



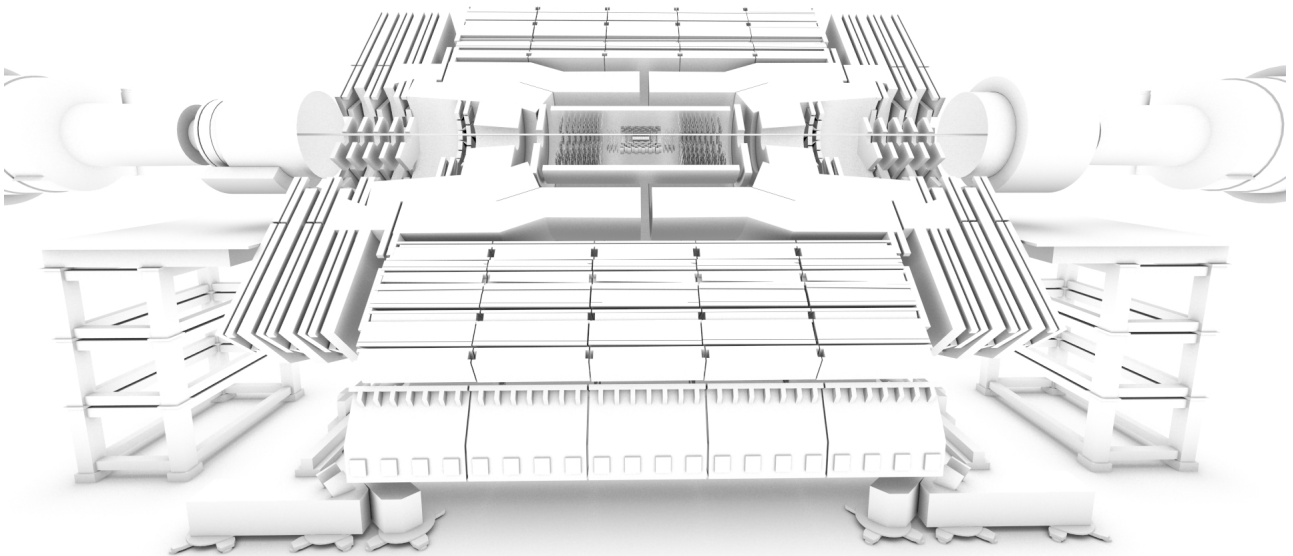
National and Kapodistrian University of Athens
Physics Department, Nuclear and Particle Physics Division

A search for compressed supersymmetry in events with soft leptons, low jet multiplicity, and missing transverse momentum with the CMS experiment at the LHC

Thesis submitted in candidacy of Doctor of Philosophy degree

Author: Antonios Agapitos, PhD candidate

Advisor: Paris Sphicas, Professor of Physics



Approval committee members:

Paris Sphicas, Prof. of Physics [Univ. of Athens & CERN]
Georgios Diamantis, Associate Prof. of Physics [Univ. of Athens]
Niki Saoulidou, Assistant Prof. of Physics [Univ. of Athens]
Theodoros Alexopoulos, Prof. of Physics [National Technical Univ. of Athens]
Alexandros Karanikas, Associate Prof. of Physics [Univ. of Athens]
Christina Kourkoumeli, Prof. of Physics [Univ. of Athens]
Efstathios Stiliaris, Associate Prof. of Physics [Univ. of Athens]

Athens, November 2015

Abstract

In the first part of this thesis a brief overview of the Standard Model physics with emphasis at its shortcomings is presented. Supersymmetry, a principle of nature which links fermions with bosons, appears as a natural extension of Standard Model which heals at once many of these shortcomings. A short description of its principle and its phenomenology is discussed.

The LHC accelerator is capable to create new particles, which Supersymmetry predicts, and CMS detectors can collect such events for further analysis. A brief description of CERN, LHC and CMS infrastructure is given.

The second part of this thesis is dedicated to a search for supersymmetry in events with soft opposite-sign leptons, large missing transverse energy and one or two hard jets. This final state is typical of supersymmetry scenarios with a small mass splitting (compressed mass spectra) between the lightest supersymmetric particle and the top squark or the chargino.

Proton-proton collision data, collected in 2012 at a centre-of-mass energy of 8 TeV and corresponding to 19.7 fb^{-1} are used in a compressed supernumerary search. The event selection strategy and the methods for estimating the Standard Model background using data are presented. In addition prediction methods are validated in real data predictions. The data observed in the search region of the analysis are found to be in agreement with the predicted background yields and as a result exclusion limits are set for different compressed signal scenarios.

Contents

1	The Standard Model of particle physics and its shortcomings	1
1.1	The Standard Model	1
1.1.1	SM particle content and their interactions	1
1.1.2	Local gauge invariance in a general Abelian field	3
1.1.3	Local gauge invariance in non-Abelian fields	4
1.1.4	Formulation of the QCD sector	6
1.1.5	Formulation of the EW sector	7
1.1.6	The Higgs field and its spontaneous symmetry breaking	8
1.1.7	Yukawa interactions	10
1.1.8	Feynman rules of the SM	12
1.1.9	Renormalisation	15
1.1.10	Tests of the SM predictions	16
1.2	The shortcomings of the SM in quantum field theory frame	19
1.2.1	Higgs mass corrections divergence and Hierarchy/Naturalness problem	19
1.2.2	The parameters of the SM	21
1.2.3	Grand unification of the three interactions in SM frame	22
1.2.4	Metastable vacuum	23
1.3	The shortcomings of the SM in Cosmology frame	24
1.3.1	Dark matter	24
1.3.2	Dark energy	28
2	Supersymmetry	29
2.1	Introduction and motivation	29
2.2	The theory	29
2.2.1	Building the SUSY concepts in a simplified toy model	29
2.2.2	Field theoretical operators	31
2.2.3	Majorana fields	32
2.2.4	Operators	34
2.3	The Minimal Supersymmetric Standard Model and its phenomenology	34
2.3.1	Particle spectrum	35
2.3.2	MSSM interactions	37
2.3.3	Spontaneous SUSY breaking	38
2.3.4	Higgs potential in the MSSM	39
2.3.5	Soft SUSY breaking	40
2.3.6	Evolution and formation of the masses in the MSSM	41
2.3.7	Summary of mass spectra	43
2.3.8	Sparticles production, decay and final state signatures at the LHC	44
3	CERN, LHC and the CMS detector	49
3.1	Introduction and motivation	49
3.2	CERN, the organization and the accelerator network	49
3.3	The Large Hadron Collider	51
3.3.1	Introduction and motivation for a TeV machine	51

3.3.2	The LHC machine aspects and performance	52
3.3.3	The LHC beams, stability, oscillations, and performance	56
3.3.4	Beams luminosity	58
3.4	The Compact Muon Solenoid detector/experiment	58
3.4.1	Introduction, motivation and the general concept	59
3.4.2	Superconducting solenoid/magnet and the iron yoke	60
3.4.3	Tracking system overview	61
3.4.4	Pixel Detector	62
3.4.5	Silicon-strip tracker	64
3.4.6	Electromagnetic Calorimeter	67
3.4.7	Hadronic Calorimeter	68
3.4.8	Muon system-chambers	72
3.4.9	Forward detectors: CASTOR and ZDC	74
3.4.10	Level one trigger	75
3.4.11	High level trigger and data acquisition	76
3.4.12	Computing infrastructure and software	77
3.5	Physics objects reconstruction and identification	77
3.5.1	Introduction and the Particle Flow reconstruction concept	77
3.5.2	Track reconstruction	78
3.5.3	Vertex reconstruction	80
3.5.4	Calorimeter clustering	80
3.5.5	Particle Flow algorithm	81
3.5.6	Muons	82
3.5.7	Electrons	83
3.5.8	Lepton isolation	84
3.5.9	Jets reconstruction/clustering	86
3.5.10	Jets energy calibration and correction	88
3.5.11	b-jets tagging	90
3.5.12	Missing transverse energy/momentum reconstruction	94
4	Analysis Strategy	98
4.1	Motivation in compressed natural SUSY search	98
4.2	Experimental frontier of compressed SUSY in terms of exclusion limit	99
4.3	The signal signatures	100
5	Event Selection	103
5.1	Data samples and triggers	103
5.2	SM background and SUSY signal simulation	103
5.3	Signal region selection cuts	103
5.3.1	Hadronic sector cuts	106
5.3.2	Leptonic sector cuts	108
5.3.3	Composite variables sector cuts	109
5.3.4	Background composition in signal region	113
6	Background Prediction	115
6.1	Dileptonic top background prediction	117
6.2	Prediction of semi-leptonic top and W+jets background	118
6.3	Prediction of the DY+jets background	122
6.3.1	Hadronic recoil correction with CR(Z)	122
6.3.2	Soft lepton correction with “SR-inv”	125
6.4	Prediction of di-boson background.	125
6.5	QCD background test	127
6.6	Prediction methods’ summary and predicted SR yields	127

7	Validation of the Background Predictions	129
7.1	Validation test for the dileptonic top prediction method	129
7.2	Validation test for all prediction methods	131
7.3	Validation test with only SR-trigger-configuration	131
8	Systematic uncertainties	136
8.1	Uncertainties applied over all backgrounds	137
8.2	Dileptonic top specific uncertainties	138
8.2.1	Spin correlation	138
8.2.2	The top-antitop p_T correction	138
8.2.3	Polarization of W-boson in dileptonic top background	140
8.3	Non-prompt background uncertainties	140
8.3.1	The W+jets over semileptonic top events abundances ratio	140
8.3.2	Source of NP leptons	141
8.3.3	Kinematics of NP leptons	141
8.4	W+jets, Z+jets, VV(γ^*)+jets, Rare background systematic uncertainties	141
8.4.1	Polarization of the W and Z bosons	141
8.4.2	Hadronic recoil systematic uncertainty	142
8.4.3	Very low invariant mass γ^* contribution	142
8.4.4	Rare background systematic uncertainty	142
8.5	Di-boson systematic uncertainty	142
8.5.1	Boson polarization	143
8.5.2	Boson transverse momentum asymmetry	143
8.6	Signal systematic uncertainties	143
8.7	Systematics summary	144
9	Results, their interpretation and conclusions	145
9.1	Results: observed data in signal region	145
9.2	Results interpretation	146
9.2.1	The SUSY signal scans and their efficiencies	146
9.2.2	Exclusion limits with the modified frequentist method	146
9.2.3	Exclusion limits	150
9.3	Summary and conclusions	152
A	Some basic kinematics	154
B	Supersymmetry, calculations and additional material	156
B.1	Superspace	156
B.2	Chiral superfield	157
B.3	Invariant action and Lagrangians	159
B.4	Feynman diagrams for sparticles hadronic production and cross sections	161
B.5	Current exclusion reach of sparticle searches	164
C	Signal region kinematics	166
C.1	Additional kinematic variables distribution in SR preselection	166
C.2	Kinematic variables distribution in SR selection	170
C.3	Explicit background cut flow	175
C.4	Tau reconstruction cases	177
D	Background prediction methods additional material	178
D.1	Kinematic variables distributions for CR($t\bar{t}2\ell$) events	178
D.2	Kinematic variables distributions, ratios and decomposition to backgrounds for CR(NP) events	180
D.3	Kinematics in CR(Z), hadronic-recoil corrected distributions	183

D.4	Kinematic variables distributions for SR-inv events	184
D.5	kinematic variables distributions for CR(VV) event	184
E	Systematic uncertainties additional material	186
E.1	Number of MC entries per region: statistics of the samples used	186
E.2	Signal uncertainties per mass point.	186
E.3	CMS performance on parameters and quantities used in analysis	186
F	The CKM and PMNS matrices, parametrization and measured values	193
G	CERN's current experiments outline	194
	Bibliography	196

Chapter 1

The Standard Model of particle physics and its shortcomings

1.1 The Standard Model

The Standard Model (SM) of particle physics contains all our current knowledge of the elementary particles and their fundamental interactions at space-scales of about 1 fm and energy-scale of about 10^2 GeV. It is the theory which describes the dynamics of electromagnetic, weak, and strong nuclear interactions in between all known elementary particles. SM is a quantum field theory(-ies) with local gauge invariance under the symmetry group $SU(3)_C \times SU(2)_L \times U(1)_Y$. In this description context spin 1/2 particles (fermions) interact each other exchanging spin 1 force-carriers particles (bosons). All particles are acquire their masses interacting with the spin 0 Higgs particle which its corresponding field fulfils timespace.

Historically, SM emerged after electromagnetic and weak forces unification, embedding theories existing before into a unibody theoretical structure based on quantum field theory (QFT) and gauge invariance principle. A brief presentation of “SM making” can be found at [104, 139] by its “fathers”, whereas an excellent extensive presentation of the SM developing and its history can be found at [125].

In this section we will very briefly present the main aspects of the SM and its prediction power. (The bibliography which is followed here is mainly [136, 40, 125], additional explicit and complete presentation of SM is beyond the scope of current document and can be found at [124, 131, 94, 95, 93]).

1.1.1 SM particle content and their interactions

The SM is comprised by 12 fermions: six leptons, three of those are electrically charged $-|e| \equiv e$, and three neutral, six charged quarks and five bosons as figure 1.1 summarizes. Each of the six quarks comes to a three “color” state and the gluon comes to an eight different color-combination states. In addition each of the fermions has an antiparticle of opposite electric charge. All these sum up to 24 fermion particles and other 24 antiparticles. These 48 fermions interact with each other with four forces: the ElectroMagnetic force (EM), weak-nuclear force, strong-nuclear force and gravity. The first three are understood and described within the SM, where the last -gravity- is not a part of it. In QFT context, where these forces are understood, each one is “mediated” by its corresponding boson(s) mediator, which sum up other 1+3+8 bosons in the SM particle context. The set closes with the newly found Higgs boson which couples with every massive SM particle; thus SM has (48+1+3+8+1=)61 particles.

A very short description of the three forces and their attributes can be as follows.

- EM force affects only the electrically-charged particles i.e. electron (e^\pm), muon (μ^\pm), tau (τ^\pm), all six quarks (u, d, c, s, t, b) and the W^\pm bosons. It is mediated by the massless and neutral photon (γ). The theory (part of SM) which describes such interactions is the Quantum ElectroDynamics (QED); a QFT, based on a local gauge invariance principle [95, 131].
- The Weak-nuclear force affects all particles caring weak-charge, i.e. all six leptons ($e, \mu, \tau, \nu_e, \nu_\mu, \nu_\tau$), six quarks and the W^\pm, Z^0 bosons. Where the last three (W^\pm, Z^0) are the mediators of the force.

Weak and EM forces are unified under the so-called ElectroWeak force (EW) described by an $SU(2)\times U(1)$ gauge symmetry. This electroweak symmetry is spontaneously broken by the vacuum, so EM and weak interactions become very different at low momentum/energy probing scales.

- Strong nuclear interaction affects only the color-charged particles i.e. the $(6\times 3\text{colors})=18$ quarks and is mediated by the eight massless, neutral, and colored-charged gluons. The theory which describes these strong interactions is the Quantum ChromoDynamics (QCD) [93, 131] which is associated with an $SU(3)$ gauge symmetry. QCD provides a description frame of understanding all hadrons and the their individual constituents (partons) interactions.

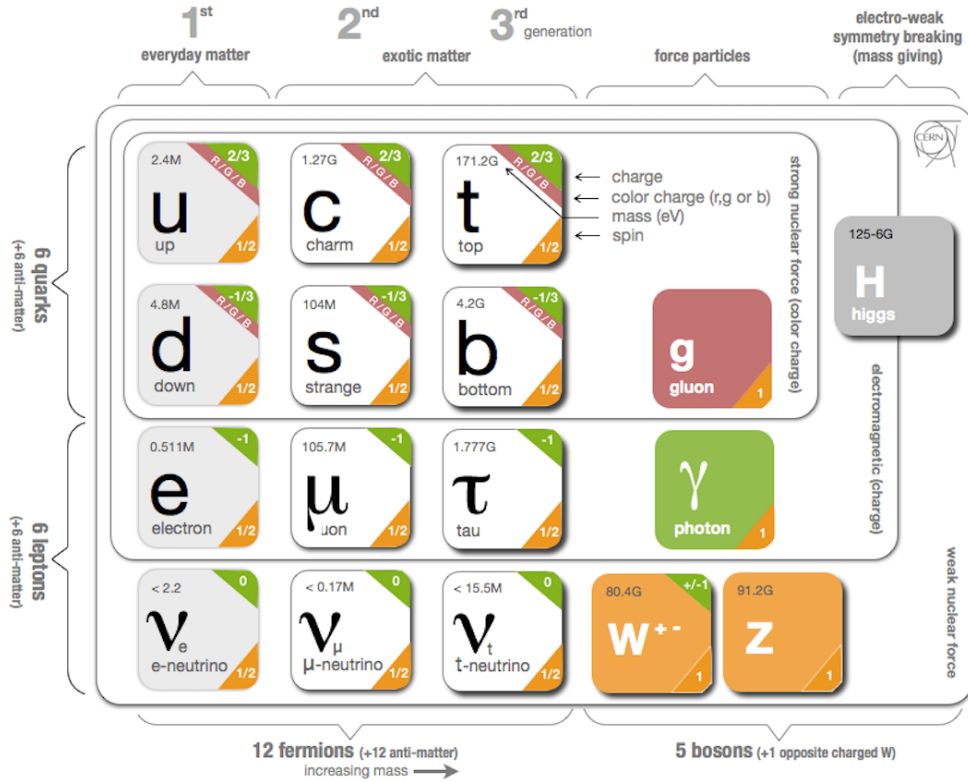


Figure 1.1: The SM particle content. In first three columns the so-called three generations of matter with distinct mass differences to each others. On top two rows the six quarks and on the bottom two rows the six leptons. Masses noted on upper-left coroners of each particle, electric charges on the top-right coroner.

Figure 1.2 summarizes the basic properties of SM fermions and bosons in tables. SM describes not only to the elementary particles physics, but also underlies larger scale phenomena, both in atomic and nuclear physics level, up to astrophysical and cosmological scale observations. Strong, weak and EM interactions are responsible for nuclear α , β and γ decays, explaining all corresponding phenomena, as well as more exotic processes observed in larger scales like nuclear fusion in stars, inverse β -decay in compact (astrophysical) object formation, cosmic rays properties and much more.

The final ingredient of the Standard Model is the Higgs boson (H), which was discovered by the ATLAS and CMS (section 3.4) experiments at the LHC (section 3.3) in 2012 [70, 74], and was predicted in 1964 by R.Brout, F.Englert and P.Higgs [85, 103]. The H boson has a mass of 125.1 GeV and spin 0^+ (scalar). It plays a crucial role in the whole SM frame since it provides the mechanism by which all (massive) particles acquire their mass. Its corresponding Higgs-field is believed to have a non-zero Vacuum Expectation Value (VEV) in contrast with the rest SM particles. It is the interaction of the -in principle- massless particles with this non-zero VEV Higgs-field that gives them their measured masses. The discovery of this (SM-like) Higgs boson was a vital importance validation for the whole SM frame.

The twelve fundamental fermions divided into quarks and leptons. The masses of the quarks are the current masses.								
Leptons					Quarks			
	Particle	Q	mass/GeV		Particle	Q	mass/GeV	
First generation	electron (e^-)	-1	0.0005		down (d)	-1/3	0.003	
	neutrino (ν_e)	0	$< 10^{-9}$		up (u)	+2/3	0.005	
Second generation	muon (μ^-)	-1	0.106		strange (s)	-1/3	0.1	
	neutrino (ν_μ)	0	$< 10^{-9}$		charm (c)	+2/3	1.3	
Third generation	tau (τ^-)	-1	1.78		bottom (b)	-1/3	4.5	
	neutrino (ν_τ)	0	$< 10^{-9}$		top (t)	+2/3	174	

The forces experienced by different particles.								
					strong	electromagnetic	weak	
Quarks	down-type	d	s	b	✓	✓	✓	
	up-type	u	c	t				
Leptons	charged	e^-	μ^-	τ^-		✓	✓	
	neutrinos	ν_e	ν_μ	ν_τ				✓

The four known forces of nature. The relative strengths are approximate indicative values for two fundamental particles at a distance of $1 \text{ fm} = 10^{-15} \text{ m}$ (roughly the radius of a proton).					
Force	Strength	Boson		Spin	Mass/GeV
Strong	1	Gluon	g	1	0
Electromagnetism	10^{-3}	Photon	γ	1	0
Weak	10^{-8}	W boson	W^\pm	1	80.4
		Z boson	Z	1	91.2
Gravity	10^{-37}	Graviton?	G	2	0

Electromagnetism	Strong interaction	Weak interaction	
All charged particles Never changes flavour $\alpha \approx 1/137$	Only quarks Never changes flavour $\alpha_S \approx 1$	All fermions Always changes flavour	All fermions Never changes flavour $\alpha_{W/Z} \approx 1/30$

Figure 1.2: Table on top: quarks and leptons with their masses and electrical charges. Table in the middle: each fermion couplings with the force carriers/mediators. Table on the bottom: the four bosons carriers of each interaction. Diagrams with fermions in coupling with the “force” bosons. (Taken from [136].)

1.1.2 Local gauge invariance in a general Abelian field

The general principle of Abelian and non-Abelian gauge invariance is what dictates the structure of the interactions between fermions and vector bosons, and also the interaction of vector bosons their self¹. The non-Abelian symmetry groups is a generalization of the Abelian gauge symmetry used in QED, thus we will first show the last one.

The Lagrangian density \mathcal{L}_0 for a free fermion field ψ , ($\psi \equiv \psi(x) \equiv \psi(x^\mu)$) with mass m , has a global U(1) symmetry, can be written as:

$$\mathcal{L}_0 = \bar{\psi}(i\gamma^\mu \partial_\mu - m)\psi \quad (1.1)$$

where $\bar{\psi} \equiv \psi^\dagger \gamma^0$ and is invariant under the global gauge (or phase) transformation:

$$\psi(x) \rightarrow \psi'(x) \equiv e^{ia}\psi(x), \quad a \in \mathbb{R} \quad (1.2)$$

We can deduce QED extending the global to local transformations, where $a \rightarrow a(x)$ is now a real function. Such change requires the insertion of a vector field A_μ , and the (minimal) modification of the derivative to the “covariant” one:

$$\partial_\mu \rightarrow D_\mu \equiv \partial_\mu + ieA_\mu \quad (1.3)$$

¹Subsection follows reference [40] by Markus Diehl and Wolfgang Hollik.

The e is at the end identified as the fermion charge. Thus the simultaneous local gauge transformations:

$$\psi(x) \rightarrow \psi'(x) = e^{ia(x)}\psi(x), \quad A_\mu(x) \rightarrow A'_\mu(x) = A_\mu(x) - \frac{1}{e}\partial_\mu a(x), \quad (1.4)$$

leaves invariant the resulting Lagrangian. Last transformations define the electromagnetic gauge group $U(1)_{EM}$. As a consequence of this transformation, the invariant Lagrangian contains now an interaction of the vector field A_μ with its corresponding (Dirac) EM-current:

$$\mathcal{L} = \bar{\psi}(i\gamma^\mu D_\mu - m)\psi = \mathcal{L}_0 - J_{EM}^\mu A_\mu, \quad \text{current} : J_{EM}^\mu \equiv e\bar{\psi}\gamma^\mu\psi, \quad (1.5)$$

The field A_μ appears as static since no kinetic term is provided yet; it can become “dynamic” by adding the kinetic term known from classical electrodynamics:

$$\mathcal{L}_A = -\frac{1}{4}F_{\mu\nu}F^{\mu\nu}, \quad F_{\mu\nu} \equiv \partial_\mu A_\nu - \partial_\nu A_\mu, \quad (1.6)$$

The field $F_{\mu\nu}$ tensor is invariant under local transformations (1.4). The A_μ vector fields then appears as the photon field obeying equations of Maxwell. Then, the full QED Lagrangian can be written as:

$$\mathcal{L}_{QED} = \bar{\psi}(i\gamma^\mu \partial_\mu - m)\psi - \frac{1}{4}F_{\mu\nu}F^{\mu\nu} - e\bar{\psi}\gamma^\mu\psi A_\mu. \quad (1.7)$$

First term allows fermion mass m existence and propagation, second, allows the existence of an electromagnetic (vector) field of massless spin 1 boson, and the third, allows interactions between the fermions and the vector field (photons) with coupling strength¹: e .

In short, the three basic steps followed in QED (\mathcal{L}_{QED}) construction as the gauge theory of the EM interaction are:

- recognize the global symmetry of the free non-interacting Lagrangian;
- change the symmetry to local by substituting ∂_μ with the covariant derivative D_μ , which contains a vector field;
- insert a kinetic term for the vector field dynamics.

1.1.3 Local gauge invariance in non-Abelian fields

With these summarized steps (subsection 1.1.2) can be extended to the non-Abelian symmetry case.² Its group’s elements are not commutative and the gauge fields turn to be self-interacting.

1. We consider the non-interacting system which is described by a multiplet $\Psi \equiv (\psi_1, \psi_2, \dots, \psi_n)^T$ of fermion fields with common masses m . An $n = 3$ example can be the triplet $(q_1, q_2, q_3)^T$ with the fields describing the three possible quark color-states. The non-interacting Lagrangian can be written as:

$$\mathcal{L}_0 = \bar{\Psi}(i\gamma^\mu \partial_\mu - m)\Psi \quad (1.8)$$

where $\bar{\Psi} \equiv (\bar{\psi}_1, \bar{\psi}_2, \dots, \bar{\psi}_n)$. The free part: \mathcal{L}_0 (in the case of common masses) is invariant under global transformations:

$$\Psi(x) \rightarrow U(a^1, \dots, a^N)\Psi(x) \quad (1.9)$$

with a unitary $n \times n$ matrix U parametrised by N real parameters a^1, \dots, a^N . This set of matrices $U(a^1, \dots, a^N)$ forms a group $U(n)$ which is the maximal symmetry. Certainly the symmetry group could be any subgroup. In this case the $n \times n$ matrices belong to a unitary representation,

¹In case of a fermion with charge eQ the preceding construction needs a small modifications to: e^{iaQ} in (1.2), $ieQA_\mu$ in (1.3) and $eQ\bar{\psi}\gamma^\mu\psi$ in (1.5).

²Subsection follows reference [40] by Markus Diehl and Wolfgang Hollik.

irreducible or reducible, of the symmetry group. The symmetry group may be chosen if not dictated by the interactions, which in general is non-Abelian. We can write:

$$U(a^1, \dots, a^N) = e^{ia^a T^a} \quad (1.10)$$

where now and on, the repeated group-indices ($a = 1, \dots, N$) imply summation. Given that U is unitary, the $n \times n$ matrices T^1, \dots, T^N are hermitian, and are called the generators of the group. They satisfy commutation relations:

$$[T^a, T^b] = if^{abc}T^c. \quad (1.11)$$

With the so-called ‘‘structure constants’’ f^{abc} being real numbers characteristic of the group. These generators are conventionally normalized as: $Tr(T^a T^b) = \delta^{ab}/2$. Typical examples for G are the groups: $SU(n)$ of the $n \times n$ unitary matrices with determinant equal to 1. In particular, the $SU(2)$ has $N = n^2 - 1 = 3$ generators given by: $T^a = \sigma^a/2$, (where σ^a are the Pauli matrices); while the $SU(3)$ has $N = 8$ generators: $T^a = \lambda^a/2$, conventionally expressed in terms of the so-called Gell-Mann matrices λ^a (representations σ^a, λ^a can be found elsewhere like [136, 93, 124, 131, 84]).

2. If we change the constants a^a of (1.10) into real functions $a^a(x)$ and simultaneously introduce a covariant derivative in the free Lagrangian (1.8) including vector fields:

$$\partial_\mu \rightarrow D_\mu \equiv \partial_\mu + igW_\mu \quad (1.12)$$

then the global symmetry can be extended to a local. We have thus introduced a new set of vector fields W_μ (one for each independent generator) together with a coupling constant g , which are similar to A_μ and e in QED. More precisely the vector field in (1.12) must be an $N \times N$ matrix, since now D_μ acts on the N -dimensional column Ψ . The set of fields $W_\mu(x)$ can explicitly be written expanded in terms of symmetry group generators as:

$$W_\mu(x) = T^a W_\mu^a(x), \quad (1.13)$$

where summation is assumed over the $a = 1, \dots, N$ (the generators’ number of the group). Thus, a set of N vector gauge fields $W_\mu^a(x)$ is introduced to the Lagrangian (1.8) and induce the following interaction terms between the N gauge fields and the n fermion fields:

$$\mathcal{L} = \mathcal{L}_0 + \mathcal{L}_{int}, \quad \mathcal{L}_{int} \equiv g\bar{\Psi}\gamma^\mu W_\mu \Psi = -J^{a,\mu}W_\mu^a, \quad (1.14)$$

which describes the interaction of currents $J^{a,\mu} \equiv -g\bar{\Psi}\gamma^\mu T^a \Psi$, with the N gauge fields W_μ^a .

The local gauge transformation under which \mathcal{L} remains invariant is constructed from the matrix $U(a^1(x), \dots, a^N(x))$ as:

$$\Psi \rightarrow \Psi' \equiv U\Psi, \quad W_\mu \rightarrow W'_\mu \equiv UW_\mu U^{-1} - \frac{i}{g}(\partial_\mu U)U^{-1} \quad (1.15)$$

Where last gauge transformation can be written for each a (in the expanded over infinitesimal $a^a(x)$ form) as:

$$W_\mu^a \rightarrow W'^a_\mu \equiv W_\mu^a + \frac{1}{g}\partial_\mu a^a + f^{abc}W_\mu^b a^c. \quad (1.16)$$

First two terms correspond to (1.4) the Abelian case, whereas the last term with f^{abc} introduces the non-Abelian nature to the group and the self-interaction of the gauge fields.

In case of a multiplet $\Phi \equiv (\phi_1, \dots, \phi_n)^T$ with scalar fields ϕ_i the Lagrangian is build in similar way, with the following substitution, and the same covariant derivative D_μ as in (1.12):

$$(\partial_\mu \Phi)^\dagger (\partial^\mu \Phi) - m^2 \Phi^\dagger \Phi \rightarrow (D_\mu \Phi)^\dagger (D^\mu \Phi) - m^2 \Phi^\dagger \Phi. \quad (1.17)$$

3. The W fields kinetic term occurs from a generalisation of the EM strength tensor $F_{\mu\nu}$ of (1.6):

$$F_{\mu\nu} = T^a F_{\mu\nu}^a = \partial_\mu W_\nu - \partial_\nu W_\mu - ig[W_\mu, W_\nu], \quad W_\nu = T^a W_\nu^a \quad (1.18)$$

with the N components:

$$F_{\mu\nu}^a = \partial_\mu W_\nu^a - \partial_\nu W_\mu^a + gf^{abc}W_\mu^b W_\nu^c. \quad (1.19)$$

The field strength $F_{\mu\nu}$ under the transformation in (1.15) changes as: $F_{\mu\nu} \rightarrow F'_{\mu\nu} \equiv UF_{\mu\nu}U^{-1}$. Consequently, the trace $Tr(F_{\mu\nu}F^{\mu\nu})$ is gauge invariant and provides the so-called Yang-Mills Lagrangian (kinetic and self-interacting field terms):

$$\mathcal{L}_W \equiv -\frac{1}{2}Tr(F_{\mu\nu}F^{\mu\nu}) = -\frac{1}{4}F_{\mu\nu}^a F^{a,\mu\nu} \quad (1.20)$$

Where the ast consists the non-Abelian version of the photon field kinetic term (1.6). The part of \mathcal{L}_W that is quadratic in the W fields describes the free propagation of the gauge bosons, whereas the cubic and quartic terms introduces self-interactions between the vector bosons in three- and four-bosons vertexes. In its explicit form is:

$$\begin{aligned} \mathcal{L}_W = & -\frac{1}{4}(\partial_\mu W_\nu^a - \partial_\nu W_\mu^a)(\partial^\mu W^{a,\nu} - \partial^\nu W^{a,\mu}) \\ & -\frac{g}{2}f^{abc}(\partial_\mu W_\nu^a - \partial_\nu W_\mu^a)W^{b,\mu}W^{c,\nu} \\ & -\frac{g^2}{4}f^{abc}f^{ade}W_\mu^b W_\nu^c W^{d,\mu}W^{e,\nu}. \end{aligned} \quad (1.21)$$

Both Lagrangians in (1.6) and (1.21) describe massless vector bosons. Mass terms: $\frac{1}{2}m^2 A_\mu A^\mu$ and $\frac{1}{2}m^2 W_\mu^a W^{a,\mu}$ for the gauge fields are not invariant under a gauge transformation and break the gauge symmetry.

1.1.4 Formulation of the QCD sector

The gauge theory of the strong interaction is Quantum ChromoDynamics (QCD) where takes place between quarks and gluons¹. It can be constructed by the principles of the previous section for the particular case of the $SU(3)_c$ symmetry group, (subscript c indicates the ‘‘colour’’, a quantum number associated with the symmetry). The quarks are the elementary fermions of the theory which appear in three different colour states (named: red, green, blue) described by triplets of fermion fields $q \equiv (q_1, q_2, q_3)^T$ for each one of the quark flavours $q : u, d, s, c, b, t$. Using the (1.12) with (1.13) the covariant derivative acting on the quark triplets can be written as:

$$D_\mu = \partial_\mu - ig_s \frac{\lambda^a}{2} G_\mu^a. \quad (1.22)$$

The g_s stands for strong coupling constant (in analogy with the fine-structure constant a or a_{EM} in QED), also expressed as $a_s \equiv g_s^2/(4\pi)$. The gauge fields G_μ^a (where for three color-states/generators counts: $a = 1, \dots, 8 = 3^2 - 1$) describe the gluon in its eight different colour-state combinations. The gluon field strengths tensors can then be introduced in accordance with general expression (1.19):

$$G_{\mu\nu}^a \equiv \partial_\mu G_\nu^a - \partial_\nu G_\mu^a + g_s f^{abc} G_\mu^b G_\nu^c. \quad (1.23)$$

According to the rules of the preceding section the Lagrangian of QCD can be written as:

$$\mathcal{L}_{QCD} \equiv \sum_q \bar{q}(i\gamma D_\mu - m_q)q + \mathcal{L}_G = \sum_q \bar{q}(i\gamma\partial_\mu - m_q)q - \sum_q J_q^{a,\mu} G_\mu^a - \frac{1}{4}G_{\mu\nu}^a G^{a,\mu\nu} \quad (1.24)$$

with summation index q running over the quark flavours. The last term is the Yang-Mills Lagrangian in accordance with (1.20) with triple and quartic gluon self-interactions (its decomposed version is in

¹Subsection follows reference [40] by Markus Diehl and Wolfgang Hollik.

(1.21)). Second term describes the interaction of the quarks (currents): $J_q^{a,\mu} \equiv g_s \bar{q} \gamma^\mu (\lambda^a/2) q$, with the eight gluon fields G_μ^a . The quark masses m_q appears in QCD as free parameters; their origin is of electroweak nature and will be discussed in Higgs sector. Even though QCD Lagrangian (1.24) appears relatively simple, the calculations in QCD dynamics is non-trivial mainly because of the non small value of its coupling a_S which in most of the cases does not allows perturbative expansions. A wide range of QCD phenomenology can be found in detail at [84, 93, 124, 125, 131].

1.1.5 Formulation of the EW sector

Fermions in SM clustered into leptons and quarks and additionally into three generations¹ (figures 1.1, 1.2). The electroweak (EW) symmetry group is the $SU(2) \times U(1)$. Where the $SU(2)$ (special unitary group with 2×2 matrices) stands as the gauge group symmetry of the double-type charges: the “chiralities” of the weak interaction, whereas the $U(1)$ for the single-type electric charge of the EM interaction. In same context strong interaction with $SU(3)$ group has triple-type charges: the color of its fermions. The EW symmetry transformations act differently on left-handed and right-handed fermion fields, which are projected out from a usual Dirac field ψ by:

$$\frac{1}{2}(1 - (+)\gamma_5)\psi = \psi_{L(R)}. \quad (1.25)$$

The $SU(2)$ group is named the weak isospin group, with associated quantum numbers the isospin I and its third projection I_3 . Left-handed fields have $I=1/2$ and form doublets, whereas the right-handed fields have $I=0$ and are singlets (treating the neutrinos as massless without right-handed states):

$$I = 1/2 : \quad \begin{pmatrix} \nu_e \\ e \end{pmatrix}_L, \begin{pmatrix} u \\ d \end{pmatrix}_L, \quad \begin{pmatrix} \nu_\mu \\ \mu \end{pmatrix}_L, \begin{pmatrix} c \\ s \end{pmatrix}_L, \quad \begin{pmatrix} \nu_\tau \\ \tau \end{pmatrix}_L, \begin{pmatrix} t \\ b \end{pmatrix}_L, \quad (1.26)$$

$$I = 0 : \quad e_R, u_R, d_R, \quad \mu_R, c_R, s_R, \quad \tau_R, t_R, b_R \quad (1.27)$$

There are no right-handed neutrinos in the SM, even we know today that this is not true, neutrinos are treated as massless and thus only left-handed. Their masses are so small ($m_\nu \lesssim 1$ eV, figure 1.2), which such consideration is valid in most cases. The $I = 1/2$ doublets transforms with a unitary matrix $U = \exp(ia^a \sigma^a/2)$, where $a = 1, 2, 3$. For each of these doublets or singlets, the $U(1)$ corresponds to an invariance of a multiplication by a phase factor $e^{iY/2}$, where Y is the so-called weak hypercharge. This Y is correlated with the EM-charge Q and “third isospin projection” I_3 of a particle by the Gell-Mann-Nishijima relation: $Q = I_3 + Y/2$.

The symmetry group underlying the (unified) EW interaction is named: $SU(2)_L \times U(1)_Y$. The EM gauge subgroup $U(1)_{EM}$ of the last, is obtained by combining a hypercharge transformation with a particular isospin transformation. For the isospin doublets (1.26) the corresponding transformation matrix is:

$$e^{ia\sigma_3/2} e^{iaY/2} = \begin{pmatrix} e^{ia/2} & 0 \\ 0 & e^{-ia/2} \end{pmatrix} e^{iaY/2} \quad (1.28)$$

which gives a phase factor e^{iaQ} for each component of the doublet field and for the isospin singlets simply $e^{iaQ} = e^{iaY/2}$. The I, I_3, Y, Q eigenvalues are shown bellow:

Given that photon γ is massless and W^\pm, Z are massive, the full symmetry described by $SU(2)_L \times U(1)_Y$ must be broken down to the EM gauge symmetry. This necessary symmetry breaking in SM is introduced by the Higgs mechanism and with a Higgs field which is a doublet under $SU(2)_L$.

Thus the full EW Lagrangian is formed by the following terms:

$$\mathcal{L}_{EW} \equiv \mathcal{L}_{WB} + \mathcal{L}_F + \mathcal{L}_H + \mathcal{L}_Y. \quad (1.29)$$

Where \mathcal{L}_{WB} : are the pure unified gauge fields, \mathcal{L}_F : fermions propagation and interaction (with W and B fields), \mathcal{L}_H : Higgs sector and \mathcal{L}_Y : Yukawa interaction sector.

¹Subsection follows reference [40] by Markus Diehl and Wolfgang Hollik.

	ν_{eL}	e_L	e_R	u_L	d_L	u_R	d_R
	$\nu_{\mu L}$	μ_L	μ_R	c_L	s_L	c_R	s_R
	$\nu_{\tau L}$	τ_L	τ_R	t_L	b_L	t_R	b_R
I_3	$+\frac{1}{2}$	$-\frac{1}{2}$	0	$+\frac{1}{2}$	$-\frac{1}{2}$	0	0
Y	-1	-1	-2	$+\frac{1}{3}$	$+\frac{1}{3}$	$+\frac{4}{3}$	$-\frac{2}{3}$
Q	0	-1	-1	$+\frac{2}{3}$	$-\frac{1}{3}$	$+\frac{2}{3}$	$-\frac{1}{3}$

Figure 1.3: Isospin with its third projection eigenstates, together with charge and hypercharge values for SM fermions, all connected by Gell-Mann-Nishijima relation: $Q = I_3 + Y/2$.

The SM gauge group full symmetry is: $SU(3)_c \times SU(2)_L \times U(1)_Y$, and its complete Lagrangian is obtained as the sum of the QCD (1.24) and EW Lagrangians¹ (1.29), where each quark fields in (1.26) and (1.27) is a colour triplet: $q = (q_1, q_2, q_3)^T$ and the colour indices are summed over.

The gauge field Lagrangian \mathcal{L}_{WB} can be derived by the three-steps method (shown in section ??) to each factor of the $SU(2)_L \times U(1)_Y$ group. Then three vector fields W_μ^a appears in association with the three $SU(2)_L$ generators and one vector field B_μ for the hypercharge $U(1)_Y$ group. The four field strength tensors can then be defined as:

$$B_{\mu\nu} \equiv \partial_\mu B_\nu - \partial_\nu B_\mu, \quad W_{\mu\nu}^a \equiv \partial_\mu W_\nu^a - \partial_\nu W_\mu^a + g_2 \epsilon^{abc} W_\mu^b W_\nu^c, \quad a = 1, 2, 3. \quad (1.30)$$

There are two independent gauge coupling constants: g_2 for the non-Abelian $SU(2)_L$ sector, and g_1 for the Abelian $U(1)_Y$ sector (and will be accosted with the B_μ field in next). Then the EW gauge field Lagrangian can be constructed as follows and is invariant under the transformations (1.4) and (1.15):

$$\mathcal{L}_{WB} \equiv -\frac{1}{4} W_{\mu\nu}^a W^{\mu\nu,a} - \frac{1}{4} B_{\mu\nu} B^{\mu\nu}. \quad (1.31)$$

The kinetic part of the fermion EW Lagrangian, together with the interaction terms between fermions and bosons, can be constructed by the covariant derivatives (according to (1.12)) for isospin doublets and singlets:

$$\mathcal{L}_F \equiv \sum_{j=1}^6 \bar{\psi}_L^j i\gamma^\mu \left(\partial_\mu - ig_2 \frac{\sigma^a}{2} W_\mu^a + ig_1 \frac{Y}{2} B_\mu \right) \psi_L^j + \sum_{j=1}^9 \bar{\psi}_R^j i\gamma^\mu \left(\partial_\mu + ig_1 \frac{Y}{2} B_\mu \right) \psi_R^j. \quad (1.32)$$

Where ψ_L^j and ψ_R^j represents left-handed doublets and right-handed singlets of (1.26), and (1.27) respectively. There are still no fermion mass terms at this stage because: $\bar{\psi}\psi = \bar{\psi}_L\psi_R + \bar{\psi}_R\psi_L$ explicitly mixes left and right-handed fields breaking the gauge invariance. Fermion masses are dynamically generated by gauge invariant Yukawa interactions with the Higgs field. (A detailed approach can be found in [124, 125]). The terms \mathcal{L}_H , \mathcal{L}_Y are discussed individually in the next subsections.

1.1.6 The Higgs field and its spontaneous symmetry breaking

The Higgs sector² of SM is constructed by an isospin doublet of complexvalued scalar fields: $\Phi(x) \equiv (\phi^+(x), \phi^0(x))^T$, with hypercharge $Y=1$ and covariant derivative:

$$D_\mu = \partial_\mu - ig_2 \frac{\sigma^a}{2} W_\mu^a + ig_1 \frac{1}{2} B_\mu. \quad (1.33)$$

According to $Q = I_3 + Y/2$ relation, ϕ^+ has EM charge +1, whereas ϕ^0 is neutral. Following the recipe (1.17), the Higgs Lagrangian is written as:

$$\mathcal{L}_H \equiv (D_\mu \Phi)^\dagger (D_\mu \Phi) - V(\Phi) \quad (1.34)$$

¹Subtracting once the free quark term $\sum_q \bar{q}(i\gamma^\mu \partial_\mu - m_q)q$ which is included in both \mathcal{L}_{QCD} and \mathcal{L}_{EW} and should not be double counted.

²Subsection follows reference [40] by Markus Diehl and Wolfgang Hollik.

with a (gauge invariant) self-interaction given by the following potential (where last constant term can be ignored):

$$V(\Phi) \equiv -\mu^2\Phi^\dagger\Phi + \frac{\lambda}{4}(\Phi^\dagger\Phi)^2 = \left(\Phi^\dagger\Phi - \frac{2\mu^2}{\lambda}\right)^2 - \frac{\mu^4}{\lambda}. \quad (1.35)$$

At the ground state of SM (i.e. in vacuum), the potential energy of the field should be at its minimum value. The Higgs potential $V(\Phi)$ has the form of a “mexican hat” (as is shown in figure 1.4) and for $\mu^2, \lambda > 0$ has its minimum value for any field fulfils the condition: $\Phi^\dagger\Phi = 2\mu^2/\lambda$. Among the possible configurations, the vacuum selects the following:

$$\langle 0|\Phi|0\rangle = \begin{pmatrix} \langle 0|\phi^+|0\rangle \\ \langle 0|\phi^0|0\rangle \end{pmatrix} = \frac{1}{\sqrt{2}} \begin{pmatrix} 0 \\ v \end{pmatrix}, \quad v \equiv 2\mu/\sqrt{\lambda} \quad (1.36)$$

where on the left is the vacuum expectation value (VEV) of the two-component Higgs fields Φ .

The VEV (1.36) is not invariant under the transformation $\exp(ia^a\sigma^a/2)$ and $\exp(iaY/2)$ thus the $SU(2)_L \times U(1)_Y$ symmetry is broken by the vacuum. (However $\langle 0|\Phi|0\rangle$ is invariant under an EM gauge transformation $U(1)_{EM}$). A “spontaneous symmetry breaking” has taken place and the initial rotationally symmetric potential $V(\Phi)$ has finally taken a fixed value as shown in figure 1.4 right.

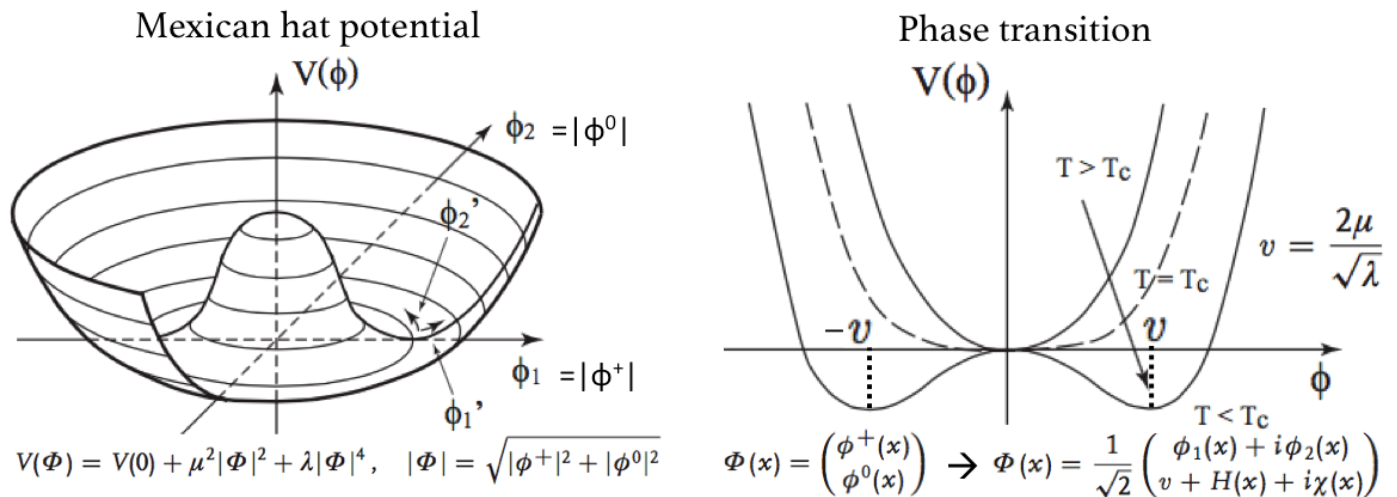


Figure 1.4: The Higgs potential illustrated as a function of its two components. Taken from [125]. According to the energy scale (which is also associated to a temperature) a theory can be in a fully symmetric phase or in a phase with broken symmetry. The transition is determined by a critical temperature [111].

The SM Vacuum is supposed to contains no particles whereas its excitations correspond to the particles of the field (which deviates from its VEV). This can be shown righting first the Higgs doublet with explicit real-valued fields (H, χ, ϕ_1 and ϕ_2) with zero VEVs:

$$\Phi = \frac{1}{\sqrt{2}} \begin{pmatrix} \phi_1(x) + i\phi_2(x) \\ v + H(x) + i\chi(x) \end{pmatrix}, \quad (1.37)$$

then the Higgs potential $V(\Phi)$ can be reformed as:

$$V(H, \chi, \phi_1, \phi_2) = \mu^2 H^2 + \frac{\mu^2}{v} H(H^2 + \chi^2 + \phi_1^2 + \phi_2^2) + \frac{\mu^2}{4v^2} (H^2 + \chi^2 + \phi_1^2 + \phi_2^2)^2. \quad (1.38)$$

Where the H describes a neutral scalar particle: the Higgs boson, with a mass $M_H = \mu\sqrt{2}$ ($=125$ GeV) and (by construction) the rest three fields are massless corresponding to the angular direction of the potential. These fields corresponds to Goldstone bosons since a continuous symmetry is broken by the vacuum. In addition (for a local symmetry), these fields in \mathcal{L}_H (1.38) can be eliminated by a proper gauge, so they do not describe physical degrees of freedom.

In such modification (using the so-called unitary gauge) the doublet field in (1.37) can be simply re-written with only the physical Higgs field as:

$$\Phi = \frac{1}{\sqrt{2}} \begin{pmatrix} 0 \\ v + H(x) \end{pmatrix}. \quad (1.39)$$

Accordingly, the Higgs potential (1.38) in same gauge is re-written as:

$$V(H) = \frac{M_H^2}{2} H^2 + \frac{M_H^2}{2v} H^3 + \frac{M_H^2}{8v^2} H^4. \quad (1.40)$$

The kinetic term of the Lagrangian (1.34) together with the Φ and D_μ expressions can reveal the couplings of Higgs to gauge fields and the mass terms for the vector bosons. An additional needed step is the transformation of the four fields W_ν^a, B_μ (using as constant the “weak mixing angle” θ_W) to the physical fields in accordance with the observed EW bosons: W^\pm, Z^0, γ . Thus the physical content of the whole \mathcal{L}_H becomes transparent after the fields transformation:

$$\begin{pmatrix} W_\mu^- \\ W_\mu^+ \end{pmatrix} = \frac{1}{\sqrt{2}} \begin{pmatrix} W_\mu^1 - iW_\mu^2 \\ W_\mu^1 + iW_\mu^2 \end{pmatrix}, \quad \begin{pmatrix} Z_\mu \\ A_\mu \end{pmatrix} = \begin{pmatrix} \cos \theta_W & \sin \theta_W \\ -\sin \theta_W & \cos \theta_W \end{pmatrix} \begin{pmatrix} W_\mu^3 \\ B_\mu \end{pmatrix}. \quad (1.41)$$

With all these in \mathcal{L}_H (1.34) we can correlate boson masses with couplings (or θ_W) as:

$$M_W = vg_2/2, \quad M_Z = v\sqrt{g_1^2 + g_2^2}/2, \quad \cos \theta_W = g_2/\sqrt{g_1^2 + g_2^2} = M_W/M_Z. \quad (1.42)$$

The field A_μ remains massless and thus can be identified as the gauge boson of the EM $U(1)_{EM}$ symmetry, i.e. the photon γ . This way the Higgs boson gives masses to the EW bosons (W^\pm, Z) by breaking the $SU(2)_L \times U(1)_Y$ symmetry rising a non zero VEV.

1.1.7 Yukawa interactions

Previous section shown the masses generation for the EW bosons, however also the fermions acquire their masses by the spontaneously broken $SU(2)_L \times U(1)_Y$ gauge symmetry¹. This is applied by introducing a gauge invariant Yukawa interactions between the Higgs and the fermion fields, the last term in (1.29). Each single fermion generation (column in figure 1.1), need the insertion of a Yukawa term in Lagrangian which can be written as:

$$\mathcal{L}_{Y,gen} \equiv -Y_\ell \bar{L}_L \Phi \ell_R - Y_d \bar{Q}_L \Phi d_R - Y_u \bar{Q}_L \Phi^c u_R + [\text{hermitian conjugate}] \quad (1.43)$$

where $L_L = (\nu_L, \ell_L)^T$ and $Q_L = (u_L, d_L)^T$ stand for the left-handed lepton and quark doublets of the first generation. The Higgs doublet, charge conjugate of $\Phi \equiv (\phi^+, \phi^0)^T$ is the: $\Phi^c \equiv i\sigma^2 \Phi^* = (\phi^{0*}, -\phi^-)^T$, where $\phi^- \equiv (\phi^+)^\dagger$.

One can substitute the last in (1.43) to reveal terms per particle (per generation). The VEV of ϕ^0 generates fermion mass terms, where the fermion masses are proportional with the Yukawa couplings given as: $m_f = Y_f v/\sqrt{2}$ (with $f = \ell, d, u$). The Yukawa Lagrangian in the unitary gauge (1.39), (and only for first generation) becomes much simpler with explicit meaningful terms:

$$\mathcal{L}_{Y,gen} = - \sum_{f=\ell,d,u} \left(m_f \bar{\psi}_f \psi_f + \frac{m_f}{v} H \bar{\psi}_f \psi_f \right). \quad (1.44)$$

Thus, Yukawa interactions between the massive fermions and the Higgs field are introduced.

In the complete version of SM, with three generations, Yukawa terms mix fermions of different generations so a complicate structure need to be introduced. The Yukawa interaction Lagrangian can be written in its most general form as:

$$\mathcal{L}_Y \equiv - \sum_{i,j} (Y_\ell^{ij} \bar{L}_L^j \Phi \ell_R^i + Y_d^{ij} \bar{Q}_L^i \Phi d_R^j + Y_u^{ij} \bar{Q}_L^i \Phi^c u_R^j) + [\text{hermitian conjugate}], \quad (1.45)$$

¹Subsection follows reference [40] by Markus Diehl and Wolfgang Hollik.

where indices i, j runs over the three generations. In (1.45) u^i and d^i denotes the u-type quarks ($u^1 = u, u^2 = c, u^3 = t$) and the d-type quarks ($d^1 = d, d^2 = s, d^3 = b$) respectively. The Yukawa couplings Y_f^{ij} turns now to 3×3 matrices in generation space with complex-valued elements. The full set of fermion mass terms are obtained from (1.45) by replacing Φ with its VEV from (1.36), thus all fermion mass terms arises:

$$\mathcal{L}_Y = -\frac{v}{\sqrt{2}} \sum_{i,j} (Y_\ell^{ij} \bar{\ell}_L^i \ell_R^j + Y_d^{ij} \bar{d}_L^i d_R^j + Y_u^{ij} \bar{u}_L^i u_R^j) + [\text{hermitian conjugate}], \quad (1.46)$$

The terms with quark can be diagonalised with the introduction of four unitary matrices $V_{L,u}, V_{R,u}, V_{L,d}, V_{R,d}$, which transform from flavour eigenstates to mass eigenstates as:

$$\tilde{q}_L^i = \sum_j V_{L,q}^{ij} q_L^j, \quad \tilde{q}_R^i = \sum_j V_{R,q}^{ij} q_R^j \quad (q = u, d). \quad (1.47)$$

The finally arose quark-mass matrices: $M_u = \text{diag}(m_u, m_c, m_t)$, $M_d = \text{diag}(m_d, m_s, m_b)$ are given by:

$$M_q = \frac{v}{\sqrt{2}} V_{L,q} Y_q (V_{R,q})^\dagger \quad (q = u, d). \quad (1.48)$$

Where the quark mass eigenstates on the left are related with the Yukawa interactions and the flavor transformation matrices. It consists the generalization of the $m_f = Y_f v / \sqrt{2}$ in a quark-mixing version.

Furthermore, introduction of the mass eigenstates (1.47) into the fermion Lagrangian \mathcal{L}_F (1.32) preserves the form of both the kinetic and interaction terms with the neutral gauge bosons, as both of these have the structure: $\sum_i \bar{q}_L^i \dots q_L^i$ or $\sum_i \bar{q}_R^i \dots q_R^i$. Hence are invariant under the unitary transformations of (1.47). The same holds for the QCD Lagrangian (1.24). The only modification occurs in the flavour changing quark interaction with the W^\pm bosons in \mathcal{L}_F , where the insertion of the mass eigenstates into $\sum_i \bar{u}_L^i \dots d_L^i$ introduces the unitary quark mixing matrix, the so-called Cabibbo-Kobayashi-Maskawa (CKM) matrix: $V_{CKM} = V_{L,u} (V_{L,d})^\dagger$. It is a unitary 3×3 matrix, with four independent physical parameters: three rotation angles and one complex phase. Figure F.1 in appendix F shown such parametrisation and the actual V_{CKM} values.

The analogues matrix for lepton mixing is the unitary matrix in the massless neutrinos consideration. Generation mixing (non-unitary matrix) in the lepton sector introduced once neutrinos masses introduced. Then the so-called Pontecorvo-Maki-Nakagawa-Sakata (PMNS) matrix V_{PMNS} mixes neutrinos flavor eigenstates to the mass eigenstates which couples the physical vector bosons (figure F.1 in appendix F shows the V_{PMNS} matrix standard parametrization as well).

The interaction term in the fermion Lagrangian (1.32), in terms of fermion mass eigenstates and physical vector boson fields, can be written as:

$$\begin{aligned} \mathcal{L}_{F,int} &= [J_{EM}^\mu] A_\mu - [J_{NC}^\mu] Z_\mu - [J_{CC}^\mu] W_\mu^+ - [J_{CC}^\mu]^\dagger W_\mu^-, \quad \text{with :} \quad (1.49) \\ \text{Electromagnetic current :} \quad & J_{EM}^\mu = g_1 \cos \theta_W \sum_f Q_f \bar{\psi}_f \gamma^\mu \psi_f, \\ \text{Neutral Weak current :} \quad & J_{NC}^\mu = -\frac{g_2}{2 \cos \theta_W} \sum_f \bar{\psi}_f \left(g_V^f \gamma^\mu - g_A^f \gamma^\mu \gamma_5 \right) \psi_f, \\ \text{Charged Weak current :} \quad & J_{CC}^\mu = -\frac{g_2}{\sqrt{2}} \left(\sum_i \bar{\nu}^i \left[\gamma^\mu \frac{1-\gamma_5}{2} \right] \ell^i + \sum_{ij} \bar{u}^i \left[\gamma^\mu \frac{1-\gamma_5}{2} \right] V_{CKM}^{ij} d^j \right). \end{aligned}$$

Where the sum over f runs over all fermions, and i, j runs over the three generations. The coupling constants of the neutral current are determined by the electric charge (Q_f) and the isospin (I_3^f), of the left-handed fermion (f_L): $g_V^f = I_3^f - 2Q_f \sin^2 \theta_W$ and $g_A^f = I_3^f$. Only the charged currents change the lepton or the quark flavour. Comparing (1.49) with previous equations one can identify that: $e = g_1 \cos \theta_W = g_2 \sin \theta_W = [g_1 g_2 / \sqrt{g_1^2 + g_2^2}]$.

The original set of parameters $g_2, g_1, \lambda, \mu^2, Y_f^{ij}$, used in the EW unification context, can be replaced with the equivalent set of more physical parameters: $e, M_W, M_Z, M_H, m_f, V_{CKM}^{ij}$. These are all experimentally known (and some of them are shown in figures 1.2, F.1).

1.1.8 Feynman rules of the SM

All interaction in the SM frame are understood (and their interaction properties are calculated) with the so-called Feynman diagrams, in which one can express each interaction as a process where a particle, or more princely, its corresponding field:

- propagates through vacuum (kinetic terms),
- interacts with Higgs field acquiring mass (Yukawa interactions),
- interacts (attracted) with gluon-fields if it has color (QCD-interactions),
- interacts with (physical) EW boson fields γ , W^\pm , Z^0 for electroweakly charged particles.

A rough taste was given in figure 1.2 bottom with the four basic Feynman diagram vertexes. Each interaction is illustrated in terms of such “vertexes” and “propagators” (particle lines which connect vertexes).

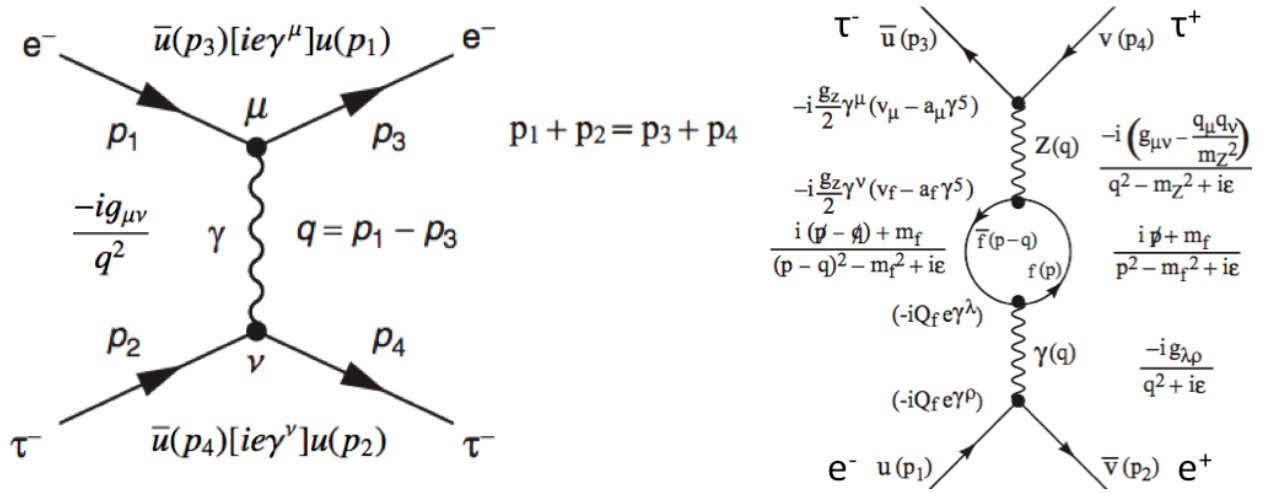


Figure 1.5: Left: a (simple) pure QED example of a Feynman diagram for the scattering: $e^- \tau^- \rightarrow e^- \tau^-$ and the associated constituents of the matrix element (equation (1.50)) constructed from the QED Feynman rules. The matrix element is comprised of a term for the electron current, a term for the tau-lepton current and a term for the photon propagator (taken from [136]). On the right: a (non-trivial) example of a Feynman diagram of second order ($O(a, a_W)$) for the annihilation $e^- e^+ \rightarrow \tau^+ \tau^-$ (the “t-Mandelstam-channel” of the left one). Loop with a fermion and propagators of photon and Z-boson are involved a virtual states. (Taken from [125]).

As a benchmark example¹, we present a QED process such $e^- \tau^- \rightarrow e^- \tau^-$ in the unpolarized scattering, as shown in figure 1.5 left. The “Feynman rules” are clearly introduced and illustrated by such example. Four-vector indices μ and ν label the two interaction vertices and u denotes the usual Dirac-spinors of each particle. Application of the Feynman rules for the “e-current”, requires the usage of the adjoint spinor for the final-state electron \bar{u} , a factor $ie\gamma^\mu$ for the interaction vertex (labelled by μ), and a spinor u for the initial-state electron. The adjoint spinor is always written first and thus the contribution to the matrix element from the electron current is: $\bar{u}(p_3)[ie\gamma^\mu]u(p_1)$. In same way the “ τ -current” gives: $\bar{u}(p_4)[ie\gamma^\nu]u(p_2)$. Finally, the photon propagator contributes with a factor: $-ig_{\mu\nu}/q^2$. The combination of these three elements, their tensor $\mu\nu$ -contraction more precisely, gives rise to an “invariant amplitude” M given from the formula:

$$-iM = (\bar{u}(p_3)[ie\gamma^\mu]u(p_1)) \frac{-ig_{\mu\nu}}{q^2} (\bar{u}(p_4)[ie\gamma^\nu]u(p_2)), \quad u(p_i) \equiv u_i \Rightarrow \quad -iM = i \frac{e^2}{q^2} (\bar{u}_3 \gamma^\mu u_1) (\bar{u}_4 \gamma_\mu u_2). \quad (1.50)$$

There are three basic ingredients[136] in this “matrix element” (or invariant amplitude) M formula:

¹The example is taken from reference [136] §5.4 by Mark Thomson.

1. the Dirac spinors for the external fermions (the initial- and final-state particles);
2. a propagator term for the virtual photon;
3. and a vertex factor at each interaction vertex.

For each of these elements, a corresponding Feynman rule is defined, and dictates the construction of the matrix element (or the $-iM$). In their simplest form, the QED Feynman rules are as listed in figure 1.6. In QED, the fundamental interaction at tree-level, i.e. leading term without loops, is between a single photon and two spin-half charged fermions (e, τ leptons in our case). At any complexity level, there is no QED vertex connecting else than three particles, else than two fermions or else than one photon. All valid QED processes, are build and described by Feynman diagrams formed by this single vertex.









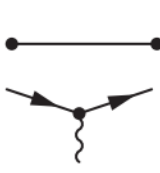
initial-state particle:	$u(p)$	
final-state particle:	$\bar{u}(p)$	
initial-state antiparticle:	$\bar{v}(p)$	
final-state antiparticle:	$v(p)$	
initial-state photon:	$\varepsilon_\mu(p)$	
final-state photon:	$\varepsilon_\mu^*(p)$	
photon propagator:	$-\frac{ig_{\mu\nu}}{q^2}$	
fermion propagator:	$-\frac{i(\gamma^\mu q_\mu + m)}{q^2 - m^2}$	
QED vertex:	$-iQe\gamma^\mu$	

Figure 1.6: The QED Feynman rules. There is only one allowed vertex and two propagators in QED. (Taken from [136]).

The computations in QED, a differential cross section for example, require first to build an expression for the $|M|^2$, and then a summation over all spin possible states. So, one must form the complex conjugate of M . A bi-spinors product can be complex-conjugated as: $(\bar{u}_3\gamma^\mu u_1)^* = u_1^\dagger(\gamma^\mu)^\dagger(\gamma^0)^\dagger u_3 = u_1^\dagger\gamma^0\gamma^\mu u_3 = \bar{u}_1\gamma^\mu u_3$. Thus the $|M|^2$ can be written:

$$|M|^2 = \frac{e^4}{q^4} [(\bar{u}_3\gamma^\mu u_1)(\bar{u}_4\gamma_\mu u_2)][(\bar{u}_1\gamma^\nu u_3)(\bar{u}_2\gamma_\nu u_4)], \quad (1.51)$$

where $u(p_i) \equiv u_i$ has been assumed. Finally, the sum over the last equation (1.51) quantity over all spin-states (initial and final); which is the actual quantity appears in proportion to both differential and total cross section is given by:

$$\langle |M|^2 \rangle \equiv \frac{1}{4} \sum_{spins} |M|^2 = \frac{e^4}{4q^4} Tr[(\not{p}_3 - m_e)\gamma^\mu(\not{p}_1 + m_e)\gamma^\nu] Tr[(\not{p}_4 - m_\tau)\gamma_\mu(\not{p}_2 + m_\tau)\gamma_\nu]. \quad (1.52)$$

Where in last, the additional definitions: $\not{p} + m \equiv \sum_s u^s(p)\bar{u}^s(p)$, $\not{p} - m \equiv \sum_s v^s(p)\bar{v}^s(p)$, have been imposed (as usual in bibliography [136, 93, 124, 131, 84]).

From the Lagrangian expressions which were discussed previously (equation (1.49)), one can derive the Feynman rules of the whole SM, which consist to the extension of the QED-rules to the EW-fields dynamics, the addition of the QCD rules, and in the addition of all Higgs interactions rules. Quadratic terms of the fields (in Lagrangians) give rise to propagators, whereas cubic and quartic terms specifying the three- and four-particle vertices in Feynman graphs. These rules allow us to formulate in a “semi-automatic” way, and to write down the invariant amplitudes ($-iM$) which contributes to each SM calculation. All SM Feynman rules are summarized in figure 1.7.

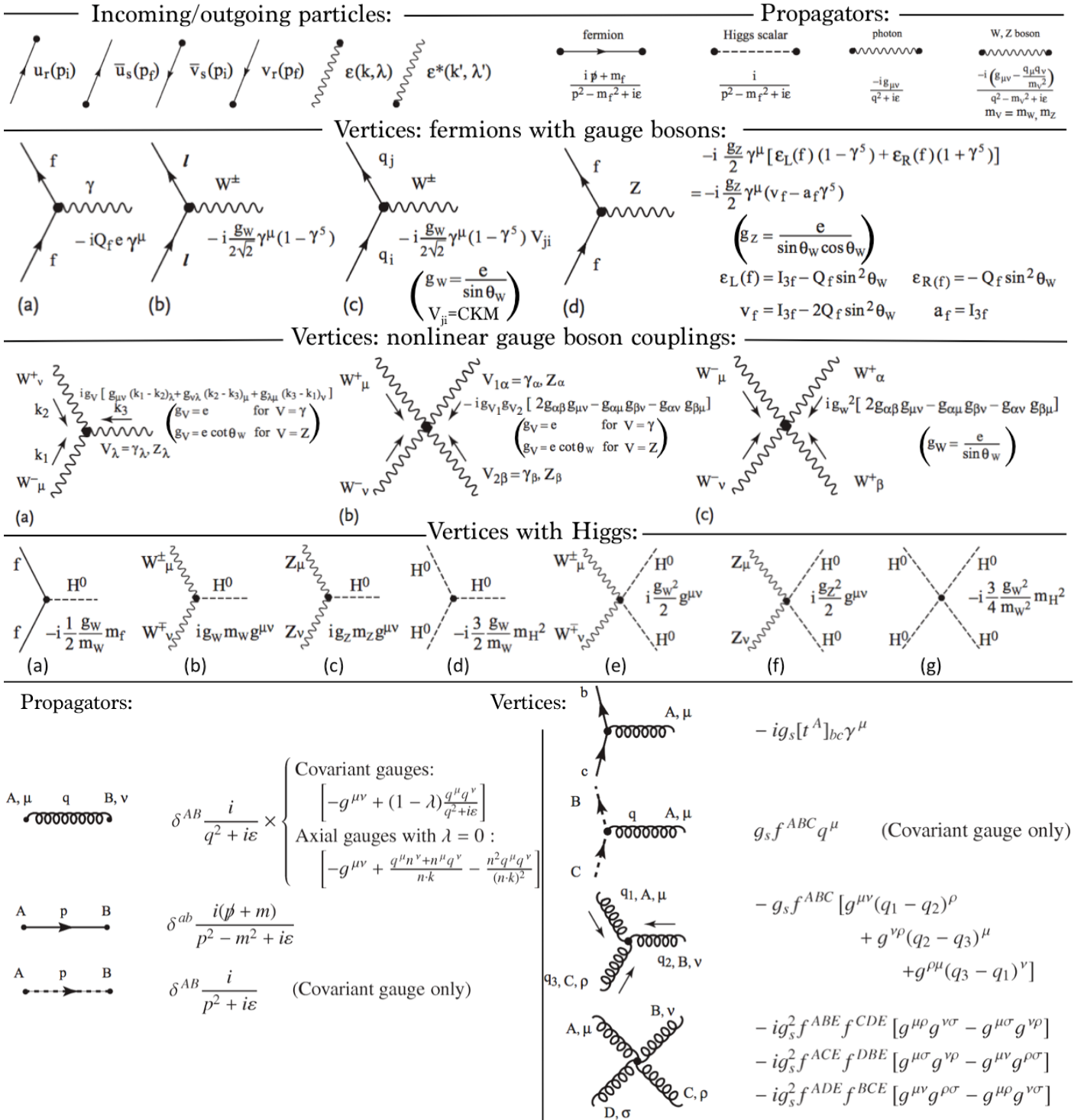


Figure 1.7: On top the full Feynman rules of EW sector. In the middle the Higgs interactions. On the bottom the QCD rules. Space-time spinor indices have been omitted. All the momenta in the three- and four-gluon vertices are inward and satisfy $\sum q_i=0$. Note there are not $\gamma ZZ, ZZZ$ vertices in the SM. (Taken from [125] §1.6).

1.1.9 Renormalisation

A process amplitude, at the lowest order (in the perturbative expansion) is given by “tree-level” graphs (like figure 1.5 left), where the momenta of all lines are fixed by the momenta of the external incoming and outgoing particles¹. Higher-order corrections involve loop graphs, where the momenta of internal lines in the graphs are integrated over, as shown in the examples of figure 1.5 right.

The momentum integrals of internal lines (propagators) in loop corrections diverge for large loop-momenta. Such processes are shown in figure 1.8, where the first row (a) shows QED-vertex leading term diagram $O(a^1)$, where in (b) to (e) diagrams are of the order of $O(a^2)$ contributions/corrections. Second and third rows left, tree-level QED and QCD full Feynman diagram of a scattering with ((b) to (d) columns) loop corrections at the propagator.

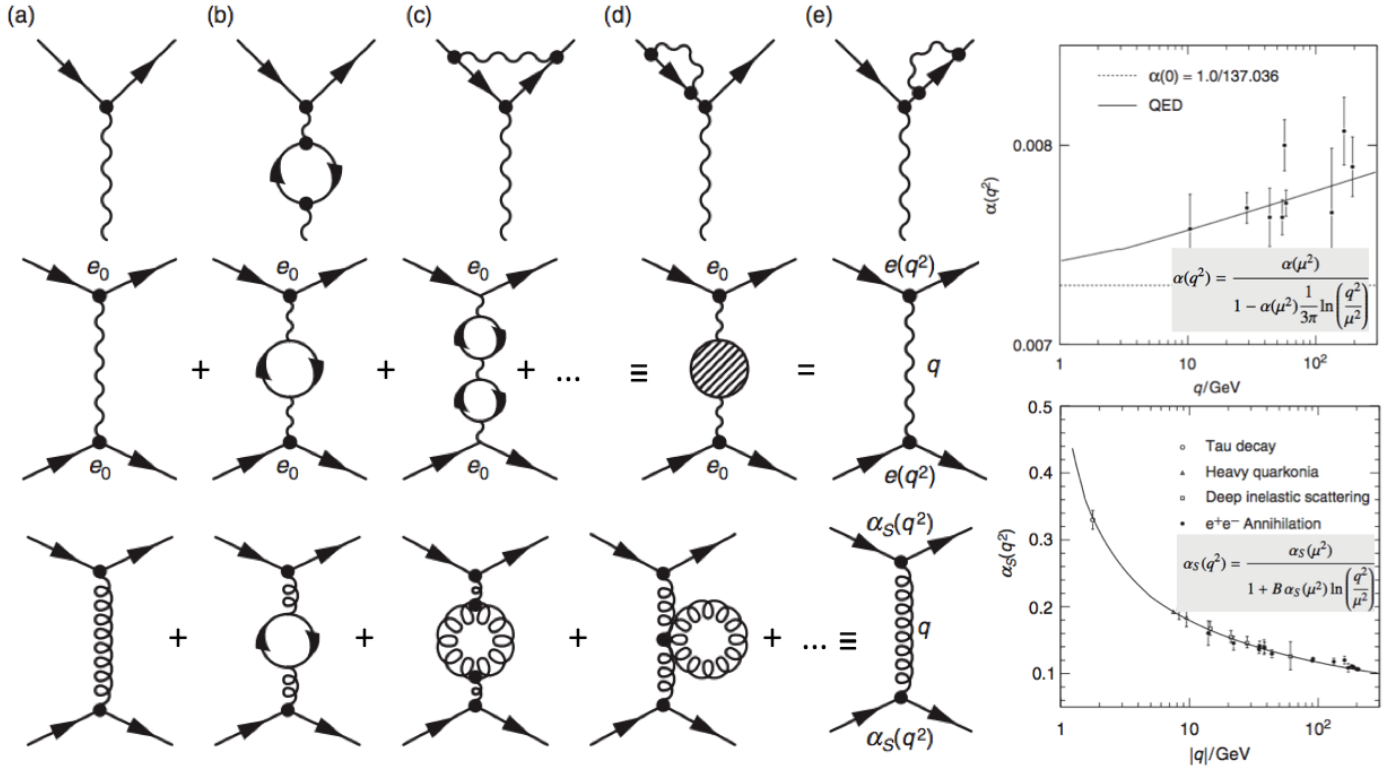


Figure 1.8: On the left column: the 0-loop diagrams of an interaction. In the rest some loop corrections cases: first row single-QED-vertex $O(a^2)$ corrections, for second and third rows full Feynman diagram higher corrections. On the right the renormalizable coupling constants a , a_s , as a function of the probing energy q . (Taken from [136]).

To maintain the theory meaningful one has to first “regularise” these divergences, by calculating loops in a number of dimensions $D = 4 - \epsilon$ where integrals converge. For instance the $O(a^2)$ graphs involved integrals such: $\int d^{4-\epsilon}l/[l^2(p-l)^2]$, with l the momentum of the particle in the loop and p the propagator where loop intervenes. The would-be divergences are then absorbed in the quantities that appear in the Lagrangian, such as coupling constants and masses. After this procedure, called “renormalisation”, the regulator is removed again ($\epsilon \rightarrow 0$) [124, 131].

In a more physical frame, renormalisation means that the effects of quantum fluctuations ($O(a^n)$ loops) with momenta much larger than the scale of a given process can be absorbed into the parameters of the theory. One has to choose a specific “renormalization scheme” which defines which part of the loop-corrections is absorbed into the renormalisable quantities.

In the modified “Minimal Subtraction” scheme (\overline{MS}) [131], (as well in most other schemes), divergent terms are expanded in powers of ϵ , the renormalised couplings and masses depend on a “renormalisation scale” μ ; which, roughly speaking, specifies the lower limit of loop momenta that have been

¹Subsection follows references: [40]§2.5 by M.Diehl and W.Hollik and [136] §10.5 by Mark Thomson.

absorbed in the renormalised parameter. The “running” of the parameter with μ is described by the “Renormalization Group Equations” (RGEs), which in the simple case of one coupling g and one mass m are [40, 131]:

$$\mu \frac{dg(\mu)}{d\mu} = \beta(g(\mu)), \quad \mu \frac{dm(\mu)}{d\mu} = m(\mu)\gamma_m(g(\mu)). \quad (1.53)$$

The “renormalisation group functions”: β and γ_m , have an expansion in the coupling and can be determined from the relevant loop graphs. If the Standard Model is renormalised in the \overline{MS} scheme, all couplings and masses, as well as the CKM matrix elements (which are closely connected to the Yukawa couplings), become dependent on μ . With the increment of μ the $U(1)_Y$ coupling g_1 increases as well (shown in figure 1.8 top right), whereas the $SU(2)_L$ and $SU(3)_c$ couplings g_2 and g_s decrease. This last QCD-case is shown on 1.8 bottom-right. (All three SM-running couplings are summarized in figure 1.16 left, which is discussed later).

An expansion in the coupling constants is only useful if these are small enough to allow the convergence of the perturbative series. The electroweak couplings g_1 and g_2 are small at all relevant scales, g_1 becomes large only for $\mu \sim 10^{15}$ GeV, where the Standard Model cannot be expected to be valid anymore. This is not true for the strong coupling, g_s , which has consequences for QCD non-allowing perturbative treatment.

Since the EW charged currents J_{CC}^μ (1.49) involve both vector and axial-vector components, (fermion-triangle anomalies) divergences could potentially break the gauge symmetry of the SM, which would prevent a consistent renormalisation of the theory ([131] §19 for more). However, it turns out that the symmetry-breaking terms cancel in the sum over all fermions running around the loop. The cancellation happens separately for each generation of quarks and leptons, where the quarks come with a factor three in the loop because of the colour-states. The consistency of the SM thus is based on the detailed quantum number assignment to the fermions under the full gauge group $SU(3)_c \times SU(2)_L \times U(1)_Y$.

1.1.10 Tests of the SM predictions

The predictivity of SM has been tested in many ways, in extreme emphasis and in high precision the last four decades. Almost always turn out that observations meets the SM predicted expectations. Here we will only summarize a few (among many) high-lighted successful predictions.

- A large set of SM cross sections, predictions and measurements, are shown in figure 1.1.10 (resent results from ATLAS and CMS collaborations). These summary plots exhibits confirmation in both EW-sector and QCD-sector (in $\geq N_{jet}$ columns). The validity of the predictions ranges up to 14 orders of magnitude over cross-sections and up $\sqrt{s} = 8$ TeV energies.
- The latest discovery of Higgs boson is undoubtedly one of the most sticking predictivity goals of the SM. Figure 1.10 shows the relevant Higgs-resonance into the $H \rightarrow \gamma\gamma$ and $H \rightarrow ZZ^* \rightarrow 4\ell$ discovery decay channels, as a function of $m_{\gamma\gamma}$ and $m_{4\ell}$ (from ATLAS and CMS collaborations). These measurements came on 2012 [70] to verify prediction from 1964 [85, 103]. Figure 1.11 shows the predicted branching ratios of the Higgs boson and their measurements in CMS as well as the Yukawa couplings measurements [74].
- Validity confirmation of the SM and in particular the renormalisation concept, coming from the evolution of coupling constants versus probing energy (figure 1.8 right).
- Quark model predicts baryon states, whereas lattice QCD calculations predicts their masses [83]. The measured hadron states and their masses are in agreement with SM prediction (figure 1.12 left). Moreover, in the QCD-sector, the differential inclusive jet cross sections is measured in great agreement with the SM predictions (figure 1.12 right).

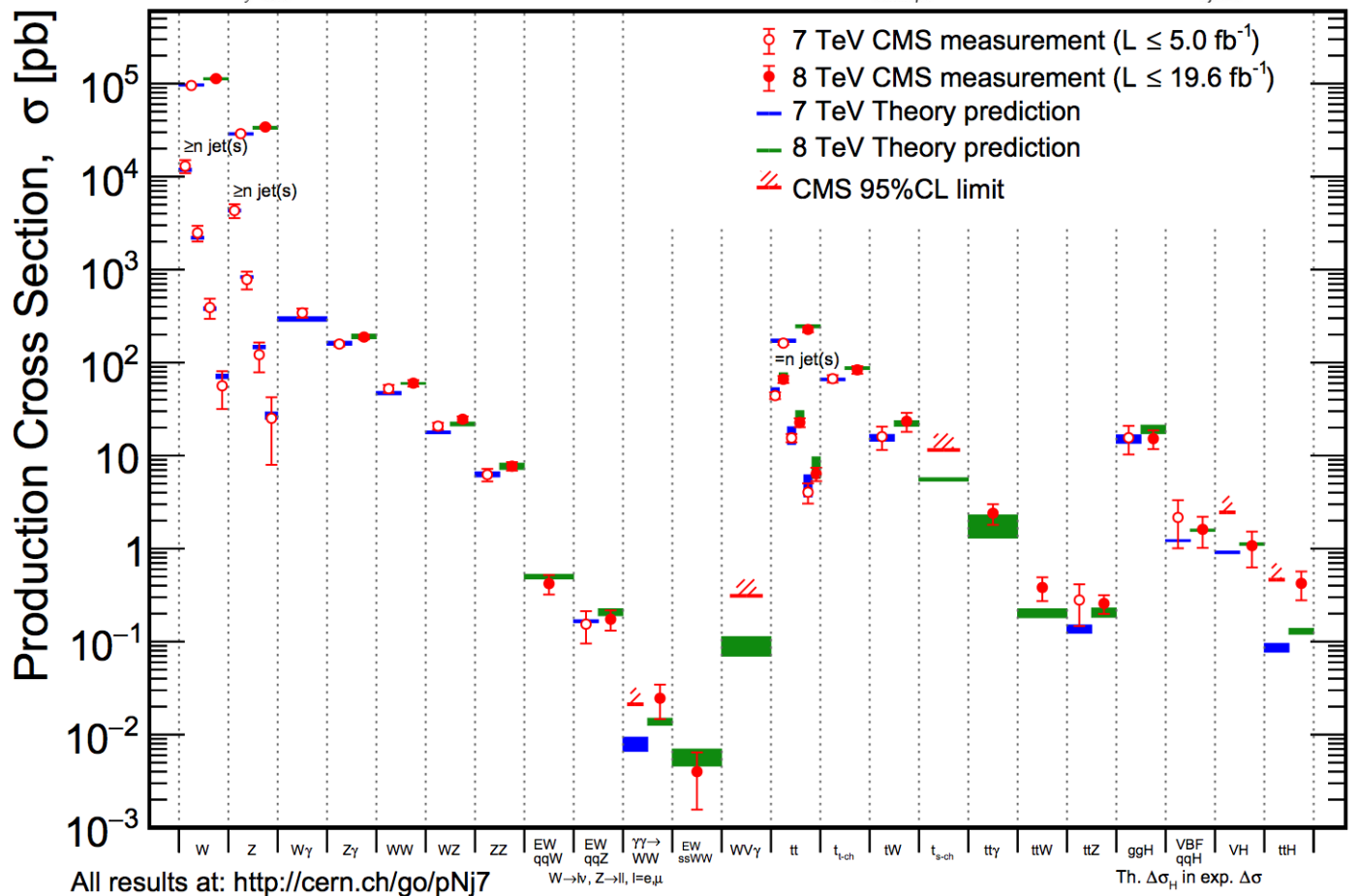
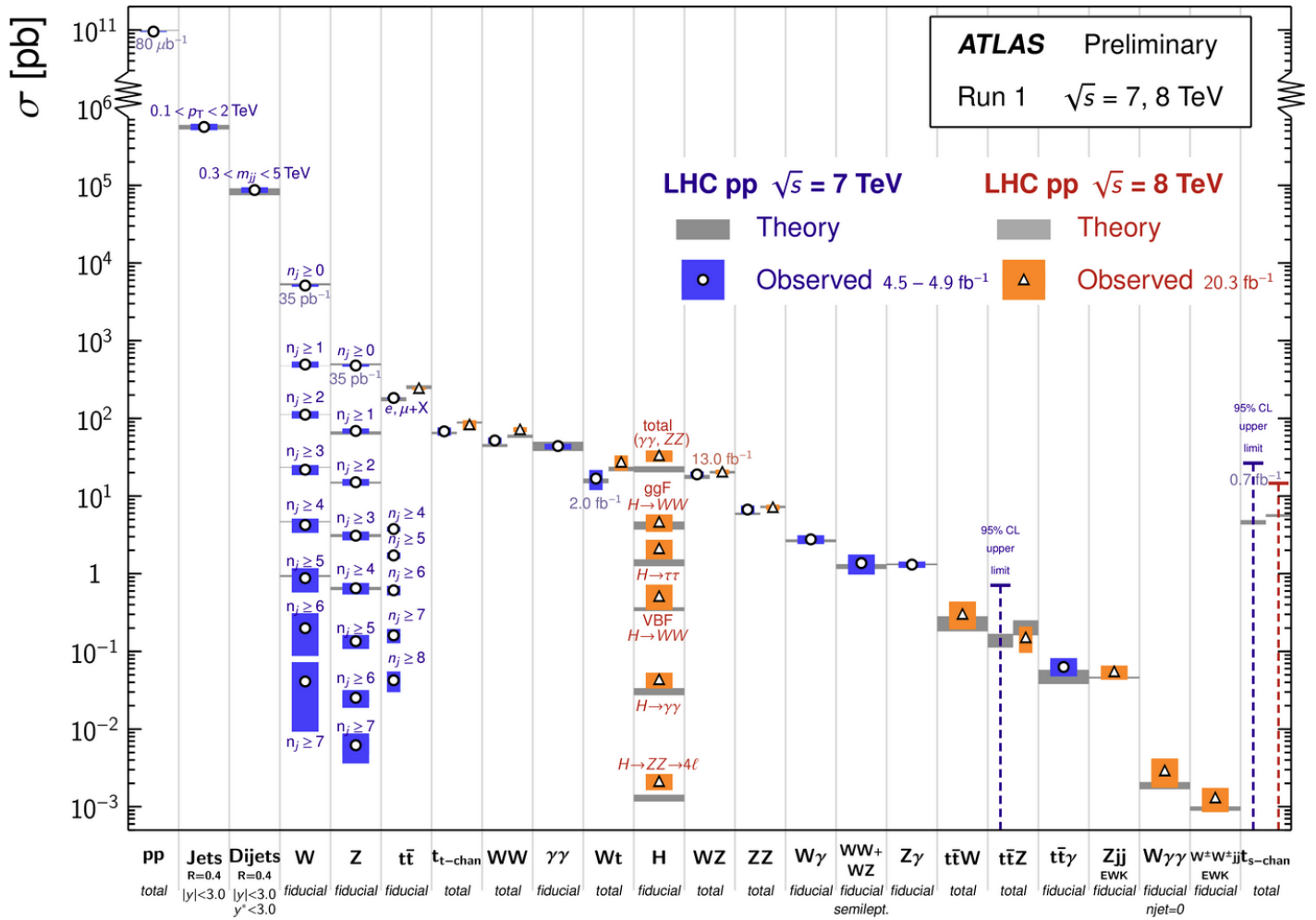


Figure 1.9: The SM production cross sections for various (mainly EW) processes as measured by ATLAS (top) and CMS (bottom) experiments at the LHC. Results up to March 2015. (Taken from [70]).

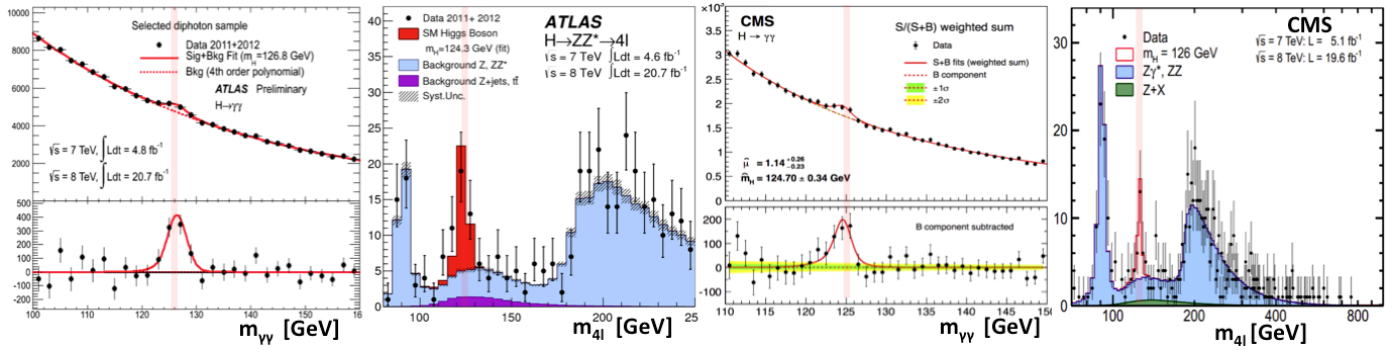


Figure 1.10: The Higgs-resonance in $H \rightarrow \gamma\gamma$ and $H \rightarrow ZZ^* \rightarrow 4l$ decay (discovery) channels at $m_{\gamma\gamma}$ and m_{4l} spectra. ATLAS and CMS collaborations results.

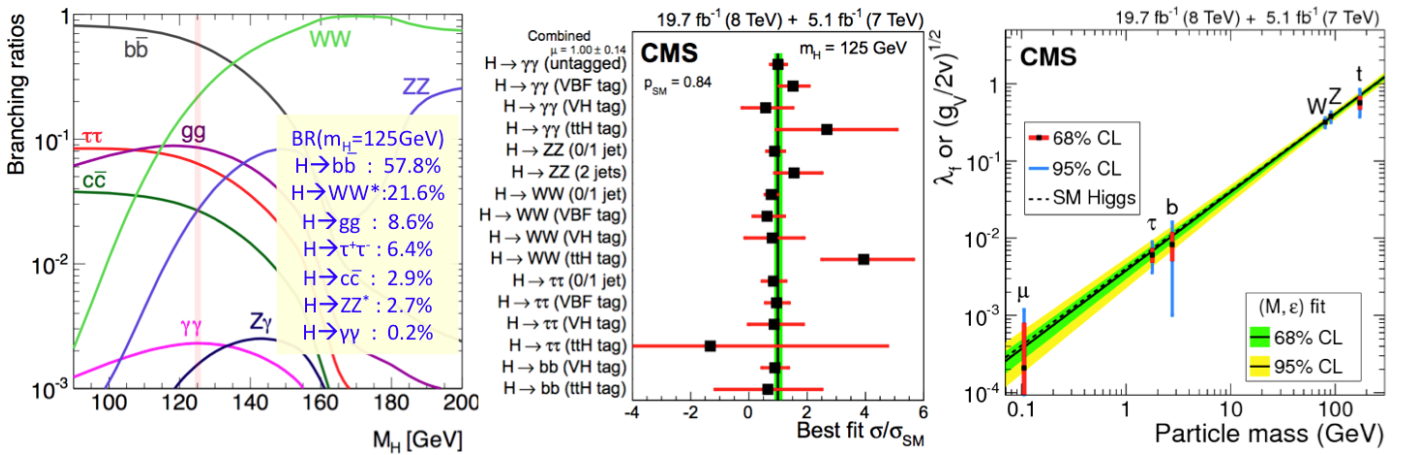


Figure 1.11: The SM predicted branching ratios of the Higgs boson, their corresponding measurements from CMS, as well as the Yukawa couplings measurements [74].

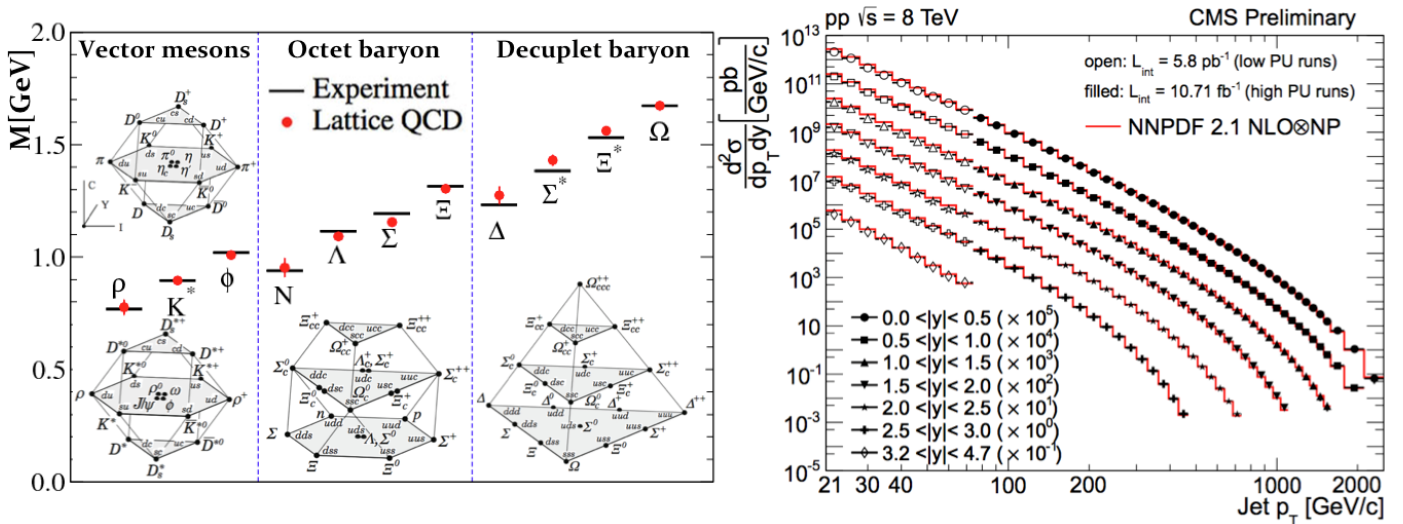


Figure 1.12: Left: light hadron spectrum obtained from lattice QCD simulations with dynamical u, d, s quarks (in the Wilson fermion formalism) taken from [83]. The hadron masses are extrapolated to the physical quark masses (determined by m_π , m_K and m_Ω). Right: the double-differential inclusive jet cross section in comparison to NLO predictions (using the NNPDF2.1 neural networks PDF set times the non-perturbative correction factor), measured by CMS [42, 112].

1.2 The shortcomings of the SM in quantum field theory frame

Even though Standard Model gives a highly successful and precise description of the physics governing the microcosm, there are strong arguments calling for an extension of this description. There are indubitable observational evidence and also conceptual issues suggesting that the SM seems to be embedded in a more fundamental theory which in our energy regime is understood as the SM. From this point of view SM is an effective theory, constructed by a number of theoretical concepts in order to reproduces the experimental data up to the accessible energy scale, rather than an ultimate fundamental theory of nature.

An obvious shortcoming of the Standard Model is that it treats neutrinos as massless, whereas neutrino oscillation experiments provided clear evidences for small but non-zero neutrino masses. SM fails to provide a natural explanation of some experimentally confirmed ingredients of the SM like the stability of higgs boson (which has non-infinite and finely-tuned mass) and the huge differences in strength of the four known forces. Does not provides any explanation why the particles come in three distinct mass generations. It also fails to describe phenomena of the macrocosm, such as gravitation (as quantized theory), dark matter, dark energy, and the baryon asymmetry of the universe.

We can clusterize these shortcomings in two basic categories: (A) those correlated with the core of theoretical particle physics i.e. with the Quantum Field Theory (QFT), and (B) those which are connected with cosmological observations and the large scale universe.

(A) In first category -QFT shortcomings- we can outline the following:

- Hierarchy problem.
- Grand Unification of the three interactions.
- Large number of free parameters imputed by hand.
- Absence of a quantum theory of gravity.

(B) Whereas in the second category -cosmology shortcomings- we can mainly refereed to:

- Dark matter.
- Dark energy.
- Matter-antimatter asymmetry, leptogenesis and baryogenesis.

In this section 1.2 we discus briefly the most important reasons signifying the presence of Beyond Standard Model physics (BSM) from the QFT perspective, whereas next section 1.3 is dedicated to the cosmology-originated shortcomings.

We will not consider the neutrino masses neither as an SM shortcoming, nor a BSM extension since massive neutrinos does not consists an intrinsic problem of the SM and does not requires any structural change. Massive neutrinos can accommodated in SM frame as massive Dirac-particles. Right-handed singlets in equations (1.27), (1.43), (1.44), (1.45), (1.46) should be turned to doublets, and the unitary lepton mixing matrix should be replaced by the PMNS-matrix.

1.2.1 Higgs mass corrections divergence and Hierarchy/Naturalness problem

The Higgs SM sector is described by the the complex scalar doublet fields Φ introduced in equations (1.35), which after a spontaneous symmetry breaking, formulated in transformation (1.37), ends up with the real-valued Higgs field H , and with the corresponding potential shown in (1.40).

Each QFT theory part of SM (QED, QCD, EW) applies the concept of renormalisation, which means that finite results are obtained for all higher-order (loop) corrections even if we extend the virtual

momenta in the loop integrals all the way to infinity; but although this certainly implies that the theory is well defined and calculable up to infinite energies. However this is not taken for granted since we know that, at least in Planck-mass energy scale ($M_{Planck} \sim 1/G_N \sim 10^{18}$), some-kind of new physics contributes and has to be taken into account into the regularization techniques of renormalization.

The four-boson vertex self-interaction¹ in (1.35,1.38,1.40) generates, at one-loop order, a contribution to the $\Phi^\dagger\Phi$ mass term, which is proportional to:

$$\int^\Lambda \frac{\lambda d^4k}{k^2 - M_H^2}. \quad (1.54)$$

Where the Λ represents the energy scale at which this new physics appears, and SM must be modified. The higgs quartic coupling contributes to the self-energy mass and its corresponding diagram is the (g) in figure 1.7. This integral diverges quadratically, producing a correction of: $\sim \lambda\Lambda^2\Phi^\dagger\Phi$, to the

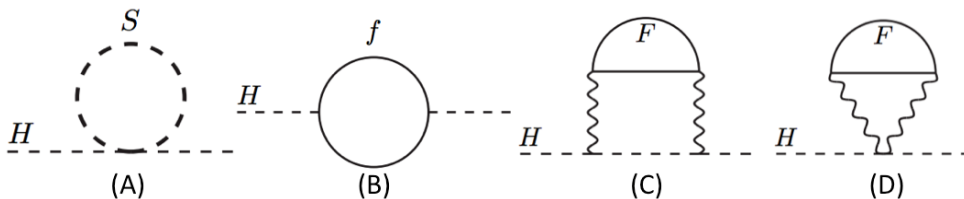


Figure 1.13: Corrections to the higgs (propagation-bare) mass. (A): diagram of one-scalar-loop correction in Higgs mass, (B): correction by an one-fermion-loop, (C) and (D) correction with two-loops processes of a heavy non-SM fermion via SM vector bosons (taken from [121]).

“bare-mass” term: $-\mu^2\Phi^\dagger\Phi$ in (1.35). The coefficient $-\mu^2$ of $\Phi^\dagger\Phi$ (“bare-mass” term) is then replaced by the one-loop corrected “physical” value $-\mu_{phys}^2$, where (ignoring the numerical factor) leads to:

$$\mu_{phys}^2 = \mu^2 + \lambda\Lambda^2 \quad \Rightarrow \quad \Delta M_H^2 \equiv \mu_{phys}^2 - \mu^2 = \lambda\Lambda^2 \quad (1.55)$$

This is the correction of the one-loop quartic self-coupling of the Higgs boson (figure 1.13 (A)) and is proportional to the new physics regime Λ^2 . However, even if the external momenta are small relatively to the scale of new physics Λ , the loop momenta have to be integrated all the way to that scale. Additional correction terms correspond to each of the SM particle (figure 1.13 (B) shows a SM-fermion loop, whereas (C) and (D) are higher order loops with a hypothetical exotic heavy fermion that couples only indirectly to higgs via EW-bosons). The main contribution of the corrections comes from the one-loop diagram of top-antitop pair loop (like (B)). This happens because the Yukawa couplings are proportional to the fermion masses and top is the mass leader of the SM-fermions. The physical mass can then approximately accounted by both diagrams (A) and (B) in figure 1.13 as:

$$\mu_{phys}^2 = (125 \text{ GeV})^2 = \mu^2 + \lambda\Lambda^2 - 3y_t^2\Lambda^2 \quad (1.56)$$

The problem is that if Λ is of order $M_{Planck} \sim 10^{18}$ GeV, (assuming the largest possible range of SM validity) then the loop corrections on M_H^2 is ~ 32 orders of magnitude larger than the required value of 125^2 GeV². In other words μ^2 and ΔM_H^2 in equation 1.55 are both huge with respect to $\mu_{phys}^2 = 125^2$ GeV²; and this would be an “un-natural”, extremely improbable as an accidental case to have such close values that performs such a “tuning” which places higgs mass into the EW-scale. This problem is characterized as the “hierarchy problem” or “naturalness problem”. Hierarchy problem refers to the very wide SM particles mass spectrum: masses from $\sim 10^0$ to $\sim 10^{11}$ eV, as received by the higgs interactions. Naturalness problem refers to the appearing un-natural “finely tuned” mass loop corrections up to many digits in order to allow higgs meet the EW-scale.

This is mainly a problem for the Higgs boson since it is scalar and its squared mass appears corrected by Λ^2 terms; in contrast, the quantum corrections for fermions and bosons which have a

¹Subsection follows references [17] §1.1 by Ian Aitchison and [122] §1 by Stephen P. Martin.

$\propto \ln \Lambda$ sensitivity to cutoff. However, all the SM particles obtain masses from Higgs, so the entire mass spectrum of the SM is much or less sensitive to the cutoff Λ . This problem consist one of the most challenging incompleteness of the SM.

Figure 1.14 illustrates and quantifies the “unnatural” case in which fine tuning needs to take place even for a $\Lambda = 10$ TeV scenario. The measured Higgs mass should somehow converges and retained to the observed value. An unknown yet mechanism “should” (is needed to) cancel-out most Λ -dependent corrections to produces as a nature consequence observed masses.

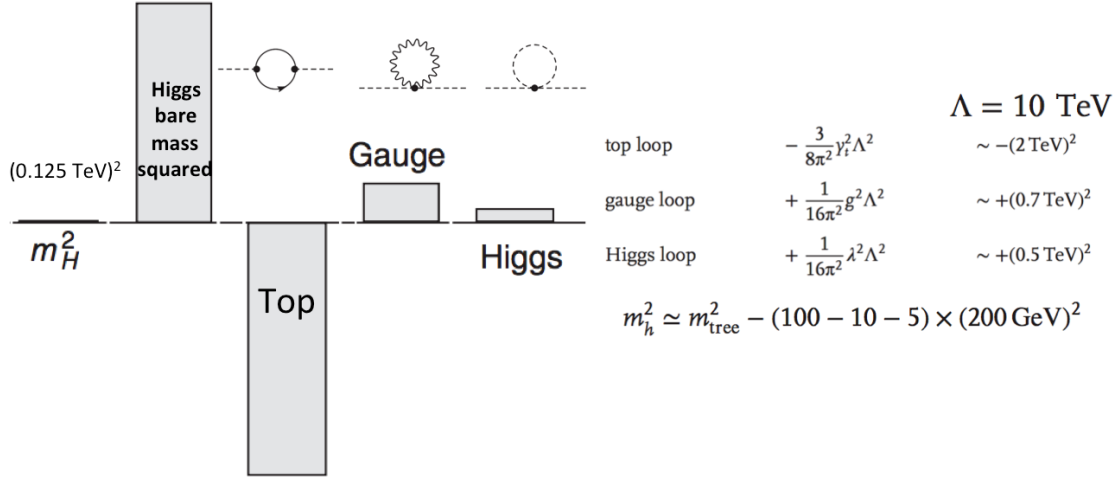


Figure 1.14: Higgs squared mass illustration as a positive and negative corrections summation under the assumption of $\Lambda = 10$ TeV (which indirectly implies new physics appears in this scale). The free parameter which supposed to be finely tuned is the higgs bare mass. Taken from [126]§1.4.

As natural scenario can considered the one which provides the framework of a small (the minimum) amount of cancellations between the many-digits correcting terms. This requires a relatively low cutoff like $\Lambda \lesssim 1$ TeV. Thus, a natural scenario would be one with some new physics (and new particles) appears in the EW-scale or up the \sim TeV scale. the contribution of these new particles would provided the needed cancellations of Λ -terms and would preserved the Higgs mass at the EW scale.

1.2.2 The parameters of the SM

If neutrinos are Dirac fermions, the SM-physics has 25 (or 26) free parameters that have to be input by hand¹. These are: the masses of the 12 fermions (or alternatively its 12 Yukawa couplings to the Higgs), the three (bare) coupling constants describing interactions’ strengths, the 2 parameters describing the Higgs potential, and the 8 mixing angles (4 of the PMNS and 4 of the CKM) matrices:

$$m_{\nu_1}, m_{\nu_2}, m_{\nu_3}, \quad m_e, m_\mu, m_\tau, \quad m_u, m_d, m_s, \quad m_c, m_b, m_t, \\ a_0(\text{or } e_0), G_F(\text{or } a_W), a_S, \quad \mu(\text{or } m_H), \lambda(\text{or } VEV), \\ V_{CKM}(\theta_{12}, \theta_{13}, \theta_{23}, \delta), \quad V_{PMNS}(\theta_{12}, \theta_{13}, \theta_{23}, \delta), \quad \theta_{QCD-CP}.$$

This relatively large number of free parameters is indicative of the Standard Model being a model where the parameters are chosen to match the observations, rather than coming from a higher theoretical principle.

Putting aside θ_{CP} , of the 26 SM parameters, 14 are associated with the Higgs field, 8 with the flavour sector and only 3 with the gauge interactions. Within each of these three broad areas, patterns emerge between these different parameters, indicating a potential presence of some unknown symmetry principle. Figure 1.15 shows the mass hierarchy in SM. With the exception of the neutrinos, the masses within a single generation are similar, and it is hard to believe that this a random fact. The flavor

¹Subsection follows reference [136] §18.1 by Mark Thomson.

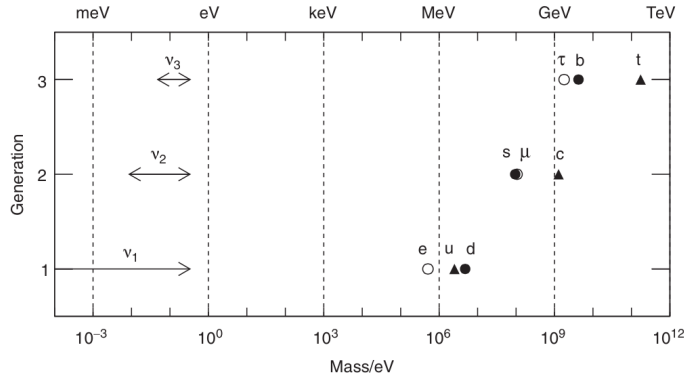


Figure 1.15: The fermion masses by generation with neutrino approximated by cosmological constraints (taken from [136]).

mixing in lepton and quark sectors are quite different as figure F.1 illustrates. This observed structure (with off-diagonal enhancement in CKM) is not understood in SM frame. In addition, the coupling constants of the three gauge interactions are of a similar order of magnitude, hinting that they might be different low-energy manifestations of a Grand Unified Theory (GUT) of the forces. These patterns provide hints for, as yet unknown, physics beyond the Standard Model.

1.2.3 Grand unification of the three interactions in SM frame

As it has been noted, the coupling constants of the three forces of the SM evolves due to the probing energy as figure 1.8 right shows.

At the electroweak scale, in probing energy $Q^2 \sim 100 \text{ GeV}^2$, the have coupling strengths are¹:

$$a^{-1} \simeq 128, \quad a_W^{-1} \simeq 30, \quad a_S^{-1} \simeq 9 \quad (1.57)$$

Furthermore, the coupling constants of QED and QCD run with energy according to:

$$[a_i(q^2)]^{-1} = [a_i(\mu^2)]^{-1} + \beta \ln(q^2/\mu^2), \quad (1.58)$$

where μ^2 represents an energy scale where the coupling is known and β depends on the numbers of fermion and boson loops contributing to the gauge boson self-energy. In QED where the photon self-energy arises from fermion loops alone a increases with energy, whereas a_S decreases with energy due to the presence of gluon loops. Because of the weak boson self-interactions, which are a consequence of the SU(2) gauge symmetry, a_W also decreases with increasing energy scale, although not as rapidly as a_S .

The running of the different coupling constants therefore tends to bring their values together. It seems plausible that at some high-energy scale, the coupling constants associated with the U(1), SU(2) and SU(3) gauge symmetries converge to a single value.

In the 1970s, it was suggested (by Georgi and Glashow) that the observed gauge symmetries of the SM could be accommodated within a larger SU(5) symmetry group. In this Grand Unified Theory (GUT), the coupling constants of the Standard Model are found to converge –although not exactly– at an energy scale of $\sim 10^{15} \text{ GeV}$. Figure 1.16 left shows the evolution of the three coupling constants as a function of probing energy. Dashed lines correspond to the higher energies extrapolation within the SM frame. The converge in GUT energy scales is not enough in the sense that not all couplings meet in the same value.

This non-complete convergent behavior is a hint that might new physics -introducing new particles which supposed to participate in the running coupling evolution- might appears in the energy range $\sim 10^3$ to $\sim 10^{16}$ and make the three forces having common unified strength. If there is physics beyond

¹Subsection follows reference [136] §18.2.3 by Mark Thomson.

the SM with new particles at a mass scale Λ , these particles also would contribute to the gauge boson self-energy terms (through extra fermionic and bosonic loops), modifying the running of the coupling constants for $q^2 > \Lambda^2$. For example, Figure 1.16 right shows how supersymmetric particles¹ at a scale of $\Lambda=0.5$ TeV (and $\Lambda=1.5$ TeV red-blue) would modify the evolution of the U(1), SU(2) and SU(3) couplings within the SU(5) GUT.

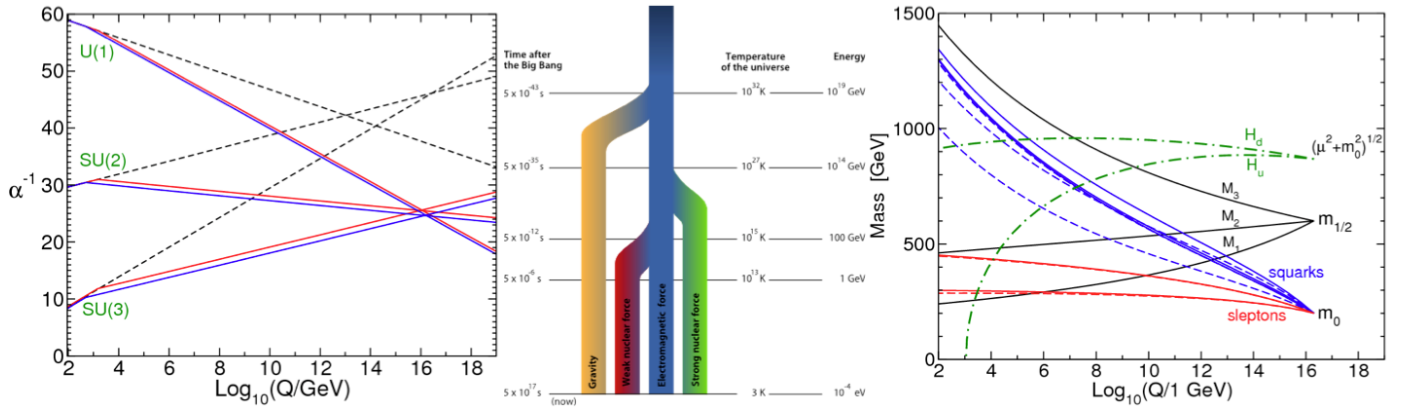


Figure 1.16: Left: the evolution of the couplings $a_i^{-1}(Q)$ in the SM SU(5) unification frame (dashed lines) and in the MSSM (solid lines). The MSSM particle masses are treated as a common threshold varied between 0.5-1.5 TeV, and ${}_3(M_Z)$ is varied between 0.117 and 0.121. Middle: a schematic evolution of the forces. Right: evolution of scalar and gaugino mass parameters in the MSSM (with MSUGRA boundary conditions imposed at $Q_0 = 2 \times 10^{16}$ GeV). Parameter $\mu^2 + M_{H_u}^2$ runs negative provoking EW symmetry breaking. Taken from [122].

The three coupling constants converge to a single value: $a_{GUT}^{-1} \simeq 26$ at $\sim 10^{16}$ GeV. In some sense, this convergence is inevitable since two non-parallel lines will always cross, and with the appropriate choice of the mass scale for new physics the three lines can always be made to meet at a single point. However it is interesting that the required mass scale turns out to be about 1 TeV.

It is now known that SU(5) is not the correct gauge group for a GUT; the predicted value for $\sin^2 \theta_W$ is incompatible with the measured value. Despite this, the convergence of the couplings strongly suggests that the three forces of the SM are the low-energy manifestations of some larger, as yet unknown, unified theory. Even more, in even higher energies, also gravity might converges to one single force of nature (Figure 1.16 middle).

A candidate theory providing such additional particles which allows the three forces convergence, is the Supersymmetry (SUSY). In the SUSY extension-frame of SM, the extra particles provides such an attribute. In addition –in one of the its versions, the so-called minimal supersymmetric SM (MSSM)– the masses of all particles (which are evolves as renormalizable parameters of the theory) meets all in 2 values as figure 1.16 right shows, the universal mass of all fermions and bosons of the model.

This masses unification in MSSM frame reduces considerably the number of free parameter of the theory, which consists an additional bonus towards GUTs and a clear hint supporting the BSM physics existence.

1.2.4 Metastable vacuum

The discovery of the Higgs boson with this particular mass of 125 GeV brings the higgs potential close to the vacuum metastability region. Figure 1.17 shows that the masses values of the Higgs and top-quark which points to a position in the metastable region. The stability condition is sensitive to these two masses and to the strong coupling constant a_S . The arising questions after the Higgs mass precise measurement are important since are directly related to how the new physics might appear.

¹Chapter 2 is dedicated to Supersymmetry, MSSM, MSUGRA.

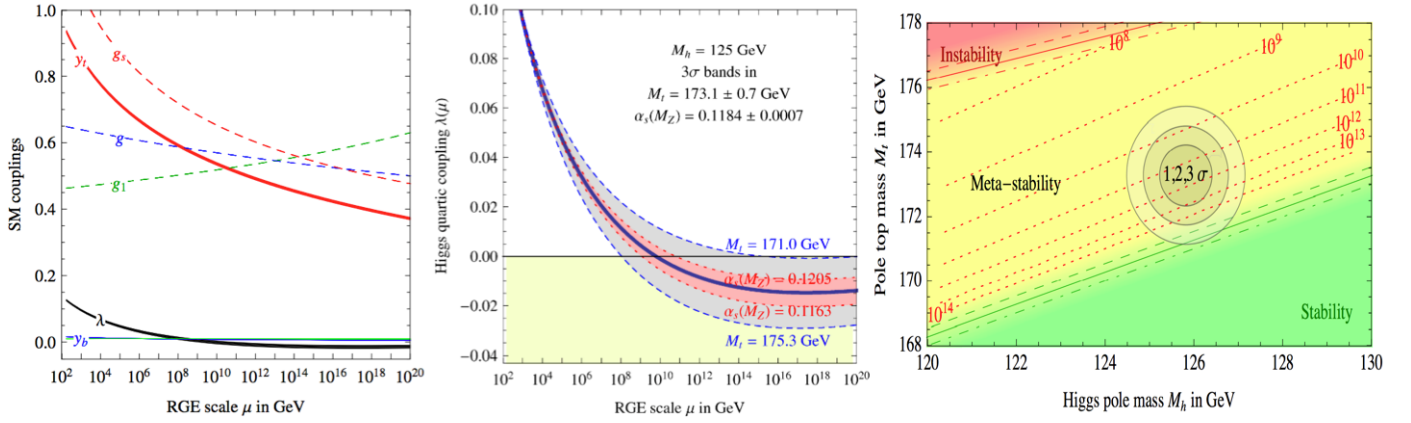


Figure 1.17: Left: SM gauge couplings g_i (in the SM, SU(5) GUT-frame), the y_t, y_b Yukawa couplings, and the Higgs quartic coupling λ with RGEs evolution in the \overline{MS} scheme. Middle: the evolution of λ varying M_t, M_H and a_s by $\pm 3\sigma$, right: stability regions in $[M_H, M_t]$ plane close to measured values. (Taken from [1, 141].)

Figure 1.17 left: SM renormalization group evolution (RGE) of the gauge couplings $g_1 = g' \sqrt{5/3}$, $g_2 = g$, $g_3 = g_s$, of the top and bottom Yukawa couplings (y_t, y_b), and of the Higgs quartic coupling λ . All couplings are defined in the \overline{MS} scheme. The thickness indicates the $\pm 1\sigma$ uncertainty. Middle: the Higgs self-coupling for $M_H = 125$ GeV for the central value of m_t and a_s , as well as for $\pm 2\sigma$ of m_t (dashed lines) and a_s (dotted lines). For negative values of λ the lifetime of the SM vacuum due to quantum tunneling at zero temperature is longer than the age of the universe as long as λ remains above the region shaded in red, which takes into account the finite corrections to the effective bounce action renormalized at the same scale as λ . Right: regions of stability, metastability and instability of the electroweak vacuum in the (M_H, M_t) plane; contours at 1,2,3 σ corresponding to the present knowledge of a_s are shown (taken from [141])

The observation of a Higgs mass of 125 GeV would give vacuum stability up to only scales between 10^9 and 10^{10} GeV, and stability up to the Planck scale would require new physics. Such new physics could be the SUSY, but other models have also been proposed [23, 47]. This is why the discovery and the determination of the Higgs mass is so important. As the dynamical properties of the Higgs are directly related to the framework of the SM, it is necessary to know how it is produced. We have to be aware that the production and detection mechanisms differ depending on the mass of the Higgs.

1.3 The shortcomings of the SM in Cosmology frame

Also from the cosmological side the Standard Model is challenged: first, the SM does not contain a theory for the description of the interactions that govern the large scale structure of the universe: there is no renormalisable quantum theory of gravity. Second, and of more direct consequence for particle physics, the SM does not provide a candidate particle to explain the large dark-matter content of the universe of close to 25%. The dark matter is necessary to account for, among other features, the rotation curves of galaxies and is also favoured by measurements of the cosmic microwave background (CMB). Also the baryon asymmetry as observed in the universe still awaits an explanation. Finally the accelerated expansion of our universe, “caused” by its so-called “dark energy” content which roughly accounts the 70%, is one of the biggest mysteries and SM provides no explanations for that observations.

1.3.1 Dark matter

The existence of dark matter in universe provides undeniable evidence for physics beyond the SM¹. Since the 1933, it has been known that a significant fraction of the mass in the universe is not bound

¹Subsection follows references [136] §18.2.1 by Mark Thomson and [126] §10.2 by Yorikiyo Nagashima.

up in the luminous matter that once were thought to comprise most of the mass of the galaxies.

The most direct evidence for dark matter comes from the velocity distributions of stars as they orbit the galactic centre. In a spiral galaxy like the Milky Way, the majority of the luminous mass is located in the central bulge. Outside this central region, the tangential velocity of a star of mass m should be given by the usual equation for centripetal acceleration in a gravitational field: $mv^2/R \simeq GmM(R)/R^2$, where $M(R)$ is the total mass within a radius R . Assuming that most of this mass is concentrated in the central bulge, the tangential velocities of the stars should decrease as $R^{-1/2}$. This is not consistent with the observed velocity distributions, which decrease only slowly with radius, implying that the distribution of mass in the galaxy is approximately $M(R) \propto R$ or rather flat. From this observation, one can conclude that the mass of a galaxy has a significant non-luminous mass component, known as dark matter. Figure 1.18 illustrates the situation.

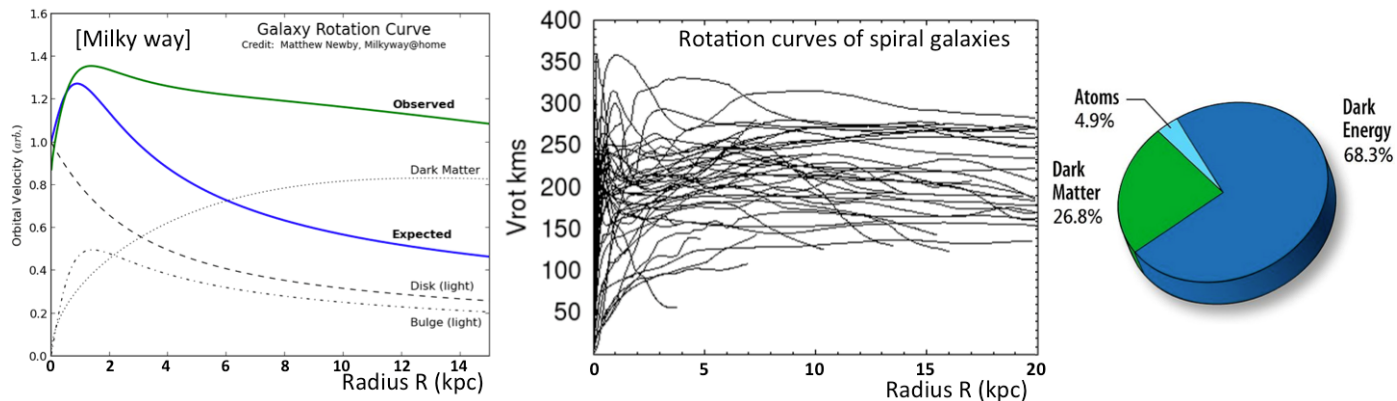


Figure 1.18: Left: our galaxy rotation curve as observed and decomposed to known (luminous) and unknown (dark) matter. Middle: rotation velocities of spiral galaxies obtained by combining CO data for the central regions, optical for disks, and HI (an interstellar cloud composed of neutral atomic hydrogen) for outer disk and halo. The graph shows that the constancy of the velocity goes beyond 30 kpc, while the typical radius of disks in spiral galaxies is ~ 10 kpc (taken from [126] §10.2). Right: the cosmic pie with “Energy-Matter” content of the universe after the recent “Planck” observations.

In addition compelling evidence for the existence of dark matter is provided by a number of cosmological and astrophysical measurements related to the precision measurements of the small fluctuations in the cosmic microwave background (CMB) from the Cosmic Microwave Background Explorer (COBE), Wilkinson Microwave Anisotropy Probe (WMAP), and Planck satellites. These have provided a firm experimental basis for the Λ CDM cosmological model, which is the standard model of cosmology. In the Λ CDM model, the total energy-matter density Ω of the universe is consistent with the flat geometry of space-time predicted by inflationary models, with $\Omega = 1$. Within the Λ CDM model, only 5% of the energy-matter density of the universe is in the form of normal baryonic matter, $\Omega_B \simeq 0.05$. A further 27% is in the form of cold dark matter (CDM), $\Omega_C \simeq 0.27$, and the majority of the energy-matter density of the universe is in the form of dark energy, $\Omega_\Lambda \simeq 0.68$. In the Λ CDM model, the dark energy is attributed to a non-zero cosmological constant of Einstein's equations of general relativity, $\Lambda \neq 0$, which tends to accelerate the expansion of the universe.

In nowadays our understanding of cosmology has reached the precision and sophistication where it now provides constraints on particle physics.

The particle content of the universe affects the way in which large-scale structure arises. Because lighter particles, such as neutrinos, remain relativistic throughout the expansion and cooling of the universe, they affect the evolution of large-scale structure differently than massive particles, which become non-relativistic during the first few years after the Big Bang. On this basis, it is known that the majority of the energy-matter density associated with the non-baryonic dark matter is due to cold (non-relativistic) matter as opposed to hot (relativistic) particles. The cosmological measurements are sufficiently precise to constrain the sum of the neutrino masses to be approximately: $(m_{\nu_1} + m_{\nu_2} + m_{\nu_3}) \lesssim 1$ eV. The current experimental evidence indicates that only a small fraction of the cold dark matter

is in the form of normal baryons, for example in low-mass brown dwarf stars.

The success of the Λ CDM standard model of cosmology, therefore strongly suggests that a significant fraction of the cold dark matter in the universe may be in the form of a new type of weakly interacting massive particle (WIMP), with a mass in the few TeV range. Such particles arise naturally in extensions to the Standard Model; for example, in many supersymmetric models the lightest supersymmetric particle (LSP) is the stable weakly interacting neutralino. WIMPs can either be observed through their production in beams collision experiments (like those at LHC) or through the direct detection of the WIMPs that are believed to pervade our galaxy.

Figure 1.19 illustrates the gravitational lensing effect (top-left) due to space-time curvature caused by a massive galaxy (or cluster) over a quasar (X-ray source) which appears behind the first. This gravitational lensing technique can be used for identifying and mapping the dark matter presented in large scale universe involving cluster(s) of galaxies. On the top-right an example with the so-called bullet nebula cluster where two clusters of galaxies have been collided. The ordinary baryonic matter (red) and behaves with a bullet-like shock, in contrast with the dark matter (blue) which passes by each other without electromagnetic interaction. Bottom-left the gravitational lensing of a single cluster of galaxies and its reconstructed mass density distribution. Bottom-right: the large scale dark matter distribution of the universe.

We can summarise the independent evidences for the presence of dark matter (completing those already mentioned) as follows:

- Rotational curves of spiral galaxies (stars kinematics).
- Virial mass of clusters of galaxies (galaxies kinematics).
- X-ray emissions from galaxy clusters (by energetic baryons bremsstrahlung in plasma).
- CMB measurements of the cosmic energy-matter densities
- Gravitational lensing in optical and x-rays either in galaxies and cluster level.
- Critical for the stability of the spiral galaxy discs (according to simulations) allowing the spiral structure formation.
- Critical for the early universe fast first cosmic structures formation (according to simulation).

All proposed explanation for dark matter candidates are comprised by some extension of the SM particle content. The suggested candidates (potential components of dark matter) can be summarized as follows:

- MACHO (massive compact halo object): It is a name given to baryonic dark matter, that is, non-luminous matter in the form of brown dwarfs, neutron stars, and black holes, that float in the galactic halo. MACHOs potential contribution to dark matter at the galactic halo is limited up to $\sim 8\%$, strengthening the need for non-baryonic dark matter.
- Heavy neutrinos: if heavy neutrinos $m_\nu \gtrsim 0.5 M_Z$ GeV exist, they can be candidates for the cold dark matter (CDM). It is a kind of WIMPs and its detection method is very similar to that of the neutralino (LSP in SUSY).
- Axions: very light ($m_a \ll O(1)$ eV). However, the so-called misalignment axion is degenerate in the Bose-Einstein condensate state and is classified as one of the CDMs. Negative results of terrestrial experiments and astrophysical observations have constrained the allowed mass range severely. Only a small window ($10^6 < m_a < 10^3$ eV) is left.
- WIMPs: Among the theories that provide the WIMPs, the supersymmetric theory is the favorite of the particle physics community because it provides a mean to unify all the forces including the gravity and to solve the hierarchy problem in grand unified theories (GUTs) as well. The coupling strength of the SUSY particle with ordinary particles is the same as its SM partner,

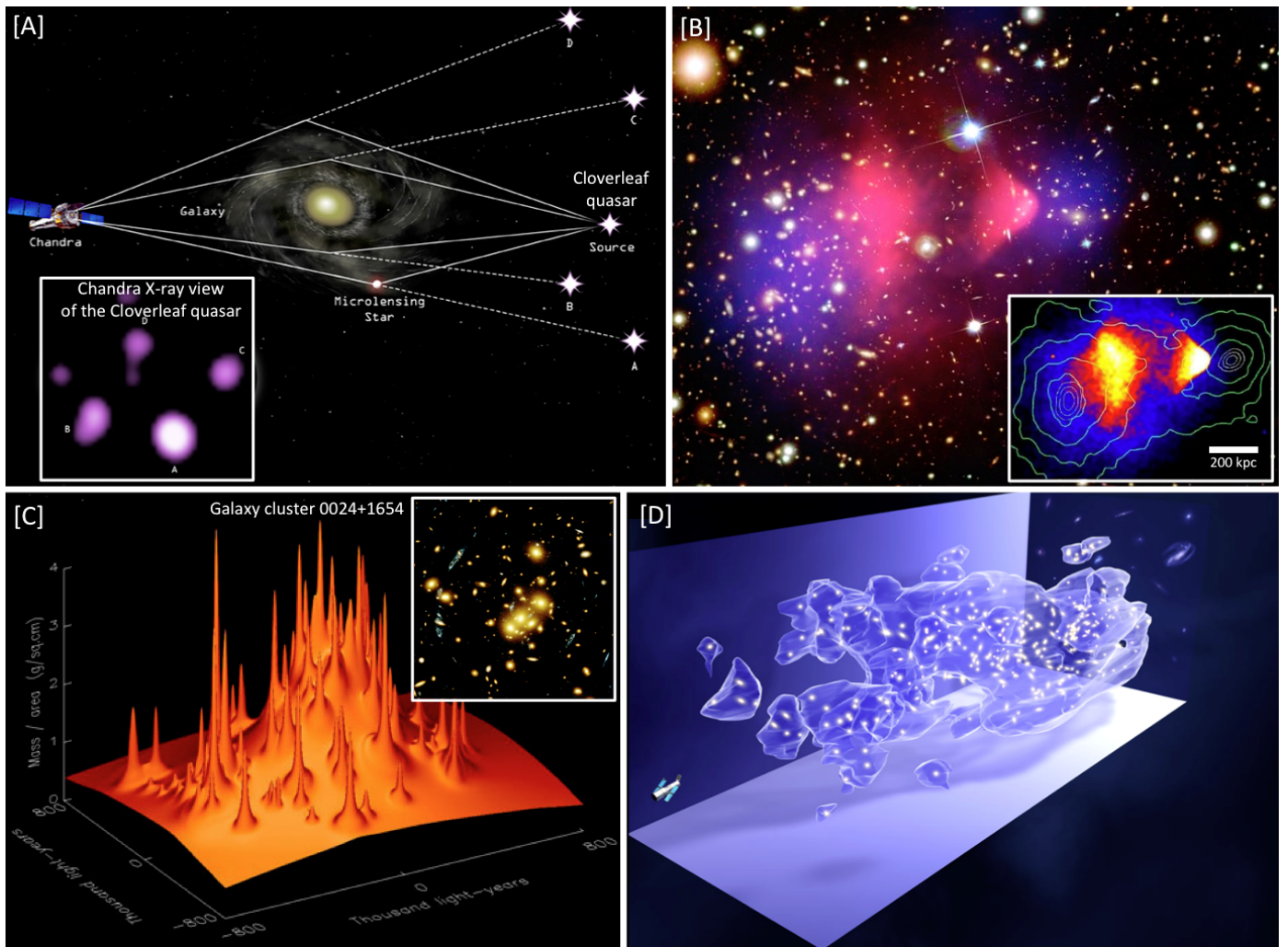


Figure 1.19: [A]: The Cloverleaf quasar is a single object whose image has been reproduced four times in a cloverleaf-like arrangement through gravitational lensing. The gravitational field of one or more foreground galaxies has bent and magnified the light from the quasar to produce the multiple images. [B]: Combined X-ray and optical image of the bullet-cluster nebula. In lines (green, white) contours of dark matter density, from the weak-lensing reconstructions method. The two figures are interpreted as follows. The two clusters passed through each other 150 million years ago. The dark matter clump, revealed by the weak-lensing map, is coincident with the collisionless galaxies and lies ahead of the collisional gas. The gas of the smaller bullet-cluster, creating a bow-shaped shock wave located near the right side of the cluster, lags behind the cluster galaxies. [C]: A computer analysis illustration of the affect of gravitational lensing over a single galaxy cluster (0024+1654). The spikes are the mass of individual galaxies. The background hump is a result of the dark matter spread between the galaxies. [D]: 3D map of the evolving distribution of the dark matter reconstructed using gravitational lensing. The distance from the Earth increases from left ($z=0$) to right ($z=1.1$) over a span of 25 Mpc. The clumping of the dark matter becomes more clear, moving right to left across the volume map, from the early universe to the more recent universe. The distribution is calibrated by measuring the cosmological red shift ($0 < z < 1.1$) of the lensing galaxies in the constellation Sextans. The structure spans over more than 25 Mpc. This dark matter map has been formed by Hubble space telescope observations.

but as its reaction typically goes through intermediate states involving heavy SUSY particles, its effective strength becomes of the order of the weak interaction. The lightest supersymmetric particle (LSP) is a Majorana particle, a mixture of SUSY partners of the B , W^0 (i.e.: γ and Z), and neutral Higgs bosons: $\tilde{\chi}_i^0 = (a)\tilde{B} + (b)\tilde{W}^0 + (c)\tilde{H}_d^0 + (d)\tilde{H}_u^0$. If R-parity of SUSY is conserved, the lightest particle is stable. The lightest neutralino $\tilde{\chi}_1^0$ is the prime candidate for the dark matter. Depending on which of the four components are dominant, its reaction rate is different.

1.3.2 Dark energy

As the figure 1.18 shows the 68% of the cosmic energy-matter budget is comprised by the so-called “dark energy”. Dark energy is simply a name of the source of the accelerating expansion of the universe; or (in other words) is the name of an “anti-gravity” effect in universe macro-scales¹. Its true nature is not known yet and definitely SM does not provides any evidences or potential sources for that. The uniform vacuum energy that appears in any quantum field theory (aka the cosmological constant) is the primary suspect, but there is a plethora of models to account for the phenomenon.

Its existence was clarified only by measuring the velocity of far away type Ia supernovae (SNe Ia) and through accumulation of indirect evidences. Figure 1.20 left shows the typical spectrum of a SNe Ia where used to estimate the expansion rate of the universe. Once an SNe Ia has been tagged as that is placed in the Hubble diagram (distance vs redshift “z” relation) which is shown in figure 1.20 middle. The data summarized in this illustration involve the measurement of the redshifts of the distant supernovae. The observed magnitudes are plotted against the redshift parameter z. Note that there are a number of Type Ia supernovae around z=0.6, which with a Hubble constant of 71 km/s/Mpc is a distance of about five billion light years. The fitted curve is laid into the accelerated expansion universe area. The same expansion trend can be seen also at the figure 1.20 right where the data fits an accelerated expanded universe.

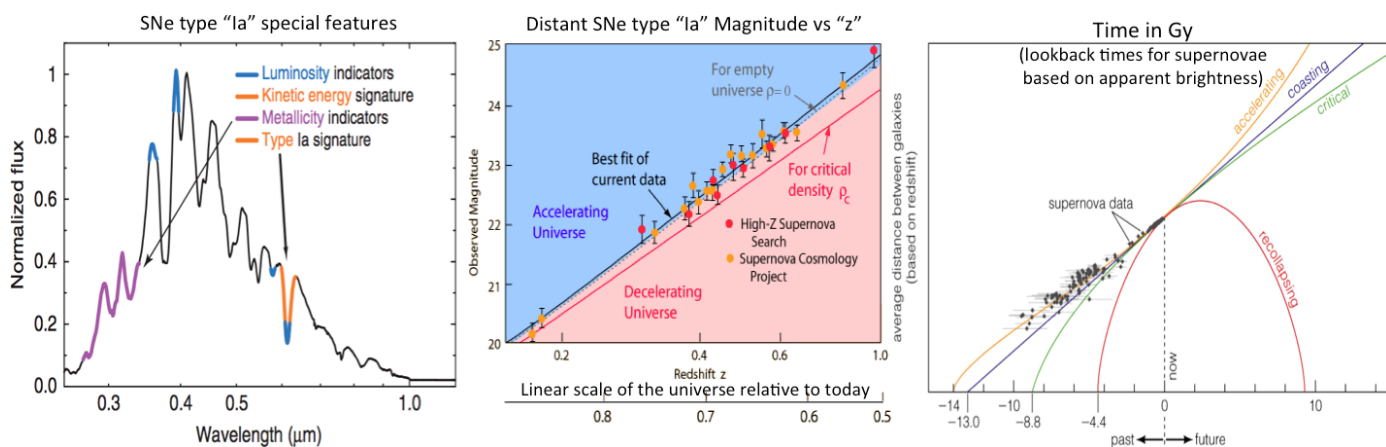


Figure 1.20: Left: Typical spectrum of the SN Ia characterized by the absence of the hydrogen line and existence of the Si line. Luminosity and metallicity indicators are also designated. Middle: effective apparent luminosity/brightness (observed magnitude) versus the redshift z. Curves for critical expansion (red), empty universe (dusted) and the fitted to data (black) which indicates an acceleration. Right: history of cosmic expansion, as measured by the redshift supernovae (black points). Given the energy compositions, time evolution curves can be calculated from the Friedmann’s equation, assuming flat cosmic geometry. Without dark energy, acceleration is always decelerating and the curve is convex upward. With dark energy, the expansion is decelerating in the beginning, turns to acceleration later. The lifetime of the universe estimated by SNe meets the Planck observation to ~ 13.8 Gy.

¹Subsection follows reference [126] §11.1 by Yorikiyo Nagashima.

Chapter 2

Supersymmetry

2.1 Introduction and motivation

Supersymmetry (SUSY) unifies fermions and bosons by introducing a super-partner or s-particle for each of the SM particles¹. The corresponding operator(s) converts fermionic fields to bosonic and vice versa. These two different field types have very different characteristics: fermions respects the Pauli exclusion principle and its number is a conserved quantity.

Supersymmetry is considered a very attractive extension of the SM because it provides:

- a solution to the hierarchy (or naturalness) problem,
- a natural candidate (the LSP) as the main dark matter constituent,
- unification of the strength of the three forces at GUT energy scales,
- it is also an necessary ingredient in attempt towards a unified theory of everything (superstring theory).

SUSY is different from all other symmetries in the sense that its operators are fermionic. Usual quantities and operators such as in the Lagrangians, the four-momentum p_μ , angular momentum $M_{\mu\nu}$ are a Lorentz scalar, vector, or tensor, and internal symmetry operators (such as the isospin operator I) are scalars. (These operators are generally polynomials of field operators). The field operator includes spinors and tensors.

One might also think that there could exist a symmetry operator in the spinor form. The SUSY operator Q_{ai} is exactly that. Here, a denotes the spinor index and i ($1 \leq i \leq N$) denotes the internal degrees of freedom. If one makes the spinor operator act on a bosonic state $|B\rangle$ which is a vacuum state multiplied by a bosonic operator, the product transforms as a spinor; hence, it represents a fermionic state $|F\rangle$. Thus we can write schematically:

$$Q_{ai}|B\rangle \propto |F\rangle, \quad Q_{ai}|F\rangle \propto |B\rangle \quad (2.1)$$

The primary effect of the SUSY operator is thus to bridge bosons with fermions.

In the following we present the main aspects of SUSY theory and SUSY phenomenology (following mainly [126] and [122] respectively). An extensive complete presentation can be found at [122, 130, 116, 17, 24, 123].

2.2 The theory

2.2.1 Building the SUSY concepts in a simplified toy model

In order to illustrate the concepts of SUSY we consider a toy model: a harmonic oscillator consisting of a fermion and a boson. The annihilation(creation) operators are $a(a^\dagger)$ for the fermion and $b(b^\dagger)$ for

¹Subsection follows reference [126] §4.1 by Yorikiyo Nagashima.

the boson. The simplest Hamiltonian¹ in quantum mechanics is expressed as:

$$H = \omega_F a^\dagger a + \omega_B b^\dagger b = \omega_F N_F + \omega_B N_B \quad (2.2)$$

with energy spectrum: $\omega_F n_F + \omega_B n_B$ corresponding to n_F fermions and n_B bosons. Assuming that:

$$\{a, a^\dagger\} = [b, b^\dagger] = 1, \quad (2.3)$$

$$\{a, a\} = \{a^\dagger, a^\dagger\} = [b, b] = [b^\dagger, b^\dagger] = 0 \quad (2.4)$$

Defining the SUSY operator Q, Q^\dagger as follows:

$$Q \equiv b^\dagger a, \quad Q^\dagger \equiv a^\dagger b, \quad (2.5)$$

The SUSY operators satisfy following relations:

$$[Q, H] = (\omega_F - \omega_B)Q, \quad [Q^\dagger, H] = -(\omega_F - \omega_B)Q^\dagger \quad (2.6)$$

Therefore, if $\omega_F = \omega_B = \omega$, Q and Q^\dagger commute with the Hamiltonian and are conserved operators. They also satisfy:

$$[N_B, Q] = [b^\dagger b, b^\dagger a] = b^\dagger a = Q, \quad [N_B, Q^\dagger] = -Q^\dagger \quad (2.7)$$

$$[N_F, Q] = [a^\dagger a, b^\dagger a] = -b^\dagger a = -Q, \quad [N_F, Q^\dagger] = Q^\dagger \quad (2.8)$$

When the operators Q, Q^\dagger act on states, they change the bosonic or fermionic numbers:

$$\begin{aligned} N_B Q |\psi\rangle &= Q N_B |\psi\rangle + Q |\psi\rangle = (n_B + 1)Q |\psi\rangle, \\ N_F Q |\psi\rangle &= Q N_F |\psi\rangle - Q |\psi\rangle = (n_F - 1)Q |\psi\rangle, \\ N_B Q^\dagger |\psi\rangle &= Q N_B |\psi\rangle - Q^\dagger |\psi\rangle = (n_B - 1)Q |\psi\rangle, \\ N_F Q^\dagger |\psi\rangle &= Q N_F |\psi\rangle + Q^\dagger |\psi\rangle = (n_F + 1)Q |\psi\rangle, \end{aligned} \quad (2.9)$$

The relations in 2.9 mean that the operator Q acting on a fermion state increases the boson number by 1 and decreases the fermion number by 1; the effect of Q^\dagger is the opposite. Defining:

$$|n_B, n_F\rangle \equiv \frac{(b^\dagger)^{n_B}}{\sqrt{n_B!}} (a^\dagger)^{n_F} |0\rangle, \quad (2.10)$$

one can easily verify that:

$$\begin{aligned} Q |n_B, n_F\rangle &= \sqrt{n_B + 1} |n_B + 1, n_F - 1\rangle & n_F \neq 0, \\ Q |n_B, n_F\rangle &= 0 & n_F = 0, \\ Q^\dagger |n_B, n_F\rangle &= \sqrt{n_B} |n_B - 1, n_F + 1\rangle & n_B \neq 0 \text{ and } n_F \neq 1, \\ Q^\dagger |n_B, n_F\rangle &= 0 & n_B = 0 \text{ or } n_F \neq 1, \end{aligned} \quad (2.11)$$

Finally, the Hamiltonian of the fermion-boson system can be expressed as follows:

$$\{Q, Q^\dagger\} = \frac{1}{\omega} H, \quad (2.12)$$

We can see that the set of operators Q, Q^\dagger, H constitute a closed algebra. Therefore, if SUSY exists, its operation exchanges a boson with a same mass fermion, and hence there are sets of multiplets whose members consist of both fermions and bosons with equal mass. Equation (2.12) shows, that the operator Q is like a square root of the Hamiltonian, reminiscent of the way in which the Klein-Gordon equation is factorized into a product of two Dirac equations. As the Hamiltonian is the time translation operator, and Q changes the spin of the states, they are both external (space-time) symmetries.

¹Subsection follows reference [126] §4.1.1 by Yorikiyo Nagashima.

An important feature of SUSY is a constraint that it makes the vacuum energy vanish. As $a|0\rangle = b|0\rangle = 0$ and $Q|0\rangle = Q^\dagger|0\rangle = 0$. If one takes vacuum expectation value (VEV) of (2.12), obtains $\langle 0|H|0\rangle = 0$. Where the last is valid if H is the Hamiltonian of the field theory.

The reason for the vanishing VEV is that the zero-point energy, created by the boson is exactly canceled by the zero-point energy created by the fermion. The zero-point energy, which is inherent to QFTs, is generally ignored for the reason that only differences from the reference point are observable. Bosons produce a divergent vacuum energy when summed over all degrees of freedom of harmonic oscillators. Fermions also produce infinite vacuum energy but with the opposite sign. SUSY provides a solid foundation for the vanishing of the vacuum energy.

2.2.2 Field theoretical operators

In the relativistic version of the “toy model”, the SUSY operator should be used in the field theory¹. In order to close the operator algebra we need both commutators and anti-commutators. Lie algebra therefore, has to be extended to include the anti-commutation relations. The notion of conventional numbers also needs to be extended to include anti-commuting numbers known as the “Grassmann numbers”. They are necessary ingredients to complete the algebra in a self-consistent mathematical framework. Here, we first introduce commutation relations among the SUSY operators that appear in the field theory and discuss what they mean.

For simplicity, let us consider a SUSY operator Q_a having spin 1/2 and only one internal degree of freedom. If we treat it as the four-component spinor, it is a Majorana spinor that satisfies the following commutation relations:

$$\begin{aligned} [Q_a, M^{\mu\nu}] &= \frac{i}{2}(\sigma^{\mu\nu} Q)_a \\ [Q_a, P^\mu] &= 0 \\ \{Q_a, \bar{Q}_\beta\} &= 2(\gamma^\mu)_{a\beta} P_\mu \\ \{Q_a, Q_\beta\} &= 0 \\ \{\bar{Q}_a, \bar{Q}_\beta\} &= 0 \end{aligned} \tag{2.13}$$

where $\sigma^{\mu\nu} \equiv (1/2i)[\gamma^\mu, \gamma^\nu]$ and $\bar{Q} \equiv Q^\dagger \gamma^0$ (we omit the index of the internal degree of freedom). The first line shows that the Q_a transforms as a spinor, and the second shows that this is a conserved operator. It also means that Q_a commutes with $P^\mu P_\mu = m^2$, i.e. the operation of Q_a does not change mass of the field: fermions and bosons that belong to the same multiplet must have the same mass.

A multiplet including both fermions and bosons, is called a supermultiplet, and the corresponding fields are called superfields. Each supermultiplet contains an equal number of fermion and boson degrees of freedom. To prove this one considers the operator $P_s \equiv (1)^{2s}$, where s is the spin angular momentum. The operator P_s has eigenvalue +1 for the bosonic state and -1 for the fermionic. The operation of Q or Q^\dagger on a state having the energy-momentum P_μ , changes a fermionic state to a bosonic and vice versa within a supermultiplet. Therefore, the operator P_s anticommutes with the SUSY operator Q or Q^\dagger . The completeness relation can be written as: $\sum_i |i\rangle\langle i| = 1$, with i running through all the states within a given supermultiplet.

Now consider the operator of: $(-1)^{2s} P_\mu$ which has as trace: $p_\mu(n_B - n_F)$. Using the completeness relation and equations (2.13) one can prove that $n_B = n_F$, i.e. there is an equal number of bosons and fermions in any given supermultiplet.

The third line of (2.13) states that a product $Q\bar{Q}$ involves the energy-momentum operator which is the generator of the space-time translation. Coordinate transformations (translation and rotation) such as Lorentz transformation are global, but when localized, their transformation matrices become functions of space-time, which means that the transformation two-component a general coordinate transformation that includes acceleration.

According to the equivalence principle of general relativity, gravity is an inertial force generated by transferring an observer from an inertial frame to an accelerating one. As the SUSY algebra includes

¹Subsection follows reference [126] §4.1.2 by Yorikiyo Nagashima.

the P_μ operator, it implies that a gauged (localized) SUSY algebra includes gravity. Therefore, the gauge theory based on the SUSY, which is referred as supergravity (SUGRA), is a candidate unified theory for all known forces.

2.2.3 Majorana fields

In order to handle the SUSY algebra two-component fermion fields ($\phi^T = (\phi_1, \phi_2)$) are usually used instead of conventional four-component Dirac spinors¹. (Strictly, the ‘‘Weyl spinor’’ applies only to massless field, however the term is used loosely to mean a two-component spinor). The Dirac field is equivalent to a set of two Weyl fields with equal masses just as a complex scalar field is a set of two real scalars.

The Weyl-representation of the γ matrices is defined as follows:

$$\gamma^\mu \equiv \begin{bmatrix} 0 & \sigma^\mu \\ \bar{\sigma}^\mu & 0 \end{bmatrix}, \quad \gamma^5 \equiv \begin{bmatrix} -1 & 0 \\ 0 & 1 \end{bmatrix}, \quad \sigma^\mu \equiv (1, \vec{\sigma}), \quad \bar{\sigma}^\mu = (1, -\vec{\sigma}). \quad (2.14)$$

where $\vec{\sigma}$ stands for the three Pauli-matrices.

$$\phi^{(4)} = \frac{1}{2}(1 - \gamma^5)\psi^{(4)} \equiv P_L\psi^{(4)} \equiv \begin{bmatrix} \phi \\ 0 \end{bmatrix}, \quad \chi^{(4)} = \frac{1}{2}(1 + \gamma^5)\psi^{(4)} \equiv P_R\psi^{(4)} \equiv \begin{bmatrix} 0 \\ \psi \end{bmatrix} \quad (2.15)$$

The index ⁽⁴⁾ is attached for the four-component spinor, ϕ, χ represents chirality \mp (or left- and right-handed particles respectively), which transform as $(1/2, 0)$ and $(0, 1/2)$ in the $SU(2) \times SU(2)$ representation of the Lorentz group.

The four-component Dirac equation can be expressed in terms of the 2-component spinors ϕ, χ of the $\psi^{(4)} = [\phi, \chi]^T$ and $\bar{\psi}^{(4)} = \psi^\dagger \gamma^0 \equiv [\phi^\dagger, \chi^\dagger]$ as follows:

$$\begin{aligned} \mathcal{L}_{Dirac} &\equiv \bar{\psi}^{(4)}(i\gamma^\mu \partial_\mu - m)\psi^{(4)} = (\phi^\dagger, \chi^\dagger) \begin{pmatrix} -m & i(\partial_0 + \vec{\sigma} \cdot \nabla) \\ i(\partial_0 - \vec{\sigma} \cdot \nabla) & -m \end{pmatrix} \begin{pmatrix} \phi \\ \chi \end{pmatrix} \\ &= \phi^\dagger \bar{\sigma}^\mu i \partial_\mu \phi + \chi^\dagger \sigma^\mu i \partial_\mu \chi - m(\phi^\dagger \chi + \chi^\dagger \phi) \end{aligned} \quad (2.16)$$

where is clear that $\phi^\dagger \sigma^\mu \phi$ and $\chi^\dagger \sigma^\mu \chi$ are Lorentz vectors. In the massless limit, the Dirac equation reduces to two equations: $\bar{\sigma}^\mu i \partial_\mu \phi = 0$, and $\sigma^\mu i \partial_\mu \chi = 0$. Which means that: $\vec{\sigma} \cdot \vec{p} \phi = -E \phi$, and $\vec{\sigma} \cdot \vec{p} \chi = E \chi$ confirming that: $\phi(\chi)$ is left(right)-handed.

If we then impose the Majorana conditions we have:

$$\psi^{(4)} = [-C\bar{\psi}^{(4)}]^T, \quad C \equiv \begin{bmatrix} i\sigma_2 & 0 \\ 0 & -i\sigma_2 \end{bmatrix}, \quad (2.17)$$

then, we can write: $\phi = -i\sigma_2 \chi^*$ and: $\chi = i\sigma_2 \phi^*$. The Lorentz transformation of the 2-component spinor is given by a 2×2 complex matrix M (with $\det[M] = 1$) and forms a group referred to as $SL(2, C)$:

$$\phi \rightarrow \phi' \equiv \begin{bmatrix} \phi'_1 \\ \phi'_2 \end{bmatrix} = M \begin{bmatrix} \phi_1 \\ \phi_2 \end{bmatrix} = \begin{bmatrix} M_1^1 & M_1^2 \\ M_2^1 & M_2^2 \end{bmatrix}, \quad \det[M] = 1 \quad \Rightarrow \quad \epsilon^{a\beta} M_a^\gamma M_\beta^\delta = \epsilon^{\gamma\delta} \quad (2.18)$$

where the $\epsilon^{a\beta}$ ($= 0, \pm 1$) is the antisymmetric symbol in the case where the indices run from 1 to 2. The complex conjugate field ϕ^* transforms as $\phi'^* = M^* \phi^*$. The M^* can not be related to M via a similarity transformation (i.e. $M^* = S M S^{-1}$ for some S). The complex conjugate of the left-handed spinor $\phi^* = -i\sigma_2 \chi$ is a right-handed Weyl spinor. Indices of the complex field ϕ^* are denoted with dots: $(\phi^*) \equiv (\bar{\phi})_{\dot{a}}$ to distinguish them from un-dotted indices used for ϕ_a .

It is straight forward to show that: $\epsilon_{a\beta} \epsilon^{\beta\gamma} = \delta_a^\gamma$, $\phi^a = \epsilon^{a\beta} \phi_\beta$, $\phi_a = \epsilon_{a\beta} \phi^\beta$ where summation over same indexes is assumed. Noting that: $(i\sigma_2)^{a\beta} = \epsilon^{a\beta}$, and $(-i\sigma_2)_{a\beta} = \epsilon_{a\beta}$ one defines:

$$(\phi^*) \equiv (\bar{\phi})_{\dot{a}} \quad \rightarrow \quad (i\sigma_2 \phi^*)^{\dot{a}} = \epsilon^{\dot{a}\beta} \bar{\phi}_{\dot{\beta}} = \bar{\phi}^{\dot{a}} \quad (2.19)$$

¹Subsection follows reference [126] §4.2.1 by Yorikiyo Nagashima.

Thus, the four-component Majorana field can be expressed as

$$\psi^{(4)} = \begin{bmatrix} \phi_a \\ \bar{\phi}^{\dot{a}} \end{bmatrix}, \quad (2.20)$$

The transformation matrix for $\bar{\phi}^{\dot{a}}$ is given by:

$$\bar{\phi}^{\dot{a}} \rightarrow \bar{\phi}^{\dot{a}'} = N^{\dot{a}\dot{\beta}} \bar{\phi}^{\dot{\beta}}, \quad N = (i\sigma_2)M^*(-i\sigma_2) \quad (2.21)$$

In such representation, the Dirac spinor is written in terms of two two-component, complex, anti-commuting variables (i.e. Grassmann numbers; details can be found at: [122, 130, 126, 116, 17, 123]) ϕ^a and $(\chi^\dagger)^{\dot{a}}$ with two distinct types of spinor indices.

The scalar products of any two Weyl spinors which are Lorentz invariant are defined as:

$$\begin{aligned} \chi\phi &\equiv \epsilon^{a\beta}\chi_\beta\phi_a = \chi^a\phi_a = -\chi_a\phi^a = \phi^a\chi_a = \phi\chi \\ \bar{\chi}\bar{\phi} &\equiv \epsilon_{\dot{a}\dot{\beta}}\bar{\chi}^{\dot{\beta}}\bar{\phi}^{\dot{a}} = \epsilon^{\dot{a}\dot{\beta}}\bar{\chi}_{\dot{a}}\bar{\phi}_{\dot{\beta}} = \bar{\chi}_{\dot{a}}\bar{\phi}^{\dot{a}} = -\bar{\chi}^{\dot{a}}\bar{\phi}_{\dot{a}} = \bar{\chi}\bar{\phi} \\ \bar{\chi}\bar{\phi} &= \chi_1^*\phi_1^{i*} + \chi_2^*\phi_2^{i*} = (\phi^1\chi_1 + \phi^2\chi_2)^* = (\chi\phi)^* \\ \chi\phi &= (\bar{\chi}\bar{\phi})^* \end{aligned} \quad (2.22)$$

The summation convention is different for dotted and non-dotted variables and that: $\chi_a\phi^a = -\chi^a\phi_a \neq \chi\phi$. The ordering is important for the anti-commuting fields. If $\chi = \phi \equiv \theta$ one can write:

$$\begin{aligned} \theta^a\theta^b &= -\frac{1}{2}\epsilon^{ab}\theta^\gamma\theta_\gamma = -\frac{1}{2}\epsilon^{ab}\theta\theta \\ \theta_a\theta_b &= \frac{1}{2}\epsilon_{ab}\theta\theta \\ \bar{\theta}^{\dot{a}}\bar{\theta}^{\dot{b}} &= \frac{1}{2}\epsilon^{\dot{a}\dot{b}}\bar{\theta}\bar{\theta} = -\frac{1}{2}\epsilon_{\dot{a}\dot{b}}\bar{\theta}_{\dot{\gamma}}\bar{\theta}^{\dot{\gamma}} \\ \bar{\theta}_{\dot{a}}\bar{\theta}_{\dot{b}} &= -\frac{1}{2}\epsilon_{\dot{a}\dot{b}}\bar{\theta}\bar{\theta} \end{aligned} \quad (2.23)$$

Substituting $\chi_a = \bar{\phi}^{\dot{a}}$ and $\chi_{\dot{a}}^\dagger = \phi^a$ in (2.16) the Majorana Lagrangian can be formed:

$$\mathcal{L}_{Majorana} \equiv \frac{1}{2} \left[\bar{\phi}_{\dot{a}} \bar{\sigma}^{\mu\dot{a}\beta} i\partial_\mu \phi_\beta + \phi^a \sigma_{a\dot{\beta}}^\mu i\partial_\mu \bar{\phi}^{\dot{\beta}} - m(\bar{\phi}_{\dot{a}} \bar{\phi}^{\dot{a}} + \phi^a \phi_a) \right] \quad (2.24)$$

The corresponding equations of motion for Majorana fields are as follows:

$$\bar{\sigma}^{\mu\dot{a}\beta} i\partial_\mu \phi_\beta - m\bar{\phi}^{\dot{a}} = 0, \quad \sigma_{a\dot{\beta}}^\mu i\partial_\mu \bar{\phi}^{\dot{\beta}} - m\phi_a = 0 \quad (2.25)$$

These equations show that $\sigma_{a\dot{\beta}}^\mu$ has natural lower indices, whereas $\sigma^{\mu\dot{a}\beta}$ has natural upper indices; one can also see that $\sigma_{a\dot{a}}^\mu$ converts a dotted spinor to an undotted and $\sigma^{\mu\dot{a}a}$ works in opposite way.

That is, the Pauli matrices $\bar{\sigma}^\mu$ convert spinors belonging to (1/2,0) to those in (0,1/2) and vice versa for σ^μ . Thus, both $\bar{\phi}\bar{\sigma}^\mu\phi$ and $\phi\sigma^\mu\bar{\phi}$ are Lorentz contravariant vectors. Similarly, $\phi\sigma^{\mu\nu}\chi$, $\bar{\phi}\bar{\sigma}^{\mu\nu}\bar{\chi}$, are Lorentz tensors where:

$$\sigma^{\mu\nu} = \frac{i}{2}(\sigma^\mu\bar{\sigma}^\nu - \sigma^\nu\bar{\sigma}^\mu), \quad \bar{\sigma}^{\mu\nu} = \frac{i}{2}(\bar{\sigma}^\mu\sigma^\nu - \bar{\sigma}^\nu\sigma^\mu) \quad (2.26)$$

The four-component Dirac spinor can be redefined as:

$$\psi_D^{(4)} = \begin{bmatrix} \phi_a \\ \bar{\chi}^{\dot{a}} \end{bmatrix}, \quad (2.27)$$

where both ϕ, χ are left-handed spinors. Thus, the four-component Dirac spinor is expressed in terms of two left-handed 2-component spinors. In this representation, the Majorana condition is simply $\phi = \chi$.

2.2.4 Operators

The supersymmetric-algebra generators¹, by construction, transform a boson to a fermion or vice versa; hence, they are fermionic operators and carry spin 1/2 (or half-odd integer). There is a theorem which states that all the symmetry operators of the Lagrangian (other than those of the Poincare group) that form a Lie algebra of commutators must be Lorentz scalars. The generators of the Poincare group satisfy the following commutation relations:

$$\begin{aligned}
[M_{\mu\nu}, M_{\rho\sigma}] &= i(g_{\nu\rho}M_{\mu\sigma} - g_{\mu\rho}M_{\nu\sigma} + g_{\mu\sigma}M_{\nu\rho} - g_{\nu\sigma}M_{\mu\rho}) \\
[P_\mu, M_{\rho\sigma}] &= i(g_{\mu\rho}P_\sigma - g_{\mu\sigma}P_\rho) \\
[P_\mu, P_\nu] &= 0
\end{aligned}
\tag{2.28}$$

If we want a fermionic operator to be a part of some Lie algebra, (which is the mathematical framework of the field operators), the Lie algebra must be generalized to contain anti-commutators. Such an extension of the Lie algebra is called a “graded” or “super algebra”. One needs Grassmann numbers to complete the algebra. To write down the extended part, we consider for simplicity a two-component SUSY operator Q_a ($a = 1, 2$). Using the two-component representation, the commutator relations of the extended Lie algebra are defined by:

$$\begin{aligned}
[M^{\mu\nu}, Q_a] &= -\frac{1}{2}(\sigma^{\mu\nu})_{a\beta}Q^\beta \\
[M^{\mu\nu}, \bar{Q}^{\dot{a}}] &= -\frac{1}{2}(\sigma^{\mu\nu})^{\dot{a}\beta}\bar{Q}_\beta \\
[Q_a, P^\mu] &= [\bar{Q}_{\dot{a}}, P^\mu] = 0 \\
\{Q_a, \bar{Q}_{\dot{\beta}}\} &= 2(\sigma^\mu)_{a\dot{\beta}}P_\mu \\
\{Q^a, \bar{Q}^{\dot{\beta}}\} &= 2(\bar{\sigma}^\mu)^{\dot{\beta}a}P_\mu \\
\{Q_a, Q_\beta\} &= \{\bar{Q}_{\dot{a}}, \bar{Q}_{\dot{\beta}}\} = 0
\end{aligned}
\tag{2.29}$$

These equations constitute an algebra that closes itself and hence can serve as generators of the SUSY group. The four-component version of the fourth and fifth is:

$$\{Q^{(4)}, \bar{Q}^{(4)}\} = 2\gamma^\mu P_\mu, \quad Q^{(4)} = [Q_a, \bar{Q}^{\dot{a}}]^T, \quad \bar{Q}^{(4)} = [Q^a, \bar{Q}_{\dot{a}}] = Q^{(4)\dagger}\gamma^0, \quad Q_a^\dagger = \bar{Q}_{\dot{a}}. \tag{2.30}$$

The form of the right-hand side of first and second of (2.29) can be determined considering the dimensionality and the Lorentz tensor structure with appropriate spinor legs.

In appendix B one can find some basic results concerning the SUSY superspace, the chiral superfields finally the invariant action and Lagrangian of SUSY is presented as well. Since we will not use this (quite advance material) further we will not emphasize to that, and we will only let the interest reader to overview it in appendix and of course in excellent available bibliography [122, 130, 116, 17, 126, 24, 123].

2.3 The Minimal Supersymmetric Standard Model and its phenomenology

Supersymmetry implies that the fermion and the boson are not different but the same particles in a different state. If SUSY exists, as a principle of nature, there must exist a supersymmetric partner to every known particle, a fermion to a boson and a boson to a fermion. This “new particle world” is schematically illustrated in figure 2.1 together with the SM particles on the left.

The partner is usually refereed to as supersymmetric particle or “superparticle” or simply “sparticle”. Particles and their partner sparticles belong to the same multiplet referred to as super-multiplet with identical mass; namely, the supersymmetric partners share the same quantum numbers with the

¹Subsection follows reference [126] §4.2.2 by Yorikiyo Nagashima.

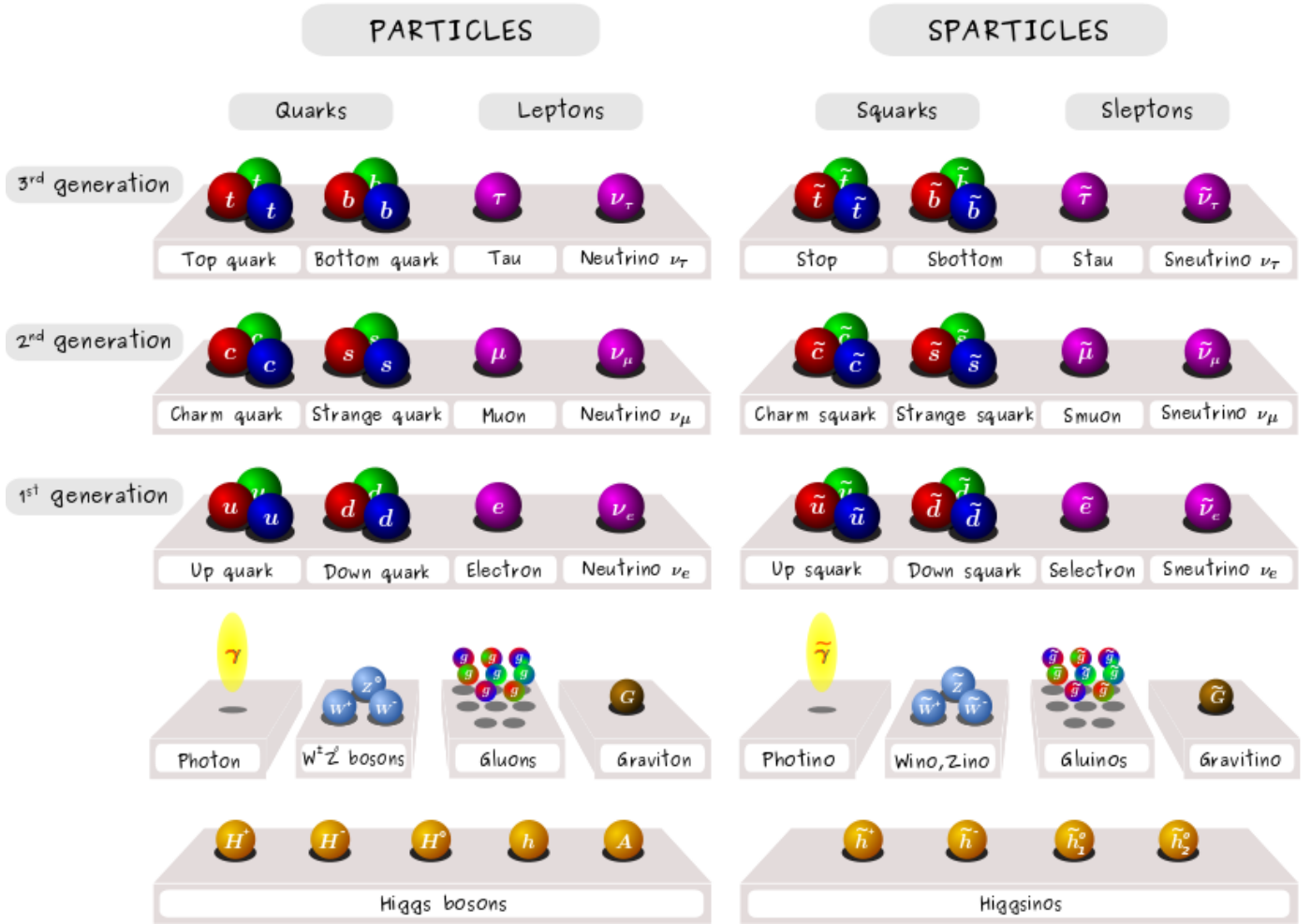


Figure 2.1: The SM Particles and the MSSM s-particles in 1-to-1 correspondence for illustration terms. Sparticles are shown in the so-called physics states, not as mass eigenstates.

SM particles but their spin differs by $1/2$, i.e.: SUSY is a spin-based symmetry of nature. They interact with other particles with the same coupling strength as the SM counterparts.

Experimentally, no degenerate fermion-boson pairs have been observed and, therefore SUSY -if it exists- must be broken, and as a consequence of this, sparticles have different (presumably higher) masses than SM-particles. If the SUSY-breaking is “small”, which corresponds to the case where the mass difference relative to the SM particles is less than a TeV, it still provides a viable solution to the hierarchy problem.

In this section we will briefly discuss a minimal version of SUSY, known as “Minimum Supersymmetric Standard Model” (MSSM), and we will explore some of its phenomenological properties.

2.3.1 Particle spectrum

The square of the SUSY operator vanishes $Q_a^2 = 0$ (shown in (2.29) and therefore the algebra closes within a doublet with helicity h differing by $1/2$ ¹. If a doublet $(h, h + 1/2)$ exists, an anti-doublet $(-h, -h - 1/2)$ must also exist by the CPT-theorem.

The Minimal Supersymmetric Standard Model (MSSM) has:

- spin $1/2$ fermions and their partners sfermions: chiral multiplets $(1/2, 0)$,
- gauge bosons and their partners: gauge multiplets $(1, 1/2)$,

¹Subsection follows reference [126] §5.2.1 by Yorikiyo Nagashima.

List of chiral super-multiplets				
Notation	Spin 0	Spin 1/2	$(SU(3)_C, SU(2)_L, Y)$	Name
Q^a	$(\tilde{u}_L, \tilde{d}_L)$	(u_L, d_L)	$(3, 2, +1/3)$	Squark
\bar{u}	\tilde{u}_R^*	u_R^\dagger	$(3^*, 1, -4/3)$	Squark
\bar{d}	\tilde{d}_R^*	d_R^\dagger	$(3^*, 1, +2/3)$	Squark
L	$(\tilde{\nu}_L, \tilde{e}_L)$	(ν_L, e_L)	$(1, 2, -1)$	Slepton
\bar{e}	\tilde{e}_R^*	e_R^\dagger	$(1, 1, +2)$	Slepton
H_u	$(H_u^+, H_u^0)^b$	$(\tilde{H}_u^+, \tilde{H}_u^0)$	$(1, 2, +1)$	Higgsino
H_d	(H_d^0, H_d^-)	$(\tilde{H}_d^0, \tilde{H}_d^-)$	$(1, 2, -1)$	Higgsino

List of vector super-multiplets			
Spin 1/2	Spin 1	$(SU(3)_C, SU(2)_L, U(1)_Y)$	Name of sparticles
\tilde{B}^a	B	$(1, 1, 0)$	Bino
$\tilde{W}^\pm{}^b$	W^\pm	$(1, 3, 0)$	Wino
$\tilde{\gamma}$	γ		Photino
\tilde{Z}	Z		Zino
\tilde{g}	g	$(8, 1, 0)$	Gluino

Figure 2.2: The list of chiral supermultiplets (top) and vector super-multiplets (bottom).

- Higgs and its partner: (a part of) chiral multiplet $(1/2, 0)$.

The MSSM is the main SUSY framework by which phenomenological studies are carried out. Its Lagrangian consists of the minimal form of equation (B.35). The super-potential is at most cubic in the chiral superfields and contains the mass and the Yukawa interaction terms.

To break SUSY, a soft-SUSY-breaking term is introduced. Soft-breaking means that it does not induce quadratically divergent radiative corrections and that their energy scales remain at the TeV scale. There is no “universally accepted” mechanism to spontaneously break the SUSY; it is instead provided as an external term to the Lagrangian put in by hand. The Lagrangian is then constructed by including all possible supersymmetric interaction terms that satisfy $SU(3) \times SU(2) \times U(1)$ gauge invariance.

The tables in figure 2.2 list the particle content of MSSM. Only first generation is shown for quarks and leptons. The column with the symmetry group lists the representation within the group and hypercharge Y of the SM.

1. In spontaneously broken SUSY, four physical Higgses states appear along with four superpartners, which are denoted as h, H, A, H^\pm and $\tilde{h}, \tilde{H}, \tilde{A}, \tilde{H}^\pm$ respectively. These higgs-states are expected to be mixed with gauginos to give $\tilde{\chi}_i^0$ and $\tilde{\chi}_i^\pm$.
2. Bino, neutral wino, and higgsinos mix to form four neutralinos: $\tilde{\chi}_1^0, \tilde{\chi}_2^0, \tilde{\chi}_3^0, \tilde{\chi}_4^0$, where the lower index orders the mass and the upper stand for the charge of the sparticle.
3. Winos and charged higgsinos mix to form two charginos: $\tilde{\chi}_1^\pm, \tilde{\chi}_2^\pm$ (same as above indexes meaning).
4. SM-fermions carry a chirality (L or R) which transforms differently under the symmetry group $SU(2) \times U(1)$, thus, they carry different quantum numbers. Therefore, they have to belong to different chiral supermultiplets: (\tilde{f}_L, f_L) and (\tilde{f}_R, f_R) . The superpartners \tilde{f}_L and \tilde{f}_R are scalar bosons, so they have no chirality, but are denoted with indexes L, R to distinguish their partners since are expected to appear in mixed mass eigenstates: \tilde{f}_1 and \tilde{f}_2 (where the index now orders the masses).

5. In the SM there is only one Higgs doublet while in SUSY we need at least two: $H_u \equiv [H_u^+, H_u^0]^T$ and $H_d \equiv [H_d^0, H_d^-]^T$. H_u couples the up-type quarks and H_d couples only to down-type quarks and charged leptons. Two Higgs doublets contain eight independent components-fields; three of them are absorbed to give masses to W^\pm , Z^0 , and the remaining five appear as physical particles: h^0, H^0, A, H^\pm . Corresponding to these five Higgses, also five higgsinos are needed in MSSM: $\tilde{h}^0, \tilde{H}^0, \tilde{A}, \tilde{H}^\pm$. Once the $SU(2)_L \times U(1)$ considered broken to $U(1)_{EM}$, mixing among them is introduced. Then \tilde{W}^\pm and \tilde{H}^\pm mix to form charginos, $\tilde{\chi}_1^\pm, \tilde{\chi}_2^\pm$, and $\tilde{B}, \tilde{W}^0, \tilde{h}^0, \tilde{H}^0$ mix to form neutralinos: $\tilde{\chi}_1^0, \tilde{\chi}_2^0, \tilde{\chi}_3^0, \tilde{\chi}_4^0$. The Photino and Zino $\tilde{\gamma}, \tilde{Z}$ are special combinations of the Bino and Wino: \tilde{B}, \tilde{W}^0 .
6. When SUSY breaks down spontaneously, Goldstone bosons associated with the SUSY appear. As the SUSY operator is a spinor, it has spin 1/2 and is referred to as the Goldstino $\tilde{G}_{1/2}$. If SUSY is a global symmetry, this is a physical particle with vanishing mass. In the supergravity (SUGRA), the symmetry is local and the Goldstino is absorbed to give mass to the spin 3/2 gravitino. However, this is not part of MSSM.
7. Sparticles and SM particles are distinguished by a multiplicative quantum number, called R-parity, which is defined as follows:

$$R \equiv (-1)^{2S+3(B-L)}, \quad S : \text{spin}, \quad B : \text{baryon number}, \quad L : \text{lepton number}. \quad (2.31)$$

All known SM-particles have R-parity $R = +1$, while all the sparticles have $R = -1$. If R-parity is violated (as the R-parity violation models of SUSY (RPV-SUSY) assume), the exchange of sparticles may lead to an unacceptable fast decay of protons. Therefore it is assumed that R-parity is conserved. As a consequence, the sparticles can only be produced in pairs, and the lightest supersymmetric particle (LSP), must be neutral and stable. The LSP is the leading candidate for dark matter since it does not radiate photons and it does not interact strongly.

2.3.2 MSSM interactions

The allowed interactions of the MSSM are dictated by the superpotential terms of equation (B.35). In spontaneous SUSY breaking, the degeneracy of particle-sparticles masses disappears¹. However the interaction coupling strengths does not changes.

Consider the case of a SM interaction of a fermion f with a vector boson V , by a coupling strength g and its corresponding sparticle pair: sfermion \tilde{f} and gaugino \tilde{V} . If we replace the set of fields $(A, \psi, \bar{\psi})$ and $(V_\mu, \lambda, \bar{\lambda})$ in equation (B.32) with the case fields: $(\tilde{f}_a, f_a, \bar{f}_a)$ and $(V^\mu, \tilde{V}, \tilde{V})$ then the interaction term becomes:

$$\mathcal{L}_{interaction}^{SM} = g \bar{f}_a \gamma^\mu f_a V_\mu + [h.c.], \quad \Rightarrow \quad \mathcal{L}_{interaction}^{MSSM} = \sqrt{2} g (\bar{f}_a \tilde{V}) \tilde{f}_a + [h.c.] \quad (2.32)$$

The form and the coupling strength of the sparticle interaction are not affected by the SUSY breaking. Only the masses change. Consequently, if the mass spectrum of the sparticles is known, the production and decay rates can be predicted up to the effects of mixing.

Figure 2.3 shows some examples of interactions vertices in the MSSM. Diagram (1) is the SM-like coupling of the top quark to the neutral complex scalar Higgs boson, (t, \bar{t} has be replaced by the more accurate notation t_L, t_R^\dagger showing the helicity states). In diagram (2), we have the coupling of the left-handed top squark \tilde{t}_L to the neutral higgsino field \tilde{H}_u^0 and right-handed top quark, while in diagram (3) the right-handed top anti-squark field (known either as \tilde{t} or \tilde{t}_R^* depending on taste) couples to \tilde{H}_u^0 and t_L . All these interactions are required to have the same strength y_t .

These couplings are dimensionless and can be modified by the introduction of soft SUSY breaking only through finite (and small) radiative corrections, so this equality of interaction strengths is also a prediction of softly broken supersymmetry. A useful mnemonic rule is that each of diagrams (1),(2),(3) can be obtained from any of the others by changing two of the particles into their superpartners.

¹Subsection follows reference [126] §5.2.2 by Yorikiyo Nagashima.

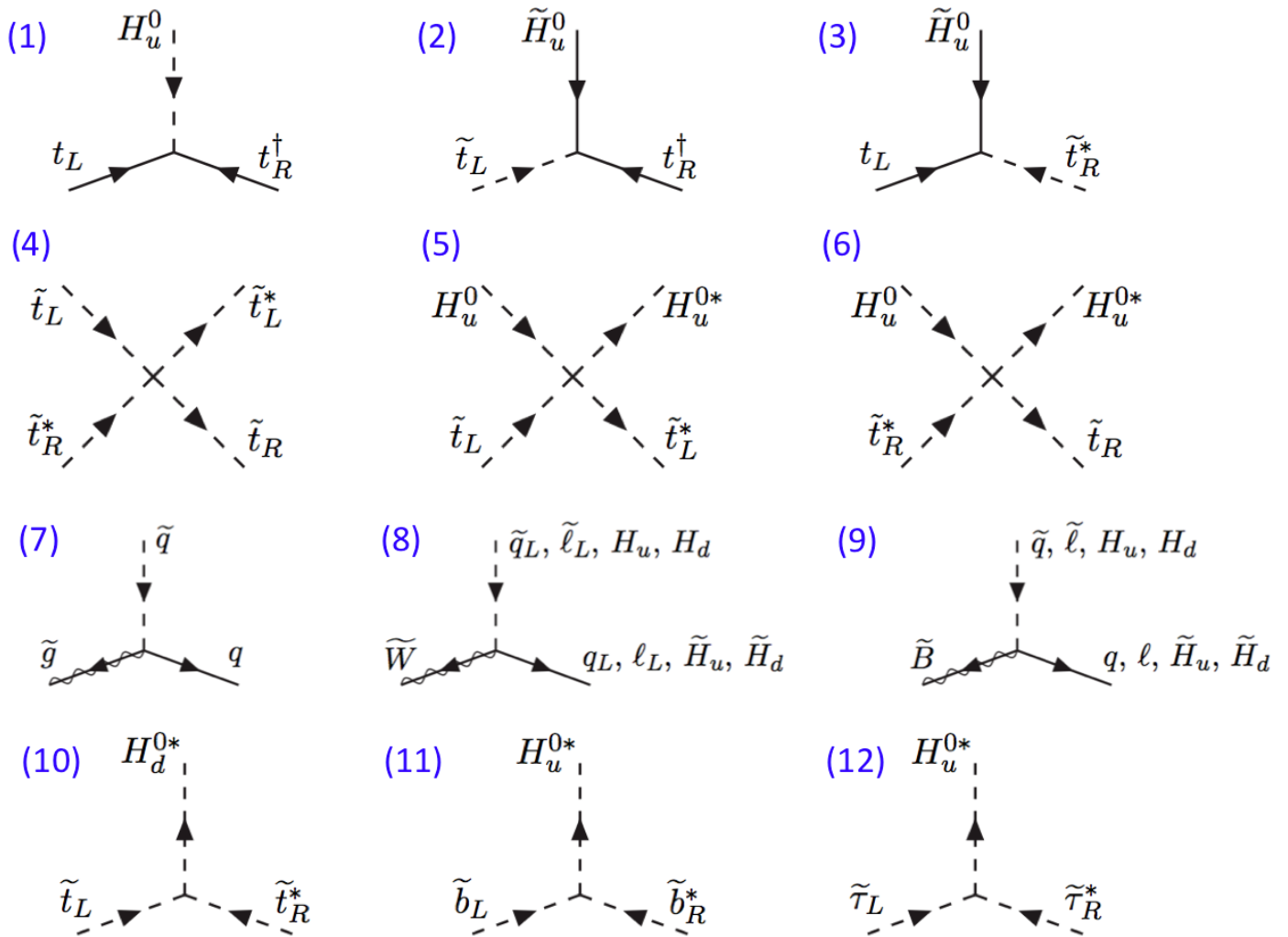


Figure 2.3: Some examples of interaction processes (vertices) in the MSSM frame. (Taken from [122]).

There are also scalar quartic interactions with strength proportional to y_t^2 , as can be seen from diagrams (4),(5),(6) (there are five more such discrete processes). Given that Yukawa couplings are known, the third generation has the dominant contribution in any process.

The gauginos can couple also with squark-quark, slepton-lepton and Higgs-higgsino pairs as illustrated in diagrams (7),(8),(9) for gluino, wino, and bino respectively. Each of the squark-quark-gaugino couplings is given by equation (2.32). For each of these diagrams, there is another diagram with all arrows reversed. Note that the winos only couple to the left-handed squarks and sleptons, and the lepton-slepton, Higgs-higgsino pairs do not couple to the gluino. The bino coupling to each scalar-fermion pair is also proportional to the weak hypercharge Y (as given in table of figure 2.2).

Diagrams (10),(11),(12) show some other couplings which play an important role in determining the mixing of top squarks, bottom squarks, and tau sleptons.

2.3.3 Spontaneous SUSY breaking

There are many ways to break SUSY, with the preferred being, as mentioned above, the so-called “soft SUSY breaking” (SSB), which is applicable to TeV-scale phenomena¹. The MSSM theoretical constraints are too weak and the number of “free parameters” is large standing at 124. The introduction of phenomenological restrictions excludes many of these parameters’ values. However, the MSSM theory is “non viable” in the sense that there is still a very large non-restricted parameter space.

A way to reduce these parameters’ space is to assume a model in which one requires some kind of

¹Subsection follows reference [126] §5.2.4 by Yorikiyo Nagashima.

unification at high energy and embed to the description the gravity. A typical restrictions imposed to MSSM requires that all the scalar particles and all gauginos are unified, having the same common mass values m_0 and m_{12} respectively. This attribute has be shown in figure 1.16 right where all physical masses of MSSM particles meet in GUT-energy scale.

Various models assume that SSB occurs in a hidden sector consisting of particles that are neutral with respect to the SM gauge group. Its effects are transmitted to the MSSM particles (referred as “visible sector”) by some “messengers”. Three theoretical scenarios are popular.

1. The “constrained” MSSM (cMSSM), traditionally also known as “minimal SuperGRAvity” (mSUGRA) in which the symmetry breaking (SB) in the hidden sector is transmitted to the visible sector by gravity.
2. The General Gauge Mediation (GGM) in which the messenger has the quantum numbers of the SM and interacts with the visible sector through ordinary gauge interaction.
3. The Anomaly Mediated Symmetry Breaking (AMSB). Scenario where the source of the SB is the quantum anomaly of the super-Weyl-scale invariance.

A detailed discussion of these SSB scenarios is beyond the scope of this document and the reader is referred to [122, 130, 17, 123].

A common feature of the above three scenarios is to assume some kind of unification in GUTs reducing the number of parameters (conventionally, masses of scalars, gauginos and Yukawa coupling at GUT scales (figure 1.16 right). These models are based on clear physical ideas and have high constraints. They suppresses effectively the large parameter space to a very limited number, which might turn out to be too restrictive.

Alternatively, a phenomenological approach can be applied to study a broader and more comprehensive subset of the MSSM the phenomenological MSSM (pMSSM). In this model, experimental data are used to eliminate parameters. Such constraints reduce the number of free parameters to 19, making it a practical compromise between the full MSSM (124 parameters) and highly constrained CMSSM (5 parameters).

2.3.4 Higgs potential in the MSSM

In the MSSM the scalar Higgs potential V_H comes from three different sources¹.

1. The “D-term”, containing the quartic Higgs interaction, which for the two Higgs fields $H_1=H_d$ and $H_2=H_u$ with $Y = -1$ and $+1$, is given by:

$$V_D \equiv \frac{g_W^2}{8} [4|H_1^\dagger H_2|^2 - 2|H_1|^2|H_2|^2 + (|H_1|^2)^2 + (|H_2|^2)^2] + \frac{g_B^2}{8} (|H_2|^2 - |H_1|^2)^2 \quad (2.33)$$

2. The “F-term” of the superpotential, which can be written as:

$$V_F \equiv \mu^2 (|H_1| + |H_2|)^2 \quad (2.34)$$

3. The soft-breaking term of the Lagrangian, given by:

$$V_{soft} \equiv m_{H_1}^2 H_1^\dagger H_1 + m_{H_2}^2 H_2^\dagger H_2 + B\mu (H_1 \cdot H_2 + h.c.) \quad (2.35)$$

Where $m_{H_1}^2$, $m_{H_2}^2$ are the Higgs masses evolved (via the RGEs) from m_0^2 down to the EW scale (by RGE, shown in figure 1.16 right). The full scalar potential V_H (expanding the Higgs doublets in terms

¹Subsection follows reference [126] §5.2.5 by Yorikiyo Nagashima.

of charged and neutral components and defining the “ μ -terms”) is:

$$\begin{aligned}
H_d \equiv \begin{bmatrix} H_d^1 \\ H_d^2 \end{bmatrix} &= \begin{bmatrix} \phi_1^{0+} \\ -\phi_1^- \end{bmatrix}, \quad H_u \equiv \begin{bmatrix} H_u^1 \\ H_u^2 \end{bmatrix} = \begin{bmatrix} \phi_2^+ \\ \phi_2^0 \end{bmatrix}, \quad \mu_1^2 \equiv |\mu|^2 + m_{H_1}^2, \quad \mu_2^2 \equiv |\mu|^2 + m_{H_2}^2, \quad \mu_3^2 \equiv -B\mu \\
V_H &= \mu_1^2(|\phi_1^0|^2 + |\phi_1^-|^2) + \mu_2^2(|\phi_2^0|^2 + |\phi_2^+|^2) - \mu_3^2(\phi_1^- \phi_2^+ + \phi_1^{-\dagger} \phi_2^0 + h.c.) \\
&\quad + \frac{g_W^2 + g_B^2}{8} (|\phi_1^0|^2 + |\phi_1^-|^2 + |\phi_2^0|^2 + |\phi_2^+|^2)^2 + \frac{g_W^2}{2} |\phi_1^{0+} \phi_2^+ - \phi_1^- \phi_2^0|^2
\end{aligned} \tag{2.36}$$

In the unification scale, we have $\mu_1^2 = \mu_2^2$ because $m_{H_1}^2 = m_{H_2}^2 = m_0^2$. We require one of the squared Higgs masses turn into negative at the EW-scale.

The conditions necessary to induce SSB are:

- the determinant of the Higgs mass matrix becomes negative: $\mu_1^2 \mu_2^2 - \mu_3^4 < 0$,
- the potential has a lower limit: $\mu_1^2 + \mu_2^2 - 2|\mu_3|^3 > 0$,
- the conditions for Higgs potential to have minimum at the EW-scale: $\partial V_H / \partial \nu_i = 0$, $i=1,2$.

The explicit equations can be found in [122, 130, 126]. We can express these equations using a limited number of parameters. For instance, in mSUGRA (or equivalently in cMSSM), it is customary to use the five parameters:

$$m_0, \quad m_{1/2}, \quad A_0, \quad \tan \beta, \quad \text{sign}[\mu] \tag{2.37}$$

Which (respectively) refers to: common scalar (s)particle mass at GUT scale, common 1/2-spin (s)particle mass at at GUT scale, the two neutral higgs VEV ratio $\tan \beta \equiv \langle 0 | H_u^2 | 0 \rangle / \langle 0 | H_d^1 | 0 \rangle$, and the sign of the potential parameter μ .

All the sparticle masses can be derived from the above parameters as using the RGEs. In order to have spontaneous breakdown of the $SU(2) \times U(1)$, either one of the Higgs masses has to go negative. If the mass of the top quark is large enough, the coupling with the Higgs H_2 is strong. If its value is positive at the SUGRA scale, it can go negative at the EW scale (as demonstrated in figure 1.16 right).

While in the SM, the EW spontaneous symmetry breakdown had to be put in by hand, whereas in SUGRA it can be derived from the SB at the Planck-scale supplemented by the RGEs. This is an excellent attribute of mSUGRA, MSSM and SUSY in general, which strongly motivates new physics. Note, however, that the (squared) mass of the squarks and sleptons should not go negative, because then the baryon and/or lepton number would no longer be conserved.

2.3.5 Soft SUSY breaking

In models that have SUGRA incorporated within them, the process that is responsible for the separation of gravity from other forces also has an effect on the EW symmetry breaking¹.

One can suppose a super-unified symmetry (with SUGRA incorporated) that is broken at some energy scale $M_X \simeq \langle F_S \rangle$, slightly below the Planck scale. The VEV of the “F-field” is $\langle F_S \rangle$ which supposes that breaks the SUSY spontaneously. At this “symmetric” stage, all the coupling constants and masses are unified at common values, and for energy scales $Q < M_X$ they evolve according to the RGEs.

We assume that the SB occurs in a “hidden sector”, which means the breaking affects only the (yet unknown) particles which do not interact neither with the SM particles nor with their superpartners. The assumption is that those particles in the hidden sector and those in the visible sector interact only through gravity. Then, even if the SB occurs at, say, a scale $\sim M_X$ (where M_X is the mass of the unknown “messenger” particle), the symmetry breaking scale is effectively reduced to $\sim 10^{11}$ GeV.

In the following we discuss only mSUGRA with simplest assumptions. We can identify chiral superfields that include SM particles. They are as follows:

$$SU(2) \text{ doublets} : \hat{Q}_i^a, \hat{L}_i^a, \hat{H}_1^a, \hat{H}_2^a, \quad SU(2) \text{ singlets} : \hat{u}_i, \hat{d}_i, \hat{l}_i, \tag{2.38}$$

¹Subsection follows reference [126] §5.3.1 by Yorikiyo Nagashima.

wherever i : generation and a : isospin(u, d). The most general superpotential compatible with gauge invariance, renormalizability, and R-parity conservation is written as (see also (B.35)):

$$W = \sum_{ij=1}^3 [y_u^{ij} \bar{u}_i \hat{Q}_j \cdot \hat{H}_u - y_d^{ij} \bar{d}_i \hat{Q}_j \cdot \hat{H}_d - y_l^{ij} \bar{l}_i \hat{L}_j \cdot \hat{H}_d] + \mu \hat{H}_u \cdot \hat{H}_d, \quad (2.39)$$

where: $y_{u,d,e}^{ij}$ denotes Yukawa couplings among generations. The first three terms are SUSY generalization of the Yukawa interactions in the SM, while the last is a SUSY-Higgs mass term. Then the effective ‘‘ultimate’’ SUSY Lagrangian \mathcal{L} can be expressed as a sum of SUSY invariant and SB Lagrangian $\mathcal{L} = \mathcal{L}_{SUSY} + \mathcal{L}_{SSB}$.

$$\mathcal{L}_{SSB} \equiv -(m_0^2 \sum_{i=\tilde{q}, \tilde{l}, H_{1,2}} |\phi_i|^2) - (m_{1/2}^2 \sum_{a=\tilde{B}, \tilde{W}, \tilde{g}} \bar{\lambda}_a \lambda_a) - B\mu H_u \cdot H_d - A_0 W_3 - h.c. \quad (2.40)$$

$$W_3 \equiv \sum_{ij=1}^3 \{y_u^{ij} \tilde{u}_i \tilde{Q}_j \cdot H_u - y_d^{ij} \tilde{d}_i \tilde{Q}_j \cdot H_d - y_l^{ij} \tilde{l}_i \tilde{L}_j \cdot H_d\}. \quad (2.41)$$

The first and the second are the mass-terms for the scalar and gaugino fields. The introduction of these mass terms only for superpartners is the cause for the SB. The third and fourth terms look like the SUSY conserving superpotential in (2.39). In this form, SB is soft (SSB) and does not induce quadratic divergences to scalar squared-mass terms. All the constants are of the TeV scale. A_0 (which is one of the five parameters of cMSSM) and B are parameters with mass dimension. m_0 and m_{12} are the common masses of the chiral scalars and gauginos and $A_0 y_{ijk}$ is the common Yukawa coupling at M_X scale.

In principle, all the SB parameters ($m_{12}, m_0, A_0, B\mu$) can be complex, although they are generally assumed to be real to avoid CP violation in the SUSY sector. As the SB mass scale m_0, m_{12} should not exceed $\sim O(1)$ TeV from a phenomenological point of view, A_0 and B should also be of the same order. In mSUGRA, governed by the renormalization equations, these parameters differ at low energies but are unified at M_X scale increasing its predictive power enormously. At low energies when the EW symmetry breaks at $\lesssim O(1)$ TeV, particles with the same quantum number mix.

2.3.6 Evolution and formation of the masses in the MSSM

The masses of all fermions and bosons in the MSSM can be derived from the cMSSM with the RGEs, given a specific combination of values of the five parameters: $m_0, m_{1/2}, A_0, \tan \beta$ and $sign[\mu]$. We will not get into details and technicalities of the mass formation (these can be found in [122, 130, 116, 17, 123]); however, we will only show some of its results as benchmarks to understand the concepts and the consequences.

We consider the ordering and the definitions of masses¹:

$$M_1 \equiv M_{\tilde{g}} < M_2 \equiv M_{\tilde{W}} < M_3 \equiv M_{\tilde{B}}. \quad (2.42)$$

The wino consists of charged \tilde{W}^\pm and neutral \tilde{W}^0 . When the $SU(2) \times U(1)$ symmetry is broken, the charged gaugino \tilde{W}^\pm mix with the charged higgsinos \tilde{H}^\pm to make two charginos $\tilde{\chi}_1^\pm, \tilde{\chi}_2^\pm$:

$$\mathcal{M}(\tilde{\chi}^\pm) \equiv \begin{bmatrix} M_2 & \sqrt{2}m_W \sin \beta \\ \sqrt{2}m_W \cos \beta & \mu \end{bmatrix}, \quad (2.43)$$

where the off-diagonal element arises from the gauge coupling of the chiral superfields, that is, between wino and higgsino ($g_W \tilde{W}^+ \tilde{H}_u^0 \tilde{H}_d^- \sim \sqrt{2}m_W \sin \beta \tilde{W}^+ \tilde{H}_d^-$).

The mass matrix is not symmetric. However, the product of $\mathcal{M}(\tilde{\chi}^\pm) \mathcal{M}(\tilde{\chi}^\pm)^T$ is symmetric. Therefore, the mass-squared eigenvalues can be obtained by diagonalizing this product which leads to the following mass eigenvalues:

$$m^2(\tilde{\chi}_{1,2}^\pm) = \frac{1}{2} [M_2^2 + \mu^2 + 2m_W^2 \mp \{ (M_2^2 + \mu^2 + 2m_W^2)^2 - 4(\mu M_2 - m_W^2 \sin 2\beta)^2 \}^{1/2}]. \quad (2.44)$$

¹Subsection follows reference [126] §5.3.2 by Yorikiyo Nagashima.

Similarly, the neutral members, bino and wino: \tilde{B}, \tilde{W}^0 , and the higgsinos \tilde{h}^0, \tilde{H}^0 , mix to constitute four neutralinos. One has to diagonalize the mass matrix of the flavor eigenstates to obtain the masses of the neutralinos $\tilde{\chi}_{1,2,3,4}^0$. They are the eigenstates of the symmetric mass matrix:

$$\mathcal{M}(\tilde{\chi}^0) \equiv \begin{bmatrix} M_1 & 0 & -\cos\beta \sin\theta_W m_Z & \sin\beta \sin\theta_W m_Z \\ 0 & M_2 & \cos\beta \cos\theta_W m_Z & -\sin\beta \cos\theta_W m_Z \\ -\cos\beta \sin\theta_W m_Z & \cos\beta \cos\theta_W m_Z & 0 & -\mu \\ \sin\beta \sin\theta_W m_Z & -\sin\beta \cos\theta_W m_Z & -\mu & 0 \end{bmatrix}. \quad (2.45)$$

The exact solutions are not presented here, are complicate and can be found in [122, 130, 17, 123, 126]. Note that the diagonal matrix may have negative or complex-valued elements. If that is true, the physical masses are the absolute values of the corresponding elements. Also should be noted that μ must be nonzero. If $\mu=0$, the determinant of (2.45) vanishes and so the lightest neutralino must be massless (this has been excluded by searches for an excess of invisible Z^0 decays). Some examples of special (extreme) cases of masses combination and dominant flavor-component in mixing are as follows [126]:

- if: $M_1, M_2 \ll m_Z, |\mu| \rightarrow \tilde{\chi}_1^0 \sim \tilde{\gamma}$ (LSP photino-like),
- if: $M_1, M_Z \ll M_2, |\mu| \rightarrow \tilde{\chi}_1^0 \sim \tilde{B}$, (LSP bino-like)
- if: $M_2, M_Z \ll M_1, |\mu| \rightarrow \tilde{\chi}_1^0 \sim \tilde{W}^0, \tilde{\chi}_1^\pm \sim \tilde{W}^\pm$ (LSP wino-like),
- if: $|\mu|, M_Z \ll M_1, M_2 \rightarrow \tilde{\chi}_1^0 \sim \tilde{h}^0, \tilde{\chi}_2^0 \sim \tilde{H}^0, \tilde{\chi}_1^\pm \sim \tilde{H}^\pm$ (LSP higgsino-like).

Figure 2.4 shows the case where $M(\tilde{\chi}_1^0)=100$ GeV, $M_1=0.5M_2$ and the ratio μ/M_2 varies. A compression or degeneracy of the $\tilde{\chi}_i^0$ and $\tilde{\chi}_j^\pm$ masses attributed in many scenarios. There are two distinct cases (regions). The first is the “gaugino region”, where $M_1, M_2 < |\mu|$, where the lightest states $\tilde{\chi}_1^0, \tilde{\chi}_1^\pm$ are mainly gauginos, while the heavy neutralinos and charginos are mainly higgsinos. In the second “higgsino region”: $M_1, M_2 > |\mu|$ the situation is reversed.

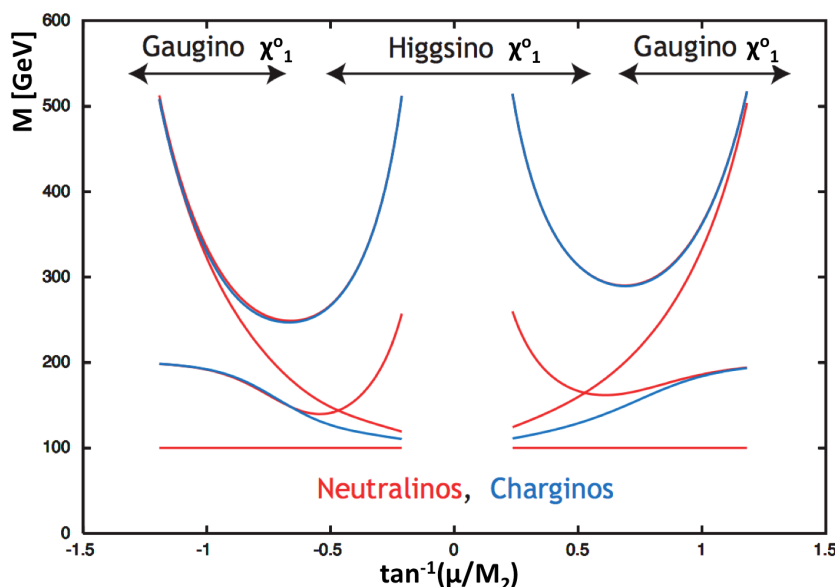


Figure 2.4: Masses of the four neutralinos and two charginos along a line in the SUSY parameter space on which $M(\tilde{\chi}_1^0)=100$ GeV, while the parameter μ moves from large negative to large positive values. The parameter M_1 is set $M_1=0.5M_2$. Note the compression of mass spectrum occurs in a large range of cases. There are four red lines for neutralinos the two for charginos, the most massive curves of both ($\tilde{\chi}_4^0, \tilde{\chi}_2^\pm$) are overlaid. (Taken from [130])

For squarks and sleptons, the mass eigenstates in the MSSM should be obtained by diagonalizing three 6×6 squared-mass matrices for up-type squarks: $(\tilde{u}_L, \tilde{c}_L, \tilde{t}_L, \tilde{u}_R, \tilde{c}_R, \tilde{t}_R)$, down-type squarks:

$(\tilde{d}_L, \tilde{s}_L, \tilde{b}_L, \tilde{d}_R, \tilde{s}_R, \tilde{b}_R)$, and charged sleptons: $(\tilde{e}_L, \tilde{\mu}_L, \tilde{\tau}_L, \tilde{e}_R, \tilde{\mu}_R, \tilde{\tau}_R)$, and one 3×3 matrix for sneutrinos $(\tilde{\nu}_e, \tilde{\nu}_\mu, \tilde{\nu}_\tau)$ there are no right-handed sneutrinos $\tilde{\nu}_R$ in the MSSM.

Most of these mixing angles are predicted to be very small (this come from a general hypothesis of flavor-blind soft parameters). Therefore, the first and second generations are almost degenerate, where the third family of squarks and sleptons can have very different masses (but the squarks are generally heavier than sleptons).

We also deduce (from the exact RGEs products) that $m(\tilde{f}_L) > m(\tilde{f}_R)$ because the SU(2) gauginos discriminate one from the other. If m_0 is very small, all the scalar particles are light. Within multiplets, one can deduce that $m(\tilde{\ell}_L)^2 = m(\tilde{\nu}_\ell)^2 - m_W^2 \cos 2\beta$. For $\tan \beta > 1$ or $\cos 2\beta < 0$, which is phenomenologically preferred.

So far we have neglect the left-right mixing effect among the same generation sfermions. The mixing is induced by the Yukawa couplings (mediated by the Higgs and its strength is proportional to the mass); hence, it can be neglected for the first and second generations. The mass eigenstates of top-squarks (called stops): \tilde{t}_1, \tilde{t}_2 can be obtained by diagonalizing the mass matrix expressed in \tilde{t}_L, \tilde{t}_R base [126, 122]:

$$\tilde{m}^2(\tilde{t}) \equiv \begin{bmatrix} \tilde{m}^2(\tilde{t}_L) & m_t(A_t - \mu^* \cot \beta) \\ m_t(A_t - \mu \cot \beta) & \tilde{m}^2(\tilde{t}_R) \end{bmatrix}, \quad \tilde{m}^2(\tilde{b}) \equiv \begin{bmatrix} \tilde{m}^2(\tilde{b}_L) & m_b(A_b - \mu^* \cot \beta) \\ m_b(A_b - \mu \cot \beta) & \tilde{m}^2(\tilde{b}_R) \end{bmatrix}. \quad (2.46)$$

The off-diagonal part of the first matrix comes from SUSY invariant contribution: $H_d \tilde{t}_L \tilde{t}_R^* \sim \nu_1 \mu y_t$ (last term of (B.35) in expression of $W(A)$) and the SB contribution term $H_u \tilde{t}_L \tilde{t}_R^* \sim \nu_2 A_t y_t$ (the first term in (2.40), expression for W_3).

Then, one using the equalities: $m_t = y_t \nu_2$, $\mu_1 = \nu \cos \beta$, and $\nu_2 = \nu \sin \beta$ can derive the mass matrix in (2.46). The soft-couplings $A_{t,b}$ (in (B.35)) are the A_0 parameter of cMSSM for the top or bottom quark, evolved down to the EW-scale. By mixing, the mass splitting between the left- and right-handed stop and sbottom occurs, simultaneously pushing their absolute values down. Especially: $\tilde{m}(\tilde{t}_1) \ll \tilde{m}(\tilde{t}_2) \lesssim \tilde{m}(\tilde{Q}_{1,2})$ and probably (with $\tan \beta \gg 1$): $\tilde{m}(\tilde{b}_1) \ll \tilde{m}(\tilde{b}_2)$ and $\tilde{m}(\tilde{\tau}_1) \ll \tilde{m}(\tilde{\tau}_2)$. Consequently, $\tilde{t}_1, \tilde{\tau}_1$ are most likely the lightest squark and slepton.

The qualitative features of what we has been described are already depicted in figure 1.16 right, which is often used as a benchmark spectrum for analyzing experimental data. The bold lines are the three gaugino masses ($\tilde{g}, \tilde{W}, \tilde{B}$). The light solid lines are the squark masses ($\tilde{q}_L, \tilde{q}_R, \tilde{t}_1, \tilde{t}_2$) and slepton masses ($\tilde{\ell}_L, \tilde{\ell}_R$). The dashed lines represent the Higgs boson masses (\tilde{H}_d, \tilde{H}_u). Because of the large top mass, the mass of the H_u is driven to negative values inducing the spontaneous symmetry breaking at the electroweak scale.

2.3.7 Summary of mass spectra

We can summarize some of the features of cMSSM (mSUGRA) model in the following statements¹. (Gauge Mediated SB, (GMSB), and AMSB models are also compared).

1. The LSP is the neutralino $\tilde{\chi}_1^0$ in mSUGRA (and the gravitino \tilde{G} in GMSB).
2. The gluino \tilde{g} is considerably heavier than charginos and neutralinos. At the EW scale the ratios for mSUGRA (and for GMSB) masses are: $M_3:M_2:M_1 \simeq 6:2:1$.
3. The squarks in first and the second generations is not lighter than 80% of the gluino in the mSUGRA (and $\sim 60\%$ in the simplest GMSB).
4. \tilde{q} is heavier than $\tilde{\ell}$ (because the gluino contribution to the RGEs is large in the evolution of the RGEs).
5. Mixing between L-R squarks is small for the first and second generation because of their small mass (i.e., Yukawa coupling); hence, they are almost degenerate. However, it is large between

¹Subsection follows reference [122] §8.5 by Stephen P. Martin.

\tilde{t}_R and \tilde{t}_L . As a result, the mass eigenstates \tilde{t}_1, \tilde{t}_2 are widely separated pushing the mass value themselves downward. For this reason, \tilde{t}_1 (actually the whole third generation) is considered as the lightest.

6. Generally, the left-handed sfermions \tilde{f}_L are slightly heavier than \tilde{f}_R (because of the wino isospin-dependent correction).
7. The light Higgs h_0 is lighter than 150 GeV, and compatible with the one observed in 125 GeV.

Figure 2.5 shows some scenarios of possible mass spectra in MSSM. Figure 2.6 shows the experimentally excluded area of cMSSM in the two parameters space: $m_0, m_{1/2}$ where the rest three are set as: $\tan\beta = 30$, $A_0 = -2m_0$, $\mu > 0$. An explicit presentation of the MSSM Feynman rules and diagrams can be found at reference [100, 82].

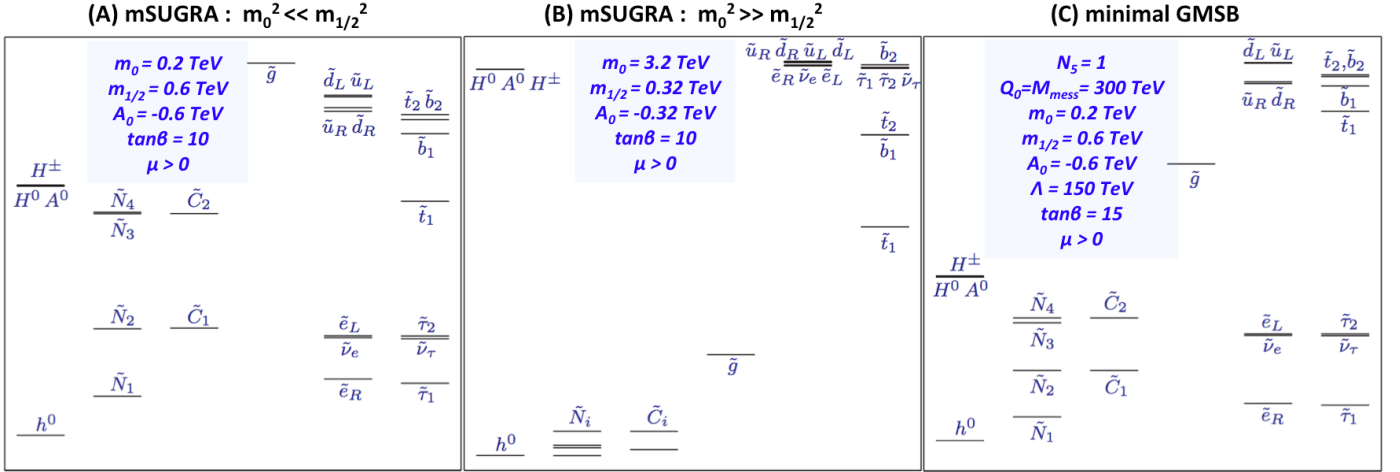


Figure 2.5: Mass spectrum for MSSM in various different SB scenarios (as hyper-titles mentions). Mass scales are not equal and are deliberately omitted. First columns have the five (non-supersymmetric) higgses, followed by sparticles: four neutralinos, two charginos, gluino, 1st, 2nd and 3rd generation sfermions. (Taken from [122]).

2.3.8 Sparticles production, decay and final state signatures at the LHC

Given that the Lagrangian and the couplings of the interactions are known, the production cross sections and the decay channels (branching ratios BR) can be predicted once a the mass spectrum is assumed (i.e. in a given set of the five cMSSM parameters values). The R-parity conservation restricts the production to an even number of sparticles at each process, i.e.: in pairs¹. Figure 2.7 shows the production cross section for various sparticle pairs in p-p collisions at energies $\sqrt{s} = 8$ TeV. Appendix B.4 and figure B.1, presents all possible production modes for sparticles in hadron collisions i.e. via $q\bar{q}, qg, gg$ parton annihilation or scattering. We can summarize these modes to the following list:

$$\begin{aligned}
q\bar{q} &\rightarrow \tilde{\chi}_i^+ \tilde{\chi}_j^-, \tilde{\chi}_i^0 \tilde{\chi}_j^0, \tilde{\chi}_i^\pm \tilde{\chi}_j^\pm, \tilde{\ell}_L^\pm \tilde{\nu}_\ell^{(*)}, & (EW - couplings), \\
gg &\rightarrow \tilde{g}\tilde{g}, \tilde{q}_i \tilde{q}_j^*, & (QCD - couplings), \\
qq &\rightarrow g\tilde{q}_i^*, & (QCD - couplings), \\
q\bar{q} &\rightarrow \tilde{g}\tilde{g}, \tilde{q}_i \tilde{q}_j^*, & (QCD - couplings), \\
qq &\rightarrow \tilde{q}_i \tilde{q}_j, & (QCD - couplings)
\end{aligned} \tag{2.47}$$

The neutralino $\tilde{\chi}_1^0$ is assumed to be the LSP. It has EW interaction, but because of R-parity conservation, the decays chains contain \tilde{q} (or $\tilde{\ell}$) loops in the intermediate states and the cross section is

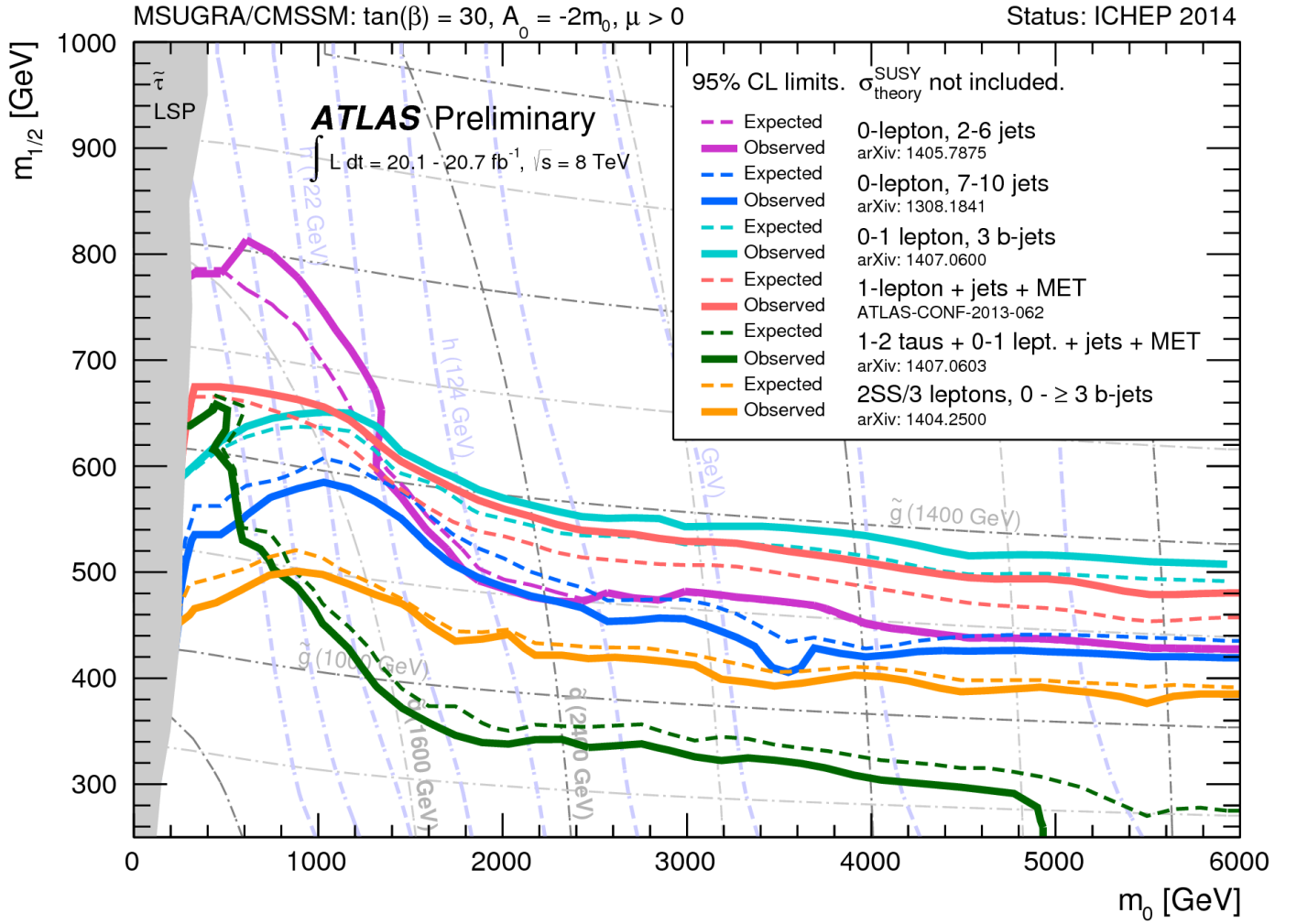


Figure 2.6: The exclusion limits at 95% CL for 8 TeV analyses in the $[m_0, m_{1/2}]$ plane for the mSUGRA/cMSSM model with the remaining parameters set to $\tan \beta = 30, A_0 = -2m_0, \mu > 0$. Part of the model plane accommodates a lightest neutral scalar Higgs boson mass of 125 GeV. Theoretical signal cross section uncertainties are not included in the limits shown. (From ATLAS ICHEP 2014).

proportional $\propto [1/m(\tilde{q})]^4$. As these masses are large, the strength of the reaction two-component of the order of weak processes or less.

The final state products are dictated by the exact mass spectrum chosen/assumed. Each neutralino $\tilde{\chi}_i^0$ and chargino $\tilde{\chi}_i^\pm$ contains at least a small admixture of the electroweak gauginos \tilde{B}, \tilde{W}^0 or \tilde{W}^\pm . So the $\tilde{\chi}_i^0$ and $\tilde{\chi}_i^\pm$ inherit couplings of weak interaction strength to (scalar, fermion) pairs as shown in figure 2.3 diagrams (8) and (9). The possible two-body decay modes for neutralinos and charginos in the R-parity conserved MSSM are:

$$\tilde{\chi}_i^0 \rightarrow Z\tilde{\chi}_j^0, W^\mp\tilde{\chi}_j^\pm, h^0\tilde{\chi}_j^0, \ell\tilde{\ell}, \nu\tilde{\nu}, [A^0\tilde{\chi}_j^0, H^0\tilde{\chi}_j^0, H^\pm\tilde{\chi}_j^\mp, q\tilde{q}], \quad (2.48)$$

$$\tilde{\chi}_i^\pm \rightarrow W^\pm\tilde{\chi}_j^0, Z\tilde{\chi}_j^\pm, h^0\tilde{\chi}_j^\pm, \ell\tilde{\nu}, \nu\tilde{\ell}, [A^0\tilde{\chi}_j^\pm, H^0\tilde{\chi}_j^\pm, H^\pm\tilde{\chi}_j^\pm, q\tilde{q}']. \quad (2.49)$$

Using a generic notation ν, ℓ, q for neutrinos, charged leptons, and quarks. The final states in brackets are the more kinematically implausible ones. For the heavier neutralinos and chargino ($\tilde{\chi}_3^0, \tilde{\chi}_4^0$ and $\tilde{\chi}_2^\pm$), one or more of the 2-body decays is likely to be kinematically allowed. If all of these two-body modes are kinematically forbidden for a given chargino or neutralino, they have three-body decays:

$$\tilde{\chi}_i^0 \rightarrow ff\tilde{\chi}_j^0, ff'\tilde{\chi}_j^\pm, \tilde{\chi}_i^\pm \rightarrow ff'\tilde{\chi}_j^0, \tilde{\chi}_2^\pm \rightarrow ff\tilde{\chi}_1^0, \quad (2.50)$$

through the same gauge bosons as in (2.48), (Higgs scalars, sleptons, and squarks that appeared in the two-body decays, but now are off-shell. Here f is generic notation for a lepton or quark, with f and f'

¹Subsection follows reference [122] (§9 and §10) by Stephen P. Martin.

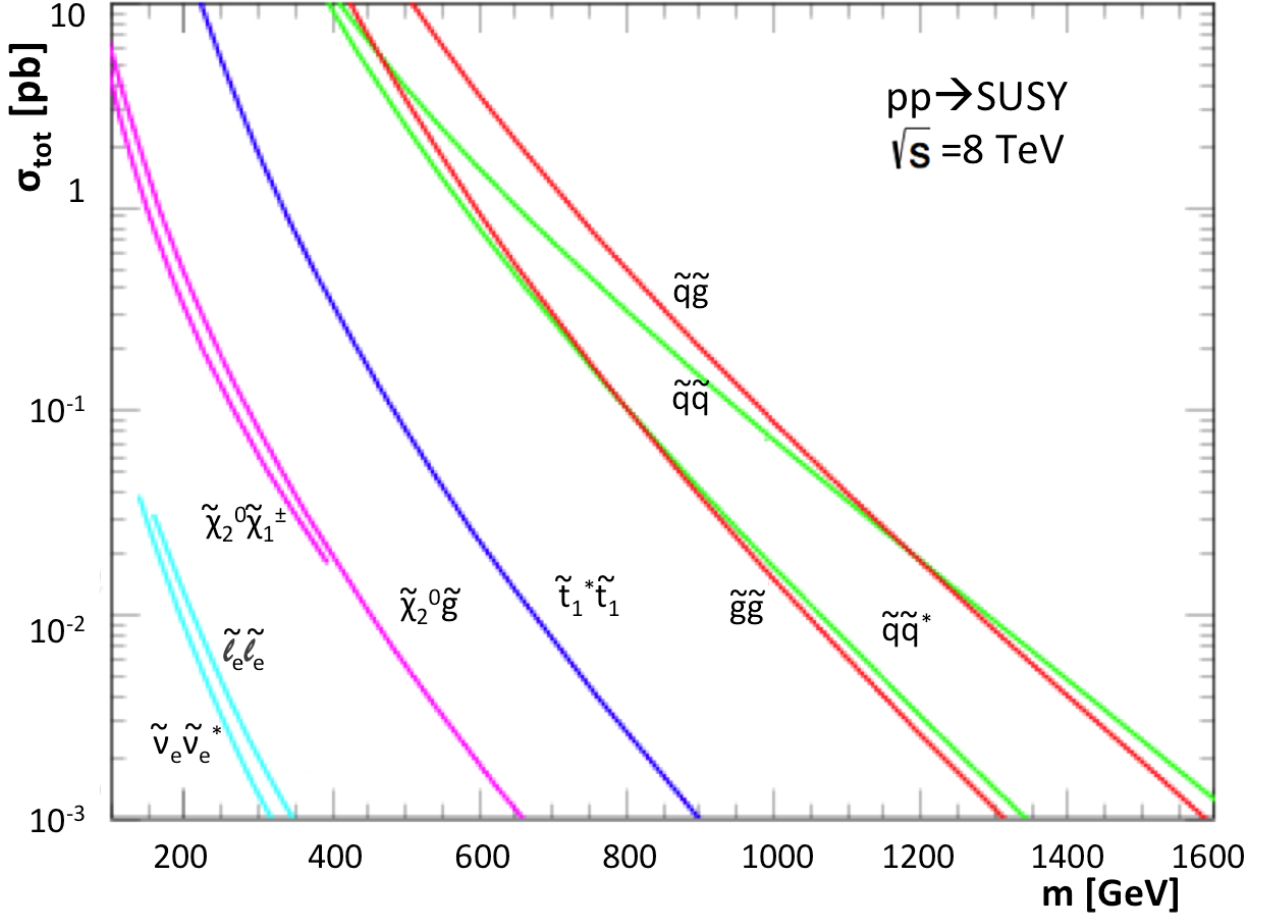


Figure 2.7: The sparticle-pair production cross section at $\sqrt{s}=8$ TeV, p-p collisions as a function of its masses. Hard SUSY production: $\tilde{g}\tilde{g}, \tilde{q}\tilde{q}, \tilde{q}\tilde{q}, \tilde{t}\tilde{t}$ and EW SUSY production $\tilde{q}\tilde{\chi}_{1,2}^0, \tilde{g}\tilde{\chi}_{1,2}^0, \tilde{\chi}_1^\pm\tilde{\chi}_{1,2}^0, \tilde{\ell}_e^\mp\tilde{\ell}_e^\pm$.

distinct members of the same $SU(2)_L$ multiplet (and of course one of the f, f' in each of these decays must be an antifermion). A set of possible sparticle decay modes can be found in figure 2.8, where the first row of diagrams shows the neutralino modes (denoted with \tilde{N}_i), the second line the charginos (denoted with \tilde{C}_i). The intermediate particle in each decay can be either off- or on-shell. In many situations, the particular decays:

$$\tilde{\chi}_1^\pm \rightarrow \ell^\pm \nu \tilde{\chi}_1^0, \quad \tilde{\chi}_2^0 \rightarrow \ell^+ \ell^- \tilde{\chi}_1^0, \quad (2.51)$$

can be important for phenomenology, because the leptons in the final state result in clean signals. These decays are more likely if the intermediate sleptons are relatively light (even if they cannot be on-shell). In particular the (three-body version) of the decays $\tilde{\chi}_2^0 \rightarrow f f' \tilde{\chi}_1^0$ and $\tilde{\chi}_1^\pm \rightarrow f f' \tilde{\chi}_1^0$ throw off-shell sleptons ($\tilde{\nu}, \tilde{\ell}$), are involved in one of the signal signatures that the current document analysis searches for.

Sleptons can have two-body decays into a lepton and a chargino or neutralino, because of their gaugino admixture, as may be seen directly from the couplings (figure 2.3, (8) and (9)). Therefore, the two-body decays:

$$\tilde{\ell} \rightarrow \ell \tilde{\chi}_i^0, \quad \tilde{\ell} \rightarrow \nu \tilde{\chi}_i^\pm, \quad \tilde{\nu} \rightarrow \nu \tilde{\chi}_i^0, \quad \tilde{\nu} \rightarrow \ell \tilde{\chi}_i^\pm, \quad (2.52)$$

can be of weak interaction strength.

In the squark-gluino sector, if the decay $\tilde{q} \rightarrow q\tilde{g}$ is kinematically allowed, it will usually dominate all production processes (figure 2.7), because the $\tilde{q}\tilde{q}\tilde{g}$ vertex (figure 2.3, diagram (7)) has QCD strength. Otherwise, the squarks can decay into a quark plus neutralino or chargino: $\tilde{q} \rightarrow q\tilde{\chi}_i^0$ or $\tilde{q} \rightarrow q'\tilde{\chi}_i^\pm$.

It is possible that the decays $\tilde{t}_1 \rightarrow t\tilde{g}$ and $\tilde{t}_1 \rightarrow t\tilde{\chi}_1^0$ are both kinematically forbidden. If so, then the lighter top-squark may decay only into charginos, by $\tilde{t}_1 \rightarrow b\tilde{\chi}_1^\pm$, or by a three-body decay $\tilde{t}_1 \rightarrow bW\tilde{\chi}_1^0$.

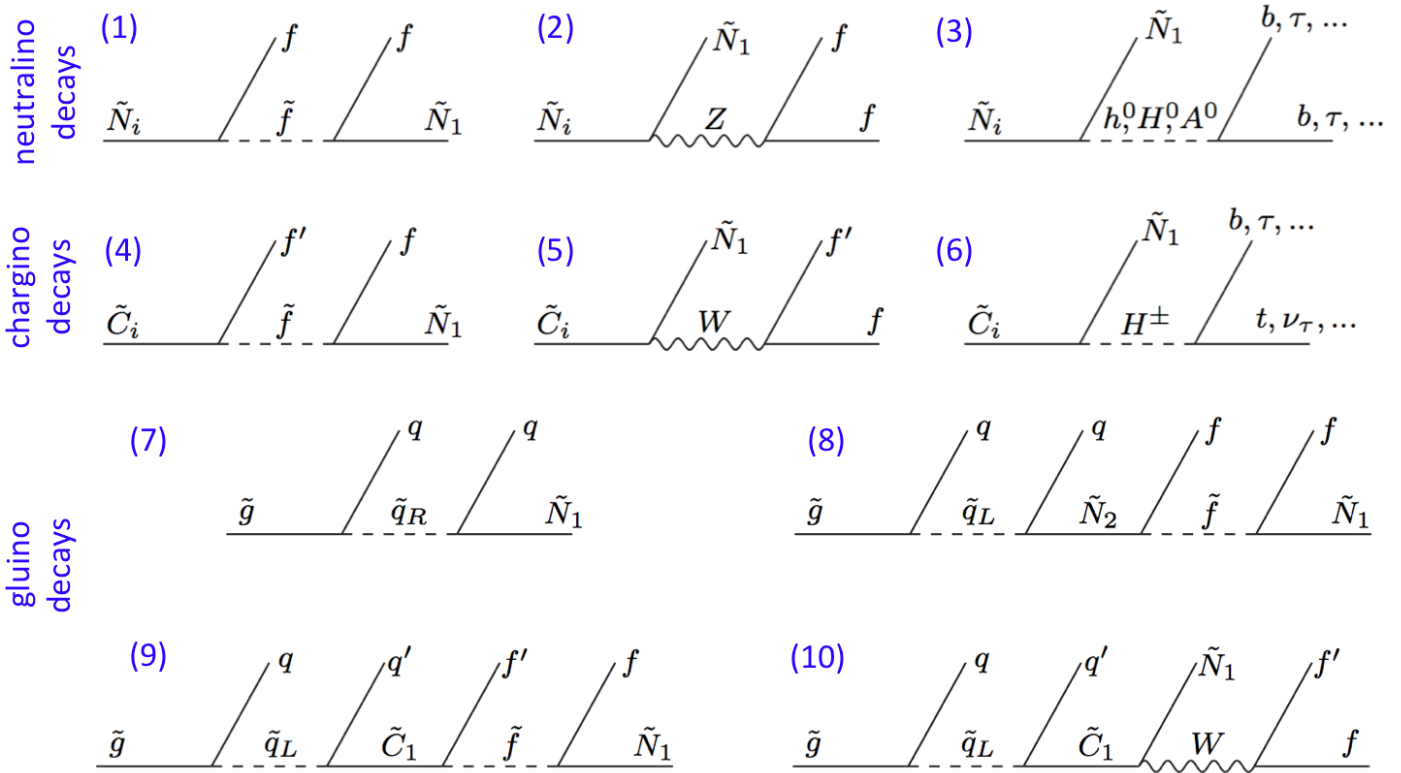


Figure 2.8: A set of possible decay channels (or chains) which sparticles can decay. First and second rows neutralinos and charginos respectively; last two rows, gluino modes. Notice that each of these has in final state the LSP $\equiv \tilde{N}_1 \equiv \tilde{\chi}_0^1$ since we consider the R-parity conservation case. (Taken from [122]).

If even this decay is kinematically closed, then it has only the flavor-suppressed decay to a charm quark, $\tilde{t}_1 \rightarrow c\tilde{\chi}_1^0$, and the four-body decay $\tilde{t}_1 \rightarrow bf'f'\tilde{\chi}_1^0$. Where the last one (four-body stop decay) consists the main signal signature of the following presented search. If indeed the stop is the lightest squark and the $\tilde{q} \rightarrow q\tilde{q}$ is kinematically inaccessible, then the $\tilde{t} \rightarrow t\tilde{\chi}_1^0$ appears as the dominant production (figure 2.7).

The decay of the gluino can only proceed through a squark, either on-shell or virtual. If two-body decays $\tilde{g} \rightarrow q\tilde{q}$ are open, they will dominate (again because the relevant gluino-quark-squark coupling has QCD strength). Since the top and bottom squarks are expected lighter than all of the other squarks, it is quite possible that $\tilde{g} \rightarrow t\tilde{t}_1$ and/or $\tilde{g} \rightarrow b\tilde{b}_1$ are the only available two-body decay mode(s) for the gluino, in which case they will dominate over all others. If instead all of the squarks are heavier than the gluino, then the gluino will decay only through off-shell squarks, so $\tilde{g} \rightarrow qq\tilde{\chi}_i^0$ and $\tilde{g} \rightarrow qq'\tilde{\chi}_i^\pm$. (There can be many competing gluino decay chains, some of the possibilities are shown in figure 2.8 diagrams (7) to (10)).

Over all, each decays of any produced sparticle-pair result in final states with two LSPs, which escape the detectors. The LSPs “absorbs” at least $2m(\tilde{\chi}_1^0)$ of the available energy ($\sqrt{\hat{s}}$) usually in the form of missing energy (\vec{E}_T). But at a hadron collider the actual collision takes place between the hadron constituents. These carry an unknown fraction of hadron energy and thus only the transverse momentum (with respect to the beam z -axis) conservation can be used. Initial p_z of colliding system is always unknown. This restrict the searches to use only the transverse component of missing energy/momentum i.e. \cancel{E}_T . So, in general, the typical observable signal-objects in SUSY production and decay are N_ℓ leptons, N_{jet} jets, and typically high \cancel{E}_T (where both N_ℓ, N_{jet} can be equal to zero).

The SM background, i.e.: known SM processes which end up decaying into the same final states observables, are mainly coming from W and Z boson productions when these decay leptonically, since produces leptons and neutrinos (where the last are identified as \vec{E}_T).

Therefore a search for supersymmetry is a challenge where one tries to discriminate sufficiently the signal from the same final-state SM background. So far, the experimental study of supersymmetry has

unfortunately been confined to setting limits. Appendix B.5 illustrates in summary plots the current experimental limits of sparticles masses (set by ATLAS and CMS experiments) over various sparticles production and decays.

Chapter 3

CERN, LHC and the CMS detector

3.1 Introduction and motivation

Discovering SUSY at the LHC is a very challenging task, even within the restricted framework of the MSSM discussed in previous chapter.

- Every corner of the parameter space needs to be covered, including all possible decay channels which provide a high number of final states with different mixtures of reconstructed objects (photon, electron, muon, tau, jets, b-jets, missing transverse energy).
- Due to the presence of many weakly interacting sparticles, cross sections are generally significantly smaller, sometimes by orders of magnitude (figure 2.7) with respect to the background SM processes (figure 1.1.10).
- The few signal events are generally located in the tails of kinematic distributions, requiring challenging trigger, powerful and sophisticated discriminating variables, and accurate SM background modeling in a complicated region of phase space.
- In other more exotic (or less natural) SUSY scenarios where R-parity is violated and/or non-prompt decays are possible, the experimental challenge generally shifts to taking the best performance of each sub-detector to improve secondary vertex reconstruction, timing resolution, jet substructure reconstruction, lepton coverage, and much more.

Thus SUSY searches provides an excellent motivation for pushing the detector and analyser capabilities to their best.

3.2 CERN, the organization and the accelerator network

CERN is the acronym of the “Conseil European pour la Recherche Nuclaire” and actually is the European Organization for Nuclear Research. It is based near Geneva extends in both France and Switzerland. It is an 61 years old organization (it was founded in 1954) that begun with 12 founding member states and today counts 22 countries as member-state contributors. CERN’s main operation is to provide the particle accelerators and other infrastructure needed (by the high-energy physics community of Europe) in order to research the fundamental aspects of matter at the sub-nuclei level. During its long lifetime, CERN has been the host of many different experiments (about 140), either in high-energy physics (HEP) probing the properties of nuclei and particles, or developing technology which afterwards is transferred to industry and the wider society. There are many “Nobel-Prize” stories that one can cite to CERN, numerous innovative practices and inventions that have been absorbed by today’s technology (we will not discuss them at all, since this is far beyond our scope).

Currently CERN hosts 26 experiments covering various experimental physics fields (a list of them can be found in appendix G with their basic description). Figure 3.1 shows the member countries of

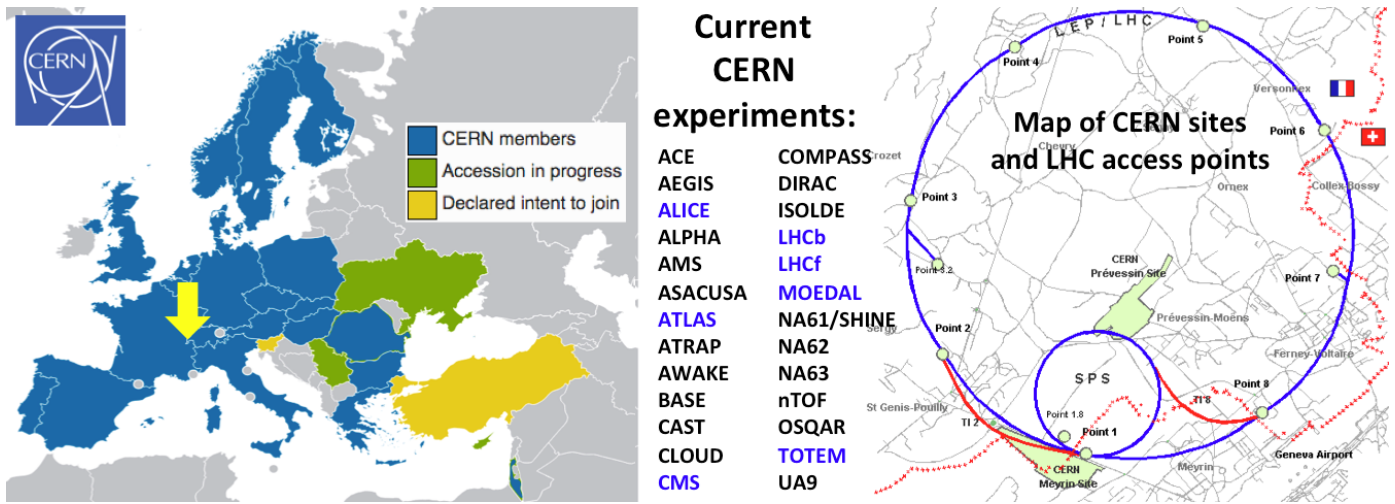


Figure 3.1: The CERN organization located near Geneva in Switzerland with its member states map (layout of its area with the LHC and SPS rings. List of the 26 current CERN’s experiments (with blue the LHC-related experiments).

CERN (left), lists its current 26 experiments (middle), and shows the layout of area (right) where the Large Hadron Collider (LHC), –its greatest machine– is located.

The accelerator complex at CERN is a succession of machines that achieve increasingly higher energies. Each machine injects a proton beam into the next one, which takes over to bring the beam to an even higher energy, and so on. In the LHC (the last element of this chain) each proton beam is accelerated up to 7 TeV, and then, they collide at center of mass energies of $\sqrt{s}=14$ TeV (s is defined in appendix A). Most accelerators in the chain have their own experimental halls, where the beams are used for experiments at lower energies.

We now explain briefly the path of a proton accelerated through the accelerator complex at CERN. (All numbers correspond to the designed performance and are not necessarily those ones of usual or so-called “Run 1” function.) For this purpose we will use the illustration of the CERN acceleration network shown if figure 3.2. Information shown in current subsection has been gathered by [88, 35, 45] and CERN official web pages [44].

- Hydrogen gas molecules (H_2) are taken from a hydrogen bottle. Ionising this gas result in protons are stripd off their electrons: accelerated electrons bombards the molecular-state H_2 (which successively turns to $H_2^+e^-$ and H^+e^-H) producing free protons. These are thus collected in a cathode to form proton beams.
- The low-energy proton beam is accelerated in the LINear ACcelerator (LINAC2) up to 50 MeV.
- Protons are injected from LINAC2 into the circular, 157 m long, Proton Synchrotron Booster (PSB). The proton beam is first distributed into four rings whereby intensities of $\sim 10^{13}$ protons per ring are achieved. The booster accelerates protons up to 1.4 GeV.
- Beam is then fed to the (628 m long) Proton Synchrotron (PS) where it is accelerated up to 25 GeV.
- Protons are then sent to Super Proton Synchrotron (SPS), underground 6.9 km accelerator, where they are accelerated to 450 GeV.
- They are finally transferred to the LHC in both clockwise and anticlockwise directions. The filling time is 4’20’’ per LHC ring, where protons are accelerated for 20’ to 7 TeV.

Beams will circulate for many hours (~ 8 h) inside the LHC beam pipes under normal operating conditions. Protons arrive at the LHC in bunches, which are prepared in the smaller machines (these

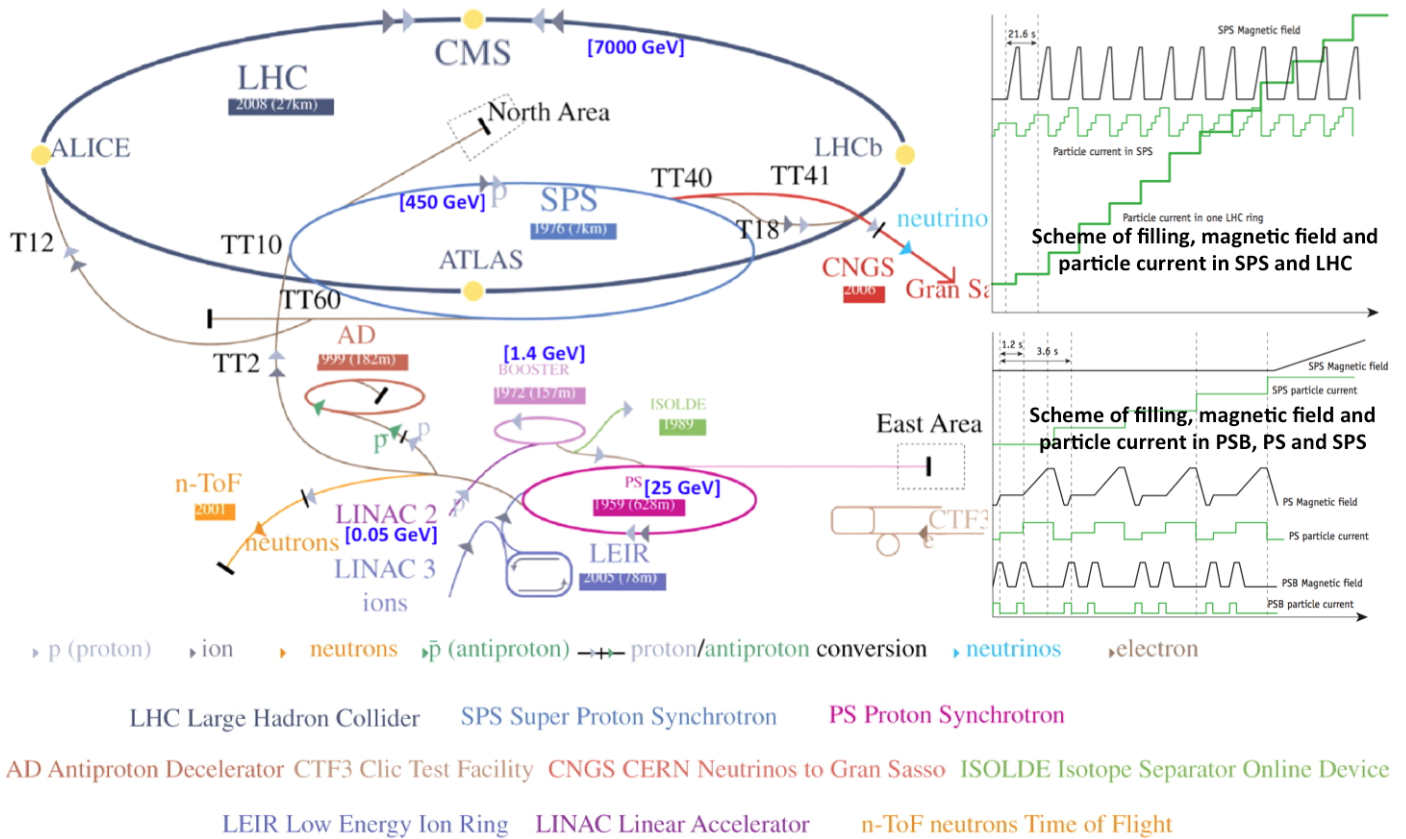


Figure 3.2: The CERN accelerator network which is followed by protons towards the LHC. Small arrows show the paths each particle (colored differently) follows. On the right: particle current (green) and the magnet-field (black) versus time for all accelerating devices (y-axis: arbitrary units).

procedures will be discussed in more detail in subsections 3.3.2 and 3.3.3). For a complete scheme of beam filling, magnetic fields imposed and particle currents induced in each accelerator figure 3.2 illustrates these quantities versus time in arbitrary units.

In addition, the accelerator complex also accelerates (and collides) lead ions. Lead ions are produced from a highly purified lead sample, heated to a temperature of about 500°C . The lead vapour is ionized by an electron current. Many different charge states are produced with a maximum around Pb^{29+} . These ions are selected and accelerated to 4.2 MeV/n (energy per nucleon) before passing through a carbon foil, which strips most of them to Pb^{54+} . The Pb^{54+} beam is accumulated, then accelerated to 72 MeV/n in the (78 m long) Low Energy Ion Ring (LEIR), which transfers them to the PS. The protons' path is followed. The PS accelerates the ion beam up to 5.9 GeV/n and sends it to the SPS after first passing it through a second foil where it is fully stripped to Pb^{82+} . The SPS accelerates it to 177 GeV/n then sends it to the LHC, which accelerates it up to 2.76 TeV/n per beam which is the final energy of each beam in the following collision.

3.3 The Large Hadron Collider

3.3.1 Introduction and motivation for a TeV machine

There are two primary objectives behind the realization of the LHC project:

- The discovery (or exclusion) of the long-sought Higgs boson in the full mass range of $[114, \sim 1000] \text{ GeV}$.
- The observation of physics beyond the SM. As explained previously the most attractive SM extension: SUSY, in its “natural” scenario, predicts sparticle pairs produced with masses down

to EW scale or at about ~ 1 TeV, answering both to hierarchy problem and the dark matter mystery.

For both of these goals, a TeV machine was necessary. In the case of an e^+e^- collider, the needed \sqrt{s} energy should only exceeds the energy or the potentially-existing (s)particles masses; therefore a machine at 1 (or 2,3) TeV would be sufficient. Unfortunately, the energy loss per turn for electron beam because would be prohibitively large. In case of hadron collisions, both the pp -option and the $p\bar{p}$ -option are available. This restriction comes from the fact that these are the only stable charged particles.

A $p\bar{p}$ -machine (such the SPS and Tevatron in the past) comes with restrictively low \bar{p} -beam luminosity due to the difficulties of antiproton production and accumulation. A pp -machine bypasses the beam-intensity limitation, however pays the cost of more rare production rates (of interesting physics) because the later usually occur through the $q\bar{q}$ production mechanism which can be only realized via the sea-antiquarks (in contrast to the valence-antiquark \bar{p} -beam). A disadvantage of hadron collisions with respect to e^+e^- are: the restriction of most physics analysis into the transverse plane of the collisions (since the z-axis partons' momenta are not known), and the intricate collision environment by the rest non primarily participated partons (rich underling-event activity).

Accounting these arguments, one can deduce that a pp -machine requires about an order of magnitude higher energies than the masses of the (s)particles to study produce, ie: ~ 10 TeV. Thus was born a powerful pp-collider with $\sqrt{s}=14$ TeV the LHC.

In the following subsections the main properties and design aspects of LHC are briefly discussed, the information presented is gathered by [35, 88, 2].

3.3.2 The LHC machine aspects and performance

The Large Hadron Collider (LHC) is the largest and most complex scientific undertaking ever attempted. It is built in a circular tunnel 27 km in circumference; the tunnel is buried 50 to 175 m underground CERN, extending both France and Switzerland sites (figure 3.1 right). It is the same one hosted in past LEP (Large Electron-Positron collider). LHC is at the edge of the accelerator based energy frontier as illustrated in the ‘‘Livingston plot’’ in figure 3.3 left.

The LHC is divided into eight arcs and eight straight sections, (figure 3.3 right) which besides the housing of the experiments serve as utility insertions. The experimental insertions are located in points 2 and 8 include the injection systems for the two beams from the SPS, while octants (points 1) and 7 contain collimation systems whereby particles with too large momentum dispersion are cleaned up. The two independent RF-systems (Radio-Frequency Cavities) that provide tangential acceleration to each LHC beam are located in octant (point) 4, while the beams are extracted and dumped into large graphite cylinders via fast-pulsed deflecting (kicker) magnets in octant 6.

Inside the LHC ring, two separate proton beams circulate in opposite directions (figure 3.4) and are accelerated up to their nominal energy of 7 TeV by eight RF-cavities per beam, which operate at 2 MV (accelerating field of 5 MV/m) and a frequency of 400 MHz [88, 35, 2]. The two beams only share the same vacuum pipe right before and after the collisions, through a distance of 126 m in IP2 (IP: Interaction Point) and IP8 where ALICE and LHCb experiments are located respectively, and 140 m in IP1 and IP5 where ATLAS and CMS experiments locations are. The long common beam pipe implies 34 parasitic collision points close to the region of the IPs and to suppress this effect the beams are separated into orbit bumps and brought to collision in a crossing angle at the IPs. The collision parameters as well as the most important nominal parameters of the LHC are summarized in table 3.1.

Within each beam, the protons are packed into up to 2808 filled proton-bunches. Each bunch contains up to $\sim 1.15 \times 10^{11}$ protons (beam intensity) and is nominally separated by $\Delta t \simeq 25$ ns (or $\Delta x = c\Delta t \simeq 7.5$ m) with the preceding/succeeding bunch, thus forming the so-called bunch trains. At peak energy, each bunch is travelling relativistically around the LHC ring with a Lorentz-factor:

$$\gamma_p = E_p/m_p c^2 \simeq 7[TeV]/938.3[MeV] \simeq 7460, \quad \beta_p \equiv v_p/c = \sqrt{1 - 1/\gamma_p^2} \simeq 0.999999991, \quad (3.1)$$

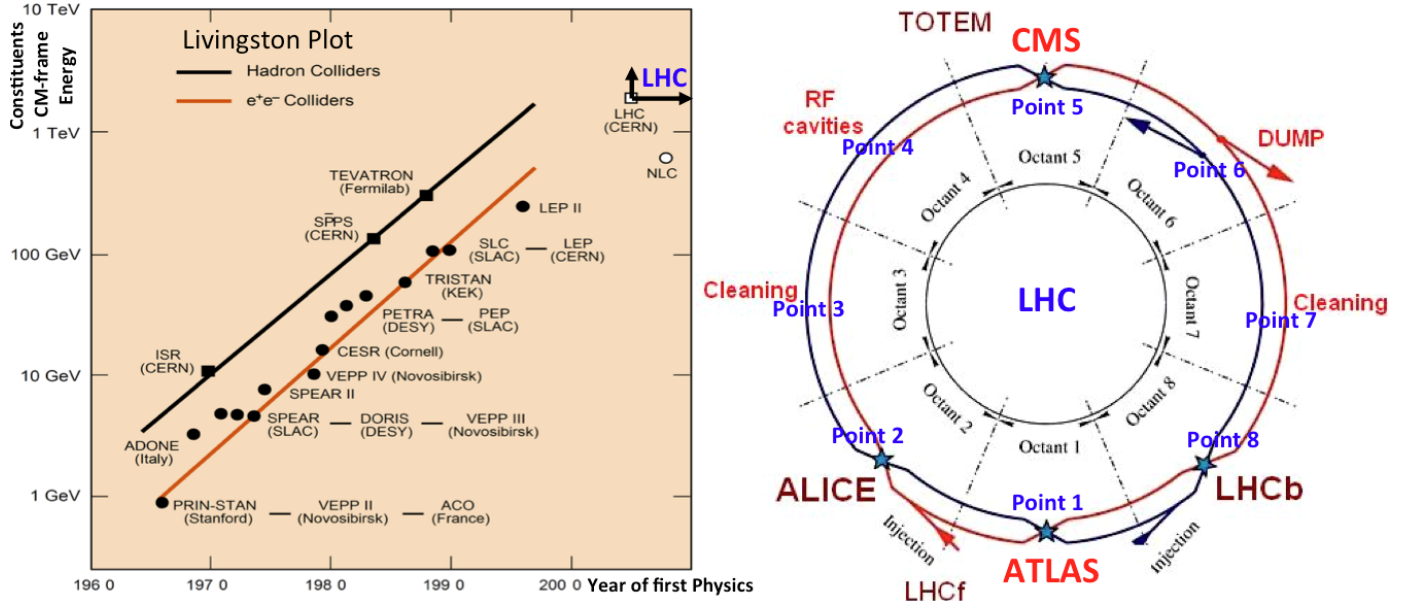


Figure 3.3: Left: the “Livingston plot” showing the energy in the constituent frame of electron-positron (filled circles) and hadron colliders partons (squares). The energy of hadron colliders has here been scaled by factors of 6-10 in accordance with the fact that the proton energy is shared among its partons (i.e. y -axis: $\sqrt{\hat{s}}$). Right: layout of the LHC, showing separation into octants, with beam-1 (beam-2) rotating clockwise (anti-clockwise). Also shows experiments, beam injection points, RF-cavities location, beam cleaning and dump locations (taken from [107, 35]).

which translates to revolution frequency $f_{rev} \simeq 11.246$ kHz or a period of $T_{rev} \simeq 89$ μ s to go around the 26.659 km long (approximately circular) ring of radius $R_{LHC} \simeq 4.3$ km.

In order to keep the beams travelling with momentum p_p in orbit, a series of superconducting dipole magnets is used to provide the required centripetal force which bends properly the beams and force them in circular orbits.

$$F_{Centripetal} = F_{Lorentz} \quad \Rightarrow \quad \frac{p_p^2}{m_p R_{LHC}} = q_p (c \vec{\beta}_p \times \vec{B}) \quad \Rightarrow \quad B[T] = \frac{p_p [TeV]}{0.3 R_{LHC} [km]}. \quad (3.2)$$

By equating the two forces, the magnetic field (\vec{B}) strength that has to be supplied normal to the plane of the orbit can be deduced. Thus, for a proton beam travelling with a momentum of 7 TeV/c, the required magnetic field is ~ 5.4 T. However, since the LHC ring cannot be completely filled with such dipole-magnets, the required bending power is provided by about 1232 superconducting dipole magnets, able to provide a homogeneous magnetic field (directed upwards/towards the center of earth) of 8.33 T into the beam pipe. Figure 3.4 (top-right) illustrates a magnetic-dipole cross section with its operational modules. The magnetic fields formed is also shown in bottom-right.

To achieve the required magnetic field, a two-in-one design strategy was chosen for the dipole magnets, to provide a uniform vertical dipole field over the width of the beam pipes for the two counter-rotating proton beams. The two vacuum pipes which carry the counter-rotating protons are held at a pressure of ~ 100 nPa ($\simeq 10^{-12}$ atm), are 55 mm in diameter and 194 mm apart. The beam vacuum pressure is imperative in order to avoid collisions with gas molecules, and for this reason close to the IP where collisions take place it is kept at even lower pressures, at < 1 nPa. The beam pipes are surrounded by the superconducting coils (as figure 3.4 bottom-left shows) and in order to counter the repulsive forces between the cables which tend to “open” the magnet, the conductors are held in place by stainless steel (non-magnetic) collars. These collars are in turn surrounded by an iron (ferromagnetic) return yoke. All these parts comprise the dipole cold mass and are contained inside a shrinking cylinder vessel. The dipole cold mass is operated at 1.9 K in superfluid He-II state. Thermal insulation is achieved by use of a vacuum vessel and a super-insulating layer. The dipole configuration

Table 3.1: Summary of the main parameters for LHC machine: modules, magnets, RF-cavities, beams and collisions performances. (Selected information from [88, 2, 35]).

Quantity	Value	Unit
Infrastructure modules		
LHC circumference (average radius)	26.659 (~ 4.3)	km
Number of arcs (straight sections)	8×2450 (8×545)	m
Nominal beam energy at injection for protons	0.45	TeV
Nominal beam energy at collision, protons (ions)	7 (2.76)	TeV
Number of magnets (discrete coils in dipoles, quadrupoles...)	9593	
Number of main dipoles/lattice quadrupoles/lattice sextupoles/lattice octupoles	1232 / 392 / 688 / 168	
Stored energy in magnets	~ 11	GJ
Radio Frequency Cavities		
Number of RF-cavities per beam	8	
Main RF System operation	400.8	MHz
Voltage of 400 MHz RF system at 7 TeV	16	MV
Magnetic dipole performance		
Magnetic field at: Injection(0.45TeV)/Nominal(7TeV)/Ultimate operation	0.54 / 8.33 / 9	T
Current at: Injection/Nominal/Ultimate operational field	0.763 / 11.850 / 12.840	kA
Energy density of the LHC magnets	500	kJ/m
Horizontal force at 8.33 T (inner and outer layer)	1.7	MN/m
Force loading 1 m of dipole	400 (35)	tonnes (MN)
Stored energy (both apertures) at nominal (ultimate) field	6.93 (8.11)	MJ
Operating temperature	1.9	K
Distance between aperture axes at 1.9 K	194	mm
Inner coil diameter at 293K	56	mm
Cold mass diameter at 293K	570	mm
Length: coils/cold mass(at 293K)/full with ancillaries	14.3 / 15.2 / 16.5	m
Total dipole mass	~ 27.5	tonnes
Superconducting coils features		
Composition of the superconducting alloy	Ni-Ti	(47Wt%Ti)
Number of strands per cable	36	
Number of Ni-Ti filaments in each strand	6500	
Beam performance		
Minimum distance between bunches	~ 7.5	m
Bunch spacing	25	ns
Design luminosity, protons (ions)	10^{34} (10^{27})	$\text{cm}^{-2}\text{s}^{-2}$
Number of harmonic buckets per beam	35640	
Number of bunches per proton beam	2808	
Number of protons per bunch	1.15×10^{11}	
Total crossing-angle	285	μrad
Proton revolution frequency	11.25	kHz
Pressure in vacuum pipes in dipoles (at IPs)	~ 100 (< 1)	nPa
Bending radius	2803.95	m
Number of turns per second	11245	
Circulating current / beam	0.54	A
Stored beam energy	~ 7360	MJ
Beam lifetime	~ 10	h
Radiated Power per beam (synchrotron radiation)	~ 6	KW
Emittance ϵ_n	3.75	μrad
Beta function β^*	0.55	m
Collision properties		
Events (primary inelastic vertexes) per bunch-crossing	~ 20	
Number of collisions points (IPs)	4	
Average crossing rate	31.6	MHz
Number of collisions per second	$0.6 \cdot 10^9$	
Elastic (inelastic) cross-section	40 (60)	mb
Number of elastic (inelastic) collisions per second	400 (600)	MHz

generates a magnetic field of nominal magnitude 8.33 T, and is opposite in direction for each beam; vertically up in the left-hand beam pipe and vertically down in the right-hand one (figure 3.4).

In order to reach the nominal field strength of 8.33 T, (necessary for stabilising the 7 TeV beams into orbit) a current of 11.850 kA is required. This is achieved by the use of 80 cables, placed in two layers, running to the beam pipe axis and back on the other side forming the coils “hugging” the beam pipes (figure 3.4). These cables house 36 strands of superconducting wire, each strand housing 6500 superconducting filaments of Niobium-Titanium (NbTi). This superconducting coils correspond to $\sim 55\%$ of full LHC budget. The main parameters of dipole magnets are summarised in table 3.1. In addition to sustaining the proton beams in orbit, the stabilisation and focussing of the proton bunches is of paramount importance, otherwise the particles might diverge and be lost. For this purpose, the

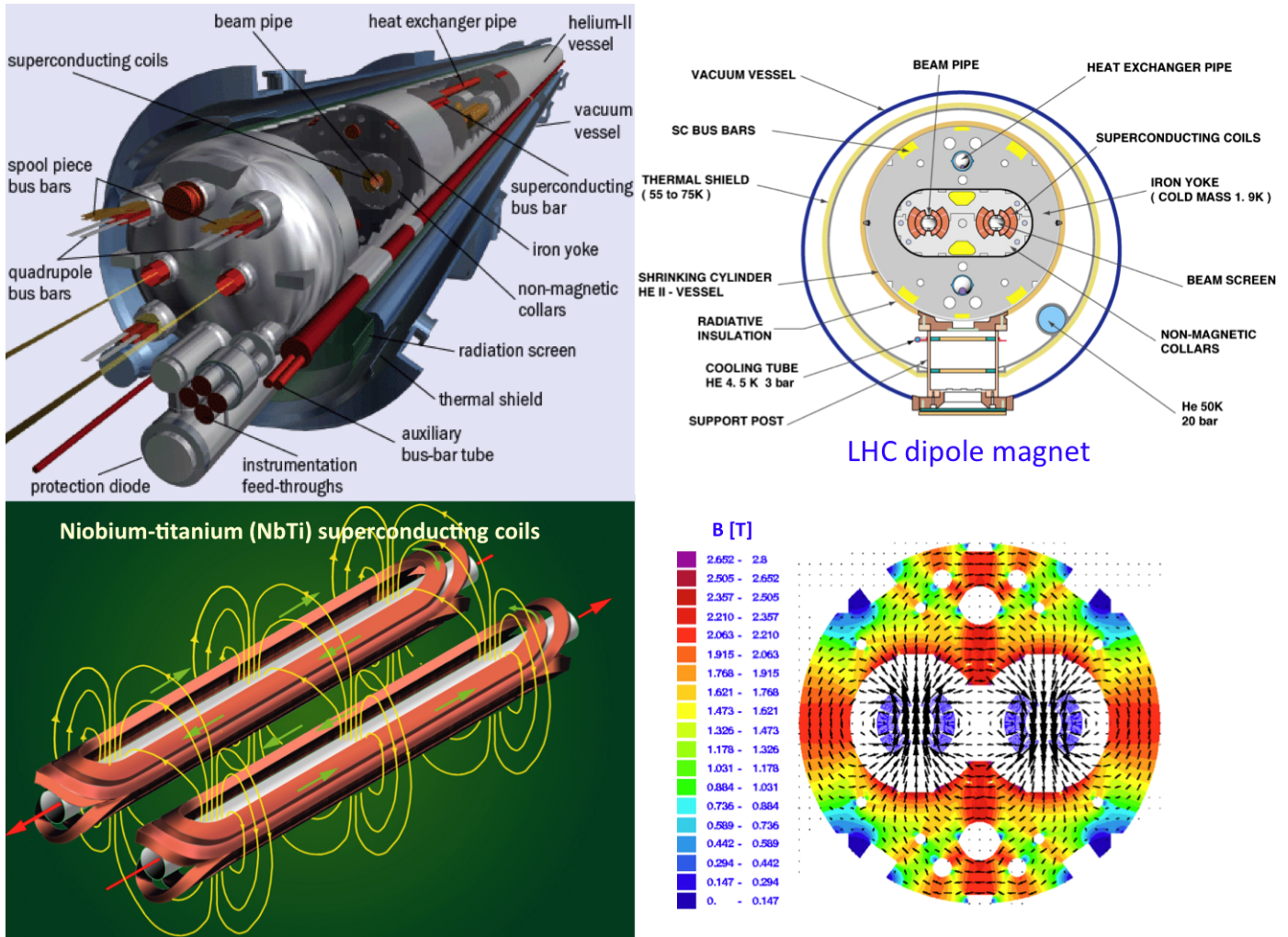


Figure 3.4: The LHC dipole magnet with its operational modules and the niobium-titanium (NbTi) superconducting coils. Cross section of the dipole and induced magnetic field.

LHC is equipped with 392 main quadrupole magnets. These magnets provide magnetic fields that are zero in the beam pipe centre but increase linearly away from it, and can thus be used as vertically focussing and horizontally defocussing, or vice-versa. For this reason, the body of the LHC machine employs alternate quadrupoles with their poles reversed, so that an alternate focussing and defocussing effect is achieved, the net effect being the focussing in both planes. However, this focussing effect on the proton bunches causes oscillations of the particles around the centre of the beam pipes. The number of oscillations in one turn of the machine is known as the “betatron tune” (Q), whose value is carefully tuned to avoid resonance with the betatron motion.

Additionally, within a proton bunch, particles tend to have different energies and hence follow slightly different orbits, which means each requires a different Q -value. The change in focusing with energy is known as the “chromaticity” and it has an adverse effect on the beam, causing instability and tune spread. To counter this, the LHC utilises sextupole magnets which are designed to provide magnetic fields that are zero in the beam pipe centre but increase quadratically away from it. In particular, there are two sextupole families per plane per beam for chromaticity corrections.

Moreover, higher magnetic multipoles are also used to support beam focussing and to compensate for other interactions that the beams suffer along their orbits, including the EM-interactions within the proton bunches, beam interaction with electron clouds from the beam pipe walls and the gravitational force experienced by the protons.

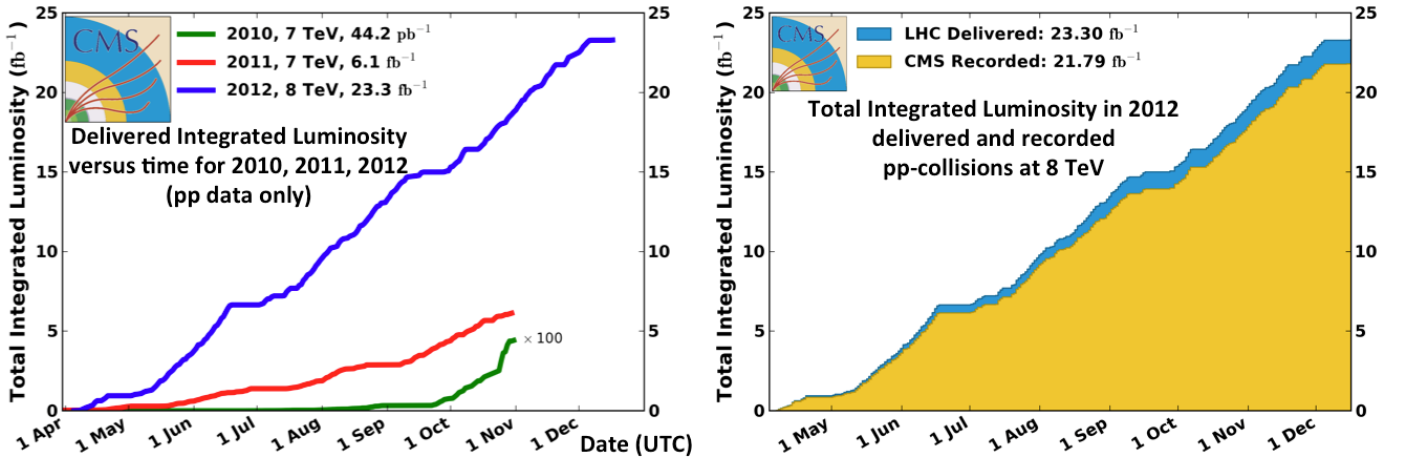


Figure 3.5: The integrated luminosity delivered from the LHC to CMS for three different runs (left), and delivered with recorded luminosities superimposed for the most important (8 TeV) run.

3.3.3 The LHC beams, stability, oscillations, and performance

Protons are tangentially accelerated from 0.45 TeV up to 7 TeV into LHC beam-pipes, by the so-called Radio-Frequency (RF) cavities.

RF-cavities are in synchronisation with both the particle's velocity (or energy) and the bending magnetic field (hence the name synchrotron). These RF-cavities generate a longitudinal oscillating voltage, which the particles see as an accelerating electrical fields.

The standing EM-waves generated inside the resonating RF-cavity capture the incident beam and contain it in what is known as an RF-bucket.

The particles are thus trapped in the RF-voltage and this is what gives bunch-structure to the beam. (The proton bunches are formed from the first level or their circular acceleration i.e.: the PSB.)

Even-though this RF-structure is present only inside the RF-cavities, the RF-buckets can be thought of as virtual positions on the LHC circumference that may or may not contain beam. If the RF-bucket contains a beam, then the beam within the bucket is referred to as a proton-bunch.

Within a given bunch, the protons do not have ideal circular orbits, but instead oscillate in and out of the orbit path in both the horizontal and transverse planes; this is known as "betatron motion".

In an alternating-gradient quadrupole magnet configuration synchrotron like the LHC, the transverse equation of motion for the particles can be approximated as a pseudo-harmonic oscillator with a path-dependent spring constant. This is described by Hills equation:

$$\frac{d^2x(s)}{ds} + K(s), \quad (3.3)$$

where $x(s)$ is the position or displacement from the longitudinal coordinate s (in the beam direction) and $K(s)$ is the varying spring constant. The simplest solution reveals that the single particle transverse motion is described by an oscillatory term analogous to the general solution of simple harmonic motion:

$$x(s) = A\sqrt{\beta[x(s)]} \cos(\phi(s) + \phi_0), \quad (3.4)$$

where A and ϕ_0 are constants connected to the amplitude and phase, respectively, and $\sqrt{\beta[s(x)]}$ is an s -dependent amplitude that modulates the evolution of the transverse motion. The betatron phase advance (μ) over one turn around the LHC ring is defined as the integral of $\beta[s(x)]$ over the closed path:

$$\mu \equiv \oint d\phi(s) = \oint \frac{ds}{\beta[s(x)]} \quad (3.5)$$

The betatron tune(Q), defined as $Q \equiv \mu/2\pi$, is the number of betatron oscillations about the closed path of the LHC ring and it is a carefully adjusted parameter to avoid betatron resonance. Moreover,

at the neighbourhood of an IP the beam optics of the ring is configured to produce a local minimum of the betatron amplitude function: $\beta^*(s)$. This transverse betatron motion of the particles evolves with the longitudinal coordinate s forming an ellipse in: $x(s), dx(s)/ds$ phase-space. For an ensemble of Gaussian-like distributed particles in: $x(s), dx(s)/ds$, the transverse emittance (ϵ_x) is defined as the area of the ellipse containing one standard deviation: $\epsilon_x \equiv \pi\sigma_x/\beta_x(s)$ (with a same expression for the other transverse direction, y). The term σ_x is the projection of the ellipse at x -axis and represents the beam size in the direction transverse to the longitudinal coordinate s . Therefore, a beam with low transverse emittance is one where the particles are confined to a small distance and have similar momenta, and it can be loosely described as the smallest opening you can squeeze the beam through.

In addition to the transverse oscillations, beam particles also oscillate longitudinally under the influence of the RF-cavities. To complement the coordinates used to describe the motion of particles, the longitudinal variables: $z, \Delta p/p$ is added to the transverse phase-space variables [i.e: $x(s), dx(s)/ds, y(s), dy(s)/ds$] mentioned above. The variable z describes the distance by which a given particle leads an ideal particle traversing the LHC ring trajectory. The quantity Δp is the particle's momentum error while $\Delta p/p$ is the momentum spread of the beam. The individual particles get in and out of step with the ideal, synchronous phase, for which the increase in momentum per turn from the RF-kick exactly matches the increase in the bending field.

Thus, if a particle is lagging with respect to the synchronous particles, it will arrive later than the RF-kick and will thus see a smaller accelerating voltage. However, since the bending field has now increased according to the exact synchronous particle, the effect will be to launch the asynchronous particle into a smaller orbit. As a consequence, during the next time around the asynchronous particle will now arrive earlier with the exact opposite outcome; experience a larger RF-kick that will launch it into a larger orbit and hence cause it to arrive later next time around.

In this way, even though the proton bunch as a whole remains stable while circulating around the LHC ring, the protons themselves undergo longitudinal oscillations, also known as “synchrotron oscillations”. Therefore, instead of the protons being uniformly distributed around the circumference of the LHC ring, they instead oscillate around the synchronous particles in the bulk of a bunch, which is in turn contained in an RF-bucket.

Now, in order (for the particles) to always see the accelerating RF-voltage, the RF-frequency (f_{RF}) must be an integer multiple (h) of the revolution frequency (f_{rev}), i.e.: $f_{RF}=hf_{rev}$, in which case h is known as the “harmonic number” and for the LHC machine it has a value of $h_{LHC}=35640$. Therefore, even though the LHC has the ability to accelerate a beam made up of 35640 bunches, the nominal number of occupied buckets is instead 2808. The reason for this is that a number of consecutive buckets are required to not contain a beam, thus forming an abort gap. An abort gap is a measure which is required in the beam-dump process, due to the fact that it takes a short yet significant time to switch on the kicker magnets that divert the beam from the LHC into the dump area.

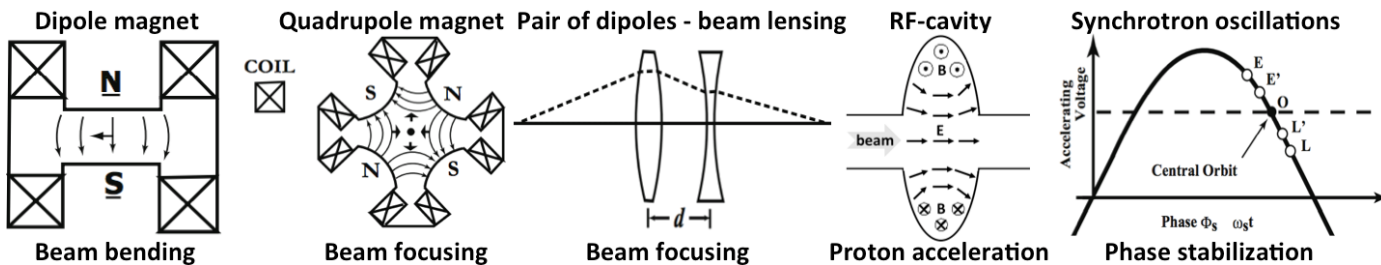


Figure 3.6: Illustration of (left to right): the dipole magnet which bends the beam; quadrupole magnet (which successive application focuses) the beam to transverse plane; the lensing induced in a quadrupole configuration; the RF-cavity “kicker” and its instant fields, and the RF-voltage which accelerates and causes longitudinal (Synchrotron) oscillations of protons around its “central orbit”.

3.3.4 Beams luminosity

Once the proton beams have reached nominal energies and have acquired stabilised orbits inside the LHC ring, they are brought to collisions in the four IPs at which the detectors are positioned. The reaction rate (R) at these regions, for a given interaction with cross-section: σ_{int} , is given by

$$R = \mathcal{L}\sigma_{int}, \quad \mathcal{L} \equiv f_{revolution} \frac{n_1 n_2}{4\pi\sigma_x\sigma_y}. \quad (3.6)$$

where \mathcal{L} is the instantaneous luminosity for two oppositely directed beams of relativistic particles with revolution frequency f_{rev} . The terms n_1, n_2 are the number of protons within the two beam bunches. The quantity $4\pi\sigma_x\sigma_y$ can be thought of as the effective cross-section area of the bunched beams (assuming they overlap completely). It can be deduced that the number of interactions at any instance is directly proportional to the intensity of each colliding beam and the revolution frequency of the bunches, and inversely proportional to the beam size (or momenta spreads within a bunch).

The equation can be recast in terms of transverse emittance and betatron amplitude functions as follows:

$$\mathcal{L} = \frac{f_{rev} n_1 n_2}{4\epsilon_x \beta_x(s) \epsilon_y \beta_y(s)}, \quad (3.7)$$

revealing that, while there are no fundamental limits to restrict the peak luminosity, the LHC luminosity is constrained by the machine's ability to maintain highly populated bunches of low transverse emittance, while being able to suppress betatron oscillations of the protons with high precision. These parameters are not constant in time, but deteriorate over a physics run. In particular, the intensity and transverse emittance of the circulating beams degrade over time and cause the initial luminosity (\mathcal{L}_0) to decay (or interact, or absorbed) exponentially as:

$$\mathcal{L}(t) = \mathcal{L}_0 e^{-t/\tau_{nuclear}}, \quad \tau_{nuclear} \equiv N_0 / (k\mathcal{L}_0\sigma_{tot}), \quad (3.8)$$

Where $\tau_{nuclear}$ the initial decay time of the bunch intensity due to beam collisions, N_0 the initial beam intensity, k is the number of IPs, and σ_{tot} is the total cross-section of the LHC at a specific centre-of-mass-energy: $\sigma_{tot} \simeq 100$ mb (at $\sqrt{s}=14$ TeV). The time required for the initial luminosity to reach 1/e of its initial value is: $(\sqrt{e} - 1)\tau_{nuclear}$, which for a nominal LHC operation is ~ 29 h.

Besides the beam losses due to collisions, luminosity lifetime is affected by ‘‘Touschek Scattering’’, whereby particle losses within a bunch are due to single particle-particle collisions. In addition to that, slow transverse emittance blow-up caused by the scattering of particles on residual gas in the beam pipes, RF-noise, beam-beam interactions and Intra-Beam Scattering (IBS) (process where particles elastically scatter off each other) can further decrease the luminosity lifetime. By approximating the luminosity decay by an exponential process, the net luminosity lifetime takes the form:

$$\frac{1}{\tau_{\mathcal{L}}} = \frac{1}{\tau_{IBS}} + \frac{1}{\tau_{nuclear}(\sqrt{e} - 1)} + \frac{1}{\tau_{RestGas}} \quad (3.9)$$

and assuming $\tau_{IBS} \simeq 80$ h and $\tau_{RestGas} \simeq 100$ h it has a value of: $\tau_{\mathcal{L}} \simeq 14.9$ h.

Therefore, luminosity lifetime can be used to estimate the integrated luminosity as: $\mathcal{L}_{int}(t) = \mathcal{L}_0(1 - e^{-t/\tau_{\mathcal{L}}})$. Once the beam losses have reached a level where the luminosity has dropped significantly, the beam is dumped and a new fill cycle begins.

The nominal beam injection time from the SPS into the LHC is 16 min, while the minimum time required for ramping the beam energy from 450 GeV up to 7 TeV is approximately 20 min. The ramping down of the magnets from the nominal 7 TeV back to 450 GeV (in case of beam abort) is 20 min, while the theoretical minimum time interval from the end of a luminosity run and a new beam at top energy (turnaround) is estimated 70 min.

3.4 The Compact Muon Solenoid detector/experiment

In this section the Compact Muon Solenoid (CMS) detector is briefly described. The CMS detector is a multi-purpose and multi-modules detecting apparatus due to operate at the LHC at CERN. CMS is

installed about 100 metres underground of LHC at point 5 (shown already at figures 3.1, 3.2 and 3.4) close to the French village Cessy between lake Geneva and the Jura mountains. The main sources of information for this section are: [77, 51, 56, 79].

3.4.1 Introduction, motivation and the general concept

The prime motivation of the CMS construction is dictated by the LHC reach; which are the study of electroweak symmetry breaking (Higgs boson/mechanism) and reveal potential SM-extensions in the TeV scale (like natural SUSY). However CMS mission is to recorded and study all LHC data and perform all kind of possible analysis extended from SM-precision physics, and Ion-collision physics up to quantum black hols studies.

At the core of the CMS detector sits a high-magnetic field and large-bore superconducting solenoid surrounding a silicon pixel and strip tracker, a lead-tungstate scintillating-crystals electromagnetic calorimeter, and a brass-scintillator sampling hadron calorimeter. The iron yoke of the flux-return is instrumented with four stations of muon detectors covering most of the 4π solid angle. Forward sampling calorimeters extend the pseudorapidity coverage to high values ($|\eta| < 5$) assuring good hermeticity and stereoscopic coverage. The overall dimensions of the CMS detector are a length of 21.6 m, a diameter of 14.6 m and a total weight of 12.5 ktonnes.

The total proton-proton (pp) cross-section at $\sqrt{s} = 14$ TeV is expected to be roughly 100 mb. At design luminosity the general-purpose detectors will therefore observe an event rate of approximately 10^9 inelastic events/sec. This leads to a number of formidable experimental challenges. The online event selection process (trigger) reduces the huge rate to about 100-150 events/sec for storage and subsequent analysis. The short time between bunch crossings, 25 ns (designed performance), has major implications for the design of the read-out and trigger systems.

At the design luminosity, a mean of about 20 inelastic collisions will be superimposed on the event of interest (within a single bunch crossing). This implies that $\sim 10^3$ charged particles will emerge from the interaction region every 25 ns. The products of an interaction under study may be confused with those from other interactions in the same bunch crossing. This problem clearly becomes more severe when the response time of a detector element and its electronic signal is longer than 25 ns.

The effect of this pile-up is reduced by using high-granularity detectors with high time-resolution, resulting in low occupancy. This requires a large number of detector channels. The resulting (~ 100) millions of detector electronic channels require excellent synchronization. The large flux of particles coming from the interaction region leads to high radiation levels, requiring radiation-hard detectors and front-end electronics.

The CMS detector/experiment requirements to meet the goals of the LHC physics programme can be summarised as follows:

- Good muon identification and momentum resolution over a wide range of momenta and angles, good di-muon mass resolution ($\sim 1\%$ at 100 GeV), and the ability to determine unambiguously the charge of muons with $p < 1$ TeV;
- Good charged-particle momentum resolution and reconstruction efficiency in the inner tracker. Efficient triggering and offline tagging of s and b-jets, requiring pixel detectors close to the interaction region;
- Good electromagnetic energy resolution, good diphoton and dielectron mass resolution ($\sim 1\%$ at 100 GeV), wide geometric coverage, π^0 rejection, and efficient photon and lepton isolation at high luminosities;
- Good missing-transverse-energy and dijet-mass resolution, requiring hadron calorimeters with a large hermetic geometric coverage and with fine lateral segmentation.

The design of CMS (detailed in the next section), meets these requirements. The main distinguishing features of CMS are a high-field solenoid magnet, a full-silicon-based inner tracking system, and a

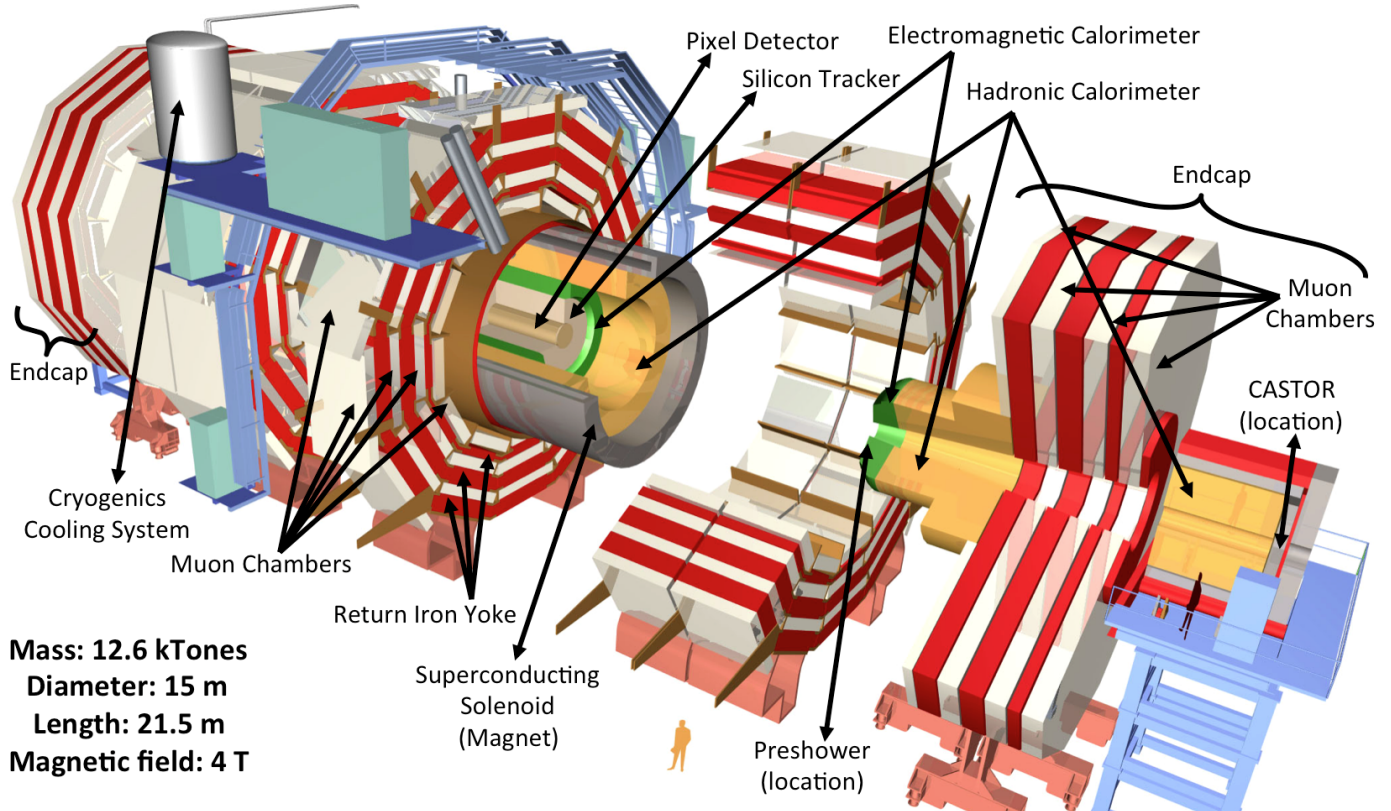


Figure 3.7: The CMS detector anatomy with its sub-devices.

homogeneous scintillating-crystals-based electromagnetic calorimeter. The coordinate system adopted by CMS has the origin centered at the nominal collision point inside the experiment, the y -axis pointing vertically upward, and the x -axis pointing radially inward toward the center of LHC ring. Thus, the z -axis points along the beam direction (toward the Jura mountains from Point 5). The azimuthal angle ϕ is measured from the x -axis in the $x - y$ plane and the radial coordinate in this plane is denoted by r . The polar angle θ is measured from the z -axis. Pseudorapidity is defined as: $\eta \equiv -\ln[\tan(\theta/2)]$. Thus, the momentum and energy transverse to the beam direction, denoted by $p_T (\equiv \sqrt{p_x^2 + p_y^2})$ and $E_T (\equiv \sqrt{p_T^2 + m^2})$, respectively, are computed from the x and y components. The imbalance of momentum measured in the transverse plane is denoted by \cancel{E}_T .

The overall layout of CMS is shown in figure 3.7, whereas transverse and longitudinal cross section are shown at figure 3.8. An complete description of the CMS performance can be found at [77]

3.4.2 Superconducting solenoid/magnet and the iron yoke

Large bending power is needed to measure precisely the momentum of energetic charged particles. This forces a choice of superconducting technology for the magnet. At the heart of CMS, sits a 13 m long, 6 m inner-diameter and field-intensity: $B=4$ T superconducting solenoid providing a large bending power: $\int \vec{B} \cdot d\vec{x} \sim 12$ Tm, with a stored energy of: 2.6 GJ at full current.

The internal space of the coil is large enough to accommodate the pixel tracker, the silicon tracker, the ECAL and the main HCAL stations. Whereas the muon chambers are installed outside of it in a 4-layer stations. The magnetic field is large enough to saturate 1.5 m iron yokes surrounding the coil. Magnetic flux returns through this 10 kilo-tonnes iron yoke comprising five barrel-wheels, two endcaps, and composed by four cylindrical-layers and three disk-layers respectively (figures: 3.7, 3.8).

The dimensions of the solenoid are: 6.3 m cold bore (diameter), 12.5 m length and weights 220 tonnes. Its distinctive feature of the coil is the NbTi superconductor. The superconductor, made from a Rutherford-type cable, co-extruded with pure aluminium, is mechanically reinforced with an aluminium alloy. Due to the number of ampere-turns required for generating a field of 4 T (41.7 MA-turn), the

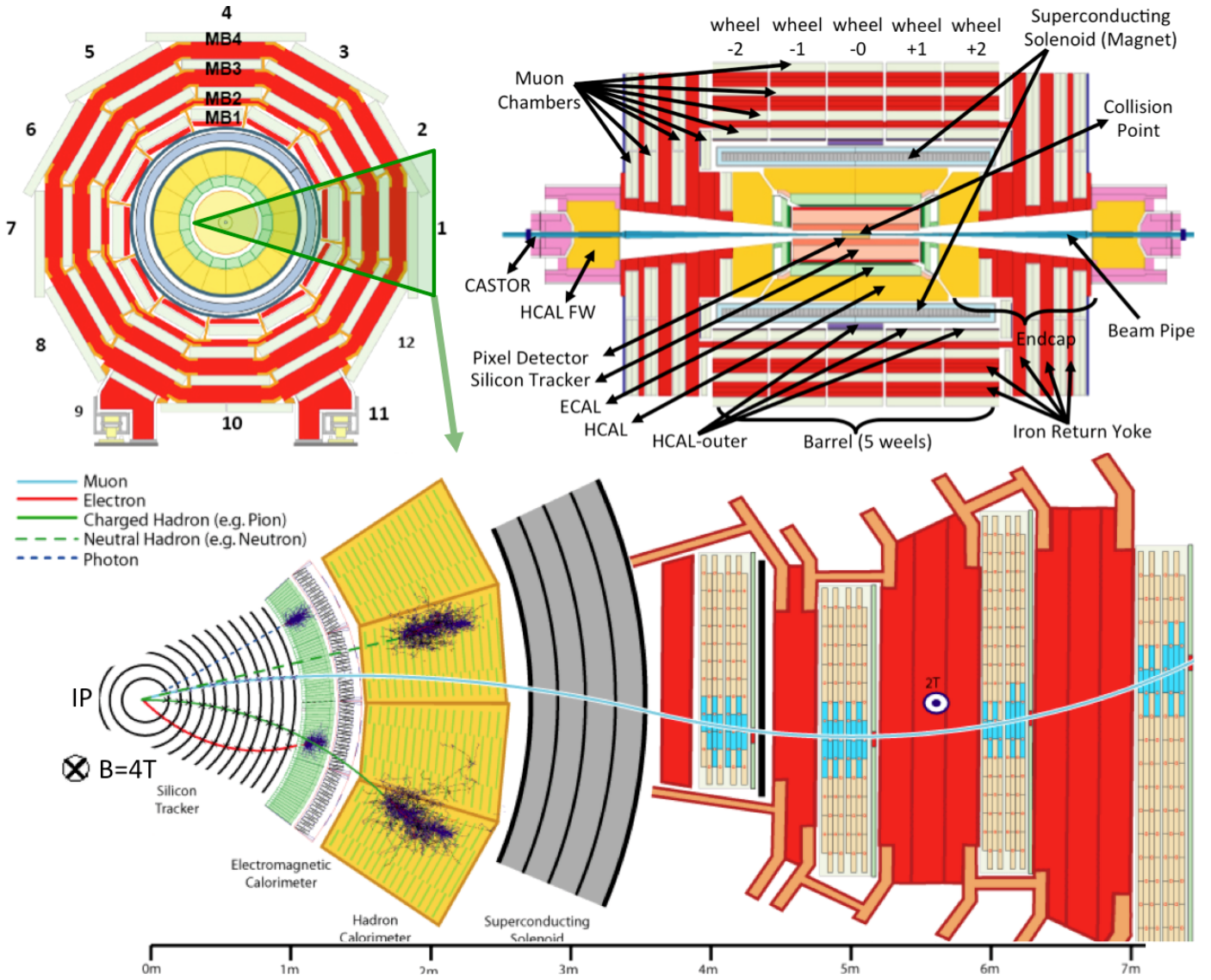


Figure 3.8: The CMS detector in the transverse and the longitudinal cross section.

winding is composed of four layers, (instead of the usual one as in Aleph, Delphi, or maximum two as in ZEUS BaBar coils).

The ratio between stored energy and cold mass is nominally: 11.6 KJ/kg, causing a large mechanical deformation (0.15%) during energising, well beyond the values of previous solenoidal detector magnets (figure 3.9 right). For physics reasons, the radial extent of the coil (ΔR) had to be kept small, and thus the CMS coil is a “thin coil”: $\Delta R/R \sim 0.1$. The magnet was designed to be assembled and tested in a surface, prior to being lowered ~ 90 m below ground to its final position in the experimental cavern.

3.4.3 Tracking system overview

The innermost part of the CMS detector is the inner tracking system [77], which is 5.8 m long and 2.5 m in diameter. It surrounds the thin beryllium beam-pipe which accommodates the LHC vacuum and is centred at the IP where beams are collide. Its mission is to provide a robust, efficient and precise measurement of the charge and trajectories of charged particles emerged from IP with transverse momenta above ~ 1 GeV and within the pseudorapidity range $|\eta| < 2.5$.

Furthermore, the efficient identification of heavy flavours requires that the tracking system is able to determine precisely secondary vertices and impact parameters d_{xy}, d_z (where are defined and illustrated in figure 3.11 bottom left).

At the LHC design luminosity, an average of ~ 1000 charged particles that originate from more than

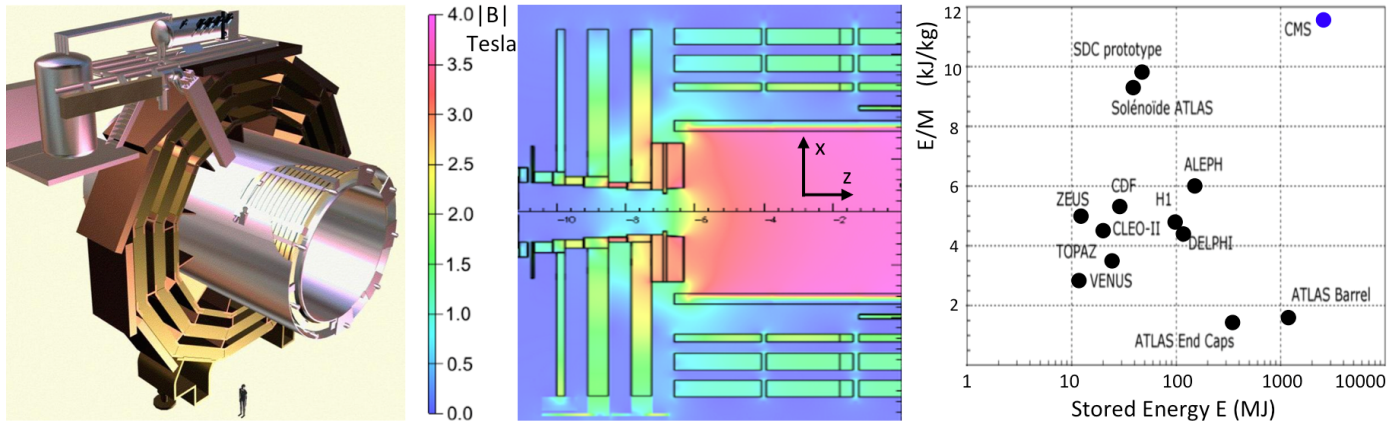


Figure 3.9: The CMS magnet, with the iron return yoke of wheel-0, and its cooling system (left). The magnetic field (parallel to z -axis) formed over the whole detector in full nominal operations conditions (middle). The energy over cold mass ratio map for CMS and other detectors (right).

20 overlapping proton-proton interactions are produced every 25 ns, and first propagate through the tracker before reaching the next detector layer, the calorimetry system.

This leads to a tracker-hit rate density of 100 MHz/cm^2 in the barrel part at a radius of 4 cm, which can have consequences in terms of detector occupancy and radiation damage to the tracking system.

In order to be able to deal with this enormous particle flux, the tracker system must have high granularity and a fast response to provide a very good position resolution, as well being able to withstand the radiation damage. However, this is contrary to the aim of keeping the amount of tracker material to as little as possible, in order to minimise the amount by which a given particle involves in multiple scatterings, bremsstrahlung, photon conversion and nuclear interactions.

To fulfil the requirements on granularity, speed and radiation hardness, the CMS tracker is entirely based on silicon technology. Two main devices/subdetectors have been implemented: the so-called Pixel detector and the Strip detector. These are composed of 1440 pixel and 15148 microstrip modules that are arranged in a barrel and endcap configuration. These corresponds to a total active silicon area of about 200 m^2 , which is the largest silicon tracker built to date. In the next subsections we will present pixel and strip detectors' main features.

3.4.4 Pixel Detector

Due to the high hit-rate density at very small distanced around CMS-IP, radiation-hard detectors with very fine granularity must be used, in order to avoid saturation and keep the tracker occupancy at the level of $\sim 1\%$. For this reason, the innermost part of the CMS tracker consists of about 66×10^6 pixel detectors, with a pixel unit cell of $100 \times 150 \mu\text{m}^2$.

The pixel detector covers a total area of $\sim 1 \text{ m}^2$, and due to the high granularity of the pixels it has an occupancy of only 10^4 per pixel at the nominal LHC operation.

There are 47923200 pixels in barrel (BPix) arranged into three homoaxial cylindrical layers, each 53.3 cm long and positioned at mean radii of: 4.4 cm, 7.3 cm and 10.2 cm around IP, providing an active area of 0.78 m^2 . These are complemented by other 17971200 pixels in endcaps (FPix) arranged into two endcap disks on each side of the barrels, at $z = \pm 34.5 \text{ cm}$ and $z = \pm 46.5 \text{ cm}$, spanning through a radius range of 615 cm and covering an area of other 0.28 m^2 . All these are illustrated in figure 3.10.

The barrel layers are composed of modular detector units (modules) placed on carbon fibre supports (ladders). Each ladder includes eight modules with pixels arranged in quadratic arrays of $n+$ implants on n substrates, with a thickness of $250 \mu\text{m}^2$. As charged particles traverse the depletion region of the junction they eject electrons from the silicon atoms-implants, causing the production of electron-hole pairs. Each pixel uses an electric field to collect these charges on the surface to metal contacts. To read out the detector, a Read-Out Chip (ROC) is bump-bonded to the pixel modules, which extracts the signal off the top by reading an array of 52×80 pixels. The ROCs, which amount to about 16000,

Table 3.2: Summary of the parameters/performances of CMS detector per sub-system: magnet, iron yoke, pixel-tracker, silicon strip-tacker, ECAL, HCAL, Muon-system, Trigger, DAQ. (Taken from [77, 51, 56, 79, 60, 38, 102, 58]).

Quantity	Value	Unit
Magnet		
Magnetic length	12.5	m
Cold bore diameter	6.3	m
Central magnetic induction	4	T
Total Ampere-turns	41.7	MA-turns
Nominal current	19.14	kA
Inductance	14.2	H
Stored energy	2.6	GJ
Radial thickness of cold mass	312	mm
Radiation thickness of cold mass	3.9	X_0
Weight of cold mass	220	t
Maximum induction on conductor	4.6	T
Temperature margin wrt operating temperature	1.8	K
Stored energy/unit cold mass	11.6	kJ/kg
Iron yoke		
Outer diameter of the iron flats	14	m
Length of barrel	13	m
Thickness of the iron layers in barrel	300, 630 and 630	mm
Thickness of iron disks in endcaps	250, 600 and 600	mm
Mass of iron in: barrel/each endcap/Total	6 / 2 / 10	kt
ECAL		
$ \eta $ coverage: EB, EE, ES	<1.479, [1.479,3], [1.653,2.6]	
Action medium / modules: EB, EE, ES	61200, 14648, -	PbWO ₄ , PbWO ₄ , Si-stripes
Radiation length: EB, EE, ES	25.8, 24.7, 3	X_0
Front(back) cross-section in EB PbWO ₄ crystals	22×22 (26×26)	mm ²
Front(back) cross-section in EE PbWO ₄ crystals	28.62×28.62 (30×30)	mm ²
Length EB, EE,	230, 220	mm
Density of PbWO ₄ crystals	8.28	g/cm ³
Refractive index n for PbWO ₄ crystals at peak wavelength	2.29	
PbWO ₄ crystals scintillation decay time (80%)	25	ns
Photo-electrons produced in PbWO ₄ crystals at 18°	4.5	MeV ¹
PbWO ₄ crystals emission spectrum maximum	420-430	nm
HCAL		
$ \eta $ coverage HB, HE, HO, HF:	<1.3, [1.3,3.0], <1.65, [3.0,5.2]	
Action medium HB, HE, HO, (HF):	plastic scintillators, (quartz fibres)	
Radiation length HB, HE, HO, HF:	[5.82,10.6], ~10, ~11, ≲11, ~10	
Absorber material	brass: Cu 70%, Zn 30%	
Brass absorber density	8.53	g/cm ³
Brass absorber radiation length: (X_0)	1.49	cm
Interaction Length: λ	16.42	cm
HB layer 0, plastic scintil.(Bicron BC408), steel:	9, 40	mm
HB layers 1-8, plastic scintil.(Kuraray SCSN81), brass:	3.7, 50.5	mm
HB layers 9-14, plastic scintil.(Kuraray SCSN81), brass:	3.7, 56.5	mm
HB layers 15-16, steel, plastic scintil.(Kuraray SCSN81):	75, 9	mm
Muon detectors		
$ \eta $ coverage DTs, CSCs, RPCs:	< 1.2, [0.9,2.4], < 1.6	
DTs gas composition	85% Ar, 15% CO ₂	
CSCs gas composition	30% Ar, 50% CO ₂ , 20% CF ₄	
RPCs gas composition	95% Freon:C ₂ H ₂ F ₄ & 5% Isobutane: C ₄ H ₁₀	
DTs anode/electrode/cathode voltage	+3.6/1.7/1.2	kV
DTs dead time:	150	ns
RPCs gas gap: number, width	2, 2	- , mm
RPCs operating voltage	8.5-9.0	kV
Trigger		
Input rate L1, HLT:	~0.1, ~1000	MHz
Output rate L1, HLT:	~100(30), ~0.1	kHz
Rate reduction factor L1, HLT:	~10 ⁴ , ~10 ³	
Time latency L1, HLT:	~3.2×10 ⁻⁶ , [0.04,1]	s

amplify the signals and apply a threshold filter before registering a hit. In the endcaps, the disks are split into half. Each half is comprised of 12 trapezoid-shaped blades which is sandwich of two back-to-back panels. Rectangular sensors of five sizes are bump-bonded to arrays of ROCs in such a way to form plaquettes. The 672 in total plaquettes are arranged to overlap, so as to provide full coverage for charged particles emerging from the IP5.

To enhance the spatial resolution by analogue signal interpolation, the effect of charge sharing

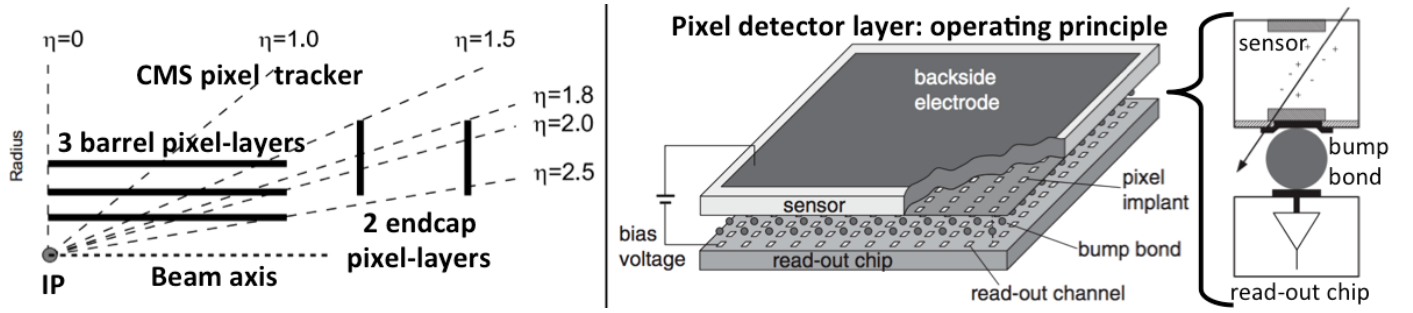


Figure 3.10: The pixel-tracker layers (which their hits allows the precise reconstruction of charged particle direction), and the operation principle of such a pixel-detector (take from [40, 77]).

induced by the Lorentz drift in the 3.8 T magnetic field is used. Charge generated by an ionising track traversing the sensor perpendicularly will be spread over $150 \mu\text{m}$ at the surface in the $r-\phi$ plane and perpendicular to the magnetic field.

Therefore, since in the barrel layers the pixels are perpendicularly oriented to the magnetic field, they are deliberately not tilted.

The resolution along the z -axis is determined by the pixel pitch (implants) in the central regions (low values of η) and by charge sharing if the tracks hit the sensors at an angle, whereby typically pixel clusters share the charge carriers created in the depletion region. Conversely, in the endcap regions, the orientation of the pixel modules is parallel to the magnetic field. Therefore, the modules are deliberately tilted to about 20° resulting in a turbine-like geometry, which enhances charge sharing between channels due to the Lorentz effect. The spatial resolution of the pixels is about $20 \mu\text{m}$ for the $r-\phi$ measurement ($\sigma_{r-\phi}$) and about $15 \mu\text{m}$ for the z measurement (σ_z). The arrangement of the pixel detector into barrel and endcap parts, provides a pseudorapidity coverage of $|\eta| \lesssim 2.5$.

In the high η regions the pixel information from the two disks has to be combined with the innermost layer of the barrel, which only covers the region up to $|\eta| \lesssim 2.2$, leaving the pseudorapidity range $2.2 < |\eta| < 2.5$ to be only covered by the endcap disks.

In this way the pixel detector provides three high precision space points (hits) on each charged particle trajectory, enabling the localization of the collision and decay vertexes, allows the determination of small impact parameter resolution ($\sigma_{d_{xy}}, \sigma_{d_z}$), which is important for good secondary vertex reconstruction for low track multiplicity of b-quark and τ -lepton decays. Moreover, the pixel detector may be used to perform fast track finding, which may be used to set coarse constrains for selecting interesting events with the trigger.

3.4.5 Silicon-strip tracker

The tracker silicon strip detector, which surrounds the pixel detector, has a total of 9.3×10^6 silicon microstrips, covering an area of 198 m^2 , and is divided into three separate subsystems; the Tracker-Inner-Barrel and Disk(s) named: (TIB), (TIDs), and the Tracker-Outer-Barrel (TOB), which surrounds the former, and the Tracker-EndCap (TEC), which seals off the TOB, as shown in figure 3.12. The placement of the barrel and endcap subsystems has been designed such that each particle must pass through at least 10 sensors, independent of pseudorapidity and, assuming they have high enough transverse momentum, to be within the tracker acceptance.

Each of the subsystems has silicon microstrip modules, designed differently for its place within the detector. The choice to use silicon sensors was based on building a compact, high resolution, efficient, reliable and cost-efficient tracker. As the pixel detector, the silicon microstrip sensors have very fast response, excellent spatial resolution, are “radiation-hard” and can be operated at nearly room temperature. These features makes it highly suited for detecting large particle flux emerging from IP and through the pixel detector.

Silicon microstrip detectors operate in similar way to the pixels. When a charged particle propagates through the sensitive region of the material, the current from the liberated electron-hole pairs can be

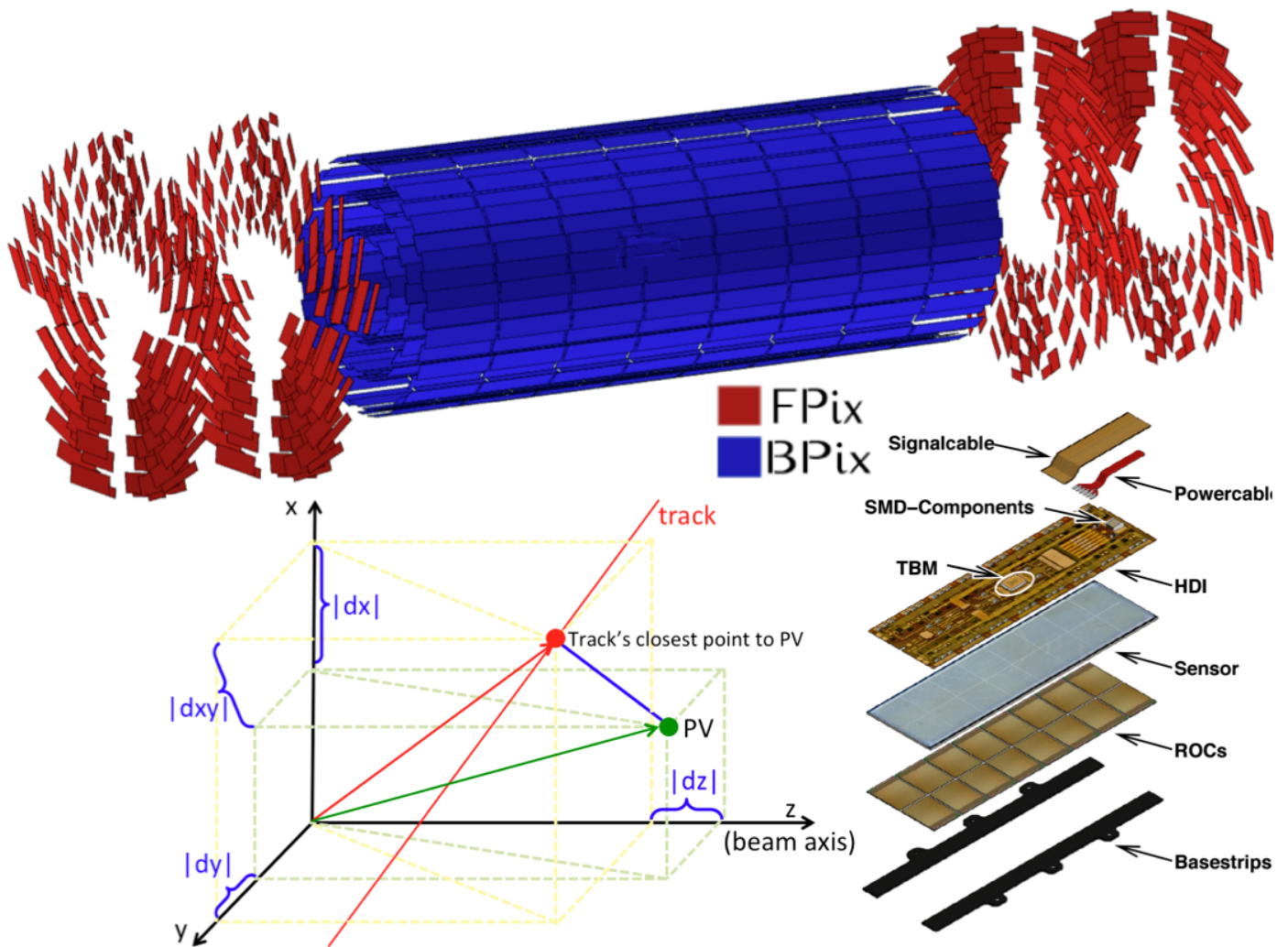


Figure 3.11: The complete picture of the CMS pixel detectors with all its plaquettes either in barrel and endcaps with also the relative spatial orientation. Bottom left: the definition of the impact parameters d_{xy}, d_z with respect to the primary vertex (PV); right: the anatomy of such a BPix module (take from [63]).

measured by collecting them to silicon strip electrodes. The small pulse of current, which typically lasts a nanoseconds, is then amplified by ROCs, thus registering a hit and allowing for the particles trajectory to be reconstructed. The layout of CMS full tracking system and the silicon-strip detector operating principle are shown in figure 3.13.

Each side of the barrel is sealed off with the TID endcaps. The TIB layers are 146 cm long and are positioned at mean radii of: 25.5 cm, 33.9 cm, 41.9 cm and 49.8 cm around IP. These are complemented by three disks in the TID on each side of the barrels at: ± 78.8 cm, ± 91.8 cm and ± 104.7 cm and spanning through a radius range of 23.5-33.5 cm, 32.6-42.6 cm and 37.7-50.2 cm, respectively. The combined TIB/TID subsystem, which has its silicon microstrips oriented parallel (radial) to the beam axis in the barrel (disks), delivers up to four r - ϕ measurements on a trajectory. The layers are fitted with 320 μm thick and 12 cm long microstrips silicon sensors, with a strip pitch in the range of 80-120 μm , leading to an occupancy of up to 2-3% per strip at the nominal LHC bunch-crossing frequency.

The two innermost layers of the TIB, and rings one and two of the TID are equipped with stereo modules that are coupled back-to-back and rotated at an angle of 100 mrad with respect to each other, hence providing measurements in both the r - ϕ and r - z coordinates. The resulting spatial resolution for TIB is about 23-35 μm for the r - ϕ measurement and about 230 μm for the z measurement.

Surrounding the TIB is the TOB, consisting of six concentric layers, each 236 cm long and positioned at mean radii of 60.8 cm, 69.2 cm, 78.0 cm, 86.2 cm, 96.5 cm and 108.0 cm around IP. Being further away from the IP than the TIB, the relatively lower particle flux enables the use of longer strip length

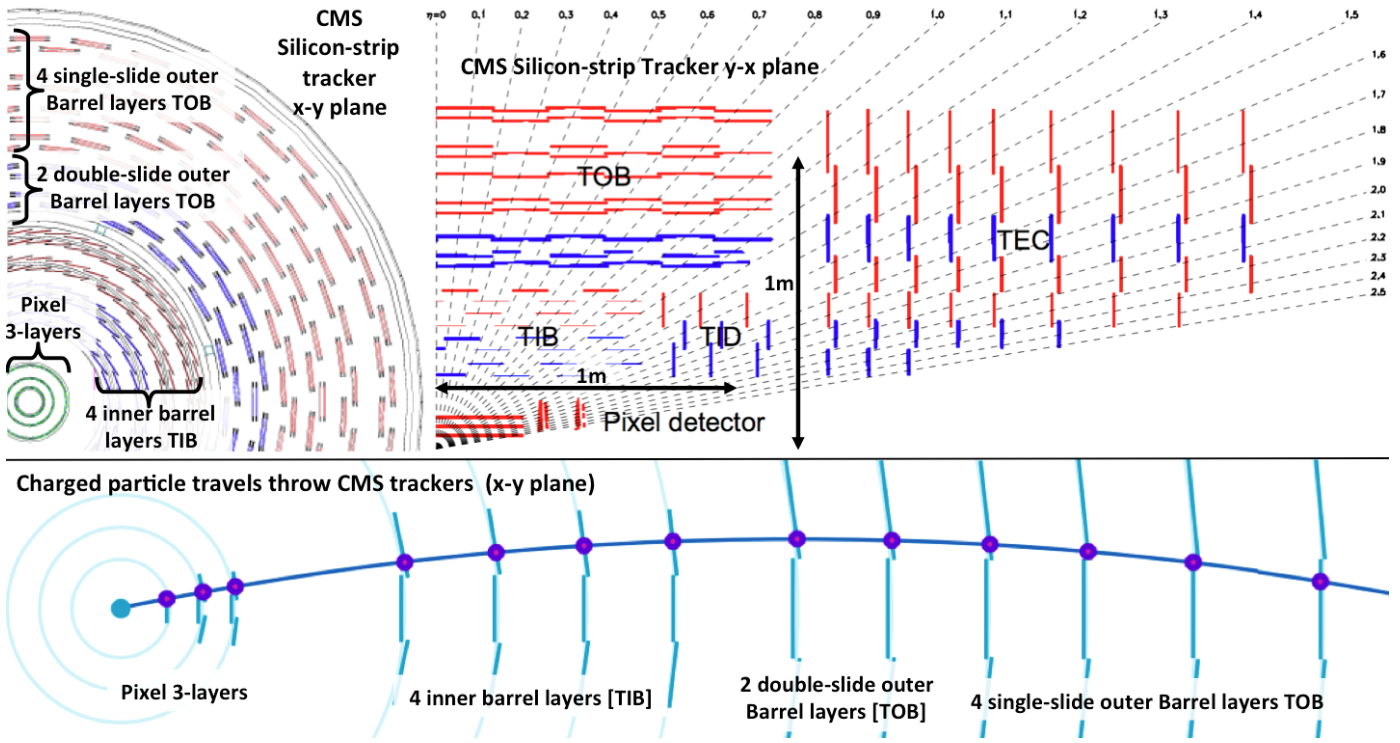


Figure 3.12: The full CMS tracking system with its sub-layers (x - y plane, and y - z plane). On the bottom: an illustration of a charged particle track with the the tracker hits.

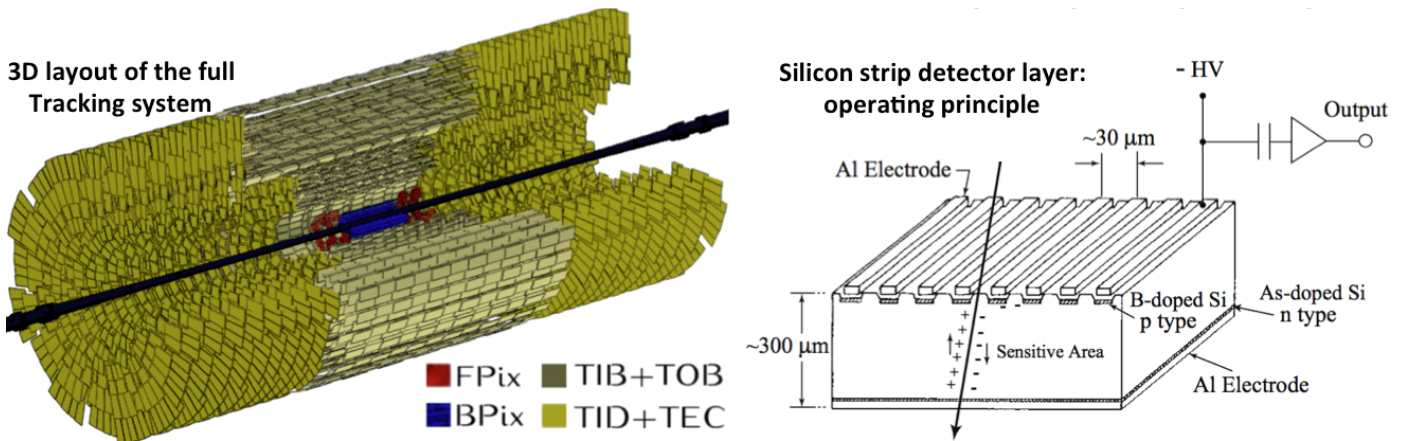


Figure 3.13: On the left, the 3D-structure of the complete CMS tracking system (pixel & strip), and on the right an illustration of the operating principle of such strip detectors. (Taken from [2, 124]).

and wider pitch. The maximum strip length is 16 cm while the pitch range is 122-183 μm .

The increase in strip length relative to the inner barrel is purely for logistical reasons, as the outer barrel has to cover a much larger area than the inner barrel, while also constraining the number of read-out channels. However, the longer strip length implies a relative increase in electronics noise, which is a linear function of strip length. To compensate for the apparent deterioration of the signal-to-noise ratio, the silicon sensors in the TOB are much thicker than those in TIB, with a thickness of 500 μm .

The thickness of the microstrips in the TOB was selected to maintain a signal/noise ratio well above 10. Additionally, and in similar fashion to the TIB, the two innermost layers of the TOB are equipped with back-to-back stereo modules, rotated at an angle of 100 mrad with respect to each other. They provide measurements in both the r - ϕ and r - z coordinates with resolutions 35-53 μm and 530 μm , respectively. The outer barrel region, is supplemented by the TEC subsystem, which is comprised of nine endcap disks on each side, thus closing the barrel gaps to form a cylindrical-like tracker volume.

Each of the disks carries 7 rings of silicon microstrip detectors, with a thickness and pitch range of 320-500 μm and 97-184 μm , respectively. This arrangement of the disks in the TEC provides another nine r -measurements per trajectory. To further enhance the performance of the TEC subsystem, the rings one, two and five carry stereo microstrip detectors that enable the measurement of the z coordinate (r coordinate) in the the barrel (disks). Similarly to the TID, the achieved single point resolution in TEC varies with the strip pitch.

The above described tracker layout provides a pseudorapidity coverage of $|\eta| < 2.4$ and ensures at least ~ 9 hits in the silicon strip tracker, with at least four of them being two dimensional measurements (stereo). The ultimate acceptance of the tracker ends at $|\eta| \sim 5$. However, despite the efforts to minimise the amount by which a given particle is perturbed, by carefully selecting the tracker design and material, the tracker does exhibit a small but finite material budget to the incoming particle flux, as shown in figure E.4 (in appendix E.3), before they penetrate the next layer of the CMS detector; the calorimetry system. The number of tracker-hits versus $|\eta|$ is shown in figure E.5 and a set of muon parameters' resolution is shown in figure E.6.

3.4.6 Electromagnetic Calorimeter

The Electromagnetic CALorimeter (ECAL) surrounds externally the tracker and its mission is to absorb and measure the energy of the electromagnetic products of the collisions i.e.: photons, electrons and positrons. ECAL covers the pseudorapidity region $|\eta| < 3$ and is composed of 75848 lead tungstate (PbWO_4) crystals. From these crystals, 61200 are installed in the central barrel while 7324 crystals are placed in each one of the endcaps.

The lead-tungstate crystals have a very good stopping power and radiation hardness as well as a high density of: 8.28 g/cm^3 . In addition, their characteristics include a short radiation length: $X_0 \simeq 0.9 \text{ cm}$, and a small Moliere radius: $r_m \simeq 2.1 \text{ cm}$, hence the ECAL is more than 25 X_0 deep. Given the fact that $\sim 80\%$ of the deposited energy can be collected in 25 ns, it is ideal for the high collision rate of the LHC. The disadvantages of PbWO_4 crystals are the low light yield per MeV ($\sim 10 \text{ e}^-/\text{MeV}$) something that is confronted with the use of photodetectors. The ECAL layout, geometry, and substructure can be shown in figure 3.14.

The ECAL barrel (EB) crystals are segmented by $\Delta\eta \times \Delta\phi = 0.0174 \times 0.0174$ with a cross section of $22 \times 22 \text{ mm}^2$ and are positioned in an angle of about 3° in both ϕ, θ directions with respect to the beam axis. The ECAL endcap (EE) covers a pseudorapidity region $1.479 < |\eta| < 3$ where the crystals are clustered in 5×5 segments (called "supercrystals"), being arranged in different angles varying from 2° to 8° with respect to the z -axis (figure 3.14 top-right shown the geometry). Their total length is $24.8 X_0 = 220 \text{ mm}$ while their cross section is $28.62 \times 28.62 \text{ mm}^2$ and $30 \times 30 \text{ mm}^2$ for the front and back side respectively.

As electrons and photons pass through the ECAL, their electromagnetic shower results in cascades giving rise to scintillations in the crystals. These signals are collected by two different types of photodetectors. The EB crystals are read with the help of avalanche-photodiodes while vacuum-photodiodes are responsible for this task in the EE as they are more radiation resistant. At the end, more than 90% of the electromagnetic shower can be contained within a single crystal.

A 20 cm thick Electromagnetic Preshower (ES) sampling calorimeter detector is contained within the ECAL, in front of the its endcaps. It is made up of two layers of lead absorbers and silicon micro-strips, which are interleaved by two silicon strip detectors. It covers effectively the region $1.653 < |\eta| < 2.6$ and is situated between the TEC and the EE (figure 3.14 bottom-left). Its main mission is to help the identification of π^0 in the forward region which otherwise could fake photons. It also helps the identification of electrons against minimum ionizing particles, and improves the position determination of electrons and photons with high granularity.

The identification of π^0 is achieved as the first lead layer is about $2 X_0$, while the second one gives another X_0 before the second sensor plate. This allows to differentiate between electrons and pions due to the fact that 95% of the photons shower before the second silicon plane is reached, therefore providing discrimination against neutral pions. The ES operates at temperature of 5C° .

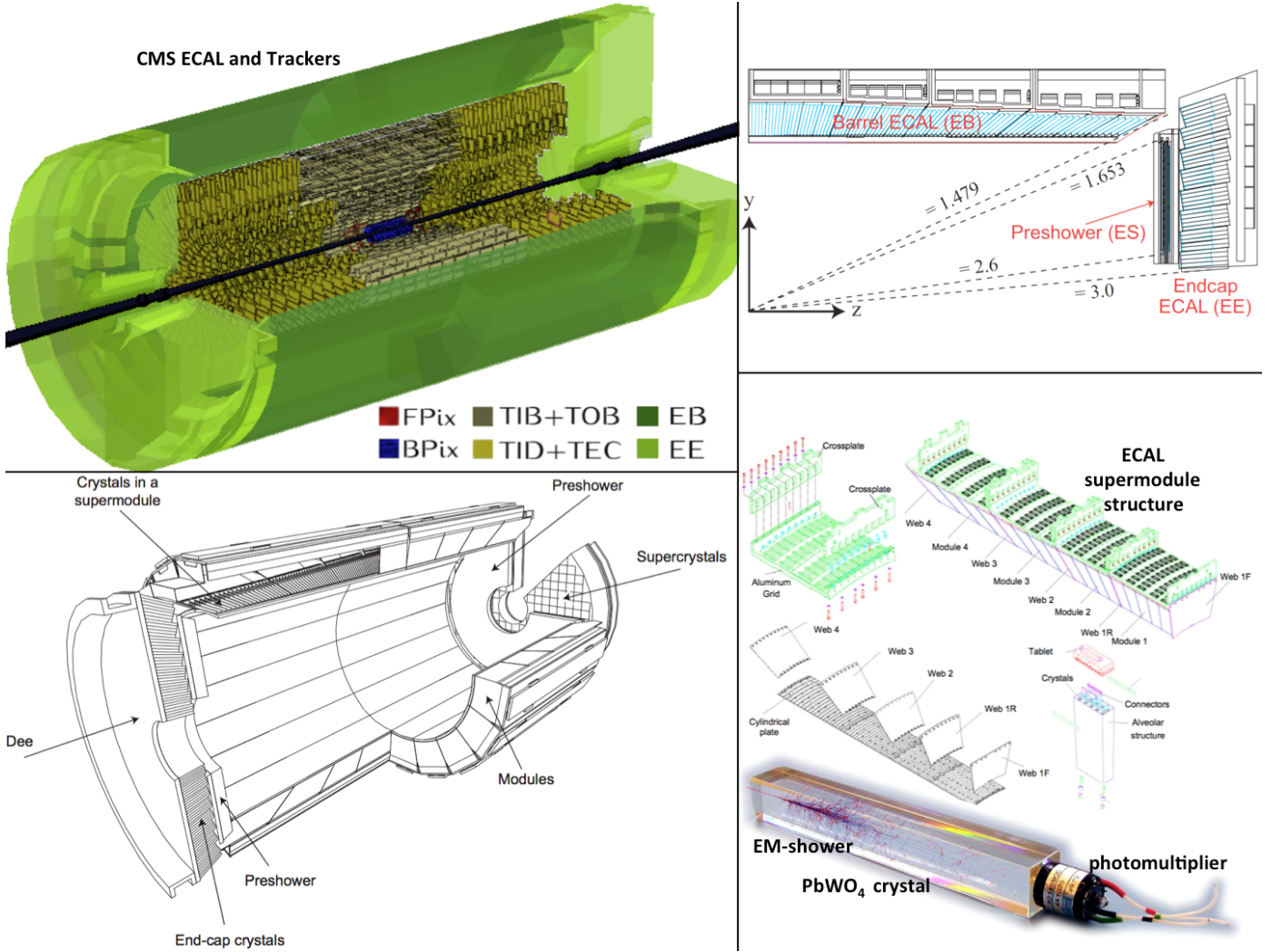


Figure 3.14: The

A very important and challenging aspect is the calibration of the electromagnetic calorimeter. The calibration is divided into two steps, the calibration of the global component, responsible for the absolute energy scale, and a channel-to-channel calibration, also known as inter-calibration. The calibration is performed both in the laboratory and with cosmic-ray and collision events. A typical energy resolution $\sigma(E)/E$ for a 3×3 crystals configuration, is modeled by the following three term function:

$$(\sigma(E)/E)^2 = (0.028/\sqrt{E})^2 + (0.12/E)^2 + (0.003)^2 \quad (3.10)$$

where E is the energy in GeV. The first term corresponds to the stochastic behavior of scintillation; it parametrizes the contribution from fluctuations of the number of photo-electrons being produced and collected due to event-by-event fluctuations. The second term is the noise contribution term, and the third term is a constant term for the non-uniformity of the readout units and miscalibrations, non perfect inter-calibration and leakage of the electromagnetic shower. At high energies, last term becomes dominant, including contributions coming from the need for stable operating conditions, such as the stable high voltage, the temperature, the non-uniform crystal yields, miscalibrations, presence of inactive material (dead-cells) or the accumulated radiation damage of the components.

A set of the ECAL main parameters and performance is listed in table 3.2.

3.4.7 Hadronic Calorimeter

The second calorimeter-layer met by a particle emerging from the tracking system is the Hadronic CALorimeter (HCAL) [56, 60, 77], whose task is to measure the energy and direction of hadron jets

(arising from hadronisation processes of quarks and gluons). Hadronic cascade showers are generated from the elastic and inelastic interactions of these hadrons with the calorimeter material. The interactions that take place between the incident particles and the nucleons of the calorimeter material produce several secondary hadrons, the majority of which are π and K mesons, neutrons and protons.

Figure 3.15 shows (on the left) the development of jets near IP of a particular $t\bar{t}$ event production decaying semileptonically, and (on the right) the shower where hadrons produce once they meet the HCAL. (Also electromagnetic shower is shown for comparison). The cascade decays and interactions processes repeated until the hadron energies are so small that they are either absorbed in a nuclear process or are stopped by ionisation energy loss.

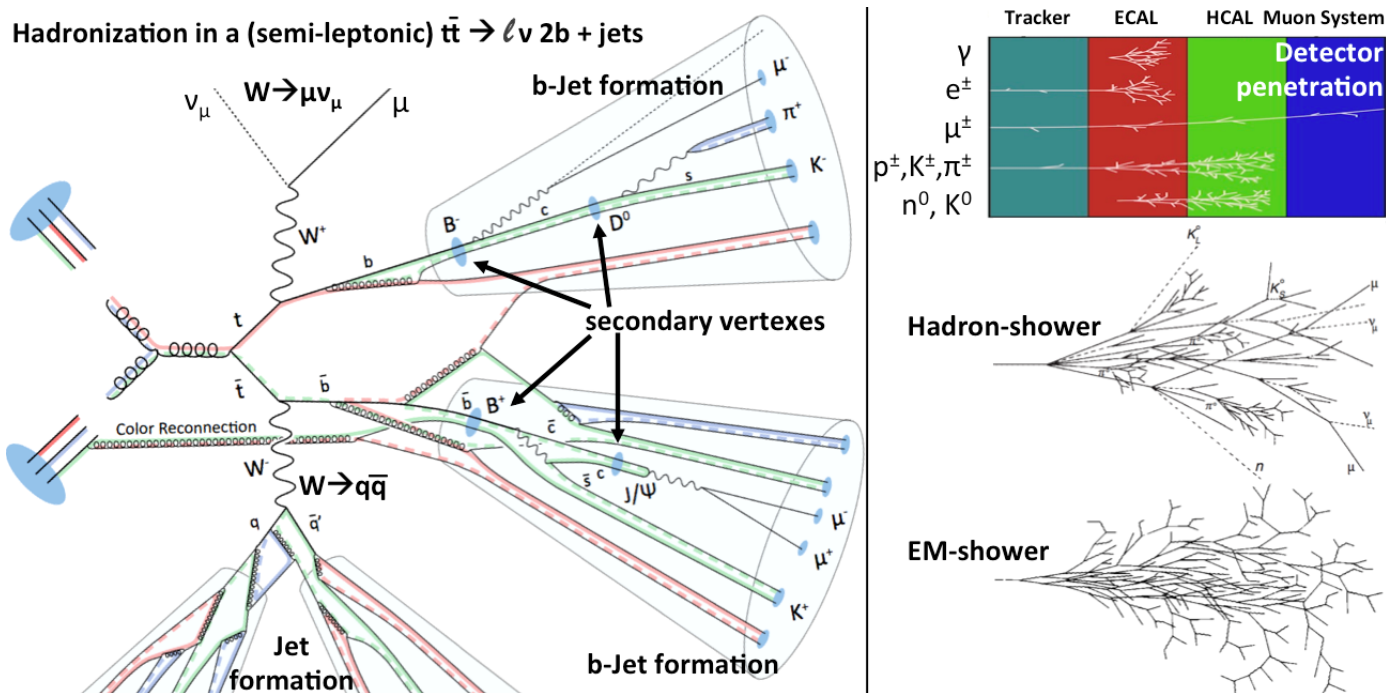


Figure 3.15: The illustration of $t\bar{t}$ production and its semi-leptonic decay. Jet and b-jet formation are illustrated where for the last secondary vertexes are noticed. On the right, examples of the showers produced by (single) hadron and photon/electron, as well as the detector module penetration of all kind of particles.

As a jet is considered, a bunch of hadrons originated by the same initial quark. The jets is then observed as a superposition of many hadron showers which also contains and an EM-component (due to e^\mp, γ) which usually is accompanied.

Compared with the values of the radiation length X_0 of high- Z materials (Z :atomic number), the size of hadronic showers is large, which correspondingly means hadron calorimeters must be also large to completely contain the hadronic showers. However, apart from energy losses due to particles leaking out longitudinally or laterally and the presence of MIPs and neutrinos which deposit little or no energy in the active calorimeter medium, hadronic sampling calorimeters have losses due to additional reasons. The inelastic collisions of shower particles induce nuclear excitations and reactions in the nuclei of the absorber material, which produces other protons, neutrons, nuclear fragments and low-energy photons. Therefore, EM cascade showers where the incident energy appears eventually in the form of ionisation, in hadron cascade showers about 30% of the incident energy is lost in such EM processes and does not give an observable signal.

In order to measure completely the energy of hadrons, HCAL must be built from high-density (ρ) materials, so as to be able to contain the showers in their active volume. For this reason as well as its non-magnetic properties, the main absorber material chosen for the CMS HCAL is brass (:alloy made of copper and zinc), whose main properties can be seen in table 3.2.

Similar to the tracker and ECAL, the HCAL is divided into a barrel and endcap parts: HB and HE respectively, with both contained within the CMS magnet. The HCAL is positioned behind the ECAL

detector as seen from IP (figure 3.16), and it is radially restricted to be between the outer extent of the ECAL (1.77 m) and the inner extent of the magnetic coil (2.95 m). Consequently, the amount of material that can be used to absorb the incident particle energy is constrained accordingly to these dimensions. For this reason, the HCAL Outer (HO) is placed outside of the magnetic solenoid, acting as an outer hadron calorimeter or a tail catcher. In the forward regions it is complemented by the HCAL Forward (HF) calorimeters, positioned at a distance of 11.2 m from the IP and outside the muon chamber. (All above details can be seen in figure 3.16 bottom-left.)

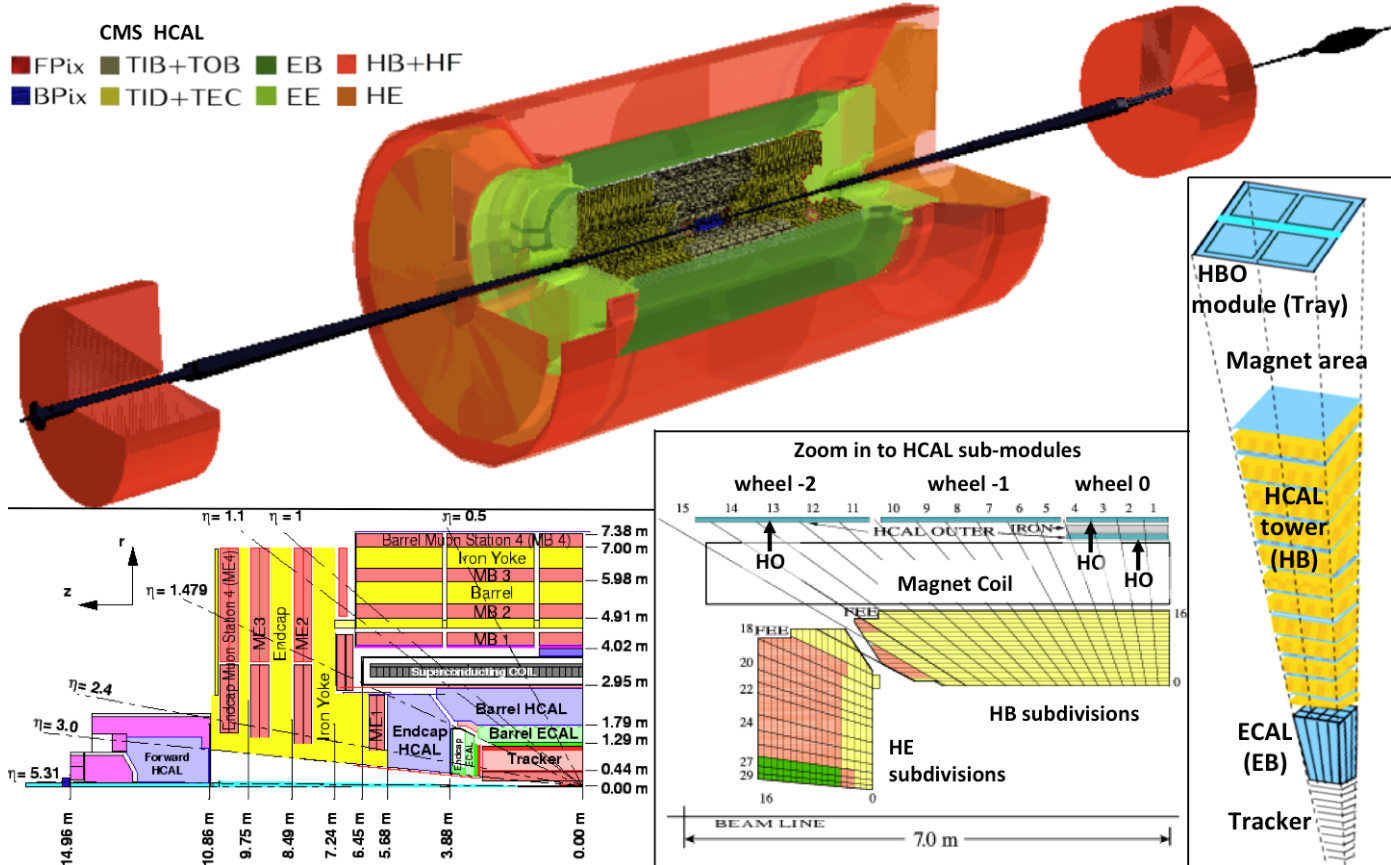


Figure 3.16: The CMS HCAL, layout, substructure, tower segmentation in the r, z plane and a tower with all sub-detectors slices. (Taken from [2, 77]).

The HCAL tower segmentation in the r, z plane

The barrel part of the HCAL (HB) is a sampling calorimeter, covering a pseudorapidity range $|\eta| < 1.3$. It consists of 36 in total identical slices/wedges which form two half-barrel, constructed of flat brass absorber plates aligned parallel to the beam axis. Each wedge, which is segmented into four ϕ -sectors, has its innermost and outermost plates made of stainless steel, to provide the necessary structural strength. A total of 14 brass plates are sandwiched between the stainless steel plates. The first layer is a 40 mm-thick stainless steel plate, followed by 50.5 mm-thick brass plates 1-8. These are followed by 56.5 mm-thick brass plates 9-14, which are finally closed by a 75 mm-thick stainless steel plate. There are 17 plastic scintillator tiles interspersed between the stainless steel and brass material. The first scintillator layer is immediately after the ECAL and it is 9 mm-thick, much thicker than the nominal scintillator tile thickness of 3.7 mm, to sample low energy showering particles from support material between the ECAL and HCAL. An identical scintillator slice is also positioned after the last stainless steel plate.

The exact plate configuration is summarised in table 3.2. The staggered wedge geometry provides a total absorber thickness of 5.82λ at $|\eta|=0$, which increases with polar angle θ as $1/\sin\theta$, resulting in 10.6λ at $|\eta| < 1.3$. Each scintillator tile is segmented to provide a granularity of $\Delta\eta \times \Delta\phi = 0.087 \times 0.087$ and it is instrumented with a WaveLength-Shifting (WLS) fibre.

As the hadronic showers develop due to brass absorber material, particles pass through the alternating scintillator layers, causing them to emit photons in the blue-violet spectrum. The gaps between tiles are filled with a reflective paint to ensure that light produced in each tile does not escape into neighbouring ones.

The WLS fibres are used to absorb this light and their wavelength to the green region of the spectrum, while clear optic fibres then carry the green light away to readout boxes located within the HCAL volume.

The optical signals are amplified and digitised by Hybrid Photo-Diode (HPD) photosensors, which use the photoelectric effect to convert light to an electric signal and a silicon diode to amplify it.

The endcap part HE covers the very active pseudorapidity range $1.3 < |\eta| < 3.0$, a region occupied by about 34% of the particles produced in each LHC bunch-crossing. Therefore, the HE is required to be radiation resistant and have enough granularity to cope with the high flux of particles.

Furthermore, as the HE has to be made of non-magnetic materials while also being thick enough to present an adequate number of interaction lengths to fully contain hadronic showers. Similarly to HB, the material chosen for these tasks was brass. The absorber design is such as to minimise crack between HB and HE, and its resolution is limited by parton fragmentation, pile-up and magnetic effects [38, 102]. The HE is divided into 18 (20° each) ϕ -sectors, in a geometry that matches the barrel part of the hadron calorimeter. The absorbers are composed entirely of 79 mm-thick brass plates with 9 mm gaps to accommodate 19 (3.7 mm-thick) scintillators. These provide a granularity of: $\Delta\eta \times \Delta\phi = 0.087 \times 0.087$ for $1.3 < |\eta| < 1.6$, thus matching the HB, which however deteriorates to $\Delta\eta \times \Delta\phi = 0.17 \times 0.17$ for $1.6 < |\eta| < 3.0$. The total length of the HE is about 10λ .

Outside the CMS HB is the magnet and above magnet there is also one more HCAL device, the Hadronic-Outer (HO). It covers the central region of pseudorapidity range $|\eta| < 1.26$, a region in which the stopping power of the EB and HB does not provide sufficient containment of the hadronic showers. The size and position of scintillator tiles in the HO approximately match the HB layers, providing a similar granularity of: $\Delta\eta \times \Delta\phi = 0.087 \times 0.087$.

The HO consists of 5, each 2.54 m wide along the z -axis and each having 12 identical ϕ -sectors. The central ring (ring 0) consists of two scintillator layers (figure 3.16) which are 10 mm thick, at a radial distance of 3850 mm and 4097 mm from IP.

The rest of the wheels ($\pm 2, \pm 1$) only have one layer of scintillator tiles, at a radial distance of 4097 mm. The scintillation light produced by hadronic showers within the detector that reach the HO calorimeter is collected by WLS fibres and transported to photodetectors with clear fibres, in similar fashion as in HB. The additional thickness provided by the HO increases the total depth of the CMS calorimeter system to a minimum of 11λ for the pseudorapidity range $|\eta| < 1.26$.

The very forward location of the HFs, results in an unprecedented average energy deposited of 760 GeV per LHC bunch-crossing, with a pronounced maximum at the highest rapidities. Compared to the rest of the detectors which receive about 100 GeV, this is a significant difference. The radiation-wise hostile environment that the HFs are exposed to was the primary factor when considering their design, aiming for a lifetime corresponding to 10 years of LHC operations.

The HF calorimeters are symmetrically positioned 11.2 m away from the IP5 and centred around the beam pipe. Each HF is essentially a cylindrical steel structure of outer radius 1.3 m, covering a pseudorapidity range of $3.0 < |\eta| < 5.2$. Each of this cylindrical structures is divided into 18 20° ϕ -wedges, composed of 5 mm-thick steel absorber plates, with quartz fibres embedded into dedicated grooves. The full depth of the absorber is 1.65 m, which corresponds to about 10λ . The quartz fibres, which were chosen as the active medium of the calorimeter, primarily due to their radiation hardness, run parallel to the beam line and are bundled in such a way as to provide a granularity of $\Delta\eta \times \Delta\phi = 0.175 \times 0.175$. They are used to generate Cherenkov light emitted by particles traversing the active medium, thereby rendering the calorimeter more sensitive to the electromagnetic component of cascade showers.

In order to enhance the ability to distinguish between electromagnetic and hadronic showers, the HF employs two set of quartz fibres which are read out separately. Half of the quartz fibres run over the full width of the steel absorber, while the other half start at a depth of 0.22 m from the face of the calorimeter. In this way, EM-showers can be distinguished from hadronic showers, due to the fact that

the former deposit a large fraction of their energy in the first 0.22 m, while the latter produce nearly equal signal on average over the two segments. The light produced in the quartz fibres is directed via light-guides into a shielded area where it is detected by Photomultiplier Tubes (PMTs).

The full HCAL properties, subsystems and features are summarised in table 3.2.

3.4.8 Muon system-chambers

The muon system of CMS [77, 56, 58] is the last subdetector layer that a particle generated at IP meets. Muon system mission is to identify and measure the momentum of the muons. Muons penetrate material and escapes detector without stopping into it, since they are MIPs, they have a modest interaction with matter (bremsstrahlung) due to their relatively-high mass. Muon system also plays an important role on triggering events based on their presence; muons usually indicates a clear (EW-content) event, candidate for “interesting” (known and new) physical process.

The muon momentum resolution and triggering capabilities are supported by the presence of the strong magnetic field (and its flux iron return yoke), which not only provides the required bending force but also absorbs hadrons that might escape HCAL and magnet. Therefore, muon chambers are placed as the last detector layer. The solenoid magnet shape led to the natural decision to design a muon system with a closed cylindrical shape, with a Muon Barrel (MB) and two Muon Endcaps (MEs) that close it, as shown in figure 3.17.

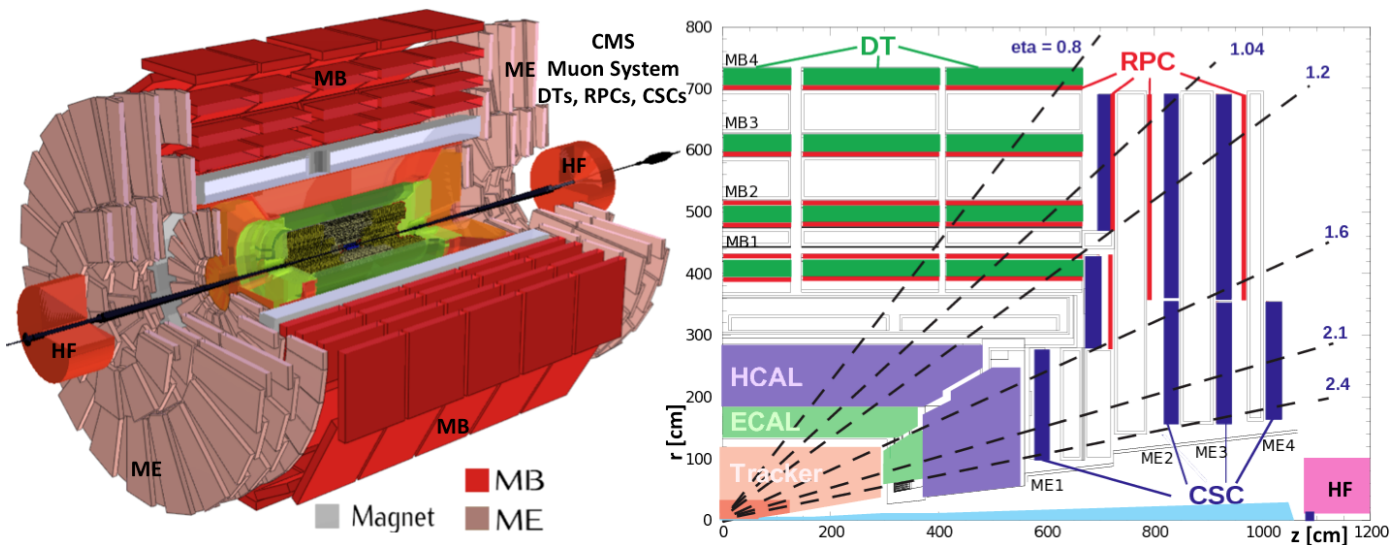


Figure 3.17: The CMS muon system, i.e.: chambers, RPCs, CSCs, DTs, at the z - x plane.

The deposition of energy and the subsequent detection of muons is implemented through the ionisation of an active gas and the collection of the resulting ions and electrons as electrical signal. The CMS muon system employs three different types of gaseous particle detectors; Drift Tubes (DTs), Cathode Strip Chambers (CSCs) and Resistive Plate Chambers (RPCs). Its position on CMS detector can be shown in figure 3.17 top-right.

1. The DTs measure muon position in the barrel part of the detector where the neutron-induced background and muon rates are small while the magnetic field is uniform and mostly contained in the iron yoke.
2. The CSCs are used in the endcaps, where the magnetic field is inhomogeneous and particle rates are high.
3. The RPCs are used in both the barrel and endcaps to provide fast decisions for the muon trigger system.

The barrel DTs, cover the pseudorapidity range $|\eta| < 1.2$ and are organised into four concentric cylindrical stations (MB1-MB4 figure 3.17 top-right), which are between the iron yoke layers and house in total 250 chambers. Each muon station consists of five wheels, each divided into 12 30° ϕ -sectors. The three innermost stations: MB1, MB2 and MB3 have 60 drift chambers each, while the outermost MB4 has 70, resulting in about 172000 sensitive wires. A DT chamber is made by three (or 2) Super-Layers (SLs), as shown in figure 3.18, and each is comprised of four successive layers of DT-cells. The DT cells geometry and SLs superposition ensure that no dead spots are present.

The operating principle is the ionisation of the active Ar/CO₂ gas volume inside and the resulting electrons are collected to the 2.4 m-long anode wire to which they drift due to the presence of electric field. The dimensions of a DT cell are 42×13 mm², which means the maximum path that the electrons have to drift is about 21 mm, corresponding to a drift time of about 380 ns. This value, which is determined by the size of the cell, the electric field and the gas mixture, is small enough to ensure a low occupancy of the DT-cells but also large enough to limit the number of active channels. DTs give two coordinates for the muon position with a single wire resolution of about 100 μ m for the r - ϕ measurement. Figure 3.18 illustrated the geometry and the operating principle of DTs.

Due to the high particle flux and the large magnetic field strength, the use of DTs in the forward regions is not suitable as the electron's drift path becomes too long. Consequently, endcap muon system employs 468 radiation resistant, fine segmented CSCs with fast response time that cover the pseudorapidity range $0.9 < |\eta| < 2.4$. In each endcap, the CSCs are organised into four stations of chambers: ME1-ME4 (figure 3.17 top-right). These chambers are mounted on the endcap disks enclosing the magnet, are oriented perpendicularly to the beam axis and interspersed in-between the iron yoke plates. The CSC chambers have a trapezoidal shape and cover 10° or 20° in the azimuthal angle ϕ . They are MultiWire Proportional Chambers (MWPCs), comprised of six anode wires interleaved with seven cathode panels that form six gas gaps.

They operate on the principle that if an electric field is established in a gas, the electrons released when a charged particle ionises the gas will drift to the anode wire (figure 3.18). With a high enough field strength, drifting electrons cause secondary ionisation and so forth, leading in numerous secondarily produced electrons which are collected as a pulse at the anode.

The anode wires are arranged in a plane between a common pair of cathode strips, each wire acting as a standalone detector. Since the cathode strips and anode wires are perpendicular to each other, two position coordinates are obtained for each passing particle traversing the active gas volume. The anode wires run azimuthally and measure a muon's radial coordinate, while strips run at constant azimuthal angle ϕ , thus providing the azimuthal angle measurement by a Gaussian fit between neighboring weirs. In total, the CSC chambers are comprised by *2times*106 wires, with an active gas volume of 50 m³ and a sensitive area of 5000 m², resulting in 220000 (180000) cathode (anode) read-out channels. The spatial resolution provided by the CSCs is about 75-150 μ m for the r - ϕ measurement. In addition the closely spaced wires make the CSCs fast detectors suitable for triggering.

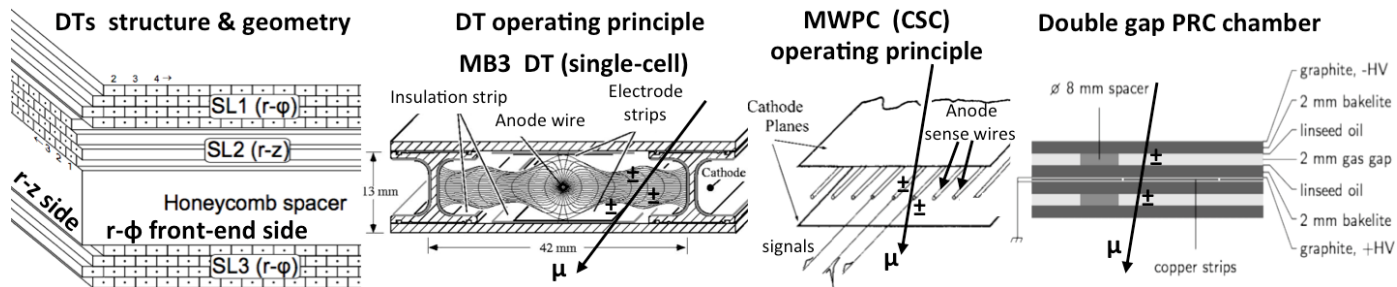


Figure 3.18: From left to right: the CMS DTs geometry, each DT individual cell, the CSCs' chambers operating principle (not CMS ones), and the CMS RPCs with its' layer substructure. (Taken from [77, 124]).

In both the barrel and endcap of CMS muon system, RPCs are employed as a dedicated muon trigger, while also contributing to the muon identification and reconstruction alongside DTs and CSCs.

In MB, 480 RPCs are sorted in six layers, two in each of the first couple stations (MB1-MB2), and one in each of the last two stations (MB3-MB4) (figure 3.17 top-right) covering the pseudorapidity range $|\eta| < 1.2$. In ME 432 RPCs are mounted in one plane in each of the first three stations (ME1-ME3), covering the pseudorapidity range $0.9 < |\eta| < 1.6$. Thus, there are six RPC layers in the central region, and three RPC layers in the forward region. The RPCs are fast gaseous detectors with a rough spatial resolution but precise time measurement, whose main properties are shown in table 3.2.

They consisted by two parallel plates, an anode and a cathode (as shown in figure 3.18 right), both made of bakelite, a plastic material of very high resistivity. These double-gap plates, which are covered with graphite to make electrodes, are separated by a gas volume that is ionised when a muon passes through chamber, and the resulting electrons are accelerated creating avalanche of electrons. These are collected by aluminium strips instead of the electrodes, which are transparent to the electrons. Each of the 912 in total RPC chambers contains a plane of strips, which are rectangularly segmented in the barrel and oriented parallel to the beam axis, whereas the endcaps are equipped with trapezoidal shaped strips of granularity: $\Delta\eta \times \Delta\phi = 0.1 \times 0.1$. Overall, the RPCs provide a spatial resolution of about 1 cm and a time resolution of less than ~ 3 ns, a time interval much shorter than the LHC bunch-crossing period of 25 ns.

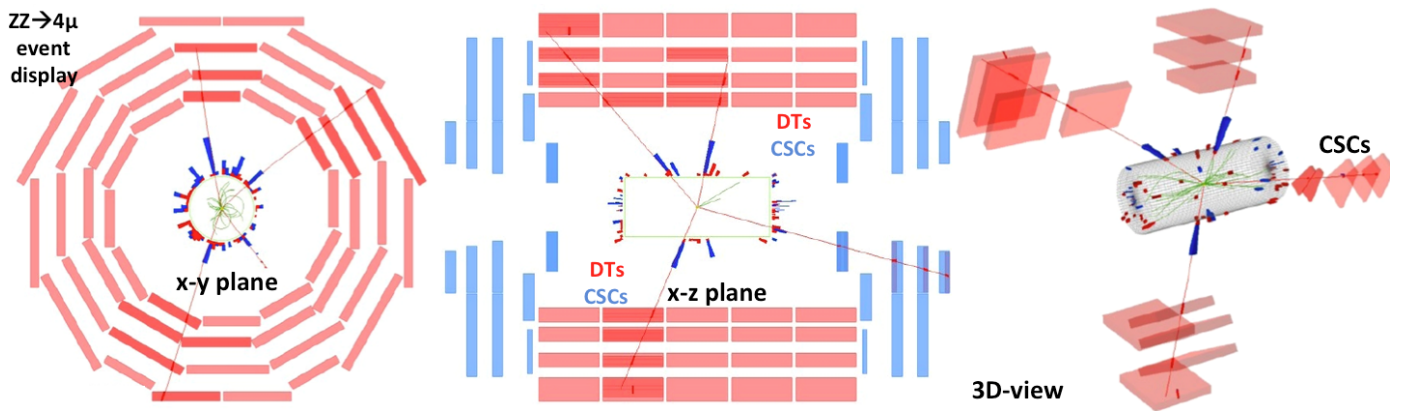


Figure 3.19: The 2D and 3D profile of a $ZZ \rightarrow 4\mu$ event. Only muon chambers are shown to illustrate their positions.

The off-line combination of the three muon-system detector information together with the rest devices provide an excellent muon reconstruction ability/resolution. Figure 3.19 shows a real $ZZ \rightarrow 4\mu$ event illustration where the four muons cross all subsystems. In conclusion, the CMS muon subsystems, provide four measurement points via the DT and CSC detectors, except for a gap at $|\eta| \sim 1.4$, where only three measurement points are provided. In addition, the RPC subsystem provides six measurements in the barrel region and three in the endcaps, enabling a relatively good muon momentum estimation even without the use of the tracking system. Furthermore, the excellent time resolution provided by the RPC subsystem provides an unambiguous identification to which a muon track is associated to, even at the in a high rates and large backgrounds environment, fully proper for muons triggering.

3.4.9 Forward detectors: CASTOR and ZDC

High pseudorapidity coverage is provided by two very forward detectors, CASTOR and ZDC [77]. CASTOR is a Cherenkov-based sampling EM/HAD-calorimeter, consisting of successive layers of tungsten (absorber) and quartz plates (active material), which covers the pseudorapidity region $5.2 < |\eta| < 6.6$. Its physics motivation is to complement the Pb-Pb collision physics program, developed essentially in the baryon-free mid-rapidity region, and also the diffractive and low- p_T physics in p-p collisions. Castor location can be seen in figures 3.7,3.8 and 3.16 and is only at the $-z$ side of the detector.

A set of two zero-degree calorimeters (ZDC), with pseudorapidity coverage of $|\eta| > 8.3$, are designed to complement HCAL for neutral particles very forward region, especially for heavy ion and p-p diffractive studies. It has a very similar design as CASTOR. Each ZDC has two independent parts: the

electromagnetic and the hadronic sections. Tungsten is used as absorber and the Cherenkov light is produced by quartz fibres. ZDCs location is ~ 140 m far from the IP and surround the two beam-pies even in-between of them.

3.4.10 Level one trigger

The LHC provides p-p and heavy-ion collisions at high interaction rates, (table 3.1) i.e.: a crossing frequency of 40 MHz. Depending on luminosity, several collisions occur, ~ 20 individual simultaneous p-p collisions occur at the nominal design luminosity of $10^{34}/(\text{cm}^2\text{s})$.

It is impossible to store and process the large amount of data resulting, a drastic rate reduction has to be applied. This task is performed by the trigger system; i.e.: trigger is the system which on-line (during the data production) filters all events and according to well defined physics criteria, decides to select and store only a small amount of them.

The rate is reduced in two steps called Level-1 (L1) Trigger and High-Level Trigger (HLT), respectively. The Level-1 Trigger consists of custom-designed, largely programmable electronics, whereas the HLT is a software system implemented in a farm of about a thousand processors. The rate reduction capability is designed to be at least a factor of 10^6 for the combined L1 and HLT triggers.

The design output rate limit of the L1 Trigger is 100 kHz, in practice the operational rate is chosen to be about 30 kHz (assuming a safety factor of 3). The L1 Trigger uses raw signal information data from the calorimeters and the muon system, while holding the high-resolution information data in pipe-lined memories in the front-end electronics.

The HLT has access to the complete read-out data and can therefore perform complex calculations similar to those made in the the analysis off-line software. The HLT algorithms evolve with time due to the accumulated experience and physics-analysis interests of the CMS collaboration.

For flexibility, the L1 Trigger hardware is implemented in FPGA technology where possible (Field-Programmable Gate Array: is an integrated circuit designed to be configured by a customer). ASICs and programmable memory Look-Up-Tables (LUT) are also widely used where speed, density and radiation resistance requirements are important. (ASIC: Application-Specific Integrated Circuit, is an integrated circuit customized for a particular use, rather than intended for general-purpose use; In computer science, an LUT is an array that replaces run-time computation with a simpler array indexing operation). A software system: the Trigger Supervisor, controls the configuration and operation of the trigger components.

The L1 Trigger has local, regional and global components.

- The Local Triggers, (also called Trigger Primitive Generators (TPG)), are based on energy deposits in calorimeter trigger towers and track segments or hit patterns in muon chambers, respectively.
- Regional Triggers combine their information and use pattern logic to determine ranked and sorted trigger objects such as electron or muon candidates in limited spatial regions. The rank is determined as a function of energy or momentum and quality, which reflects the level of confidence of the L1 parameter measurements, based on detailed knowledge of the L1-electronics and on the amount of available information.
- The global calorimeter and global muon triggers determine the highest-rank calorimeter and muon objects across the entire experiment and transfer them to the global trigger, the top entity of the Level-1 hierarchy.

The latter takes the decision to reject an event or to accept it (~ 1 per 10^5 events) for further evaluation by the HLT.

The decision is based on algorithm calculations and on the readiness of the sub-detectors and the DAQ (Data Acquisition System), which is determined by the Trigger Control System (TCS). The Level-1-Accept (L1A) decision is communicated to the sub-detectors through the Timing, Trigger and Control (TTC) system. The architecture of the L1 Trigger is depicted in figure 3.20. The L1 Trigger

has to analyze every bunch crossing. The allowed L1 latency, between a given bunch crossing and the distribution of the trigger decision to the detector front-end electronics, is: $\sim 3.2 \mu\text{s}$. The processing must therefore be pipelined in order to enable a downtime-free operation. The L1 Trigger electronics is housed partly on the detectors, partly in the underground control room located at a distance of approximately 90 m from the experimental cavern. An overview of the CMS L1 properties is given in table 3.2.

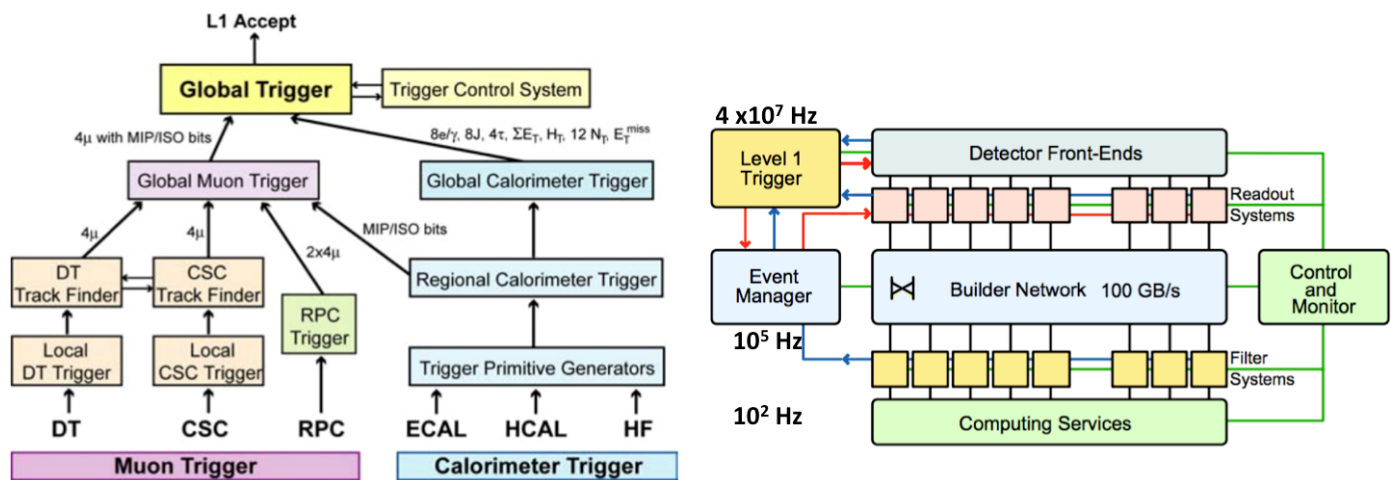


Figure 3.20: The architecture of CMS L-1 trigger (left), and the CMS DAQ (right). (Taken from [77]).

3.4.11 High level trigger and data acquisition

The L1 Trigger processes fast trigger information coming from calorimeters and muon systems, and only selects events with interesting content. It is able to analyse all forwarded information for further filtering at a maximum rate of 100 kHz. With a mean event size of 1 MB of zero-suppressed data in the CMS read-out systems, this rate corresponds to a data flow of about 100 GB/s fed by the L1 to the DAQ system. The DAQ system must thus be able to sustain such rates and provide enough computing power for the HLT, which is a software-based filter system.

The HLT task is to provide a further event-rate reduction of the order of 10^3 , reducing the incoming L1 trigger input of 100 kHz to a rate of 100 Hz. These 100 events per second will be recorded for offline processing and analysis. In order to achieve the required rate reduction 100 Hz, a computing power corresponding to ~ 1000 processing nodes is required running the corresponding selection algorithms. An overview of the CMS HLT parameters is shown in table 3.2.

To achieve the required rate reduction, all events that pass the L1 Trigger are sent to a computer farm known as the Event Filter, located in a dedicated room on the surface of the CMS cavern, not far away from the CMS detector. The Event Filter uses access to the full read-out data from the CMS detector to perform physics selections using faster versions of the offline reconstruction software, in order to filter events and reduce the output rate within a time interval of: 0.04 to ~ 1 second.

The various subdetector Front-End Systems (FESs) store data continuously in 40 MHz pipelined buffers, and upon the arrival of a L1A decision via the TTC system, the full detector data are extracted and pushed to the DAQ system by the Front-End Drivers (FEDs). The Event Builder assembles the data from all FEDs into a single complete event and transmits it to a Filter Unit (FU) in the Event Filter for further processing.

CMS HLT implements trigger paths using a combination of more than one trigger physics object, like for example high lading jet momentum of lepton momentum together with a second or third jet or a second lepton etc. Such trigger paths are referred to as cross-triggers. An example could be the trigger which looks for events with at least one jets with $p_T > 30 \text{ GeV}$ each, along with an isolated muon with $p_T > 25 \text{ GeV}$. In order to trigger physics-process which are not rare but still interesting

(in analysis perspective) without increase HLT output rate, prescaled trigger paths are implemented selecting a defined fraction of events of a particular topology.

3.4.12 Computing infrastructure and software

During data taking periods, the output of the HLT is directly reconstructed at the so-called Tier-0 which is located at CERN Computing Center (CCC). Because of the huge amount of data that can be more than: ~ 1 GB/sec, or ~ 1 PB/year, the need to properly distribute both the collision as well as the simulation data, is of vital importance for the CMS collaboration.

To achieve that, several Tier-1 and Tier-2 computing clusters have been accommodated in various institutes all over the world. Together they constitute the so-called CMS computing infrastructure which is implemented on top of the WorldWide LHC Computing Grid (WLCG), a very powerful network of computers which allows analysts to use the required computational resources for analysis. No matter if it is collision or simulated events, both can be accessed from any grid enabled machine using appropriate software tools (like CRAB). Figure 3.21 illustrates the data flow between CMS data centers and Tiers.

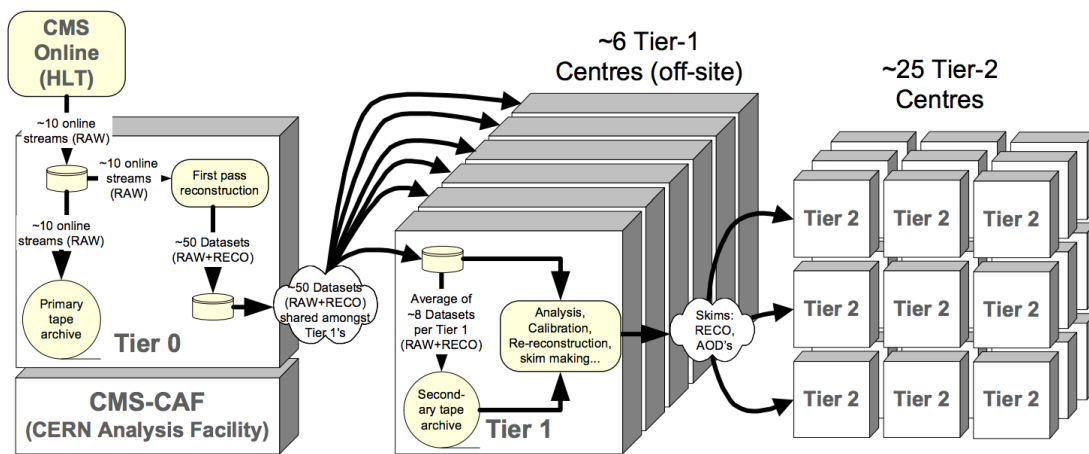


Figure 3.21: A schematic illustration of data processing flow after HLT selection towards the analysis final-object extraction. (Taken from [77]).

The backbone of data analysis is the CMS Software called CMSSW which is written in Python and C++, and it is the result of the combined efforts of thousands of CMS members over the past ~ 15 years. This software, is a rather sophisticated mixture of various integrated software packages, which allows users to explore and use different tools. These can include the generation of simulated events, detector-level reconstruction, or even data analysis using of the reconstructed final objects.

3.5 Physics objects reconstruction and identification

3.5.1 Introduction and the Particle Flow reconstruction concept

As has been discussed every 25 ns (nominally) about 20 p-p pairs come to inelastic collision producing $\sim 10^3$ new particles which then travels through the detector material interacting in various ways. Most of these particles have a rather low momenta and does not corresponds to the process where we are interested in study. However a good understanding of all particle content of a bunch crossing is necessary.

One of the CMS primer objectives in order to do physics analysis is first to identify and reconstruct those particles in the highest possible efficiency and purity (lowest misidentification “fake” rate). We can have a feeling of the challenge by looking the figure 3.22, which illustrates a real CMS bunch-

crossing reconstruction picture with multiple primary vertexes. We can see the particles' tracks which has been clustered in colors due to their parent p-p vertex.

The CMS collaboration employs the so-called “Particle Flow” (PF) approach for the physics object reconstruction mission. This approach combines in the most efficient way information from all sub-detector components, prior to jet clustering and missing energy calculation, to identify, reconstruct and classify all stable particles (of an event) into five main categories/objects: photons, muons, electrons, neutral and charged hadrons. From these particles, composite objects such as jets, (hadronic) taus and \cancel{E}_T , are reconstructed in an optimal determination of their direction, energy and type [59].

The input information to the PF event reconstruction are: the charged-particle tracks, the clusters of energy deposits in the calorimeters and the hits (tracks) from the muon system. The output of the PF event reconstruction is a collection of particle candidates (belonging in one of the five categories above) associated to an p-p event. Compared to calorimeter-based reconstruction methods, the PF event reconstruction has been found to be superior with respect to the spatial and energy resolution of the reconstructed jets [66], while it also gives a more accurate measurement of the \cancel{E}_T of the event [59, 98].

In the next subsections we will briefly overview the physics objects identification and reconstruction techniques; information shown is gathered from references: [59, 128, 86, 61, 66, 98, 68, 64, 71, 67, 28, 65, 16, 40, 2, 92].

3.5.2 Track reconstruction

Track pattern recognition is very important for CMS since two thirds of the produced particles are charged. It is also a very challenging task under the high track densities (figure 3.22), and a main consumer of CPU resources in the overall event reconstruction.

In principle the trajectory of each charged particle consists in general of a deterministic and a stochastic component. The deterministic aspect of the trajectory is due to the known magnetic field and leads to a helical (3D) track if the field is homogeneous (which roughly is the case for CMS tracker). This part of the trajectory is entirely determined by the equations of motion, material effects like multiple scattering or energy loss give rise to stochastic components. Thus the realistic track pattern turn to circular helical, with gradually decreased radii and step, which often including knees (angles). A proper accounting for stochastic effects is essential in order to obtain an unbiased estimation of the track parameters (and their covariance matrix).

The track reconstruction is decomposed into five logical parts [56]:

- Hit reconstruction, which in turn consists of clustering of strips or pixels and estimating a position and its uncertainty
- Seed generation
- Pattern recognition or trajectory building
- Ambiguity resolution
- Final track fit

First step is the clustering of the signals produced by charged particles in the pixel and strip subdetectors into hits. After estimating the position and the uncertainty of the hits, they are used to generate the seeds of tracks.

The minimum information needed to construct a curvature is three seeds or a pair of seeds with an additional constraint from beam-spot or vertex. To increase the tracks reconstruction efficiency, tracks are generated in four different ways: pixel triplets, pixel or strip pairs with beam-spot or vertex constraint, or strip-only pairs with beam-spot constraint.

The pattern recognition and the track building starts from the collection of seeds and proceeds by including successive detection layers. The track reconstruction procedure (and the estimation of the its parameters) implements the method “Combinatorial Kalman Filter” (CKF) [61, 68, 64, 40]. It is also

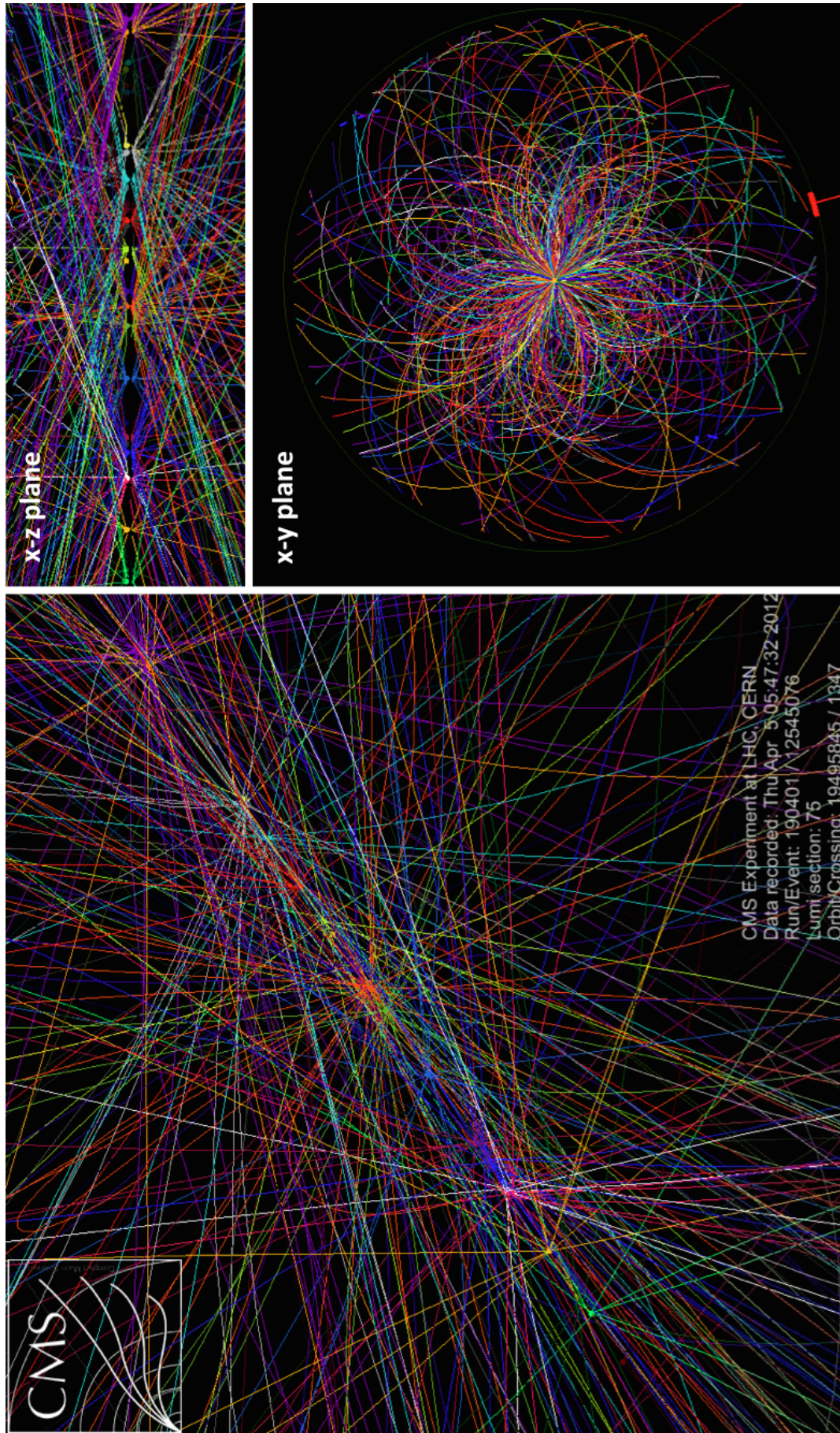


Figure 3.22: CMS events with 29 distinct p-p vertices within a single bunch crossing. Tracks of generated particles tagged with colors due to their parent p-p vertex.

known as Combinatorial Track Finder (CTF), and is the default CMS track reconstruction algorithm as it provides the best performance both in terms of physics results and computing time. The CKF addresses ambiguities which consist the main complication of track pattern recognition in complex events. Ambiguities arise from the passage of several particles through the same detector areas or the presence of noise hits, also the possibility that the expected hit is missing due to limited efficiency. As soon as a new layer is included, the track parameters are re-calculated leading to a more precise estimation of the trajectory. The procedure is repeated until the last detection layer is reached. In each step, track candidates are rejected based on quality criteria (χ^2 method, or number of valid and invalid hits).

During the track reconstruction, the same tracks may be created multiple times starting from different seeds or a given seed may be included into many track candidates. The final track collection consists of cleaned candidates that share maximum 50% of their seeds. Before the final track fit, spurious hits are removed and the track is refitted. The track collection consists of many fake tracks, that are significantly reduced by applying appropriate selection on their quality criteria.

3.5.3 Vertex reconstruction

An example of reconstructed primary vertices (PV) by CMS can be shown in figure 3.22. By primary vertex one means the exact 3D-location where an individual p-p collision took place. This PV reconstruction comes with its corresponding set of tracks – particles originated by this vertex. The accurate reconstruction of vertices and the correct assignment of their corresponding tracks is very important for the correct description of the event final state content. This is a challenging task when multiple collisions take place in the same bunch-crossing (high pile-up).

At a first step, the reconstructed tracks are grouped into clusters based on the z -coordinate of their shortest (to the beam line) point. Then, as second step, a 3D vertex-fit is performed with the tracks in each cluster, using the full track information [92, 132].

The main challenge for the clustering step in the presence of high pile-up is to avoid merging tracks from separate p-p collisions into a single cluster, while at the same time preserving a good efficiency of assigning tracks to the proper clusters, and a low rate of fake clusters not corresponding to a p-p interaction. The algorithm used in CMS to perform clustering is the “deterministic annealing” [134, 46, 132]: starting from a very loose clustering in which the same track can contribute to multiple clusters, the association between tracks and clusters is iteratively tightened to produce narrower clusters and more definite track-cluster assignments. With this algorithm it is possible to resolve vertices with separations down to about 1 mm, appropriate for a multiplicity of interactions per bunch crossing up to 20.

Vertex fitting is performed with the “adaptive vertex fitter algorithm” [138, 132], which addresses the issue of secondaries and fake tracks in the cluster by iteratively under-weighting the tracks which are not compatible with the common vertex being fitted. The resolution on the vertex position depends on the number of tracks in the vertex, and is in the 2050 μm range.

3.5.4 Calorimeter clustering

The calorimeter clustering is taking place with algorithm for the four following reposes:

- detect and measure the energy and direction of stable neutral particles such as photons and neutral hadrons,
- separate these neutral particles from energy deposits from charged hadrons,
- reconstruct and identify electrons and all accompanying “bremsstrahlung” photons,
- help the energy measurement of charged hadrons for which the track parameters were not determined accurately, which is the case for low-quality, or high- p_T tracks.

A specific clustering algorithm has therefore been developed for the particle-flow event reconstruction [59], aiming high detection efficiency (even for low-energy particles), and towards a separation of close energy deposits (as the example in figure 3.23). The clustering is performed separately to each sub-detector: ECAL barrel, ECAL endcap, HCAL barrel, HCAL endcap, Preshower-first layer and Preshower-second layer. In the HF, no clustering is performed so far, so that each cell gives rise to one cluster.

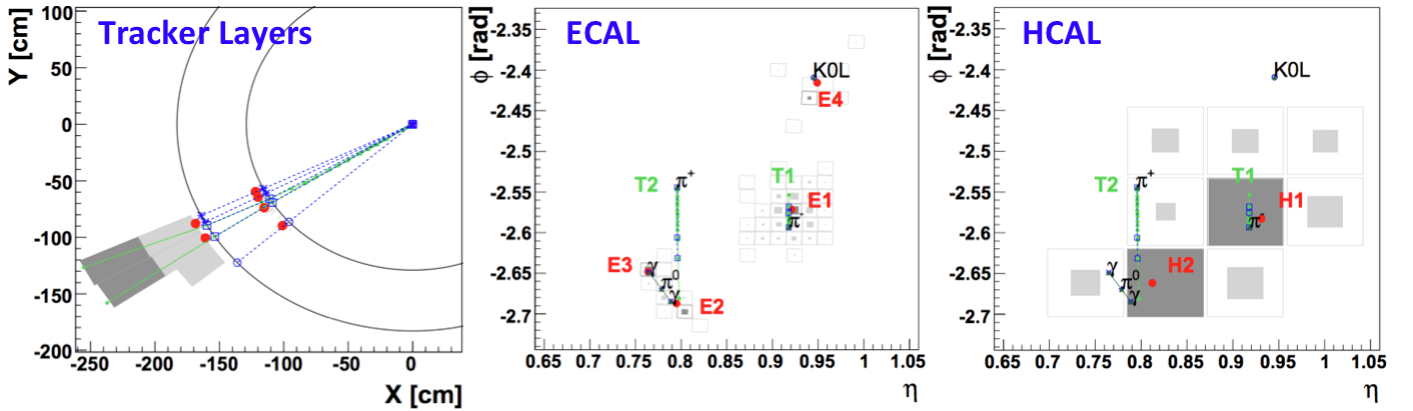


Figure 3.23: An event display of a simple jet in the x - y view left, in η - ϕ in the middle and right with the ECAL and HCAL surfaces respectively. The K_L^0 , the π^- and the two photons from the π^0 decay are detected as four well separated ECAL clusters (middle). The π^+ leaves no energy in the ECAL. The two charged pions are reconstructed as charged-particle tracks, appearing as vertical solid lines in the $\eta - \phi$ views and circular arcs in the $x - y$ view. These tracks point towards two HCAL clusters (right). In all three views, the cluster positions are represented by dots, the simulated particles by dashed lines, and the position of their impact on the calorimeter surfaces by various open markers. Taken from [59].

The clustering algorithm firsts identifies “cluster seeds” as local calo-energy maxima above a given energy, then “topological clusters” are grown from the seeds by gathering cells with at least one side in common with a cell already in the cluster, and with an energy in excess of a given threshold. (These thresholds represent two standard deviations of the electronics noise [59].) A topological cluster gives rise to as many “particle-flow clusters” as seeds. The calorimeter granularity is exploited by sharing the energy of each cell among all particle-flow clusters according to the cell-cluster distance, with an iterative determination of the cluster energies and positions. In a simple jet example the resulting clusters, four of which are resolved from two topological clusters (one in ECAL, one in HCAL), are represented by dots in figure 3.23.

3.5.5 Particle Flow algorithm

A given particle is, expected to give rise to several particle-flow elements in the various sub-detectors (charged-particle track, calorimeter clusters, muon track). A simple example is shown in figure 3.23. These elements must be connected to each other by a “link algorithm” to fully reconstruct each single particle, and getting rid of any possible double counting.

The link algorithm is performed for each pair of elements in the event and defines a distance between any two linked elements to quantify the quality of the link. The algorithm then produces “blocks” of elements linked. Thanks to the granularity of the CMS detectors, blocks typically contain only one, two or three elements, and constitute simple inputs for the particle reconstruction and identification algorithm.

The smallness of the blocks ensures the algorithm performance to be essentially independent of the event complexity, for example, jets as simple as that of figure 3.23, made of one to four blocks, turn out to have the same energy response and resolution as regular jets found in QCD events, which typically

feature a larger number of blocks, but of the same size. More specifically, a “link” between a charged-particle track and a calorimeter cluster proceeds as follows. The track is first extrapolated from its last measured hit in the tracker to the layers of Preshower, ECAL and HCAL, at a proper depth typical of a hadron shower. The track is linked to any given calorimeter cluster if the extrapolated position is within the cluster boundaries. The link distance is defined as the distance in the $\eta - \phi$ plane between the extrapolated track position and the cluster position.

Algorithms are dedicated to reconstruct individual electrons and muons [127] which also accounts the potential radiated energy and accurately reconstruct the object. These method will be discussed in the next subsections. Charged hadrons are reconstructed [59] from the tracks in the central tracker. Photons and neutral hadrons are reconstructed from energy clusters in calorimeters. Clusters separated from the extrapolated position of tracks in the calorimeters constitute a clear signature of these neutral particles. A neutral particle overlapping with charged particles in the calorimeters can be detected as a calorimeter energy excess with respect to the sum of the associated track momenta. The resulting list of reconstructed particles constitute a global description of each event, available for subsequent physics analysis.

3.5.6 Muons

As has been indirectly mentioned muons are considered “stable” in the sense that: they have mean lifetime $\tau_\mu \sim 2.2 \mu\text{s}$, mass $m_\mu \simeq 0.1 \text{ GeV}$; so, even an 1 GeV muon (with $\gamma \simeq 10$) has a 50% provability to survive and travel a distance of $(c\tau_\mu 10 \ln 2) \simeq 5 \text{ km}$ before decay. Therefore one can safely consider that the muons generated in p-p collision are only decade away the ($\sim 10 \text{ m}$ long) detector devices and we can treat them as stable. (The fraction of the 50 GeV muons which decay before they escape last level of detection is $(1 - \exp[-\Delta x/(c\gamma\tau)]) \times 100 \sim 0.005\%$).

Muons are reconstructed using information from the silicon tracker and the muon system [92, 71, 67, 128], leading in the following three reconstruction approaches:

1. Tracker reconstructed muons (local reconstruction).

Tracks reconstructed (almost only) by the silicon tracker, (with $p_T > 0.5 \text{ GeV}$ and $p > 2.5 \text{ GeV}$), are considered as muon candidates and are extrapolated to the muon system, while taking into account effects from multiple scattering. If at least one compatible muon segment is found, then the corresponding track is promoted to tracker muon. In such tracker-muons, momentum and position assignment is estimated only from the strip-track. This approach is very efficient for relatively low p_T muons, exploiting the excellent tracker performance.

2. Standalone (only muon-chambers) reconstructed muon (local reconstruction).

The standalone muon reconstruction uses information only from the muon system. Tracks in the muon chambers are reconstructed following a very similar method as the one described for the track reconstruction (CKF). The trajectories found are then propagated to the closest vertex to reject reconstruction of cosmic ray muons. Hence, position and momentum are estimated using only the muon system. This approach serves L1-trigger purposes and is mainly used as input for the global muon reconstruction.

3. Global muon reconstruction.

Global muons are reconstructed from standalone muons which are matched to the most compatible tracker-muon track. The hits from both the tracker and the muon system are used to perform a fit, (using the CKF technique) to create the global track. For transverse momenta with $p_T < 200 \text{ GeV}$ the momentum estimation is driven by the tracker resolution, while for larger momenta the global muon fit can improve the estimation compared to the tracker only estimation.

In general, several sources can lead to muon (or a muon-like) objects. We can roughly classify the muon candidates as follows:

- Prompt muons. These are muons that can be associated directly with the IP and an individual PV near by. These are mostly coming from an on-shell, Z or W boson leptonic decays, or even can

produced by a tau-leptonic decay near the IP. Their features are basically relatively low momenta ($p \gtrsim 15$ GeV), high isolation, small impact parameters: d_{xy}, d_z (distances of track from the PV).

- Non-prompt muons. These are muons coming from hadron decays. These can be further separated between muons coming from heavy or light flavour quark transition. The light-flavour category includes decays of in-flight π or K mesons, or even particles produced while interacting with the detector material. In the case of heavy-flavours, the muon can come from a charmed or a beauty quark transition (via an off-shell W-boson). Typical non-prompt (NP) muon profile is relatively low momentum, usually appears in a busy-track environment i.e.: non isolated and without necessarily small impact parameters.
- Fake muons. Hadron punch-through from the remnants of a hadron shower that penetrates the calorimeter detector and reaches the muon-chambers. These misidentified “muon-like” objects give hits in the muon chamber, however typically are not matched with inner tracker seeds. An other case of fake reconstruction is by duplicate false-reconstruction of single (real) candidate muons are due to the largest number of neighboring hits. Fakes and non-prompt have the same profile in terms of p_T , isolation and impact parameters.

In the following chapters analysis we will refered to non-prompt and fakes inclusively as non-prompt (NP) muons (and we will also generalize this to leptons including electrons accordingly).

The full set of the muon parameters where we cut over to define the reconstructed muons is listed in table 3.3. With these selections cuts a high identification and reconstruction efficiency is achieved together with high purity. Figure E.7 in appendix E.3 shows the identification and reconstruction efficiencies for muons versus p_T and $|\eta|$. The data which are used are from $Z \rightarrow \mu\mu$ and $J/\psi \rightarrow \mu\mu$ processes for above and bellow the $p_T = 20$ GeV respectively, and tag and probe method has been used.

Table 3.3: Muons and electrons identification requirements for “Loose” and “Tight” selections. First block muons, second block electrons broken down into barrel and endcap electrons (Taken from [96, 97, 92]).

Muons ID variable	Muons Tight ID	Muons Loose ID
μ -reco type	Tracker & Global	Tracker or Global
p_T	> 20 GeV	> 15 GeV
$ \eta $	< 2.1	< 2.5
$I_{rel} = I_{abs}/p_T(\mu)$	< 0.12	< 0.2
Global- μ track fit χ^2/ndf	≤ 10	-
Valid muon hits	> 0	-
Matched stations	> 1	-
Pixel hits	> 0	-
Track layers with hit	> 5	-
Transverse distance from PV: d_{xy}	< 0.02 cm	< 0.2 cm
Longitudinal distance from PV: d_z	< 0.5 cm	< 0.5 cm
Electrons ID variable	Electrons Tight ID Barrel, Endcap	Electrons Loose ID Barrel, Endcap
p_T	> 20 GeV, > 20 GeV	> 15 GeV, > 15 GeV
$I_{rel} = I_{abs}/p_T(\mu)$	$< 0.15, < 0.15$	$< 0.15, < 0.15$
H/E	$< 0.12, < 0.10$	$< 0.15, < -$
$ \Delta\phi_{in} $	$< 0.06, < 0.03$	$< 0.8, < 0.7$
$ \Delta\eta_{in} $	$< 0.004, < 0.007$	$< 0.007, < 0.01$
$ \sigma_{i\eta i\eta} $	$< 0.01, < 0.03$	$< 0.01, < 0.03$
Missing hits	$\leq 0, \leq 1$	- , -
Conversion Rejection	true, true	- , -
Transverse distance from PV: d_{xy}	< 0.02 , < 0.02 cm	$< 0.04, < 0.04$ cm
Longitudinal distance from PV: d_z	$< 0.1, < 0.1$ cm	$< 0.2, < 0.2$ cm

3.5.7 Electrons

The electrons in CMS are reconstructed using two algorithms varying to the initial seed. The first uses energy deposits in ECAL as seed for the electron reconstruction, whereas the second starts from a track seed to build the electron candidate.

1. The ECAL-driven algorithm [28, 65, 92].

For electrons with $p_T > 5$ GeV, It has the advantage of increased purity compared to the track-driven approach for a similar efficiency. The algorithm starts by clustering deposits of energy in several crystals of the ECAL, creating ECAL clusters. The clustering algorithm accounts for the effects induced by the passage of electrons through the tracker; when an electrons traversing the tracker interact with its material (shown in figure E.4 appendix E.3) and radiate photons (figure 3.24), hence the energy deposits on ECAL are spread in a ϕ range (due to the bended track). This effect is very important since electrons typically radiate $\sim 50\%$ of their initial energy before they reach the ECAL. These additional energy-deposits are identified and summed with the ECAL clusters to form the ECAL super-clusters. Super-clusters with $E_T > 4$ GeV are matched with the most compatible track seeds and then, using the Gaussian Sum Filter (GSF) algorithm [16, 40]. The GSF (is an extension of Kalman Filter method) able to deal with profoundly non-Gaussian random variables, which can deals with radiative energy-loss, (at a significant expense of computing power). Information of both ECAL and tracker is combined for the most precise momentum assignment in reconstruct of the electron's final trajectory.

2. The track-driven algorithm [64, 92].

This is used mainly to reconstruct very low p_T electrons, or electrons inside jets, where the energy deposits on ECAL are very widely spread across ϕ , leading to mismeasurement of the actual electron's energy. The procedure starts from the reconstructed tracks fitted by the GSF algorithm which is extrapolated from the outermost hit to the closest possible ECAL cluster candidate. If no compatible ECAL-seed is found, the track is not considered appropriate for the electron reconstruction. Then again, important fraction of electron's energy is carried out by bremsstrahlung photons (as illustrated in figure 3.24). To account for this effect, for each hit used to estimate the GSF track, a straight line tangential to the direction of the track is extrapolated up to the ECAL. If an ECAL cluster, which is not already linked to any track, is found, the energy is added to the total electron energy. The final selection of electrons is based on the output of a Boosted Decision Tree (BDT) [137] which combines information from several observables related to tracker and ECAL.

Additional selections are applied on the reconstructed electrons to suppress backgrounds originating by photon-converted electrons or pions misidentified as electrons. Electrons from photon conversions are reconstructed by selecting two opposite sign tracks and estimating the conversion vertex. In addition, an electron from a photon conversion is expected to have missing hits in the pixel. Therefore, the distance from the primary vertex, the conversion vertex fit probability and the number of missing hits in the pixel, are used to discriminate them. Table 3.3 shows the variables and their cuts witch define the a tight and a loose selection of electrons with different purity and reconstruction efficiency $\sim 80\%$ and $\sim 95\%$ respectively. The most important are: the energy-momentum match between the seed cluster and track, defined as E_{seed}/p_{in} , the transverse shower profile along the direction, $\sigma_{i\eta i\eta}$, the spatial matching in η and ϕ between track and super-cluster, $\Delta\eta_{in}$ and $\Delta\phi_{in}$, and the ratio of the energy deposit in HCAL and ECAL, defined as H/E . These variables distributions can bee seen in figure E.8 in appendix E.3.

Electrons, as like muons, can be characterized and categorization as: prompt, non-prompt and fakes (and usually last two are merged into non-prompt NP). This categorization follows the same criteria as for NP muons and also leads to the same kinematic features in terms of isolation, impact parameters and momenta. However the fake electrons are significantly larger compared to muons and hence the reconstructed efficiency for prompt electrons is smaller (compared to muons) and depends strongly on the identification algorithm. To increase the purity of the electron collection, tight selection on the identification variables is applied.

3.5.8 Lepton isolation

Isolation requirements are imposed to charged leptons: e and μ as a handle to suppress the QCD background and reduce leptons arising from heavy flavor decays and decays in hadron flight. Two

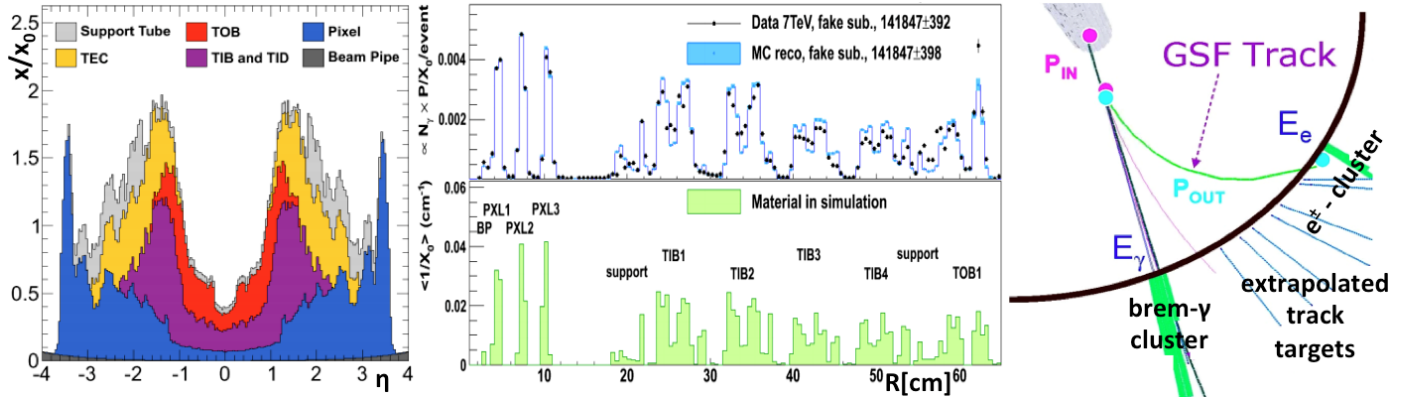


Figure 3.24: Left: material budget of tracker up to ECAL in units of radiation length as a function of η , extracted from simulation. Middle: material budget in the tracker as function of the radius R , measured using reconstructed photon conversions in data and simulation and extracted from simulation (top-bottom respectively). Right: illustration of an electron undergoing a large radiative energy loss in the material, depicted in the transverse plane: the local curvature of the GSF track close to the interaction point provides an estimate of the initial momentum p_{in} , while that close to the ECAL surface allows to estimate the final one p_{out} . The tangents to the trajectory are used to collect the bremsstrahlung clusters in the particle flow. (Taken from [132].)

methods are used to estimate the degree of isolation of a given particle [92]. The more traditional method estimates the level of isolation based on the sum of the p_T of the tracks and the energy deposits in the calorimeters in a cone $\Delta R < 0.4$ around the charged lepton. The subdetector-based isolation, I_{comb}^{rel} (calo), is defined as:

$$[CALO] \quad I_{comb}^{rel} \equiv \frac{1}{p_T(\ell)} \left[\sum_i p_{T,i}^{tracker} + \sum_i E_{T,i}^{ECAL} + \sum_i E_{T,i}^{HCAL} \right], \quad \Delta R(\ell, i) < 0.4. \quad (3.11)$$

An other more advanced method is used to estimate the isolation variable using objects reconstructed by particle flow. Similarly, the isolation is calculated in a cone $\Delta R < 0.4$ around the charged lepton. In this case particle flow based isolation, I_{rel}^{comb} (PF), is defined as:

$$[PF] \quad I_{comb}^{rel} \equiv \frac{1}{p_T(\ell)} \left[\sum_i p_{T,i}^{charged \ hadrons} + \sum_i E_{T,i}^{photons} + \sum_i E_{T,i}^{neutral \ hadrons} \right], \quad \Delta R(\ell, i) < 0.4. \quad (3.12)$$

Where the first term is the sum of the p_T of the charged hadrons, the second is the sum of the E_T of the photons and the last is the sum of the E_T of the neutral hadrons. (To reduce contributions from electronics noise, photons and neutral hadrons are required to have $E_T > 0.5$ GeV). In parallel to the luminosity increase, the number of pile-up interactions increases as well, leading to a degradation in the isolation efficiency. The contribution in the calculation of isolation from particles originating from minimum bias interactions becomes significant and has to be reduced. Charged particles are rejected by using the vertex information. For the neutral particles this approach is not feasible and a specific correction, known as $\Delta\beta$ correction, is implemented [27]. The $\Delta\beta$ correction relies on the fact that, on average, the relative fraction of the jet energy carried out by charged and neutral particles is $\sim 2:1$. The correction is calculated by estimating the isolation from all charged particles that do not originate from the primary vertex, which are particles from PU interactions, and then using the average “charge-to-neutral energy fraction”, the contribution of PU due to neutral particles is extracted. The $\Delta\beta$ corrected isolation has the form [92, 27]:

$$[PF, \Delta\beta] \quad I_{comb}^{rel} \equiv \frac{1}{p_T(\ell)} \left[\sum_i p_{T,i}^{chd.Had.} + \max\left(0, \left(\sum_i E_{T,i}^{\gamma} + \sum_i E_{T,i}^{neut.Had.} - \frac{1}{2} \sum_i E_{T,i,\Delta\beta}^{chd.Had.} \right) \right) \right], \quad \Delta R_{li} < 0.4. \quad (3.13)$$

This method exhibits an improved performance and hence used for the analysis presented next. The numerator of each I^{rel} defines the corresponding absolute isolation I^{abs} . Both relative and absolute isolation are used in the analysis follows and always $\Delta R(\ell, i) < 0.4$ is considered.. In cases with soft leptons (low $p_T(\ell)$), where the I^{abs} is comparable with $p_T(\ell)$: $I^{abs}/p_T(\ell) \gtrsim 0.2$) then the I^{rel} is needed to guaranty isolated lepton.

3.5.9 Jets reconstruction/clustering

Quarks and gluons in final state products hadronize immediately after their production, as shown in figure 3.15 left, leading to a spray of energetic hadrons boosted in similar directions. These hadrons are then naturally clustered in what is refereed as a jets.

A jet reconstruction is defined by a set of objects, and an algorithm to clusterize them [132]. Several options are available for both these choices but the vast majority of the analyses, rely on jets from particles reconstructed using particle flow approach and clustered according to the “anti-kT” algorithm with distance parameter $\Delta R = 0.5$. ΔR is defined in appendix A, it is also called clustering radius (also shown in figure A.1 over the $\eta - \phi$ plane). The PF approach (one of the three available), exploiting the precision of the tracker and the full granularity of ECAL, provides a very significant improvement to the jet energy and direction resolutions compared to calorimetric-only approaches. The use of PF reconstruction also allows a high reconstruction efficiency for jet constituents with low momentum achieving a jet energy response close to unity even before calibrations.

Detector jets belong to three types, depending on the way which the contributions from subdetectors are combined: “Calorimeter jets”, “Jet-Plus-Track jets” and “Particle-Flow jets”. Figure 3.25 (top left) helps the visualization of the following three definitions.

- Calorimeter jets (“CALO-jets”) [69]: are reconstructed from energy deposits in the calorimeter towers. A calorimeter tower consists of one or more HCAL cells and the geometrically corresponding ECAL crystals. A four-momentum is associated to each tower deposit above a certain threshold, assuming zero mass, and taking as a direction the tower position as seen from the interaction point.
- Jet-Plus-Track (JPT) jets [69]: are reconstructed calorimeter jets whose energy response and resolution are improved by incorporating tracking information (according to the Jet-Plus-Track algorithm [57]). “Calo-jets” are first reconstructed as described above, and then charged particle tracks are associated with each jet, based on the spatial separation between the jet axis and the track momentum vector, measured at the interaction vertex, in $\eta - \phi$ plane. The associated tracks are projected onto the front surface of the calorimeter and are classified as in-cone tracks if they point to within the jet cone around the jet axis on the calorimeter surface. The tracks that are bent out of the jet cone because of the CMS magnetic field are classified as out-of-cone tracks. The momenta of charged tracks are then used to improve the measurement of the energy of the associated calorimeter jet: for in-cone tracks, the expected average energy deposition in the calorimeters is subtracted and the momentum of the tracks is added to the jet energy. For out-of-cone tracks the momentum is added directly to the jet energy. The Jet-Plus-Track algorithm corrects both the energy and the direction of the axis of the original calorimeter jet.
- Particle-Flow jets (PF-jets) [69]: are reconstructed by clustering the four-momentum vectors of particle-flow candidates. The PF algorithm [59] combines the information from all relevant CMS sub-detectors to identify and reconstruct all visible particles in the event (muons, electrons, photons, charged and neutral hadrons). Charged hadrons electrons and muons, are reconstructed from tracks. Photons and neutral hadrons are reconstructed from energy clusters separated from the extrapolated positions of tracks in ECAL and HCAL, respectively. A neutral particle overlapping with charged particles in the calorimeters is identified as a “calorimeter energy excess” with respect to the sum of the associated track momenta. The energy of photons is then obtained from the ECAL measurement (corrected for zero-suppression effects). The energy of electrons is determined from a combination of the track momentum at the main interaction vertex, the

corresponding ECAL cluster energy, and the energy sum of all bremsstrahlung photons associated with its track. The energy of muons is obtained from the corresponding track momentum. The energy of charged hadrons is determined from a combination of the track momentum and the corresponding ECAL and HCAL energy (corrected for zero-suppression effects, and calibrated for the non-linear response of the calorimeters). Finally, the energy of neutral hadrons is obtained from the corresponding calibrated ECAL and HCAL energy.

As has been already mentioned the PF-jets provides the greatest performances and thus are used in most analysis.

Jet clusterization is performed by the “anti- k_T ” algorithm [41]. The anti- k_T algorithm is a sequential clustering of individual particles. It basically tries to combine near by entities (particles) noted here with indexes i, j . The input to the jet-clustering routine is the collection of PF candidates of the event from which a list of pseudo-jets is defined. These pseudo-jets are recombined to form the final jets object according to following algorithmic steps [125].

- For each particle i (PF-objects), and for each pair of them i, j in a given event, the following metrics are calculated:

$$d_i \equiv \frac{1}{p_{T,i}^2}, \quad d_{ij} \equiv \min \left[\frac{1}{p_{T,i}^2}, \frac{1}{p_{T,j}^2} \right] \frac{\Delta R_{ij}^2}{\Delta R^2},$$

where : $\Delta R_{ij}^2 \equiv (\eta_i - \eta_j)^2 + (\phi_i - \phi_j)^2$, $i \neq j$, $\Delta R = 0.5$: constant. (3.14)

- Find the minimum of all d_i, d_{ij} and label it d_{min} .
- If d_{min} is d_{ij} , remove particles i and j from the list (of event’s PF-objects) and replace them with a new, merged pseudoparticle (denoted with c), with parameters are given by the recombination scheme of centroid method [125]:

$$E_{Tc} \equiv E_{Ti} + E_{Tj}, \quad \eta_c \equiv \frac{E_i}{E_{Tc}}\eta_i + \frac{E_j}{E_{Tc}}\eta_j, \quad \phi_c \equiv \frac{E_i}{E_{Tc}}\phi_i + \frac{E_j}{E_{Tc}}\phi_j. \quad (3.15)$$

- Else if d_{min} is d_i , remove particle i from the list of pseudoparticle and add it to the list of final reconstructed jets.
- If any particles (PF-object) remains non jet-clusterized, then go to step 1: recalculate d_i, d_{ij} ...

This algorithm produces a list of jets, each separated by $\Delta R_{ij} > \Delta R$. The metric d_{ij} between a hard and a soft entity (pseudoparticle) is exclusively determined by the momentum of the hard one and ΔR_{ij} , and typically has small values. For two soft entities d_{ij} is much larger. Hence, the anti- k_T algorithm leads to jet configurations with one hard particle at the center of a circle and many other softer on the edge. If there is no other hard particle within $2\Delta R$, the jet would have a perfectly conical shape. If there is a second hard entity such that $\Delta R < \Delta R_{ij} < 2\Delta R$, two hard jets will be created, and the shape would depend on the momentum of each hard particle. Finally, if both hard particles have $\Delta R_{ij} < \Delta R$, they will cluster into a single jet [41, 92]. The key feature above is that the soft particles do not modify the shape of the jet, while hard particles do; i.e. the jet boundary in this algorithm is resilient with respect to soft radiation, but flexible with respect to hard radiation.

The anti- k_T is both infrared and collinear safe [41]. Being collinear safe, means that all collinear splitting does not change the final output of the algorithm. Being infrared safe (IR) means that the presence of soft QCD emissions should not change the structure of the jet [106]. Figure 3.25 shows an example of jets reconstruction over the $\eta - \phi$ plane, the separation patterns mentioned above can be seen as well. Also, the jet resolution appears well modeled with the anti- k_T algorithm.

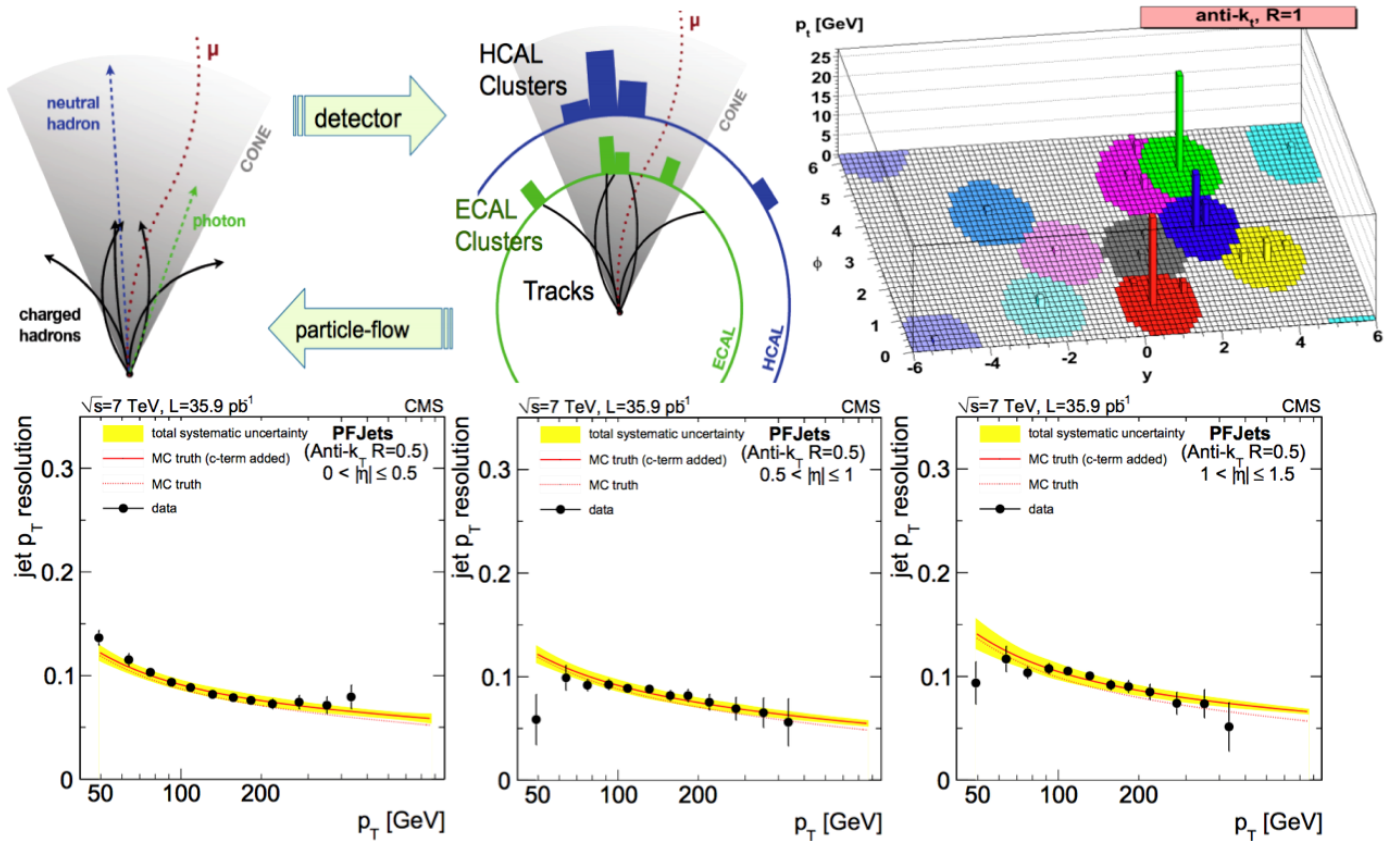


Figure 3.25: Top left: Illustration of a jet substructure and its layout over detector. Top right: a sample parton-level event (generated with Herwig), together with many random soft “QCD-ghosts”, clustered with anti- k_T jets algorithm (“active” areas of the resulting clustered hard jets shown with colors). Bottom: jet resolution with bias-corrected data, compared to the generator-level MC (denoted as MC-truth) p_T resolution before (red-dashed line) and after correction for the measured discrepancy between data and simulation (red-solid line) for PF jets in three bins of $|\eta|$. Taken from [41, 69]

3.5.10 Jets energy calibration and correction

Since the reconstructed jets are affected by both the imperfections of the detector and the weaknesses of jet clustering algorithms, jet-energy calibration and corrections have to be applied. These are needed to get the most accurate reconstructed object derived from the constituents of the jets. On average, they connect the measured jets to a more generic and universal jet definition, hence, independent of the detector’s geometry and response. Problems arise since the theoretical definition of a jet can be very different compared to the final output of a given jet-algorithm, because of the interaction of particles with matter. Thus, one needs to calibrate and correct the reconstructed jet energy to be close to the energy of the initial parton or the “GenJet”. In this section we discuss the various levels of jet corrections that CMS implements.

The adopted work-flow for CMS is the so-called “factorized approach” [69, 92, 106] where the jet-energy calibration can be divided into different levels as illustrated in figure 3.26. Once this sequence of different levels of corrections is applied, a non-negligible reduction of the systematic errors and uncertainties is achieved. Each one of these, is studied in detail by dedicated working groups, which are trying to get a better understanding and control of the different sources of systematic uncertainties involved.

The CMS collaboration derives the jet-energy corrections from both simulation and by using data-driven methods. The different corrections are applied as successive multiplication factors to the raw jet four-vector ($p_\mu^{corr.} \equiv L1(p_\mu) \times L2(\eta) \times L3(p_T) \times \dots p_\mu^{raw}$). These multiplication factors corresponds to the following corrections:

1. Offset correction (L1).

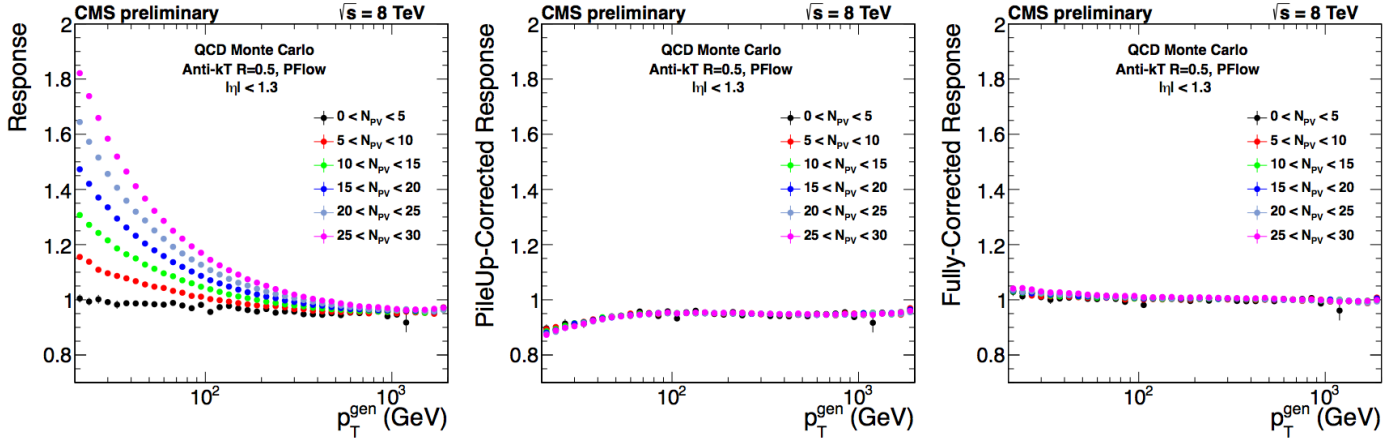
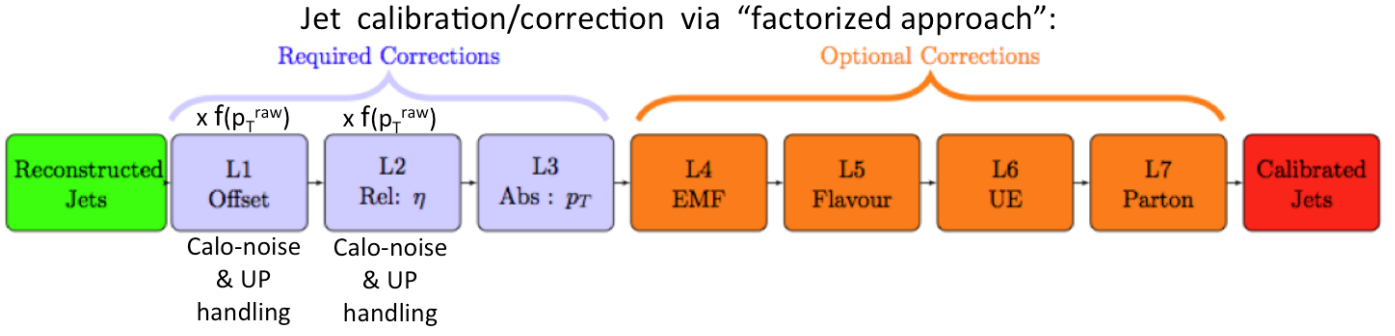


Figure 3.27: Response versus Gen-Jet p_T for PF-jets (left) before correcting for pileup, (middle) after correcting for pileup, and (right) after the required MC correction chain (L2,L3). (The same plots can be made for the Calo jets with similar results). Taken from [129].

When the jet energy has been measured, there are still sources that result in additional calorimeter energy deposits. These contributions are due to electronic noise in calorimeters and PU events. As a consequence, they cause an offset of the jet energy scale. The PU correction subtracts from the jet the average extra energy from other vertices present in the event, but are not associated with the jet itself. The correction formula is parametrized as a function of the median jet energy, or alternatively of the number of primary vertices N_{PV} . There are three way to perform this correction which can be found here [69] and their presentation is far beyond our scope. Figure 3.27 shows the p_T of the jet before and after the PU correction.

2. Relative η dependence (L2).

The L2 correction aims to correct for the effects of the dependence of the jet energy response with the pseudo-rapidity. Studies based on MC [129] show a need for a correction at the level of 0.5-1.5% for jets with $p_T > 30$ GeV, depending on the flavour of the jet.

3. Absolute p_T dependence (L3).

The L3 correction aims to correct the jet energy due to the non-uniform response of the detector as a function of their p_T and correcting back to the jet energy scale. Figure 3.27 (right) demonstrates some of the relative uncertainty sources as a function of p_T and η for the PF jets collection.

4. Electromagnetic fraction (L4).

The electromagnetic fraction (EMF) of the jet (i.e. the fraction of energy measured in ECAL compared the total energy measured in both HCAL and ECAL), can result in a different jet energy scale. The L4 correction is the first of the “optional” corrections and is depending on the

EMF value. The L4 correction can be derived both from simulation studies or from data-driven approach.

5. Correction for the dependency on the jet flavour (L5).

Given the fact that jets originate either from gluons or (u, d, c, s, b) quarks, the jet energy scale can be different depending on the flavour of the jet as small differences are expected due to the way jets fragment depending on their the flavour. On top of that, gluons are responsible for the presence of extra radiation in the jet activity. The L5 corrections can be derived from simulation studies by matching the jet flavour to the GenJet. Details of this correction can be found here [87].

6. Correction for the underlying event (L6).

This correction accounts for the extra amount of energy that is attributed to a jet due to the UE. Hence, the L6 correction aims to subtract this contribution which gives an extra hadronic activity that shifts the jet energy to higher values.

7. Parton correction (L7).

The L1-L6 corrections aim to correct the jet energy back to the energy of the GenJet collection. The L7 calibration targets to correct the jet energy back to the energy of the originating parton [106]. However, the connection between the jet p_T and the patron p_T , is far from trivial. Consequently, the correction strongly depends on the implementation and modelling of the UE and the MPIs in the MC generator. It also depends somehow from the choice of the used jet reconstruction algorithm and the details of the physics process in question.

3.5.11 b-jets tagging

The jets originated by b-quarks can be identified and tagged as these, by taking into account the following two properties of the b-quarks:

- b-quarks hadrons have relatively long lifetime, so they fly a bit before they disintegrate: $b \rightarrow W, c(u)$, providing a signature of a secondary vertex (displaced from the primary PV) in the event. This property comes from the decay suppression imposed by the corresponding CKM matrix elements (figure F.1).
- b-quark is heavier than the rest (figure 1.2, with the exception of top quark), hence the higher final-initial-quark mass difference leads to more energetic final state hadrons and wider jets.

These two characteristics allow us to separate and tag b-jets from the rest light-flavoured jets. This b-tagging opportunity is a vital importance attribute for every analysis includes signal or background with b or t quarks.

There are three main b-tagging algorithms used in CMS [72]. The ‘‘Impact Parameter significance’’ algorithm, the ‘‘Secondary Vertex’’ algorithm, and the ‘‘Soft Lepton’’ algorithm. Each one, combines one or more discriminating observables (associated with jets properties), providing finally a single discriminating value per jet which characterise it as b-jet or non-b-jet with a certain probability.

In all cases, a common selection over the jets candidates is applied to ensuring quality of their input PF-objects and robustness of the algorithm. This is applied by the following selection cuts over each considered jet [72]:

1. Only well-reconstructed tracks with high purity are considered by requiring: $p_T > 1$ GeV.
2. Number of track-hits present: in Strip Tracker $N_{hits}^{strip} \geq 8$, and in Pixel Detector $N_{hits}^{pixel} \geq 2$.
3. Track fit requirement: $(\chi^2/\text{n.d.o.f.}) < 5$.
4. Loose restriction on impact parameters (defined in figure 3.11): $|d_{xy}| < 0.2$ cm, $|d_z| < 17$ cm. These cuts suppress the track contamination by long-lived particle decay products’ like kaons.

5. Cone $\Delta R < 0.5$ around the jet axis and the track is required to associate a track with the jet (jet axis is defined by the PV and the direction of its momentum).
6. The minimum distance (in 3D-space) between the jet-axis and a track (which is supposed to be part of it) has to be less than 0.07 cm. This way one rejects track contributions from PU.
7. The point of closest jet-track distance must be less than 5 cm away from the PV.

Figure 3.28 shows the aforementioned track properties (cut variables) for a jet-sample with $p_T > 60$ GeV.

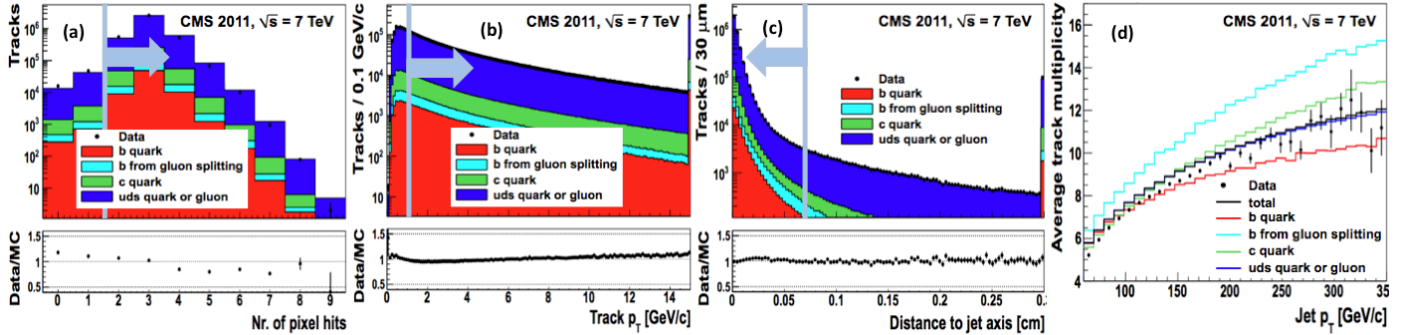


Figure 3.28: Track properties after basic selection (except for the variable plotted): (a) number of hits in the pixel system, (b) transverse momentum, (c) distance to the jet axis. The average number of tracks passing the basic selection is shown in (d) as a function of the transverse momentum of the jet. In (a)-(c) the distributions from simulation have been normalized to match the counts in data. The filled circles correspond to data. The stacked, coloured histograms indicate the contributions of different components from simulated multijet (QCD) samples. Simulated events involving gluon splitting to b-quarks (b from gluon splitting) are indicated separately from the other b production processes (b-quark). In each histogram, the rightmost bin includes all events from the overflow. The sample corresponds to a trigger selection with $p_T(jet) > 60$ GeV. (Taken from [72]).

The reconstruction of the secondary vertices: SV (decay points) of b or c hadrons is more challenging in the presence of multiple p-p interactions. In order to minimize this complexity an additional track selection is required. Tracks must be:

1. within a cone of $\Delta R < 0.3$ around the jet axis,
2. with minimum (jet-axis,track) distance less of 0.2 cm,
3. and pass a “high-purity criterion” as defined in [62].

Where the last uses the normalized χ^2 of the track fit, the track length, and the impact parameters to cut and optimize the purity of tracks.

The SV finding procedure begins with tracks defined by this selection and proceeds iteratively. A vertex candidate is identified by applying an “adaptive vertex fit” [?] which estimates the SV position and assigns a weight (between 0 and 1) to each track based on its compatibility with the SV. Tracks with weights > 0.5 are then rejected as SV content. The fit procedure is repeated until no new vertex candidate can be found.

The aforementioned properties are used in the three b-tagging algorithms [72] which are briefly explained in the following:

1. Impact Parameters (IPs) b-jet identification algorithm (“b-IP-tag”).
The IPs: d_z, d_{xy} are used to distinguish the SV decay products (tracks) of a b-hadron from prompt tracks coming from PV. The IPs have the same sign as the scalar product of the vector pointing from the PV to the closest point of jet axis. Tracks originating from the SV decay travelling

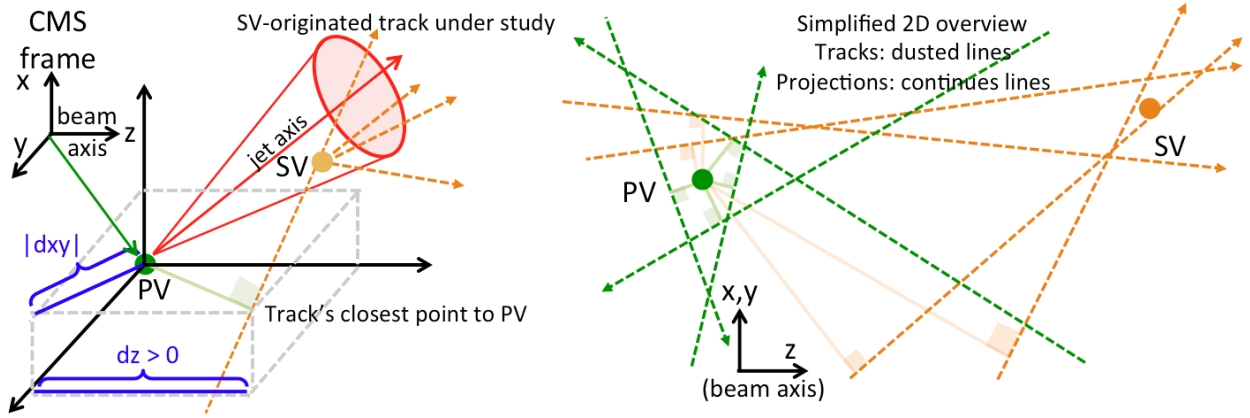


Figure 3.29: Left: an illustration of an SV in a jet. One jet’s track is shown with its closes point to the PV and with its IP quantities. Right: a 2D example of tracks associated to the PV (green) and to the SV (orange). We can deduce that: $\langle d_z^{PV} \rangle < \langle d_z^{SV} \rangle$, and $\langle d_z^{PV} \rangle \simeq 0$, $\langle d_z^{SV} \rangle > 0$.

along the jet axis tend to have positive IP values, whereas for PV originated tracks IPs signs are balanced. Figure 3.29 illustrates the situation.

The “impact parameter significance” (S_{IP}), defined as the ratio of the IP to its estimated uncertainty, has discriminating power between the decay products of b and non-b jets. The distributions of IP values and their significance are shown in figure 3.30. The “Track Counting” (TC) algorithm sorts tracks in a jet by decreasing values of the IP significance. Although the ranking tends to bias the values for the first track to high positive IP significances, the probability to have several tracks with high positive values is low for light-parton jets. Therefore the two different versions of the algorithm use the IP significance of the second and third ranked track as the discriminator value. These two versions of the algorithm are called “Track Counting High Efficiency” (TCHE) and “Track Counting High Purity” (TCHP), respectively. The distribution of the TCHE discriminator is shown in figure 3.30 left as well. A natural extension of the TC algorithms is the combination of the IP information of several tracks in a jet. Two discriminators are computed from additional algorithms. The “Jet Probability” (JP) algorithm uses an estimate of the likelihood that all tracks associated to the jet come from the primary vertex. The “Jet B Probability” (JBP) algorithm gives more weight to the tracks with the highest IP significance, up to a maximum of four such tracks, which matches the average number of reconstructed charged particles from b-hadron decays.

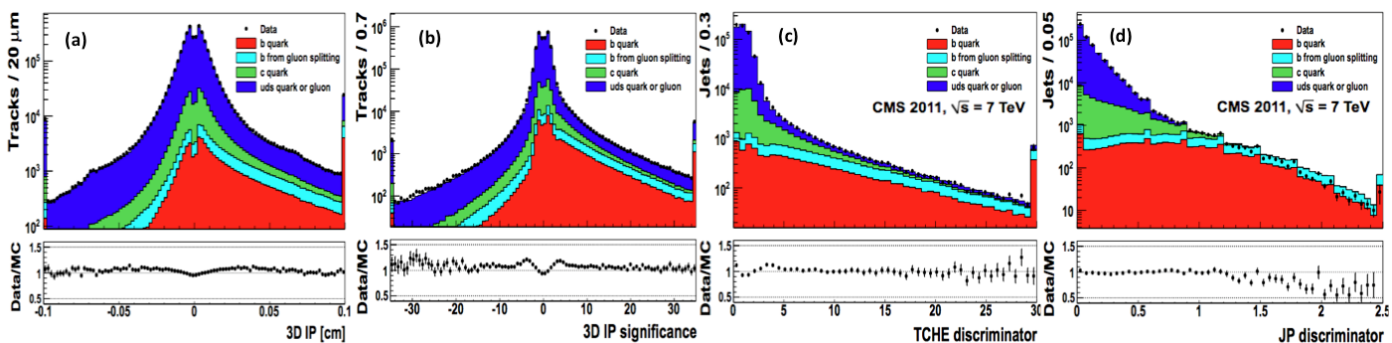


Figure 3.30: Distributions of (a) the 3D impact parameter, (b) the significance of the 3D impact parameter for all selected tracks, discriminator values for (c) the TCHE and (d) the JP algorithms respectively. Taken from [72].

The distribution of the JP discriminator in data and simulation is shown in figure 3.30 (d). The IP is calculated in the 3D-plane and carries the same sign as the scalar product of the vector

pointing from the PV to the point of closest approach with the jet direction. Hence, it will be positive (negative) if the track was produced downstream (upstream) compared to the PV along the jet direction (figure 3.29 left). That practically means that those tracks originating from the particles along the jet axis direction will tend to have positive values.

2. The presence of a SV and its associated kinematic variables can be used to discriminate b from non-b jets. Two such variables are the “flight distance” and “flight direction”, using the vector between PV and SV. The SV candidates must fulfill the following requirements in order to enhance the b-jet purity:

- An SV must share less than 65% of their associated tracks with PV.
- The significance of radial distance (between PV and SV) has to exceed 3σ .
- The SV candidates with a radial distance of more than 2.5 cm (with respect to the PV), with masses compatible to K^0 or exceeding 6.5 GeV are rejected. (Reducing the contamination by vertices from long-lived meson decays and interactions with the detector material.)
- The flight direction of each SV has to be within a cone of $\Delta R < 0.5$ around the jet direction.

The Simple Secondary Vertex (SSV) algorithm uses the significance of the flight distance (defined as the ratio of the flight distance to its estimated uncertainty) as the discriminating variable. The algorithms’ efficiencies are limited by the SV reconstruction efficiency to $\sim 65\%$. There exist two versions: the High Efficiency (SSVHE) and the High Purity (SSVHP) version (requiring at least two and three respectively associated tracks). Figure 3.31 left shows the flight distance significance.

A more sophisticated approach involves the use of SV, together with track-based lifetime information. By using these additional variables, the “Combined Secondary Vertex” (CSV) algorithm provides discrimination also in cases when no secondary vertices are found, increasing the maximum efficiency (with respect to the SSV). In many cases, tracks with $S_{IP} > 2$, can be combined in a “pseudo vertex”, allowing the computation of a subset of SV-based quantities even without an actual vertex fit. When even this is not possible, a “no vertex” category reverts to track-based variables that are combined. The following set of variables with high discriminating power and low correlations is used (in “no vertex” case only the last two variables are available):

- vertex category: “real”, “pseudo”, or “no vertex”,
- flight distance significance in the transverse plane,
- the vertex mass,
- number of tracks at the vertex,
- ratio of the energy carried by tracks at the vertex with respect to all tracks in the jet,
- the η of the tracks at the vertex with respect to the jet axis,
- the 2D-IP significance of the first track that raises the invariant mass above the charm threshold of 1.5 GeV (tracks are ordered by decreasing IP significance and the mass of the system is recalculated after adding each track),
- number of tracks in the jet,
- the 3D-IP significances for each track in the jet.

Two likelihood ratios are built from these variables and are used to discriminate between b and c jets, and between b and light-parton jets. They are combined with prior weights of 0.25 and 0.75, respectively. The distributions of the SV mass, vertex multiplicity and the CSV discriminator are presented in figure 3.31. For the CSV variable, three thresholds are shown: define loose (“L”), medium (“M”), and tight (“T”) operating points with a misidentification probability for light-parton jets of about 10%, 1%, and 0.1% respectively (at an average jet with $p_T > 80$ GeV). In the next chapters’ analysis the CVS discriminator is used in its medium working point: “CVSM”, i.e: a jet is a b-jet if: $CVS > 0.679$.

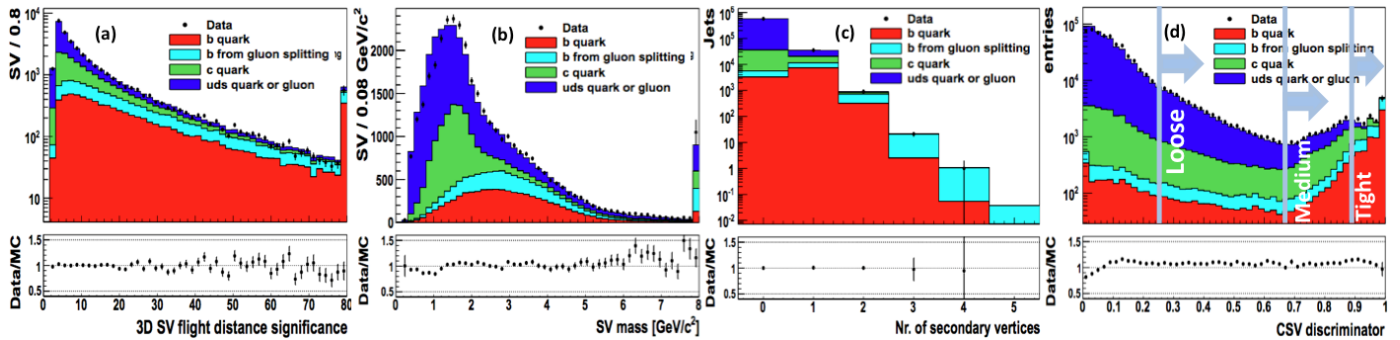


Figure 3.31: Properties of reconstructed decay vertices: (a) the significance of the 3D-SV flight distance, (b) the mass associated with the SV, (c) the SV multiplicity, and (d) the CSV discriminator. Taken from [72].

The performance of these algorithms are summarized in figure 3.32, at (a) the misidentification provability for a given b-tag efficiency. The three working points (L,M,T) are defined by this curve accepting a fixed percentage ($\sim 10\%$, 1% , 0.1%) of wrongly light-quark or gluon jets tagged as b-jets. The b-jet efficiency for the CSVM point is ~ 0.67 . For this efficiency the fraction of c-jets which are wrongly tagged as b are $\sim 15\%$ figure 3.32 (b). Over all the CSVM algorithm reconstructs on average two out of three b-jets, with purity of $\sim 85\%$. In the same figure at plots (c,d,e,f) one can see the variation of b-tagging efficiency versus p_T and η for the two best algorithms: CSV and JPL. Even if the b-jet efficiency is higher (by ~ 1.2) for JPL, the c and light quark jet have also higher misidentification rate (by ~ 2), and the optimal choice for most analysis turns to be the CSV algorithm at medium point: CSVM (figure: d,f). Explanation for the histograms' trends can be found at [72].

The b-jet tagging algorithms are tested and their efficiencies are measured in data. Many techniques are employed for that purpose [72] using the multijet or the $t\bar{t}$ event samples:

- Efficiency measurement with kinematic properties of “muon jets”: jets with near by muon ($\Delta R < 0.4$) originated from its sequential decay.
- Efficiency measurements with the “System8” method [52, 15] using muon jets.
- Efficiency measurements with “reference lifetime algorithm”.

The key aspect of a “muon jets” selection usage (in order to obtain a rich in b-jets selection) is that the muons coming for b-jets ($b \rightarrow c\mu\nu_\mu$) have relatively higher transverse to the jet momenta (p_T^{rel}). Corrections can be applied to simulated events using a scale factor SF_b , defined as the ratio of the efficiency measured in data to the efficiency found in the equivalent MC samples, using MC generator-level information to identify the jet flavour. Figure 3.33 shows the fits of MC over data samples applied with the first method above. The p_T^{rel} and $\ln(|P|)$ variable are shown in cases where muon jets are tagged (a,c) and not tagged (b,d) as b-jets. On the bottom, the b-tagging scale factor for the CSVM method are shown (on average are $\sim 0.95 \pm 0.02$ with a small variance over $p_T(b)$ between $[0.94, 0.98]$).

3.5.12 Missing transverse energy/momentum reconstruction

The missing transverse momentum, $\vec{\cancel{E}}_T$, is reconstructed as the negative of the vector sum of the transverse momenta of all final-state particles reconstructed in the detector: $\vec{\cancel{E}}_T \equiv -\sum_i \vec{p}_{T,i}$. There are three distinct algorithms developed in CMS to reconstruct $\vec{\cancel{E}}_T$:

- Particle Flow $\vec{\cancel{E}}_T$ (pf- $\vec{\cancel{E}}_T$): calculated from all reconstructed PF particles,
- Calo $\vec{\cancel{E}}_T$: calculated using the energies contained in calorimeter towers and their direction, relative to the center of the detector, to define pseudo-particles

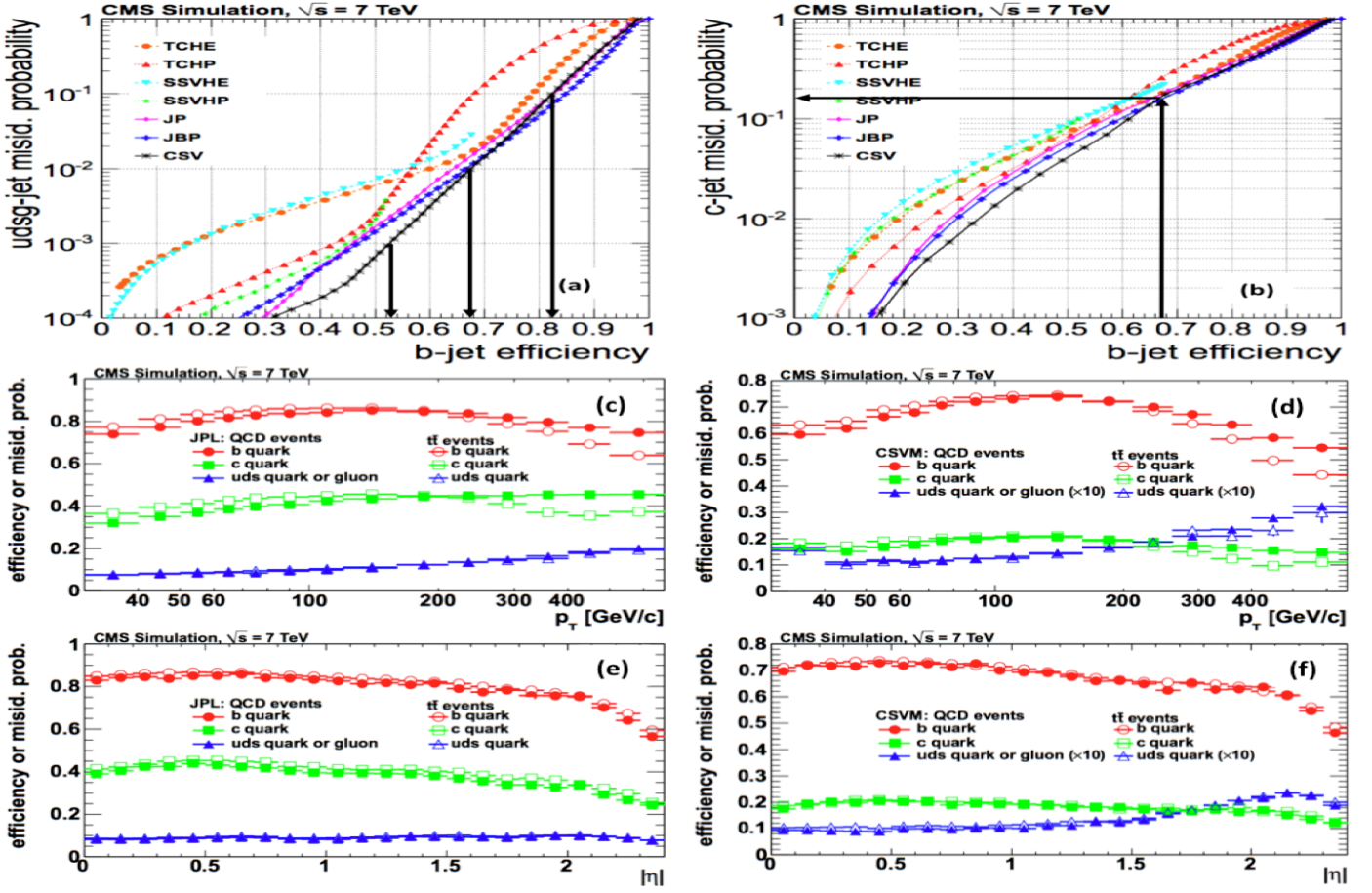


Figure 3.32: Top: performance curves obtained from MC for many algorithms. (a) light parton- and (b) c-jet misidentification probabilities as a function of the b-jet efficiency. Jets with $p_T > 60$ GeV in a sample of MC multijet events are used to obtain the efficiency and miss-ID probability values. Bottom: efficiency for b-jets and misidentification probabilities for c and light-parton jets of the JPL (c, e) and CSVM (d, f) taggers as a function of $p_T(jet)$ and $|\eta_{jet}|$. Overflows are accounted for p_T . Taken from [72].

- TC $\vec{\cancel{E}}_T$: is based on Calo-MET, but the response and resolution is improved using tracks reconstructed in the inner tracker.

A three-step correction is used to remove the bias in the \cancel{E}_T magnitude due to the non-linearity of the calorimeter response for neutral and charged hadrons, caused by event pile-up (PU), large bending of low p_T tracks due to strong magnetic field in CMS, etc.. The correction procedure relies on the fact that \cancel{E}_T can be factorized into contributions from jets, isolated high p_T photons, electrons, muons and un-clustered energies. The jet energy scale corrections are propagated \cancel{E}_T using the so called “type-I” correction:

$$\vec{\cancel{E}}_T^{Corrected} \equiv \vec{\cancel{E}}_T^{Raw} - \sum_i (p_{T,i}^{Corrected jets} - p_{T,i}^{Raw jets}), \quad (3.16)$$

In order to correct for the soft jets below the threshold used for “type-I” correction and energy deposits not clustered in any jet, a second correction can be applied to the un-clustered energy, which is called “type-II” correction. This correction is obtained from $Z \rightarrow ee$ events, as discussed in [99]. To reduce the dependency of \cancel{E}_T on event pile-up, a so called “type-0” correction has been developed only for PF- \cancel{E}_T . For each pile-up vertex the expected missing neutral momentum is calculated using an improved PF candidate to vertex association technique and added it vectorially to PF- \cancel{E}_T .

The performance of \cancel{E}_T is studied using events containing a Z or γ boson sample where the \cancel{E}_T can be induced by removing the vector boson from the event. The well measured Z boson: $Z \rightarrow \mu\mu(ee)$, provides the momentum scale, q_T and a unique event axis (figure 3.34 top). The hadronic recoil,

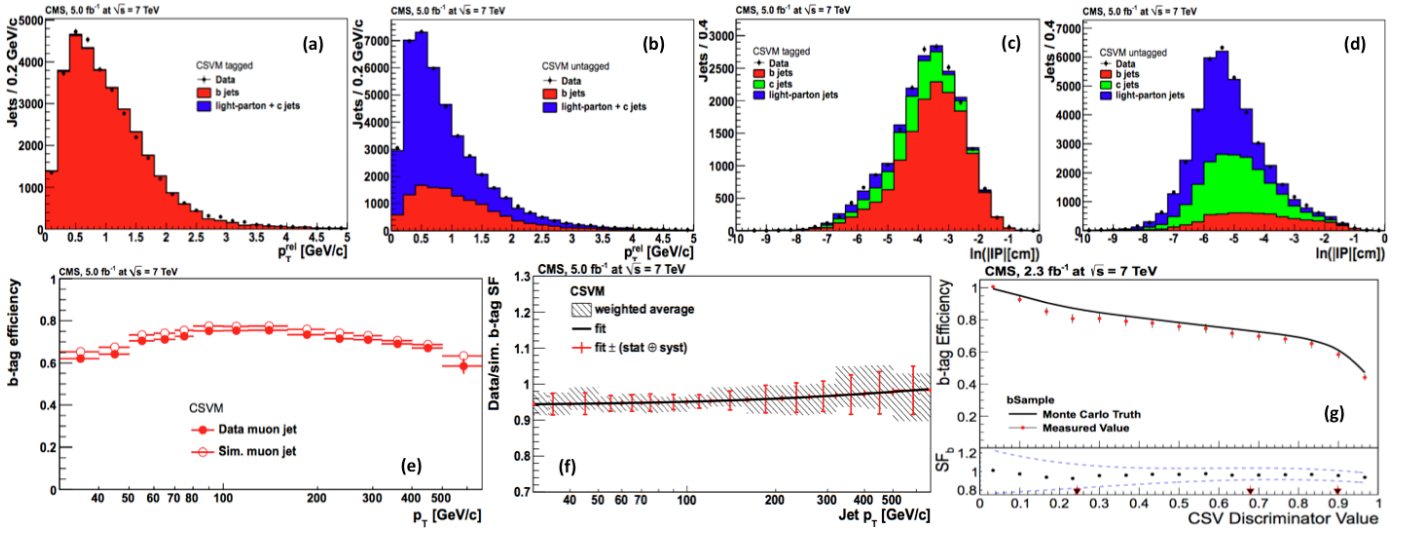


Figure 3.33: Top: fits of the summed b and non-b templates, for simulated muon jets, to the muon p_T^{rel} distributions from data. (a) and (c) show the results for muon jets that pass (tagged) and or in (b) and (d) fail (untagged) the b-jet tagging criteria of the CSV method. The muon jet p_T is [80,120] GeV. Bottom: (e) the efficiencies for the identification of b-jets measured with the “Life-Time” method in data with the muon-jet sample. (f) the combined measurements (fit) of the data/MC ratio which formed the SF_b . (g) the measured b-tagging efficiency and the SF_b as a function of the flavour discriminator threshold for the CSV algorithm, measured with “bSample” method. Taken from [72].

\vec{u}_T , is defined as the vector sum of the transverse momenta of all particles except the vector boson. Momentum conservation in the transverse plane requires: $-\vec{q}_T = \vec{u}_T + \vec{\cancel{E}}_T$. The projection of the hadronic recoil onto the axis \hat{q}_T yields two signed components, parallel: u_{\parallel} and perpendicular: u_{\perp} to the event axis, where u_{\parallel} is typically negative.

$$-\vec{q}_T \equiv \vec{u}_T + \vec{\cancel{E}}_T = [u_{\parallel} + u_{\perp}] + \vec{\cancel{E}}_T \quad (3.17)$$

The mean value of the scalar quantity $\langle u_{\parallel} \rangle / q_T$ is the correction factor required for $\vec{\cancel{E}}_T$ measurements and is closely related to jet energy scale corrections. The $-\langle u_{\parallel} \rangle / q_T$ is referred also as $\vec{\cancel{E}}_T$ response, and its dependence of the q_T as $\vec{\cancel{E}}_T$ response curve. This is shown in figure 3.34 (e). The component u_{\perp} is expected to be centred at zero by construction, and to be symmetric as it arises primarily from random detector noise and the underlying event, whereas by construction u_{\parallel} is balanced with q_T , thus making $u_{\parallel} + q_T$ centred around zero and approximately symmetric. Deviations from unity indicate a biased hadronic recoil energy scale. The curves fit to data indicate that the PF- $\vec{\cancel{E}}_T$ is able to fully recover the hadronic recoil activity corresponding to a Lorentz boosted boson with $q_T \sim 40$ GeV.

Since the vast majority of pileup interactions do not have significant $\vec{\cancel{E}}_T$ and its average value projected on any axis is zero, the effect of pileup interactions on the $\vec{\cancel{E}}_T$ response is small. However, as shown in figure 3.34 (f), (g), pileup interactions have a considerable effect on the $\vec{\cancel{E}}_T$ resolution. CMS employs two algorithms that reduce the effect of pileup interactions on the $\vec{\cancel{E}}_T$ reconstruction, referred to as the “No-PU PF- $\vec{\cancel{E}}_T$ ” and “MVA PF- $\vec{\cancel{E}}_T$ ” algorithms [76]. These algorithms divide each event into two components: particles that are likely to originate from the primary hard-scattering pp interaction (HS particles) and particles that are likely to originate from pileup interactions (PU particles). The implementation of these show a significantly reduced dependence of the resolution on pileup interactions in both data and simulation. This reduced pileup dependence can significantly increase the sensitivity of searches for new physics.

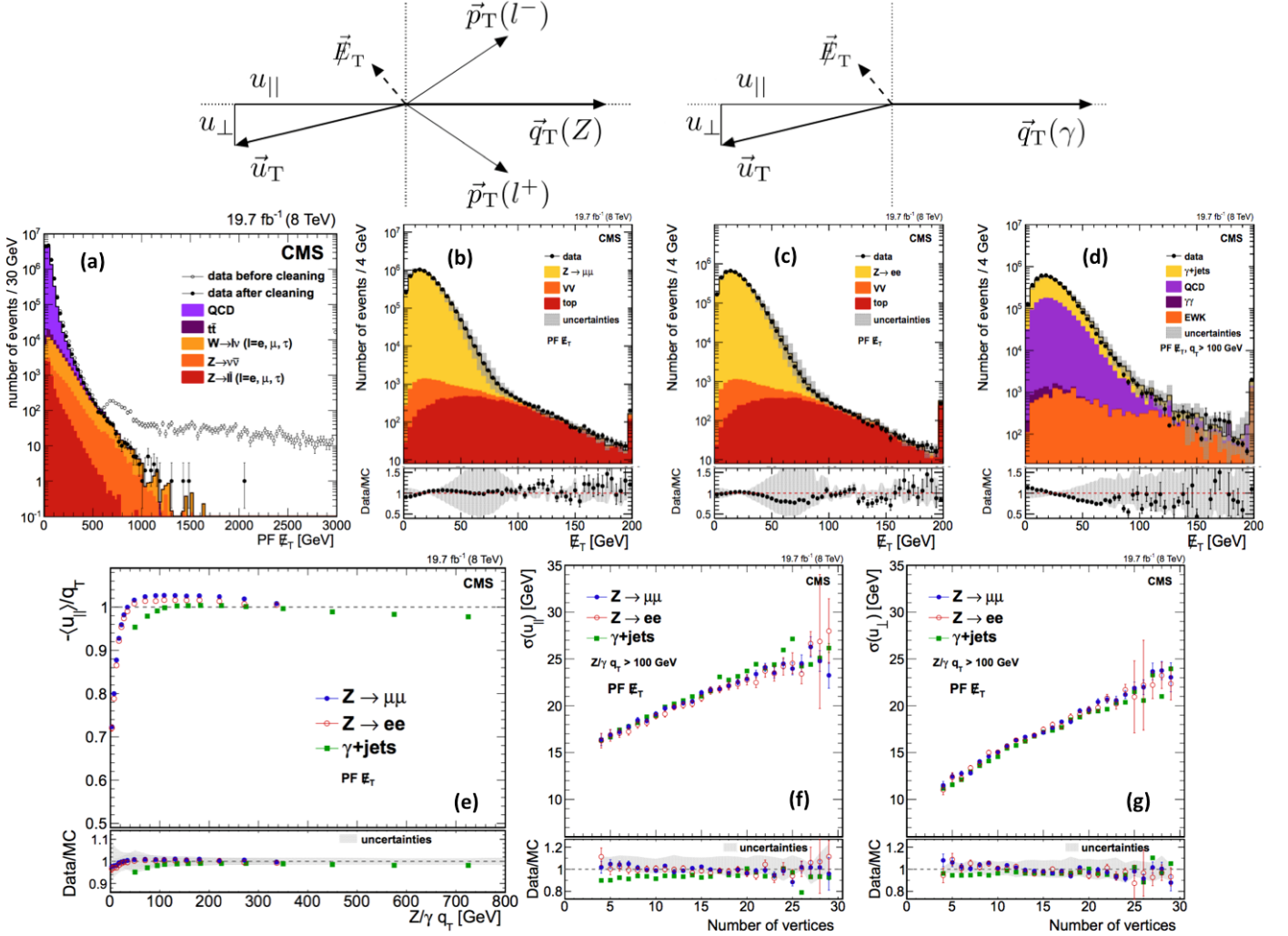


Figure 3.34: On the top: schematic illustration of momentum conservation in transverse plane for Z and γ events. The $\vec{u}_T, \vec{q}_T, u_{||}, u_{\perp}$ definitions can be seen. Plot (a): the $\text{PF}-\cancel{E}_T$ distributions for events passing a di-jet selection without and with cleaning algorithms applied. Plots (b),(c),(d) shows the $\text{PF}-\cancel{E}_T$ distribution in $Z \rightarrow \mu^+\mu^-$, $Z \rightarrow e^+e^-$, and direct-photon events respectively. The lower panel of each plot show the data/MC ratio. Plot (e) response curves for $\text{PF}-\cancel{E}_T$ in events with a Z/γ -boson. Upper frame shows the response in data; the lower frame shows the ratio of data over simulation. Plots (f),(g) parallel and perpendicular recoil component resolution curves versus the number of reconstructed vertices (PU) for $\text{PF}-\cancel{E}_T$. Upper frames show the resolution in data; lower frames show the ratio of data/MC. Taken from [76].

Chapter 4

Analysis Strategy

Recent results for the mass of the newly found Higgs boson [?, ?] (fully consistent with the SM Higgs boson so far) at 125 GeV, put a strain on the Minimal Supersymmetric extension to the Standard Model (MSSM), the absence of SUSY can be explained and its “naturalness” being preserved, in the so-called compressed SUSY models.

In this analysis, results from a search for natural SUSY in R-parity conservation scenario, and considering small sparticle mass-splittings are reported.

4.1 Motivation in compressed natural SUSY search

Discovering supersymmetry at the LHC requires distinguishing the signal decay products of SUSY particles (sparticles) from large standard model (SM) backgrounds. In R-parity conserving SUSY in which the Lightest Super Partner (LSP) is stable and invisible to the detector, methods commonly used to separate signal from backgrounds take advantage of the signals large missing transverse momentum (\cancel{E}_T), numerous jets from visible final state products, or highly energetic leptons. However, this becomes more challenging in the case of electroweak (EW) SUSY production where cross sections are modest (figure 2.7). More over is especially difficult for compressed EW SUSY scenarios in which the mass difference between the SUSY produced sparticle (initial) and the LSP (final) is small.

Not only are such processes harder to pick out of backgrounds during an analysis, but they may not even pass typical trigger requirements for the LHC detectors (requiring for example high $\cancel{E}_T, p_T(\ell), H_T$). As a result, both CMS and ATLAS remain “blind” in a vast majority of compressed SUSY scenarios.

In compressed natural SUSY models the mass spectrum of SUSY particles is more compressed, i.e. parent sparticle is closer in mass to the LSP and as a result, less visible energy is available in the final state, in form of detected objects. Also a modest amount of energy escapes detection as it stored in the (not necessarily energetic) LSP’s, making it very hard to distinguish between signal and QCD, $t\bar{t}$ and electroweak backgrounds.

The main motivation for a search in natural SUSY compressed spectra is listed bellow.

- Such phase-space regions has been remained unexplored (even two years after the end of “Run-I”) due to their kinematic inaccessibility. Instead CMS and ATLAS emphasize in signal searches with higher cross sections signatures and which probe broad (more kinetically accessible) areas of the sparticles masses parametric space.
- A small mass splitting $\Delta M \sim [10,30]$ GeV (of LSP and next-to-LSP (NLSP) particles) is compatible with the observed dark matter relic. In such scenario the co-annihilation of LSP-NLSP to SM particles is enhanced and produces the observed DM relic [29, 118, 18].
- Also compressed SUSY in third generation is particularly well motivated since the dominant correction to the Higgs mass comes from the top quark loop, therefore it is necessary for the stop quark to be in the TeV range in order to effectively cancel most of this correction thus preserving “naturalness” [31, 78, 80, 140, 119, 81, 135, 108].

4.2 Experimental frontier of compressed SUSY in terms of exclusion limit

Before the publication of current analysis result the landscape of exclusion limits in stop-LSP and chargino-LSP productions was as shown in figure 4.1. Exclusion limit curves corresponds to 95% confidence level and exclude a wide range of the two masses parametric space. The non excluded areas across and between the (dusted straight) lines $m_{\tilde{\chi}_1^0} = m_{\tilde{t}} - m_W$, $m_{\tilde{\chi}_1^0} = m_{\tilde{t}} - m_t$ are characterized as the compressed spectra.

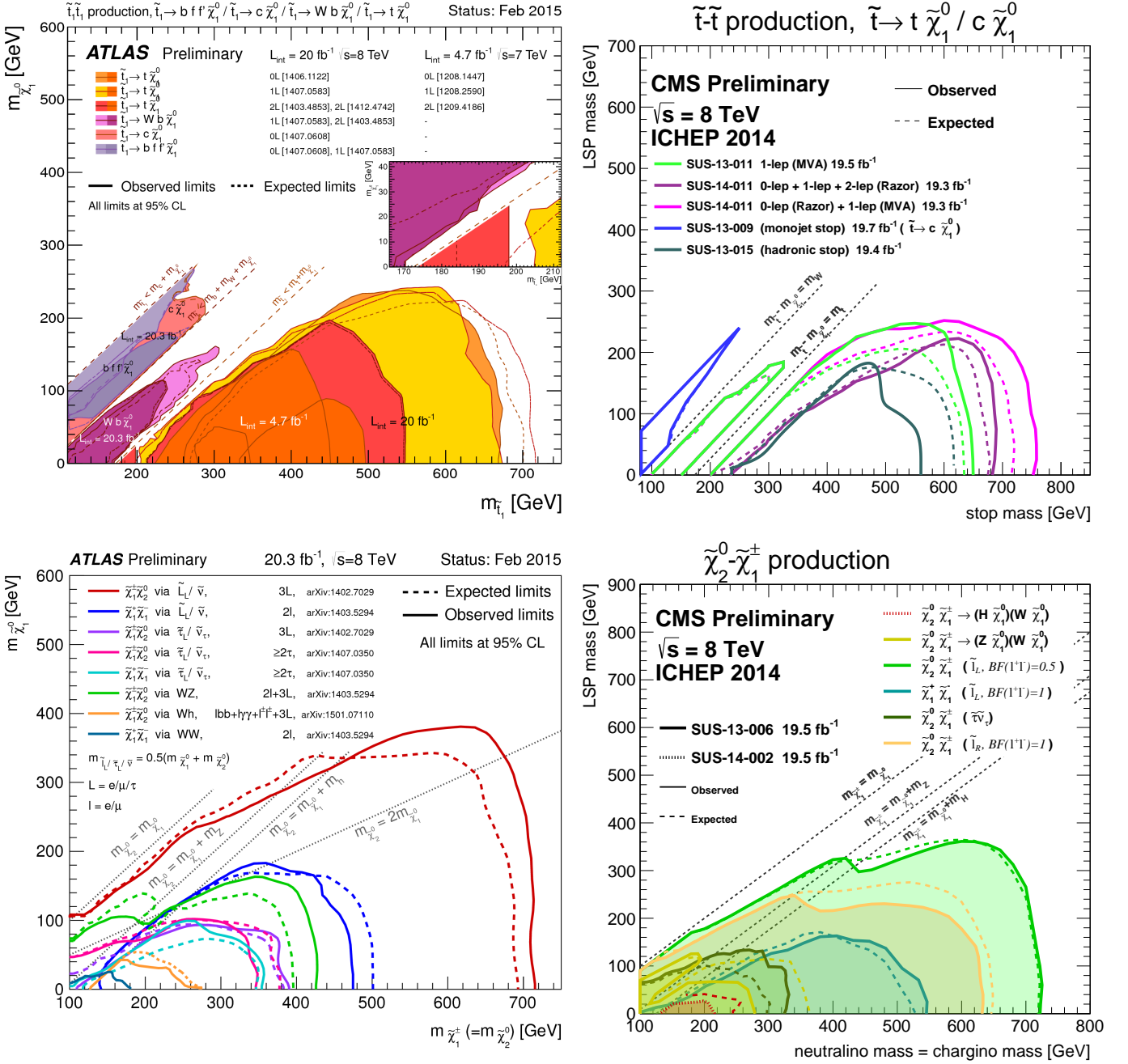


Figure 4.1: Exclusion limits from ATLAS (left) and CMS (right). The stop-pair production on top, the chargino-neutralino production on the bottom. Various different analysis in different channels are superimposed. (Taken from ATLAS and CMS public results summary web-page).

For the $m_{\tilde{t}} - m_{\tilde{\chi}_1^0} < m_t$ the top quark appear off-shell and if $m_{\tilde{t}} - m_{\tilde{\chi}_1^0} < m_W$ also its daughter W ($t \rightarrow bW$) appears off-shell. The corresponding search regions are kinematically inaccessible in the sense which described above: it leads to low p_T objects and modest \cancel{E}_T , buried under huge SM background processes.

After the LHC “Run-I” data collection period a lot of effort were put in investigation of the accessible on-shell sparticle productions. Analysis were designed and optimized to probe such events and not the compressed scenarios. The later period (and mainly the end of the LS1 period) the compressed scenarios attracted the interest since natural SUSY could be hidden it.

4.3 The signal signatures

In this analysis three different signal signatures are probed. The main one is a stop-pair production with stop-LSP mass-splitting: $\Delta M(\tilde{t}\tilde{\chi}_1^0) < M_W$. This is shown in figure 4.2 left. The exact decay chain for each of the stops which will be considered is: $\tilde{t} \rightarrow t\tilde{\chi}_1^0 \rightarrow Wb\tilde{\chi}_1^0 \rightarrow \ell\nu b\tilde{\chi}_1^0$, i.e. we only the leptonic decay of the stops: “dileptonic” channel. Accounting only the electron and muon as leptonic final states of a single W-decay (accounting that τ disintegrate rapidly into these or into quarks) we have the following % branching ratios (BR):

- $2W \rightarrow 2q\bar{q}$ ($\sim 55\%$) full-hadronic,
- $2W \rightarrow \ell\nu q\bar{q}$ ($\sim 38\%$) semi-leptonic,
- $2W \rightarrow \ell^+\ell^-\nu\nu$ ($\sim 7\%$) di-leptonic.

The final state is characterized by jets, (originating from the fragmentation and hadronization of b-quarks), soft oppositely charged leptons and neutrinos (originating from the decays of W bosons in the leptonic decay of it). The search is therefore based on events with soft opposite-sign (OS) leptons.

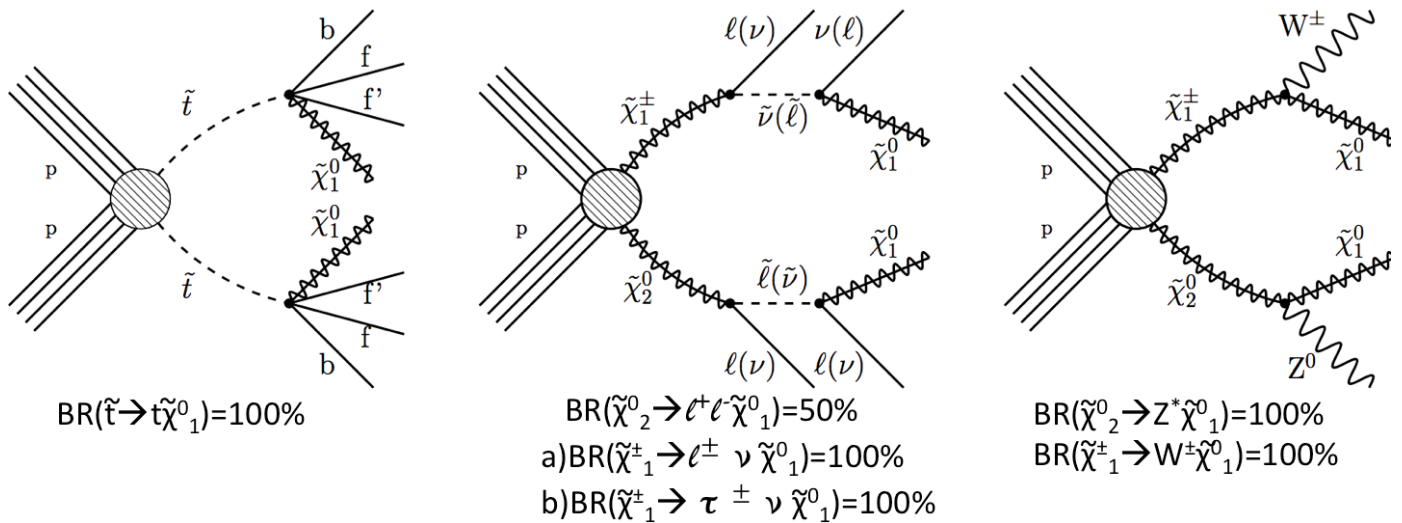


Figure 4.2: SUSY signal models considered in the analysis. Left: stop-squark pair production with subsequent four-body decays (where both t^* , W^* appears off-shell). Middle: chargino-neutralino pair production in final states with three leptons with two LSPs, right: chargino-neutralino pair production in W^*Z^* final state with two LSPs. The considered branching ratios are also shown (two sub-cases for the one in the middle are probed).

As mentioned, stop with a mass similar to LSP mass are difficult to discover, as only few missing transverse momentum is produced in each stop decay and also the two decay legs (stops) are not oriented necessarily in same direction. To see this lets consider the four-body decay of the stop at its center of mass frame, the energy and momentum conservation (for massless b, ℓ, ν_ℓ) can be written as:

$$m_{\tilde{t}} = |\vec{p}_b| + |\vec{p}_\nu| + |\vec{p}_\ell| + \sqrt{\vec{p}_\chi^2 + m_\chi^2}, \quad \vec{p}_b + \vec{p}_\nu + \vec{p}_\ell + \vec{p}_\chi = 0 \quad (4.1)$$

We can see that even at the extreme scenario where the LSP produced at rest the three fermions have to share the energy corresponding to the stop-LSP mass split which does not exceeds m_W . In

such example there is not \cancel{E}_T produced at all. In the other regime the maximum LSP momenta is: $|\vec{p}_{\tilde{\chi}}| = |\vec{p}_b| + |\vec{p}_\nu| + |\vec{p}_\ell|$ (where the three fermions are collinear and back-to-back with LSP), and we substitute to the energy conservation relation above we can easily deduce: $|\vec{p}_{\tilde{\chi}}| = m_{\tilde{\ell}}[1 - (m_{\tilde{\chi}}/m_{\tilde{\ell}})^2]/2$. For a typical mass combination of $(m_{\tilde{\ell}}, m_{\tilde{\chi}}) = (200, 150)$ GeV (or $(300, 250)$ GeV) we have: $|\vec{p}_{\tilde{\chi}}| \simeq 45$ GeV. This momenta add up vectorially with the other LSP and the two neutrinos which typically forms a $\cancel{E}_T \lesssim 100$ GeV. Thus in principle, if stops are not produced boosted, the process has modes \cancel{E}_T and low momentum leptons and b-jets. As has been mentioned is hard to trigger such events since no such trigger (with soft leptons and low \cancel{E}_T) was employed in “Run-I”.

One way to circumvent this challenge of compressed SUSY (of low \cancel{E}_T and soft objects) is to search for events with an energetic jet from Initial State Radiation (ISR). In such events the sparticles will recoil against the ISR, increasing the energy of visible decay products but mainly increasing \cancel{E}_T , up to a level that makes such events able to be triggered.

Indeed if we consider that the stop-pair is produced in association with an ISR-jet and that each stop inherits $p_T \sim 200$ GeV, then a Lorentz boost of $\gamma \simeq 1.4$ (1.2) boost all the stop decay products. The final p_{TS} at the CMS frame then are given by the relation:

$$p_T^{CMS-frame} = \gamma\beta E + \gamma p_T^{CM-frame}, \quad \vec{\gamma} \parallel -\vec{p}_T(jet_{ISR}) \quad (4.2)$$

which for the above LSP masses and p_{TS} cases the $p_T^{CMS-frame}(\tilde{\chi})$ ranges in $[150, 220]$ GeV (only for one LSP). Thus LSPs, and the whole event, acquire artificially high momenta and induces high \cancel{E}_T sufficient to be triggered. The same does not happens to the rest soft object. Dues to their very small masses the first term in equation 4.2 is relatively small thus for example a $|p| = 15$ GeV object is boosted to a $|p|$ range $[0, 35]$ GeV depending to its orientation with respect to the boost ($\vec{\gamma}$). Consequently, the b-jet, the lepton and the neutrino remains low p_T objects, and \cancel{E}_T (induced mainly by the two LSPs) is back-to-back with the hard ISR-jet. Figure 4.3 illustrates this situation.

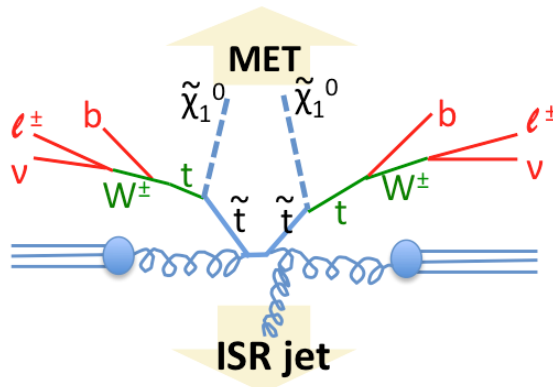


Figure 4.3: The stop-pair production illustration showing the back-to-back behavior of the \cancel{E}_T and ISR-jet. With red the soft objects, with green the off-shell mediators.

Such ISR-strategy searches are usually called “mono-jet” searches and similar analysis can be found here [4, 5, 6] (also the same signature in the full-hadronic channel). Analysis in the full-hadronic channel have to deal with huge irreducible SM background stemming from $Z \rightarrow \nu\nu$ (invisible) and W +jets (with “missing” charged lepton or having hadronically decayed tau). Both these SM processes give exactly the same mono-jet-like signature as the signal. The single lepton final state leads to smaller BR but bypasses the $Z \rightarrow \nu\nu$ contribution and the W +jets, with the $t\bar{t}$ becomes then dominant. A soft lepton requirement (and soft b-jet) can suppress these backgrounds effectively for the search.

These backgrounds can be further suppressed by requiring two soft lepton at the price of a smaller branching ratio as only fully leptonically decaying stop pairs are selected. This search is therefore based on events with soft opposite-sign leptons, high missing transverse energy and one or two hard jets from initial state radiation.

The search presented in next section has small event yield for the SM backgrounds (<10 events), which is very complementary situation to the mono-jet searches [3, 75]. The SM yields are so small

that the SM prediction do not need to reach e.g. 10% precision level as the statistical uncertainties are the dominant. This search not only add sensitivity, but as well would potentially give corroborative evidence in cases of excesses in mono-jet like searches.

Similar processes, e.g. boosted EWKinos [101] or other BSM models, could give similar signatures as those in the figure 4.2 middle and right. The topology in the middle, with chargino-neutralino production, leads to three soft lepton final state, however the di-lepton search can probe the cases where one of the two same-sign leptons is missed, or is very soft, or is a hadronically-decay tau. Thus, two decay scenarios are considered for this signal as well. The topology in the right is the the same chargino-neutralino production where now are both rapidly disintegrates to off-shell W^* , Z^* boson leading also in a 0,1,2 and 3 lepton final states.

1. $pp \rightarrow \tilde{t}\tilde{t} + jets \rightarrow \ell^+\ell^-\nu\nu(\nu_\tau\nu_\tau\nu_\tau\nu_\tau)\tilde{\chi}_1^0\tilde{\chi}_1^0bb + jets$,
(with $\text{BR}(\tilde{t} \rightarrow t^*\tilde{\chi}_1^0) = 100\%$)
2. $pp \rightarrow \tilde{\chi}_1^\pm\tilde{\chi}_2^0 + jets \rightarrow \ell^\pm\ell^\mp\ell^\pm\nu(\nu\nu\nu\nu\nu_\tau\nu_\tau)\tilde{\chi}_1^0\tilde{\chi}_1^0 + jets$,
(“flavor-democratic” with $\text{BR}(\tilde{\chi}_2^0) = 50\%$ and $\text{BR}(\tilde{\chi}_1^\pm) = 100\%$)
3. $pp \rightarrow \tilde{\chi}_1^\pm\tilde{\chi}_2^0 + jets \rightarrow \ell^\pm\ell^\mp\tau^\pm\nu_\tau(\nu\nu\nu\nu\nu_\tau\nu_\tau)\tilde{\chi}_1^0\tilde{\chi}_1^0 + jets$,
(“tau-enriched” with $\text{BR}(\tilde{\chi}_2^0) = 100\%$ and $\text{BR}(\tilde{\chi}_1^\pm) = 100\%$)
4. $pp \rightarrow \tilde{\chi}_1^\pm\tilde{\chi}_2^0 + jets \rightarrow W^*Z^*\tilde{\chi}_1^0\tilde{\chi}_1^0 + jets \rightarrow \ell^\pm\ell^\mp(\ell^\pm\nu\nu\nu\nu\nu_\tau\nu_\tau)\tilde{\chi}_1^0\tilde{\chi}_1^0 + jets$,
(with $\text{BR}(\tilde{\chi}_2^0) = 100\%$ and $\text{BR}(\tilde{\chi}_1^\pm) = 100\%$)

Where ℓ can be e or μ . The τ has been considered decayed either leptonically or hadronically. Particles appears in parenthesis stands for those may or may not appear depending on tau decays. For the first one as mentioned we will search the: $\Delta M(\tilde{t} - \tilde{\chi}_1^0) \leq 80$ GeV band, for second and third only the: $M(\tilde{\chi}_1^\pm) = M(\tilde{\chi}_2^0) = M(\tilde{\chi}_1^0) + 20$ GeV slice, and for the last the: $M(\tilde{\chi}_1^\pm) = M(\tilde{\chi}_2^0) = M(\tilde{\chi}_1^0) + 10$ GeV. Obviously the third decay is a special case of the second.

Chapter 5

Event Selection

5.1 Data samples and triggers

The data sample used for the search is proton-proton collisions collected in 2012 at a center-of-mass energy of $\sqrt{s}=8$ TeV. These were recorded by the CMS experiment and corresponds to an integrated luminosity (L) of: $L=19.7 \text{ fb}^{-1}$. As the leptons for the signal are very soft and are produced in association with high \cancel{E}_T and ISR jet(s) we use the following hadronic triggers for the signal region:

- HLT_MET_120_HBHENoiseCleaned,
- HLT_Mono_CentralPFJet80_PFMETno_Mu105_NHEF0p95,
- HLT_Mono_CentralPFJet80_PFMETno_Mu95_NHEF0p95,

No soft muon triggers were in place at 8 TeV. Triggers evolved over the data taking period and require either $\cancel{E}_T > 120$ GeV, where \cancel{E}_T is reconstructed from the energy deposited in the calorimeters, or $\cancel{E}_T > 95$ GeV and a jet with $p_T > 80$ GeV and $|\eta| < 2.6$, where both objects are reconstructed using the PF algorithm. In the second part of the data taking period the threshold on \cancel{E}_T was raised from 95 to 105 GeV. The “or” combination of these three triggers leads to an efficiency above 98% for events with \cancel{E}_T above 200 GeV. The turn-on curves for this trigger (in their “or” combination) for the data, SM background, and SUSY signal can be seen in the figure 5.1. Alternatively, also the HLT_PFMET_150 GeV trigger was investigated, which had a slightly slower turn-on figure 5.2 and was discarded.

Each triggers response for background and signal generated events is simulated and taken into account. Control samples were collected based on a single-muon trigger with a p_T threshold of 24 GeV.

5.2 SM background and SUSY signal simulation

The Monte Carlo (MC) samples and the data samples that are used in the signal and control regions are listed in Table 5.2. These are produced mainly with MadGraph generator (the decays) where the Pythia generator implemented in final state radiation and hadronization of the decay products.

5.3 Signal region selection cuts

In principle the event selections defines the so-called signal or search region (SR) of the events selected for the Analysis. It is a set of “cuts” which are applied in order to discriminate signal from background. With term cuts we mean a set of requirements/restriction, over various kinematic variables of each event, which discriminate the signal over the same (final state) signature SM background. The SR selection is dictated by the signal features of the dilepton final state topology of stop-pair production (shown in figure 4.3). Even the analysis is optimised and designed for stop-pair production, is also applied for the other chargino-neutralino production (shown if figure 4.2 middle and right).

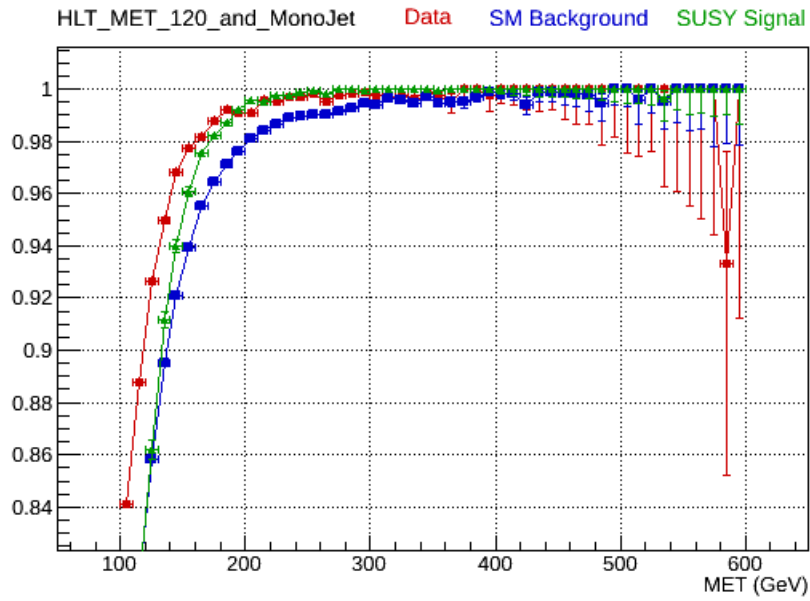


Figure 5.1: Offline Efficiency of the “or” combination of: HLT_MET_120 _HBHENoiseCleaned, HLT_Mono _Central PFJet80 _PFMETno_Mu105 _NHEF0p95, and HLT_Mono _Central PFJet80 _PFMETno_Mu95 _NHEF0p95 triggers in data and MC measured using the single muon trigger.

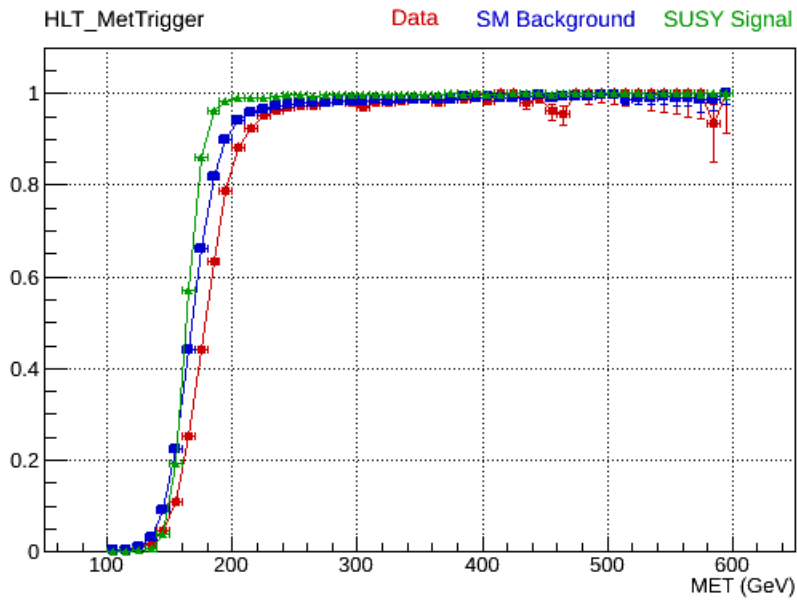


Figure 5.2: Performance of the MET trigger on data measured and MC using the single muon trigger.

Table 5.1: MC background, signal simulation and the data samples used in the analysis.

Samples	Cross Section [pb]	Name
$t\bar{t}(2\ell)$	25.80	TTJets_FullLeptMGDecays_8TeV-madgraph/Summer12_DR53X-PU_S10_START53_V7A-v2
$t\bar{t}(1\ell)$	116.15	TTJets_SemiLeptMGDecays_8TeV-madgraph/Summer12_DR53X-PU_S10_START53_V7A_ext-v1
$t\bar{t}(1\ell)$	116.15	TTJets_SemiLeptMGDecays_8TeV-madgraph/Summer12_DR53X-PU_S10_START53_V7A_ext-v2
$W + jets$	282.00	WJetsToLNu_TuneZ2Star_8TeV-madgraph-tarball/Summer12_DR53X-PU_S10_START53_V7A-v2
$Z(2\ell)$	40.50	DYJetsToLL_PtZ_100_TuneZ2star_8TeV-madgraph/Summer12_DR53X-PU_S10_START53_V7A-v2
$Z(2\ell)$	810.00	DYJetsToLL_M-10To50filter_8TeV-madgraph/Summer12_DR53X-PU_S10_START53_V7A-v1
$Z(2\nu)$	456.30	ZJetsToNuNu_50_HT_100_TuneZ2Star_8TeV-madgraph/Summer12_DR53X-PU_S10_START53_V7A-v1
$Z(2\nu)$	191.80	ZJetsToNuNu_100_HT_200_TuneZ2Star_8TeV-madgraph/Summer12_DR53X-PU_S10_START53_V7A-v1
$Z(2\nu)$	46.67	ZJetsToNuNu_200_HT_400_TuneZ2Star_8TeV-madgraph/Summer12_DR53X-PU_S10_START53_V7A-v1
$Z(2\nu)$	6.30	ZJetsToNuNu_400_HT_inf_TuneZ2Star_8TeV-madgraph/Summer12_DR53X-PU_S10_START53_V7A-v1
WW	5.995	WWJetsTo2LNu_TuneZ2star_8TeV-madgraph-taola/Summer12_DR53X-PU_S10_START53_V7A-v1
WZ	1.057	WZJetsTo3LNu_TuneZ2_8TeV-madgraph-taola/Summer12_DR53X-PU_S10_START53_V7A-v1
$WZ (1 \leq M_{ll} \leq 12\text{GeV})$	0.226	WZJetstollnu_8TeV-madgraph_DR53X-PU_S10_START53_V7A-v1
ZZ	0.339	ZZJetsTo4L_TuneZ2star_8TeV-madgraph-taola/Summer12_DR53X-PU_S10_START53_V7A-v1
$ZZ (1 \leq M_{ll} \leq 12\text{GeV})$	0.012	ZZJetsnull_8TeV-madgraph_START53_V7A-v1
$tW(\text{single top})$	11.10	T_tW-channel-DR_TuneZ2star_8TeV-powheg-taola/Summer12_DR53X-PU_S10_START53_V7A-v1
$\bar{t}W(\text{single top})$	11.10	Tbar_tW-channel-DR_TuneZ2star_8TeV-powheg-taola/Summer12_DR53X-PU_S10_START53_V7A-v1
$t\bar{t}W$	0.232	TTWJets_8TeV-madgraph/Summer12_DR53X-PU_S10_START53_V7A-v1
$t\bar{t}Z$	0.208	TTZJets_8TeV-madgraph_v2/Summer12_DR53X-PU_S10_START53_V7A-v1
$t\bar{t}H$	0.127	TTH_Inclusive_M-125_8TeV_pythia6/Summer12_DR53X-PU_S10_START53_V7A-v1
$W^-W^- + jets$	0.0889	WmWmq_8TeV-madgraph/Summer12_DR53X-PU_S10_START53_V7A-v1
$W^+W^+ + Jets$	0.2482	WpWpqq_8TeV-madgraph/Summer12_DR53X-PU_S10_START53_V7A-v1
$WWW + jets$	0.0822	WWWJets_8TeV-madgraph/Summer12_DR53X-PU_S10_START53_V7A-v1
$WWZ + Jets$	0.0633	WWZNoGstarJets_8TeV-madgraph/Summer12_DR53X-PU_S10_START53_V7A-v1
$WZZ + Jets$	0.0197	WZZNoGstarJets_8TeV-madgraph/Summer12_DR53X-PU_S10_START53_V7A-v1
$ZZZ + Jets$	0.0055	ZZZNoGstarJets_8TeV-madgraph/Summer12_DR53X-PU_S10_START53_V7A-v1
SUSY Scan $[\tilde{t}, \tilde{t}]$		SMS-T2DegenerateStop_2J_mStop-XY_mLSP-20to140_TuneZ2star_8TeV-madgraph-taolapp/Summer12-START53_V19-FSIM_PU_S12-v1
SUSY Scan $[\tilde{\chi}_1^\pm, \tilde{\chi}_2^0]$		TChiStepSnuTauEn & TChiStepSnuDemo
MET+Jets Data		MET/Run2012A(BC)-22Jan2013 & METParked/Run2012D-22Jan2013 & HLT_Mono_CentralPFJet80_PFMETNo_Mu105(95)_NHFEF0p95
Single Muon Data		SingleMu/Run2012A(BCD)-22Jan2013

Thus, we require two leptons: $N_\ell = 2$, either an electron or a muon, with opposite-sign (OS) charges: $Q(\ell_1)Q(\ell_2) = -1$, with the additional requirement that at least one of the two leptons must be a muon: $N_\mu \geq 1$ (i.e. $[\mu\mu], [\mu e]$ channels). The rejection of the $[ee]$ was due to the lower reconstruction efficiency that electrons have, in combination their smaller kinematic acceptance with respect to muons.

Muons (electrons) with $p_T > 5(7)$ GeV, with $|\eta| < 1.5$, relative isolation $Iso_{(rel)} < 0.5$, and absolute isolation $Iso_{(abs)} < 5$ GeV were accepted in the SR of the analysis. (Isolation is defined in subsection 3.5.8, is the sum of all objects p_{T_S} within a $\Delta R = 0.4$ cone around the lepton, relative isolation is the absolute over its p_T ; the p_T , η and much more useful variables definitions can be found in appendix A.) For the muon identification we select loose ID (POG) muons and require the soft lepton ID as well (defined in table 3.3). For electrons we use GSF electron (defined in subsection 3.5.7) with the Egamma POG non-triggering MVA ID at the same working point used in the $H \rightarrow ZZ \rightarrow 4\ell$ analysis with the additional requirement of at most one inner tracker lost hit.

In order to motivate those and the additional cuts of our signal region (SR) definition we use a selection named ‘‘Preselecton’’. This is by construction looser than the SR and is defined by the cuts shown in table 5.2. We stress that this preselection sample is only to allow us explore the discrimination power of each variable we tempting to cut over. This could be done with the so-called ‘‘N-1’’ plots, (i.e. showing distributions excluding only the cut over the plotted variable), but in our case the very low yields is SR requires an enriched preselection with sufficient conclusive statistics; thus we implement preselection. The three horizontal lines on table separates the cuts to leptonic-sector, hadronic-sector, and composite variable sector cuts.

Table 5.2: Preselection cuts used for the plots which motivates the SR cuts. (For the N_b multiplicity plot we remove the $N_b=0$ requirement). The ‘‘-’’ means no cut is imposed in preselection.

Variable	Preselection cut value:
N_ℓ	= 2
N_μ	≥ 1 (soft μ ID)
$Q(\ell_1)Q(\ell_2)$	= -1
$p_T(\ell_1)$	[5(7),45] GeV
$p_T(\ell_2)$	[5(7),25] GeV
$ \eta (\ell_{1,2})$	< 2.1
$d_z(\ell_{1,2}) \& d_{xy}(\ell_{1,2})$	< 0.1 cm
$Iso_{rel}(\ell_{1,2}), Iso_{abs}(\ell_{1,2})$	- , -
$p_T(jet1)$	> 100 GeV
$p_T(jet3)$	-
$ \eta (jet1)$	< 2.4
$N_b(\text{CSVM})$	= 0, (-)
\cancel{E}_T	> 175 GeV
\cancel{E}_T / H_T	-
$M_{\ell\ell}$	-
$M_{\tau\tau}$	-
Simulated Trigger	pfMET120 or MonoJet

We illustrate each SR cut choice in plots using this preselection. For the signal, three points are shown (two from the stop-pair case with considerably different mass splittings, and one from the ‘‘democratic’’ chargino-neutralino production). Signal histograms are scaled by $\times 10$ to be visible.

5.3.1 Hadronic sector cuts

The trigger requires an offline selection of at least 200 GeV in missing transverse momentum and a leading hard jet (jet1) of more than 150 GeV. Conditions which perfectly meet our signal discrimination requirements. These are the values we cut over. The simulated distributions, for SUSY signal and background, for missing transverse momentum (\cancel{E}_T) and leading jet p_T ($p_T(jet1)$) are presented in figure 5.3 left and right respectively. Signal appears clearly harder distributed than the background.

Thus, in the hadronic sector of our selection we require a hard central ($|\eta| < 2.4$) jet1 and we allow the presence of a second hard jet (with $|\eta| < 4.5$). The sub-leading jet (jet2) p_T distribution does not discriminates the signal (shown in appendix C.1, figure C.1). These (one or two) ISR-originated hard jet(s) gives the boost to the sparticle pair and allows the triggering of such events. We veto events

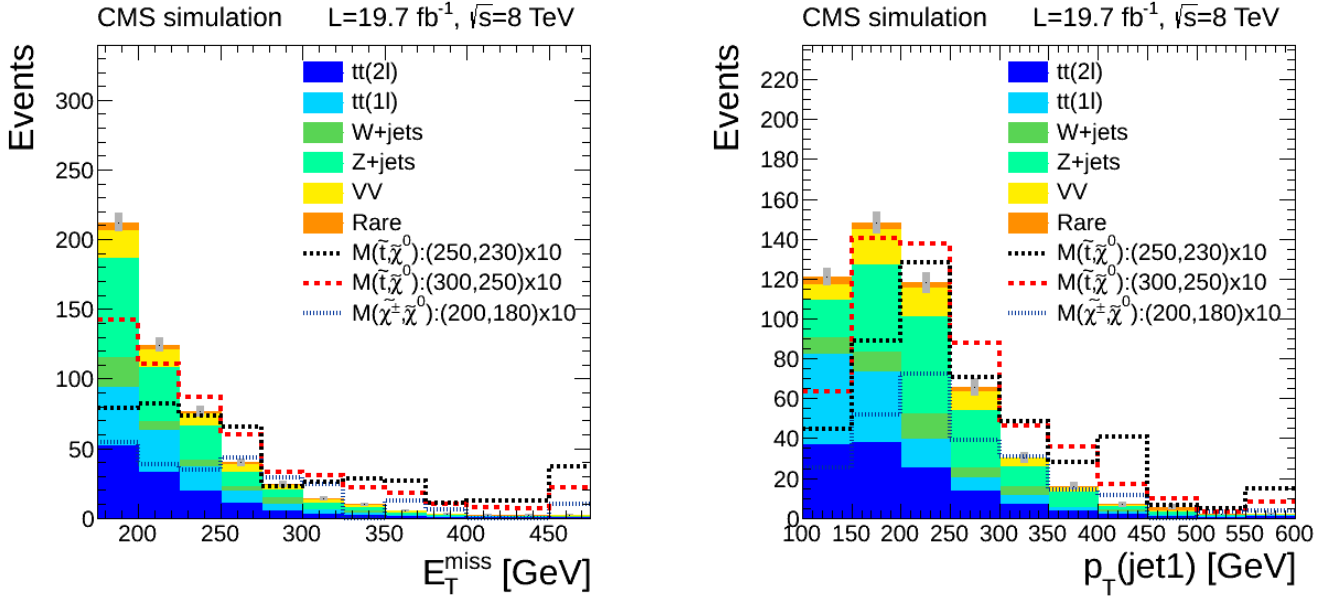


Figure 5.3: The missing transverse energy \cancel{E}_T (left) and the leading jet p_T (right). SM background processes and signal (scaled by $\times 10$) are superimposed in the preselection.

with a third hard jet if $p_T(\text{jet}3) > 60$ GeV, to suppress the $t\bar{t}$ backgrounds. $p_T(\text{jet}3)$ distribution is presented in figure 5.4 left.

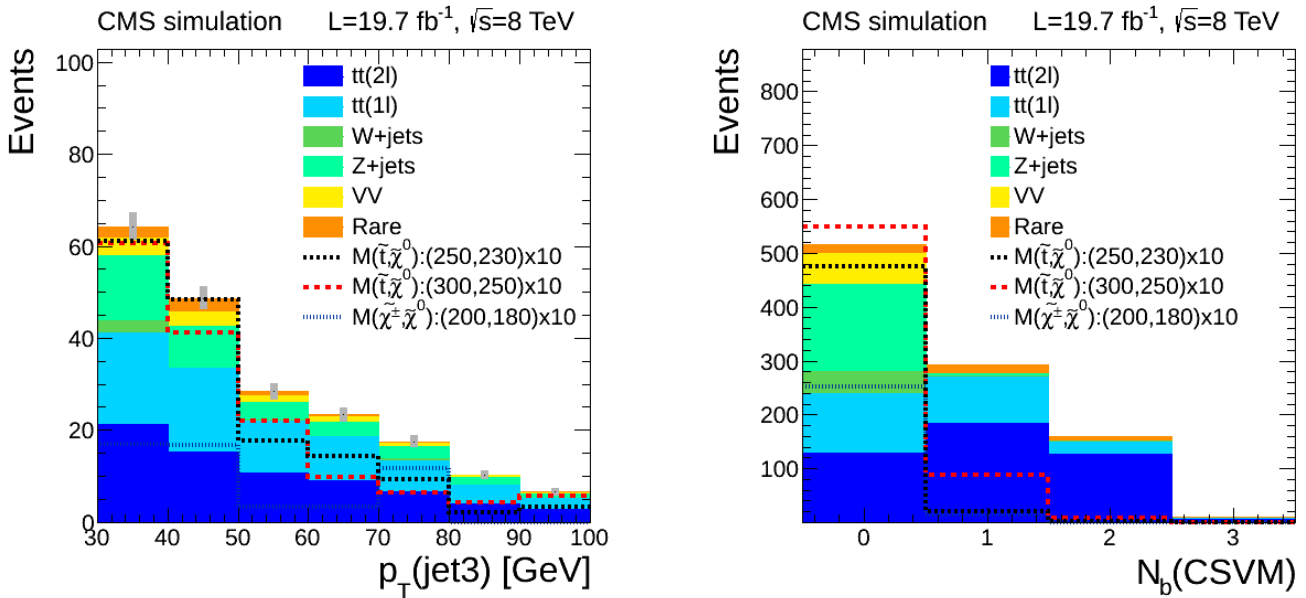


Figure 5.4: The distribution of third jet p_T (if exists) left, and the b-jet multiplicity right. Signal and background in preselection. SM background processes and two SUSY signal scenarios scaled by $\times 10$ are superimposed.

To suppress the instrumental and beam-related backgrounds additional quality requirements are imposed to the leading jet. Events are selected only if jet1 charged and neutral electromagnetic energy fraction is below 50% and 70%, respectively. In addition events are rejected if less than 20% of its energy is carried by charged hadrons or more than 70% of this energy is carried by either neutral hadrons or photons [3, 75]. Such spurious jets primarily arise from instrumental noise, where the energy deposition is limited to one sub-detector. Jets resulting from energy deposition by beam halo or cosmic-ray muons do not have associated tracks and are also rejected by these selections. The application of these data

“clean-up requirements” are very effective in rejecting non-collision backgrounds. (The distributions over these variables in preselection are presented in appendix C.1, figures C.11 and C.10.)

Even though the stop-pair production has two b-jets in final state (figure 4.2) these appears in most cases softer than the jet p_T threshold of our analysis which is 30 GeV and the b-jet multiplicity distribution peaks at $N_b = 0$. This is shown in figure 5.4 right. We select $N_b = 0$ and thus we further suppress $t\bar{t}$ events. (The b-jet tagging is performed with the method described in subsection 3.5.11 using the “Combined Secondary Vertex” CSV discriminator at the “Medium” working point which provides $\sim 65\%$ reconstruction efficiency with $\sim 85\%$ b-jet purity [72]). The exact jets’ requirements are summarised bellow.

- $p_T(\text{jet}) > 30$ GeV and $|\eta_{\text{jet}}| < 4.5$ for all the jets to be considered in the analysis
- $p_T(\text{jet1}) > 150$ GeV and $|\eta|(\text{jet1}) < 2.5$
- $CHEF(\text{jet1}) > 0.2$ charged hadrons energy fraction
- $NHEF(\text{jet1}) < 0.7$ neutral hadrons energy fraction
- $NEEF(\text{jet1}) < 0.7$ neutral electromagnetic energy fraction
- $CEEF(\text{jet1}) < 0.5$ charged electromagnetic energy fraction
- $p_T(\text{jet3}) < 60$ GeV
- $N_b(\text{CSVM}) = 0$

5.3.2 Leptonic sector cuts

The transverse momentum of the two leptons is shown in plots of figure 5.5, which motivates a cut of the first lepton to be below 25 GeV and the second to be less than 15 GeV. Further, the first lepton p_T is split into two search bins, one with: $5(7)$ GeV $< p_T(\ell_1) < 15$ GeV and one with: $15 < p_T(\ell_1) < 25$ GeV. This binning extends the sensitivity of the search to a wide range of mass-splittings. The higher the $\Delta M(\tilde{t} - \tilde{\chi}_1^0)$ is, the most extended (higher) the $p_T(\ell_1)$ is as well, (this can be shown from the equation 4.1 where ΔM limits the momenta of soft objects). The pseudorapidity of the leptons is shown in figure 5.6 whereas the relative and absolute isolation in figure 5.8.

Absolute pseudorapidity $|\eta_\ell|$ of each lepton is required to be less than 1.5. Lepton originated by heavy objects decay (in our case \tilde{t} which are produced modestly boosted) tends to have more central direction. Such cut restricts to central leptons. The relevant distributions are shown in figure 5.6.

Among the plotted backgrounds one can notice processes with in principle one lepton like the $W+\text{Jet}$ ($W \rightarrow \ell\nu$) and $t\bar{t}(1\ell)$. In such events a second (usually soft) lepton may occur from a hadron decay in a jet, and that makes the events laid in dileptonic selection. Such leptons and events are called “Non-Prompt” (NP) in contrast with the other lepton (coming from on-shell W) which is the prompt. To suppress such the NP-events we proceed to the following cuts:

- We require an impact parameter (IP) in the transverse plane z, y and along the z (beam) axis direction with respect to the primary vertex, satisfying the requirements: $|d_{xy}| < 0.01$ cm and $|d_z| < 0.01$ cm. (The illustration of IP’s definition has been shown in figure 3.11). Thus NP-lepton coming from relatively long-lived and flight hadrons tend to have higher $|d_{xy}|, |d_z|$ values and are suppressed with such cut.
- We apply both relative and absolute isolation cuts (as has been mentioned: $ISO_{rel} < 0.5, ISO_{abs} < 5$ GeV) and thus NP-leptons close to jets are suppressed.

Main motivation for these cuts is to suppress the NP background events (which in general tends to be the most difficult to predict) and not the discrimination power or the variables. The corresponding distribution of $|d_{xy}|, |d_z|$ are shown in figure 5.7, whereas the isolation in figure 5.8. (For each individual lepton, IPs, and isolation are shown in figures C.6, C.7, C.8 and C.9, in the appendix C.1).

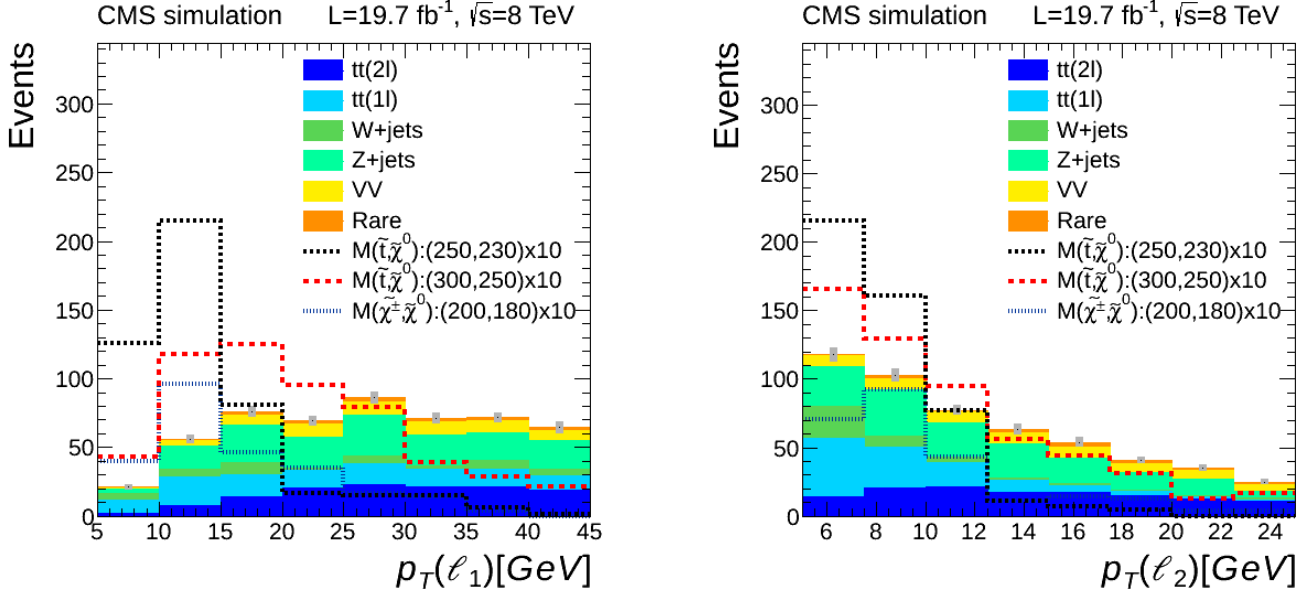


Figure 5.5: Leading lepton p_T distribution (left), and the sub-leading lepton p_T distribution (right). A looser than the signal region selection (preselection) is used. SM background processes and signal scaled by $\times 10$ are superimposed in preselection.

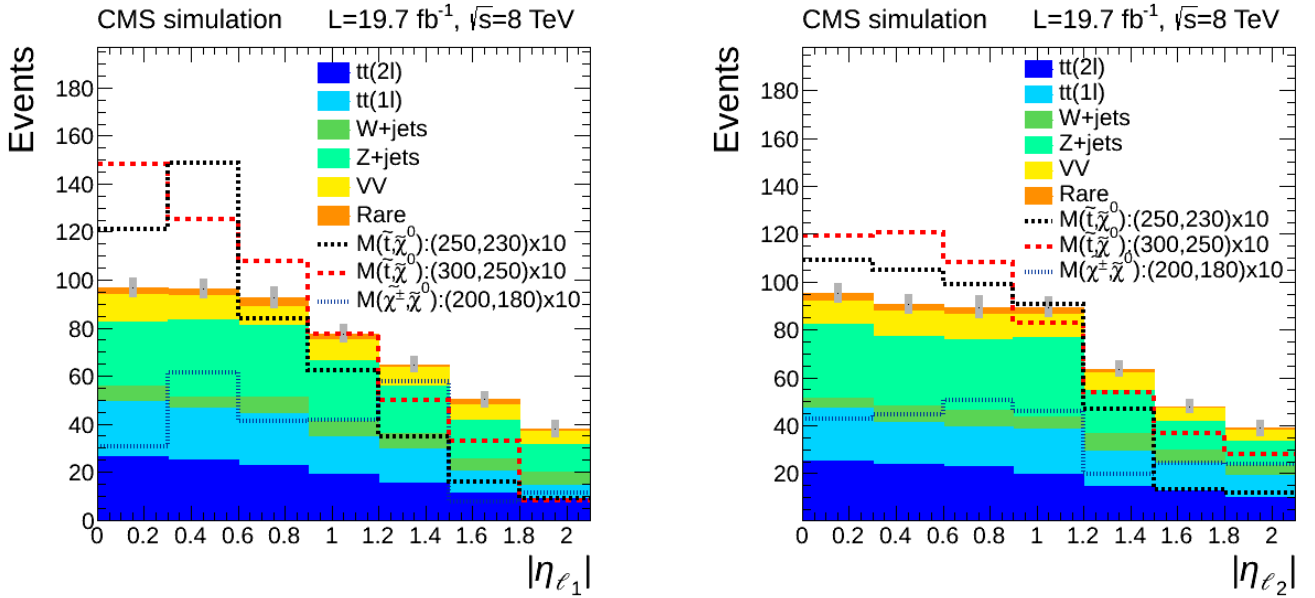


Figure 5.6: The $|\eta_\ell|$ distribution of leading (left) and sub-leading (right) leptons for signal and background. SM background processes and signal scaled by $\times 10$ are superimposed in preselection.

5.3.3 Composite variables sector cuts

The \cancel{E}_T / H_T ratio (where the H_T is the sum of p_T of all considered jets) is presented in figure 5.9 (left). It is used to guard our selection from QCD events, which are not simulated in sufficient statistics. QCD events are expected to have small \cancel{E}_T with respect to the H_T and therefore to appear at the left tail of ratio distribution. \cancel{E}_T / H_T is known also from hadronic searches to be a very effective QCD “killer” and we select events with $\cancel{E}_T / H_T > 2/3$.

After all previous cuts, the dominant remaining background is the Z+jets. Where the boosted Z is initially decayed into two taus were decayed finally leptonically in a final-state with four neutrinos and two soft leptons. Due to the boost that taus inherit from Z ($p_T(\tau) \gg m_\tau$) the flight direction of the

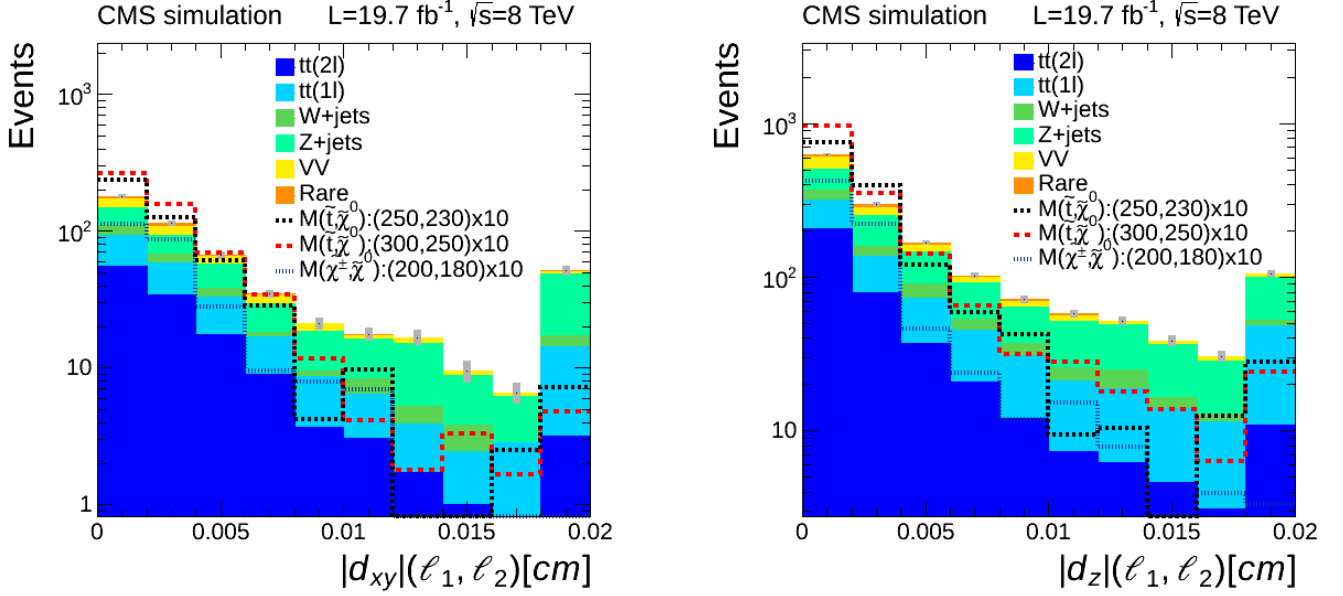


Figure 5.7: The $|d_{xy}|$ (left) and $|d_z|$ (right) impact parameters distributions for signal and background. SM background processes and signal scaled by $\times 10$ are superimposed in preselection.

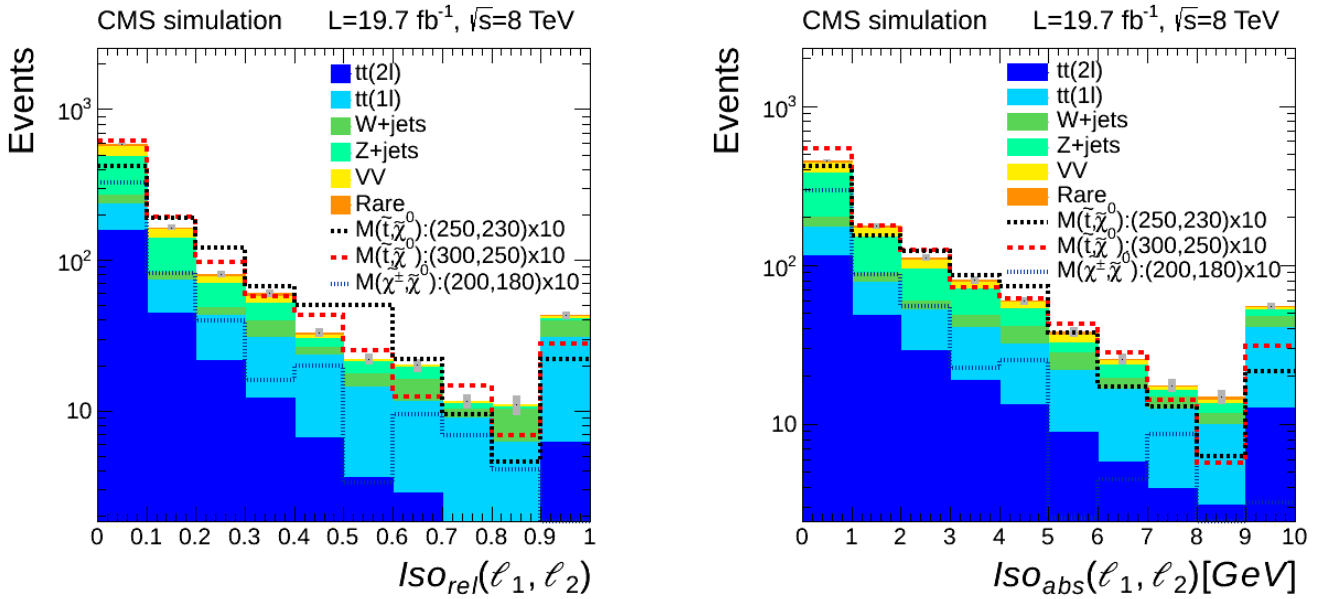


Figure 5.8: The relative isolation distributions (left) and absolute isolation distributions (right) for signal and background. SM background processes and signal scaled by $\times 10$ are superimposed in preselection.

final lepton is roughly the same with its parent tau i.e. $\Delta R(\ell, \tau) \simeq 0$. Assuming equality to the last, we can calculate the original tau four-momentum setting the two taus momenta equal to the measured hadronic recoil:

$$\vec{p}_{(Z)} = \vec{p}_{(\tau_1)} + \vec{p}_{(\tau_2)} = -\vec{H}_T = \vec{p}_{(\ell_1)} + \vec{p}_{(\ell_2)} + \sum_i \vec{p}_{i(\nu)}, \quad (5.1)$$

$$\begin{aligned} x-y \text{ plane} \Rightarrow [\vec{p}_{T(\tau_1)}] + [\vec{p}_{T(\tau_2)}] &= \vec{p}_{T(\ell_1)} + \vec{p}_{T(\ell_2)} + \vec{\cancel{E}}_T = [\vec{p}_{T(\ell_1)} + \vec{\cancel{E}}_{T \ 1} \hat{p}_{T(\ell_1)}] + [\vec{p}_{T(\ell_2)} + \vec{\cancel{E}}_{T \ 2} \hat{p}_{T(\ell_2)}] \\ \Rightarrow \vec{p}_{T(\tau_i)} &= \vec{p}_{T(\ell_i)} \left(1 + \frac{\cancel{E}_{T \ i}}{|\vec{p}_{T(\ell_i)}|}\right), \quad p_{z(\tau_i)} = p_{z(\ell_i)} \left(1 + \frac{\cancel{E}_{T \ i}}{p_{z(\ell_i)}}\right) \end{aligned}$$

This equation projected in the transverse plane gives a trivial equation with two unknowns that can be solved ($\vec{\cancel{E}}_{T \ 1}, \vec{\cancel{E}}_{T \ 2}$ in the above). With the tau four-vectors we then reconstruct the (effective)

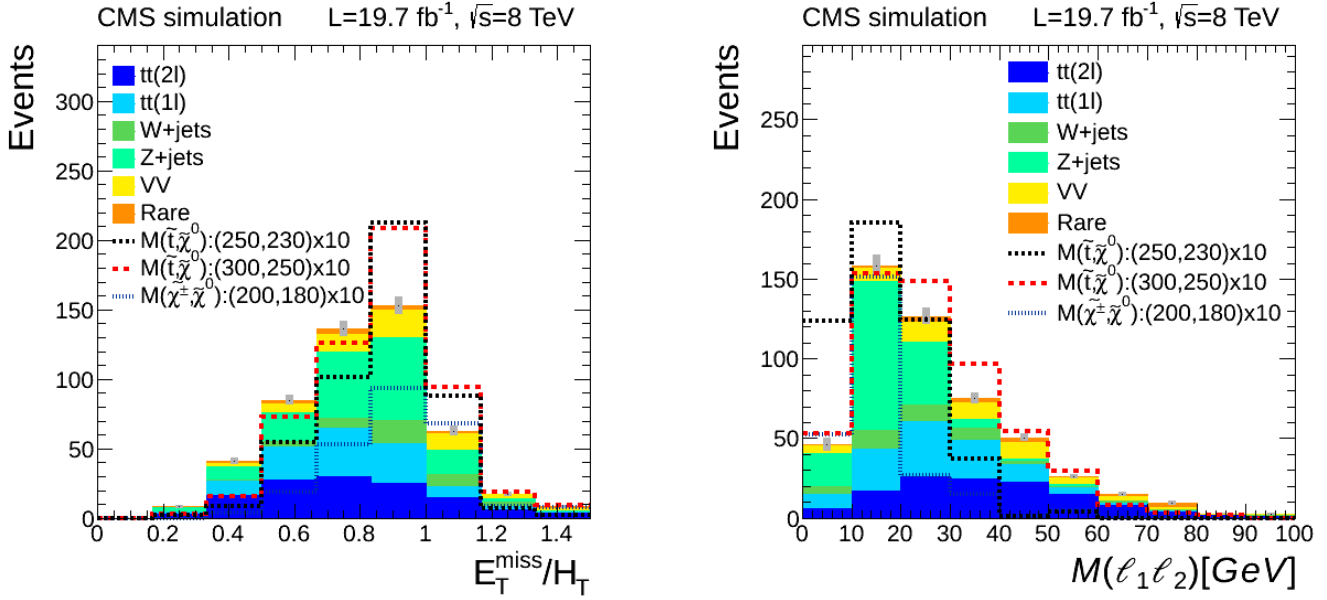


Figure 5.9: The \cancel{E}_T / H_T distribution (left) and the invariant mass of lepton pair (right). SM background processes and signal scaled by $\times 10$ are superimposed.

invariant mass of the tau-pair $M_{\tau\tau}$ which correspond to their parent Z -mass.

In other words: we decompose $\vec{\cancel{E}}_T$ along the two soft lepton directions, we add together these two components ($\vec{p}_{T(\ell_i)} + \cancel{E}_T \cdot \hat{p}_{T(\ell_i)}$) into the effective $\vec{p}_{T(\tau)}$ and we scale the $p_Z(\ell)$ by the same factor (as for $p_T(\ell)$) to form $p_Z(\tau)$ and receive each tau four-vector.

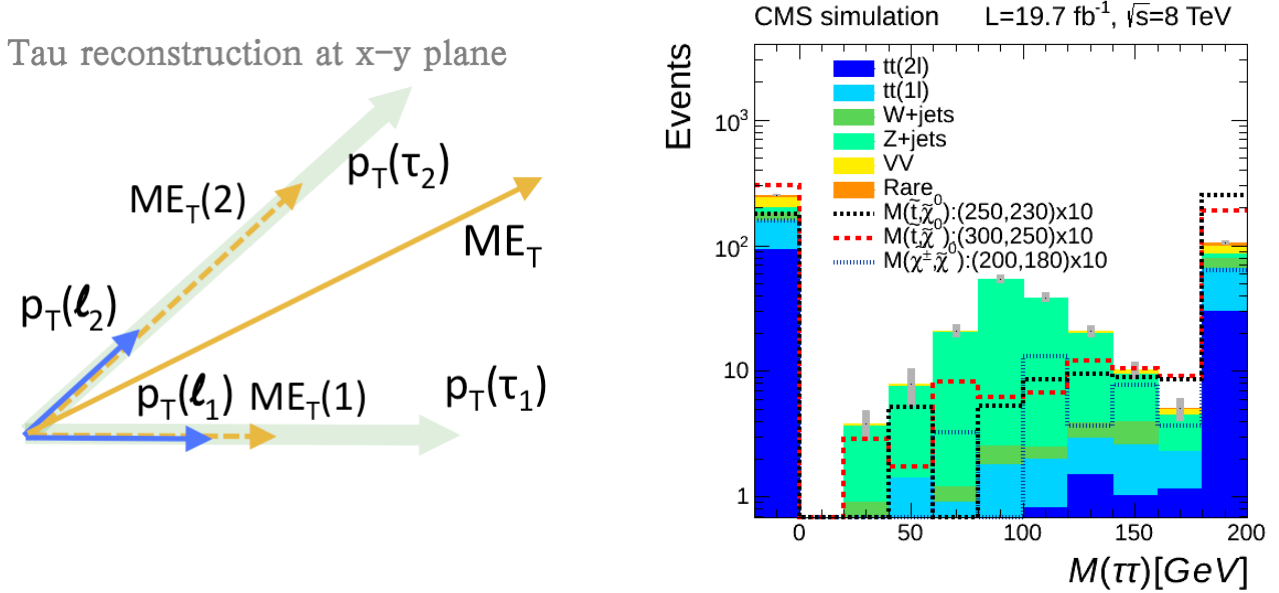


Figure 5.10: The decomposition of \cancel{E}_T along the two lepton directions in transverse plane (left). Each $p_T(\ell_i) + \cancel{E}_T \cdot \hat{p}_{T(\ell_i)}$ component forms each tau $p_T(\tau_i)$. Each $p_Z(\tau_i)$ is formed as: $p_Z(\tau_i) = p_Z(\ell_i) [p_T(\tau_i) / p_T(\ell_i)]$. Invariant mass of the effective taus $M_{\tau\tau}$ (right) for a looser than the signal region selection (preselection). SM background processes and two SUSY signal scenarios scaled by $\times 10$ are superimposed.

Figure 5.10 illustrates the tau's reconstruction (left) in the transverse plane and the distribution of their corresponding effective invariant mass $M_{\tau\tau}$ (right). If the \cancel{E}_T doesn't lying in-between the two soft leptons the $\cancel{E}_T \cdot \hat{p}_{T(\ell_i)}$ is negative; case which corresponds to taus having opposite direction than their

soft lepton. We set the reconstructed invariant mass to be negative for these cases ($M_{\tau\tau} = -|M_{\tau\tau}|$). An explicit study of all possible tau-reconstruction cases can be found in appendix C.4, figure C.25. Finally, we impose a cut excluding the $0 < M_{\tau\tau} < 160$ GeV region which corresponds the Z mass-peak of di-tau reconstructed mass. Thus, we subtract the $Z \rightarrow \tau\tau \rightarrow \ell\ell\nu\nu\nu\nu$ events from SR.

Some other potential soft OS-lepton background contribution is coming from the processes:

- heavy hadron decays like $j/\psi \rightarrow \mu\mu$, with lepton invariant mass: $M_{\ell\ell} \simeq 3.1$ GeV,
- b-hadron proceeding in “double sequential decay”: $b \rightarrow cW \rightarrow dWW \rightarrow d\ell^+\ell^-\nu\nu$, with $M_{\ell\ell} < M_b \simeq 4.5$ GeV,
- photons conversion: $\gamma \rightarrow \ell^+\ell^-$.

In order to shield our SR selection from their presence we impose a rejection of all events with $M_{\ell\ell} < 5$ GeV.

The complete set of all cut define the SR are listed in table 5.3. An explicit cut-flow can be shown in figure 5.11 and in table 5.4, whereas each bin corresponds to a selection one step closer to the final SR selection. An additional set of kinematic variable distributions, under preselection requirements, can be found in appendix C.1. Similar set of all kinematic variable distributions, after applying all SR selection cuts are presented in appendix C.2 where signal is scaled to data luminosity 19.7 fb^{-1} .

Table 5.3: Selection cut for the signal regions. The p_T s in parenthesis stands for electrons.

Variable:	SR selection cut:
N_ℓ	= 2
N_μ	≥ 1 (& soft Muon ID)
$Q(\ell_1)Q(\ell_2)$	-1
$p_T(\ell_1)$	[5(7), 25] GeV
$p_T(\ell_2)$	[5(7), 15] GeV
$ \eta (\ell_{1,2})$	< 1.5
$d_z(\ell_{1,2})\&d_{xy}(\ell_{1,2})$	< 0.01 cm
$Iso_{rel}(\ell_{1,2})\&Iso_{Abs}(\ell_{1,2})$	< 0.5, < 5 GeV
$p_T(jet1)$	> 150 GeV (& quality requirements)
$p_T(jet3)$	< 60 GeV
$ \eta (jet1)$	< 2.4
N_b (CSVM)	= 0
\cancel{E}_T	> 200 GeV
\cancel{E}_T / H_T	> 2/3
$M_{\ell\ell}$	> 5 GeV
$M_{\tau\tau}$	cut:[0, 160] GeV
	HLT_MET_120_HBHENoiseCleaned
Triggers used	HLT_Mono_CentralPFJet80_PFMETno_Mu105_NHEF0p95 HLT_Mono_CentralPFJet80_PFMETno_Mu95_NHEF0p95

Table 5.4: The cut-flow yields for simulated background and two signal points. (In the appendix C.3, Table C.1 an explicit cut-flow per each background is shown).

bin	Selection cuts	Total SM background	$M(\bar{t}), M(\bar{\chi}_1^0)$: (250,230) GeV	$M(\bar{t}), M(\bar{\chi}_1^0)$: (300,250) GeV
1	$\cancel{E}_T > 200$ GeV	147533±229	6640±39	2563±15
2	$N_\ell = 2$	6247±32	132±6	125.9±3.4
3	$N_\mu \geq 2$	4472±26	117±6	102.8±3.1
4	$Q(\ell_1)Q(\ell_2) = -1$	3712±23	92.5±4.9	83.5±2.8
5	$p_{Tj1} > 150$ GeV, $ \eta < 2.4$	2610±19	76.2±4.4	69.7±2.5
6	$p_{Tj3} < 60$ GeV	1887±18	69.2±4.2	63.1±2.3
7	$N_b = 0$	1003±15	64.3±4.1	53.2±2.2
8	$\cancel{E}_T / H_T > 2/3$	667±13	57.5±3.6	46.3±2.0
9	$p_{T\ell}: [5, 25(15)]$ GeV, $ \eta < 1.5$	41.0±3.0	23.2±2.3	14.3±1.1
10	$ d_z , d_{xy} < 0.01$ cm	18.5±1.9	20.3±2.2	12.1±1.1
11	$I_{Rel} < 0.5, \&I_{Abs} < 5$ GeV	12.7±1.5	15.3±1.9	9.0±0.9
12	$M_{\ell\ell} > 5$ GeV	12.4±1.5	14.6±1.8	8.4±0.9
13	$M_{\tau\tau}$ cut:[0, 160] GeV	8.0±0.8	13.5±1.8	7.8±0.8

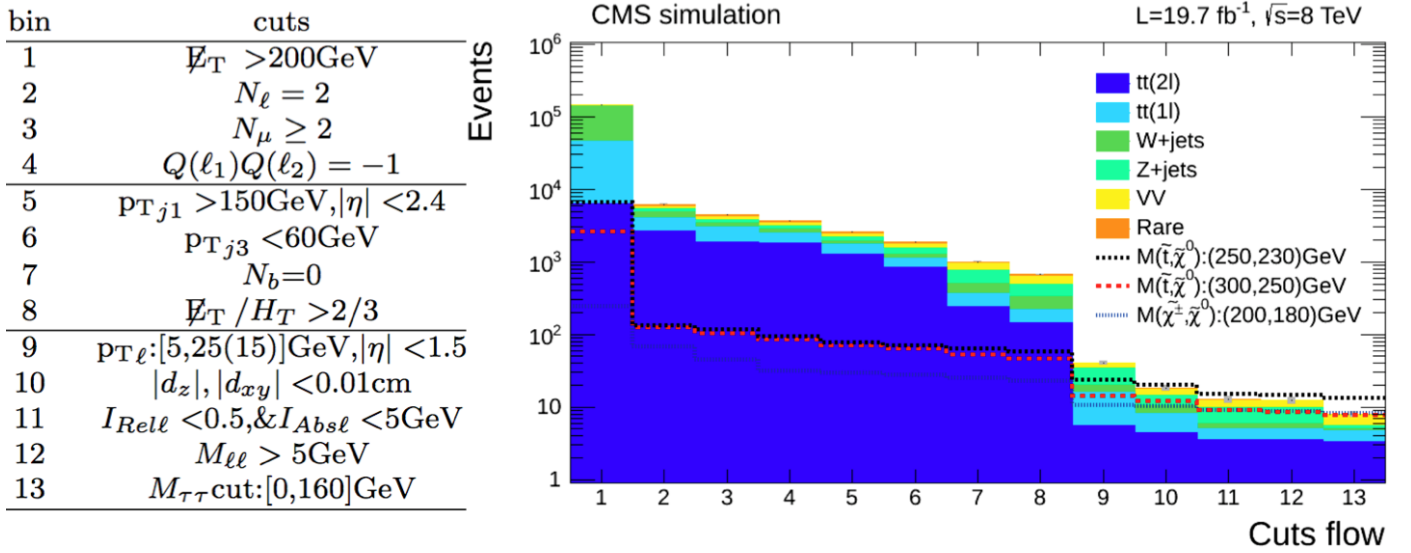


Figure 5.11: The cut-flow in a histogram. Each bin correspond to different selection cuts which are defined (adding always the listed cut) in table on the left. Last bin has the final event yields of the SR. (Pile-up correction, ISR-reweigh corrections, b-tagging Scale Factors correction and trigger simulations cuts are applied from the 0-level of the cut-flow).

5.3.4 Background composition in signal region

The yielded SM background is presented in table 5.5 accompanied by the three signal scenarios. The SM background composition –according to simulation– is comprised mainly from $t\bar{t}(2\ell) \sim 42\%$, and di-boson $\sim 30\%$ (where W^+W^- , WZ , ZZ merged together under the collective legend “VV”), and the subdominant $t\bar{t}(1\ell) \sim 18\%$, W +jets $\sim 4\%$, and Z +jets $\sim 6\%$. All these corresponds to ~ 8 events according to raw MC.

Table 5.5 also shows three signal points. First two corresponds to stop-pair production decaying into LSPs via the four-body decay (figure 4.2 left) for masses $(m(\tilde{t}), m(\tilde{\chi}_1^0))$. The third signal scenario stands for figure 4.2 middle (democratic), and for masses $(m(\tilde{\chi}_1^\pm), m(\tilde{\chi}_1^0))$. The chargino-neutralino pair decayed (via slepton-neutralino) at 50% BR to the three lepton final state (where lepton can equi-probable be e , μ or τ).

Table 5.5: Simulation yields in SR. The SM background and three signal point are shown.

Sample: / Bins:	$p_T(\ell_1) : [5, 15]\text{GeV}$	$p_T(\ell_1) : [15, 25]\text{GeV}$	Inclusive
$t\bar{t}(2\ell)$	0.90 ± 0.20	2.48 ± 0.34	3.38 ± 0.39
$t\bar{t}(1\ell)$	0.53 ± 0.20	0.89 ± 0.27	1.42 ± 0.33
$W + jets$	0	0.28 ± 0.28	0.28 ± 0.28
$Z + jets$	0	0.45 ± 0.33	0.45 ± 0.33
VV	0.70 ± 0.21	1.64 ± 0.33	2.34 ± 0.39
Rare	0.03 ± 0.01	0.08 ± 0.04	0.11 ± 0.04
SM Total	2.16 ± 0.35	5.81 ± 0.69	7.97 ± 0.78
SUSY(250,230)	10.0 ± 1.5	3.41 ± 0.90	13.5 ± 1.8
SUSY(300,250)	3.98 ± 0.61	3.83 ± 0.58	7.80 ± 0.84
SUSY(200,180)	6.2 ± 1.5	1.90 ± 0.88	8.1 ± 1.7

The % background abundances can be shown in chart at figure 5.12 as well the per bin distribution. The collective “Rare” legend stands for the very small contribution of: tW , $\bar{t}W$ (i.e.: “single-top”), $t\bar{t}W$, $t\bar{t}Z$, $t\bar{t}H$, WWW , WWZ , WZZ , ZZZ , $W^\pm W^\pm$ (i.e.: same-sign WW).

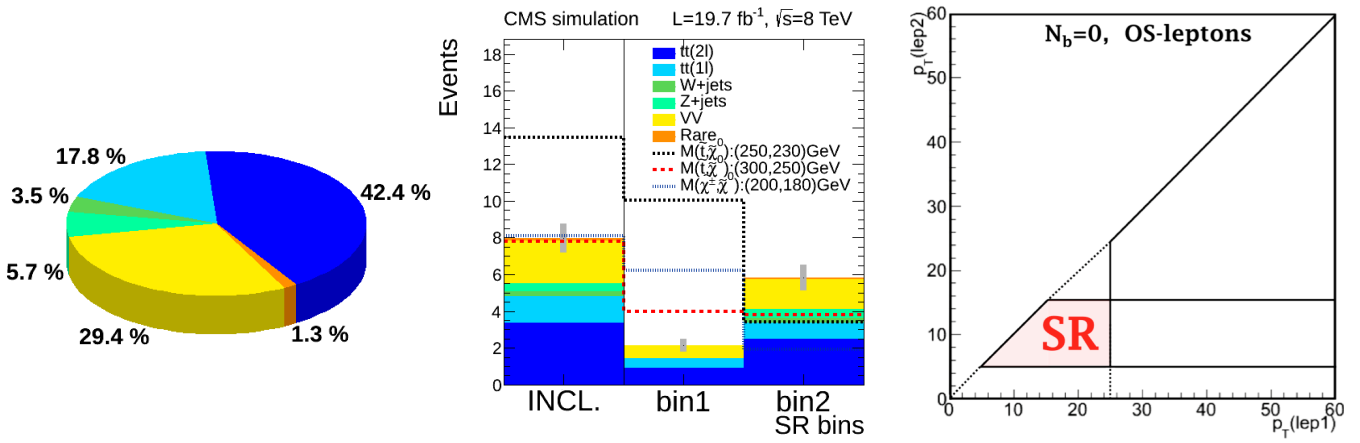


Figure 5.12: The SR decomposed in its % SM background (left), broken-down into the two bins event yields (middle), and the SR-position in a $p_T(\ell_1) - p_T(\ell_2)$ plane (right). Region above the diagonal is forbidden due to convention $p_T(\ell_1) > p_T(\ell_2)$.

Chapter 6

Background Prediction

In this chapter we exhibit the methods used for the background prediction in SR.

We predict four different background categories individually. One is $t\bar{t}(2\ell)$, which is the biggest background (table 5.5, figure 5.12), the second largest background stems from di-boson events. Another background is DY+jets (to $\tau\tau$) where the latest decayed leptonically (to $e\mu$ or $\mu\mu$). Background with one “non-prompt” lepton, i.e. W+jets and $t\bar{t}$ semi-leptonic, are the fourth category. For the negligible ($\sim 1\%$) contribution of “Rare”, we use as predicted the MC simulated yields. The SM events yielded with such soft leptons have in a level of $\sim 50\%$ at least one tau-originated lepton.

For each of these four categories we introduced a Control Region (CR), enriched in such processes, in which we derive correction factors from data to correct the SR yields from MC. The explicit motivation of each CR selection and the explicit prediction formulas are presented in next sections.

The table 6.1 presents collectively all variables that we cut over (first column), repeats the SR selection (second column), and shows for each each CR definition cuts. On the bottom the corresponding event yields in data and simulation are presented as well. No cut value, is imposed where a cut is the same with the one in SR. The three signal points presence shows that all CR are relatively “signal-free”. Figure 6.1 illustrates the % purity of each CR. All the content of the table will be detailed discussed in the next.

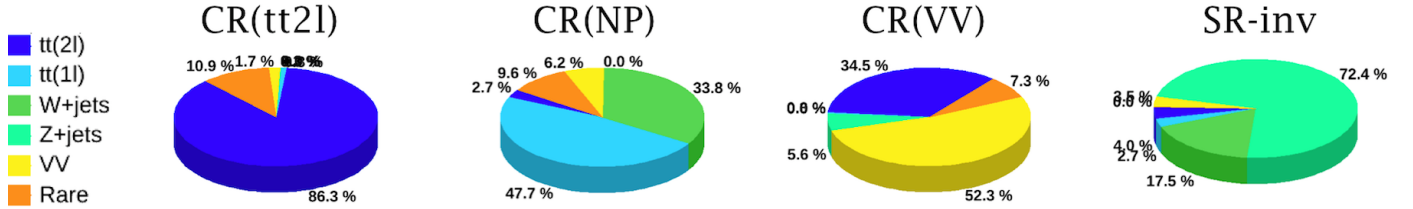


Figure 6.1: The % abundances (purity) of the four main control regions used for each or the corresponding background prediction.

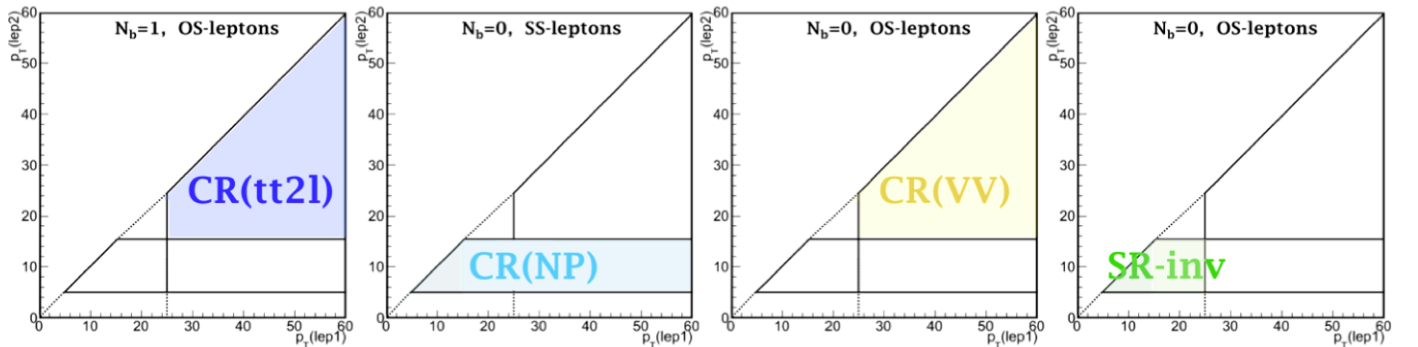


Figure 6.2: The $p_{T\ell_1} - p_{T\ell_2}$ plane and each control region selection over this.

Table 6.1: Top: selection cuts for SR and each control region used for the background prediction. Only the changes with respect to the SR cut are shown. Bottom: simulation and data event yields per region. Isolation values in square brackets stands for the soft leptons with: $p_T(\ell) < 25$ GeV.

Regions: Sub Regions:	SR	CR($t\bar{t}2\ell$)	CR(NP) SR(SS) CR(SS)	CR(VV)	CR(Z)	SR-inv
Cut variables	Cut values/thresholds					
N_ℓ	2		==+1	==+1		
$Q(\ell_1)Q(\ell_2)$	=-1					= 2
N_μ	1 or 2					μ , (tight ID)
ℓ_1 flavor, (ID)	μ or e	μ , (tight ID)		μ , (tight ID)	μ , (tight ID)	μ , (tight ID)
$p_T(\ell_1)$	[5(7),25] GeV	> 25 GeV		> 25 GeV	> 25 GeV	> 125 GeV
$p_T(\ell_2)$	[5(7),15] GeV	> 15 GeV				> 10 GeV
$ \eta (\ell_{1,2})$	<1.5					< 2.1
$ d_z , d_{xy} (\ell_{1,2})$	<0.01 cm					<0.5, <0.02 cm
$I_{Rel}(\ell_{1,2})$	<0.5	< 0.12 [<0.5]		0.12 [<0.5]	<0.12 [<0.5]	<0.12 [<0.5]
$I_{Abs}(\ell_{1,2})$	<5 GeV	- [<5 GeV]		- [<5 GeV]	- [<5 GeV]	- [<5 GeV]
$p_T(jet1)$	>150 GeV					
$p_T(jet3)$	<60 GeV					
$ \eta (jet1)$	<2.4					
N_j	≥ 1				1 or 2	
N_b	=0	=1 & jet1: non b			=0 (loose id)	
$ \Delta\phi(\ell_1, jet1) $	-				>1	
\cancel{E}_T	>200 GeV	>125 GeV		>125 GeV	> 125 GeV	-
\cancel{E}_T / H_T	> 2/3	-		-	-	-
$\cancel{E}_T + p_T(\ell_1) \equiv L_T$	-	> 225 GeV		>225 GeV	>225 GeV	-
L_T / H_T	-	>2/3		>2/3	>2/3	-
$ \vec{p}_T(\mu_1) + \vec{p}_T(\mu_2) $	-					>200 GeV
$ \vec{p}_T(\mu_1) + \vec{p}_T(\mu_2) / H_T$	-					>2/3
$M_{\ell\ell}$	>5 GeV				>50 GeV	>10 GeV
$M_{\tau\tau}$	<0, >160 GeV					-
Trigger(s) used	MET or ISR	Single_Mu		Single_Mu	Single_Mu	Single_Mu
						[0,160] GeV
Samples	Simulation and data event yields					
$t\bar{t}(2\ell)$	3.38 \pm 0.39	119.1 \pm 2.4	0.27 \pm 0.11	30.3 \pm 1.2	12.5 \pm 0.8	0.15 \pm 0.08
$t\bar{t}(1\ell)$	1.42 \pm 0.33	1.09 \pm 0.29	4.7 \pm 0.6	0.30 \pm 0.14	2.19 \pm 0.42	0.11 \pm 0.11
W+jets	0.28 \pm 0.28	0	3.4 \pm 1.3	0	0	0.7 \pm 0.7
DY+jets	0.45 \pm 0.33	0.35 \pm 0.35	0	4.9 \pm 1.3	9464 \pm 62	3.3(2.8) \pm 1.1
VV	2.34 \pm 0.39	2.4 \pm 0.6	0.62 \pm 0.11	45.9 \pm 1.8	33.6 \pm 1.4	0.13 \pm 0.09
Rare	0.11 \pm 0.04	15.1 \pm 2.7	1.0 \pm 0.5	6.4 \pm 1.7	3.7 \pm 0.9	0
Total SM background	8.0 \pm 0.8	138.0 \pm 3.7	10.0 \pm 1.5	87.8 \pm 3.0	9516 \pm 62	4.4(3.9) \pm 1.3
Data	results section	119	11	81	7610	5
SUSY(250,230)	13.5 \pm 1.8	0	1.0 \pm 0.5	0	0	1.1 \pm 0.5
SUSY(300,250)	7.8 \pm 0.8	0.16 \pm 0.11	0.72 \pm 0.24	0.50 \pm 0.20	0	0.57 \pm 0.22
SUSY(200,180)	8.1 \pm 1.7	0	1.8 \pm 0.8	0	0	0.51 \pm 0.42

6.1 Dileptonic top background prediction

For the control region of $t\bar{t}(2\ell)$ background we apply the same selection on hadronic level as in SR, i.e. same jet requirements, but we use higher p_T leptons. The first lepton p_T is required to be: $p_T(\ell_1) > 25$ GeV and the second: $p_T(\ell_2) > 15$ GeV. (The inversion of the second lepton p_T is necessary to eliminate non-prompt event contribution as will be clear in following sections.)

In order to avoid an increment at the scale of leptonic activity (sum of neutrinos and leptons p_T s) by going higher in lepton p_T , we replace the missing transverse momentum cut with the sum of transverse momentum of the first lepton $p_T(\ell_1)$ and \cancel{E}_T . In the following we call this sum L_T . We also replace the \cancel{E}_T/H_T cut by the $L_T/H_T > 2/3$ correspondingly. The \cancel{E}_T cut is relaxed to: $\cancel{E}_T > 125$ GeV and an L_T cut is set to: $L_T > 225$ GeV (which is the value of the \cancel{E}_T cut plus the upper threshold of $p_T(\ell_1)$ in signal region).

Apart from assuring that the scale of the leptonic activity is similar (between \cancel{E}_T and L_T cuts) also the yields are larger (by factor of $\times 4$) compared to those only changing the leptons p_T ranges.

We use the single muon trigger: HLT_IsoMu24_eta2p1, to trigger also lower \cancel{E}_T events with large L_T . The standard muon ID from the POG, and isolation (relative PF isolation: $I_{rel} < 0.12$) are used for the leading lepton which required to be a muon. The trigger and reconstruction efficiencies for this selection are very well understood. For the subleading lepton, (which can be either electron or muon) we require same as for the leading lepton requirements for p_T s above 25 GeV, and in case of a soft second lepton (i.e. $15 < p_T(\ell_2) < 25$ GeV), we stay in the SR requirements (demanding $I_{rel} < 0.5$ and $I_{abs} < 5$ GeV). This selection gives a sample with dileptonic tops but has a large di-boson contribution (mainly WW) and thus we require exactly one b-tagged jet to reject them ($N_b(CSVM) = 1$).

What remain is a rather pure $t\bar{t}(2\ell)$ sample, however it is not yet assured that it is kinetically similar as the high missing transverse momentum in SR can either stem from a top pair (which is boosted by an initial state radiation) or it can stem from a high p_T top from a top pair that is back-to-back in the transverse plane, but not boosted as a pair. Figure 6.3 left shows the momentum of the top-pair: $p_T(t\bar{t}) \equiv |\vec{p}_T(t) + \vec{p}_T(\bar{t})|$ for the signal region and it can be seen that it is dominated by boosted stop pairs balanced by \cancel{E}_T . Same figure the second, third, fourth plots shows the same distribution for our control sample for three cases; second: all events, third: the events where the leading jet is b-tagged and fourth the events for which the leading jet is not b-tagged. It can be seen that events for which the first jet is required to not be b-tagged have a similar $p_T(t\bar{t})$ distribution as the signal region and thus is the preferred control region. Therefor we require the first jet to be non b-tagged.

In the following this control sample is called CR($t\bar{t}(2\ell)$). Its detailed cuts are listed in table 6.1 at the corresponding CR($t\bar{t}(2\ell)$) column. The event yields in simulation and in data are listed in the same table (bottom).

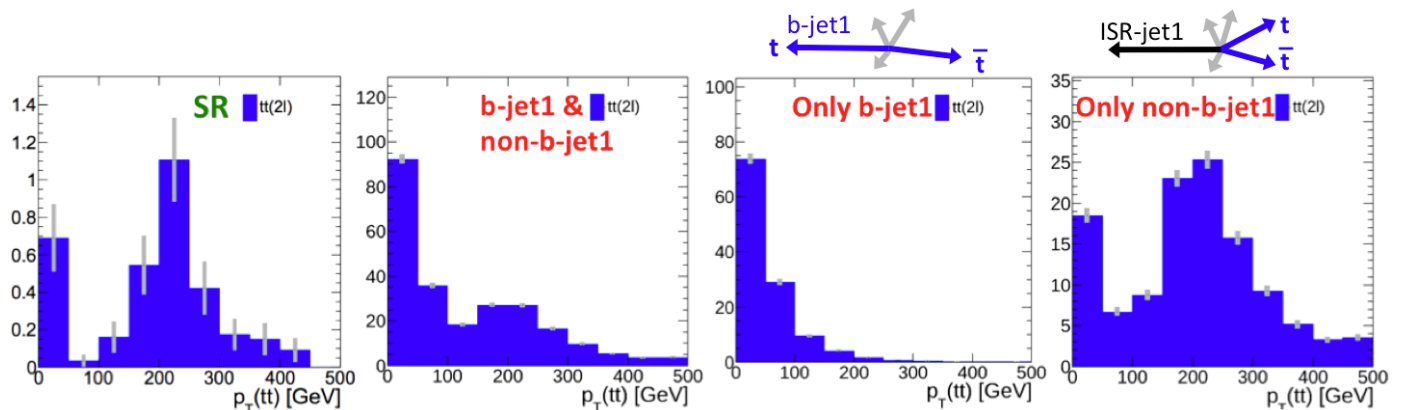


Figure 6.3: On the left first plot, the transverse momentum of top pair of di-leptonic $t\bar{t}$ events in the SR. On the second plot: the $p_T(t\bar{t})$ distributions for any kind of leading jet for $N_b = 1$ events. In third plot the $p_T(t\bar{t})$ distribution for only b-tagged as leading jet events and on the fourth plot the non-b-tagged leading jet events (third and fourth plots are the breakdown of the second).

In order to predict the SR $t\bar{t}(2\ell)$ events we measure the data events yielded in CR($t\bar{t}2\ell$), we subtract the non- $t\bar{t}(2\ell)$ events ($\sim 14\%$) and we multiply these with the MC ration of $t\bar{t}(2\ell)$ events for the SR over the CR($t\bar{t}2\ell$). Explicitly, the prediction formula for $t\bar{t}(2\ell)$ can be written as:

$$PRED_{SR}^{t\bar{t}(2\ell)} = \left(DATA_{CR(t\bar{t}2\ell)} - MC_{CR(t\bar{t}2\ell)}^{non-t\bar{t}(2\ell)} \right) \left(\frac{MC_{SR}^{t\bar{t}(2\ell)}}{MC_{CR(t\bar{t}2\ell)}^{t\bar{t}(2\ell)}} \right), \quad (6.1)$$

where DATA, MC, represent the number of events in data and simulation respectively, and PRED is the predicted yield in the signal region. Upper indexes stands for the background sample(s) in MC, PRED, and the lower indexes characterise the region of each yield has be measured/calculated.

Some kinematic variable distributions of CR($t\bar{t}2\ell$) events (in data and simulation) are shown in appendix D.1, where reasonable agreement is observed.

6.2 Prediction of semi-leptonic top and W+jets background

The background stemming from $t\bar{t}(1\ell)$ and W+jet consists of events with at least one non-prompt ‘‘NP’’ lepton. The prompt lepton comes from the on-shell W-boson leptonic decay whereas the non-prompt one can be either occurs from a hadron decay or as a miss-reconstructed (‘‘fake’’) object accounted as lepton. In order to measure in data the rate for these ‘‘NP’’ events we again define control regions that are expected to have a similar ‘‘NP’’ contribution.

The main strategy is to use exactly the same SR selection and only change from OS to same-sign (SS) lepton events. Indeed, since the non-prompt lepton does not have necessarily opposite than the prompt lepton charge, $t\bar{t}(1\ell)$ and W+jet occupies also the SS event slice of SR-cuts. Its cuts are presented in the collective table 6.1, whereas the MC and data yields are presented in table 6.2.

We have carefully checked that the lepton kinematics as well as the source of non-prompt is very similar between the SR and SR(SS). Although kinematics is very similar the actual events yields are too poor to be used for prediction.

To further gain statistics we make use of the fact that predominantly the second lepton is the non-prompt one (NP or ℓ_{NP}). We apply exactly same cuts (as in SR) for the subleading lepton and we allow higher transverse momentum muons for the first lepton: $p_T(\ell_1) > 25$ GeV. Further more, in accordance with the CR($t\bar{t}2\ell$), we exchange \cancel{E}_T with L_T variable. (Whereas, in one W-boson backgrounds is true that: $L_T^2 = M_T^2 + p_{T(W)}^2$. The L_T is very similar to $p_T(W)$ between SR and the L_T -configuration extension: $p_T(W) \sim \cancel{E}_T$).

Since kinematics depends on $p_T(W)$, we get a similar kinematics between SR and CR by using L_T . The extension to $p_T(\ell_1) > 25$ GeV events increase statistics by $\times 5$. This (second) control region is called CR(SS). Exact data and MC yields of SR(SS) and CR(SS) are presented in table: 6.2.

Table 6.2: Simulation and data Yields for SR(SS) and CR(SS); the sum of those two form the CR(NP). The CR(NP) total yields are presented in 6.1 as well.

Sample: / Region	SR(SS)	CR(SS)
$t\bar{t}(2\ell)$	0	0.27 ± 0.11
$t\bar{t}(1\ell)$	1.48 ± 0.33	3.27 ± 0.51
W+jets	1.47 ± 0.85	1.89 ± 0.94
DY+jets	0	0
VV	0.17 ± 0.08	0.45 ± 0.08
Rare	0.52 ± 0.45	0.44 ± 0.14
SM Total	3.6 ± 1.0	6.3 ± 1.1
SUSY(250,230)	1.00 ± 0.51	0
SUSY(300,250)	0.54 ± 0.21	0.17 ± 0.12
SUSY(200,180)	1.35 ± 0.63	0.49 ± 0.49
DATA	2	9

These two regions combined SR(SS)+CR(SS) provide a control sample rich in $t\bar{t}(1\ell)$ and W+jets events with similar relative abundances. The combined selection is named CR(NP). figure 6.4 Illustrates

this extension to $p_T(\ell_1) > 25$ in the $p_T(\ell_1), p_T(\ell_2)$ plane, and also shows the relative background abundances. The collective table 6.1 lists its full selection cuts for the two sub-regions and the inclusive CR(NP) data and MC yields.

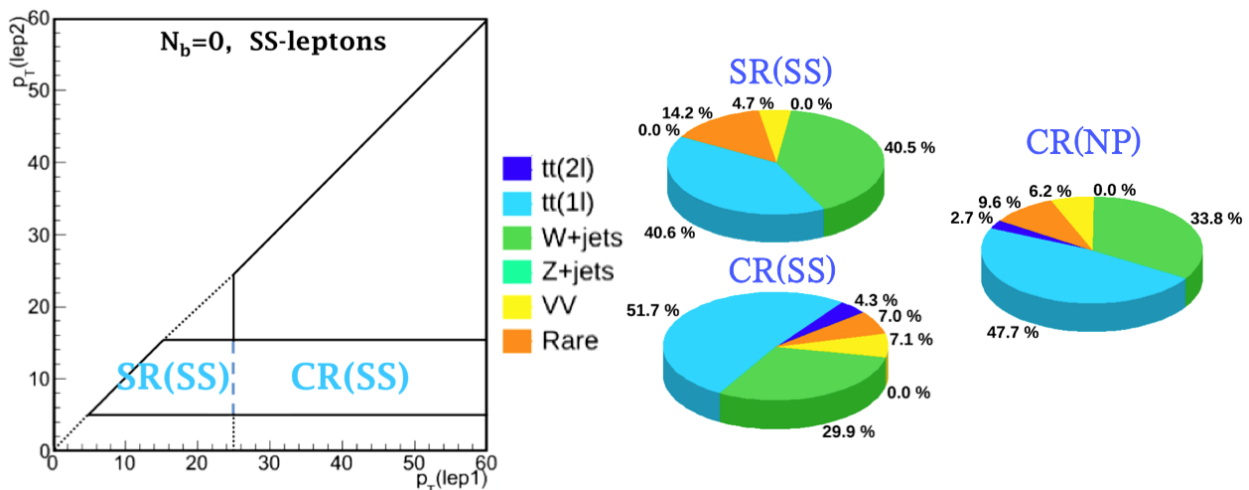


Figure 6.4: The SR(SS), CR(SS) and CR(NP) in the $p_T(\ell_1), p_T(\ell_2)$ plane and their % background contribution. The purity of the final CR(NP) in NP-events is $\sim 80\%$.

In order to check if the CR(NP) is indeed consists a proper representative sample (due NP-lepton kinematics and origination) to predict the SR NP-events we plot (superimposed) various distributions. Figure 6.5 shows the categorization of the NP-events due to four aspects of each NP-lepton (p_T , charge, flavor, channel). The plots on top stands for the (standard) SR selection whereas those on the bottom for a looser one which allow us robust conclusions in higher statics. It shows that indeed the second lepton is always the non-prompt one as assumed to motivate CR(SS) extension. Consequently the ℓ_1, ℓ_2 small asymmetry (first two bins) is an artifact of CR(SS) leading lepton which is always the prompt one.

Further, the plots shows the fraction of positively and negatively charged “NP” leptons. As expected, the SS events have a small enhancement of ℓ_{NP}^+ (or prompt ℓ_{Prompt}^-). The OS selection prefers positively charged prompts. The positive charge preference stems from the dominance of u quarks in the protons and the polarization of W-boson at the LHC. As the fake rate is not expected to be dependent on the charge these very small differences between control and signal region can be safely ignored.

Also the fractions of the lepton-flavor, (e or μ as the NP-lepton) are shown and reasonably agree between the three samples. The small difference in flavor is understood as well. If we decompose the events into its channels, where events are ordered by p_T , we have: $[\mu\mu], [e\mu], [\mu e]$ for SR and SR(SS), and only $[\mu\mu], [\mu e]$ for CR(SS) i.e. the relative presence of μ is 2/3 for SR,SR(SS) and 1/2 for CR(SS). Thus we expect an enhancement of μ_{NP} due to that ordering, also because the electron acceptance is shorter ($p_{T(e)} > 7$ GeV). This effects can be shown in 6.5 bottom left.

The fraction of electron-muon and muon-muon channels is presented as well; here CR(SS) is biased as the first lepton is required to be a muon, however the other two samples agree well. The bias for CR(SS) is not a problem, as only the non-prompt, i.e. the second lepton and unbiased one, does matter for our method.

The similarity of these regions with respect to the NP-lepton origin can be seen in figures 6.6 and 6.7 left column, which illustrates the decomposition of non-prompt leptons over four different parenthood sources. The three regions appears very similar in the origin of non-prompt lepton. Same figures 6.6 and 6.7 in second, third and forth columns shows the p_T , $|\eta|$, and $|\Delta\phi(\ell_{NP}, jet1)|$ distributions of the non-prompt lepton respectively.

The first row of plots in figures 6.6, 6.7 confirms the similarity in kinematics between the three samples and therefore supports and allows the combination of SR(SS)+CR(SS) into one: CR(NP).

The second row plots (figures 6.6, 6.7, contains actually very similar information) motivates the usage of the CR(NP) as the one kinematic representative sample to be used in the SR NP-event prediction.

Additional plots with separated $t\bar{t}(1\ell)$ and W+jets samples and with ratios of SR/CR(NP) of distributions can be found in appendix D. A set of kinematic variable distributions of CR(NP) events (in data and simulation) are shown in same appendix figure D.5, where reasonable agreement is observed.

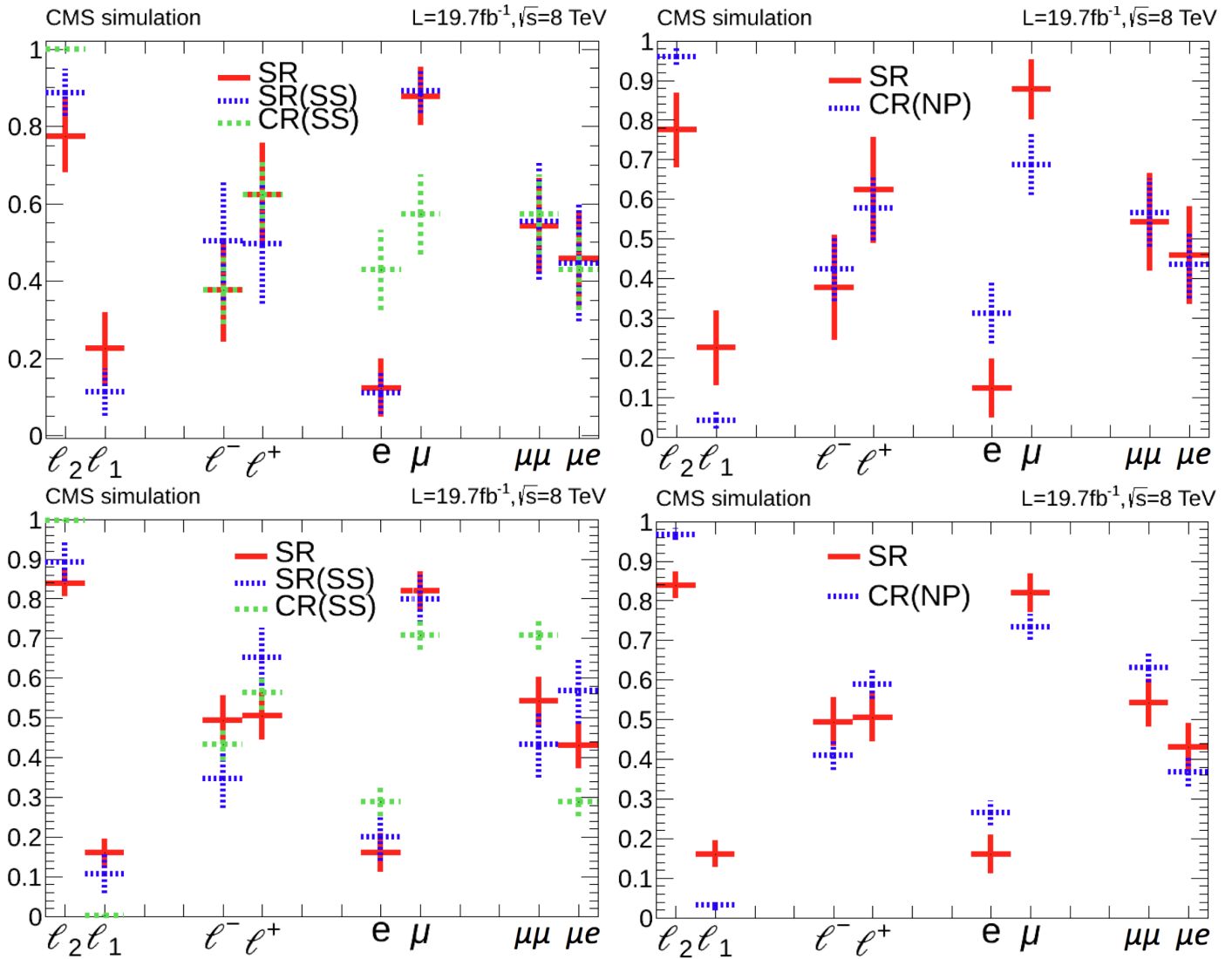


Figure 6.5: Decomposition of non-prompt events in cases where [a] second(first) lepton is the non-prompt, [b] negative(positive) lepton is the non-prompt, [c] non-prompt is an electron(muon) and [d] the non-prompt lepton is in a $\mu\mu(e\mu)$ event. Each pair of bin values' is normalized to 1. Comparison between SR, SR(SS), CR(SS) on the left, and comparison between SR, CR(NP) on the right. Standard SR-selection on top, looser selection on the bottom for a higher statistics ($\times 7$) cross check. The looser selection differs to the SR b removing the impact parameter and relative isolation cuts, and relaxing absolute isolation cut at 10 GeV.

The prediction is preformed by taking the data events from the combined CR(NP), subtracting the non $t\bar{t}(1\ell)$ or non W+jets events in simulation (prompt background); and then, multiplying with the ratio (transfer factor) of $t\bar{t}(1\ell)$ and W+jets events in SR over the those appear in CR(NP) region. The explicit prediction formula for $t\bar{t}(1\ell)$ and W+jets events is:

$$PRED_{SR}^{t\bar{t}(1\ell),W+jets} = \left(DATA_{CR(NP)} - MC_{CR(NP)}^{non[t\bar{t}(1\ell),W+jets]} \right) \left(\frac{MC_{SR}^{t\bar{t}(1\ell),W+jets}}{MC_{CR(NP)}^{t\bar{t}(1\ell),W+jets}} \right) \quad (6.2)$$

where (as before) DATA, MC, represent the number of events in data and simulation respectively, and PRED is the predicted yield in the signal region. Upper indexes stands for the background samples

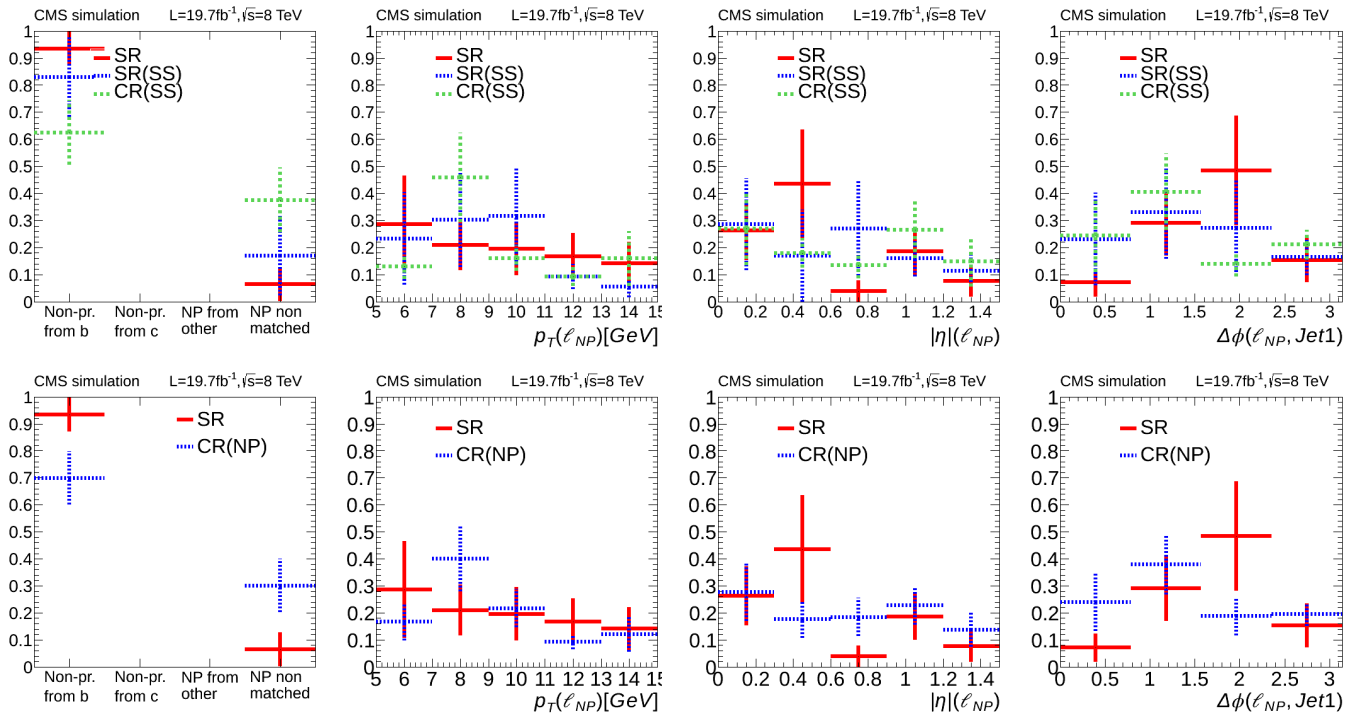


Figure 6.6: Top row: comparison between the SR, SR(SS) and CR(SS) non-prompt lepton parenthood and kinematics. Bottom row: comparison between the SR, and CR(NP) non-prompt lepton parenthood and kinematics. First column: the available examined origins which are considered for non-prompt lepton, bin1: from b to c quark transition, bin2: form c to s, bin3: from other quark, bin4: non-matched to object. Rest three columns the p_T , $|\eta|$ and $|\Delta\phi(\ell, jet1)|$ distributions of the non-prompt leptons respectively. Distribution stands for SR selection, figure 6.7 shows the same in a looser selection providing conclusive statics.

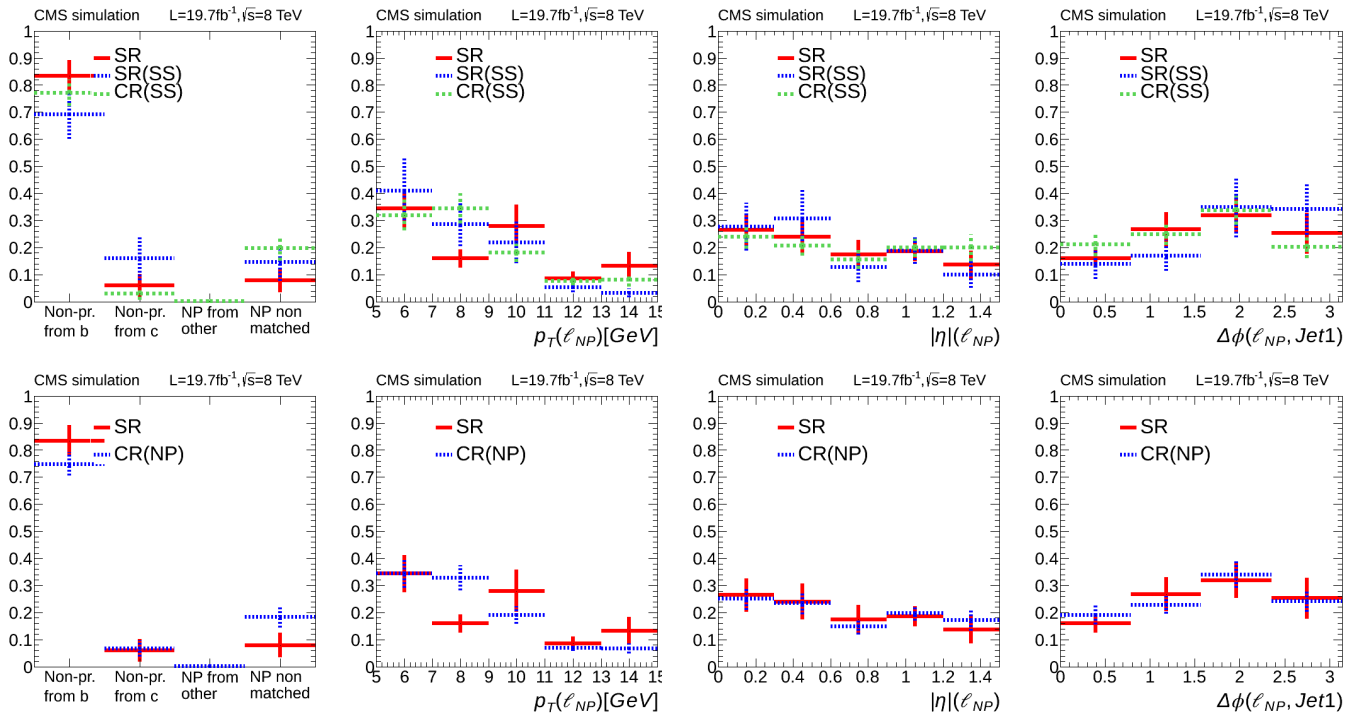


Figure 6.7: Same as in figure 6.6 distributions but for a looser than the SR selection, i.e. removing the impact parameter and Iso_{rel} cuts, and relaxing absolute isolation at 10 GeV ($\times 7$ higher statistics).

whereas the lower indexes characterise the region of each yield. The background components which are subtracted from data are $\sim 20\%$, mainly WZ events (under the collective legend VV) and $t\bar{t}(2\ell)$ which one of the prompt leptons has been missed.

6.3 Prediction of the DY+jets background

The DY+jets background yielded in SR is very small, less than 0.5 events, 6% over total (according to simulation) as listed in table 5.5, and shown in figure 5.12.

The selected events are: $Z \rightarrow \tau^+\tau^- \rightarrow \ell^+\ell^-\nu_\tau\bar{\nu}_\tau\nu_\ell\bar{\nu}_\ell$, as this leads to soft lepton and missing transverse momentum. These are the events where the \cancel{E}_T is laid aside the two soft lepton (smallest) angle $|\Delta\phi(\vec{p}_{T(\ell_1)}, \vec{p}_{T(\ell_2)})|$ (details are shown in appendix C.4), or the invariant di-tau reconstructed mass arise higher than the threshold of 160 GeV.

The prediction method for the Z+jets events is performed in two steps and uses two different control regions.

- step-1: We apply an event-per-event reweigh of each event MC-yield based on data, correcting a potential miss-modeling of hadronic recoil resolution.
- step-2: We measure in the control region the effect of potential miss-modeling of the soft lepton spectra due to miss-modeling of the tau decays and correct for it.

For these two correction steps we define two control samples, referred as CR(Z) and ‘‘SR-inv’’ for step-1 and step-2 respectively. Both are highly pure in Z+jets events.

6.3.1 Hadronic recoil correction with CR(Z)

The CR(Z) is used for the hadronic recoil correction. For this, we select the $Z \rightarrow \mu\mu$ events with $p_T(Z) > 200$ GeV, by requiring $|\vec{p}_T(\mu_1) + \vec{p}_T(\mu_2)| > 200$ GeV in accordance with the SR corresponding $\cancel{E}_T > 200$ GeV. Consequently we ask for $|\vec{p}_T(\mu_1) + \vec{p}_T(\mu_2)|/H_T > 2/3$. This way we preserve the Z boson properties same as in SR. Isolation changes and impact parameters relaxed to the POG officially proposed selection. The exact full set of cuts are explicitly presented in table 6.1 as well data and MC events yields. The obtained sample CR(Z) is consisted by 99.5% of Z+jets events (according to simulation). The $p_T(Z)$, $p_T(Z)/H_T$, $M_{\mu\mu}$ and $M_{\tau\tau}$ distribution of CR(Z) events are presented in figure 6.8.

The $\sim 20\%$ MC-overestimation is a well known fact and is due to missing higher order corrections in simulation.

We analyze the hadronic recoil: $[\cancel{E}_T + \vec{p}_T(\mu_1) + \vec{p}_T(\mu_2)]$ of each CR(Z) event in longitudinal and transverse components with respect to $\vec{p}_T(\mu\mu) = \vec{p}_T(Z)$ direction. (This is the same with the \cancel{E}_T correction procedure shown in top of figure 3.34). Then, we calculate the difference of longitudinal component and the $|\vec{p}_T(Z)|$, named in following: U_{\parallel} . The transverse component is noted as U_{\perp} . (Assuming same behavior for negative and positive angular deviations we use the $|U_{\perp}|$.) The 2D-distributions of U_{\parallel} , $|U_{\perp}|$ versus $|p_T(Z)|$ are presented in figure 6.9. On the first, second, row the U_{\parallel} , $|U_{\perp}|$ respectively. Columns: first, second, third: the MC in generation level, the MC in reconstruction level, the data respectively. The 1-D (profile) distributions using MC_{reco} and data superimposed are presented in figure 6.10. The U_{\parallel} and $|U_{\perp}|$ are in first and second rows respectively.

We observe a modest miss-modeling of the U_{\parallel} and $|U_{\perp}|$ distributions. As ‘‘step-1’’ correction we heal this hadronic recoil miss-modeling together with the 20% cross-section divergence by:

- forming the data/MC ratios in 3D-variable binning over: $p_T(Z), U_{\parallel}, |U_{\perp}|$,
- reweighing each SR event yield by multiplying with its corresponding 3D-ratio.

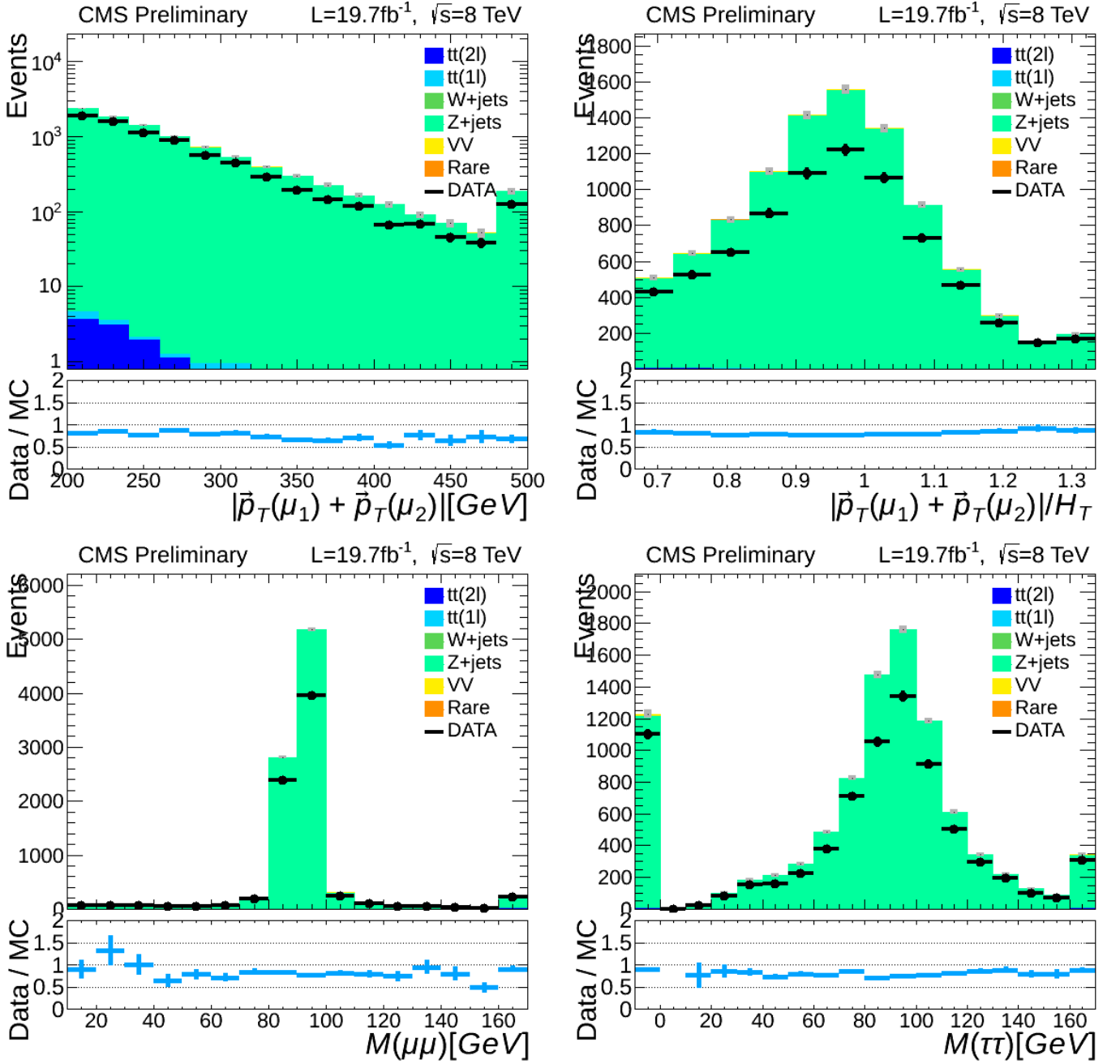


Figure 6.8: On top: the two main variables distributions which their cuts defines the CR(Z). Bottom: the di-muon invariant mass $M_{\mu\mu}$ distribution (left) and the di-tau invariant mass $M_{\tau\tau}$ distribution (right). All histograms stands for the CR(Z) control region selection.

Since for SR we do not have two muons we access the $\vec{p}_T(\mu\mu)$ in generator level as $\vec{p}_T(Z)$. The data/MC ratios are presented in figure 6.11, were into the bulk the reweigh ranges from 0.6 to 0.9 and at the tails of $U_{\parallel}, |U_{\perp}|$ is up to ~ 1.6 . We can express the correction formula for a single event yield as:

$$\left(MC_{SR}^{Z+jets}\right)_{recoil-corr} = MC_{SR}^{Z+jets} \left(\frac{DATA_{CR(Z)}}{MC_{CR(Z)}}\right)_{p_T(Z), U_{\parallel}, |U_{\perp}|} \quad (6.3)$$

where on the left is a single SR event corrected yield. The indexes in ratio stands for the 3D-binning. Upper indexes stands for the background sample, and the lower for the region of the events.

Using this correction formula (equation 6.3) we can also correct the CR(Z) events and compare data over MC-corrected. Figures D.6 and D.7 in appendix D.3 shows figures' 6.8 and 6.10 distributions with the hadronic recoil corrected according to equation 6.3, where by construction are in agreement. The Z+jets raw MC yields in SR-inv are decreased by $\sim 15\%$ after this step-1 correction.

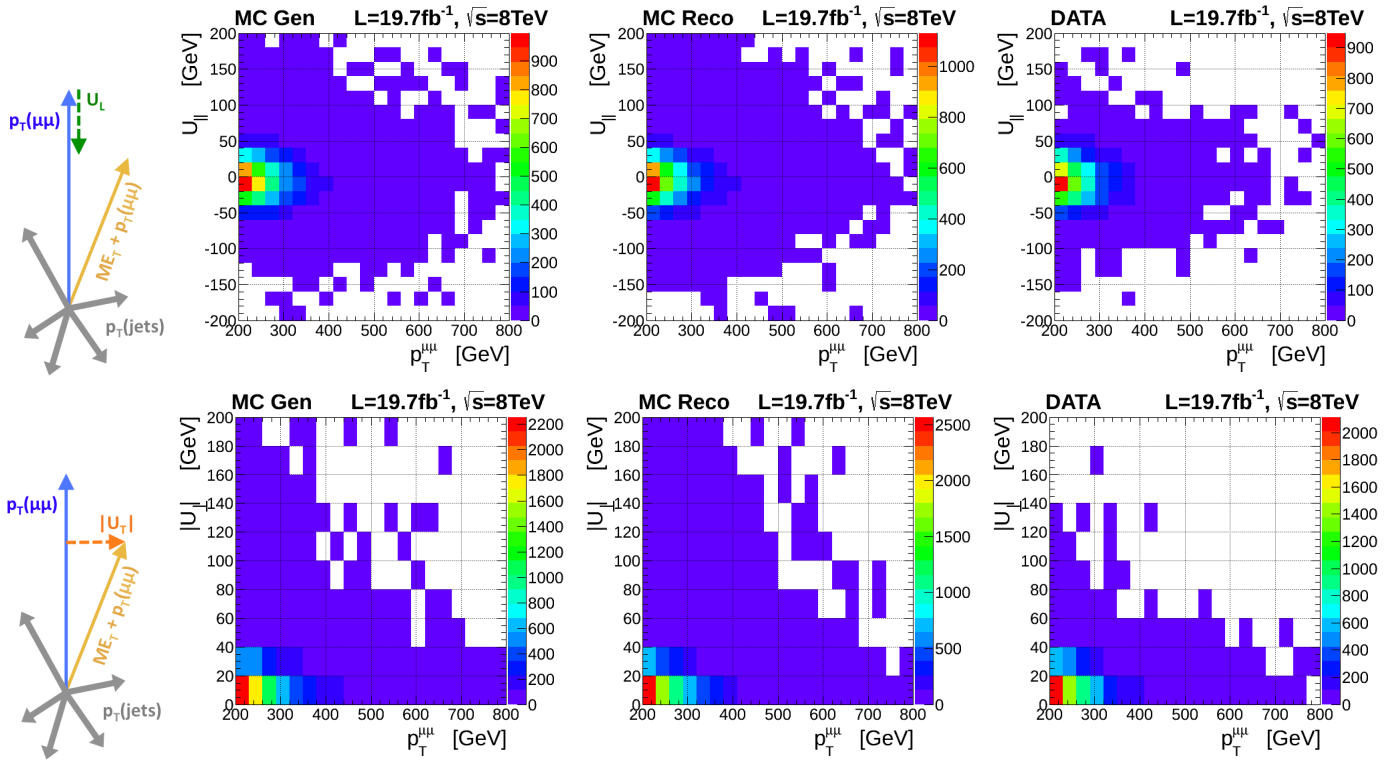


Figure 6.9: Top row: the MC_{gen} (left), MC_{reco} (middle) and data (right) distributions of the longitudinal component U_{\parallel} of the hadronic recoil resolution (projected to $\vec{p}_T(Z)$) versus the $|p_T(Z)|$. Bottom: the MC_{gen} (left), MC_{reco} (middle) and data distributions (right) of the difference of transverse hadronic recoil component and the $\vec{p}_T(Z)$, ($|U_{\perp}|$) versus the $|p_T(Z)|$ (for CR(Z) events). All distributions are for CR(Z) selection.

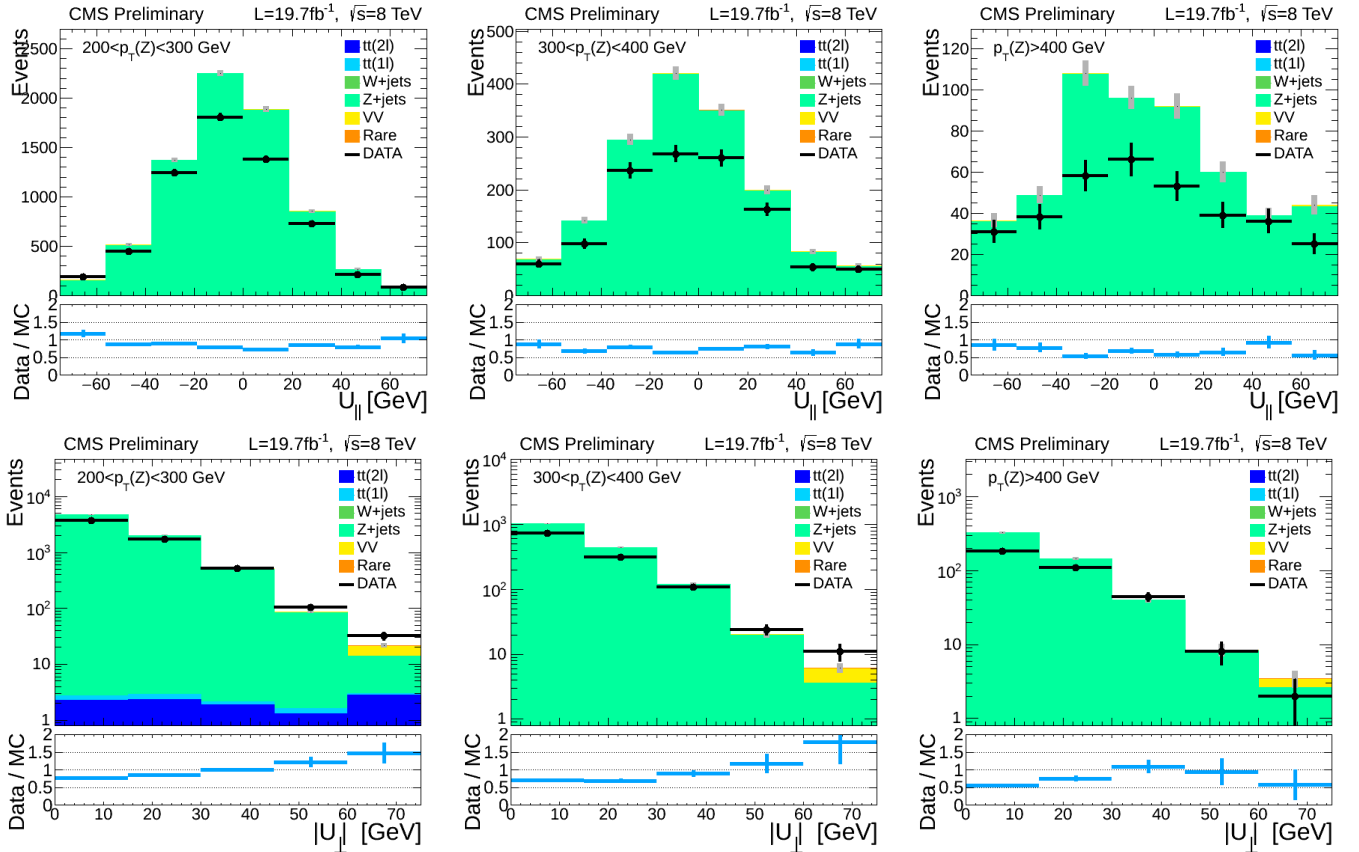


Figure 6.10: Top row: data and MC(reco) distributions of the $|U_{\perp}|$. Bottom row: data and MC(reco) distributions of the U_{\parallel} . All plots are in CR(Z) events. From left to right the bins: $200 < p_T(Z) < 300$ GeV, $300 < p_T(Z) < 400$ GeV, $p_T(Z) > 400$ GeV. All distributions are for CR(Z) selection.

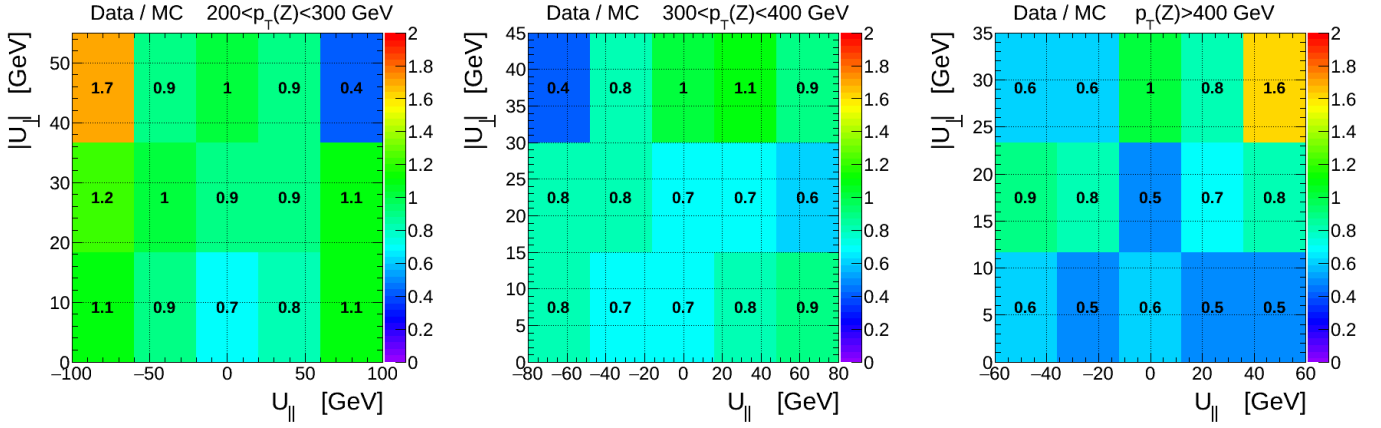


Figure 6.11: The data over MC(reco) ratios of the CR(Z) events, as distributed over the: $p_T(Z), U_{\parallel}, |U_{\perp}|$ variables. From left to right bins: $200 < p_T(Z) < 300$ GeV, $300 < p_T(Z) < 400$ GeV, $p_T(Z) > 400$ GeV. These are the values used for the event-per-event first-step correction.

6.3.2 Soft lepton correction with “SR-inv”

In step-2 we define an additional control region with two soft OS leptons. The most natural choice is to use the exact SR selection with inverted $M_{\tau\tau}$ cut, i.e. we select the events with: $0 < M_{\tau\tau} < 160$ GeV. This region is named “SR-inv”. Table 6.1 shows the cuts and the yields of the region. The Z+jets yields in parenthesis stands for the hadronic-recoil-corrected (step-1 correction) events yield. This region allows to correct for a potential miss-modeled in isolation, in impact parameters, (where we cut tighter in SR than in CR(Z)), as well prevents SR from a tau-decay potential miss-modeled. SR-inv is dominated by Z+jets (purity: $\sim 70\%$, shown in figure 6.1), and the rest is mainly non-prompt $\sim 20\%$. The yielded raw MC Z+jets events (and the data) are about $\times 7$ higher in SR-inv than these in SR (so, sufficiently larger to be used in prediction).

We measure the data in SR-inv, then we subtract predicted values of all rest $\sim 30\%$ non Z+jets processes, and we transfer the yields to SR by multiply with the ratio of (hadronic-recoil-corrected) Z+jets yields in SR over SR-inv. The explicit prediction formula can be expressed as:

$$PRED_{SR}^{Z+jets} = \left(DATA_{SR-inv} - PRED_{SR-inv}^{non-Z+jets} \right) \left(\frac{MC_{SR}^{Z+jets}}{MC_{SR-inv}^{Z+jets}} \right)_{recoil-corr.} \quad (6.4)$$

where “DATA”, the “MC” and the “PRED” represents total events yields, upper indexes stands for the background sample, and the lower for the region.

figure D.8 in appendix D.3 shows the distribution of $p_T(\ell_1), M_{\ell\ell}, M_{\tau\tau}$ of SR-inv region. Despite the poor statistics in SR-inv, the prediction is precise enough since we extrapolate from a region with 5 (data) events in one with less than 0.5 events expected according to MC.

6.4 Prediction of di-boson background.

The dominant di-boson (VV) contribution in the SR comes form WW ($\sim 90\%$ over the VV), which in principle has two prompt leptons and \cancel{E}_T .

To define a control region for this background we do the hadronic selection as for the SR and the same lepton selection as for CR($t\bar{t}2\ell$), i.e. $p_T(\ell_1) > 25$ GeV, $p_T(\ell_2) > 15$ GeV and the replacement $\cancel{E}_T \rightarrow L_T$. As mentioned in the section 6.1 ($t\bar{t}(2\ell)$ prediction), after such a selection we have a mixed sample of $t\bar{t}(2\ell)$ and VV events. For $t\bar{t}(2\ell)$ prediction we changed to the $N_{b(CVSM)} = 1$ events to suppress the VV, whereas in VV prediction we keep $N_{b(CVSM)} = 0$.

We introduce further cuts to enhance the VV purity over the dileptonic top. Inspired by di-boson analysis (measurements) which were using zero-jet multiplicity events (triggered by photon) we demand low jet multiplicity: $N_j \leq 2$. The dileptonic top can be even harder suppressed by using the b-tagged jet

multiplicity at the loose selection point: $N_{b(CSVL)} = 0$, and by requiring $|\Delta\phi(\ell_1, jet1)| > 1$. After these cuts we apply also the $M_{\ell\ell} > 50$ GeV to suppress DY+jets contribution. These variable distributions are presented (for the selection without these four cuts) in figure 6.12.

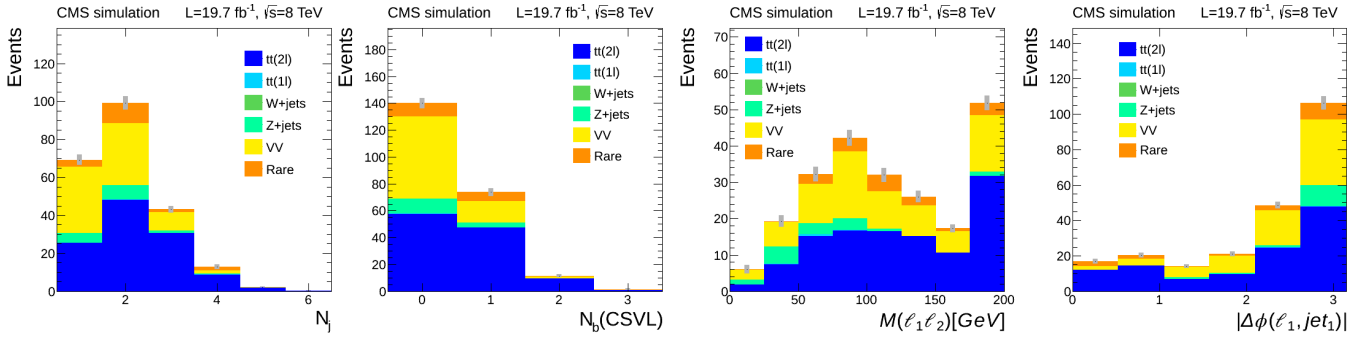


Figure 6.12: The N_j , $N_{b(CSVL)}$, $M_{\ell\ell}$ and $|\Delta\phi(\ell_1, jet1)|$ distributions for events in a region with same leptonic cuts as CR($t\bar{t}2\ell$) and hadronic as SR. The additional selection cuts: $N_j \leq 2$, $N_b(CVSL) = 0$, $|\Delta\phi(\ell_1, jet1)| > 1$, $M_{\ell\ell} > 50$ define the CR(VV).

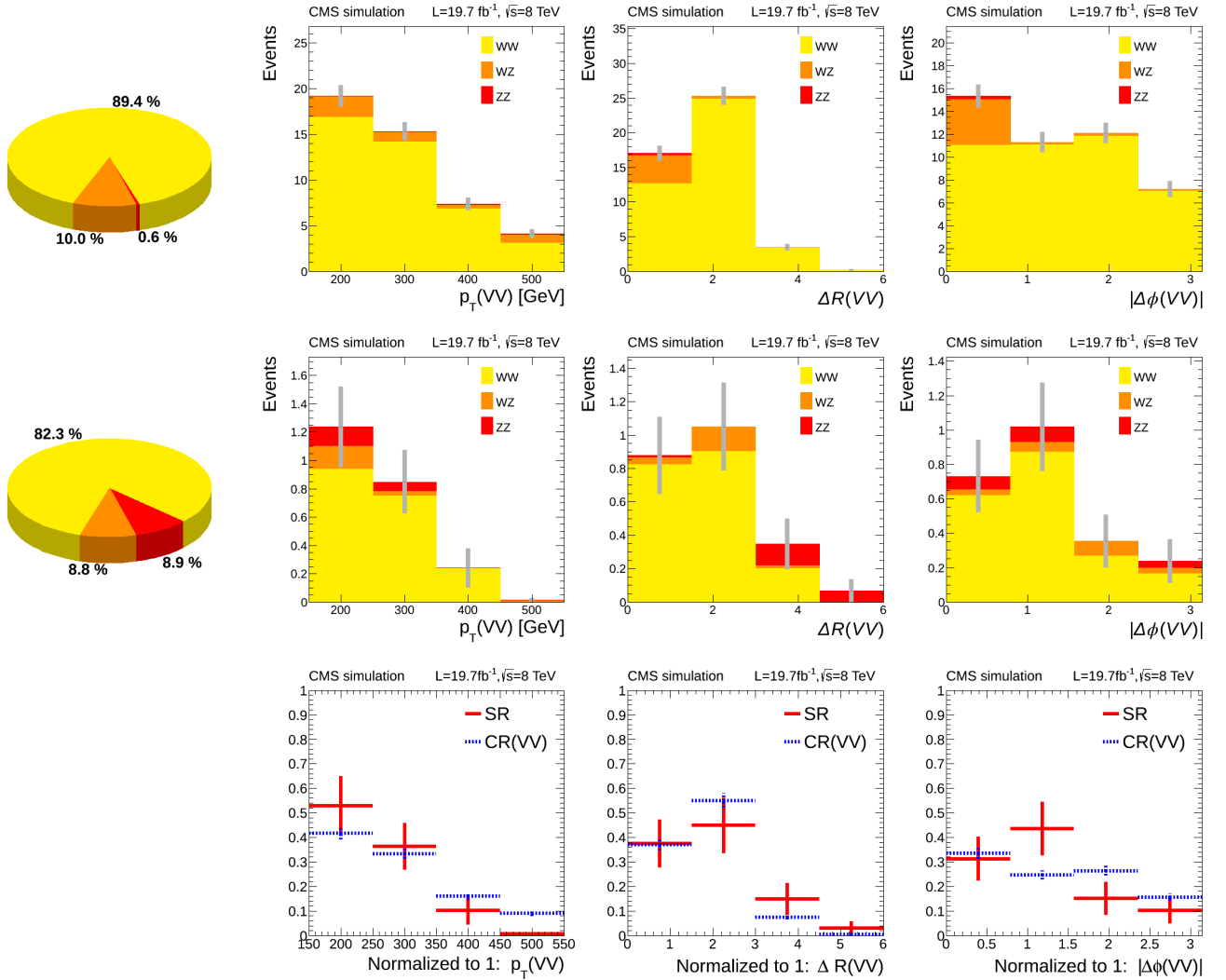


Figure 6.13: The $p_T(VV)$, $\Delta R(V,V)$ and $|\Delta\phi(V,V)|$ distributions for only VV events decomposed to WW, WZ, ZZ. Top row the CR(VV), middle the SR (and on the bottom both normalised superimposed).

The full selection details are summarized in table 6.1 and we refer to this selection as CR(VV). The

VV purity of CR(VV) is $\sim 50\%$ and the rest is mainly ($\sim 30\%$) $t\bar{t}(2\ell)$. The explicit event yields in data and MC are presented at the bottom of the same table.

The distributions of $p_T(\text{VV})$, $\Delta R(\text{V,V})$ and $|\Delta\phi(\text{V,V})|$ of the VV pair in SR and in CR(VV) are shown and compared in Figures 6.13. The relative abundances of WW, WZ, ZZ ($Z\gamma^*$ merged to ZZ) are very similar in two regions. CR(VV) has about $\times 20$ the SR yields (high statistics). We observe a rough similarity of the vector boson kinematics between the control samples and the SR, which supports its usage for prediction.

The prediction methods for the VV yield in the SR is very similar to the procedure followed in $t\bar{t}(2\ell)$ and non-prompt predictions. We measure the data yielded in CR(VV); since the rest background is 50% we subtract its predicted yield value for each of the processes. Then, we transfer this yield to the SR by multiplying by an MC-formed ratio of VV events in SR over CR(VV). For this method the exact prediction formula is:

$$PRED_{SR}^{VV} = \left(DATA_{CR(VV)} - PRED_{CR(VV)}^{t\bar{t},Z,W} - MC_{CR(VV)}^{Rare} \right) \left(\frac{MC_{SR}^{VV}}{MC_{CR(VV)}^{VV}} \right) \quad (6.5)$$

where DATA, MC, and PRED are the number of events in data, in simulation and the predicted yields respectively and indexes stand for region (lower) and SM-process (upper).

6.5 QCD background test

Apart from requiring high \cancel{E}_T and two leptons, we also apply the $\cancel{E}_T / H_T > 2/3$ in standard SR selection to reject any residual QCD. \cancel{E}_T / H_T is a known QCD “killer” and an integral part of e.g. the QCD save α_T variable in relevant analysis. QCD background from miss-measurements is expected to be enhanced -if exists- at lower \cancel{E}_T / H_T values.

We thus form such a control region, designed to potentially accommodate the maximum QCD contribution in our SR. Thus we apply the following cuts:

- invert the \cancel{E}_T / H_T cut selecting events with: $\cancel{E}_T / H_T < 2/3$,
- select events in the three dilepton channels i.e. including also the [ee] one,
- select events in both OS and SS events, slices QCD is expected (in principle) charge symmetric,
- relax the impact parameters from 0.01 cm to $|d_z|, |d_{xy}| < 0.05$ cm,
- relax the subleading lepton cut from 15 to: $p_T(\ell_2) < 25$ GeV in order to enlarge statistics,
- extend to N_b : any, maintaining leading-b-jet veto, and check the per bin agreement.

However, since this selection (named CR(QCD)) diverges from the one in SR, we plot the data vs simulated distributions over these variables to check the agreement also in individual bins. figure 6.14 shows the distribution of this CR(QCD)-selection.

All results-distributions are fully compatible with no QCD contribution even in this CR(QCD) selection. In particular the $N_b=0$ and $\cancel{E}_T / H_T < 0.44$ bins are in good agreement. Similar conclusions can be derived if (instead of simulated) predicted yields where used.

6.6 Prediction methods’ summary and predicted SR yields

The semi-data-driven prediction recipe is in principle the same for the four different backgrounds categories. It can be summarized in the following steps:

- define a CR highly pure in each SM background sub-process events,
- ensure similarity in kinematics (at the maximum possible extend) between CR and SR,

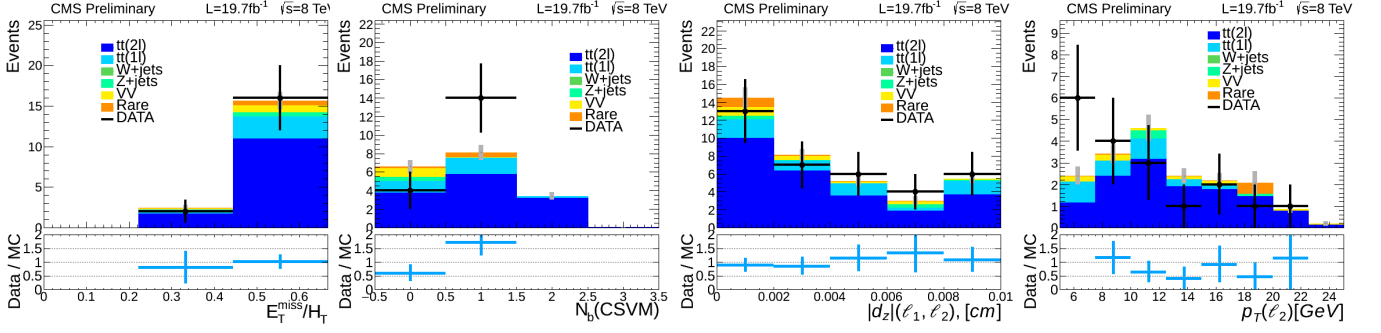


Figure 6.14: Kinematic variable distributions of the CR(QCD) selection to test potential QCD contribution. Simulated background and data.

- ensure that CR has sufficiently higher events yields with respect to SR and that is signal free,
- measure data yielded in each background CR,
- subtract the rest background (those which contaminate CR purity) either using simulated or (if purity $\lesssim 70\%$) predicted yields,
- multiply the above measurement with the MC-made yields ratio of events in SR over CR.

Implementing all prediction methods we derive the following predicted yields as listed in table 6.3.

Table 6.3: Predicted and data yields for SR.

Sample: / Bins:	$p_T(\ell_1) : [5, 15] GeV$	$p_T(\ell_1) : [15, 25] GeV$	Inclusive
$t\bar{t}(2\ell)$	0.75 ± 0.19	2.08 ± 0.37	2.84 ± 0.42
$t\bar{t}(1\ell), W+jets$	0.60 ± 0.33	1.32 ± 0.69	1.92 ± 0.76
DY+jets	0 ± 0	0.48 ± 0.45	0.48 ± 0.45
VV	0.74 ± 0.27	1.61 ± 0.48	2.35 ± 0.55
Rare	0.03 ± 0.01	0.08 ± 0.04	0.11 ± 0.04
Total SM Prediction	2.12 ± 0.47	5.6 ± 1.0	7.7 ± 1.1
SUSY(250,230)	10.0 ± 1.5	3.41 ± 0.90	13.5 ± 1.8
SUSY(300,250)	3.98 ± 0.61	3.83 ± 0.58	7.80 ± 0.84
SUSY(200,180)	6.2 ± 1.5	1.90 ± 0.88	8.1 ± 1.7

Small differences with respect to the raw MC yields are observed. In particular, (comparing tables 6.3 and 5.5) for the two bins inclusively we have -16% for dileptonic top, $+9\%$ for NP-events, $+6\%$ for VV events and 0% for Z+jets. The total predicted yields decreased at -4% , and for the most sensitive bin (low p_T s) by -2% . However the statistical uncertainty is increased about $+33\%$ for both SR bins.

Chapter 7

Validation of the Background Predictions

The CRs used for each prediction methods were designed under the concept of providing the most consistent kinematic behavior with respect to SR events, and thus to provide robust predictions in SR. However, even if CR are conceptual properly chosen, we need to verify (if possible) that predictions works in data, both individually and inclusively validating their usage.

Regions which are not used as control samples (for the prediction method measurements) are used for validation of these predictions. We perform an exclusive validation of the $t\bar{t}(2\ell)$ background prediction method in two independent validation regions, a combined one for the $t\bar{t}(2\ell)$ and VV backgrounds, and a validations for all methods inclusively. For each of these four independent validation we define a dedicated validation region (VR).

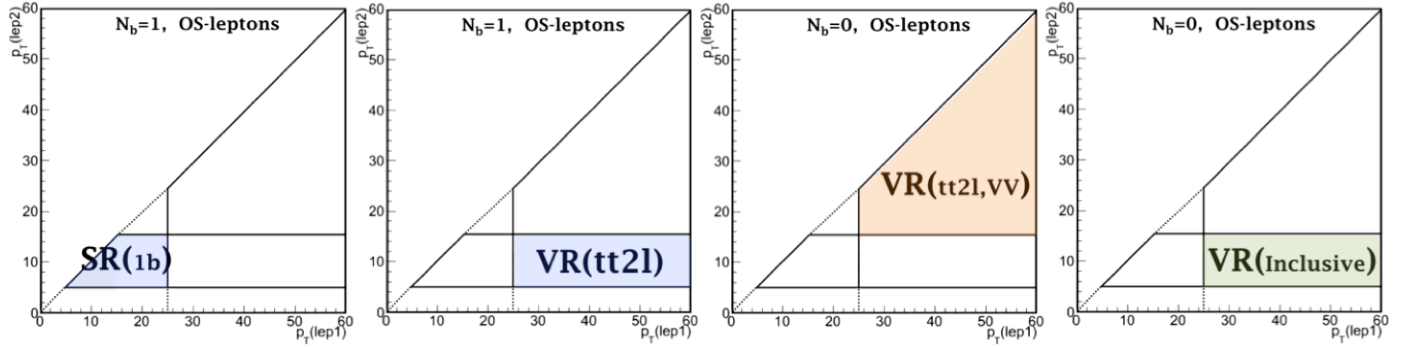


Figure 7.1: The four validation regions in a $p_T(\ell_1) - p_T(\ell_2)$ plane illustration. Their full cut selection is shown in table 7.1.

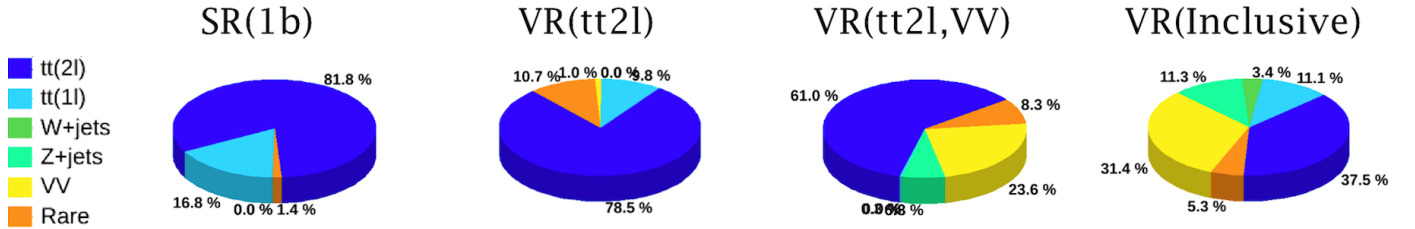


Figure 7.2: The four validation regions % background abundances.

7.1 Validation test for the dileptonic top prediction method

In the $N_b=1$ event-slice (with non b-tagged jet1) we invert the $p_T(\ell_2)$ cut of $\text{CR}(t\bar{t}2\ell)$ as it is required in SR: $5 < p_T(\ell_2) < 15$ GeV. The obtained region is further divided into two:

Table 7.1: Top: selection cuts for each validation region used. Only the changes with respect to the SR are shown. For VR($t\bar{t}2\ell, VV$) we demand at least one of the “{}” conditions being true i.e. “or” combination. Isolation values in “[]” stands for soft leptons with: $15 < p_T < 25$ GeV. Middle: each region simulated yields (SM background and signal contamination). Bottom: predicted SM yields and observed data.

Validation Region:	SR(1b)	VR($t\bar{t}(2\ell)$)	VR($t\bar{t}2\ell, VV$)	VR(Inclusive)
Cut variables	cut values/thresholds			
N_ℓ $Q(\ell_1)Q(\ell_2)$ N_μ 1st lepton flavor and ID $p_T(\ell_1)$ $p_T(\ell_2)$ $ \eta (\ell_{1,2})$ $d_z(\ell_{1,2}) \& d_{xy}(\ell_{1,2})$ $Rel.Iso(\ell_{1,2})$ $Ab.Iso(\ell_{1,2})$		μ (tight ID) > 25 GeV	μ (tight ID) > 25 GeV > 15 GeV	μ (tight ID) > 25 GeV
$p_T(jet1)$ $p_T(jet3)$ $ \eta (jet1)$ N_j $N_{b(CSVM)}$ $N_{b(CSVL)}$ $ \Delta\phi(\ell_1, jet1) $	= 1 & jet1: non b-tag	= 1 & jet1: non b-tag	{ ≥ 3 }	{ ≥ 1 }
\cancel{E}_T $\cancel{E}_T + p_T(\ell_1) \equiv L_T$ $ \vec{p}_T(\ell_1) + \vec{p}_T(\ell_2) $ \cancel{E}_T / H_T L_T / H_T $ \vec{p}_T(\ell_1) + \vec{p}_T(\ell_2) / H_T$ $M_{\ell\ell}$ $M_{\tau\tau}$		> 125 GeV > 225 GeV none > 2/3	> 125 GeV > 225 GeV none > 2/3	> 125 GeV > 225 GeV none > 2/3
Trigger used		Single_Mu_*	Single_Mu_*	Single_Mu_*
Samples	Simulated (raw MC) background yields and signal contamination			
$t\bar{t}(2\ell)$ $t\bar{t}(1\ell)$ W+jets DY+jets VV Rare	2.95±0.37 0.61±0.22 0 0 0 0.05±0.03	21.3±1.0 2.66±0.45 0 0 0.27±0.13 2.9±1.1	84.7±2.0 0.42±0.17 0 9.5±2.1 32.8±1.5 11.5±2.2	18.9±0.9 5.6±0.7 1.7±0.9 5.7±1.3 15.8±1.0 2.7±1.1
Total MC background	3.60±0.43	27.1±1.6	139.0±4.0	50.2±2.5
SUSY(250,230) SUSY(300,250) SUSY(200,180)	0.29±0.21 1.31±0.31 0.14±0.14	0 0.28±0.15 0	0.39±0.28 1.56±0.36 0.37±0.37	0.03±0.03 1.71±0.38 1.1±0.6
Samples	SM predicted background yields			
$t\bar{t}(2\ell)$ Non-Prompt: $t\bar{t}(1\ell), W$ +jets DY+jets VV Rare	2.48±0.38 0.68±0.32 0 0 0.05±0.03	17.9±2.2 3.0±1.3 0 0.27±0.14 2.9±1.1	71±8 0.47±0.28 6.8±1.9 32±7 11.5±2.2	15.8±2.0 8.2±3.6 7.1±2.5 15.5±3.6 2.7±1.1
Total predicted background	3.2±0.5	24.0±2.8	122±11	49±6
Data	4	31	134	39
Significance σ_{stat}	0.4	1.2	0.7	-1.1

- one with $p_T(\ell_1) < 25$ GeV, which has exactly the same as SR cuts except the $N_b=1$, and into
- one with the $p_T(\ell_1) > 25$ GeV where, as for the CR($t\bar{t}2\ell$), the L_T and L_T/H_T replaces \cancel{E}_T and \cancel{E}_T/H_T cuts respectively.

We name these two validation regions as: SR(1b) and VR($t\bar{t}2\ell$) respectively. Figure 7.1 illustrates both VRs in first and second diagrams, whereas figure 7.2 shows the purities. The explicit list of cuts of these VRs are presented in table 7.1, where only the differences with respect to SR selection (left column) are listed.

According to simulation, these two regions are dominated by $t\bar{t}(2\ell)$ events (as same tables in the middle shows and also figure 7.2 illustrates in pie-charts). Thus is mainly tested the $t\bar{t}(2\ell)$ prediction method.

We use (all) our prediction methods to predict each VR yields. The corresponding predicted yields for SR(1b) and VR($t\bar{t}2\ell$) are presented in table 7.1 on the bottom and also observed data are listed. The total predicted yields are in agreement within statistical uncertainties.

7.2 Validation test for all prediction methods

For the $N_{b(CSVM)} = 0$ selection we can use as VR the events which are not selected in the CR(VV). Two region can be formed bellow and above the $p_T(\ell_2) = 15$ GeV (figure 7.1 third and fourth diagrams).

- Events with same as CR(VV) cuts but inverted at least one of the N_j , $N_{b(CSVL)}$, $M_{\ell\ell}$, $|\Delta\phi(\ell_1, jet1)|$ cut requirements. This sample is the complementary of the CR(VV) with respect to the “and” combination of these four variables. The deduced VR is name VR($t\bar{t}2\ell, VV$) due to its main background content (figure 7.2).
- Events with same as SR hadronic-cuts, $p_T(\ell_1) > 25$ GeV, and L_T cut configuration (instead of \cancel{E}_T) forms a VR very similar in background composition and abundances with the SR. We name this VR(Inclusive) and we test all background methods inclusively there.

The explicit cuts, the MC, predicted and data yields of VR($t\bar{t}2\ell, VV$) and VR(Inclusive) are presented in table 7.1. Figure 7.1 illustrates both VRs in third and fourth diagrams, whereas figure 7.2 shows the purities. We perform again prediction using all background prediction methods. We observe once more agreement within statics between data and predictions.

Figure 7.3 present all four implemented validation regions (predicted vs data yields) with the background decomposition left, and with the $\pm 1\sigma$, $\pm 2\sigma$ statistical uncertainties right. We observe over all agreement. The methods can successfully extrapolate the yields form non-soft to soft leptons and also from the single-muon trigger to the triple-combination of trigger used in SR.

7.3 Validation test with only SR-trigger-configuration

The extrapolation of single-muon triggered events which mainly CR uses, to “ \cancel{E}_T -ISR-triggered” SR events is a step which requires additional study and tests.

The straightforward (and obvious) extension of SR to CRs would be an maintenance of a $\cancel{E}_T > 200$ GeV cut in all CRs (i.e. CR($t\bar{t}2\ell$), CR(SS), CR(VV)) without changing to L_T -cut concept, and consequently use of same trigger configuration in both SR and CRs. We name this triple trigger “or” configuration “SR-trigger-configuration”.

The implementation of single-muon triggered events introduced in section 6.1 in order to enlarge the statistics of the corresponding CR($t\bar{t}2\ell$) region. However the low statistics appears as a critical issue only for the CR(NP) and more specifically for CR(SS) sub-region. The CR(NP) has a factor of about $\times 7$ higher yields than those in SR. For that purpose (to select more NP-events in CR(SS)) we introduced the L_T variable and relaxed \cancel{E}_T in such a way which maintains the W-products p_T s. Since the SR-trigger-configuration turn-on curve has the plateau for $\cancel{E}_T > 200$ GeV we needed an other trigger to go lower in \cancel{E}_T , thus we implement the single-muon one.

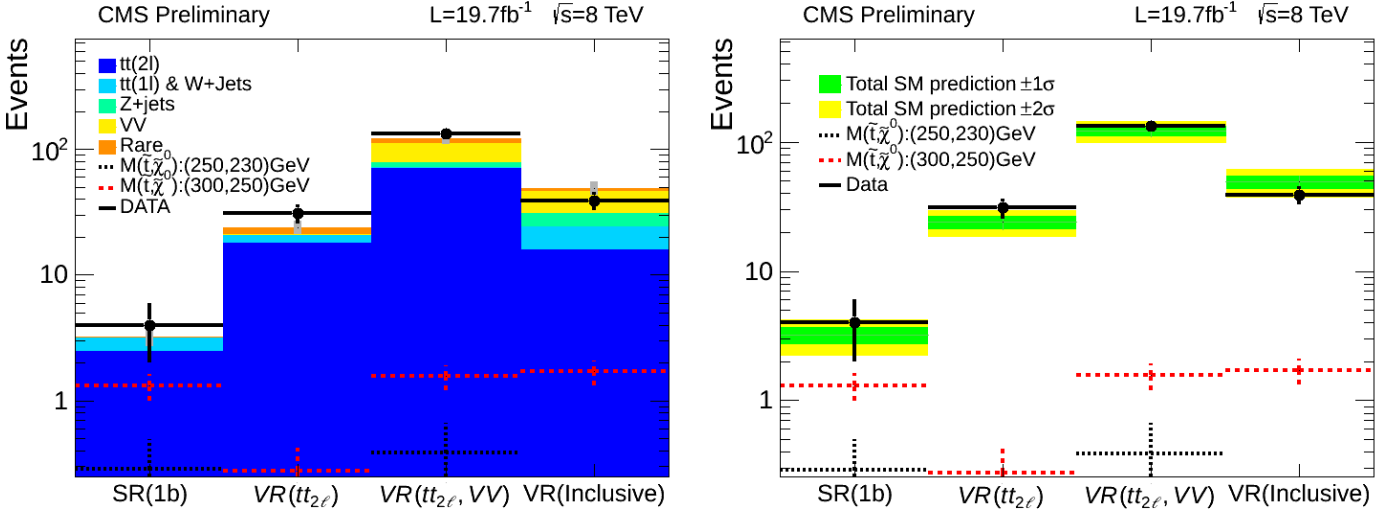


Figure 7.3: The predicted and data event yields in all validation regions with (left) explicit background decomposition and (right) with $\pm 1\sigma, \pm 2\sigma$ statistical uncertainty bands.

However we can perform the full analysis and use every prediction method in the only $\cancel{E}_T > 200$ GeV cut configuration without introducing L_T . This variation of analysis is named: “only SR-trigger-configuration”. The exact CR cuts of this variation as well as the MC and data yields are presented in table 7.2 which is analogous to the table 6.1 (original CRs setup/configuration i.e. with single-muon triggered events). Only the columns CR($t\bar{t}2\ell$), CR(SS), CR(VV) are different and only for the rows: “1st lep.flavor”, \cancel{E}_T , \cancel{E}_T/H_T , L_T , L_T/H_T , “Trigger(s) used”. This way we have a simple (and closer to SR) definition of the CR($t\bar{t}2\ell$), CR(SS), CR(VV). We perform two tests:

- Test 1: the SR predicted yields in “only SR-trigger-configuration” (formed by tables’ 7.2 CRs) are shown in table 7.3. Compared with the original predictions (those formed by single-muon triggered CRs in table 6.3) we can conclude that prediction are very close each other and they agree within statistics. The original one has slightly smaller uncertainties. So the SR prediction is roughly invariant under the change of \cancel{E}_T to L_T and the change from “single-muon triggered CRs” to “only SR-trigger-configuration”.
- Test 2: the VRs’ tests can be repeated in the “only SR-trigger-configuration” of the analysis. We redefine the VRs accordingly (without L_T) as shown in table 7.4, the SR(1b) remains same as no L_T cut is involved in its definition. Raw MC, predictions and data yields are also listed in the same table. The data in VRs are in agreement with the predictions within statistical uncertainties. Figure 7.4 shows the analogous of figure 7.3 illustration in “only SR-trigger-configuration” version, i.e. data versus predicted yields in four VRs.

We can conclude that the single-muon trigger, and the corresponding L_T -cut configuration, leads in same predictions/results for SR, and also leads to correct predictions in VRs triggered with “only SR-trigger-configuration”. These validation tests offers the robustness and reliability to the prediction methods and the two different trigger-configuration strategy.

Table 7.2: “Only SR-trigger-configuration” CR definitions. Top: selection cuts for each CR used for prediction. Only the changes with respect to the SR are shown. Bottom: simulation and data event yields. (Isolation values in “[]” stands for the soft leptons with: $15 < p_T < 25$ GeV).

Control Regions: Sub Regions:	CR($t\bar{t}\ell$)	CR(NP)		CR(VV)	CR(Z)	SR-inv
		SR(SS)	CR(SS)			
Cut variables		cut values/thresholds				
N_ℓ $Q(\ell_1)Q(\ell_2)$ N_μ 1st lep. flavor & ID $p_T(\ell_1)$ $p_T(\ell_2)$ $ \eta (\ell_{1,2})$ $d_z(\ell_{1,2}), d_{xy}(\ell_{1,2})$ $Rel.Iso(\ell_{1,2})$ $Ab.Iso(\ell_{1,2})$	> 25 GeV > 15 GeV	$=+1$	$=+1$ > 25 GeV	> 25 GeV	$= 2$ μ tight ID > 125 GeV > 10 GeV < 2.1 $< .02, < .5$ cm < 0.12 < 0.12 none	
$p_T(jet1)$ $p_T(jet3)$ $ \eta (jet1)$ N_j N_b (CSVM) N_b (CSVL) $ \Delta\phi(\ell_1, jet1) $	$= 1$ & jet1: non b			≤ 2 $= 0$ > 1		
\cancel{E}_T $\cancel{E}_T + p_T(\ell_1) \equiv L_T$ $ \vec{p}_T(\ell_1) + \vec{p}_T(\ell_2) $ \cancel{E}_T / H_T L_T / H_T $ \vec{p}_T(\ell_1) + \vec{p}_T(\ell_2) / H_T$ $M_{\ell\ell}$ $M_{\tau\tau}$				> 50 GeV	none > 200 GeV none $> 2/3$ > 10 GeV none (0,160)GeV	
Trigger(s) used					Single_Mu	
Samples		Simulation and data event yields				
$t\bar{t}(2\ell)$	33.2 ± 1.3	0.09 ± 0.07		10.5 ± 0.7	12.5 ± 0.8	0.15 ± 0.08
$t\bar{t}(1\ell)$	0.14 ± 0.09	2.8 ± 0.5		0.13 ± 0.09	2.19 ± 0.42	0.11 ± 0.11
W+jets	0	3.0 ± 1.2		0.5 ± 0.5	0	0.7 ± 0.7
DY+jets	0	0		0.60 ± 0.43	9464 ± 62	2.8 ± 0.9
VV	1.39 ± 0.32	0.47 ± 0.10		20.5 ± 1.2	33.6 ± 1.4	0.13 ± 0.09
Rare	6.2 ± 1.8	0.7 ± 0.5		3.0 ± 1.3	3.7 ± 0.9	0
Total background	41.0 ± 2.2	7.1 ± 1.4		35.2 ± 2.0	9516 ± 62	3.9 ± 1.1
Data	31	8		27	7610	5

Table 7.3: Predicted and data yields for SR in the “only SR-trigger-configuration”.

Sample: / Bins:	$p_T(\ell_1) : [5, 15] \text{ GeV}$	$p_T(\ell_1) : [15, 25] \text{ GeV}$	Inclusive
$t\bar{t}(2\ell)$	0.63 ± 0.21	1.73 ± 0.50	2.36 ± 0.54
$t\bar{t}(1\ell), W+\text{jets}$	0.62 ± 0.37	1.36 ± 0.79	1.97 ± 0.87
DY+jets	0 ± 0	0.48 ± 0.45	0.48 ± 0.45
VV	0.54 ± 0.26	1.24 ± 0.53	1.78 ± 0.59
Rare	0.03 ± 0.01	0.08 ± 0.04	0.11 ± 0.04
Total SM Prediction	1.82 ± 0.50	4.9 ± 1.2	6.7 ± 1.3

Table 7.4: “Only SR-trigger-configuration” VRs definitions. Top: selection cuts for each VR. Only the changes with respect to the SR are shown. For VR($t\bar{t}2\ell, VV$) we demand at least one of the “{ }” conditions being true. Isolation values in “[]” stands for soft leptons with: $15 < p_T < 25 \text{ GeV}$. Middle: each region simulated yields. Bottom: predicted SM yields and observed data.

Validation Region:	SR(1b)	VR($t\bar{t}(2\ell)$)	VR($t\bar{t}2\ell, VV$)	VR(Inclusive)
Cut variables	cut values/thresholds			
N_ℓ $Q(\ell_1)Q(\ell_2)$ N_μ 1st lepton flavor and ID $p_T(\ell_1)$ $p_T(\ell_2)$ $ \eta (\ell_{1,2})$ $d_z(\ell_{1,2}) \& d_{xy}(\ell_{1,2})$ $Rel.Iso(\ell_{1,2})$ $Ab.Iso(\ell_{1,2})$		$> 25 \text{ GeV}$	$> 25 \text{ GeV}$ $> 15 \text{ GeV}$	$> 25 \text{ GeV}$
		$< 0.12[0.5]$	$< 0.12[0.5]$	$< 0.12[0.5]$
		none [$< 5 \text{ GeV}$]	none [$< 5 \text{ GeV}$]	none [$< 5 \text{ GeV}$]
$p_T(jet1)$ $p_T(jet3)$ $ \eta (jet1)$ N_j N_b (CSVM) N_b (CSVL) $ \Delta\phi(\ell_1, jet1) $	$= 1 \& jet1: \text{non b-tag}$	$= 1 \& jet1: \text{non b-tag}$	$\{\geq 3\}$	$\{\geq 1\}$ $\{< 1\}$
\cancel{E}_T $\cancel{E}_T + p_T(\ell_1) \equiv L_T$ $ \vec{p}_T(\ell_1) + \vec{p}_T(\ell_2) $ \cancel{E}_T / H_T L_T / H_T $ \vec{p}_T(\ell_1) + \vec{p}_T(\ell_2) / H_T$ $M_{\ell\ell}$ $M_{\tau\tau}$			$\{< 50 \text{ GeV}\}$	
Trigger used				
Samples	Simulated (raw MC) background yields and signal contamination			
$t\bar{t}(2\ell)$	2.95 ± 0.37	9.8 ± 0.7	31.7 ± 1.2	12.3 ± 0.8
$t\bar{t}(1\ell)$	0.61 ± 0.22	0.83 ± 0.24	0.18 ± 0.12	2.11 ± 0.41
W+jets	0	0	0	0.5 ± 0.5
DY+jets	0	0	2.4 ± 1.0	0.9 ± 0.5
VV	0	0.19 ± 0.10	18.7 ± 1.2	10.9 ± 0.9
Rare	0.05 ± 0.03	2.1 ± 1.0	5.1 ± 1.5	1.8 ± 0.9
Total MC background	3.60 ± 0.43	12.9 ± 1.3	58.1 ± 2.5	28.5 ± 1.7
Samples	SM predicted background yields			
$t\bar{t}(2\ell)$	2.1 ± 0.5	6.9 ± 1.8	22 ± 6	8.6 ± 2.2
Non-Prompt: $t\bar{t}(1\ell), W+\text{jets}$	0.70 ± 0.35	1.0 ± 0.5	0.21 ± 0.17	3.0 ± 1.6
DY+jets	0	0	2.1 ± 1.1	1.8 ± 1.2
VV	0	0.14 ± 0.09	14±5	8.2 ± 3.2
Rare	0.05 ± 0.03	2.1 ± 1.0	5.1 ± 1.5	1.8 ± 0.9
Total predicted background	2.8 ± 0.6	10.1 ± 2.2	44 ± 8	23.4 ± 4.5
Data	4	5	42	26
σ_{stat}	0.7	-1.3	-0.2	0.4

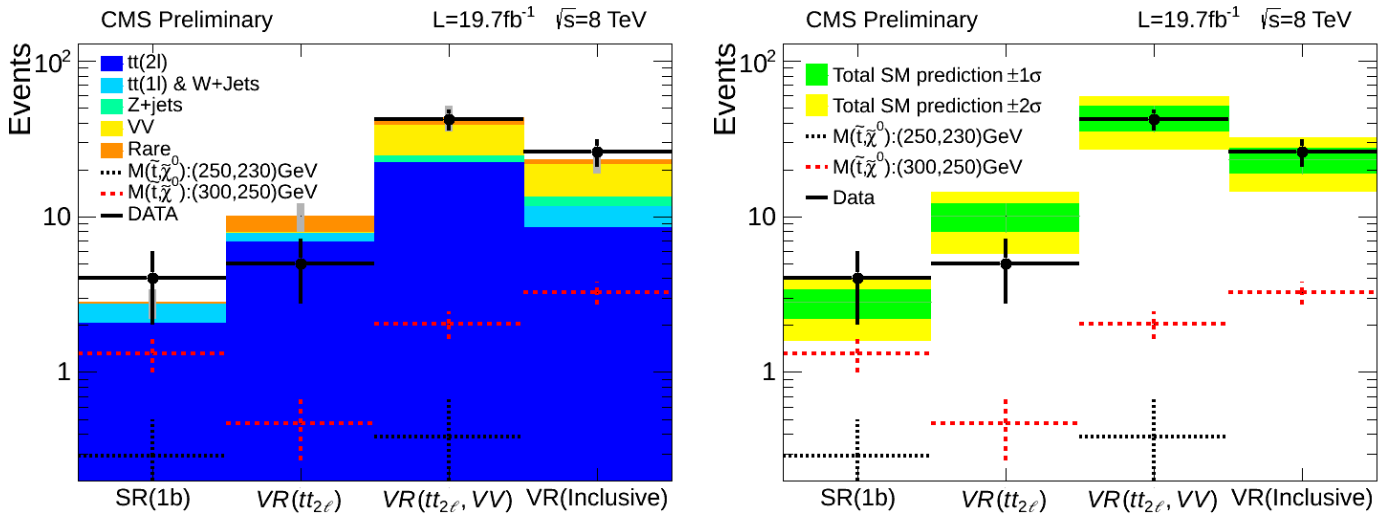


Figure 7.4: SR-trigger-configuration, the predicted and data event yields in all VRs with (left) explicit background decomposition and (right) with $\pm 1\sigma$, $\pm 2\sigma$ statistical uncertainty bands.

Chapter 8

Systematic uncertainties

This chapter describes the systematic uncertainties. As systematic is considered every source of uncertainty which is not induced by statistical fluctuation of data or MC event. All sources are considered uncorrelated and the total uncertainties are accounted as the quadratic sum of the individuals per search bin. In this chapter we present the methods which were used in each uncertainty estimation.

Table 8.1 presents each systematic uncertainty per individual source (rows) and per search bin (columns). More specifically, the % absolute difference of the total predicted yields between the default prediction and the prediction yielded with the variation shown. The simple formula can be expressed as in equations 8.1 or, in cases that the variation of a parameter has two (\pm) “directions” equations 8.2. The U is the % uncertainty and P each predicted value.

$$U_{SR}^{Source} = \frac{1}{P_{SR}^{Default}} |P_{SR}^{Default} - P_{SR}^{Variation}| 100\% \quad (8.1)$$

$$U_{SR}^{\pm Source} = \frac{1}{2P_{SR}^{Default}} \left[|P_{SR}^{Default} - P_{SR}^{(+)\text{Variation}}| + |P_{SR}^{Default} - P_{SR}^{(-)\text{Variation}}| \right] 100\% \quad (8.2)$$

Table 8.1: Uncertainty on SR predicted yield for each individual systematic uncertainty source.

Bins	$p_T(\ell_1):[5,15]$ GeV	$p_T(\ell_1):[15,25]$ GeV	Inclusive
Default SM total predicted yields:	2.12	5.57	7.69
Relative statistical uncertainty ($\delta Pred/Pred$):	21.9 %	18.3 %	14.6 %
Uncertainty Source			
JES ($\pm 1\sigma$):	1.0 %	2.8 %	2.1 %
SF btag c-b quark ($\pm 1\sigma$):	0.9 %	0.9 %	0.7 %
SF btag light partons ($\pm 1\sigma$):	1.3 %	1.1 %	1.1 %
electron efficiency (with/without SFs):	1.3 %	1.1 %	1.1 %
Muon efficiency ($\pm 5\%$ for soft μ):	6.0 %	4.5 %	4.9 %
$t\bar{t}(2\ell)$ spin correlation ($\pm 20\%$):	4.1%	3.5%	3.6 %
$t\bar{t}(2\ell)$ W polarization ($\pm 10\%$):	2.5 %	2.6 %	2.6 %
$t\bar{t} p_T$ reweigh $t\bar{t}(1\ell, 2\ell, W, Z, H)$ (with/without):	1.7 %	3.3 %	2.9 %
Non-prompt W+jets/ $t\bar{t}(1\ell)$ ratio ($\pm 20\%$):	6.1 %	2.7 %	3.6 %
Non-prompt b-originated NP ($\pm 50\%$):	4.9 %	3.5 %	3.9 %
Non-prompt c-originated NP ($\pm 100\%$):	0.4 %	0.4 %	0.2 %
Non-prompt $p_T(\ell_{NP})$ ratio SR/CR(NP) ($\pm 100\%$):	2.3 %	1.7 %	1.9 %
Non-prompt $\eta(\ell_{NP})$ ratio SR/CR(NP) ($\pm 100\%$):	1.6 %	1.9 %	1.8 %
Non-prompt CR(NP) VV-yield ($\pm 50\%$):	5.7%	2.4%	3.3%
VV W&Z polarization ($\pm 10\%$):	2.5%	1.9 %	1.4 %
VV ($p_T^+/[p_T^+ + p_T^-]$) ($\pm 50\%$):	2.5%	1.7 %	0.7 %
VV $M(\ell\ell):[1,12]$ GeV (“private” samples, $\pm 100\%$):	7.2%	0.7 %	2.5%
W,Z polarization $\pm 10\%$:	0.6 %	0.8%	0.4%
DY \cancel{E}_T resolution:	0.0 %	2.3 %	1.7 %
Rare reweigh ($\pm 50\%$):	3.7%	3.3 %	3.4 %
Rare $t\bar{t}$ spin correlation ($\pm 20\%$):	0.2%	0.0 %	0.0 %
Rare W & Z polarization ($\pm 10\%$):	0.1%	0.2 %	0.2 %
Total systematic uncertainty:	15.7%	10.7 %	11.3 %
Total uncertainty [statistical+systematic]:	26.9%	21.1 %	18.3 %

We should stress that the analysis is dominated by statistical-uncertainty. This is listed also in same table as first row ($\delta Pred/Pred$ %) which includes all error propagation from the prediction methods formulas. In the following we examine most of the techniques uncertainties accounting.

8.1 Uncertainties applied over all backgrounds

The uncertainties applied over all backgrounds inclusively are:

- b-tagging scale factor (SF) for b and c quarks. A long discussion about the “b-tag-SF” (SF_b) definition and construction can be found in subsection 3.5.11. The b-tagging with CSVM algorithm has a small divergence compared with data; thus, by default we apply the SF_b to correct the MC yields. A potential miss-modeling of the SF_b is a source of systematic uncertainty. We scale up/down the heavy flavor (b,c) quark tagging according to the BTV POG (b Tag & Vertexing Physics Object Group) recommended uncertainty and use the differences in predicted yields as uncertainty (according to formula 8.2).
- b-tagging scale factor for light partons: we scale up/down the colored light particles (g,u,d,s) according to the BTV POG recommended uncertainty and use the differences in predicted yields as uncertainty (with formula 8.2).
- Electrons efficiency: we apply SF for the electron efficiency in the default predictions. Theses SF s again correct for the differences of electron reconstruction between data and MC. The corresponding SF s were determined by the EGamma POG for “not-triggered MVA ID” that we use. As there are small differences between their and our selection, we apply the full SF s as uncertainty. (The only difference between the selection we use and the one used for the SF s is the “3D-IP significance” cut, which should not have a large effect on the SF s.) Formula 8.1 is used. Figure 8.1 shows the specific SF -values.
- Muons efficiency: we scale up/down each event by $(1 \pm 5\%)^N$, with N being the number of soft muons $5 < p_T(\mu) < 25$ GeV. The efficiencies for the control region with the muon POG tight ID and the single lepton trigger is much better determined than 5% and the SF s are negligible small. (Also for the low p_T regime SF s have been determined for the loose ID). Again the uncertainties and values are well below 5%. We apply the SF s only for soft leptons and we calculate the corresponding uncertainty according to formula 8.1).
- JES (Jet Energy Scale): we apply the recommended JES factors to estimate the JES uncertainty.
- Trigger efficiency: the trigger is $\sim 100\%$ efficient and the uncertainty on this is small enough to be negligible with respect to the other systematic uncertainties.

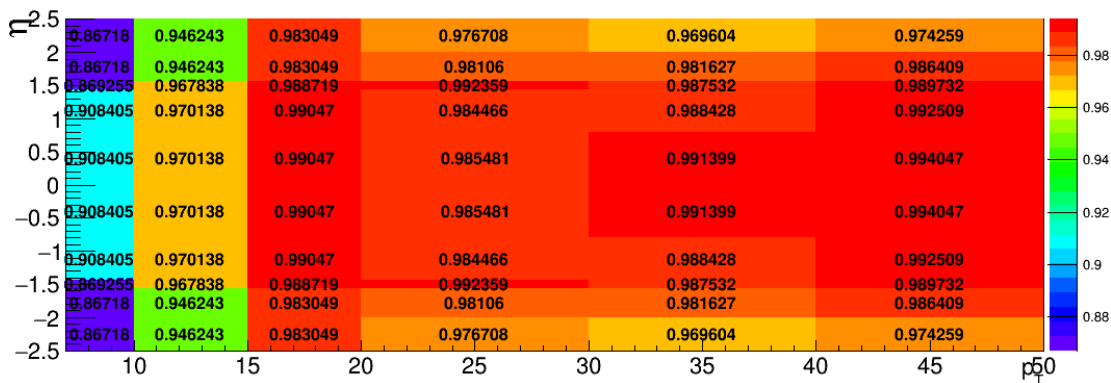


Figure 8.1: Electron efficiency SF s as a function of p_T , η . Used by default to rescale every $[e\mu]$ event.

All resulting uncertainties are displayed in table 8.1 (upper block).

8.2 Dileptonic top specific uncertainties

8.2.1 Spin correlation

The top and antitop quarks are produced essentially unpolarised. The gg -fusion dominates the $t\bar{t}$ production at the LHC $\sim 90\%$, while the $q\bar{q}$ -annihilation contributes about $\sim 10\%$ (figure 8.2). The $t\bar{t}$ spins tend to be anti-parallel in the gg -fusion i.e. the spin tend to be anti-correlated: and thus the system has same helicities [37, 14, ?]. Due to the very short lifetime of top the spin correlation is inherit also at its decay products: $t \rightarrow bW$. The SM dictates that the top quark has the ‘‘V-A’’ charged-current EW interaction which implies that the W-boson in its decay must be left-handed $\sim 30\%$ or longitudinally polarized $\sim 70\%$.

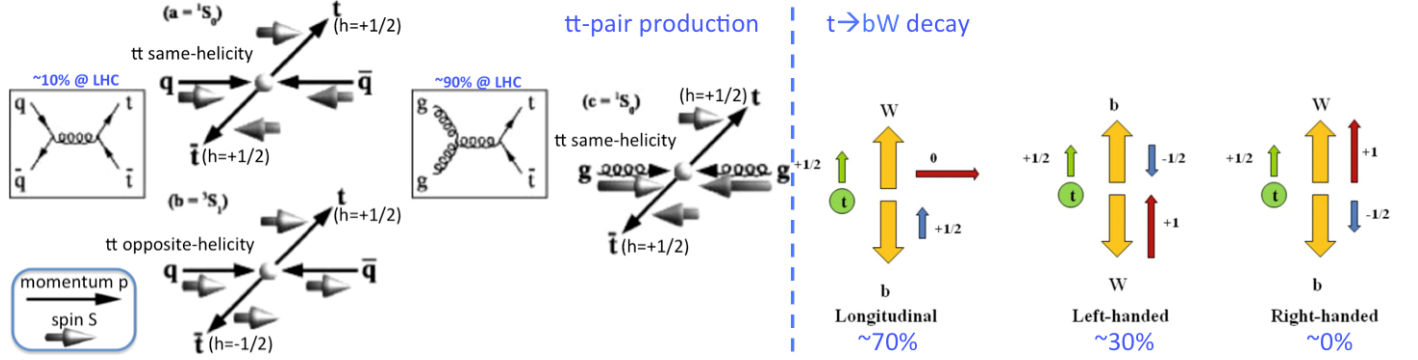


Figure 8.2: Left: the $t\bar{t}$ production mechanisms and its spin correlation. Configurations with reversed spin directions are not shown explicitly, but are meant to be included. Right the top/antitop decay and the helicity conservation. (Taken from [?].)

The $t\bar{t}(2\ell)$ spin correlation potential miss-modeling is a source of systematic uncertainty. We measure the correlation of the $t\bar{t}$ -pair using the variables $\cos\theta_i^*$ where the angle is the one between the lepton ℓ_i and its corresponding top/anti-top flight direction at the rest frame of it. The correlation C of two variables x, y is defined as:

$$\text{Correlation : } C(x, y) \equiv \text{cov}(x, y) / (\sigma_x \sigma_y) = [\langle xy \rangle - \langle x \rangle \langle y \rangle] / (\sigma_x \sigma_y) \quad (8.3)$$

which in our case x, y are: $\cos(\theta_{(\ell^+, t)}^*)$, $\cos(\theta_{(\ell^-, \bar{t})}^*)$, and according to simulation (in generator level) the correlation is: $C_{\text{default}} = -0.151$. The distribution of $t\bar{t}$ -events over $[\cos\theta_{(\ell^+, t)}^*, \cos\theta_{(\ell^-, \bar{t})}^*]$ plane is presented in figure 8.3 left.

In order to account a potential miss-modeling of the $t\bar{t}$ correlation we decompose this 2D distribution into two: the flat component with 0-correlation and the one with the shape (and consequently with correlation $C_{\text{shape}} = C_{\text{default}} = -0.151$). Then we add the two components back, once multiplying the non-flat with 0.8, and once with 1.2. Thus we obtained two new 2D-histograms with weaker and stronger correlation (with values: $C_{-20\%} = -0.134$ and $C_{+20\%} = -0.164$, or $+11\%$, -8% with respect to the default). The last step is to divide these distributions with the default one to obtain the weights over the $\cos\theta_{(\ell^+, t)}^*, \cos\theta_{(\ell^-, \bar{t})}^*$ plane. These reweighed distributions are presented in figure 8.3 middle and right. (The variation of $\sim 20\%$ is inspired by the measurement at LHC in data [11].)

To account the systematic we use these 2D reweigh function to multiply each $t\bar{t}(2\ell)$ MC event according to its $\cos\theta_{(\ell^+, t)}^*, \cos\theta_{(\ell^-, \bar{t})}^*$ values. The estimated uncertainty with formula 8.2 on the SR predicted total yield is $\sim 4\%$ (table 8.1).

8.2.2 The top-antitop p_T correction

It is a known feature that $t\bar{t}$ MC used shows modest disagreement of the top p_T distribution with respect to data. Formulas have been developed (by fitting in data) in order to correct the observed disagreement. The data over simulation ratios for top-antitop p_T s are presented in figure 8.4. The

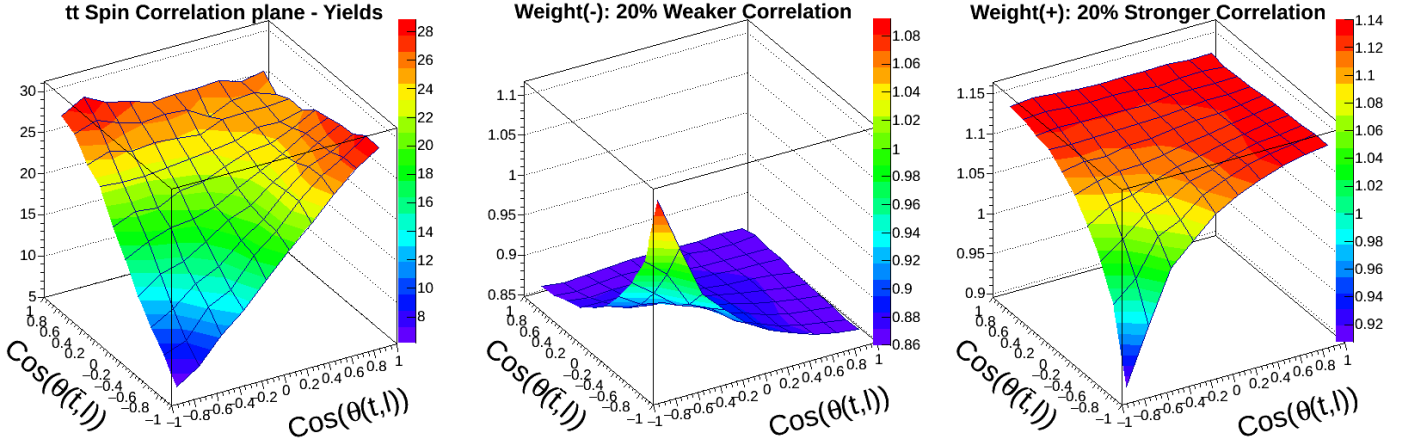


Figure 8.3: Left: the distribution of $t\bar{t}(2\ell)$ events, at generator level over the $\cos(\theta_{(\ell^+, t)}^*)$, $\cos(\theta_{(\ell^-, \bar{t})}^*)$ plane. Middle and right: the reweigh functions obtained by a $\pm 20\%$ enhancement of the non-flat component of the default distribution.

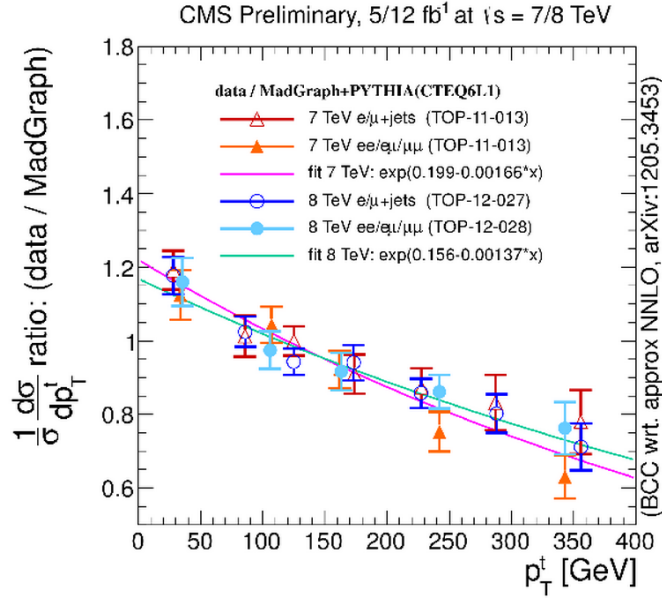


Figure 8.4: The distribution of top (or antitop) p_T -ratios of data over simulation.

data-driven formed scale factor (for each top-leg) which corrects MC are given by the formula:

- weight per t (or \bar{t}) leg: $W(p_T; t) = e^{a+bp_T}$, for $t\bar{t}(1\ell)$ with $a=0.159$, $b=-0.00141$,
- weight per t (or \bar{t}) leg: $W(p_T; t) = e^{a+bp_T}$, for $t\bar{t}(2\ell)$ with $a=0.148$, $b=-0.00129$,
- weight per $t\bar{t}$ event: $W(p_{T1}, p_{T2}; a, b) = \sqrt{e^{a+bp_{T1}}} \sqrt{e^{a+bp_{T2}}}$.

We do not reweigh by default our MC selections since these studies do not apply directly to our situation, as the high p_T of the tops in our case mainly stem from the ISR boost (as figure 6.3 illustrates). However, to proof that our data-driven correction really does cancel miss-modeling of a plausible size we take the suggest corrections to calculate an uncertainty. This uncertainty due to a potential MC $p_T(t)$ miss-modeling is accounted by producing the predictions with and without the top- p_T correction and accounting the difference as a systematic uncertainty. As expected the resulting uncertainty is tiny (table 8.1).

8.2.3 Polarization of W-boson in dileptonic top background

A potential miss-modeling of the W-boson polarization (originated by top: $(t^\pm \rightarrow b, W^\pm)$) is taken into account as a systematic uncertainty. The W-bosons coming from $t\bar{t}$ decay are left-handed $\sim 30\%$ or longitudinally polarized $\sim 70\%$ (right-handed is suppressed of the small b quark mass), when taking using the top rest-frame to determine these numbers.

We scale $\pm 10\%$ the left-handed polarization state component: $[(1 - \cos\theta^*)^2/4]$ which dominates the SR events (shown in figure 8.6). The W boson polarization in top decays is well known and measured, thus the usage of $\pm 10\%$ is conservative approach. The weights stemming from each W-boson are multiplied and applied to the $t\bar{t}(2\ell)$ on event-by-event basis. The difference with respect to default predicted yield is accounted as systematic uncertainty. The $\cos\theta^*$ distributions for the two leptons, of SR and CR($t\bar{t}2\ell$) are presented in figure 8.6.

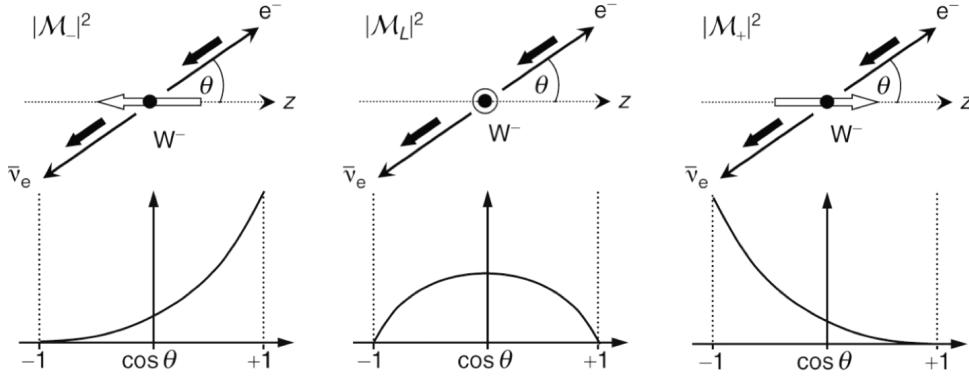


Figure 8.5: The polarization states of W-boson and its corresponding distributions over the $\cos\theta^*$ variable (where $\theta^* = \theta_{\ell,t}^*$ at the cm-frame of parent top).

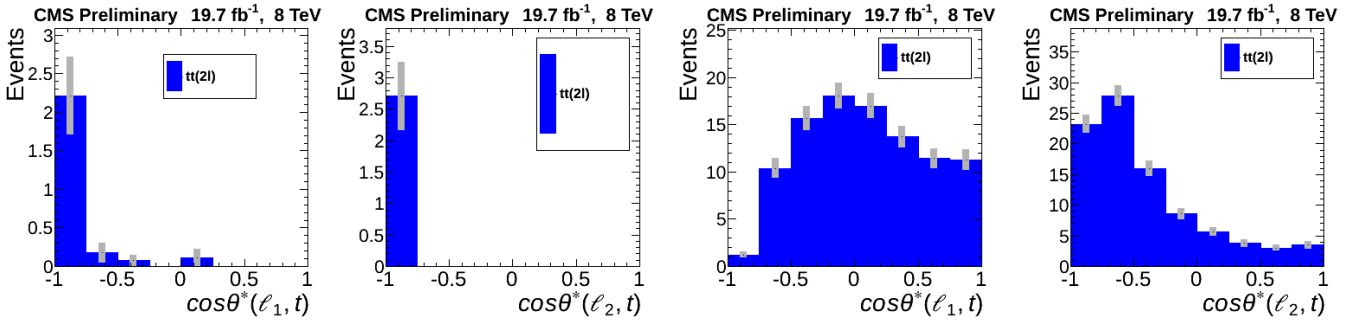


Figure 8.6: The $\cos\theta^*$ distribution for the SR events (left 2 plots), and for the CR($t\bar{t}2\ell$) (right 2 plots).

8.3 Non-prompt background uncertainties

8.3.1 The W+jets over semileptonic top events abundances ratio

The relative abundances (r) of W+jets over W+jets & $t\bar{t}(1\ell)$ events are different between SR ($r \simeq 20\%$) and CR(NP) ($r \simeq 40\%$). This can be shown in table 6.2 and figure 6.4. In order to estimate a systematic uncertainty coming from this different ratio we rescale by $\pm 50\%$ the W+jets events in CR(NP) and we use the difference in prediction (formula 8.2) as uncertainty estimate. Thus, a wide range of ratios r are accounted as potential miss-modeling. Also the $t\bar{t}(1\ell)$ was rescaled by $\pm 50\%$ and the yielded systematic was smaller than the W+jet case. In order to be conservative we use the highest estimated uncertainty from these variations as final uncertainty on the W+jet to $t\bar{t}(1\ell)$ cross-section ratio.

8.3.2 Source of NP leptons

Concerning the origin of each non-prompt lepton the parenthood decomposition (for the processes $t\bar{t}(1\ell)$, $W+\text{jets}$) is shown in figures 6.6, 6.7 bottom left. An enhancement of $\pm 50\%$ of non-prompt leptons originating from b quarks ($b \rightarrow (c/u)\ell_{NP}^\pm\nu_\ell$) is applied. Additionally, in the same context, a $\pm 100\%$ enhancement of the c-quark originated non-prompt leptons ($c \rightarrow d\ell_{NP}^\pm\nu_\ell$) is used to estimate the uncertainties. The differences of predicted yields (with respect to default) are used as estimation of the uncertainties. Both variations are used as two separate systematic uncertainties.

8.3.3 Kinematics of NP leptons

We consider the differences of NP-leptons (ℓ_{NP}) kinematic distributions between SR and CR(NP) (for $W+\text{jets}$ & $t\bar{t}1\ell$ events), as a potential source of systematic uncertainty.

The non-prompt lepton's p_T and $|\eta|$ distributions for SR and CR(NP) events are presented in figure 6.6 (bottom row). Since the statistics is poor and the plots are inconclusive, we relaxed the isolation and the impact parameters cuts to obtain the collection of plots in figure 6.7. To quantify the potential uncertainty coming the usage of CR(NP) events due to different kinematics with respect to SR we follow the steps:

- we form the $p_T(\ell_{NP})$ ratios of SR over CR(NP) normalized distribution in loose selection as shown in figure 8.7,
- we reweigh the CR(NP) events per non-prompt lepton once by multiplying with the ratio and once dividing with it; reducing and enhancing the “SR-like” kinematics in CR(NP) per $p_T(\ell_{NP})$ -bin,
- we take as systematic uncertainty the difference in SR prediction (as usual formula: 8.2),
- We do the same independently for $|\eta_{\ell_{NP}}|$ ratio distribution (figure 8.7 third plot).

The delivered uncertainties are about 2% as table 8.1 shows.

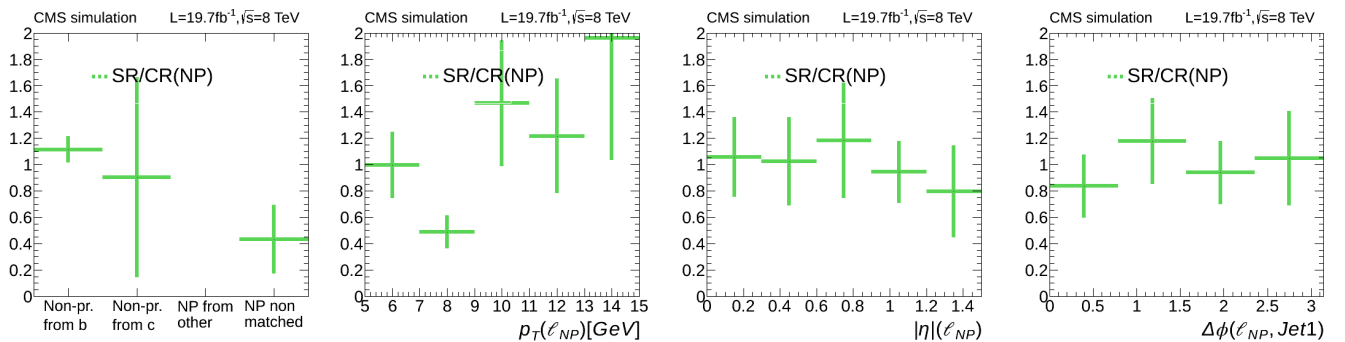


Figure 8.7: The ratios: SR/CR(NP) for normalized distribution of ℓ_{NP} -parenthood, $p_T(\ell_{NP})$, $|\eta|(\ell_{NP})$ and $|\Delta\phi|(\ell_{NP}, jet1)$ for both $t\bar{t}(1\ell)$ and $W+\text{jets}$ events. The looser selection has been used formed by SR removing the impact parameter and relative isolation cuts, and relaxing absolute isolation cut at 10 GeV (thus we gain statistics $\times 7$).

8.4 $W+\text{jets}$, $Z+\text{jets}$, $VV(\gamma^*)+\text{jets}$, Rare background systematic uncertainties

8.4.1 Polarization of the W and Z bosons

The differential cross-section of the boson decay expressed in terms of $\cos\theta^*$, where θ^* is the angle between lepton and boson flight direction, of the $W(Z)$ is determined by its helicity. The total $W(Z)$

decay rate is proportional to the amplitude [?]:

$$\langle |M_{if}|^2 \rangle \propto g_W^2 m_W^2 \left[A \frac{1}{2} (1 + \cos\theta^*)^2 + B (\sin\theta^*)^2 + C \frac{1}{2} (1 - \cos\theta^*)^2 \right] \quad (8.4)$$

where each term corresponds to the three possible polarization states illustrated in figure 8.5, and in the non-polarized case we have $A = B = C = 1$.

Mainly left-handed W boson are selected in our signal region “C” term dominates SR. Thus we reweigh this left-handed fraction of events by $\pm 10\%$ i.e. $C \rightarrow C(1 \pm 0.1)$ in order to estimate the uncertainty from a potential miss-modeling of this polarization. The factors A, B, C are known as function of η_ℓ and are different for lepton coming from W^+, W^-, Z^0 or W^\pm from $t\bar{t}$ production. However approximately are: $A(t) \approx A(\bar{t}) \approx 0$, $B(t) \approx C(\bar{t}) \approx 0.3$, $C(t) \approx B(\bar{t}) \approx 0.7$.

The variation $\pm 10\%$ is derived from the data measurements [48, 7] and theory uncertainties [36]. We use the difference between the prediction with reweighed and the default one as the systematic uncertainty.

8.4.2 Hadronic recoil systematic uncertainty

The Z+jets prediction method corrects for potential miss-modeling of hadronic recoil. This is performed via the formula 6.3. As explained in subsection 6.3, this step-1 correction scales down the SR-inv region MC yields by $\sim 15\%$ and increases the transfer factor used in step-2 by $\sim 10\%$. We conservatively use the difference between predictions with and without this correction as uncertainty. Given the very small contribution of Z+jets in our SR this appears negligible effect.

8.4.3 Very low invariant mass γ^* contribution

The $\gamma^* M_{\ell\ell}$ region of [1,12] GeV of the $WZ(\gamma^*)$ and $ZZ(\gamma^*)$ samples is covered by “privately produced” samples using massive leptons. As a conservative approach to account for the different treatment of lepton masses we perform the prediction once without the samples and once with double weights i.e: ± 100 reweighing. The difference (with respect to the default one) is used as systematic uncertainty. The cut $M_{\ell\ell} > 5$ GeV imposed in all regions used in the analysis protects for a further miss-modeling of γ^* with momentum close to ~ 1 GeV.

8.4.4 Rare background systematic uncertainty

The rare background processes are: $t\bar{t}W, t\bar{t}Z, t\bar{t}H, tW, VVV$ and $W^\pm W^\pm$. We do not form a prediction method for them since the yields about 1% in SR. Instead, we use the raw MC and for uncertainty we change their nominal cross-section by $\pm 50\%$. The yielded difference on prediction is used as uncertainty. The relatively high value occurs from the fact that rare background contribute by $\sim 11\%$ and $\sim 7\%$ in $CR(t\bar{t}2\ell)$ and $CR(VV)$ respectively, in combination with the fact that these regions have both less than one transfer factors. (It is like a simultaneous scaling of their transfer factors by $\pm 5.5\%$ and $\pm 3.5\%$ respectively.)

8.5 Di-boson systematic uncertainty

The WW, WZ and ZZ have been measured at the LHC [9, 49, 8, 110, 10] and typically show reasonable description even of the shapes of distribution. The small difference observed in the inclusive cross-section of WW [9, 49] will largely cancel by design of the prediction method. We varied physics quantities that could affect the transfer factors.

8.5.1 Boson polarization

Same recipe with subsection 8.2.3. We enhance(suppress) the contribution of the a specific helicity state (the dominant one in SR) by +10%(−10%) and we use change in predicted yields as systematic uncertainty (formula 8.2).

8.5.2 Boson transverse momentum asymmetry

The p_T of the boson pair in the signal region is similar by design to those in the control region. Also the ΔR and $\Delta\phi$ shows reasonable agreement as figure 6.13 illustrates. However, for the translation factor the asymmetry in the two boson p_T could have an effect. In order to account this we do the following procedure.

- we form the distributions ratios: $[p_T^{V+}/(p_T^{V+} + p_T^{V-})]$ in a high statistics selection (requiring only $\cancel{E}_T > 200$ GeV) figure 8.8 left,
- we de-compose this distribution into a flat one and one component with the shape,
- we re-compose back the two components by scaling the one with the shape by $\pm 50\%$,
- finally we divide the last by the initial distribution to obtain the $\pm 50\%$ reweigh functions.

With these weight functions (presented in figure 8.8 right) we perform an event-per-event reweighing of all VV events. The difference in predicted values is taken as systematic uncertainty.

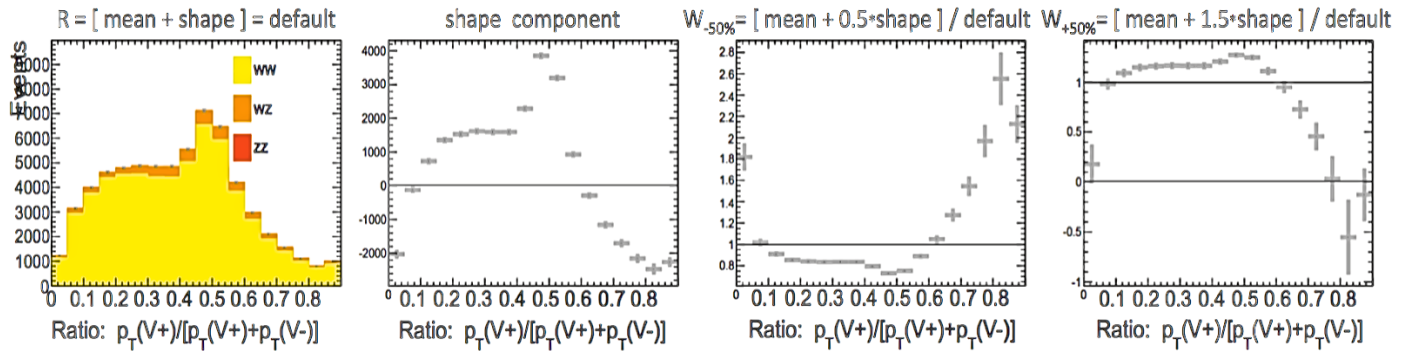


Figure 8.8: First: the distributions of the boson asymmetry: $[p_T^{V+}/(p_T^{V+} + p_T^{V-})]$ in a loose selection. Second: the shape-component of the ratio. In third and fourth: the distributions of the ratio re-composed by scaling with $\pm 50\%$ the shape-component and the result divided by the original. In other words, last two are the reweighing functions. (Negative weights are treated as zeros.)

8.6 Signal systematic uncertainties

For the signal we consider the similar as for the background systematic uncertainties.

For b-tagging SF, and for muon/electron efficiencies the uncertainties were found to be roughly flat over the different mass point (2D masses scan) of each of the three different signal scans. Table 8.2 shows these uncertainties in summary, whereas the figure E.1 in appendix E.2 present an explicit per $M_{\tilde{t}}, M_{\tilde{\chi}_1^0}$ mass-point calculation of the % uncertainties for the stop-scan.

For JES, ISR signal correction and MC statistics the uncertainties are accounted per each individual mass point. Again figure E.1 shows the % uncertainties per point only for stop scan.

A potential miss-modeling of the $|d_z|$ cut efficiency is accounted as systematic uncertainty in signal. This cut efficiency is calculated as the fraction of events accepted with the analysis $|d_z| < 0.01$ cm cut over those accepted with a much loosed (that CMS usually uses): $|d_z| < 0.5$ cm. To measure the efficiency in data and in background (MC-calculation) we use all electrons and muons in every accepted

event in all CRs and VRs used in analysis. (We only veto leading muon in CR(Z) to avoid an overuse of CR(Z) muons). The efficiencies are shown in appendix E.3, figure E.3 and seams perfectly modeled $|\Delta E f f_{DATA,MC}| < 3\%$.

For the signal the efficiency is higher ($\sim 5\%$) than the background as expected, since signal isn't dominantly consisted by tau-originated-leptons. In order to account a potential miss-modeling of the efficiency we assign a $\pm 2.5\%$ systematic uncertainty over the signal yield.

Table 8.2: Systematic uncertainties for SR yields per source. The three different signal scans (stop-pair, chargino-democratic and chargino-tau-enriched) are shown. Case where the corresponding uncertainty differs significantly versus mass point are shown separately. The typical uncertainty ranges (in stead of single values) are shown for cases where the per-mass-point treatment has been implemented.

Bin:	$p_T(\ell_1) : [5, 15] GeV$	$p_T(\ell_1) : [15, 25] GeV$
Uncertainty sources / Signal scan:	$\tilde{t}\tilde{t}(2\ell), \tilde{\chi}_1^\pm \tilde{\chi}_2^0(3\ell), \tilde{\chi}_1^\pm \tilde{\chi}_2^0(2\ell 1\tau)$	$\tilde{t}\tilde{t}(2\ell), \tilde{\chi}_1^\pm \tilde{\chi}_2^0(3\ell), \tilde{\chi}_1^\pm \tilde{\chi}_2^0(2\ell 1\tau)$
Flat in the whole scan uncertainties:		
btag-SF (b,c-quarks & light partons $\pm 1\sigma$)	0.6%	0.6%
PDF	6.0%	6.0%
Luminosity	2.6%	2.6%
$ d_z $ cut efficiency	2.5%	2.5%
Electron efficiency	3.4%, 1.0%, 0.7%	1.8%, 0.7%, 0.6%
Muons efficiency	7.2%, 8.7%, 9.8%	7.2%, 8.7%, 9.8%
Per mass-point accounted uncertainties:		
JES $f(M_{\tilde{t}}, M_{\tilde{\chi}_1^0})$	$\sim [0, 5]\%$	$\sim [0, 5]\%$
ISR correction	$\sim [15, 20]\%, 14.8\%, 13.7\%$	$\sim [15, 20]\%, 16.9\%, 16.6\%$
Statistical uncertainty $f(M_{\tilde{t}}, M_{\tilde{\chi}_1^0})$	$\sim [10, 25]\%, \sim [20, 40]\%, \sim [15, 30]\%$	$\sim [10, 25]\%, \sim [20, 40]\%, \sim [20, 35]\%$

8.7 Systematics summary

Table 8.1 also summarizes systematics uncertainties without the statistical which is around 15% in the low lepton p_T -bin and 10% in the high p_T -bin. The statistical uncertainty of the each search bin yield is presented on the top of the same table list. For these we accounted both the propagated transfer factor statistical uncertainty and the data yielded (in each CR) uncertainty. The combined systematic uncertainties are much smaller than each corresponding statistical uncertainties (16% and 11% versus 22% and 18% for the two p_T -bins). Therefore the leading uncertainty is the statistical one from MC on the translation factors.

Chapter 9

Results, their interpretation and conclusions

9.1 Results: observed data in signal region

The predicted yields and the observed data for the SR are presented in table 9.1 (same information as in table 6.3 with data) and in figure 9.1. Observed and predicted yields are in good agreement and give no indication of the presence of signal. In particular we have 2 events in the sensitive bin expecting 2.1 ± 0.5 events and 6 over all expecting 7.7 ± 1.1 .

Table 9.1: Predicted and data yields for SR. Systematic uncertainties shown in parenthesis.

Sample: / Bins:	$p_T(\ell_1) : [5, 15] GeV$	$p_T(\ell_1) : [15, 25] GeV$	Inclusive
$t\bar{t}(2\ell)$	0.75 ± 0.19	2.08 ± 0.37	2.84 ± 0.42
$t\bar{t}(1\ell), W+jets$	0.60 ± 0.33	1.32 ± 0.69	1.92 ± 0.76
DY+jets	0 ± 0	0.48 ± 0.45	0.48 ± 0.45
VV	0.74 ± 0.27	1.61 ± 0.48	2.35 ± 0.55
Rare	0.03 ± 0.01	0.08 ± 0.04	0.11 ± 0.04
Total SM Prediction	$2.12 \pm 0.47(\pm 0.33)$	$5.6 \pm 1.0(\pm 0.60)$	$7.70 \pm 1.1(\pm 0.87)$
SUSY(250,230)	10.0 ± 1.5	3.41 ± 0.90	13.50 ± 1.8
SUSY(300,250)	3.98 ± 0.61	3.83 ± 0.58	7.80 ± 0.84
SUSY(200,180)	6.2 ± 1.5	1.90 ± 0.88	8.1 ± 1.7
DATA	2	4	6
σ_{stat}	-0.1	-0.6	-0.6

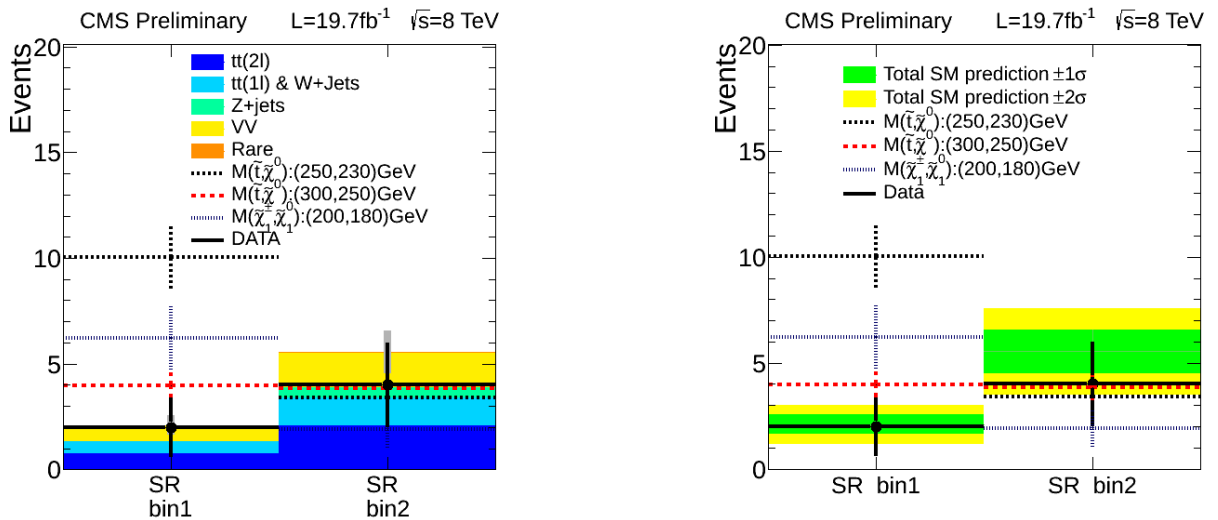


Figure 9.1: The predicted and data event yields in two search bins. Left: the background decomposition, right: the $\pm 1\sigma, \pm 2\sigma$ bands with only statistical uncertainties.

9.2 Results interpretation

9.2.1 The SUSY signal scans and their efficiencies

The search performed have shown no evidence of SUSY signals. Therefore, results obtained are interpreted using a statistical methodology to constrain a parameter space. This parameter space is in the context of the Simplified ModelS “SMS” where only the LSP and the next-to-LSP sparticles are considered with various masses combinations.

The SUSY models considered are those mentioned in section 4.3, shown in figure 4.2.

- For the stop-pair production (figure 4.2 left) we use a full “2D-scan” over the parameter space of stop-LSP masses, with 25×10 GeV binning respectively, and with the restriction of $\Delta M(\tilde{t}, \tilde{\chi}_1^0) \leq 80$ GeV.
- For the chargino-neutralino production (figure 4.2 middle) we have a 2D parametric space with Chargino-LSP masses in 20×20 GeV step-binning however we only use the $\Delta M(\tilde{\chi}_0^\pm, \tilde{\chi}_1^0) = 20$ GeV “slice” (the smallest one) where the analysis is sensitive. Two scenarios are considered differing on the chargino decay: the “democratic” and the “tau-enriched”.
- Finally we interpret the results in the topology shown in figure 4.2 right; 2D-scan over Chargino-LSP masses in 10×10 GeV step-binning, again we consider only the minimum $\Delta M(\tilde{\chi}_0^\pm, \tilde{\chi}_1^0) = 10$ GeV slice.

The signal efficiency % (SR-accepted over all signal events) for the first scan and for the two cases of the second scan can be shown in figure 9.2. In these figures where (cross-sections are not accounted) the observed pater is high efficiencies in high masses. This is an artifact of the LSP-mass, which is silently and indirectly implied to be relatively high ($M(\tilde{\chi}_1^0) \sim \cancel{E}_T^{CUT}$) in order to gain momentum from the ISR-boost and therefore induce \cancel{E}_T at the event.

9.2.2 Exclusion limits with the modified frequentist method

In order to quantify the level of incompatibility of observed experimental data with a signal+background (“B+S”) hypothesis, it is common practise to express it in Confidence Level (CL). The commonly accepted convention is to require a 95% CL for the exclusion of an “B+S” hypothesis.

The official LHC guideline for imposing exclusion limits for Higgs boson searches is based on the “modified frequentist method” [55]. The limit calculation method is defined by the choice of the test-statistic (q_μ) and the way that nuisance parameters (θ) are treated.

The null results of the “B+S” hypothesis will be expressed in terms of a given “signal strength” modifier, denoted μ , which is taken to change the signal cross-section by a scale μ . The predictions of both S and B event yields are subject to multiple uncertainties, which are all incorporated to the signal and background event yields by introducing a nuisance parameter vector space, such that $S \equiv S(\vec{\theta})$ and $B \equiv B(\vec{\theta})$. In this way, the signal and background event yields become functions of the nuisance parameters [2, 55].

Systematic uncertainties treatment of the limits

The systematic error Probability Density Functions (PDFs), denoted $\rho(\theta|\tilde{\theta})$, reflect the degree of belief on what the true value of the nuisance parameters θ is, with $\tilde{\theta}$ being the default nuisance parameter value. This can be expressed as [2, 55]:

$$\rho(\theta|\tilde{\theta}) = \frac{1}{\sqrt{2\pi} \ln k} \exp \left[-\frac{(\ln(\theta/\tilde{\theta}))^2}{2(\ln k)^2} \right] \frac{1}{\theta}, \quad k \equiv 1 + \delta, \quad \lim_{\delta \rightarrow 0} \rho(\theta) = \frac{1}{\sqrt{2\pi}\delta} \exp \left[-\frac{(\theta - \tilde{\theta})^2}{2\delta^2} \right] \frac{1}{\theta} \quad (9.1)$$

where k incorporates the relative systematic uncertainty (δ) associated with the best estimate of $\tilde{\theta}$. Example of log-normal distributions are presented in figure 9.3. From equation 9.1, by writing $\ln(\theta/\tilde{\theta}) =$

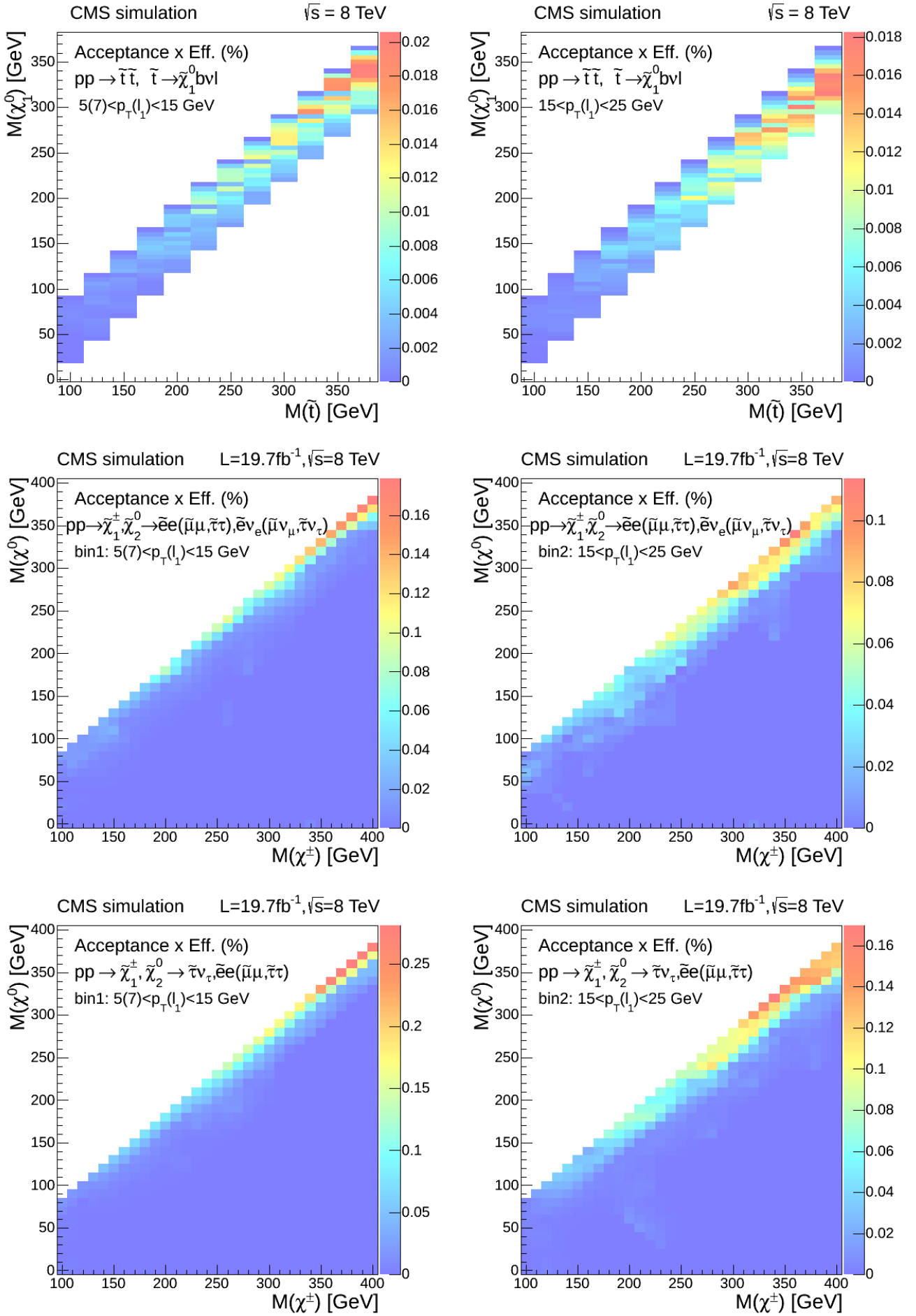


Figure 9.2: Signal efficiency %, first row: $\tilde{t}\tilde{t}$ -pair production (stop-LSP masses), second row: $\tilde{\chi}_1^\pm \tilde{\chi}_2^0$ -production “democratic”, third: $\tilde{\chi}_1^\pm \tilde{\chi}_2^0$ -production “tau-enriched”. High efficiencies for small mass splittings and high LSP-masses (\cancel{E}_T) as the SR selections imposes.

$\ln \theta / - \ln \tilde{\theta}$ one sees that the log-normal distribution is just a Gaussian with mean $\ln \tilde{\theta}$ and variance $\sigma^2 = (\ln k)^2$. Therefore, the lognormal PDF is simply a Gaussian distribution in the x-axis log-scale, which assigns equal probabilities for the nuisance parameter θ to be a factor k^n larger (or smaller) than the best estimate $\tilde{\theta}$. In the limiting case where the relative systematic uncertainty approaches zero, the log-normal distribution becomes a Gaussian with mean $\tilde{\theta}$ and variance $\sigma^2 = \delta^2$, as it can be seen in figure 9.3 (a). The log-normal distribution's connection to the Gaussian becomes increasingly inappropriate for higher values of δ as shown in same figure plot (b). It is convenient to reinterpret the systematic uncertainty PDFs $\rho(\theta|\tilde{\theta})$ as posteriors of some real or imaginary measurements, thus decoupling the need for Bayesian a priori information, and allow a purely frequentist approach. In this conceptual step, the systematic uncertainty PDFs can be re-formulated using Bayes' theorem as: $\rho(\theta|\tilde{\theta}) \sim p(\tilde{\theta}|\theta)\pi_\theta(\theta)$ where the functions $\pi_\theta(\theta)$ are hyper-priors of the hypothetical measurements. By choosing flat hyper-prior functions, the mapping of Bayesian posterior PDFs $\rho(\theta|\tilde{\theta})$ to frequentist auxiliary measurements PDFs $p(\tilde{\theta}|\theta)$, allows one to represent all systematic uncertainties in the frequentist context. In this way, a systematic uncertainty PDF is expressed as the posterior $\rho(\theta|\tilde{\theta})$ constructed from a fictional auxiliary measurement, whose systematic PDF is $p(\theta|\tilde{\theta})$. The latter can be used to constrain the main measurement and to construct sampling distributions of the test-statistic in pure frequentist calculations.

Calculation of observed limit method

For a given experimental observation with a set of observed events N_i (i runs over search bins), a likelihood function is constructed of the form:

$$\mathcal{L}(data|\mu, \vec{\theta}) = \prod_i \frac{1}{N_i!} \left[\mu S_i(\vec{\theta}) + B_i(\vec{\theta}) \right]^{N_i} \exp \left[-\mu S_i(\vec{\theta}) - B_i(\vec{\theta}) \right] p(\vec{\theta}|\vec{\theta}). \quad (9.2)$$

This expression quantifies the probability that a given set of data, (poissonianly distributed), will be observed for the specified parameters $\mu, S(\vec{\theta})$ and $B(\vec{\theta})$. The Poisson product describes the combined probability that, in each of the bins, which has Poisson mean of: $\mu S_i(\theta) + B_i(\theta)$, an event yield of N_i will be observed. The signal strength modifier μ is a parameter that can be used to adjust the event yield expected from a given ‘‘B+S’’ hypothesis, while the term $\vec{\theta}$ represents the full set of nuisance parameters.

In order to assess the degree of compatibility between the data and the ‘‘B+S’’ hypothesis for a given signal strength modifier (μ), and the background-only (‘‘B+0’’) hypothesis (with zero signal $\mu = 0$), the construction of a test-statistic is required. The chosen test-statistic is based on the profile likelihood ratio:

$$\tilde{q}_\mu = -2 \ln \frac{\mathcal{L}(data|\mu, \vec{\theta}_\mu)}{\mathcal{L}(data|\hat{\mu}, \vec{\theta})}, \quad 0 \leq \hat{\mu} \leq \mu, \quad (9.3)$$

The term $\vec{\theta}_\mu$ refers to the nuisance parameter vector that maximises the likelihood $\mathcal{L}(data|\mu, \vec{\theta}_\mu)$ for a given value of μ and for a given set of experimentally observed data. The pair of parameter estimators $\hat{\mu}$ and $\vec{\theta}$ correspond to the parameters that yield the global maximum of the likelihood, for any of the allowed μ .

Having defined the test-statistic \tilde{q}_μ in equation 9.3, three variables are needed for the calculation of the observed limit on the μ :

- the observed test-statistic value \tilde{q}_μ^{obs} , which is unique for a given trial μ ,
- the nuisance parameter vector $\vec{\theta}_\mu^{obs}$, deduced form maximisation: $\frac{d}{d\vec{\theta}} \mathcal{L}(data|\mu, \vec{\theta}) = 0$, and
- the nuisance parameter vector $\vec{\theta}_{\mu=0}^{obs}$, deduced form maximisation: $\frac{d}{d\vec{\theta}} \mathcal{L}(data|\mu = 0, \vec{\theta}) = 0$.

Where vectors derived from the likelihood maximisation and describe best the observed data, for the “B+S” hypothesis and “B+0” hypothesis respectively.

Once the above values/vectors are determined, the next step is to generate toy MC pseudo-data in order to construct the PDFs of the test-statistic \tilde{q}_μ for the “B+S”, and “B+0” hypothesis, denoted $f(\tilde{q}_\mu|\mu, \vec{\theta}_\mu^{\text{obs}})$ and $f(\tilde{q}_{\mu=0}|\mu=0, \vec{\theta}_{\mu=0}^{\text{obs}})$, respectively. Details of the procedure can be found at [2, 55]. In this way, the likelihoods are constructed using events yields that account for fluctuations, from systematic uncertainties sources, and for possible statistical fluctuations of the data.

The PDF distributions $f(\tilde{q}_\mu|\mu, \vec{\theta}_\mu^{\text{obs}})$ and $f(\tilde{q}_{\mu=0}|\mu=0, \vec{\theta}_{\mu=0}^{\text{obs}})$, are used to quantify the “p-values” of “B+S” and “B+0” hypothesis, denoted p_μ and $p_{\mu=0}$, respectively:

$$p_\mu \equiv P(\tilde{q}_\mu \geq \tilde{q}_\mu^{\text{obs}} | \text{“B+S”}) = CL_{B+S}, \quad \Rightarrow \quad CL_{B+S} = \int_{\tilde{q}_\mu^{\text{obs}}}^{\infty} f(\tilde{q}_\mu|\mu, \vec{\theta}_\mu^{\text{obs}}) d\tilde{q}_\mu, \quad (9.4)$$

$$1 - p_{\mu=0} \equiv P(\tilde{q}_\mu \geq \tilde{q}_\mu^{\text{obs}} | \text{“B+0”}) = CL_{B+0}, \quad \Rightarrow \quad CL_{B+0} = \int_{\tilde{q}_\mu^{\text{obs}}}^{\infty} f(\tilde{q}_\mu|\mu=0, \vec{\theta}_{\mu=0}^{\text{obs}}) d\tilde{q}_\mu. \quad (9.5)$$

The CL_{B+S} describes the probability that a test-statistic with a value greater to the one evaluated from data $\tilde{q}_\mu^{\text{obs}}$ will be observed under the “B+S” hypothesis; that is, how compatible is the test-statistic value of $\tilde{q}_\mu^{\text{obs}}$ with the “B+S” hypothesis hypothesis. Similarly, CL_{B+0} describes the probability that the observed value is compatible with the “B+0” hypothesis. By calculating the ratio of these two probabilities as: $CL_s(\mu) \equiv CL_{B+S}/CL_{B+0}$, one has the final ingredient for quantifying the probability that a given “B+S” hypothesis, with a certain trial signal strength modifier μ , is compatible with the observed data. In particular $CL_s(\mu)$ is compared by convention with the 0.05 (since 1-0.05 corresponding to 2σ confidence level). The “B+S” hypothesis is then excluded with 95% confidence level if: $CL_s(\mu) < 0.05$. The “B+S” hypothesis is set to be excluded with a 95% CL upper limit on the signal strength modifier μ , and is denoted as $\mu^{95\%CL}$.

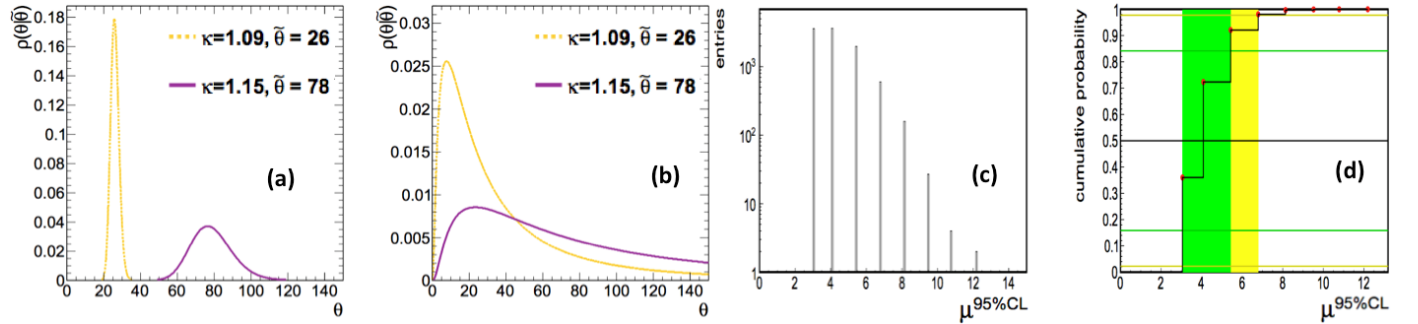


Figure 9.3: Left: example log-normal distributions with typical (a) and 200% (b) systematic uncertainties. Right: an example of differential distribution of possible limits on μ (c) for the “B+0” hypothesis (no systematic errors); and the Cumulative probability distribution (d) of the plot (c) (horizontal lines defining the median expected limit as well as the $\pm 1, 2\sigma$). Taken from [2, 55].

Calculation of expected limit method

The procedure starts with the generation of a large set (indexed with j) of toy MC pseudo-data, under the assumption of a “B+0” hypothesis ($\mu=0$), to obtain a set of event yields: N_{ij} . The N_{ij} replaces the N_i (used in equation 9.2) for observed data over i -bin. The generated pseudo-yields follows a poisson distribution of the form:

$$p(N_{ij}; B) = \frac{B^{N_{ij}} e^{-B}}{N_{ij}!}, \quad B = \sum_k b_k(\vec{\theta}_k) \quad (9.6)$$

Where B stands for the total predicted event background and is a sum of k individual background components b_k with different “set” of systematic uncertainties $\vec{\theta}$. These toy MC pseudo-data are

treated as if they were in fact real experimental data and are used in calculating of the $\mathcal{L}(data|\mu, \vec{\theta})$ and the \tilde{q}_μ as described before.

The p-values, p_μ and $p_{\mu=0}$, are also evaluated using dedicated toy MC pseudo-data for the “B+S” and “B+0” hypothesis. Once the p-values are determined, the value of $CL_s(\mu)$ is compared to 0.05 to determine whether the requirement $CL_s(\mu) \leq 0.05$ is met. The procedure is repeated by adjusting the trial value of the signal strength modifier μ until $CL_s(\mu) = 0.05$ and a corresponding $\mu^{95\%CL}$ is obtained. By repeating this iteration several times, a distribution of $\mu^{95\%CL}$ can be obtained, which can be converted to a PDF distribution and consequently into a “cumulative” CDF (see figure 9.3 right). The CDF distribution is then used to finally obtain the expected limit in terms of signal strength modifier μ , by simply reading the $\mu^{95\%CL}$ which corresponds to the CDF 95%.

9.2.3 Exclusion limits

The modified-frequentist CLs method [105, 133, 26] with a one-sided profile likelihood ratio test statistic is used to define 95% confidence level (CL) upper limits on the production cross section as a function of the sparticle masses.

Statistical uncertainties related to the observed number of events in control regions are modelled as Poisson distributions. All other uncertainties are assumed to be multiplicative and are modelled with lognormal distributions. The impact of a potential signal contamination in the control regions is taken into account in the calculation of the limits for each signal point. The CRs with highest signal contamination are those with the same selection as the SR, i.e.: the CR(NP) (actually the SR(SS) sub-region of it) and the SR-inv. Their corresponding signal event yields per mass point are shown in figure 9.4 and are negligible with respect to the SR yield.

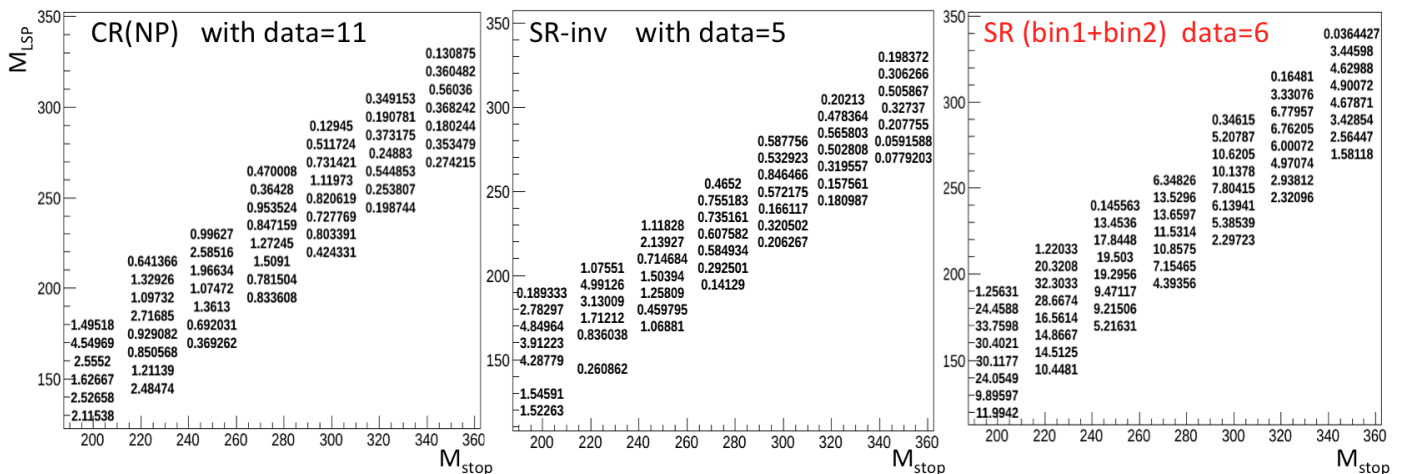


Figure 9.4: The signal contamination in the two most contaminated CRs. The signal events yields per mass-point; on the left the CR(NP), middle the SR-inv and right SR.

Systematic uncertainties on signal yields related to the determination of the integrated luminosity [53], pileup, energy scales, object identification efficiencies, and uncertainties in the parton distribution functions [19, 39, 30, 120, 117] and the modelling of ISR [50] have been evaluated. Section 8.6 and appendix E presents most of them. The dominant term is related to ISR and amounts to approximately 20% (table 8.2, figure E.1). Correlations between the systematic uncertainties in different signal regions are taken into account, where applicable.

Limits for this work are set in the context of a simplified model [25, 22, 21, 20]. In our particular case of stop-pair and chargino-neutralino pairs the cross sections are shown in figure B.3.

Interpretation in the stop-pair production, limits over the stop-LSP mass scan

Using the stop-pair production cross section calculated at next-to-leading order (NLO) and “next-to-leading logarithm” (NLL) precision [34, 115, 114, 33, 32, 113] the cross section limits can be converted

into excluded regions in the stop-LSP mass plane. The limits obtained for top squark pair production are shown in figure 9.5, under the assumption of a 100% branching ratio of the four-body decay.

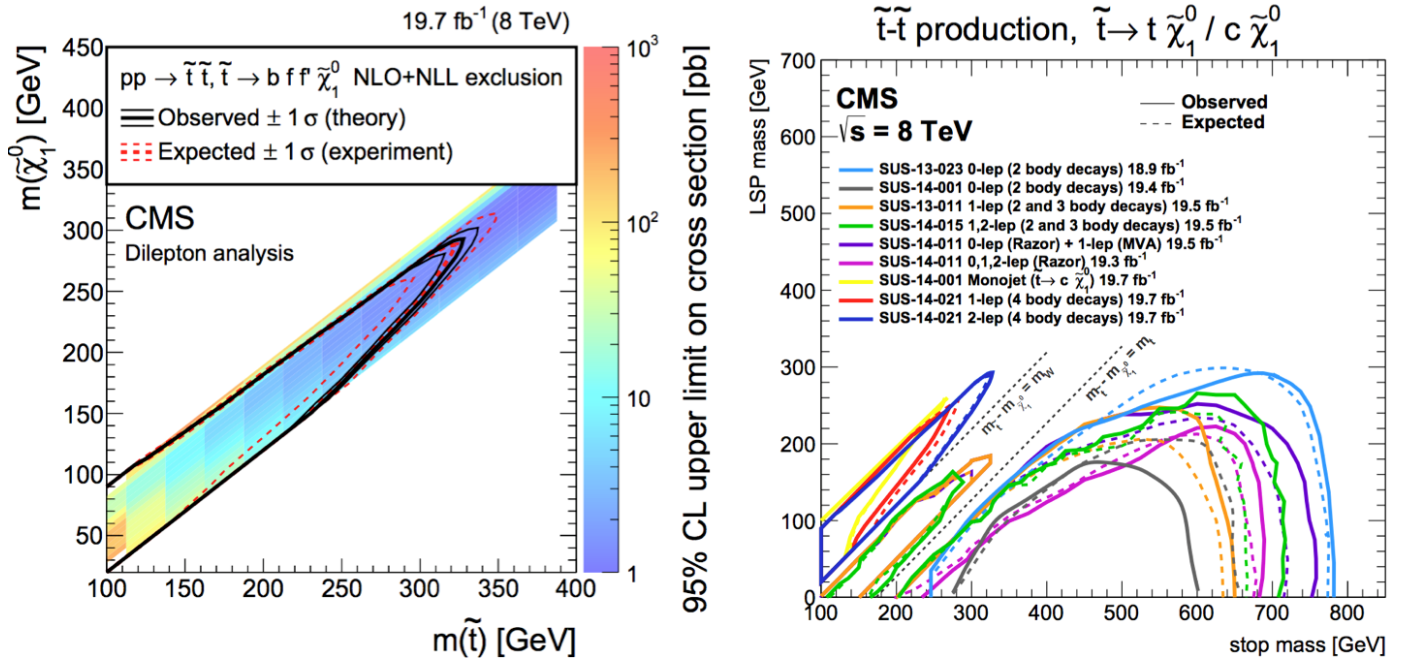


Figure 9.5: Left the expected (red) and observed (black) upper limits at 95% CL with its corresponding $\pm 1\sigma$ bands. Right the status of CMS searches over the whole 2D-space including the 0,1,2-lepton searches in compressed spectra.

- stop masses below 325 GeV are excluded for $\Delta M(\text{stop} - \text{LSP}) \sim 30$ GeV.
- stop masses below 300 GeV are excluded for $\Delta M(\text{stop} - \text{LSP})$ range: $\sim [20, 50]$ GeV.
- stop masses below 250 GeV are excluded for $\Delta M(\text{stop} - \text{LSP}) \sim$ range: $\sim [15, 80]$ GeV.

This result considerably extends existing limit [13, 12] shown in figure 4.1. It is complementary to the results of searches in the monojet topology targeting the decay to $\tilde{t} \rightarrow c\tilde{\chi}_1^0$ [54, 13] into the 0-lepton final state (figure 9.5 right yellow curve). Also complements and exceed the exclusion result of the 1-lepton final state of the same four-body decay (figure 4.2 left). This 1-lepton search (which was developed in parallel with the current 2-lepton one), results into the red exclusion limit presented in figure 9.5 right, and complement the 2-lepton result extending at $\Delta M(\text{stop} - \text{LSP}) \sim 10$ GeV. Both these 1,2-lepton results are submitted to be published together under the same paper.

Interpretation in chargino-neutralino production, limits over the chargino-LSP mass scan

In the case of chargino-neutralino pair production three models are studied as explained in section 4.3, figure 4.2 middle and right. If only the supersymmetric partners of left-handed leptons ($\tilde{\ell}_L$) and neutrinos ($\tilde{\nu}$) participate in the process, we expect a “flavour-democratic” scenario with identical branching fractions into all lepton flavours, both for the chargino and the neutralino. In this scenario the fraction of events with at least two charged leptons is reduced by 50% due to the $\tilde{\chi}_2^0 \rightarrow \nu\nu\tilde{\chi}_1^0$ decay channel.

If only the supersymmetric partners of right-handed leptons ($\tilde{\ell}_R$) are involved the production of τ leptons is increased since the $\tilde{\ell}_R$ would couple to the higgsino component of the chargino. For this case we use the τ -enriched scenario where the chargino decays exclusively to a τ lepton, while the neutralino decays democratically as in the first case.

In our interpretation we set $M(\tilde{\ell}) = [M(\tilde{\chi}_1^\pm) + M(\tilde{\chi}_1^0)]/2$. Figure 9.6 left, shows the 95% CL limits for the three cases in a compressed scenario with $\Delta M(\tilde{\chi}_1^\pm, \tilde{\chi}_1^0) = 20(10)$ GeV. On the right the contribution of the 2-lepton search (dotted slices) over the general-status of CMS scan-plane. The theoretical cross

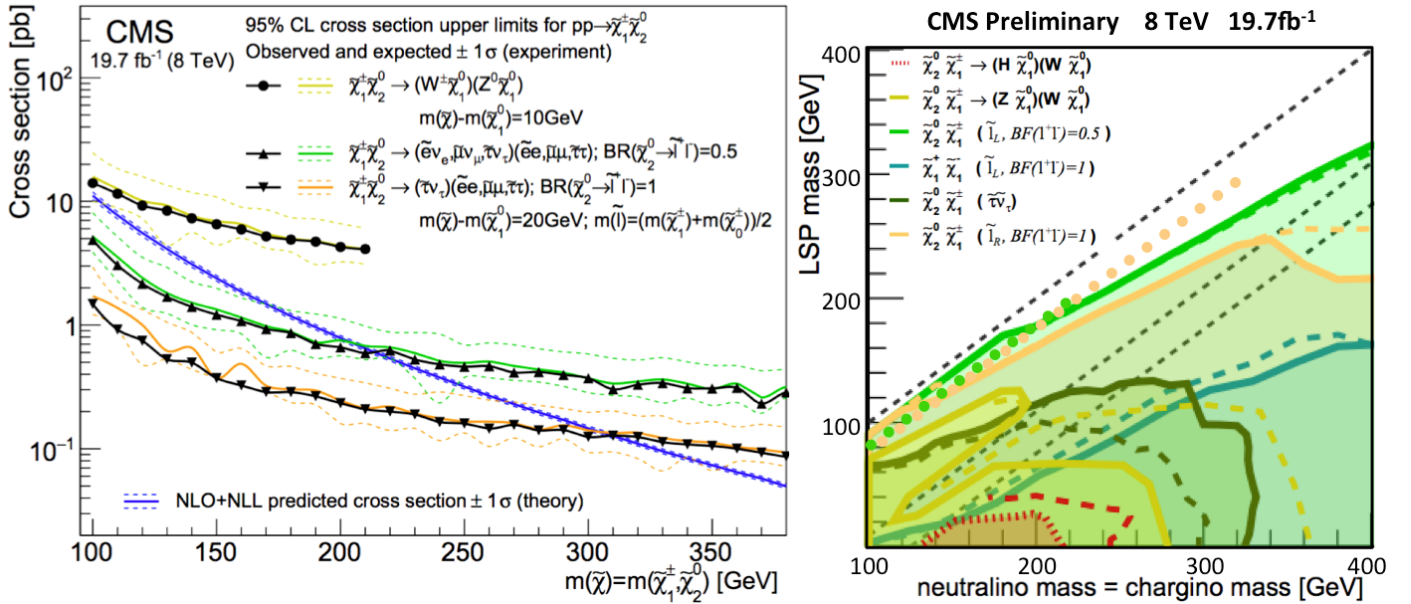


Figure 9.6: Left: expected and observed exclusion limits at 95% CL with its corresponding $\pm 1\sigma$ bands for the chargino-neutralino production cross section. Three different scenarios are considered (with mass differences $\Delta M(\tilde{\chi}_1^\pm, \tilde{\chi}_1^0) = 20(10)$ GeV). Right: the contribution of the result in the general status CMS limits graph. The two newly excluded slices by soft-2-lepton search are shown in (orange and green) dots.

section is calculated at NLO+NLL precision with the RESUMMINO [89, 90, 91] program. The 95% CL limits on $m(\tilde{\chi}_1^\pm)$ are set as follows:

- chargino masses below ~ 210 GeV are excluded in flavour-democratic scenario,
- chargino masses below ~ 310 GeV are excluded in τ -enriched scenario.
- non exclusion for any chargino mass for the third (WZ) scenario shown in figure 4.2 right.

In this compressed scenario the new limits slightly improve current results in the flavour-democratic scenario (green) and exceed them by ~ 200 GeV for the τ -enriched scenario (orange) [109], as for the latter the dominant decays lead to final states with opposite-sign leptons.

9.3 Summary and conclusions

A search for supersymmetry with compressed mass spectra is performed in events with one or two hard jets, \cancel{E}_T , and two oppositely-charged soft leptons, compatible with the emission of initial state radiation. In particular, the search targets the pair production of top squarks with a mass splitting of at most 80 GeV with respect to the LSP.

The data sample consists of proton-proton collisions at $\sqrt{s}=8$ TeV, recorded by the CMS detector in 2012. Signal region is defined requiring one or two hard jets (ISR candidate), no b-tagged jet, two low p_T OS leptons ($\mu\mu$ or $e\mu$) and high \cancel{E}_T . A leading-lepton transverse mass binning is used as discriminating variable between low and high mass splittings, extending the range of sensitivity.

The most crucial cuts which can be underlined as the “golden cuts” of the search are: (a) the di-tau (effective) invariant mass $M_{\tau\tau}$ cut, which drastically reduces the Z +jets($Z \rightarrow \tau\tau$) background, and (b) the tight impact parameters cuts (with respect to primary vertex) which suppresses the soft lepton coming from a tau decays ($\sim 50\%$) since taus (accompanied by their neutrinos) are preferably selected in our high \cancel{E}_T , soft-lepton selection. In addition the tight impact parameter cuts reduces the non-prompt background which introduces the highest systematic and statistical uncertainty.

The search is clearly dominated by the low $p_T(\ell_1)$ -bin and its statistical uncertainty. The backgrounds to this search-bin are $t\bar{t}(2\ell)$, $t\bar{t}(2\ell)$ and VV in almost equivalent abundances and only 2 ($\pm 30\%$) expected/predicted events.

The expected event yield prediction is performed by data-driver methods using control regions similar in kinematic properties (as much as possible) to the signal region. The main assumption which were used for the prediction is that: event yielded in SR over CR are correctly modeled in MC. Under this assumption we predict in SR with the basic formula: $PRED_{SR} = [MC_{SR}/MC_{CR}]DATA_{CR}$, correcting the $DATA_{CR}$ yields properly for non 100% purity.

An essential ingredient of the search is (a) the test of all prediction methods in four different validation regions, and (b) a test of all prediction (in either SR and VRs) in an alternative approach based on a single trigger configuration (in contrast with the default usage of two different triggers). Figure 9.7 left summarizes the SR and VRs prediction and data for the dual-trigger configuration (default strategy used), whereas plots on the right shows same six bins in the single trigger configuration. (Left histogram information re-presents inclusively the figures 9.1 and 7.3 whereas right histogram re-presents inclusively information of figure 7.4 and table 7.3).

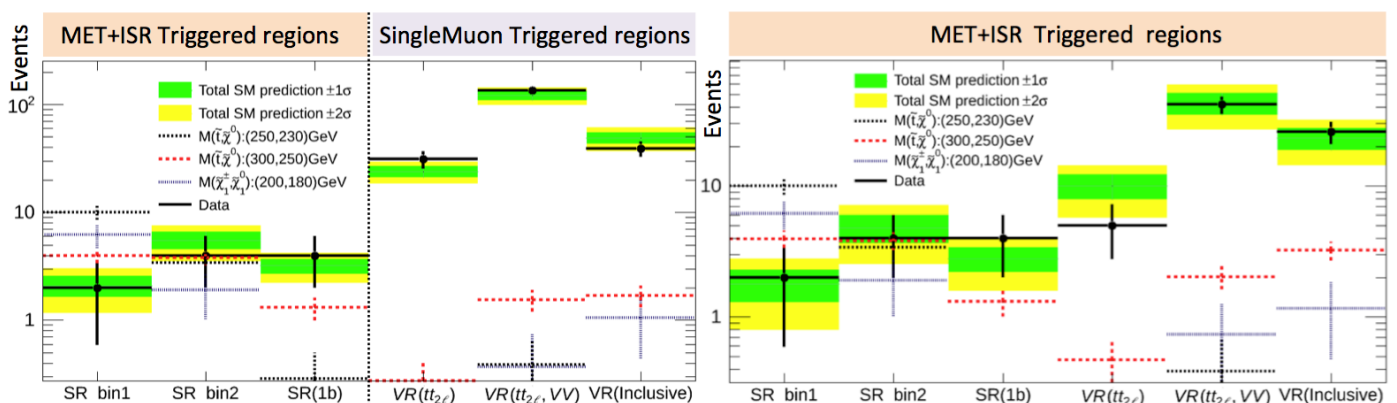


Figure 9.7: On the left, the predicted and data yields for the two SR bins and the four VRs with the default trigger configuration (i.e. single muon trigger for $p_T(\ell_1) > 25$ GeV). On the right, the same information where all predictions have been derived using data by a single trigger configuration (the “MET+ISR” triggers only) and the VRs are defined accordingly with high \cancel{E}_T cut.

Observed data are compatible with the SM background predictions within statistical uncertainties. In the absence of any indication for supersymmetry, cross section limits are set at 95% CL in the LSP-top squark mass plane. These limits are used to derive mass limits based on a reference cross section for top squark pair production and assuming a 100% branching ratio for the four-body decay $\tilde{t} \rightarrow bff'\tilde{\chi}_1^0$ where $M_{\tilde{t}}$ points are excluded up to ~ 325 GeV. The result extend existing limits in the four-body decay channel of the top squark [13, 12] and complement the analyses performed in the 0 and 1 soft lepton final state channel [54].

The result is also capable, even without optimization, to set limits on various chargino-neutralino production in compressed spectrum scenarios with a mass difference of $\Delta M(\tilde{\chi}_1^\pm, \tilde{\chi}_1^0)$ 20 GeV. In case of flavour-democratic leptonic decays of these sparticles, and for 95% CL, a lower limit on the common $M_{\tilde{\chi}_1^\pm}/M_{\tilde{0}_2^\pm}$ mass is set at 210 GeV. If chargino decays proceeds exclusively via the τ -channel the limit increases to 310 GeV.

The dileptonic final state search has shown that at least for the stop-pair productions leads to the best sensitivity with respect to the full-hadronic and semi-leptonic channel searches. In addition, the exclusion results in the chargino-scan are very promising for a reload of the search optimized for that topologies.

Appendix A

Some basic kinematics

The CMS experiment uses a right-handed coordinate system, with the origin at the interaction point (IP), the x-axis pointing to the centre of the LHC ring and the y-axis pointing vertically upwards perpendicular to the LHC plane. It then follows that the z-axis, from which the polar angle θ is measured, is oriented to be parallel to the beam and the anti-clockwise rotating proton beam. The azimuthal angle ϕ is measured from the positive x-axis in the x-y plane whereas the radius (r) denotes the distance from the z-axis.

In high energy physics where hadron beam collisions takes place, the actual colliding particles are not the hadrons but their constituent partons. Due to different momentum carried by these, the center of mass of the colliding partons is moving along the z-direction (with respect to the lab-frame). Consequently since LHC collides protons only the x-y plane conservation of momentum can be used in most analysis. Thus, a set of proper variables using the transverse plane aer defined and used in analysis. The most commonly used variable is pseudorapidity: $\eta(\theta) \equiv -\ln[\tan(\theta/2)]$ is presented in figure A.1. The $\theta \rightarrow \eta$ change have the great advantage to enables the use of the invariant quantity $\Delta\eta$. More kinematic variables used in high energy particle collisions physics are listed bellow.

1. Mandelstam invariant variables: s, t, u

where momenta ($p_i \equiv p_i^\mu$) stands for the generic interaction “1+2→3+4” with $p_1 + p_2 = p_3 + p_4$.

$$s \equiv (p_1 + p_2)^2 = (p_3 + p_4)^2 = (E_1 + E_2)^2 + (\vec{p}_1 + \vec{p}_2)^2,$$

$$t \equiv (p_1 - p_3)^2 = (p_2 - p_4)^2 = (E_1 - E_3)^2 + (\vec{p}_1 - \vec{p}_3)^2,$$

$$u \equiv (p_1 - p_4)^2 = (p_2 - p_3)^2 = (E_1 - E_4)^2 + (\vec{p}_1 - \vec{p}_4)^2,$$

where in the relativistic limit (p_i/E_i) $\rightarrow 1$ turn to:

$$s = 2p_1p_2 = 2p_3p_4$$

$$t = -2p_1p_3 = -2p_2p_4$$

$$u = -2p_1p_4 = -2p_2p_3$$

$$s + t + u = m_1^2 + m_2^2 + m_3^2 + m_4^2.$$

2. Total (initial and final) collision energy in any frame: $\sqrt{s} = \sqrt{2p_1p_2} = \sqrt{2p_3p_4}$.

3. Transverse momentum: $p_T \equiv \sqrt{p_x^2 + p_y^2} = |p| \sin \theta$.

4. Transverse energy : $E_T \equiv E \sin \theta = p_T(E/|p|)$.

5. Transverse mass (of a single particle): $m_T \equiv \sqrt{p_T^2 + m^2}$.

6. Rapidity: $y \equiv \frac{1}{2} \ln[(E + p_z)/(E - p_z)]$.

7. Pseudorapidity: $\eta \equiv \lim_{(E/p) \rightarrow 1} y = -\ln[\tan(\theta/2)]$.

8. Invariant η - ϕ “3D-angle”: $\Delta R \equiv \sqrt{(\Delta\eta)^2 + (\Delta\phi)^2}$.

9. Four-momentum of a particle as function of different variables:

$$f(E, p_x, p_y, p_z): p^\mu \equiv (E; p_x, p_y, p_z),$$

$$f(m_T, p_x, p_y, y): p^\mu = (m_T \cosh y; p_x, p_y, m_T \sinh y),$$

$$f(m_T, p_T, y, \phi): p^\mu = (m_T \cosh y; p_T \cos \phi, p_T \sin \phi, m_T \sinh y),$$

$$f(m, p_T, \eta, \phi): p^\mu = (\sqrt{m^2 + p_T^2 \cosh^2 \eta}; p_T \cos \phi, p_T \sin \phi, p_T \sinh \eta).$$

10. Invariant mass of n particles: $M \equiv \sqrt{(p_1^\mu + p_2^\mu + \dots + p_n^\mu)^2} = \sqrt{(E_1 + E_2 + \dots)^2 - (\vec{p}_1 + \vec{p}_2 + \dots)^2}$.
11. Invariant mass of 2 particles: $M = \sqrt{E_1^2 + E_2^2 + 2E_1E_2 - p_1^2 - p_2^2 - 2\vec{p}_1 \cdot \vec{p}_2}$.
12. Invariant mass of 2 particles for $(E_i/p_i) \rightarrow 1$: $M = \sqrt{2p_1p_2(1 - \cos \theta)}$.
13. Transverse mass of 2 particles: $M_T \equiv \sqrt{(E_1 + E_2)^2 - (\vec{p}_{T1} + \vec{p}_{T2})^2}$.
14. Transverse mass of 2 particles for $(E_i/p_i) \rightarrow 1$: $M_T = \sqrt{2p_{T1}p_{T2}(1 - \cos \theta)}$.
15. Transverse hadronic activity: $H_T \equiv \sum_i p_T(jet_i)$ (where the sum runs over all jets above some thresholds, which in particular analysis are $p_T > 30$ GeV, $|\eta| < 4.5$).
16. Hadronic recoil: $\vec{H}_T^{miss} \equiv -\sum_i \vec{p}_T(jet_i)$ where the sum runs over all jets. (Usually used in Z+jets samples where is equal with the $p_T(Z)$). It is true that: $|\vec{H}_T^{miss}| \neq H_T$ due to the threshold(s) imposed to selected jets in H_T .
17. Transverse missing energy (or momentum): $\vec{E}_T \equiv -\sum_i \vec{p}_T(i)$ where the sum runs over, all reconstructed objects: jets, leptons, taus, photons (without cut thresholds).
18. Transverse leptonic activity: $L_T \equiv p_T(\ell_1) + \vec{E}_T$ (definition used only in current analysis)
19. Lepton (absolute) isolation: $I^{abs} \equiv \sum_i p_{T,i}^{charged\ hadr.} + \sum_i E_{T,i}^\gamma + \sum_i E_{T,i}^{neutral\ hadr.}$, for all particles with: $\Delta R(\ell, i) < 0.4$.
20. Lepton relative isolation: $I^{rel} \equiv I^{abs}/p_T(\ell)$.

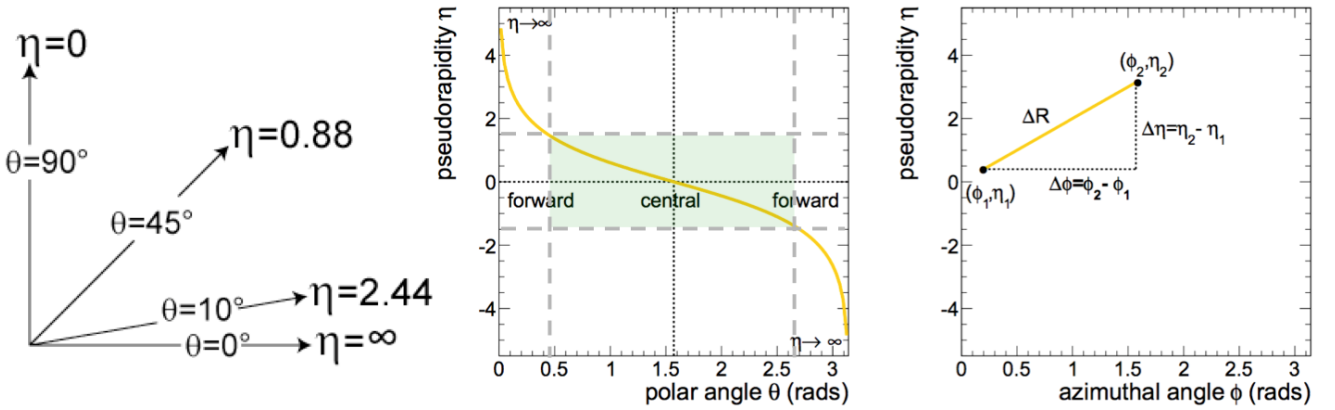


Figure A.1: The pseudorapidity η versus θ . Leptons with $|\eta| < 1.5$ or $25^\circ < \theta < 155^\circ$ are considered in the signal region of the analysis. (Taken from [2]).

Appendix B

Supersymmetry, calculations and additional material

B.1 Superspace

The four-momentum P_μ is a translation symmetry operator¹; it is defined by:

$$\Phi(x + a) = e^{-a^\mu P_\mu} \Phi(x) e^{ia^\mu P_\mu}, \quad (\text{B.1})$$

where $a = a^\mu$, ($\mu : 0, 1, 2, 3$) is a set of four constant space-time coordinates. In parallel to the energy-momentum operator (P_μ), we consider the superfield operators $Q_a, \bar{Q}_{\dot{a}}$ as generators of the translation in the fermionic coordinate system expressed by the Grassmann numbers. To match the four (space-time) dimensions, we consider four fermionic coordinates as elements of a Majorana spinor or as a pair of 2-component Weyl spinors. Points in super-space are identified by the coordinates: $z = (x^\mu, \theta^\mu, \bar{\theta}_{\dot{a}}) = (x^\mu, \theta^1, \theta^2, \bar{\theta}_{\dot{1}}, \bar{\theta}_{\dot{2}})$. Commutators of the super-coordinates satisfy the following relations:

$$\begin{aligned} \{\theta^a, \theta^\beta\} &= \{\bar{\theta}_{\dot{a}}, \bar{\theta}_{\dot{\beta}}\} = \{\theta^a, \bar{\theta}_{\dot{\beta}}\} = 0 \\ [x^\mu, \theta^a] &= [x^\mu, \bar{\theta}_{\dot{\beta}}] = 0 \end{aligned} \quad (\text{B.2})$$

where always the indices a, \dot{a} runs from 1 to 2 and $(\theta^a)^* \equiv \bar{\theta}^{\dot{a}}$.

A translational operator (an element of the super group) $L(x, \theta, \bar{\theta})$ is then defined. The superfield $\Phi(x, \theta, \bar{\theta})$ is the operand of the SUSY generators, which is a function of space-time and superspace coordinate variables:

$$\begin{aligned} L(x, \theta, \bar{\theta}) &\equiv \exp[i(-x^\mu P_\mu + \theta^a Q_a + \bar{\theta}_{\dot{a}} \bar{Q}^{\dot{a}})] \\ \Phi(x, \theta, \bar{\theta}) &= L(x, \theta, \bar{\theta}) \Phi_0 L^{-1}(x, \theta, \bar{\theta}) \end{aligned} \quad (\text{B.3})$$

Using the ‘‘Poincare algebra’’ and the ‘‘Baker-Campbell-Hausdorff’’ formula:

$$e^A e^B = e^{A+B+[A,B]/2+[A,[A,B]]/12-[B,[B,A]]/12+\dots}, \quad (\text{B.4})$$

one can prove that:

$$\begin{aligned} [\xi Q, \bar{\theta} \bar{Q}] &= 2(\xi \sigma^\mu \bar{\theta}) P_\mu, \\ [\bar{\xi} \bar{Q}, \theta Q] &= -2(\theta \sigma^\mu \bar{\xi}) P_\mu, \\ [\xi Q, \theta Q] &= 0, \\ [\bar{\xi} \bar{Q}, \bar{\theta} \bar{Q}] &= 0. \end{aligned} \quad (\text{B.5})$$

And with these relations the transformation property of the super-generator is obtained:

$$S \Phi(x, \theta, \bar{\theta}) \equiv L(0, \xi, \bar{\xi}) \Phi(x, \theta, \bar{\theta}) L^{-1}(0, \xi, \bar{\xi}) = \Phi(x^\mu + i[\theta \sigma^\mu \bar{\xi} - \xi \sigma^\mu \bar{\theta}], \theta^a + \xi^a, \bar{\theta}_{\dot{a}} + \bar{\xi}_{\dot{a}}). \quad (\text{B.6})$$

¹Subsection follows reference [126] §4.2.3 by Yorikiyo Nagashima.

The important thing to notice is that translations in the super-coordinates necessarily induce translations in the space-time coordinates as well. The interpretation of the super-generator as a translation operator of the fermionic coordinates is valid, but unlike the space-time translation, does not have a simple expression. For most purposes, it is sufficient to consider infinitesimal transformations, which can be written as follows:

$$\delta_S(\xi, \bar{\xi})\Phi(x, \theta, \bar{\theta}) = i[\xi Q + \bar{\xi}\bar{Q}, \Phi(x, \theta, \bar{\theta})] = (\dots)\Phi(x, \theta, \bar{\theta}) \quad (\text{B.7})$$

which corresponds to the following explicit representation of the SUSY generators:

$$iQ_a \equiv \nabla_a - i(\sigma_{a\dot{a}}^\mu)\bar{\theta}^{\dot{a}}\partial_\mu = D_a, \quad i\bar{Q}_{\dot{a}} \equiv -\bar{\nabla}_{\dot{a}} + i\theta^a(\sigma_{a\dot{a}}^\mu)\partial_\mu = \bar{D}_{\dot{a}} \quad (\text{B.8})$$

where the definitions: $\nabla_a \equiv \partial/\partial\theta^a$, $\bar{\nabla}_{\dot{a}} \equiv \partial/\partial\bar{\theta}^{\dot{a}} = -\epsilon_{\dot{a}\beta}\partial/\partial\bar{\theta}^{\dot{\beta}}$, have been introduced in order to avoid confusion with the space-time derivatives ∂_μ . A valid global symmetry should apply also to the derivatives of the field as both the field itself (f) and its derivatives appear in the Lagrangian. An important notion in SUSY is that $\nabla_a f$ and $\bar{\nabla}_{\dot{a}} f$ do not satisfy the global SUSY transformation hence they are not superfields. By global symmetry, we mean that SUSY operators satisfy the commutation relations defined by equations (2.29). Notice that $\partial_\mu f$ is a superfield because it satisfies the global SUSY but: $\nabla_a f$, $\bar{\nabla}_{\dot{a}} f$ are not (this can be seen by looking at its commutators with the symmetry operators.) We have to find differential operators that commute with the SUSY operators. This can be achieved by defining the covariant derivatives D_a , $\bar{D}_{\dot{a}}$ (equation B.8) which satisfy the following relations:

$$\begin{aligned} \{D_\beta, Q_a\} = \{D_\beta, \bar{Q}_{\dot{a}}\} = \{\bar{Q}_{\dot{\beta}}, D_a\} = \{\bar{D}_{\dot{\beta}}, \bar{Q}_{\dot{a}}\} = \{D_a, D_\beta\} = \{\bar{D}_{\dot{a}}, \bar{D}_{\dot{\beta}}\} = 0, \\ \{D_a, \bar{D}_{\dot{\beta}}\} = -2i(\sigma_{\dot{a}\beta}^\mu)\partial_\mu, \\ (D^3)_a \equiv (D^\beta D_\beta)D_a = (\bar{D}^3)_{\dot{a}} \equiv (\bar{D}^{\dot{\beta}}\bar{D}_{\dot{\beta}})\bar{D}_{\dot{a}} = 0. \end{aligned}$$

For reference, in the four-component representation, we have:

$$\Theta^{(4)} \equiv (\theta_a, \bar{\theta}^{\dot{a}})^T, \quad \bar{\Theta}^{(4)} \equiv (\theta^a, \bar{\theta}_{\dot{a}}) \Rightarrow \left(\frac{\partial}{\partial\Theta}\right)_a^{(4)} \equiv \left(\frac{\partial}{\partial\theta_a}, \frac{\partial}{\partial\bar{\theta}^{\dot{a}}}\right), \quad \left(\frac{\partial}{\partial\bar{\Theta}}\right)_a^{(4)} \equiv \left(\frac{\partial}{\partial\theta^a}, \frac{\partial}{\partial\bar{\theta}_{\dot{a}}}\right)^T \quad (\text{B.9})$$

We can re-write and summarize the four-component operators as, follows:

$$Q^{(4)} = \begin{bmatrix} Q_a \\ \bar{Q}_{\dot{a}} \end{bmatrix} = \begin{bmatrix} \nabla_a \\ \bar{\nabla}_{\dot{a}} \end{bmatrix} = -i \begin{bmatrix} 0 & \sigma_{a\dot{\beta}}^\mu \\ \bar{\sigma}^{\mu\dot{a}\beta} & 0 \end{bmatrix} \begin{bmatrix} \theta_\beta \\ \bar{\theta}^{\dot{\beta}} \end{bmatrix} \partial_\mu = \left[\frac{\partial}{\partial\bar{\Theta}}\right]^{(4)} - i\gamma^\mu\Theta\partial_\mu \quad (\text{B.10})$$

$$D_a^{(4)} = \begin{bmatrix} D_a \\ \bar{D}_{\dot{a}} \end{bmatrix} = \left(\frac{\partial}{\partial\bar{\Theta}}\right)_a^{(4)} + i(\gamma^\mu\Theta)_a\partial_\mu \quad (\text{B.11})$$

B.2 Chiral superfield

Consider a superfield $F(x, \theta, \bar{\theta})$, which is a function of $x^\mu, \theta^a, \bar{\theta}_{\dot{a}}$, then F could belong to an arbitrary representation of the Lorentz group but first we consider a scalar field¹. The Taylor expansion in powers of θ and $\bar{\theta}$ terminates at finite order $\theta\theta, \bar{\theta}\bar{\theta}$, since the variables are anti-commuting Grassmann numbers. Thus F can be expanded [123, 126] as follows:

$$F(x, \theta, \bar{\theta}) = A + \theta\psi + \bar{\theta}\bar{\chi} + m\theta\theta + n\bar{\theta}\bar{\theta} + \theta\sigma^\mu\bar{\theta}V_\mu + \theta\theta\bar{\theta}\bar{\lambda} + \bar{\theta}\bar{\theta}\theta\xi + \theta\theta\bar{\theta}\bar{d} \quad (\text{B.12})$$

There are four complex scalar components A, m, n, d , a complex vector V^μ , two Weyl spinors: ψ, ξ that belong to $(1/2, 0)$, and two more Weyl spinors χ, λ , belonging to $(0, 1/2)$. All these are functions of x^μ . Altogether, there are 16 real bosonic and 16 fermionic degrees of freedom.

¹Subsection follows reference [126] §4.3 by Yorikiyo Nagashima.

The transformation laws for each component under the SUSY operator can be obtained by comparing powers of θ and $\bar{\theta}$ in the equation $\delta F = \delta_\eta F + \delta_{\bar{\eta}} F = \delta A + \theta\delta\psi + \dots$; with the definitions:

$$\delta_\eta F = \eta^a i Q_a F, \quad \delta_{\bar{\eta}} F = \bar{\eta}_{\dot{a}} i \bar{Q}^{\dot{a}} F \quad (\text{B.13})$$

and $Q_a, \bar{Q}_{\dot{a}}$ defined in (B.8). A set of constraints can be derived for $\delta A, \delta\psi_a, \delta\bar{\chi}^{\dot{a}}, \delta m, \delta n, \delta V_\mu, \delta\bar{\lambda}^{\dot{a}}, \delta\xi_a, \delta d$. Given that the components are reducible under SUSY operations, which means that not all of the derived conditions are required to close the algebra, a condition to make them irreducible is imposed. One widely used set of conditions is the following:

$$\begin{aligned} \bar{D}_{\dot{a}} \Phi_L(x, \theta, \bar{\theta}) &= [-\bar{\nabla}_a + i\theta^a (\sigma_{a\dot{a}}^\mu \partial_\mu) \Phi_L(x, \theta, \bar{\theta}) = 0, \\ D_a \Phi_R(x, \theta, \bar{\theta}) &= [\nabla_a - i(\sigma_{a\dot{a}}^\mu \bar{\theta}^{\dot{a}} \partial_\mu) \Phi_R(x, \theta, \bar{\theta}) = 0, \end{aligned} \quad (\text{B.14})$$

where the first defines a chiral (left-handed) superfield Φ_L and similarly the second, a chiral (right-handed) superfield Φ_R .

The chiral superfield Φ_L can be solved in terms of new variables defined by: $y^\mu \equiv x^\mu + i\theta\sigma^\mu\bar{\theta}$. It can be shown that $\bar{D}_{\dot{a}} y^\mu = \bar{D}_{\dot{a}} \theta_a$. Therefore, any function of y, θ is a solution to $\bar{D}_{\dot{a}} \Phi$. That is:

$$\Phi_L(x, \theta, \bar{\theta}) = \Phi'(y, \theta) = \Phi'(x^\mu + i\theta\sigma^\mu\bar{\theta}, \theta) \quad (\text{B.15})$$

where Φ' can be any function of y, θ . Using a Taylor expansion, the field Φ' can be expressed as: $\Phi'(y, \theta) = A(y) + \sqrt{2}\theta^a \psi_a(y) + \theta\theta F(y)$.

The superfield satisfying the first condition of (B.14), contains only two scalar fields A, F and a left-handed Weyl spinor ψ . Notice that the chiral superfield has dimension $[E]$. It follows that the field $F(x)$ has dimension $[E^2]$, which is an indication that it is not a conventional scalar field. The expression for $\Phi_L(x, \theta, \bar{\theta})$ can be derived by going back to the original variable x .

Finally after some calculations the chiral superfield can be expressed as:

$$\Phi'(x, \theta, \bar{\theta}) = A + \sqrt{2}\theta^a \psi_a + \theta\theta F + i(\theta\sigma^\mu\bar{\theta})\partial_\mu A + \frac{i}{\sqrt{2}}\theta\theta\bar{\theta}_{\dot{a}}\sigma^{\mu\dot{a}a}\partial_\mu\bar{\psi} - \frac{1}{4}\theta\theta\bar{\theta}\bar{\theta}\partial_\mu\partial^\mu A \quad (\text{B.16})$$

Variations under the super-translation of the component fields A, ψ, F in the chiral superfield Φ_L follow by applying the formulas $\delta_\eta A, \delta_\eta \psi_a, \delta_\eta \phi$ and for the infinitesimal $\eta\bar{\eta}$ are given by:

$$\begin{aligned} \delta_\eta A &= \sqrt{2}\eta^a \psi_a, \\ \delta_\eta \psi_a &= \sqrt{2}[\eta_a F + i(\sigma^\mu\bar{\eta})\partial_\mu A], \\ \delta_\eta \phi &= \sqrt{2}i\bar{\eta}\bar{\sigma}^\mu\theta_\mu\psi. \end{aligned} \quad (\text{B.17})$$

Where we can see that no fields other than A, ψ, F appear in the transformed fields. Every component in equation (B.16) transforms to each other, and hence the SUSY algebra is closed by itself. The chiral left-handed superfield constitutes an irreducible representation. It also means that the field F is a necessary ingredient to have a consistent SUSY algebra.

In a similar set of steps one can derive the (right-handed) superfield Φ_R relation which is:

$$\Phi_R(x, \theta, \bar{\theta}) = \Phi'(z, \bar{\theta}) = \Phi'(x^\mu - i\theta\sigma^\mu\bar{\theta}, \theta), \quad Taylor \Rightarrow \Phi'_R = A^*(z) + \sqrt{2}\bar{\theta}_{\dot{a}}\bar{\psi}^{\dot{a}}(z) + \bar{\theta}\bar{\theta}F^*(z) \quad (\text{B.18})$$

where: $z^\mu \equiv x^\mu - i\theta\sigma^\mu\bar{\theta}$, and: $D_a z^\mu = D_a \bar{\theta}_{\dot{a}} = 0$. From the above equation, one can see that the right-handed chiral superfield is the one of the left-handed field. A right-handed superfield is a complex conjugate of a left-handed superfield and contains only the complex conjugate of a scalar field and a right-handed Weyl field.

Products of chiral superfields are again chiral superfields. This can be seen by explicitly making products of two left-handed scalar chiral fields. By induction, product of three left-handed chiral superfields is again a left-handed chiral superfield. Similar results hold for the conjugate, that is, right-handed chiral fields. Note that products of left- and right-handed chiral superfields are in general neither chiral nor anti-chiral.

B.3 Invariant action and Lagrangians

The action for SUSY in superspace is given by¹:

$$S = \int d^4x L(x), \quad L(x) = \int d^2\theta d^2\bar{\theta} \mathcal{L}(x)[\Phi(x, \theta, \bar{\theta}), V(x, \theta, \bar{\theta})], \quad (\text{B.19})$$

where the integration is over four-dimensional super-coordinates: $\theta^1, \theta^2, \bar{\theta}_1, \bar{\theta}_2$ as well as over space-time. We will ignore the vector field for a while in terms of simplicity. We use the following identities for intergration over a Grassmann variable η :

$$\int d\eta = 0, \quad \int \eta d\eta = 1, \quad \theta\theta = \theta^a\theta_a = \theta^a\epsilon_{ab}\theta^b = -\theta^1\theta^2. \quad (\text{B.20})$$

One thus obtains:

$$\int \theta\theta d^2\theta \equiv c \int (-2\theta^1\theta^2) d\theta^1 d\theta^2 = 2c \int \theta^1 d\theta^1 \int \theta^2 d\theta^2 = 2c \quad (\text{B.21})$$

therefore, we have $c=1/2$. The $d^2\theta$ and $d^2\bar{\theta}$ can be expressed as:

$$d^2\theta = -\frac{1}{4}\epsilon_{ab}d\theta^a d\theta^b, \quad \int \theta\theta d^2\theta = 1, \quad d^2\bar{\theta} = -\frac{1}{4}\epsilon^{\dot{a}\dot{b}}d\bar{\theta}_{\dot{a}}d\bar{\theta}_{\dot{b}}, \quad \int \bar{\theta}\bar{\theta} d^2\bar{\theta} = 1 \quad (\text{B.22})$$

We will consider the integration of a superfield that is at most quadratic in θ :

$$f(\theta) = A + \theta^a B_a + C\theta\theta, \quad \Rightarrow \quad \int d^2\theta(A + \theta^a B_a + C\theta\theta) = C \quad (\text{B.23})$$

with a similar equation for the $\int d^2\bar{\theta}g(\bar{\theta})$. Consequently, the only non vanishing terms in equation (B.19) are those proportional to: $\theta\theta\bar{\theta}\bar{\theta}$. When the integrand contains a function of: θ or $\bar{\theta}$ only, the $L(x)$ is to be understood to stands for the following:

$$L(x) = \int d^2\theta d^2\bar{\theta} [\mathcal{L}_L[\Phi_L(x, \theta)]\delta(\bar{\theta}\bar{\theta}) + \mathcal{L}_R[\Phi_R(x, \bar{\theta})]\delta(\theta\theta) + \mathcal{L}[\Phi(x, \theta, \bar{\theta})]] \quad (\text{B.24})$$

where $\delta(\theta\theta)$ is a δ -function whose integral gives 1. That is, the superspace integral picks up the highest order component of the Lagrangian made of superfields. All other terms vanish upon integration.

The action that is invariant under the SUSY should satisfy the relation

$$\delta_S S = \int \delta_S \mathcal{L}(x) d^4x = 0 \quad (\text{B.25})$$

This means that the SUSY action should give $\delta_S \mathcal{L}=0$ up to a total divergence. We have seen that the highest component of a superfield always gives a total divergence upon the symmetry operation (B.17). If they also have the proper Lorentz structure, like those of kinetic energy, a mass term or a potential, they are candidates of the Lagrangian. By demonstrating that the superspace integration of the action picks up only the highest component of the superfields, we have just proven that the action defined by equation (B.19) is SUSY-invariant.

In the following, we consider building a Lagrangian using irreducible representations of the superfields, namely the chiral fields and the vector fields. The vector fields are real. The chiral fields contain either θ only (left-handed) or $\bar{\theta}$ only (right-handed). As the Lagrangian has to be Hermitian and the right-handed chiral fields are obtained by taking the Hermitian conjugate of the left-handed fields, we can separate the Lagrangian into two:

$$L(x) = \int \left[\left(\int d^2\theta \mathcal{L}_L + h.c. \right) + \int d^2\theta d^2\bar{\theta} \mathcal{L} \right] = \int d^2\theta d^2\bar{\theta} [(\mathcal{L}_L \delta(\theta\theta) + h.c.) + \mathcal{L}] \quad (\text{B.26})$$

¹Subsection follows reference [126] §4.5 by Yorikiyo Nagashima.

where $\delta(\theta\theta)$ is the δ -function. From now on we omit to attach the index “ L ” to the chiral superfield and simply denote it as Φ unless otherwise specified.

It can be seen that the products of chiral fields contain mass terms and Yukawa interactions, which are candidates to be included in the chiral part of the Lagrangian (B.26).

We now briefly discuss the kinetic energy of the chiral superfield. A second order or square of the derivatives is necessary to construct the kinetic energy part of the Lagrangian. We have seen already that chiral fields or their products contain no derivatives at least in the L or R representation. Let us consider the product of a left-chiral field and its conjugate. As the left-handed field is in the L representation and its conjugate is in the R representation, we need to unify the representation to handle their product. Expressing the left-chiral field as in (B.16) we have:

$$\Phi(x, \theta, \bar{\theta}) = [A] + [\sqrt{2}\theta^a\psi_a] + [\theta\theta F] + [i(\theta^a\sigma_{\dot{a}a}^\mu\bar{\theta}^{\dot{a}})\partial_\mu A] + \left[\frac{i}{\sqrt{2}}\theta\theta\bar{\theta}^{\dot{a}}(\sigma_{\dot{a}a}^\mu\partial_\mu\psi^a)\right] - \left[\frac{1}{4}\theta\theta\bar{\theta}\bar{\theta}\partial_\mu\partial^\mu A\right] \quad (\text{B.27})$$

Where the fields: A, ψ_a, F are time-space function: $A(x), \psi_a(x), F(x)$. Taking the hermitian conjugate and noting the hermitian nature of the Grassmann variables, that is: $(\theta^a\bar{\theta}^{\dot{b}})^* = (\bar{\theta}^{\dot{b}})^*(\theta^a)^* = \theta^{\dot{b}}\bar{\theta}^a$, we have:

$$\Phi^\dagger(x, \theta, \bar{\theta}) = [A^*] + [\sqrt{2}\bar{\theta}_{\dot{a}}\bar{\psi}^{\dot{a}}] + [\bar{\theta}\bar{\theta}F^*] - [i(\theta^a\sigma_{\dot{a}a}^\mu\bar{\theta}^{\dot{a}})\partial_\mu A^*] + \left[\frac{i}{\sqrt{2}}\bar{\theta}\bar{\theta}\theta^a(\sigma_{\dot{a}a}^\mu\partial_\mu\bar{\psi}^{\dot{a}})\right] - \left[\frac{1}{4}\theta\theta\bar{\theta}\bar{\theta}\partial_\mu\partial^\mu A^*\right] \quad (\text{B.28})$$

We only need to consider the coefficients of $\theta\theta\bar{\theta}\bar{\theta}$ in the product $\Phi^\dagger\Phi$. The fermionic kinetic energy terms then arise from the crossed terms: $(2^{nd-term}\Phi \times 5^{th-term}\Phi^\dagger)$, and $(2^{nd-term}\Phi^\dagger \times 5^{th-term}\Phi)$; and the results after some algebra is:

$$= \frac{i}{2}[\partial_\mu\bar{\psi}^{\dot{a}}\bar{\sigma}_{\dot{a}a}^\mu\psi^a - \bar{\psi}^{\dot{a}}\bar{\sigma}_{\dot{a}a}^\mu\partial_\mu\psi^a]\theta\theta\bar{\theta}\bar{\theta} \quad (\text{B.29})$$

In the bosonic sector, the kinetic energy terms are: $(1^{st-term}\Phi \times 6^{th-term}\Phi^\dagger) + (6^{nd-term}\Phi^\dagger \times 1^{st-term}\Phi) + (3^{rd-term}\Phi \times 3^{rd-term}\Phi^\dagger) + (4^{nd-term}\Phi^\dagger \times 4^{th-term}\Phi)$; and the results after some algebra is:

$$= \left[\left(\frac{1}{2}\partial_\mu A^*\partial^\mu A - \frac{1}{4}\partial_\mu(A^*\partial^\mu A + \partial^\mu A^*A) \right) + FF^* + \frac{1}{2}g^{\mu\nu}\partial_\mu A^*\partial_\nu A \right] \theta\theta\bar{\theta}\bar{\theta} \\ = [\partial_\mu A^*\partial^\mu A + FF^* + \text{divergence terms}]\theta\theta\bar{\theta}\bar{\theta} \quad (\text{B.30})$$

Combining Eqs. (B.29) and (B.30), the Lagrangian for the kinetic energy part of the chiral fields two-component:

$$\mathcal{L}_{KE}^{Chiral}(x) = \int d^2\theta d^2\bar{\theta}\Phi^\dagger\Phi = \partial A^*\partial^\mu A + \frac{1}{2}[\partial_\mu\bar{\psi}^{\dot{a}}\bar{\sigma}_{\dot{a}a}^\mu\psi^a - \bar{\psi}^{\dot{a}}\bar{\sigma}_{\dot{a}a}^\mu\partial_\mu\psi^a] + FF^* \quad (\text{B.31})$$

The first two terms represent the kinetic energy of a scalar field and its super-partner left-handed Weyl field.

For a detailed extraction of all lagrangian terms one can see at: [122, 130, 116, 17, 123], here we further present only some final the results. Starting from definitions of the following chiral superfields: Φ_L, Φ_R and a vector superfield V_{WZ} (in the so-called “Wess-Zumino” gauge):

$$\Phi_L(x, \theta, \bar{\theta}) = \Phi'(y, \theta) = A(y) + \sqrt{2}\theta\psi(y) + \theta\theta F(y), \quad (\text{B.32})$$

$$\Phi_R(x, \theta, \bar{\theta}) = \Phi'(z, \theta) = A^*(z) + \sqrt{2}\bar{\theta}\bar{\psi}(z) + \bar{\theta}\bar{\theta}F^*(z), \quad (\text{B.33})$$

$$y = x - i(\theta^a\sigma_{\dot{a}a}^\mu\bar{\theta}^{\dot{a}}), \quad z = x + i(\theta^a\sigma_{\dot{a}a}^\mu\bar{\theta}^{\dot{a}}),$$

$$V_{WZ}(x, \theta, \bar{\theta}) = (\theta\sigma^\mu\bar{\theta})V_\mu(x) + \theta\theta\bar{\theta}\bar{\lambda}(x) + \bar{\theta}\bar{\theta}\theta\lambda(x) + \theta\theta\bar{\theta}\bar{\theta}\frac{1}{2}D(x) \quad (\text{B.34})$$

we will give the full Lagrangian describing all its interactions. The SUSY-invariant Lagrangian containing the chiral superfield (A_i, ψ_i) and the gauge superfield λ_a, V_a^μ in an explicit representation is

expressed as:

$$\mathcal{L}_{SUSY} \equiv \mathcal{L}_{gauge\ KE} + \mathcal{L}_{chiral\ KE} + \mathcal{L}_{superpotential}, \quad (\text{B.35})$$

$$\mathcal{L}_{gauge\ KE} \equiv \sum_a \left[\frac{1}{2} |D^a(x)|^2 - \frac{1}{4} F_{\mu\nu}^a F^{\mu\nu a} - i \lambda^a \sigma^\mu \partial_\mu \bar{\lambda}^a \right], \quad (\text{B.36})$$

$$\mathcal{L}_{chiral\ KE} \equiv \sum_i \left[|F_i(x)|^2 + i (D_\mu^* \bar{\psi}_i(x)) \bar{\sigma}^\mu \psi_i(x) + D_\mu^* A^*(x) D^\mu A(x) \right] + \quad (\text{B.37})$$

$$\sum_a \left[-\{ \sqrt{2} g \bar{\lambda}^a(x) [\bar{\psi}(x) T^a A(x)] + (c.c.) \} + g D^a(x) (A^*(x) T^a A(x)) \right],$$

$$[D_\mu]_{ij} \equiv \delta_{ij} \partial_\mu - i g \sum_a V_\mu^a [T^a]_{ij}$$

$$\mathcal{L}_{superpotential} \equiv \sum_i W_i F_i - \frac{1}{2} \sum_{j,k} W_{jk} \psi_j \psi_k + (h.c.) \quad (\text{B.38})$$

$$W_i = \frac{\partial W(A)}{\partial A_i}, \quad W_{ij} = \frac{\partial^2 W(A)}{\partial A_i \partial A_j}, \quad F_i = -W_i^* \equiv \left[\frac{\partial W(A)}{\partial A_i} \right]^*,$$

$$W(A) \equiv t_i A_i + \frac{1}{2} m_{ij} A_i A_j + \frac{1}{3} y_{ijk} A_i A_j A_k$$

where T^a is the gauge group generators and i, j, k denote the flavor of the chiral fields. The superpotential $W(A)$ is an analytic function of $A(x)$ treated as a complex number. That is, it does not contain the complex conjugate fields $A(x)$ or derivatives of the field.

B.4 Feynman diagrams for sparticles hadronic production and cross sections

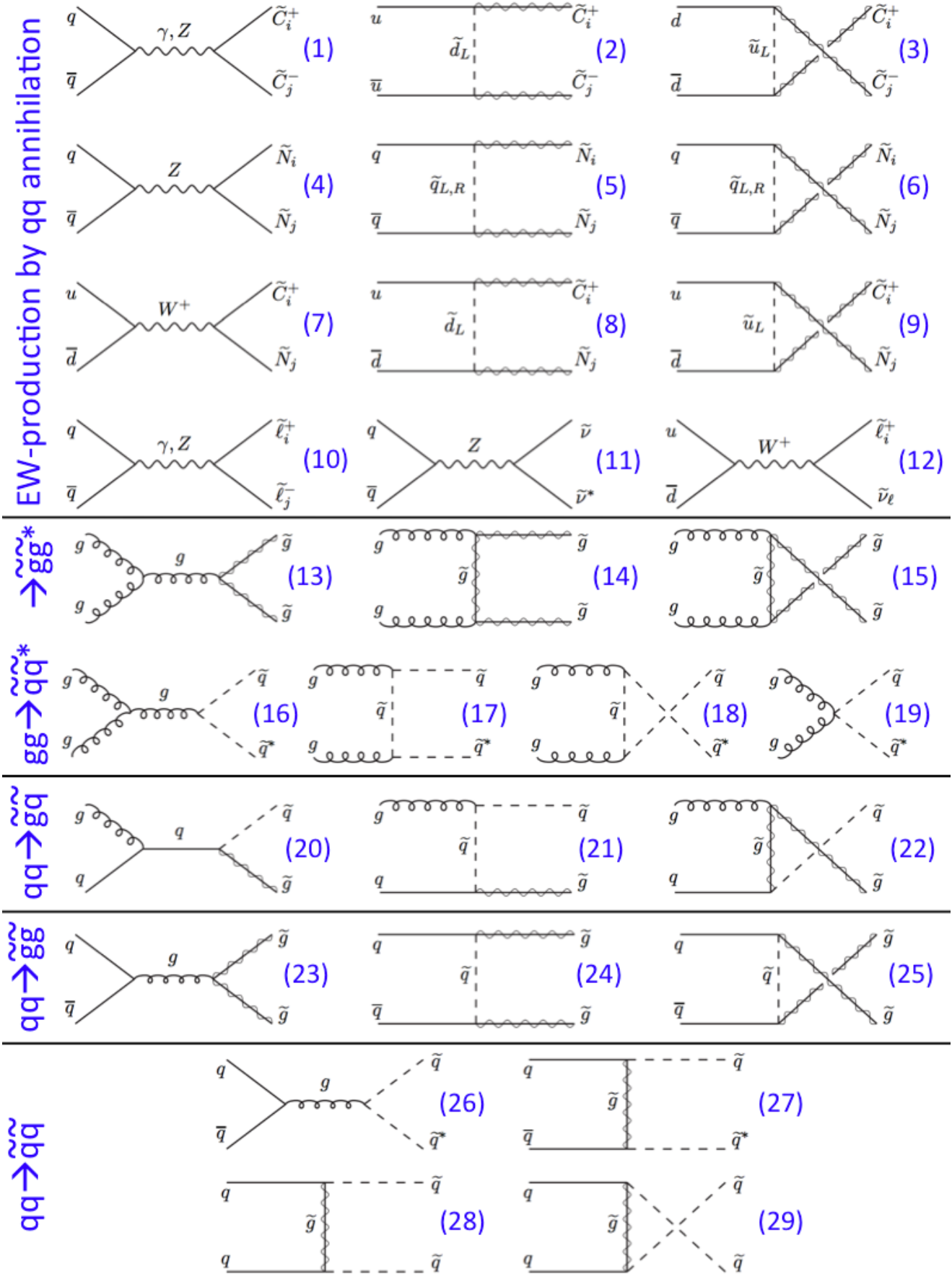


Figure B.1: Feynman diagrams for all possible particles production modes in hadronic collisions, i.e.: by annihilation or scattering of $q\bar{q}$, qg , gg . R-parity conservation is assumed and sparticles are produced in pairs. (Taken from [122]).

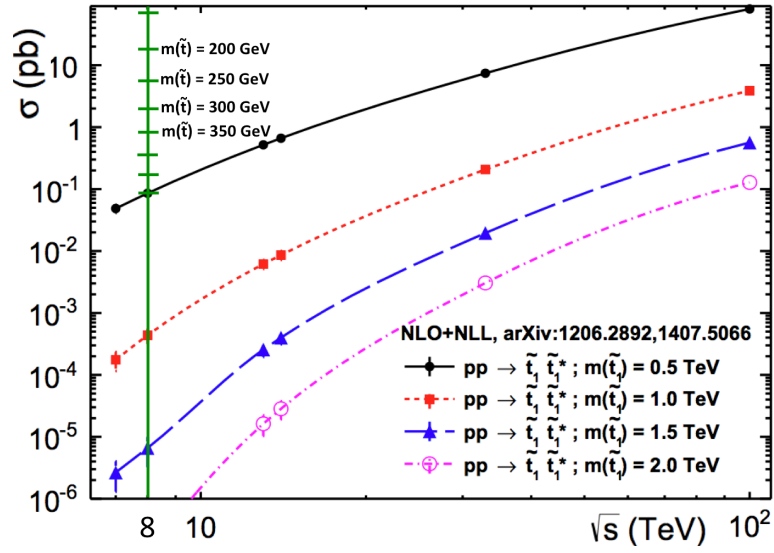


Figure B.2: The cross sections for $\tilde{t}\tilde{t}^*$ pair production as a function of \sqrt{s} for four different stop masses.

Stop-pair production in pp at 8 TeV						Chargino-Neutralino pair production, pp, 8 TeV								
$m(\tilde{t})$ [GeV]	σ [pb] \pm unc.	$m(\tilde{t})$ [GeV]	σ [pb] \pm unc.	$m(\tilde{t})$ [GeV]	σ [pb] \pm unc.	$m(\tilde{\chi}^\pm)$ [GeV]	σ [pb]	\pm unc.	$m(\tilde{\chi}^\pm)$ [GeV]	σ [pb]	\pm unc.	$m(\tilde{\chi}^\pm)$ [GeV]	σ [pb]	\pm unc.
105	448.456 \pm 15.9732%	205	16.2439 \pm 15.117%	305	1.81486 \pm 14.4434%	105	9.20	0.626	205	0.712	0.0326	305	0.136	0.00581
110	361.917 \pm 16.1134%	210	14.3201 \pm 14.8495%	310	1.64956 \pm 14.4769%	110	7.71	0.506	210	0.647	0.0300	310	0.127	0.00530
115	293.281 \pm 15.9763%	215	12.6497 \pm 14.8689%	315	1.50385 \pm 14.4549%	115	6.52	0.418	215	0.588	0.0273	315	0.118	0.00494
120	240.077 \pm 15.9212%	220	11.1808 \pm 14.9108%	320	1.3733 \pm 14.7503%	120	5.55	0.350	220	0.536	0.0237	320	0.110	0.00462
125	197.122 \pm 15.7303%	225	9.90959 \pm 14.9662%	325	1.25277 \pm 14.2875%	125	4.76	0.284	225	0.491	0.0214	325	0.102	0.00436
130	163.376 \pm 15.8101%	230	8.78125 \pm 14.796%	330	1.14277 \pm 14.578%	130	4.12	0.255	230	0.447	0.0199	330	0.0956	0.00408
135	135.791 \pm 15.8086%	235	7.81646 \pm 14.7983%	335	1.04713 \pm 14.3659%	135	3.55	0.204	235	0.411	0.0172	335	0.0894	0.00383
140	113.319 \pm 15.7234%	240	6.96892 \pm 14.7878%	340	0.959617 \pm 14.39%	140	3.10	0.172	240	0.377	0.0165	340	0.0837	0.00356
145	95.0292 \pm 15.649%	245	6.22701 \pm 14.7897%	345	0.879793 \pm 14.388%	145	2.71	0.154	245	0.346	0.0150	345	0.0787	0.00337
150	80.268 \pm 15.5946%	250	5.57596 \pm 14.7529%	350	0.807323 \pm 14.360%	150	2.39	0.126	250	0.318	0.0142	350	0.0737	0.00313
155	68.0456 \pm 15.5232%	255	5.00108 \pm 14.729%	355	0.74141 \pm 14.368%	155	2.11	0.118	255	0.293	0.0127	355	0.0690	0.00296
160	58.01 \pm 15.3899%	260	4.48773 \pm 14.6782%	360	0.681346 \pm 14.336%	160	1.86	0.0932	260	0.268	0.0115	360	0.0647	0.00277
165	49.6639 \pm 15.3711%	265	4.03416 \pm 14.7964%	365	0.626913 \pm 14.363%	165	1.66	0.0871	265	0.249	0.0109	365	0.0607	0.00262
170	42.6441 \pm 15.3017%	270	3.63085 \pm 14.6565%	370	0.576882 \pm 14.271%	170	1.48	0.0751	270	0.230	0.0962	370	0.0576	0.00245
175	36.7994 \pm 15.1749%	275	3.2781 \pm 14.7341%	375	0.531443 \pm 14.27%	175	1.32	0.0672	275	0.213	0.0915	375	0.0541	0.00228
180	31.8695 \pm 15.2449%	280	2.95613 \pm 14.7816%	380	0.489973 \pm 14.396%	180	1.18	0.0587	280	0.197	0.00870	380	0.0498	0.00221
185	27.7028 \pm 15.063%	285	2.67442 \pm 14.7661%	385	0.452072 \pm 14.223%	185	1.06	0.0525	285	0.182	0.00752	385	0.0473	2.07E-03
190	24.1585 \pm 15.16%	290	2.42299 \pm 14.6805%	390	0.4176 \pm 14.3166%	190	0.960	0.0461	290	0.171	0.00728	390	0.0445	0.00199
195	21.1597 \pm 14.9422%	295	2.19684 \pm 14.8465%	395	0.385775 \pm 14.311%	195	0.869	0.0407	295	0.158	0.00699	395	0.0418	0.00178
200	18.5245 \pm 14.9147%	300	1.99608 \pm 14.6905%	400	0.35683 \pm 14.2848%	200	0.785	0.0373	300	0.146	0.00661	400	0.0393	0.00167

Figure B.3: Production cross sections at pp-collisions in $\sqrt{s} = 8$ TeV used in the analysis. Left the $\tilde{t}\tilde{t}^*$ pair production, right the $\tilde{\chi}_1^\pm \tilde{\chi}_2^0$ pair production.

B.5 Current exclusion reach of sparticle searches

ATLAS SUSY Searches* - 95% CL Lower Limits

Status: Feb 2015

ATLAS Preliminary

$\sqrt{s} = 7, 8 \text{ TeV}$

Model	e, μ, τ, γ	Jets	$E_{T, \text{miss}} [L dT(fb^{-1})]$	Mass limit	Reference	
Inclusive Searches	MSUGRA/CMSSM	0	2-6 jets	Yes	\tilde{q}, \tilde{g}	1405.7875
	$\tilde{q}\tilde{q}, \tilde{q} \rightarrow q\tilde{\chi}_1^0$	0	2-6 jets	Yes	\tilde{q}	1405.7875
	$\tilde{q}\tilde{q}, \tilde{q} \rightarrow q\tilde{\chi}_1^0$ (compressed)	1 γ	0-1 jet	Yes	\tilde{q}	1411.1559
	$\tilde{g}\tilde{g}, \tilde{g} \rightarrow q\tilde{q}\tilde{\chi}_1^0$	0	2-6 jets	Yes	\tilde{g}	1405.7875
	$\tilde{g}\tilde{g}, \tilde{g} \rightarrow q\tilde{q}\tilde{\chi}_1^0$	1 e, μ	3-6 jets	Yes	\tilde{g}	1501.03555
	$\tilde{g}\tilde{g}, \tilde{g} \rightarrow q\tilde{q}\tilde{\chi}_1^0$	2 e, μ	0-3 jets	-	\tilde{g}	1501.03555
	GMSB ($\tilde{\chi}$ NLSP)	1-2 $\tau + 0-1 \ell$	0-2 jets	Yes	\tilde{g}	1407.0603
	GGM (bino NLSP)	2 γ	-	Yes	\tilde{g}	ATLAS-CONF-2014-001
	GGM (wino NLSP)	1 $e, \mu + \gamma$	1 b	Yes	\tilde{g}	ATLAS-CONF-2012-144
	GGM (higgsino-bino NLSP)	γ	0-3 jets	Yes	\tilde{g}	1211.1167
3 rd gen. \tilde{g} med.	GGM (higgsino NLSP)	2 $e, \mu (Z)$	0-3 jets	Yes	\tilde{g}	ATLAS-CONF-2012-152
	Gravitino LSP	0	mono-jet	Yes	$F^{1/2}$ scale	1502.01518
	$\tilde{g} \rightarrow h\tilde{\chi}_1^0$	0	3 b	Yes	\tilde{g}	1407.0600
	$\tilde{g} \rightarrow t\tilde{\chi}_1^0$	0	7-10 jets	Yes	\tilde{g}	1308.1841
	$\tilde{g} \rightarrow b\tilde{\chi}_1^0$	0-1 e, μ	3 b	Yes	\tilde{g}	1407.0600
	$\tilde{g} \rightarrow h\tilde{\chi}_1^0$	0-1 e, μ	3 b	Yes	\tilde{g}	1407.0600
	$\tilde{g} \rightarrow h\tilde{\chi}_1^0$	0	2 b	Yes	\tilde{g}	1308.2631
	$\tilde{g} \rightarrow h\tilde{\chi}_1^0$	2 e, μ (SS)	0-3 b	Yes	\tilde{g}	1404.2500
	$\tilde{g} \rightarrow h\tilde{\chi}_1^0$	1-2 e, μ	1-2 b	Yes	\tilde{g}	1209.2102, 1407.0583
	$\tilde{g} \rightarrow h\tilde{\chi}_1^0$	2 e, μ	0-2 jets	Yes	\tilde{g}	1403.4853, 1412.4742
3 rd gen. squarks	$\tilde{t}_1\tilde{t}_1, \tilde{t}_1 \rightarrow b\tilde{\chi}_1^0$	0	2 b	Yes	\tilde{t}_1	1407.0583, 1406.1122
	$\tilde{t}_1\tilde{t}_1, \tilde{t}_1 \rightarrow b\tilde{\chi}_1^0$	2 e, μ (SS)	0-3 b	Yes	\tilde{t}_1	1407.0608
	$\tilde{t}_1\tilde{t}_1, \tilde{t}_1 \rightarrow b\tilde{\chi}_1^0$	1-2 e, μ	1-2 b	Yes	\tilde{t}_1	1403.5222
	$\tilde{t}_1\tilde{t}_1, \tilde{t}_1 \rightarrow W\tilde{\chi}_1^0$ or $\tilde{\chi}_1^0$	2 e, μ	0-2 jets	Yes	\tilde{t}_1	1403.5294
	$\tilde{t}_1\tilde{t}_1, \tilde{t}_1 \rightarrow W\tilde{\chi}_1^0$	0-1 e, μ	1-2 b	Yes	\tilde{t}_1	1407.7029
	$\tilde{t}_1\tilde{t}_1, \tilde{t}_1 \rightarrow W\tilde{\chi}_1^0$	0	mono-jet/c-tag	Yes	\tilde{t}_1	1403.5294, 1402.7029
	$\tilde{t}_1\tilde{t}_1, \tilde{t}_1 \rightarrow W\tilde{\chi}_1^0$	2 $e, \mu (Z)$	1 b	Yes	\tilde{t}_1	1501.07110
	$\tilde{t}_1\tilde{t}_1$ (natural GMSB)	3 $e, \mu (Z)$	1 b	Yes	\tilde{t}_1	1405.5086
	$\tilde{t}_1\tilde{t}_1, \tilde{t}_1 \rightarrow \tilde{t}_1 + Z$	0	0	Yes	\tilde{t}_1	1403.5222
	$\tilde{t}_1\tilde{t}_1, \tilde{t}_1 \rightarrow \tilde{t}_1 + Z$	2 e, μ	0	Yes	\tilde{t}_1	1403.5294
EW direct	$\tilde{\chi}_1^0\tilde{\chi}_1^0, \tilde{\chi}_1^0 \rightarrow \tilde{\chi}_1^0$	2 e, μ	0	Yes	$\tilde{\chi}_1^0$	1403.5294
	$\tilde{\chi}_1^0\tilde{\chi}_1^0, \tilde{\chi}_1^0 \rightarrow \tilde{\chi}_1^0$	2 τ	-	Yes	$\tilde{\chi}_1^0$	1407.0350
	$\tilde{\chi}_1^0\tilde{\chi}_1^0, \tilde{\chi}_1^0 \rightarrow \tilde{\chi}_1^0$	3 e, μ	0	Yes	$\tilde{\chi}_1^0$	1402.7029
	$\tilde{\chi}_1^0\tilde{\chi}_1^0, \tilde{\chi}_1^0 \rightarrow \tilde{\chi}_1^0$	2-3 e, μ	0-2 jets	Yes	$\tilde{\chi}_1^0$	1403.5294, 1402.7029
	$\tilde{\chi}_1^0\tilde{\chi}_1^0, \tilde{\chi}_1^0 \rightarrow \tilde{\chi}_1^0$	e, μ, γ	0-2 b	Yes	$\tilde{\chi}_1^0$	1501.07110
	$\tilde{\chi}_1^0\tilde{\chi}_1^0, \tilde{\chi}_1^0 \rightarrow \tilde{\chi}_1^0$	4 e, μ	0	Yes	$\tilde{\chi}_1^0$	1405.5086
	Direct $\tilde{\chi}_1^0\tilde{\chi}_1^0$ prod., long-lived $\tilde{\chi}_1^0$	Disapp. trk	1 jet	Yes	$\tilde{\chi}_1^0$	1310.3675
	Stable, stopped \tilde{g} R-hadron	0	1-5 jets	Yes	\tilde{g}	1310.6584
	Stable \tilde{g} R-hadron	trk	-	19.1	\tilde{g}	1411.6795
	GMSB, stable $\tilde{\chi}_1^0 \rightarrow \tilde{\chi}_1^0 + \tau(\ell, \mu)$	1-2 μ	-	19.1	$\tilde{\chi}_1^0$	1411.6795
GMSB, $\tilde{\chi}_1^0 \rightarrow \tilde{\chi}_1^0 + G$, long-lived $\tilde{\chi}_1^0$	2 γ	-	20.3	$\tilde{\chi}_1^0$	1409.5542	
Long-lived particles	$\tilde{q}\tilde{q}, \tilde{\chi}_1^0 \rightarrow q\tilde{q}$ (RPV)	1 μ , displ. vtx	-	20.3	\tilde{q}	ATLAS-CONF-2013-092
	LFV $p\tilde{p} \rightarrow \tilde{\nu}_\tau + X, \tilde{\nu}_\tau \rightarrow e\mu + \mu$	2 e, μ	-	4.6	$\tilde{\nu}_\tau$	1212.1272
	LFV $p\tilde{p} \rightarrow \tilde{\nu}_\tau + X, \tilde{\nu}_\tau \rightarrow e(\mu) + \tau$	1 $e, \mu + \tau$	-	4.6	$\tilde{\nu}_\tau$	1212.1272
	Bi-linear RPV CMSSM	2 e, μ (SS)	0-3 b	Yes	\tilde{g}, \tilde{q}	1404.2500
	$\tilde{\chi}_1^0\tilde{\chi}_1^0, \tilde{\chi}_1^0 \rightarrow W\tilde{\chi}_1^0, \tilde{\chi}_1^0 \rightarrow e\tilde{\nu}_\mu, e\tilde{\mu}_\tau$	4 e, μ	-	20.3	$\tilde{\chi}_1^0$	1405.5086
	$\tilde{\chi}_1^0\tilde{\chi}_1^0, \tilde{\chi}_1^0 \rightarrow W\tilde{\chi}_1^0, \tilde{\chi}_1^0 \rightarrow \tau\tilde{\nu}_\tau, e\tilde{\nu}_\tau$	3 $e, \mu + \tau$	-	20.3	$\tilde{\chi}_1^0$	1405.5086
	$\tilde{g} \rightarrow q\tilde{q}$	0	6-7 jets	-	\tilde{g}	ATLAS-CONF-2013-091
	$\tilde{g} \rightarrow t\tilde{t}, \tilde{t}_1 \rightarrow b\tilde{s}$	2 e, μ (SS)	0-3 b	Yes	\tilde{g}	1404.250
	Scalar charm, $\tilde{c} \rightarrow c\tilde{\chi}_1^0$	0	2 c	Yes	\tilde{c}	1501.01325
	Other					

*Only a selection of the available mass limits on new states or phenomena is shown. All limits quoted are observed minus 1σ theoretical signal cross section uncertainty.

Appendix C

Signal region kinematics

C.1 Additional kinematic variables distribution in SR preselection

All plots in this subsection stands for the preselection cuts listed in table 5.2. The SM simulated background processes with three SUSY signal points scaled by $\times 10$ are superimposed.

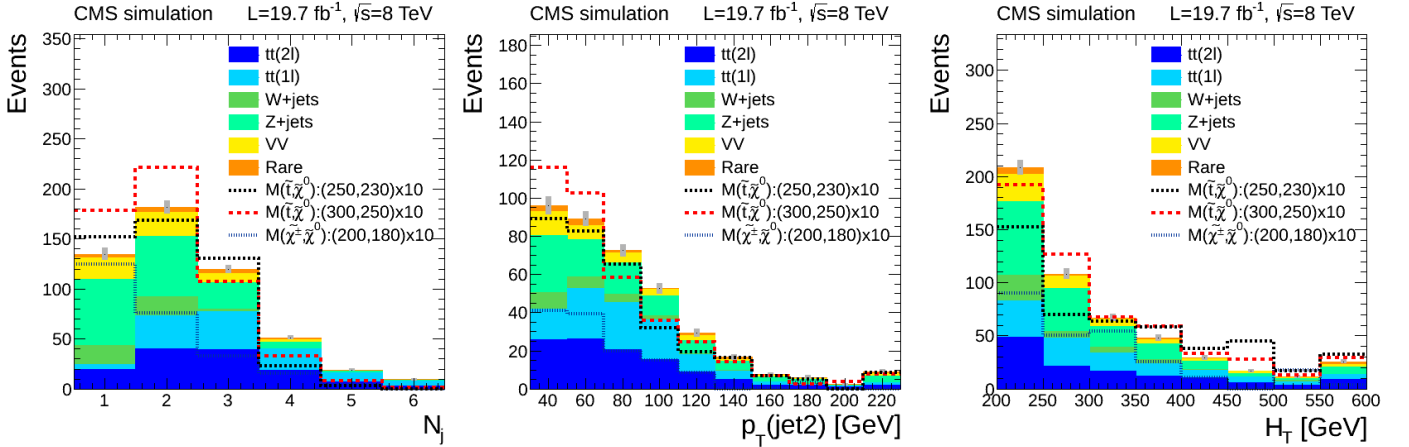


Figure C.1: The jet multiplicity N_j , $p_T(jet2)$, and H_T distributions for SR preselection.

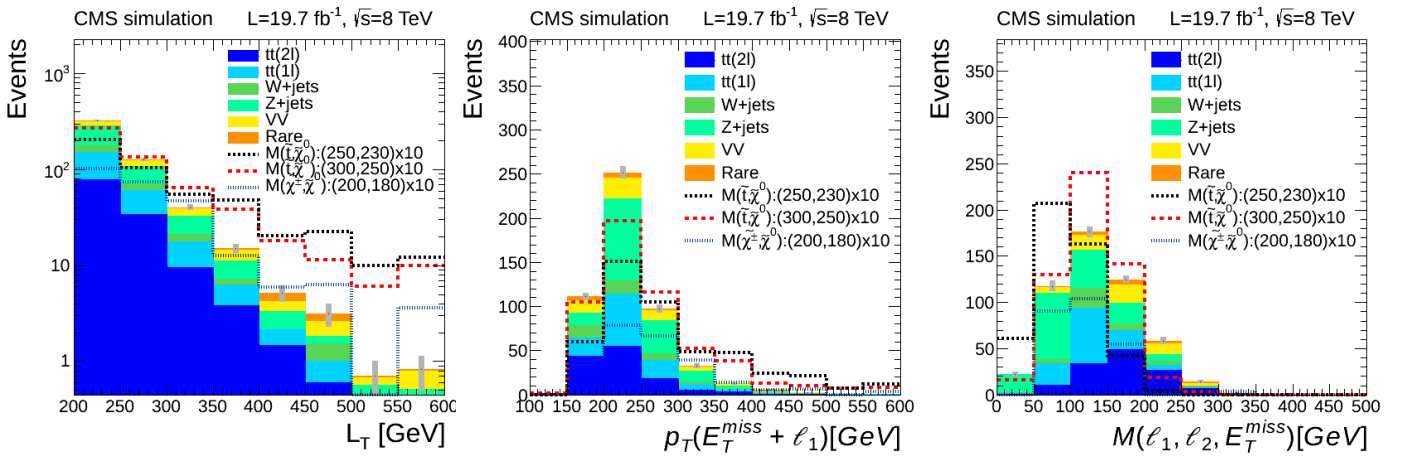


Figure C.2: The $L_T \equiv p_T(l_1) + \cancel{E}_T$, $|\vec{\cancel{E}}_T + \vec{p}_T(l_1)|$ and the $M(l_1, l_2, \cancel{E}_T) = [(p_{l_1} + p_{l_2} + \cancel{E}_T)^\mu (p_{l_1} + p_{l_2} + \cancel{E}_T)_\mu]^{0.5}$ distribution for preselected events.

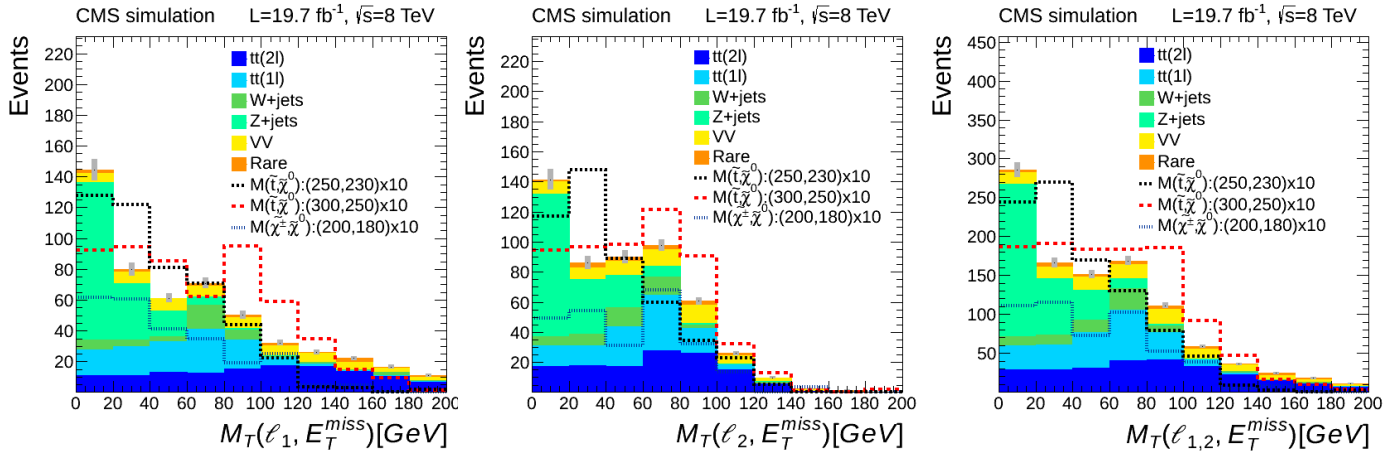


Figure C.3: The leading and subleading lepton transverse masses $M_T(\ell_1, \cancel{E}_T)$, $M_T(\ell_2, \cancel{E}_T)$ distributions, and both together.

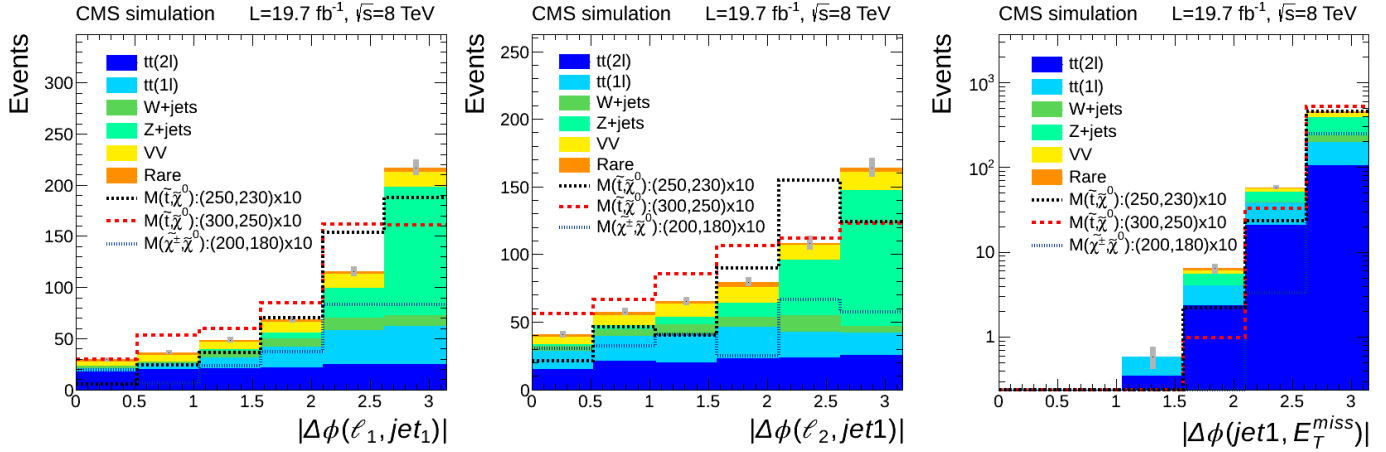


Figure C.4: The $|\Delta\phi(\ell_1, jet1)|$, $|\Delta\phi(\ell_2, jet1)|$, and $|\Delta\phi(\ell_1, \cancel{E}_T)|$ distributions for preselected events.

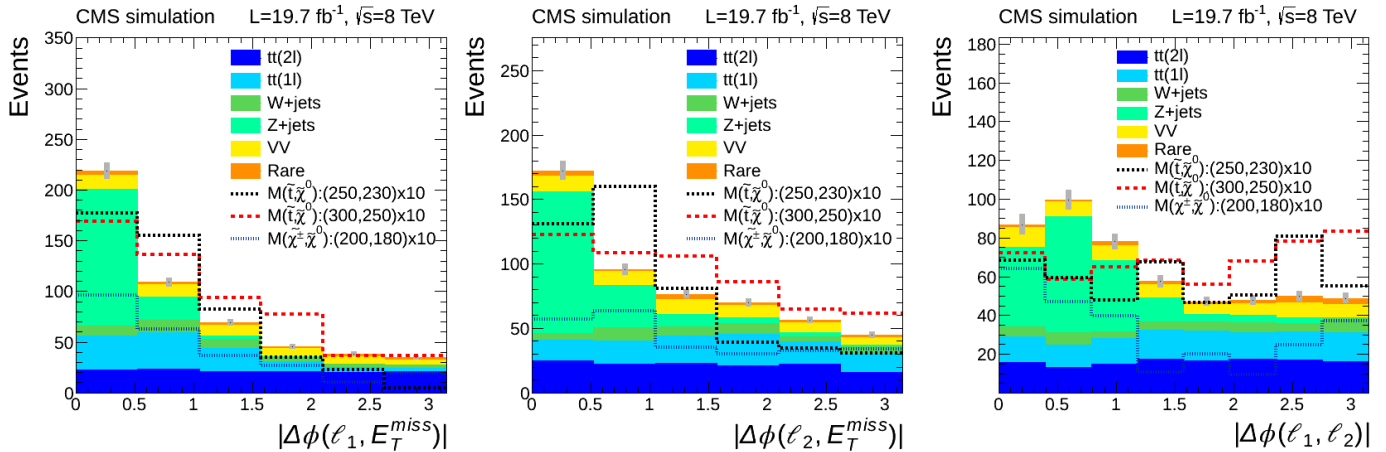


Figure C.5: The $|\Delta\phi(\ell_1, \cancel{E}_T)|$, $|\Delta\phi(\ell_2, \cancel{E}_T)|$, and $|\Delta\phi(jet1, \cancel{E}_T)|$ distribution for preselected events.

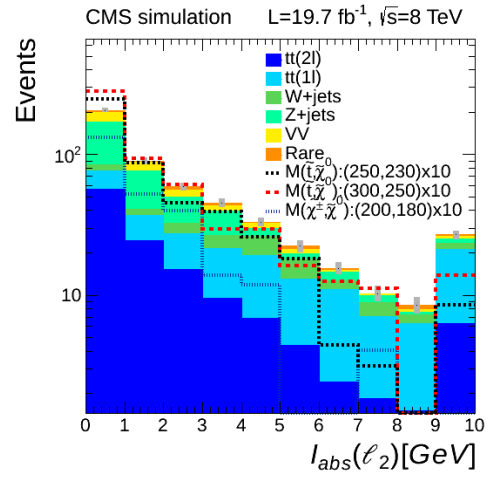
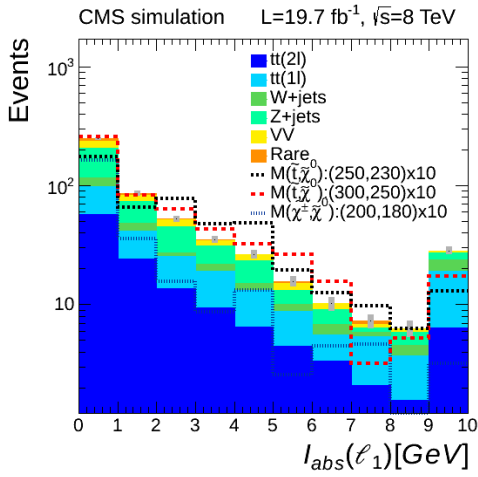


Figure C.6: Absolute isolation distributions for leading and sub-leading lepton in preselection.

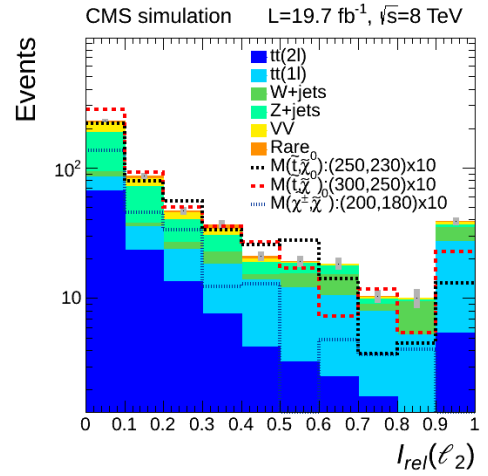
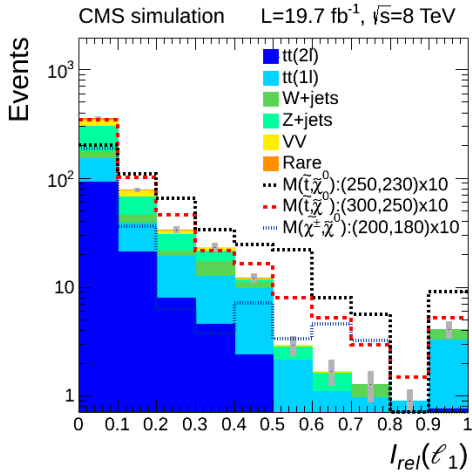


Figure C.7: Relative isolation distributions for leading and sub-leading lepton in preselection.

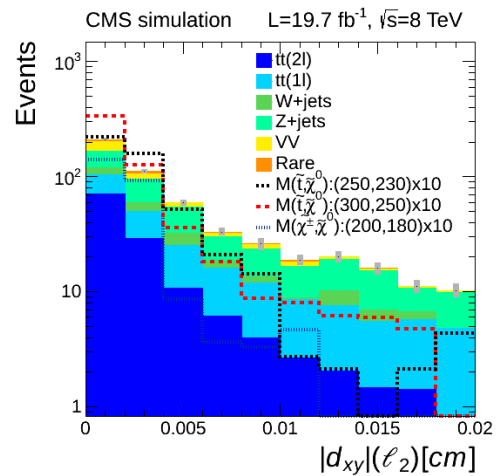
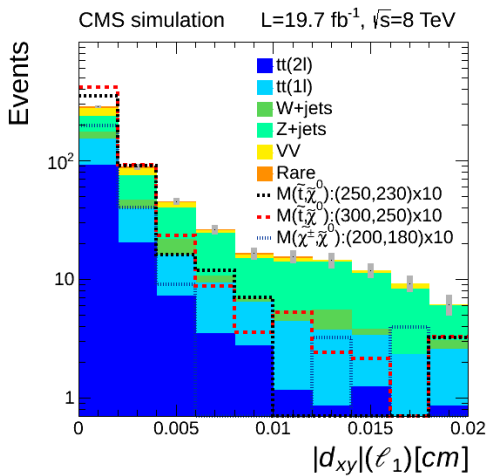


Figure C.8: Impact parameter $|d_{xy}|$ for leading lepton and sub-leading in preselection.

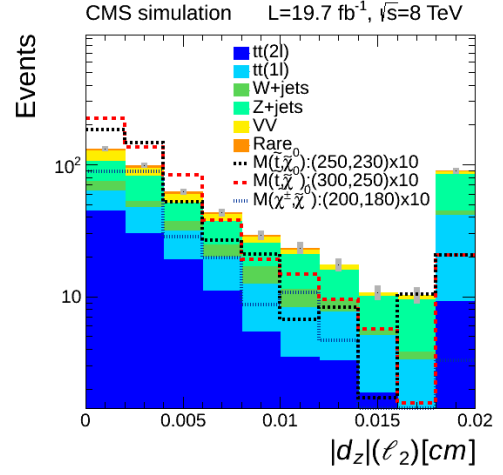
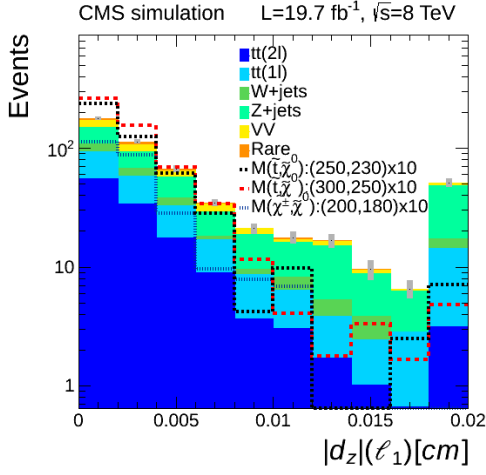


Figure C.9: Impact parameter $|d_z|$ for leading lepton and sub-leading in preselection.

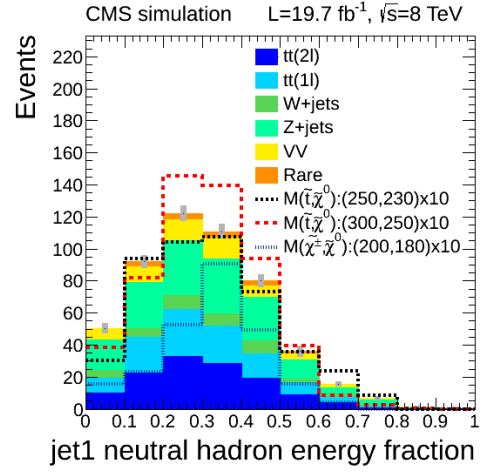
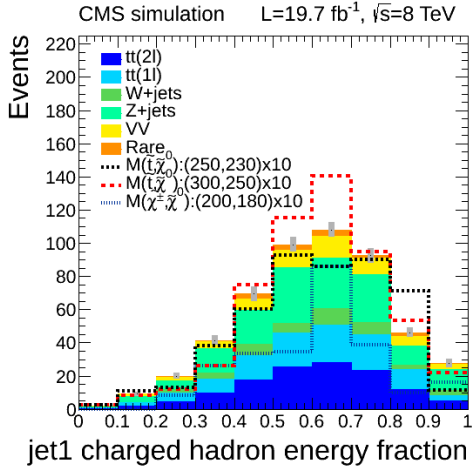


Figure C.10: The charged-hadrons-energy-fraction distribution of jet1 (left) and the neutral-hadrons-energy-fraction distribution distribution (right), for the leading jet in preselection.

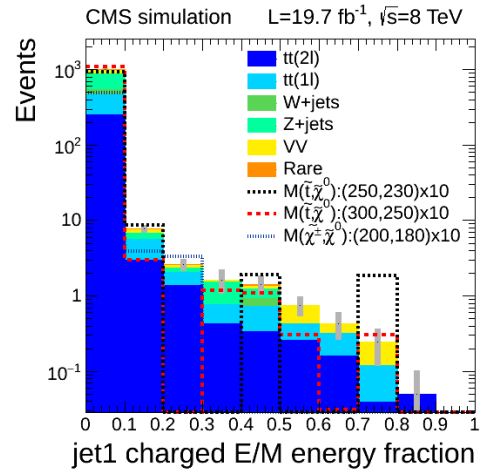
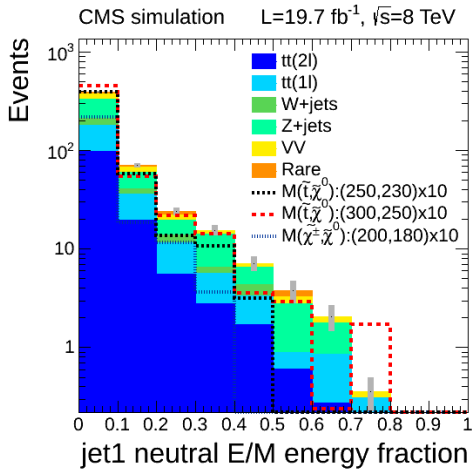


Figure C.11: The jet1 neutral electromagnetically-originated (photons) energy fraction distribution (left). The jet1 charged electromagnetically-originated energy fraction distribution (right).

C.2 Kinematic variables distribution in SR selection

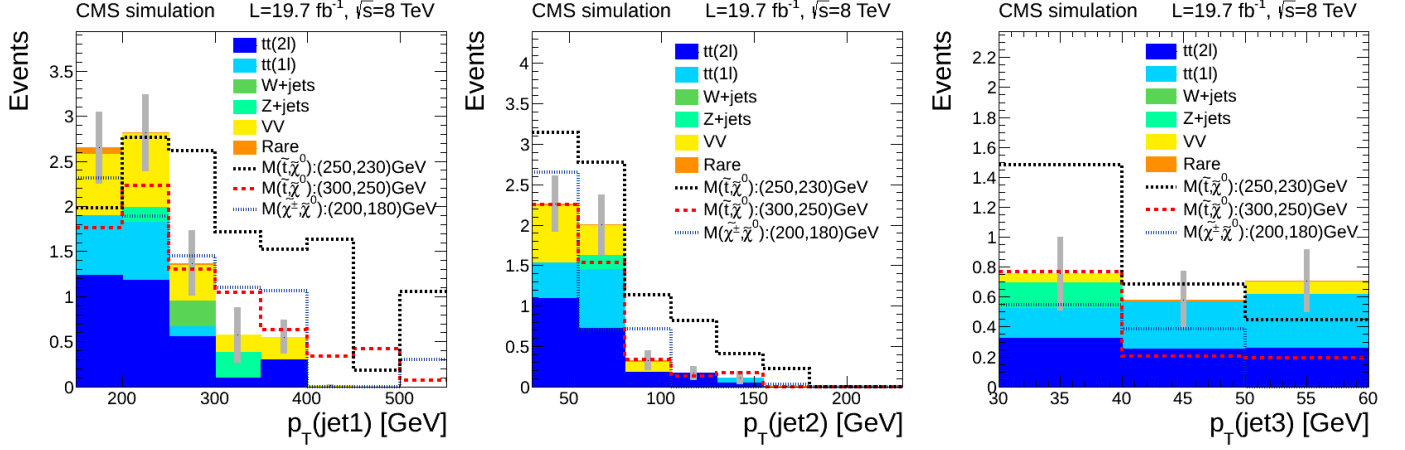


Figure C.12: The jet1, jet2 and jet3 p_T distributions in SR selection.

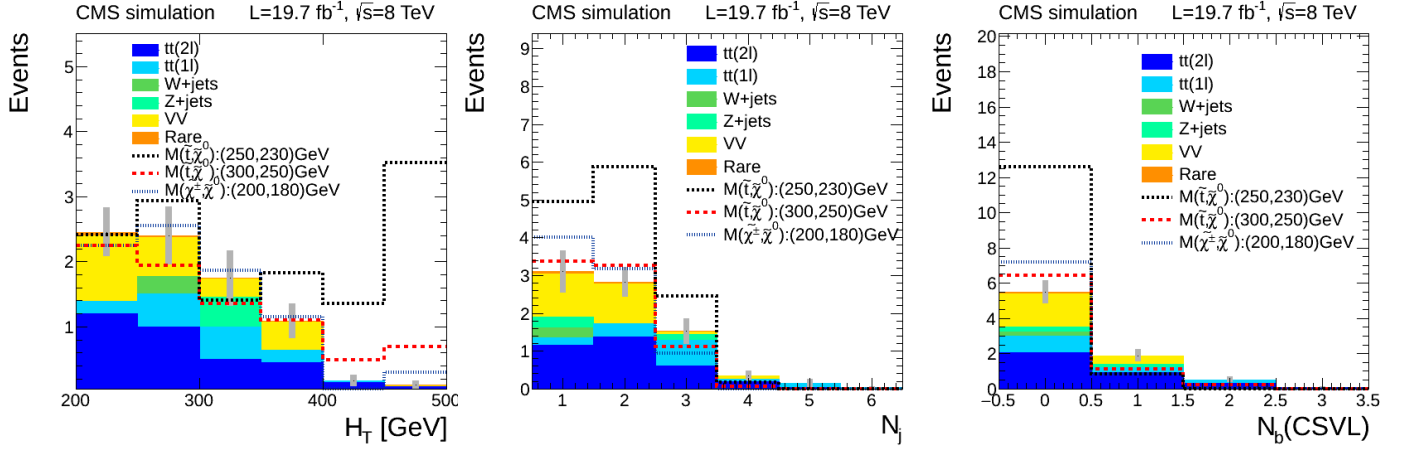


Figure C.13: The H_T , N_j and $N_b(CSVL)$ distributions in SR selection.

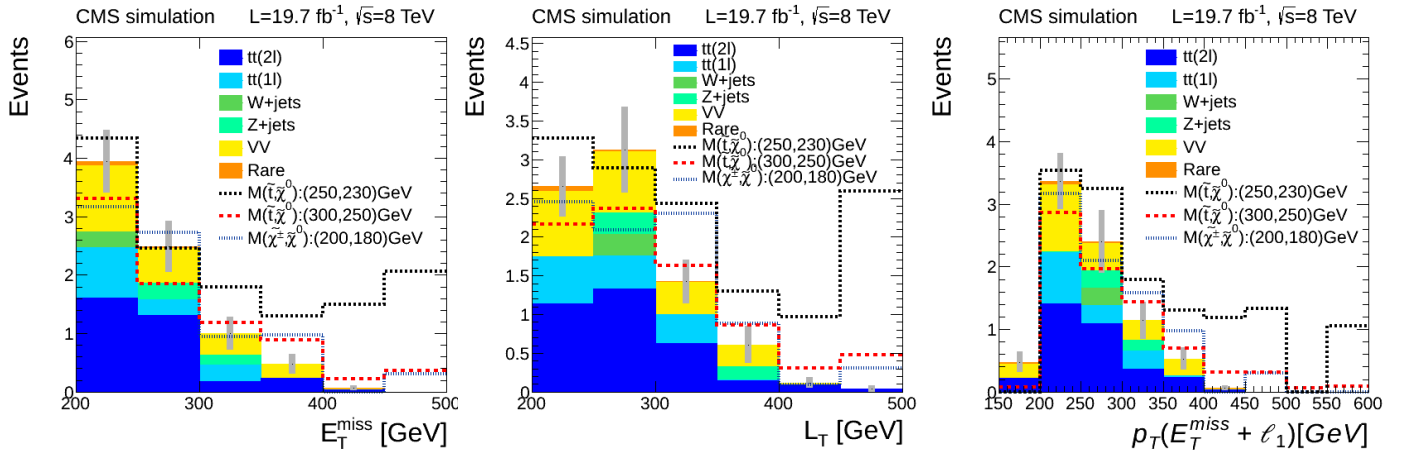


Figure C.14: The \cancel{E}_T , L_T and $p_T(W) = |\vec{\cancel{E}}_T + \vec{p}_T(\ell_1)|$ distributions in SR selection.

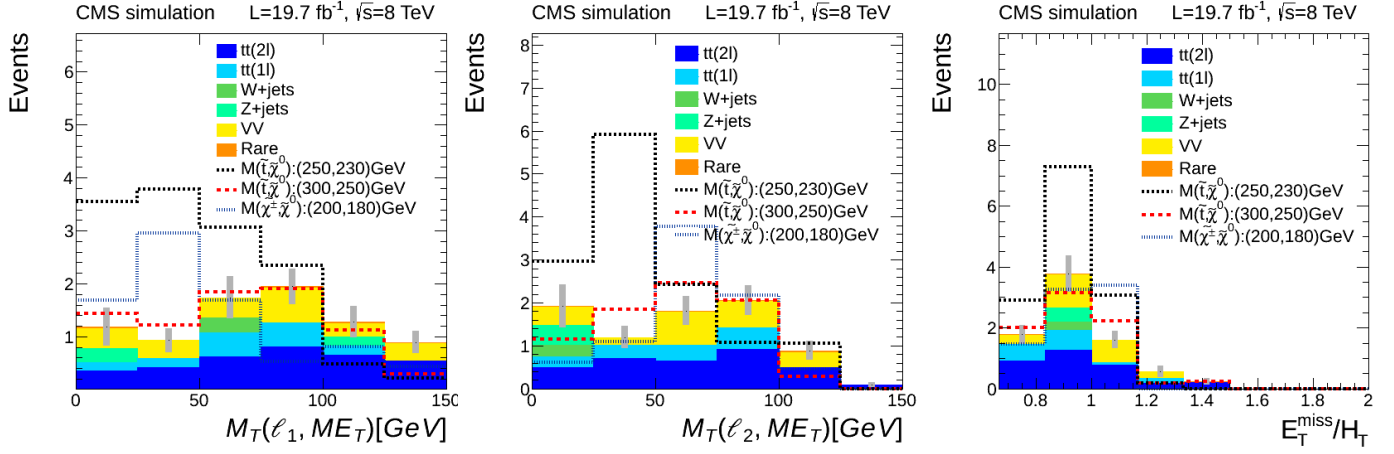


Figure C.15: The $M_T(\ell_1, \cancel{E}_T)$, $M_T(\ell_2, \cancel{E}_T)$ and \cancel{E}_T / H_T distributions in SR selection.

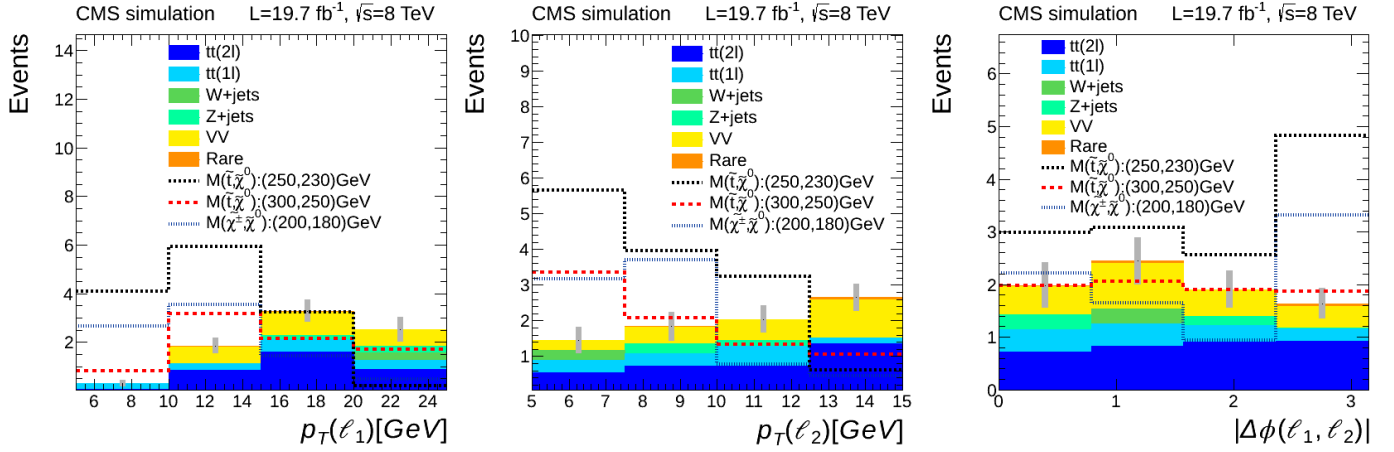


Figure C.16: The $p_T(\ell_1)$, $p_T(\ell_2)$ and $|\Delta\phi(\ell_1, \ell_2)|$ distributions in SR selection.

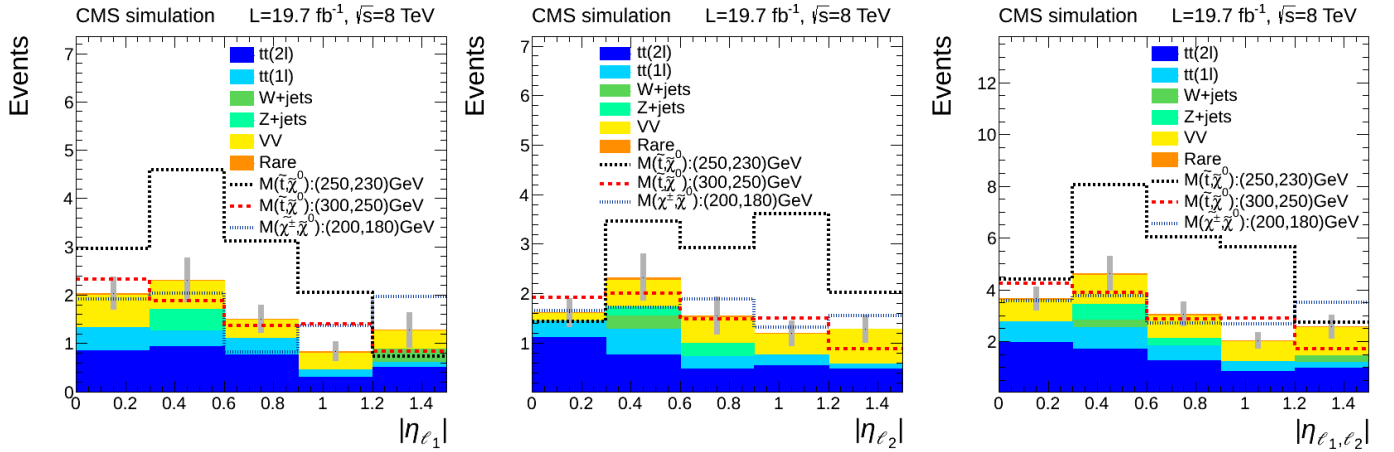


Figure C.17: The $|\eta|$ distributions of leading lepton, sub-leading and both in SR selection.

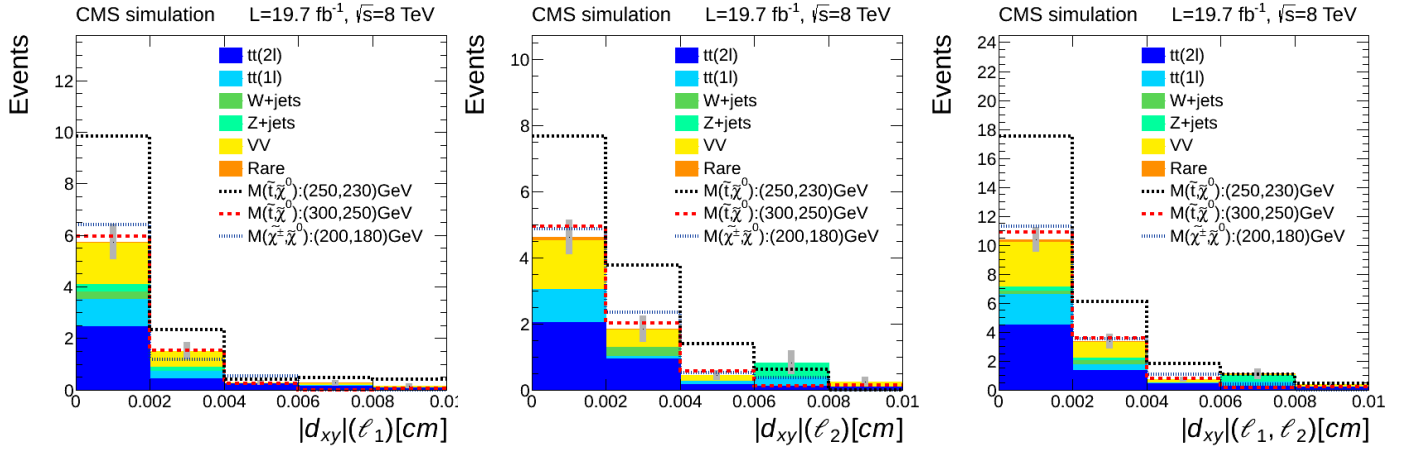


Figure C.18: The impact parameter $|d_{xy}|$ distributions for leading lepton (left), sub-leading lepton (middle) and both leptons (right) for SR selection.

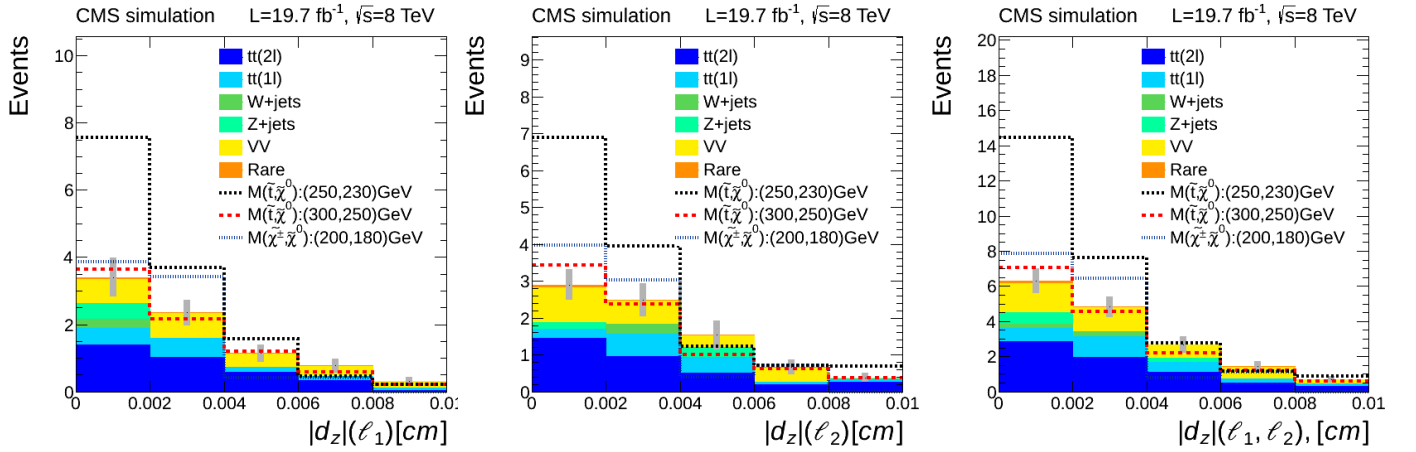


Figure C.19: The impact parameter $|d_z|$ distributions for leading lepton (left), sub-leading lepton (middle) and both leptons (right) for SR selection.

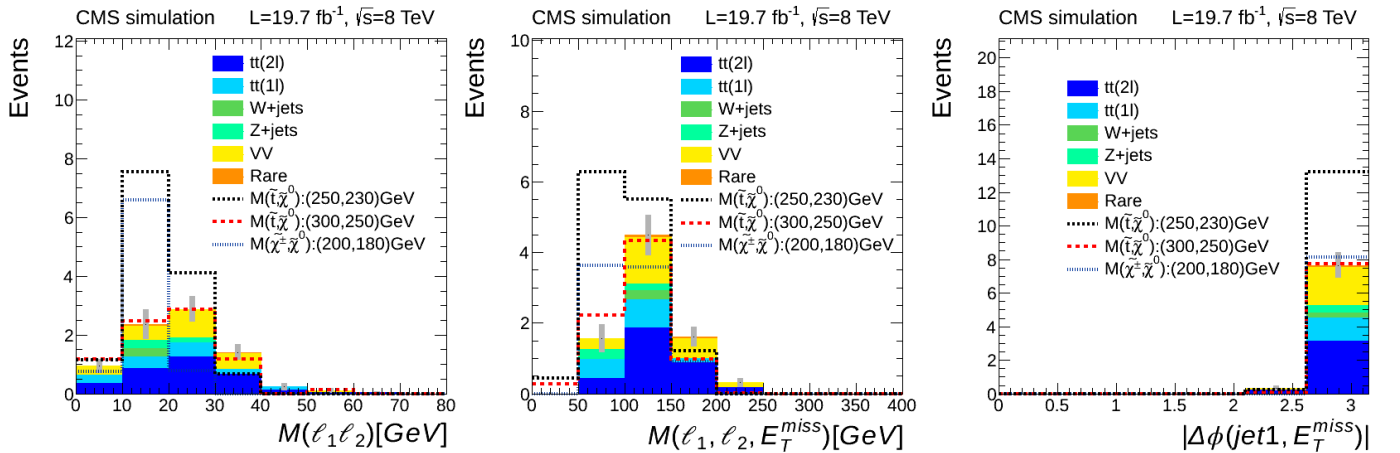


Figure C.20: The $M(\ell_1, \ell_2)$, $M(\ell_1, \ell_2, \cancel{E}_T)$ and $|\Delta\phi(\cancel{E}_T, jet1)|$ distributions in SR selection.

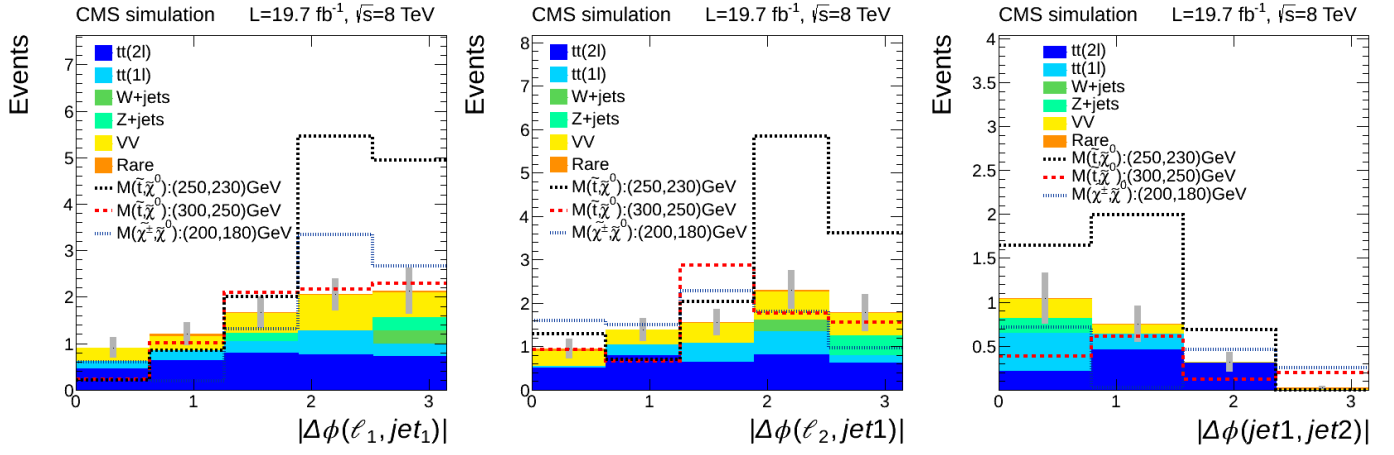


Figure C.21: The $|\Delta\phi(\ell_1, jet_1)|$, $|\Delta\phi(\ell_2, jet_1)|$ and $|\Delta\phi(jet_1, jet_2)|$ distributions in SR selection.

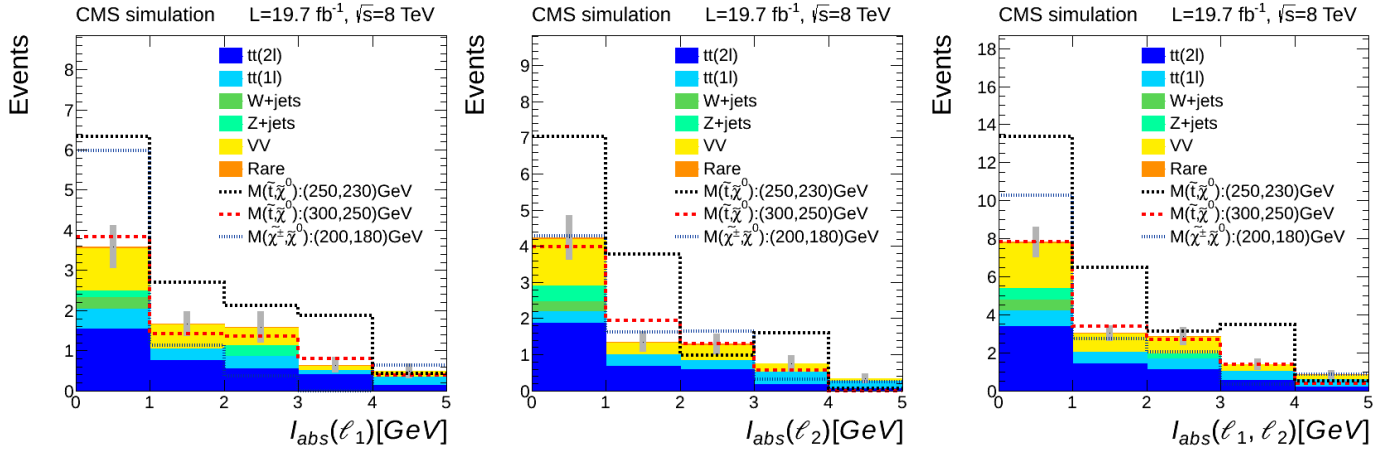


Figure C.22: The absolute isolation distributions for leading lepton (left), sub-leading lepton (middle) and both leptons (right) for SR selection.

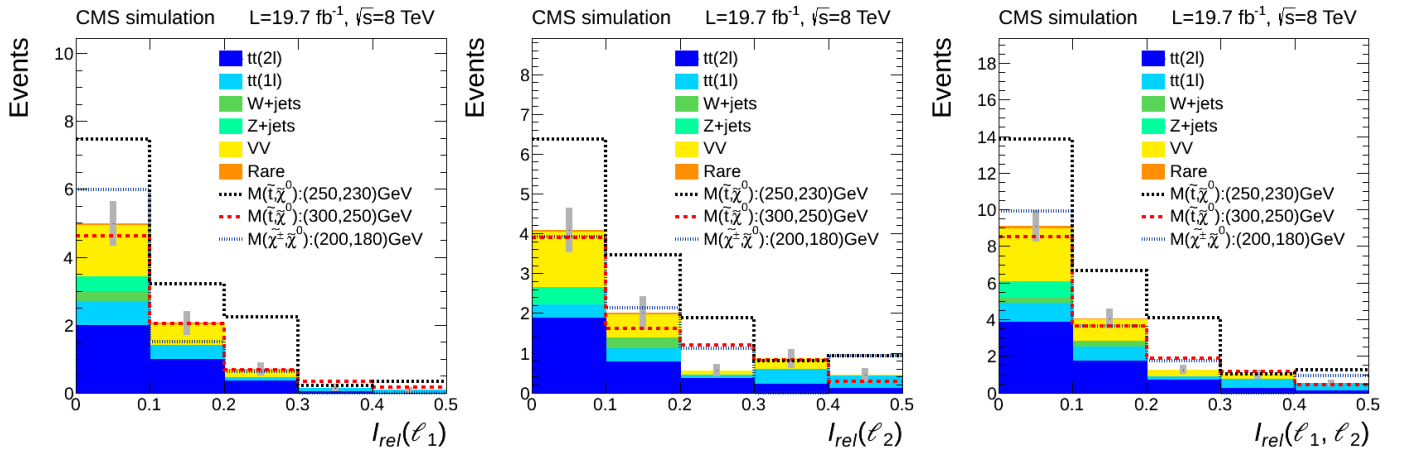


Figure C.23: The relative isolation distributions for leading lepton (left), sub-leading lepton (middle) and both leptons (right) for SR selection.

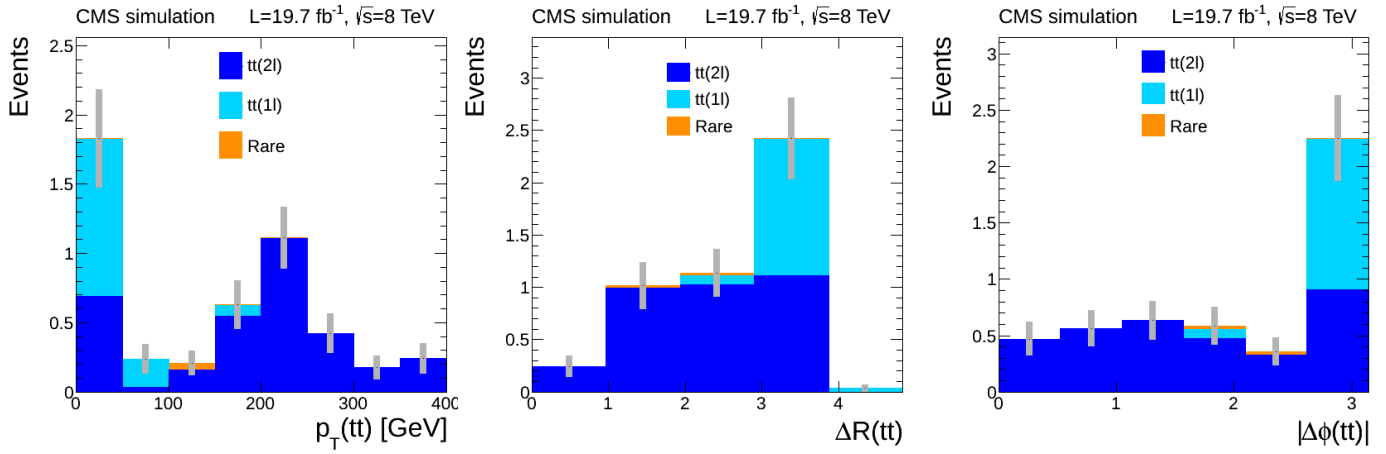


Figure C.24: The $p_T(tt)$, $\Delta R(t, \bar{t})$ (left) and the $|\Delta\phi(t, \bar{t})|$ distributions in SR selection. The $p_T(tt)$ shape indicates that the peak at ~ 200 GeV corresponds to the ISR-boost which pushes back-to-back $t\bar{t}$ -pair and ISR-Jet. The $|\Delta\phi|$ however indicates that these $t\bar{t}$ -quarks have all possible angles in almost flat distribution. These means that the two tops are not necessarily in the same direction, but rather in all possible directions/angle but in such a way that their vectorial momentum sum appears back-to-back with leading jet. In addition, we see that the $p_T(tt) \lesssim 100$ GeV region is populated by the events with t back-to-back with \bar{t} and probably one of the b-jets has not been tagged as a b-jet consisting the jet1 in stead of an ISR one. As expected this non-tagging effect is about 1/3 as the b-jet efficiency of CSV algorithm at medium working point indicates.

C.3 Explicit background cut flow

Table C.1: Explicit background cut flow yields for each simulated background, and two signal points in 13 steps. Same information is presented in figure 5.11 in log scale. We successively (per row) impose cuts towards the SR selection. Last row corresponds to the full SR-selection and the SR event yields.

Selection cuts	$t\bar{t}(2\ell)$	$t\bar{t}(1\ell)$	W+jets	Z+jets	VV	Rare	TotalSM background	$M(t), M(\tilde{\chi}_1^0)$: (250,230)	$M(t), M(\tilde{\chi}_1^0)$: (300,250)
$\cancel{E}_T > 200\text{GeV}$	6384±17	39289±55	94093±216	3848±36	1074±9	2844±35	147533±229	6640±39	2563±15
$N_\ell = 2$	2649±11	1468±11	742±19	498±14	460±6	430±13	6247±32	132±6	125.9±3.4
$N_\mu \geq 2$	1904±9	1122±9	477±15	335±11	325±5	308±11	4472±26	117±6	102.8±3.1
$Q(\ell_1)Q(\ell_2) = -1$	1852±9	681±7	281±12	327±11	310±5	261±11	3712±23	92.5±4.9	83.5±2.8
$p_{Tj1} > 150\text{GeV}, \eta < 2.4$	1301±8	468±6	149±9	290±11	224±4	178±9	2610±19	76.2±4.4	69.7±2.5
$p_{Tj3} < 60\text{GeV}$	842±6	292±5	147±8	265±10	206.1±3.9	135±8	1887±18	69.2±4.2	63.1±2.3
$N_b = 0$	245.0±3.4	124.7±3.1	141±9	249±10	190.1±3.7	53±5	1003±15	64.3±4.1	53.2±2.2
$\cancel{E}_T / H_T > 2/3$	147.1±2.6	74.5±2.4	115±8	162±8	137.5±3.1	30.0±3.8	667±13	57.5±3.6	46.3±2.0
$p_{T\ell} [5, 25(15)]\text{GeV}, \eta < 1.5$	5.6±0.5	10.5±0.9	3.8±1.4	15.0±2.2	5.4±0.7	0.62±0.45	41.0±3.0	23.2±2.3	14.3±1.1
$ d_z , d_{xy} < 0.01\text{cm}$	4.45±0.45	3.9±0.6	2.4±1.1	4.1±1.2	3.11±0.45	0.56±0.44	18.5±1.9	20.3±2.2	12.1±1.1
$I_{Reit} < 0.5, \&I_{Abs\ell} < 5\text{GeV}$	3.53±0.40	1.52±0.35	1.0±0.7	3.8±1.1	2.77±0.43	0.11±0.04	12.7±1.5	15.3±1.9	9.0±0.9
$M_{\ell\ell} > 5\text{GeV}$	3.53±0.40	1.52±0.35	1.0±0.7	3.8±1.1	2.47±0.40	0.11±0.04	12.4±1.5	14.6±1.8	8.4±0.9
$M_{\tau\tau} \text{ cut: } [0, 160]\text{GeV}$	3.38±0.39	1.42±0.33	0.28±0.28	0.45±0.33	2.34±0.39	0.11±0.04	8.0±0.8	13.5±1.8	7.8±0.8

C.4 Tau reconstruction cases

Since we require high met and two soft leptons, the Z +jets events (appearing in signal region) are boosted and dominated by $Z \rightarrow \tau^+\tau^- \rightarrow \ell^+\ell^-\nu\nu\nu\nu$. Consequently \cancel{E}_T appearing mainly in-between the two leptons (smallest) angle. However the \cancel{E}_T vector can appear aside this angle. Figure C.25 analyze all possible cases. In our analysis we perform the $M_{\tau\tau}$ reconstruction only for case A, while for B, C and D we assign a negative value i.e.: $M_{\tau\tau} = -[(p_{\tau_1} + p_{\tau_2})^\mu (p_{\tau_1} + p_{\tau_2})_\mu]^{0.5}$.

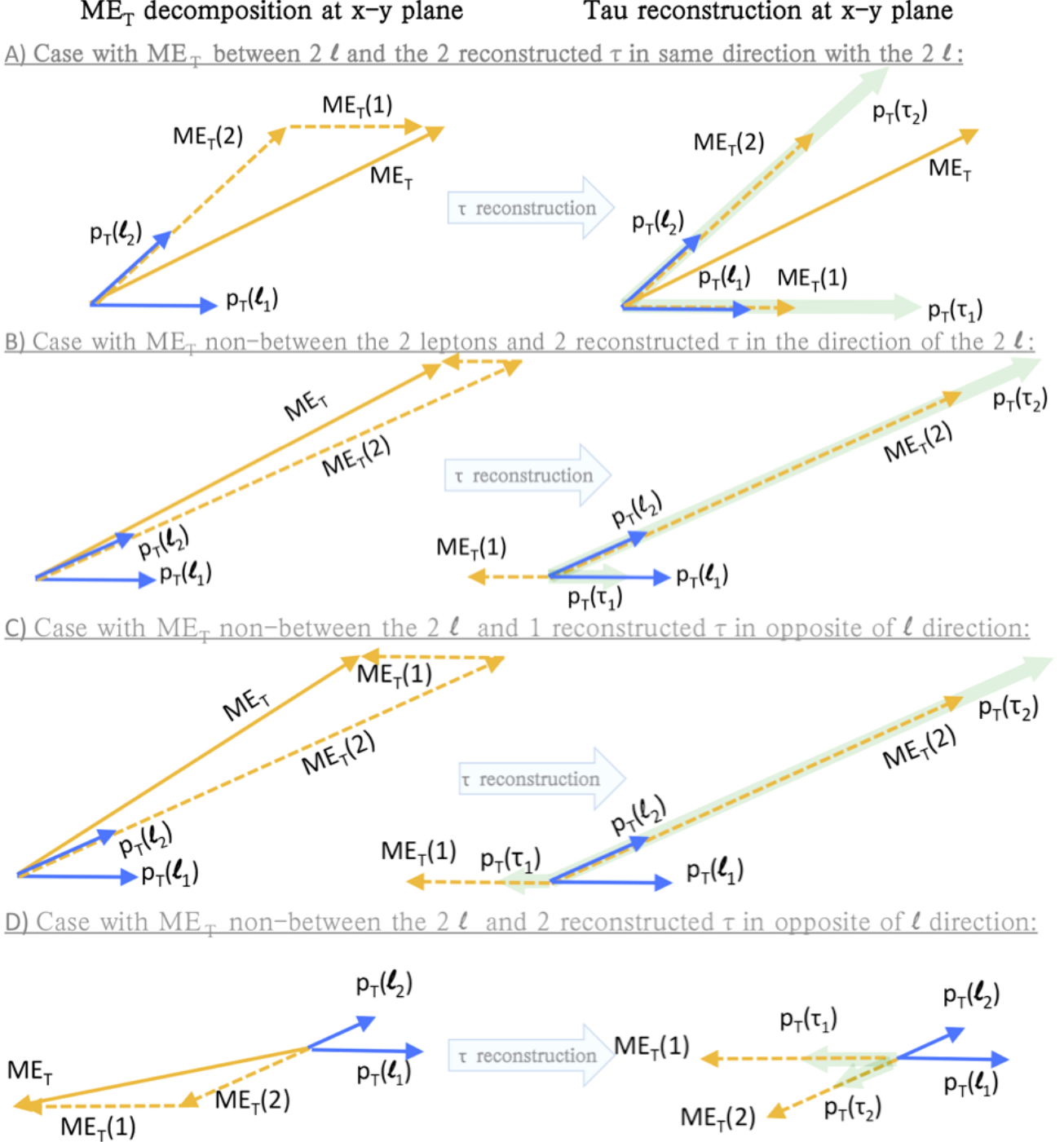


Figure C.25: The four different reconstruction cases for the “effective-taus” (A-D). A) The \cancel{E}_T is in-between the two leptons and the direction of reconstructed taus is the same as the leptons. B) The \cancel{E}_T is not in-between the two leptons but reconstructed taus’ direction is still same with the corresponding lepton. C) When the \cancel{E}_T is not in-between the two leptons and only one direction of reconstructed tau is same with its corresponding lepton. D) \cancel{E}_T is not in-between and both tau directions are opposite of the leptons. (Blue: leptons’ p_T , yellow: \cancel{E}_T , green: reconstructed taus’ p_T .)

Appendix D

Background prediction methods additional material

D.1 Kinematic variables distributions for CR($t\bar{t}2\ell$) events

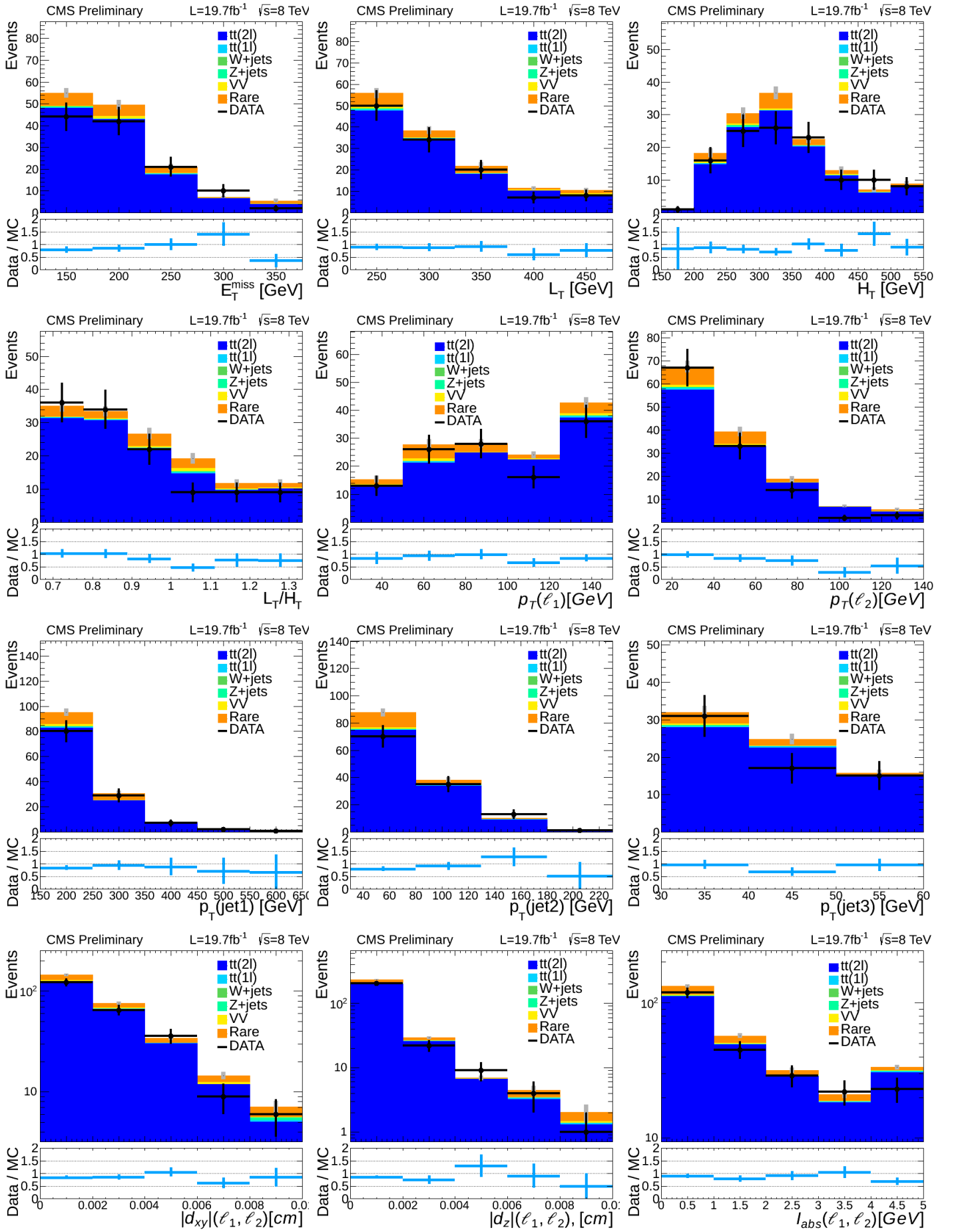


Figure D.1: Some kinematic variables distribution for $CR(tt2l)$. Raw MC versus data.

D.2 Kinematic variables distributions, ratios and decomposition to backgrounds for CR(NP) events

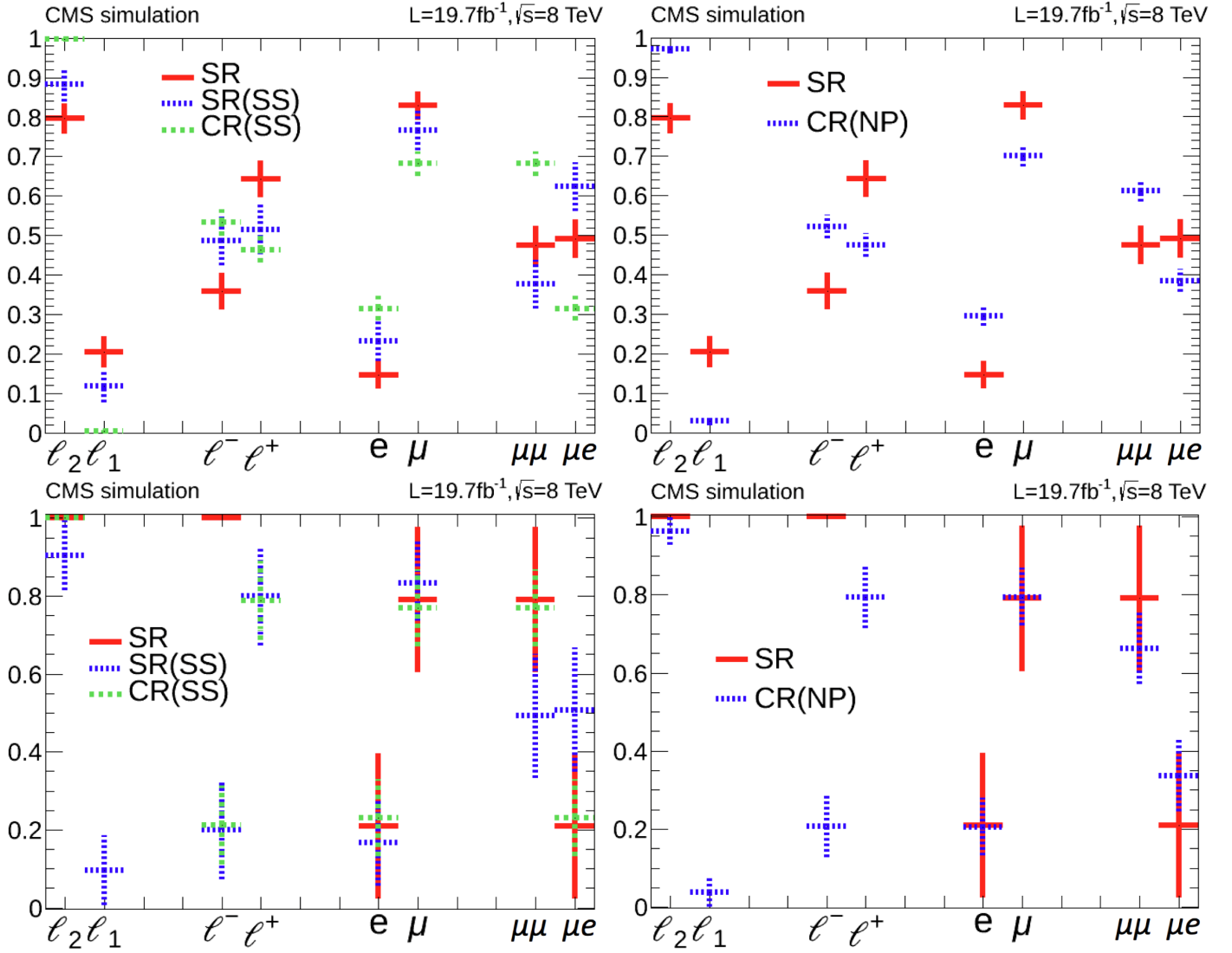


Figure D.2: Top row $t\bar{t}(1l)$ events, bottom W +jets. Left the three region explicitly, right the combination to CR(NP). Decomposition of non-prompt events in cases where [a] second(first) lepton is the non-prompt, [b] negative(positive) lepton is the non-prompt, [c] non-prompt is an electron(muon) and [d] the non-prompt lepton is in a $\mu\mu(e\mu)$ event. Each pair of bin values' is normalized to 1. Comparison between SR, SR(SS), CR(SS) on the left, and comparison between SR, CR(NP) on the right. The looser selection has been used which stands for SR removing the impact parameter and relative isolation cuts, and relaxing absolute isolation cut at 10 GeV (thus we gain statistics $\times 7$).

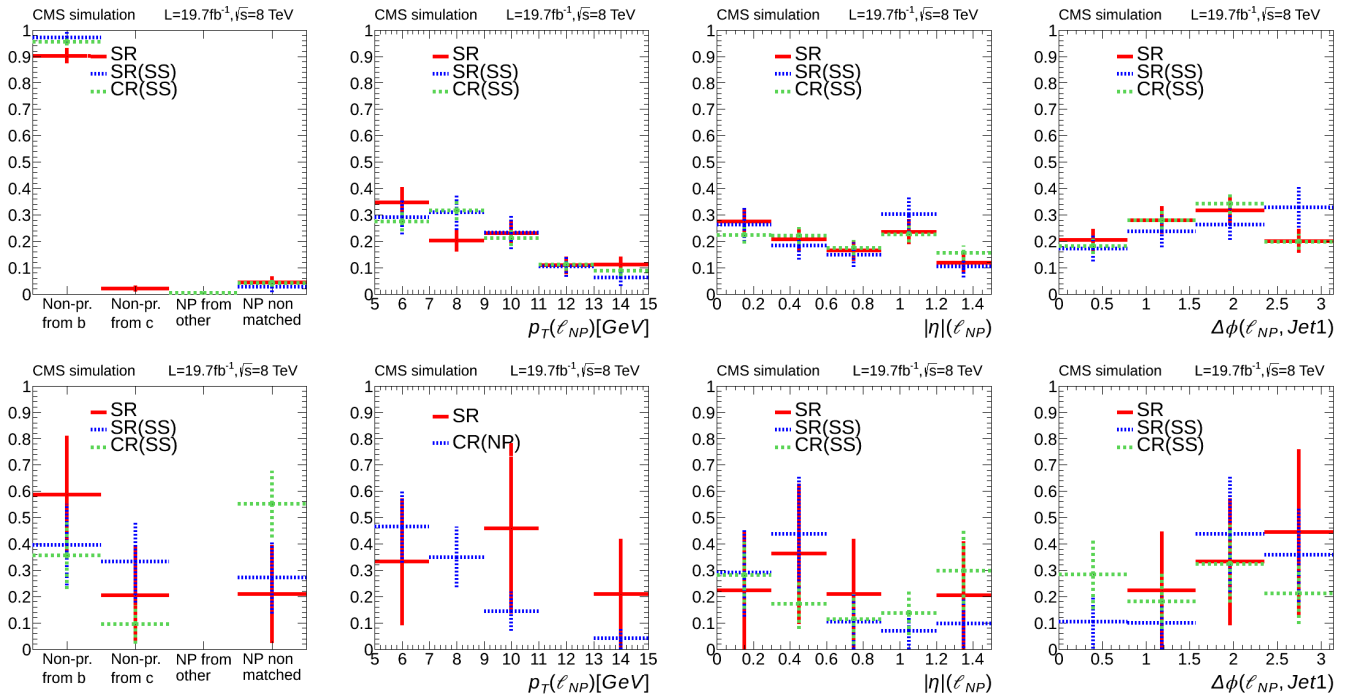


Figure D.3: Top row $t\bar{t}(1\ell)$ events, bottom W +jets. First column: the available examined origins which are considered for non-prompt lepton, bin1: from b to c quark transition, bin2: form c to s , bin3: from other quark, bin4: non-matched to object. Rest three column the p_T , $|\eta|$ and $|\Delta\phi(\ell, jet1)|$ distributions of the non-prompt leptons respectively. Distribution stands for the loose selection with removed IP & I_{rel} cuts, and relaxed I_{abs} to 10 GeV. Figure D.4 shows the same with combined the SR(SS) and CR(SS) to CR(NP).

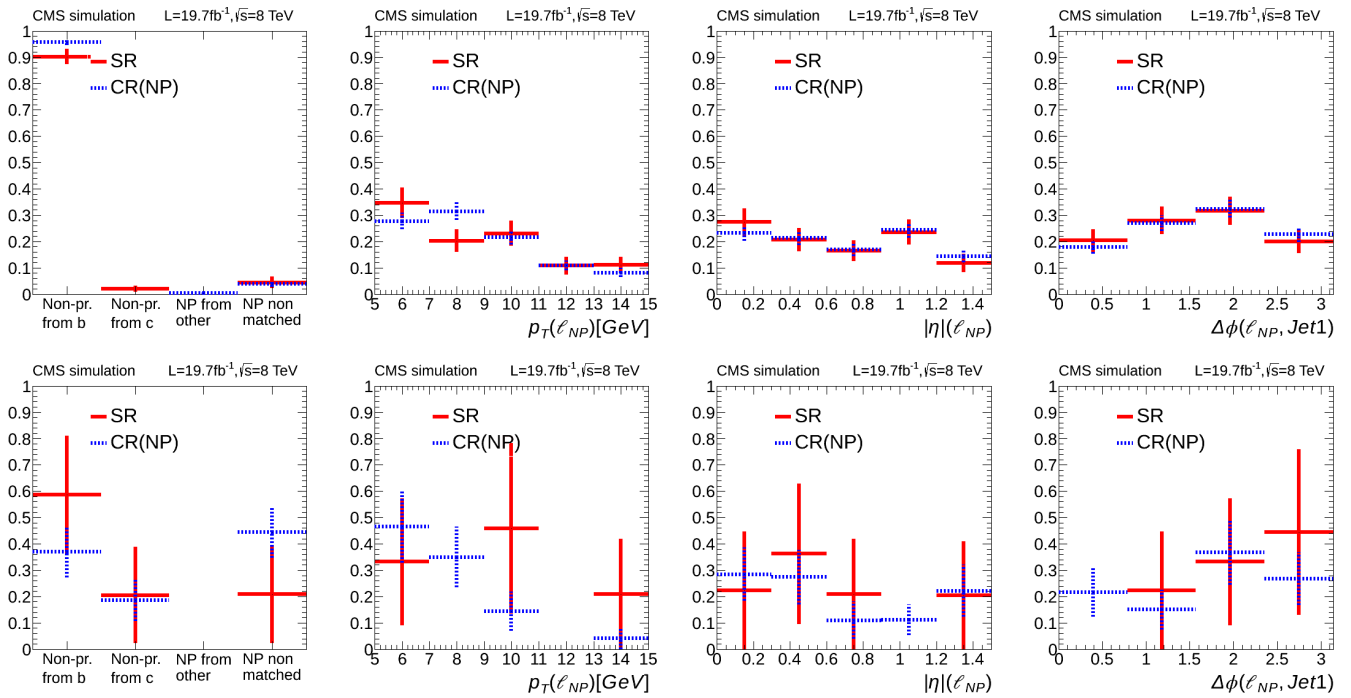


Figure D.4: Top row $t\bar{t}(1\ell)$ events, bottom W +jets. First column: origins which are considered for non-prompt lepton origin. Rest three column the p_T , $|\eta|$ and $|\Delta\phi(\ell, jet1)|$ distributions of the NP-leptons respectively. Distribution stands for the loose selection with removed IP & I_{rel} cuts, and relaxed I_{abs} cut to 10 GeV.

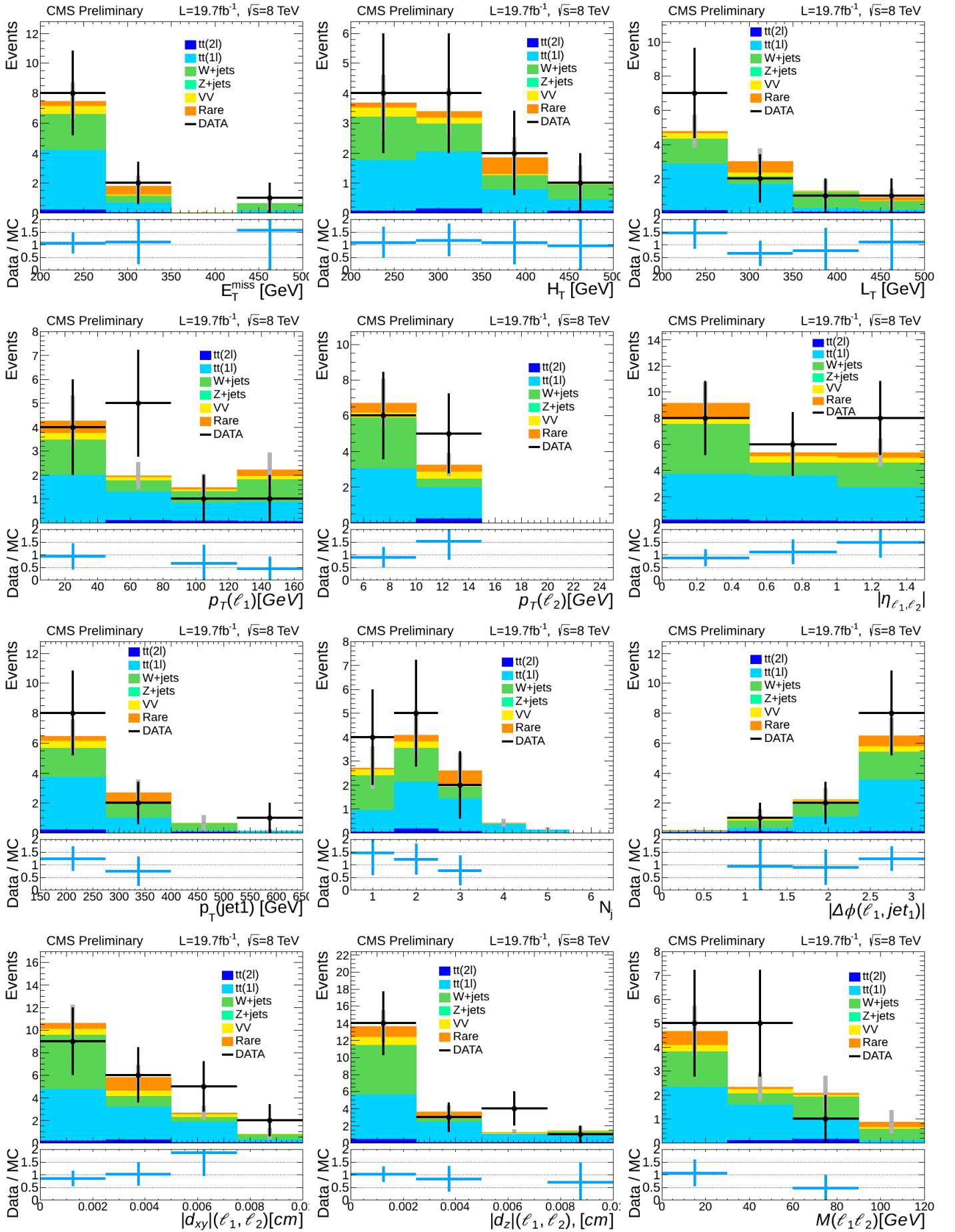


Figure D.5: Set of some kinematic variables distribution for CR(NP) events selection. Raw simulation background versus data.

D.3 Kinematics in CR(Z), hadronic-recoil corrected distributions

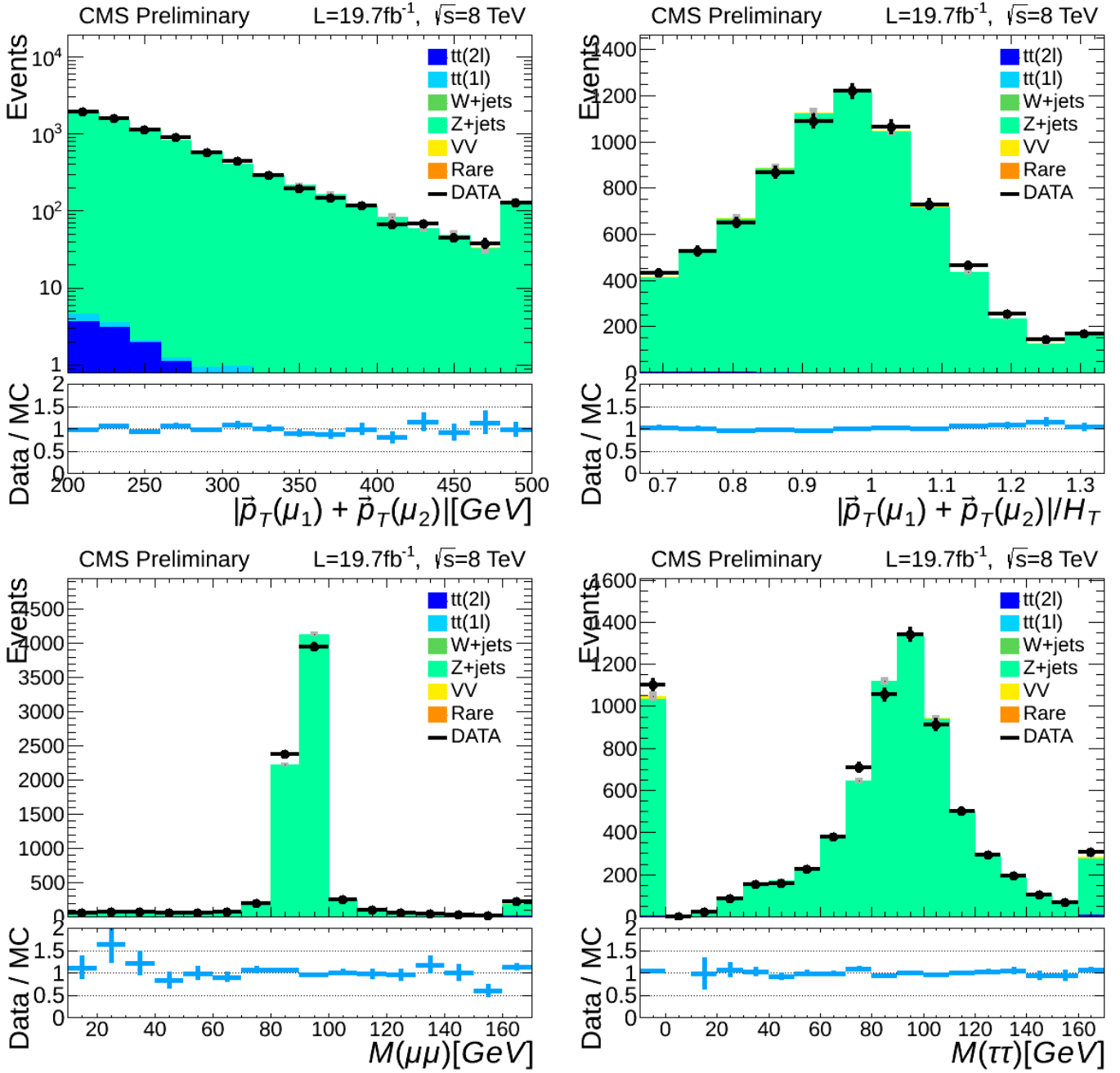


Figure D.6: Hadronic recoil corrected distributions for CR(Z) events (corrected version of figure 6.8). On top: the two main variables distributions which their cuts defines the CR(Z). Bottom: the di-muon invariant mass $M_{\mu\mu}$ distribution (left) and the di-tau invariant mass $M_{\tau\tau}$ distribution (right).

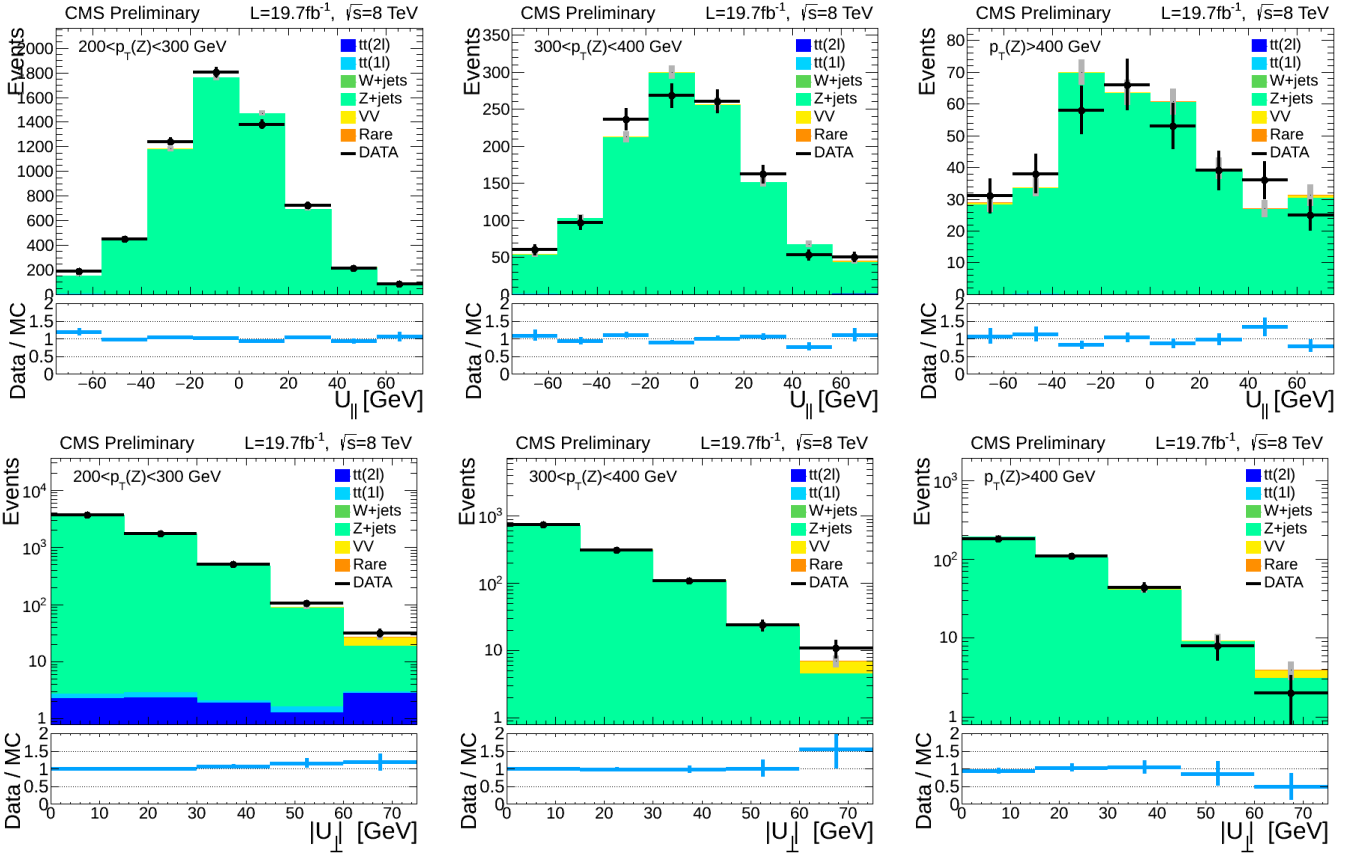


Figure D.7: Hadronic recoil corrected distributions for CR(Z) events (corrected version of figure 6.10). Top row: data and MC(reco) distributions of the $|U_T|$. Bottom row: data and MC(reco) distributions of the U_L . All plots are in CR(Z) events. From left to right the bins: $200 < p_T(Z) < 300$ GeV, $300 < p_T(Z) < 400$ GeV, $p_T(Z) > 400$ GeV.

D.4 Kinematic variables distributions for SR-inv events

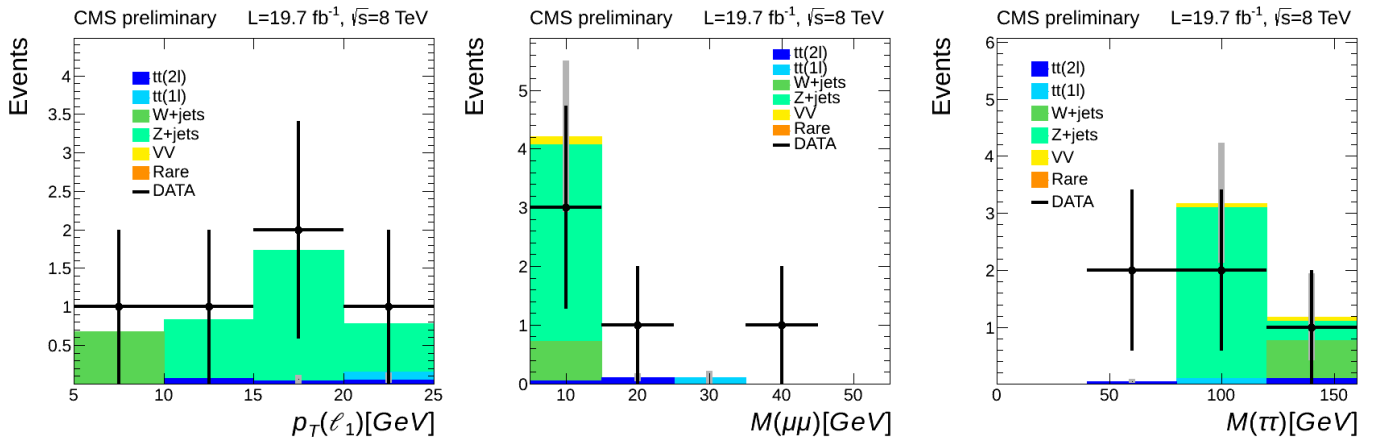


Figure D.8: The $p_T(\ell_1)$, $M_{\ell\ell}$ and $M_{\tau\tau}$ distributions of SR-inv region. MC background and data.

D.5 kinematic variables distributions for CR(VV) event

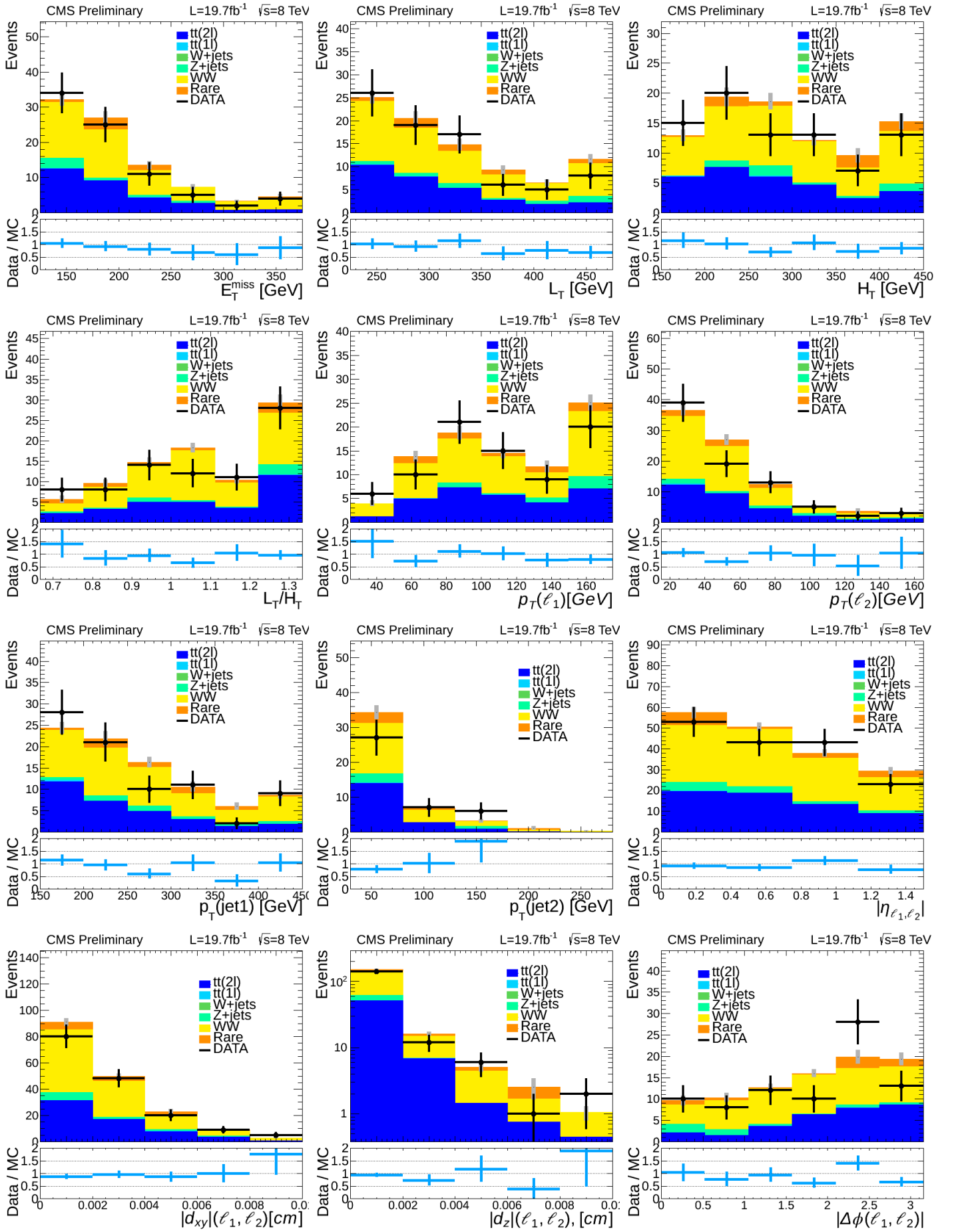


Figure D.9: Some kinematic variables distribution for CR(VV) events selection. Raw simulation background versus data.

Appendix E

Systematic uncertainties additional material

E.1 Number of MC entries per region: statistics of the samples used

Table E.1: Number of entries in simulated MC events for SR and CRs. These numbers indicate the statistics of the simulation. We deduce that entries are relatively poor for some of the backgrounds of SR(bin1): $t\bar{t}(1\ell)$, W+jets, however still a factor of about $\times 10$ higher than the predicted yields.

Sample	SR(bin1)+SR(bin2)	CR($t\bar{t}\ell$)	CR(NP)	CR(VV)	CR(Z)	SR-inv
$t\bar{t}(2\ell)$	22 + 60	2896	6	721	301	5
$t\bar{t}(1\ell)$	8 + 14	17	72	5	30	1
W+jets	0 + 1	0	7	0	0	1
DY+jets	0 + 4	1	0	15	30733	11
VV	26 + 40	60	56	1498	1941	3
Rare	6 + 6	162	24	190	545	0
Total Background	62 + 125	3136	165	2429	33550	21
Data Observed	2 + 4	119	11	81	9516	5
SUSY(250,230)	51 + 15	0	5	0	0	7
SUSY(300,250)	52 + 53	2	10	8	0	8
SUSY(200,180)	20 + 6	0	6	0	0	2

E.2 Signal uncertainties per mass point.

E.3 CMS performance on parameters and quantities used in analysis

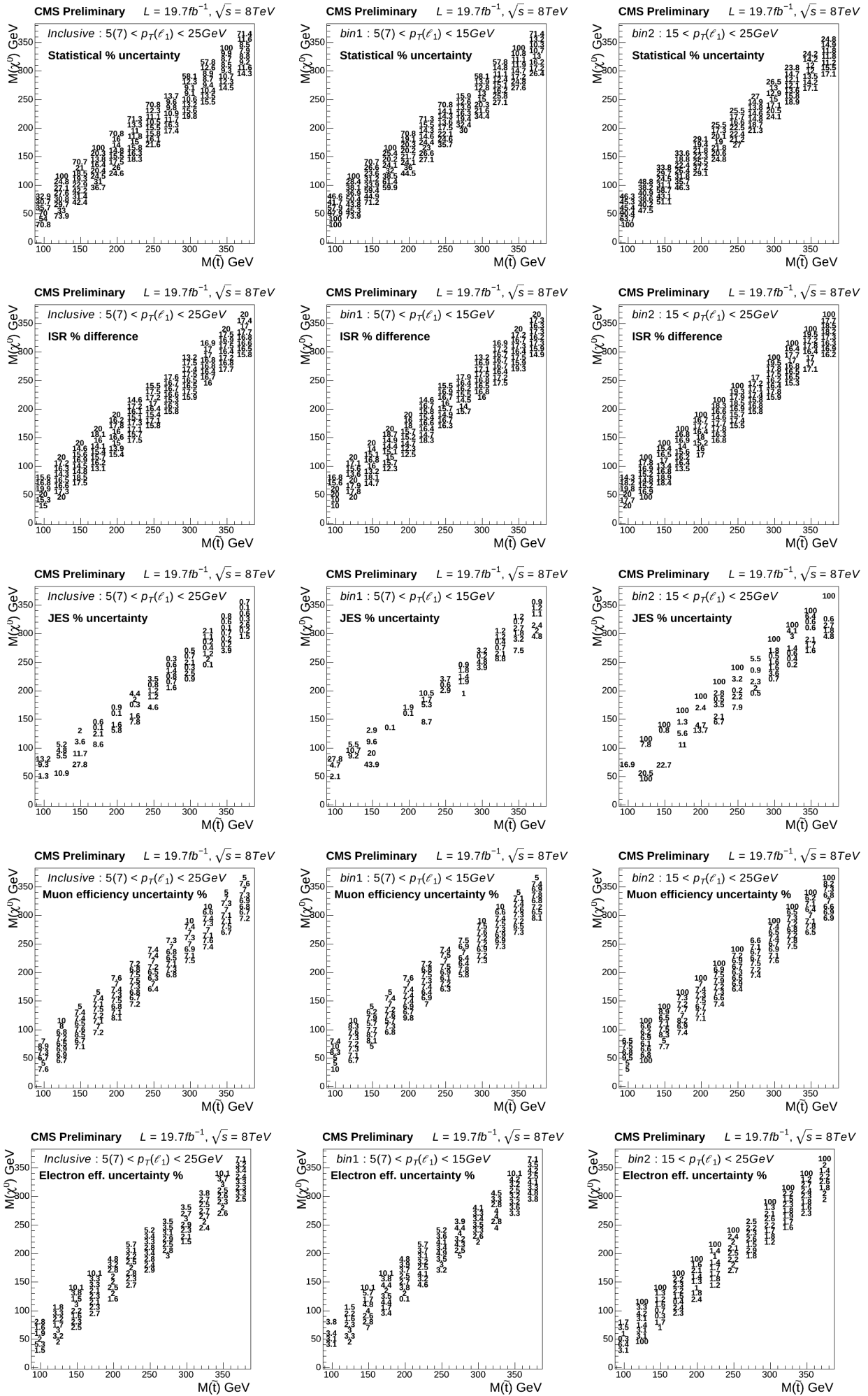


Figure E.1: Signal % uncertainties. Rows: statistical,ISR,JES,eff(μ),eff(e). Columns: incl.,bin1,bin2.

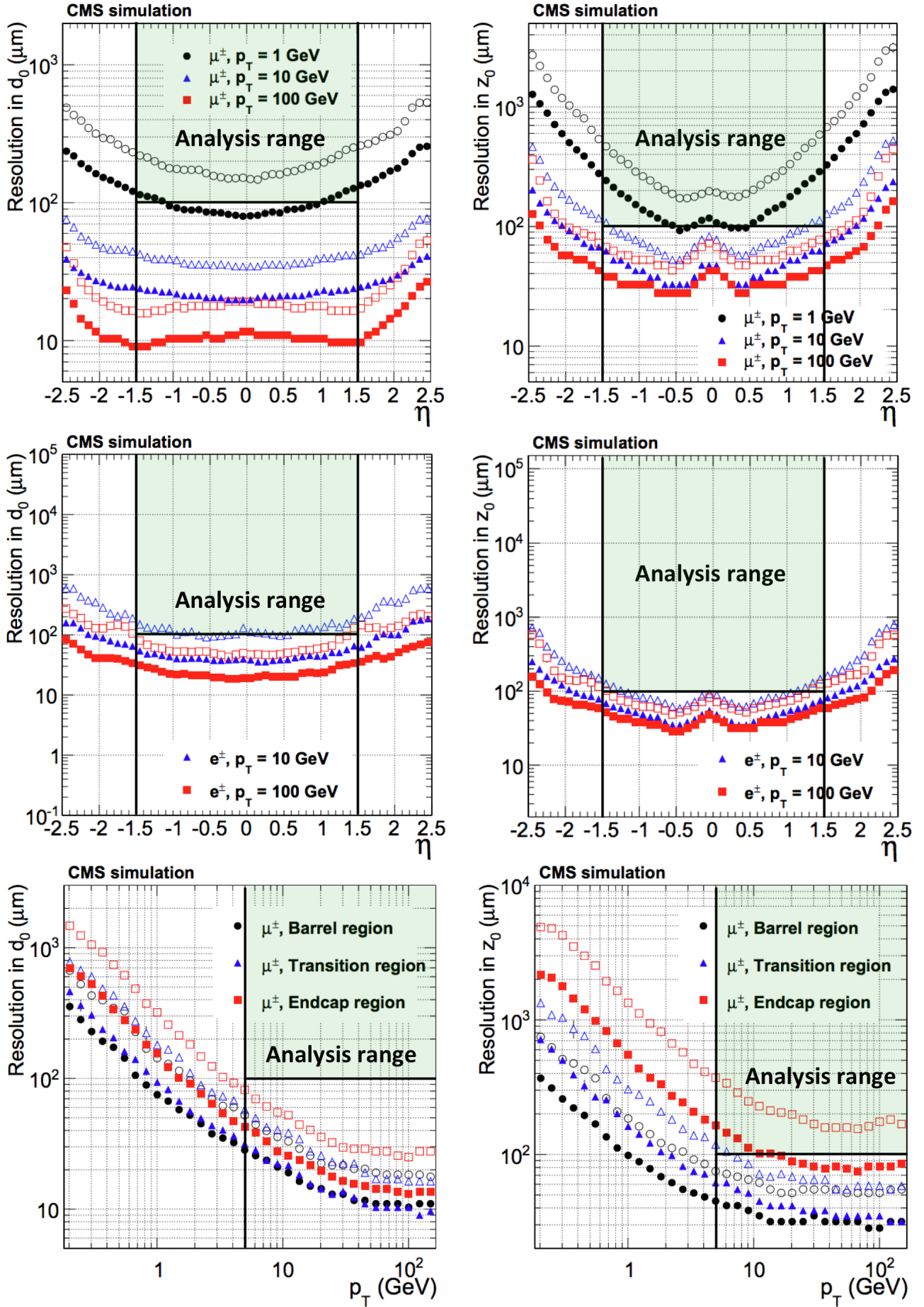


Figure E.2: Tracker performance on impact parameters. Transverse and longitudinal impact parameters $|d_{xy}|$ ($\equiv d_0$) and $|d_z|$ ($\equiv z_0$) resolution, as a function of η and p_T , for single isolated muons with $p_T = 1, 10,$ and 100 GeV. Barrel, transition-area, and endcap regions, defined by η intervals of $0-0.9, 0.9-1.4$ and $1.4-2.5$ respectively. For each bin in η , the solid (open) symbols correspond to the half-width for 68% (90%) intervals centered on the mode of the distribution in residuals [73].

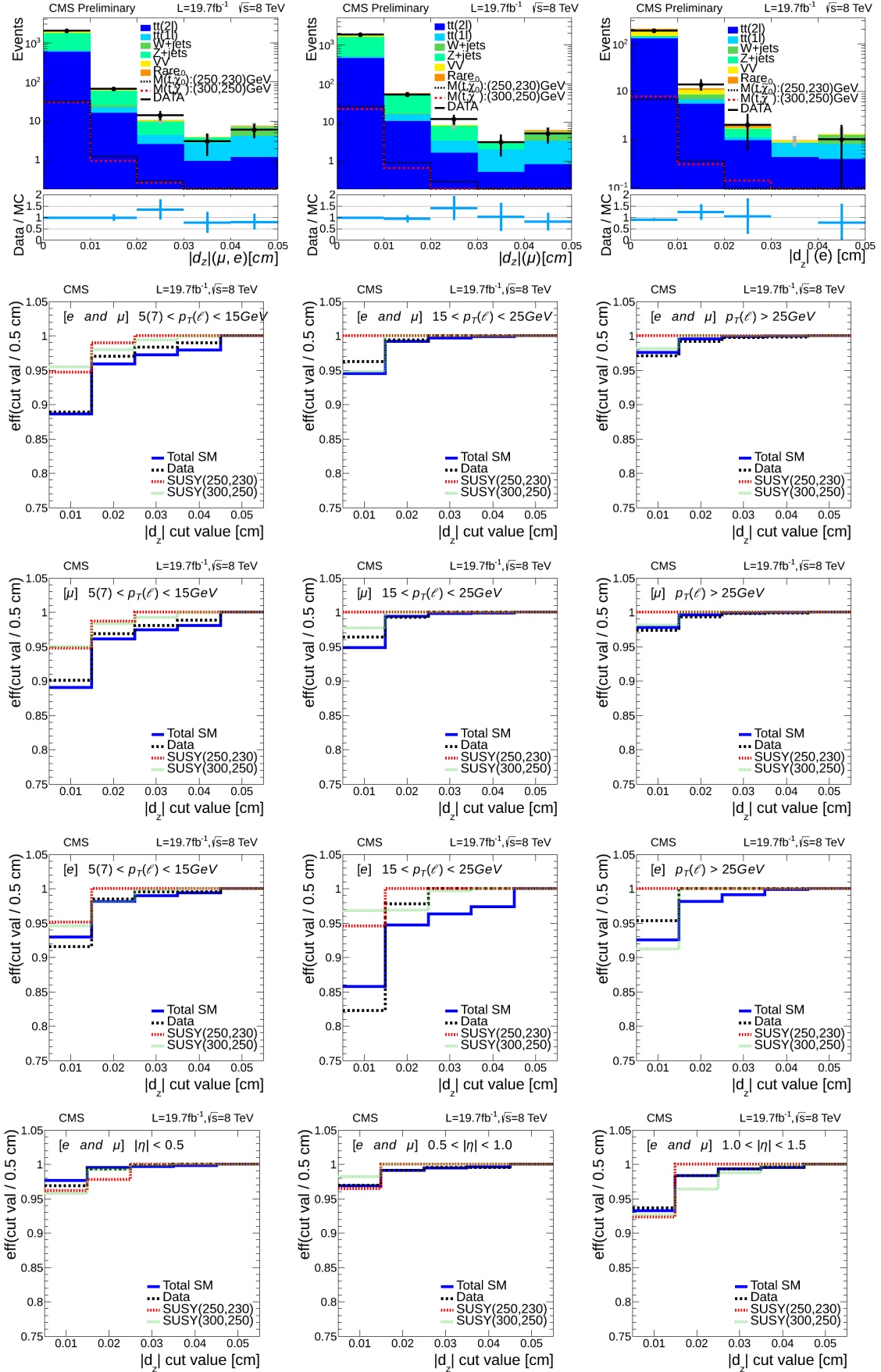


Figure E.3: 1st row: background and data $|d_z|$ distributions including leptons from CRs and VRs (vetoing leading muon of CR(Z)). From left to right: both leptons, only μ , and only e . Signal leptons includes all regions ie: +SR. Z+jets background is corrected due to hadronic recoil according to formula 6.3. 2nd row: the d_z -cut efficiency as a function of different cut value (with respect to 0.5 cm cut: last overflow-bin). Three different p_T ranges are shown from left to right. (3rd and 4th rows: the breakdown of 2nd into only μ and e respectively). 5th row: three η ranges (inclusive over p_T ranges), for both leptons, for e , and for μ left to right respectively.

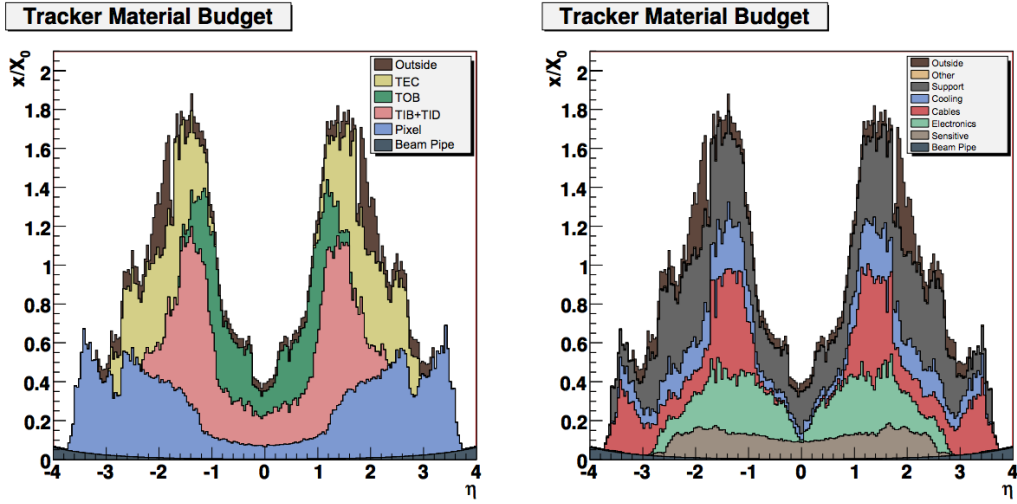


Figure E.4: The material budget of the CMS tracker in units of radiation length (X_0) as a function of η for the different sub-detectors (left) and functionalites (right). The radiation length is the mean distance over which the energy of an electron drops to $1/e$ by bremsstrahlung. (Taken from [77]).

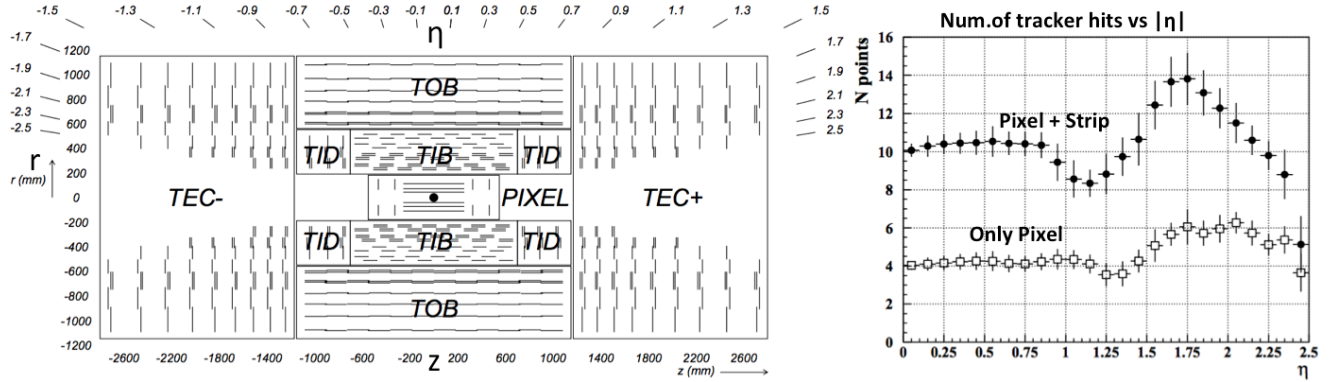


Figure E.5: Left: a schematic cross section through the CMS tracker. Each line represents a detector module. Double lines indicate back-to-back modules which deliver stereo hits. Right: Number of measurement points in the strip tracker as a function of pseudorapidity. (Taken from [77]).

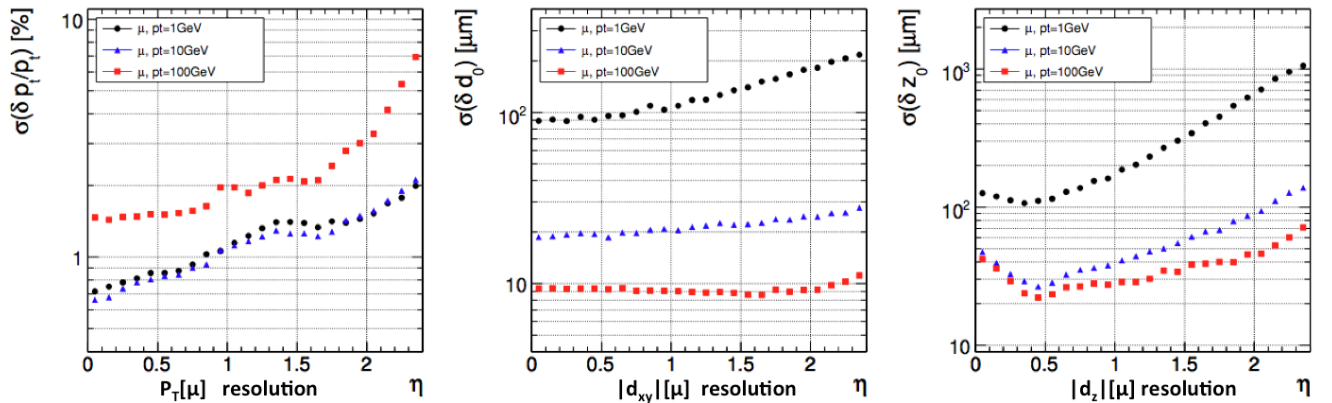


Figure E.6: Resolution of track parameters for single muons with transverse momenta of 1, 10 and 100 GeV: transverse momentum (left), transverse and longitudinal impact parameters (middle) and (right) respectively. (Taken from [77]).

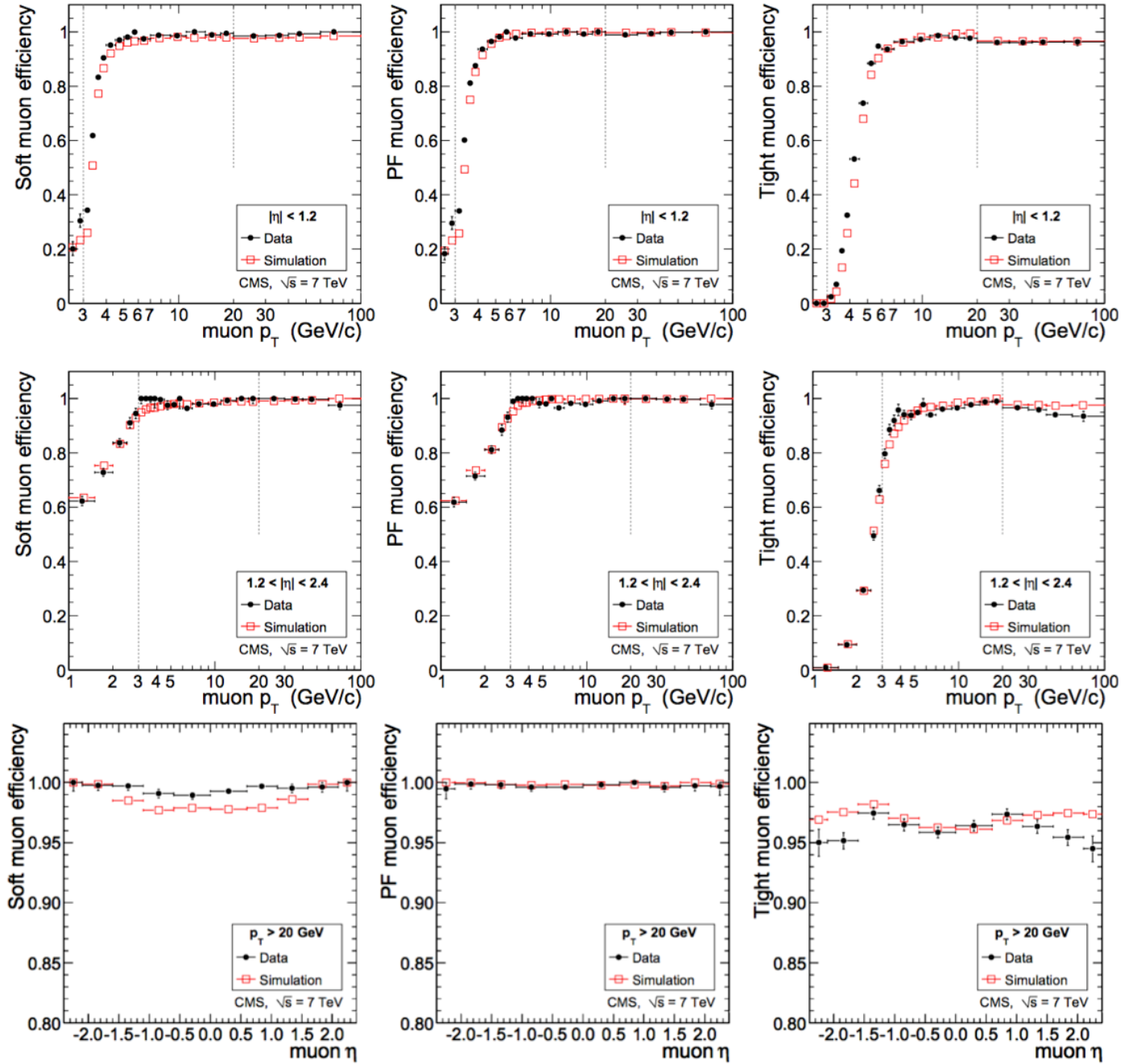


Figure E.7: Tag-and-probe results for the muon efficiency in data compared to simulation. Given that a tracker track exists, the plots show the efficiency as a function of muon p_T for Soft Muons (left), Particle-Flow Muons (middle), and Tight Muons (right) in the barrel and overlap regions (top), and in the endcaps (middle). On the bottom muon deficiencies versus η . The measurement is made using $J/\psi \rightarrow \mu^- \mu^+$ events for $p_T < 20$ GeV/c and $Z \rightarrow \mu^- \mu^+$ events for $p_T > 20$ GeV/c. For $p_T < 3$ GeV/c, to reduce the background, only tracks with MIP signature are considered. (Taken from [67]).

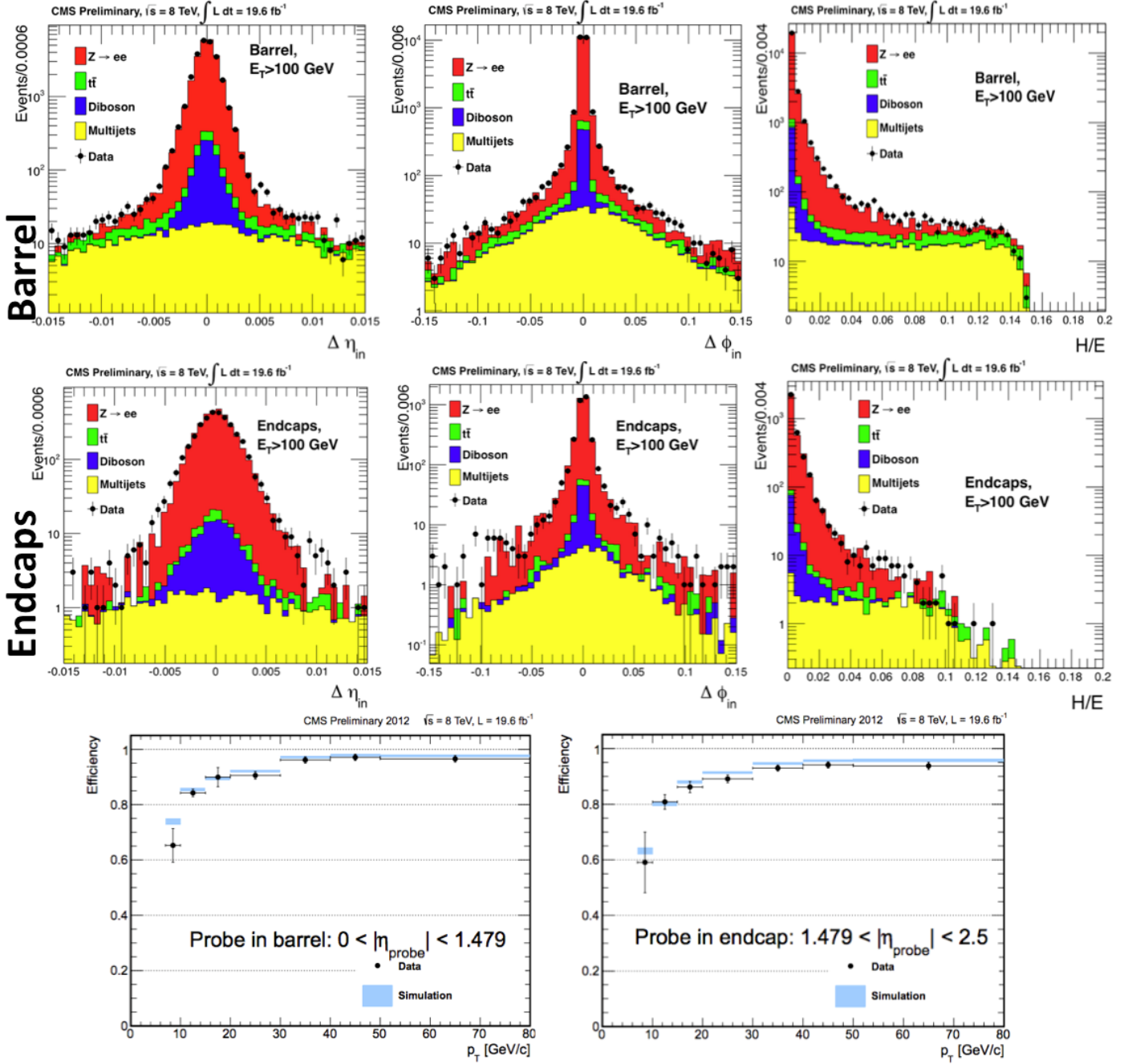


Figure E.8: Electron distributions over: $\Delta\eta_{in}$, $\Delta\phi_{in}$ and H/E , variables used for pure and efficient selection reconstruction. First row for barrel, second for endcaps. Bottom row the reconstruction efficiency versus p_T starting from 7 GeV as used in the analysis. (Taken from [97]).

Appendix F

The CKM and PMNS matrices, parametrization and measured values

$$\begin{bmatrix} \nu_e \\ \nu_\mu \\ \nu_\tau \end{bmatrix} = U_{\text{PMNS}} \begin{bmatrix} \nu_1 \\ \nu_2 \\ \nu_3 \end{bmatrix}, \quad U_{\text{PMNS}} \equiv \begin{pmatrix} U_{e1} & U_{e2} & U_{e3} \\ U_{\mu1} & U_{\mu2} & U_{\mu3} \\ U_{\tau1} & U_{\tau2} & U_{\tau3} \end{pmatrix} \begin{pmatrix} e^{i\frac{\alpha_1}{2}} & 0 & 0 \\ 0 & e^{i\frac{\alpha_2}{2}} & 0 \\ 0 & 0 & 1 \end{pmatrix} \equiv UV$$

Majorana phase

$$U = \begin{bmatrix} 1 & 0 & 0 \\ 0 & c_{23} & s_{23} \\ 0 & -s_{23} & c_{23} \end{bmatrix} \begin{bmatrix} c_{13} & 0 & s_{13}e^{-i\delta} \\ 0 & 1 & 0 \\ -s_{13}e^{i\delta} & 0 & c_{13} \end{bmatrix} \begin{bmatrix} c_{12} & s_{12} & 0 \\ -s_{12} & c_{12} & 0 \\ 0 & 0 & 1 \end{bmatrix}$$

where c_{ij}, s_{ij} denote $\cos \theta_{ij}, \sin \theta_{ij}$

$$= \begin{pmatrix} c_{12}c_{13} & s_{12}c_{13} & s_{13}e^{-i\delta} \\ -s_{12}c_{23} - c_{12}s_{23}s_{13}e^{i\delta} & c_{12}c_{23} - s_{12}s_{23}s_{13}e^{i\delta} & s_{23}c_{13} \\ s_{12}s_{23} - c_{12}c_{23}s_{13}e^{i\delta} & -c_{12}s_{23} - s_{12}c_{23}s_{13}e^{i\delta} & c_{23}c_{13} \end{pmatrix}$$

$$= \begin{pmatrix} 0.795 - 0.846 & 0.513 - 0.585 & 0.126 - 0.178 \\ 0.205 - 0.543 & 0.416 - 0.730 & 0.579 - 0.808 \\ 0.215 - 0.548 & 0.409 - 0.725 & 0.567 - 0.800 \end{pmatrix}$$

PMNS

	ν_1	ν_2	ν_3
ν_e			
ν_μ			
ν_τ			

$$\begin{pmatrix} d' \\ s' \\ b' \end{pmatrix} = V_{\text{CKM}} \begin{pmatrix} d \\ s \\ b \end{pmatrix}, \quad V_{\text{CKM}} \equiv \begin{bmatrix} V_{ud} & V_{us} & V_{ub} \\ V_{cd} & V_{cs} & V_{cb} \\ V_{td} & V_{ts} & V_{tb} \end{bmatrix} = R_{23}(I_{\delta_D} R_{13} I_{\delta_D}^\dagger) R_{12}$$

$$= \begin{bmatrix} 1 & 0 & 0 \\ 0 & c_{23} & s_{23} \\ 0 & -s_{23} & c_{23} \end{bmatrix} \begin{bmatrix} c_{13} & 0 & s_{13}e^{-i\delta} \\ 0 & 1 & 0 \\ -s_{13}e^{i\delta} & 0 & c_{13} \end{bmatrix} \begin{bmatrix} c_{12} & s_{12} & 0 \\ -s_{12} & c_{12} & 0 \\ 0 & 0 & 1 \end{bmatrix}$$

where c_{ij}, s_{ij} denote $\cos \theta_{ij}, \sin \theta_{ij}$

$$= \begin{pmatrix} c_{12}c_{13} & s_{12}c_{13} & s_{13}e^{-i\delta} \\ -s_{12}c_{23} - c_{12}s_{23}s_{13}e^{i\delta} & c_{12}c_{23} - s_{12}s_{23}s_{13}e^{i\delta} & s_{23}c_{13} \\ s_{12}s_{23} - c_{12}c_{23}s_{13}e^{i\delta} & -c_{12}s_{23} - s_{12}c_{23}s_{13}e^{i\delta} & c_{23}c_{13} \end{pmatrix}$$

$$= \begin{bmatrix} 0.97425 \pm 0.00022 & 0.2252 \pm 0.0009 & 0.0039 \pm 0.00044 \\ -0.230 \pm 0.011 & 1.023 \pm 0.036 & 0.0415 \pm 0.0007 \\ 0.0084 \pm 0.0006 & -0.0387 \pm 0.0023 & 0.9991 \pm 0.0001 \end{bmatrix}$$

CKM

	d	s	b
u			
c			
t			

Figure F.1: The CKM and PMNS matrices parametrized. Illustration with the squares representing the square of the matrix elements. (Values taken from [125, 126]).

Appendix G

CERN's current experiments outline

A full list with current CERN's experiments together with their main purposes and description can be found here. (Information taken from [43]).

1. ACE: brings together an international team of physicists, biologists and medics to study the biological effects of antiprotons.
2. AEGIS: (Antihydrogen Experiment: Gravity, Interferometry, Spectroscopy) uses a beam of antiprotons from the antiproton decelerator to measure the value of Earth's gravitational acceleration
3. ALICE: (A Large Ion Collider Experiment) detects quark-gluon plasma, a state of matter thought to have formed just after the big bang.
4. ALPHA: makes, captures and studies atoms of antihydrogen and compares them with hydrogen atoms.
5. AMS: (Alpha Magnetic Spectrometer) multipurpose high precision detector, looks for dark matter, antimatter, SM-matter distributions and abundances, and missing matter from a module on the International Space Station.
6. ASACUSA: compares matter and antimatter using atoms of antiprotonic helium and antihydrogen, and studies the properties of matter-antimatter collisions.
7. ATLAS: from a cavern 100 metres below ground, the 7000-tonne ATLAS detector is probing for fundamental particles doing general-purpose physics analyses.
8. ATRAP: compares hydrogen atoms with their antimatter equivalents - antihydrogen atoms.
9. AWAKE: (proton-driven plasma wakefield acceleration experiment) is an accelerator project, explores the use of plasma to accelerate particles to high energies over short distances.
10. BASE: is aiming for the most precise measurements of the magnetic moments of protons and antiprotons - to compare matter with antimatter.
11. CAST: (Cern Axion Solar Telescope) axions could explain differences between matter and antimatter - and we may find them at the centre of the Sun.
12. CLOUD: (Cosmics Leaving Outdoor Droplets) experiment uses a special cloud chamber to study the possible link between galactic cosmic rays and cloud formation.
13. CMS: (Compact Muon Solenoid) is a general-purpose detector at the LHC. It has a broad physics programme ranging from studying the SM and probe the BSM physics at the Terascale (as well as ATLAS).

14. COMPASS: (Common Muon and Proton Apparatus for Structure and Spectroscopy) experiment is a multipurpose experiment uses the Super Proton Synchrotron to probe fix targets with muon and pion beams.
15. DIRAC: (DImeson Relativistic Atom Complex) studies the decay of unstable ponium atoms to gain insight into the strong force.
16. ISOLDE: (Isotope mass Separator On-Line facility) is a source of low-energy beams of radioactive nuclides, which aim to study the properties of atomic nuclei, with further applications in fundamental studies, astrophysics, material and life sciences.
17. LHCb: (LHC-beauty) experiment specializes in investigating the slight differences between matter and antimatter by studying the “beauty quark” hadron decays.
18. LHCf: (LHC-forward) experiment uses particles thrown forward by collisions in the LHC as a source to simulate cosmic rays in laboratory conditions.
19. MOEDAL: (MOнопole and Exotics Detector At the LHC) its prime motivation is to search directly for the magnetic monopole.
20. NA61/SHINE: studies the properties of the production of hadrons in collisions of beam particles (pions, and protons, beryllium, argon and xenon) with a variety of fixed nuclear targets.
21. NA62: studies rare kaon decays. Understanding these decays will help to check some of the predictions the SM makes about short-distance interactions.
22. NA63: experiment directs beams of electrons and positrons onto a variety of targets to study radiation processes in strong electromagnetic fields.
23. nTOF: (neutron Time-Of-Flight) studies neutron-nucleus interactions for neutron energies ranging from a few meV to several GeV.
24. OSQAR: (Optical Search for QED vacuum birefringence, Axions and photon Regeneration) experiment searches for axions, and studies the properties of a vacuum.
25. TOTEM: (TOTAl, Elastic and diffractive cross-section Measurement) experiment studies particles thrust forward by collisions in the LHC.
26. UA9: is investigating how tiny bent crystals could improve how beams are collimated in modern hadron colliders such as the LHC.

References and Bibliography

- [1]
- [2]
- [3]
- [4] Discovery potential and search strategy for the standard model Higgs boson in the $H \rightarrow ZZ^* \rightarrow 4\mu$ decay channel using a mass-independent analysis. CMS SUS PAS 2013/009, 2013.
- [5] Search for pair-produced third-generation squarks decaying via charm quarks or in compressed supersymmetric scenarios in pp collisions at $\sqrt{s}=8$ TeV with the atlas detector. *Phys. Rev. D*, 90:052008, 2014.
- [6] Search for top squark pair production in final states with one isolated lepton, jets, and missing transverse momentum in $\sqrt{s}=8$ TeV pp collisions with the atlas detector. ATLAS note CERN-PH-EP-2014-143, 2014.
- [7] Georges Aad et al. Measurement of the polarisation of W bosons produced with large transverse momentum in pp collisions at $\sqrt{s} = 7$ TeV with the ATLAS experiment. *Eur. Phys. J. C*, 72:2001, 2012.
- [8] Georges Aad et al. Measurement of WZ production in proton-proton collisions at $\sqrt{s} = 7$ TeV with the ATLAS detector. *Eur. Phys. J. C*, 72:2173, 2012.
- [9] Georges Aad et al. Measurement of W^+W^- production in pp collisions at $\sqrt{s}=7$ TeV with the ATLAS detector and limits on anomalous WWZ and $WW\gamma$ couplings. *Phys.Rev.*, D87(11):112001, 2013.
- [10] Georges Aad et al. Measurement of ZZ production in pp collisions at $\sqrt{s} = 7$ TeV and limits on anomalous ZZZ and $zz\gamma$ couplings with the ATLAS detector. *JHEP*, 03:128, 2013.
- [11] Georges Aad et al. Measurement of Spin Correlation in Top-Antitop Quark Events and Search for Top Squark Pair Production in pp Collisions at $\sqrt{s} = 8$ TeV Using the ATLAS Detector. 2014.
- [12] Georges Aad et al. Search for pair-produced third-generation squarks decaying via charm quarks or in compressed supersymmetric scenarios in pp collisions at $\sqrt{s} = 8$ TeV with the ATLAS detector. *Phys.Rev.*, D90(5):052008, 2014.
- [13] Georges Aad et al. Search for top squark pair production in final states with one isolated lepton, jets, and missing transverse momentum in $\sqrt{s} =8$ TeV pp collisions with the ATLAS detector. *JHEP*, 1411:118, 2014.
- [14] VM Abazov, B Abbott, M Abolins, BS Acharya, M Adams, T Adams, M Agelou, E Aguilo, SH Ahn, M Ahsan, et al. Measurement of the top quark mass in the lepton+ jets final state with the matrix element method. *Physical Review D*, 74(9):092005, 2006.

- [15] VM Abazov, B Abbott, M Abolins, BS Acharya, M Adams, T Adams, E Aguilo, GD Alexeev, G Alkhazov, A Alton, et al. b-jet identification in the d0 experiment. *Nuclear Instruments and Methods in Physics Research Section A: Accelerators, Spectrometers, Detectors and Associated Equipment*, 620(2):490–517, 2010.
- [16] W Adam, T Todorov, A Strandlie, and R Frühwirth. Reconstruction of electron tracks with the gaussian-sum filter. Technical report, 2003.
- [17] Ian Aitchison. *Supersymmetry in particle physics: an elementary introduction*. Cambridge University Press, 2007.
- [18] M Adeel Ajaib, Tong Li, and Qaisar Shafi. Stop-neutralino coannihilation in the light of the lhc. *Physical Review D*, 85(5):055021, 2012.
- [19] Sergey Alekhin et al. The PDF4LHC Working Group Interim Report. 2011.
- [20] Daniele Alves et al. Simplified Models for LHC New Physics Searches. 2011.
- [21] Johan Alwall, My-Phuong Le, Mariangela Lisanti, and Jay G. Wacker. Model-Independent Jets plus Missing Energy Searches. *Phys.Rev.*, D79:015005, 2009.
- [22] Johan Alwall, Philip Schuster, and Natalia Toro. Simplified Models for a First Characterization of New Physics at the LHC. *Phys. Rev.*, D79:075020, 2009.
- [23] Luis A Anchordoqui, Ignatios Antoniadis, Haim Goldberg, Xing Huang, Dieter Lust, Tomasz R Taylor, and Brian Vlcek. Vacuum stability of standard model⁺⁺. *arXiv preprint arXiv:1208.2821*, 2012.
- [24] Ignatios Antoniadis and Dumitru Ghilencea. Supersymmetry after the higgs discovery. *The European Physical Journal C*, 74(5):1–2, 2014.
- [25] Nima Arkani-Hamed et al. MARMOSSET: The Path from LHC Data to the New Standard Model via On-Shell Effective Theories. 2007.
- [26] ATLAS and CMS Collaborations, LHC Higgs Combination Group. Procedure for the LHC higgs boson search combination in summer 2011. Technical Report ATL-PHYS-PUB/2011-11, CMS NOTE 2011/005, 2011.
- [27] Michail Bachtis. Heavy neutral particle decays to tau pairs in proton collisions at the square root of $s=7\text{TeV}$ with cms at the cern large hadron collider. 2012.
- [28] Stephanie Baffioni, Claude Charlot, Federico Ferri, David Futyan, Paolo Meridiani, Ivica Puljak, Chiara Rovelli, Roberto Salerno, and Yves Sirois. Electron reconstruction in cms. *The European Physical Journal C*, 49(4):1099–1116, 2007.
- [29] C. Balazs et al. Dark matter, light stops and electroweak baryogenesis. *Phys. Rev. D*, 70:015007, 2004.
- [30] Richard D. Ball, Valerio Bertone, Stefano Carrazza, Christopher S. Deans, Luigi Del Debbio, Stefano Forte, Alberto Guffanti, Nathan P. Hartland, Josè I. Latorre, Juan Rojo, and Maria Ubiali. Parton distributions with LHC data. *Nucl. Phys. B*, 867:244, 2013.
- [31] R. Barbieri and G. Giudice. Upper bounds on supersymmetric particle masses. *Nucl. Phys.*, B306:63, 1988.
- [32] Wim Beenakker, Silja Brensing, Michael Krämer, Anna Kulesza, Eric Laenen, Leszek Motyka, and Irene Niessen. Squark and gluino hadroproduction. *Int. J. Mod. Phys. A*, 26:2637, 2011.

- [33] Wim Beenakker, Silja Brensing, Michael Krämer, Anna Kulesza, Eric Laenen, and Irene Niessen. Soft-gluon resummation for squark and gluino hadroproduction. *JHEP*, 12:041, 2009.
- [34] Wim Beenakker, R. Höpker, M. Spira, and P. M. Zerwas. Squark and gluino production at hadron colliders. *Nucl. Phys. B*, 492:51, 1997.
- [35] Michael Benedikt, Paul Collier, V Mertens, John Poole, and Karlheinz Schindl. LHC design report. *CERN, Geneva*, 3:3–1, 2004.
- [36] Z. Bern, G. Diana, L.J. Dixon, F. Febres Cordero, D. Forde, et al. Left-handed W bosons at the LHC. *Phys. Rev. D*, 84:034008, 2011.
- [37] Werner Bernreuther, A Brandenburg, ZG Si, and P Uwer. Top quark pair production and decay at hadron colliders. *Nuclear Physics B*, 690(1):81–137, 2004.
- [38] Philippe Bloch, Robert Brown, Paul Lecoq, and Hans Rykaczewski. Changes to cms ecal electronics: addendum to the technical design report. *Technical Design Report CMS. CERN, Geneva*, 2002.
- [39] Michiel Botje, Jon Butterworth, Amanda Cooper-Sarkar, Albert de Roeck, Joel Feltesse, Stefano Forte, Alexander Glazov, Joey Huston, Ronan McNulty, Torbjörn Sjöstrand, and Robert S. Thorne. The PDF4LHC Working Group Interim Recommendations. 2011.
- [40] Ian Brock and Thomas Schörner-Sadenius. *Physics at the Terascale*. John Wiley & Sons, 2011.
- [41] Matteo Cacciari, Gavin P Salam, and Gregory Soyez. The anti-kt jet clustering algorithm. *Journal of High Energy Physics*, 2008(04):063, 2008.
- [42] Deniz Sunar Cerci, CMS Collaboration, et al. Hadronic results from cms experiment at the LHC. In *Journal of Physics: Conference Series*, volume 562, page 012015. IOP Publishing, 2014.
- [43] CERN. Experiments, www.cern.ch/about/experiments.
- [44] CERN. The large hadron collider, www.cern.ch/topics/large-hadron-collider.
- [45] FAQ CERN. Lhc the guide, 2009.
- [46] Eric Chabanat and N Estre. Deterministic annealing for vertex finding at cms. 2005.
- [47] Ali H Chamseddine and Alain Connes. Resilience of the spectral standard model. *Journal of High Energy Physics*, 2012(9):1–11, 2012.
- [48] Serguei Chatrchyan et al. Measurement of the polarization of W bosons with large transverse momenta in W+Jets events at the LHC. *Phys. Rev. Lett.*, 107:021802, 2011.
- [49] Serguei Chatrchyan et al. Measurement of W+W- and ZZ production cross sections in pp collisions at $\sqrt{s} = 8$ TeV. *Phys.Lett.*, B721:190–211, 2013.
- [50] Serguei Chatrchyan et al. Search for top-squark pair production in the single-lepton final state in pp collisions at $\sqrt{s} = 8$ TeV. *Eur .Phys. J. C*, 73:2677, 2013.
- [51] Sergio Cittolin, Attila Rcz, and Paris Sphicas. Cms the tridas project: Technical design report, volume 2: Data acquisition and high-level trigger. *CMS trigger and data-acquisition project. Technical Design Report CMS. CERN, Geneva*, 2002.
- [52] Benoit Clement. Electroweak production of the top quark in the run ii of the d0 experiment. Technical report, Fermi National Accelerator Laboratory (FNAL), Batavia, IL, 2006.
- [53] CMS Collaboration. Cms luminosity based on pixel cluster counting - summer 2013 update. CMS Physics Analysis Summary CMS-PAS-LUM-13-001, 2013.

- [54] CMS Collaboration. Searches for third-generation squark production in fully hadronic final states in proton-proton collisions at $\sqrt{s} = 8\text{tev}$. CMS Physics Analysis Summary CMS-PAS-SUS-14-001, 2014. to be published.
- [55] ATLAS Collaboration and CMS Collaboration. Procedure for the lhc higgs boson search combination in summer 375 2011. Technical report, Technical Report CMS-NOTE-2011-005. ATLAS-PHYS-PUB-2011-11, CERN, Geneva, 376 Aug, 2011. 377.
- [56] CMS Collaboration. Cms detector performance and software. *Physics Technical Design Report*, 1:2006–001.
- [57] CMS Collaboration, R Bainbridge, et al. The jet plus tracks algorithm for calorimeter jet energy corrections in cms. *CMS AN*, (2010/031), 2009.
- [58] CMS Collaboration, G Bayatian, et al. The cms muon project: Technical design report. *CERN, Geneva, Switzerland, CERN Internal Rep., CERN/LHCC/97-32*, 1997.
- [59] CMS collaboration, CMS Collaboration, et al. Particle-flow event reconstruction in cms and performance for jets, taus and met. Technical report, CMS-PAS-PFT-09-001, 2009.
- [60] CMS collaboration et al. The cms tracker: addendum to the technical design report. *CMS TDR, CERN, Geneva, CERN-LHCC-2000-016*, 2000.
- [61] CMS collaboration et al. Alignment of the cms silicon tracker during commissioning with cosmic rays. *Journal of Instrumentation*, 5(03):T03009, 2010.
- [62] CMS collaboration et al. Cms tracking performance results from early lhc operation. *arXiv preprint arXiv:1007.1988*, 2010.
- [63] CMS collaboration et al. Commissioning and performance of the cms pixel tracker with cosmic ray muons. *Journal of Instrumentation*, 5(03):T03007, 2010.
- [64] CMS collaboration et al. Commissioning of the particle-flow event reconstruction with the first LHC collisions recorded in the cms detector. *CMS Physics Analysis Summary CMS-PAS-PFT-10-001*, 30, 2010.
- [65] CMS collaboration et al. Electron reconstruction and identification at $\sqrt{s}= 7\text{ TeV}$. *CMS Physics Analysis Summary CMS-PAS-EGM-10-004*, 34, 2010.
- [66] CMS collaboration et al. Jet performance in pp collisions at $\sqrt{s}= 7\text{ TeV}$. *CMS Physics Analysis Summary CMS-PAS-JME-10-003*, 2010.
- [67] CMS collaboration et al. Performance of muon identification in pp collisions at $\sqrt{s}= 7\text{ TeV}$. *CMS Physics Analysis Summary CMS-PAS-MUO-10-002*, 13(14):8, 2010.
- [68] CMS collaboration et al. Tracking and primary vertex results in first 7 TeV collisions. *CMS Physics Analysis Summary CMS-PAS-TRK-10-005*, 17(18):9, 2010.
- [69] CMS collaboration et al. Determination of jet energy calibration and transverse momentum resolution in cms. *Journal of Instrumentation*, 6(11):P11002, 2011.
- [70] CMS collaboration et al. Observation of a new boson at a mass of 125 gev with the cms experiment at the lhc. *Physics Letters B*, 716(1):30–61, 2012.
- [71] CMS collaboration et al. Performance of cms muon reconstruction in pp collision events at $\sqrt{s}= 7\text{ TeV}$. *Journal of Instrumentation*, 7(10):P10002, 2012.
- [72] CMS collaboration et al. Identification of b-quark jets with the cms experiment. *Journal of Instrumentation*, 8(04):P04013, 2013.

- [73] CMS collaboration et al. Description and performance of track and primary-vertex reconstruction with the cms tracker. *Journal of Instrumentation*, 9(10):P10009, 2014.
- [74] CMS collaboration et al. Precise determination of the mass of the higgs boson and tests of compatibility of its couplings with the standard model predictions using proton collisions at 7 and 8 tev. *arXiv preprint arXiv:1412.8662*, 2014.
- [75] CMS Collaboration et al. Search for dark matter, extra dimensions, and unparticles in monojet events in proton-proton collisions at $\sqrt{s}= 8$ tev. *arXiv preprint arXiv:1408.3583*, 2014.
- [76] CMS collaboration et al. Performance of the cms missing transverse momentum reconstruction in pp data at s= 8 tev. *Journal of Instrumentation*, 10(02):P02006, 2015.
- [77] The CMS collaborators. The cms experiment at the cern LHC. *Jinst*, 803:S08004–2008, 2008.
- [78] B. de Carlos and J. Casas. One loop analysis of the electroweak breaking in supersymmetric models and the fine tuning problem. *Phys.Lett.*, B309:320, 1993.
- [79] Albert De Roeck. Cms technical design report, volume II: Physics performance. *Journal of Physics G: Nuclear and Particle Physics*, 34(6):null, 2007.
- [80] S. Dimopoulos and H. Georgi. Softly broken supersymmetry and su(5). *Nucl. Phys.*, B193:150, 1981.
- [81] S. Dimopoulos and S. Raby. Supercolor. *Nucl. Phys.*, B182:353, 1981.
- [82] Herbi K Dreiner, Howard E Haber, and Stephen P Martin. Two-component spinor techniques and feynman rules for quantum field theory and supersymmetry. *Physics Reports*, 494(1):1–196, 2010.
- [83] S Dürr, Zoltan Fodor, Christian Hoelbling, Sandor D Katz, Stephan Krieg, T Kurth, L Lellouch, T Lippert, KK Szabó, G Vulvert, et al. Lattice qcd at the physical point: Simulation and analysis details. *Journal of High Energy Physics*, 2011(8):1–47, 2011.
- [84] R Keith Ellis, W James Stirling, and Bryan R Webber. *QCD and collider physics*, volume 8. Cambridge university press, 2003.
- [85] Francois Englert and Robert Brout. Broken symmetry and the mass of gauge vector mesons. *Physical Review Letters*, 13(9):321, 1964.
- [86] W Erdmann. Offline primary vertex reconstruction with deterministic annealing clustering. *CMS Internal note*, 14:2011, 2011.
- [87] S Esen and G Landsberg. Mc truth l4 emf-based factorized jet corrections in cms. *CMS Analysis Note*, 51, 2009.
- [88] Lyndon R Evans. *The large hadron collider: a marvel of technology*. EPFL Press, 2009.
- [89] Benjamin Fuks, Michael Klasen, David R. Lamprea, and Marcel Rothering. Gaugino production in proton-proton collisions at a center-of-mass energy of 8 TeV. *JHEP*, 10:081, 2012.
- [90] Benjamin Fuks, Michael Klasen, David R. Lamprea, and Marcel Rothering. Precision predictions for electroweak superpartner production at hadron colliders with RESUMMINO. *Eur. Phys. J. C*, 73:2480, 2013.
- [91] Benjamin Fuks, Michael Klasen, David R. Lamprea, and Marcel Rothering. Revisiting slepton pair production at the Large Hadron Collider. *JHEP*, 01:168, 2014.

- [92] Loukas Gouskos. *Ph.D. Thesis: Search for supersymmetry in events with a single lepton, jets and missing transverse energy with the CMS detector at LHC*. PhD thesis, National and Kapodistrian University of Athens, 2014.
- [93] Walter Greiner, DA Bromley, Stefan Schramm, and Eckart Stein. *Quantum chromodynamics*. Springer Science & Business Media, 2007.
- [94] Walter Greiner and Joachim Reinhardt. *Field quantization*. Springer Science & Business Media, 1996.
- [95] Walter Greiner and Joachim Reinhardt. *Quantum electrodynamics*. Springer Science & Business Media, 2008.
- [96] CMS Physics Object Group. CMS official TWiki: Baseline muon selections for Run-I data. https://twiki.cern.ch/twiki/bin/view/CMSPublic/SWGuideMuonId#New_HighPT_Version_recommendation, 2012.
- [97] CMS Physics Object Group. CMS official TWiki: Cms 2013 public electron performance results. <https://twiki.cern.ch/twiki/bin/view/CMSPublic/EGMElectronsMoriond2013>, 2013.
- [98] A Gurtu et al. Missing transverse energy performance of the cms detector. *Journal of Instrumentation*, 6(9):No-pp, 2011.
- [99] A Gurtu et al. Missing transverse energy performance of the cms detector. *Journal of Instrumentation*, 6(9):No-pp, 2011.
- [100] Howard E Haber and Gordon L Kane. The search for supersymmetry: probing physics beyond the standard model. *Physics Reports*, 117(2):75–263, 1985.
- [101] Zhenyu Han et al. Hunting quasidegenerate higgsinos. *Phys. Rev. D*, 89:075007, 2014.
- [102] Arno Heister, Viktor Konoplyanikov, Christopher Tully, Sergey Petrushanko, James Rohlf, Olga Kodolova, and A Ulyanov. Measurement of jets with the cms detector at the LHC. Technical report, CERN-CMS-NOTE-2006-036, 2006.
- [103] Peter W Higgs. Broken symmetries and the masses of gauge bosons. *Physical Review Letters*, 13(16):508, 1964.
- [104] Gerard't Hooft. The making of the standard model. *Nature*, 448(7151):271–273, 2007.
- [105] T. Junk. Confidence level computation for combining searches with small statistics. *Nucl. Instrum. Meth. A*, 434:435, 1999.
- [106] Alexis Kalogeropoulos. Ph.D. thesis: Search for direct stop quark pair production at the lhc with the cms experiment. 2013.
- [107] Gordon L Kane and Aaron Pierce. *Perspectives on LHC physics*. World Scientific, 2008.
- [108] R. Kaul and P. Majumdar. Cancellation of quadratically divergent mass corrections in globally supersymmetric spontaneously broken gauge theories. *Nucl. Phys.*, B199:36, 1982.
- [109] Vardan Khachatryan et al. Searches for electroweak production of charginos, neutralinos, and sleptons decaying to leptons and W, Z, and Higgs bosons in pp collisions at 8 TeV. *Eur.Phys.J.*, C74(9):3036, 2014.
- [110] Vardan Khachatryan et al. Measurement of the $pp \rightarrow ZZ$ production cross section and constraints on anomalous triple gauge couplings in four-lepton final states at $\sqrt{s} = 8$ TeV. *Phys. Lett. B*, 740:250, 2015.

- [111] David A Kirzhnits and Andrei D Linde. Symmetry behavior in gauge theories. *Annals of Physics*, 101(1):195–238, 1976.
- [112] Panagiotis Kokkas. Jet production measurements at cms. Technical report, 2014.
- [113] Michael Krämer, Anna Kulesza, Robin van der Leeuw, Michelangelo Mangano, Sanjay Padhi, Tilman Plehn, and Xavier Portell. Supersymmetry production cross sections in pp collisions at $\sqrt{s} = 7$ TeV. 2012.
- [114] Anna Kulesza and L. Motyka. Soft gluon resummation for the production of gluino-gluino and squark-antisquark pairs at the LHC. *Phys. Rev. D*, 80:095004, 2009.
- [115] Anna Kulesza and L. Motyka. Threshold resummation for squark-antisquark and gluino-pair production at the LHC. *Phys. Rev. Lett.*, 102:111802, 2009.
- [116] Patrick Labelle. *Supersymmetry demystified*. Mcgraw-hill, 2010.
- [117] Hung-Liang Lai, Marco Guzzi, Joey Huston, Zhao Li, Pavel M. Nadolsky, Jon Pumplin, and C.-P. Yuan. New parton distributions for collider physics. *Phys. Rev. D*, 82:074024, 2010.
- [118] Matthew Low and Lian-Tao Wang. Neutralino dark matter at 14 and 100 tev. *arXiv preprint arXiv:1404.0682*, 2014.
- [119] W. Fischler M. Dine and M. Srednicki. Supersymmetric technicolor. *Nucl. Phys.*, B189:575, 1981.
- [120] A. D. Martin, W. J. Stirling, R. S. Thorne, and G. Watt. Parton distributions for the LHC. *Eur. Phys. J. C*, 63:189, 2009.
- [121] J.P. Martin. A supersymmetry primer. 1997.
- [122] Stephen P Martin. A supersymmetry primer. *Perspectives on supersymmetry II*, pages 1–153, 1997.
- [123] Harald JW Müller-Kirsten and Armin Wiedemann. *Introduction to supersymmetry*, volume 80. World Scientific, 2010.
- [124] Yorikiyo Nagashima. *Elementary Particle Physics: Quantum field theory and particles*, volume 1. John Wiley & Sons, 2011.
- [125] Yorikiyo Nagashima. *Elementary Particle Physics: Foundations of the Standard Model*, volume 2. John Wiley & Sons, 2013.
- [126] Yorikiyo Nagashima. *Beyond the Standard Model of Elementary Particle Physics*. John Wiley & Sons, 2014.
- [127] Aruna Kumar Nayak et al. Reconstruction of physics objects in the cms detector. *arXiv preprint arXiv:1310.7408*, 2013.
- [128] Carmen Diez Pardos, Cms Collaboration, et al. Object definition and performance at cms. In *Journal of Physics: Conference Series*, volume 452, page 012015. IOP Publishing, 2013.
- [129] A Perloff, CMS collaboration, et al. Pileup measurement and mitigation techniques in cms. In *Journal of Physics: Conference Series*, volume 404, page 012045. IOP Publishing, 2012.
- [130] Michael E Peskin. Supersymmetry in elementary particle physics. *arXiv preprint arXiv:0801.1928*, 2008.
- [131] Michael E Peskin and Daniel V Schroeder. *An introduction to quantum field theory*. Westview, 1995.

- [132] Giovanni Petrucciani. *Ph.D. Thesis: Observation of a new state in the search for the Higgs boson at CMS*, volume 18. Springer, 2014.
- [133] A L Read. Presentation of search results: the CL_S technique. *J. Phys. G*, 28:2693, 2002.
- [134] Kenneth Rose. Deterministic annealing for clustering, compression, classification, regression, and related optimization problems. *Proceedings of the IEEE*, 86(11):2210–2239, 1998.
- [135] S. Sakai. Naturalness in supersymmetric guts. *Zeit. Phys.*, C11:153, 1981.
- [136] Mark Thomson. *Modern particle physics*. Cambridge University Press, 2013.
- [137] Helge Voss, F Tegenfeldt, H Höcker, and J Stelzer. Tmva: Toolkit for multivariate data analysis with root. *PoS*, page 040, 2007.
- [138] Wolfgang Waltenberger, Rudolf Frühwirth, and Pascal Vanlaer. Adaptive vertex fitting. *Journal of Physics G: Nuclear and Particle Physics*, 34(12):N343, 2007.
- [139] Steven Weinberg. The making of the standard model. In *Prestigious Discoveries at CERN*, pages 9–23. Springer, 2003.
- [140] E. Witten. Dynamical breaking of supersymmetry. *Nucl. Phys.*, B188:513, 1981.
- [141] Fabio Zwirner. Theory summary. *arXiv preprint arXiv:1310.3292*, 2013.